ADELAIDE UNIVERSITY
AUSTRALIA

Department of Geology and Geophysics

MID-PALAEOZOIC SHEAR ZONES IN THE STRANGWAYS RANGE:

A RECORD OF INTRACRATONIC TECTONISM IN THE ARUNTA INLIER, CENTRAL AUSTRALIA

Betina Bendall

December, 2000

Thesis submitted for the degree of Doctor of Philosophy
at the University of Adelaide, Faculty of Science

TABLE OF CONTENTS

LIST OF FIGURES

LIST OF TABLES

ABSTRACT

In the Strangways Metamorphic Complex in the Arunta Inlier central Australia, amphibolite facies shear zones which cross cut Palaeoproterozoic granulite, record two phases of prograde Palaeozoic metamorphism associated with the intracratonic Alice Springs Orogeny. In the north-western Strangways Metamorphic Complex, a system of predominantly east-west trending, steeply north dipping shear zones contain mid-amphibolite facies assemblages commonly consisting of kyanite + mica ± (garnet, staurolite) assemblages in metapelites, hornblende + plagioclase ± garnet assemblages in metabasic rocks and hornblende + plagioclase + garnet + staurolite assemblages in rare aluminous metabasic rocks. Garnet + hornblende + staurolite assemblages from these shear zones yield Sm-Nd mineral ages ranging between 379 ± 30 Ma (MSWD = 0.09) and 438 ± 54 (MSWD = 0.3). Compositional mapping of garnets coupled with thermobarometric calculations indicates that prograde metamorphism at around 380 Ma reached peak conditions of around 600°C and 6 kbar. These P-T conditions are consistent with calculated phase diagrams for unusual aluminous metabasic assemblages which indicate that mineral textures are also consistent with prograde metamorphism.

In the south-eastern Strangways Metamorphic Complex, shear zones also containing kyanite + mica ± (garnet, staurolite) assemblages in metapelites and hornblende + plagioclase ± garnet assemblages in metabasic rocks. The shear zones are generally east-west trending and dip steeply north. Shear zones in the Winnecke area yield garnet-staurolite-biotite-whole rock isochrons of 312 ± 18 Ma (MSWD = 0.8) and 322 ± 6 Ma (MSWD = 0.7). A combined isochron of these samples yields 332 ± 7 Ma (MSWD = 1.3). In the Pinnacles Bore region a garnet-staurolite-biotite-whole rock assemblage produced an isochron of 318 ± 24 Ma (MSWD = 0.6). Phase equilibria and P-T estimates on garnet-bearing assemblages from these shear zones indicate peak metamorphism occurred at about 600°C and 6 kbar during a clockwise prograde P-T path.

In comparison to the granulites which they cross cut, the shear zones contain significantly hydrated assemblages suggesting the infiltration of water to the precursor granulites facilitated the crystallisation of the amphibolite facies assemblages. Stable isotope studies indicate that an exotic fluid, probably sourced from the lowest units of the Amadeus Basin sediments, were channelled through the shear zones during progressive diagenesis-prograde metamorphism. The oxygen isotope values of fluids from these deeply buried basin segments vary significantly from fluids which have interacted with shear zone rocks in the Reynolds and Anmatjira Ranges about 150 km north-west of the Strangways Metamorphic Complex, reflecting differences in the basin architecture, in response to local variations in rift geometry.

Correlations between the syn-orogenic sedimentary record and isotopic, structural and metamorphic evidence from the basement consistently demonstrates a strong link between the development of local structures and epeirogenetic movements in the adjacent Amadeus, Georgina and Ngalia Basins and basement activity during the ASO. It is also evident however that the majority of the sediment record associated with most of the exhumation of the SE Arunta has been lost from the these basins, probably to the south-east.

The recognition that the Strangways Metamorphic Complex records at least two prograde mid-Palaeozoic metamorphic events in essentially similar shear zones, indicates that the Alice Springs Orogeny was more thermally complex than previously thought, and suggests that the metamorphic character of shear zones in the Arunta Inlier is not a reliable guide for regional correlation.

DISCLAIMER

This thesis contains no material which has been accepted for the award of any other degree or diploma in any university or other tertiary institution and, to the best of my knowledge and belief, contains no material previously published or written by any other person, except where due reference has been made in the text.

I give consent to this copy of my thesis, when deposited in the University Library, being available for loan and photocopying.

Betina Bendall

ACKNOWLEDGEMENTS

I would like to sincerely thank my supervisors Martin Hand, John Foden, Ian Cartwright and Kurt Stüwe for the opportunity to take on this project and for their support and stimulus throughout. Special thanks to Martin in particular, for his enthusiasm and generosity in sharing his ideas and views on central Australian geology and the zen of geology in general.

Thank you also to Jo Arnold, Roger Powell and Brenton Worley who were incredibly patient and generous in helping me understand the business of calculating of phase diagrams, compatibility diagrams and pseudosections, and answering so many tedious questions about the workings of that marvelous beast THERMOCALC.

Without the support of the Hayes family at The Garden and Undoolya and the Gorrie Family at Yambah, field work for this project would have been nearly impossible. Thanks so much to Jim, Richie, Andy, Jane, Katie and Stevie for keeping me sane during those long weeks alone in the field. Thank you also to traditional owners Silas and Max Turner of the Arnapipa Estate for permission to enter their lands, and to the NTGS staff especially Bunge, Dot, Carmel and Kerry for access to aerial photos, geophysical images, stereoscopes, references and other equipment.

The technical and adminstration staff of the department and CEMMSA helped me with many different facets of this project from computing to thin sections and everything in between, but more importantly I think provided me a haven of normalcy when I couldn't bear to think about my thesis for one more moment. Thanks to Gerald, Sherry, Geoff, John, Yvonne, David, Keith and especially Wayne for great discussions on Ducatis, mudbrick houses, hobby farms, quandongs and the vagaries of ex-pacers.

Thanks too to all the students and post-docs who have made my experience of uni life such great fun, especially to Bruce, J.T., Scotty, Rob, Gary, Paul, JDP, Kathy, Karin, Jo, Narelle, Sandra, Marlina, Mary and my good friend Eike for all their laughter and support. Special thanks to my friend Andrea Smith who shared my office as well as so many of the ups and downs that happened during these past few years.

Finally and most of all thanks to my family who helped me through everything. Thanks to Mum and Dad, my sisters Deborah and Cheryle and their families Trevor, Chad and Danielle, Peter, Breanne and Marc, and also my family-in-law Paola, Giuseppe and Claudio for your love and support and tolerance of my obsession with rocks. My greatest thanks go to Mauro, for just being.

DEDICATION

To my Dad
Geoff Bendall

Chapter 1

INTRODUCTION

1.1 Project overview and aims

Investigating the tectono-thermal evolution of high-grade polymetamorphic terrains is complicated by the tendency for high-grade metamorphic assemblages to readily equilibrate with their pressure-temperature environment. As a result, direct evidence for the prograde path of high-grade metamorphic rocks is not often preserved, whereas retrograde assemblages and structural fabrics are more frequently recorded. As a consequence, retrograde features are commonly used to make inferences about the entire P-T trajectory of a terrain, including it's prograde path.

The presence of post-peak shear zones within high-grade metamorphic terrains is invaluable for investigating terrain evolution, as shear zones effectively provide a discrete marker horizon which records the structural and metamorphic character of the terrain at a point in its geological history. This is particularly the case in granulite facies terrains where the loss of volatile components during the prograde development of the terrain generally produces anhydrous mineral assemblages which are less able to re-equilibrate during the retrograde path. In such terrains, shear zones acting as channels for fluid flow may be the only areas capable of reacting during the retrograde path, and hence provide the only information available on the direction of the terrain's movement through P-T space. However such shear zones also constitute a separate geological entity. That is, despite being 'hosted' by a metamorphic terrain which must therefore have experienced the same ambient P-T conditions, the shear zones have encountered a deformational and chemical environment not experienced or recorded by the enclosing country rocks. In this scenario, interpreting the geological history of the terrain on the basis of evidence from shear zones may be misleading, as without direct geochronological evidence there may be no way to determine whether the development of the shear zones occurred as part of the retrograde path of a single metamorphic continuum, or as part of a second lower grade metamorphic cycle distinct and unrelated to the preceding high-grade event.

The Arunta Inlier in central Australia is an excellent example of the scenario described above. Central Australia has experienced two episodes of intraplate orogenesis, the Petermann and Alice Springs Orogenies, which resulted in the reworking and exhumation of Palaeo-Mesoproterozoic to Palaeozoic igneous and metamorphic rocks in both the Musgrave and Arunta Inliers (Figure 1.1). Although the Alice Springs Orogeny (ASO) was a major tectonic event responsible for exhuming the Arunta Inlier from beneath the overlying sediments of the Amadeus and Georgina Basins, the extent and magnitude of

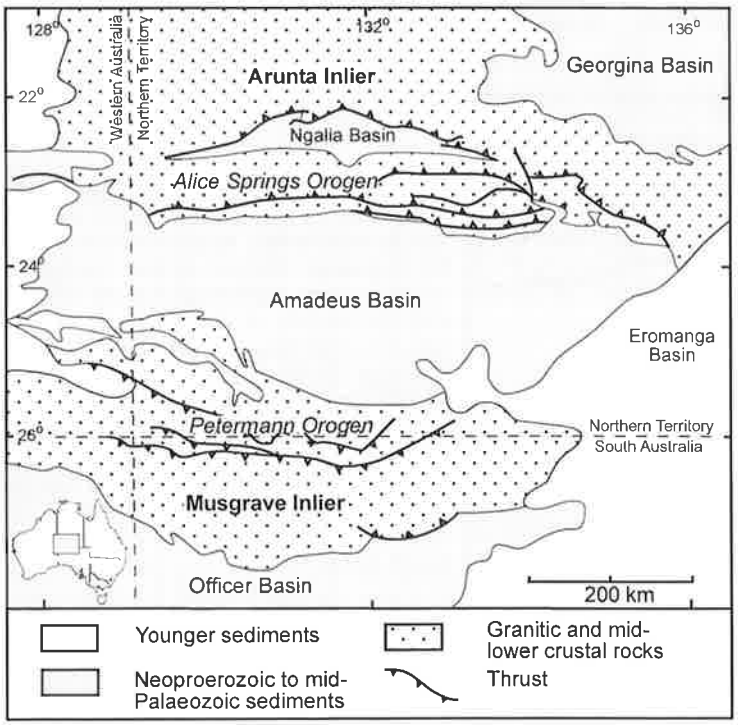

Figure 1.1. Generalized map of the Central Australian region indicating the location of major Neoproterozoic to mid-Palaeozoic basins and the position of the Arunta and Musgrave Inliers (after Hand and Sandiford, 1999).

ASO reworking within the Arunta Inlier is still poorly resolved. This is largely due to the geological complexity of the inlier, and the inherent difficulties in distinguishing between the effects of high-grade Proterozoic metamorphism and high-grade Palaeozoic reworking.

An anastomosing set of mid-amphibolite to greenschist facies retrograde shear zones cross-cuts the amphibolite to granulite facies Palaeo- to Mesoproterozoic basement complex of the Arunta Inlier (Figure 1.2). However the age of many of these shear zones is poorly defined, as the thermochronometers used to date them have had closure temperatures lower than temperatures recorded by the peak metamorphic assemblages within the shear zone rocks (e.g. Iyer et al, 1976; Woodford et al, 1975; Collins and Shaw, 1995). Therefore the thermochronometers have recorded cooling ages rather than crystallisation ages. In addition the polymetamorphic nature of the inlier complicates the identification and selection of rock specimens which uniquely sample each stage of metamorphic development (e.g. Allen and Stubbs, 1982; Windrim and McCulloch, 1986). As a result, it is uncertain whether the amphibolite-facies assemblages in the shear zones record part of the retrograde path of Proterozoic metamorphism (e.g. Dirks et al, 1991) or whether they are a response to Palaeozoic reworking during the Alice Springs Orogeny (e.g. Collins and Teyssier, 1989a). As the youngest major geological features in the inlier, the shear zones provide an obvious starting point for unraveling the geological history of the terrain since they overprint all other structures and potentially record the most information on the last stage of the tectono-thermal development of the inlier.

The Strangways Metamorphic Complex (SMC) (Figure 1.2) is a particularly good location to investigate the history of the shear zones since shear zones in this area are widely distributed and show a systematic change in metamorphic grade from greenschist to mid-amphibolite facies. Thus determining the geological history of these shear zones is important, in that they provide a good example of the inlier-wide system of shear zones.

The aim of this thesis is to use the geological information recorded in shear zones in the Strangways Metamorphic Complex to:

1) establish the timing of amphibolite-facies metamorphism and associated deformation;

2) document and investigate the metamorphic conditions associated with the deformation within the shear zones;

3) establish the effect and source of fluids associated with the development of the shear zones, and

4) characterise the timing and architecture of the controlling tectonic regime.

1.2 Thesis outline

This thesis is organised in a manner which systematically addresses a number of fundamental elements relating to the timing, metamorphic environment and fluid flow regime which prevailed in shear zones in the Strangways Metamorphic Complex.

Chapter 2 presents a brief overview of the geology of the Strangways Metamorphic Complex focusing particularly on describing the geology of the shear zones.

Chapter 3 examines the existing geochronological database from the Strangways Metamorphic Complex and discusses the application of Sm-Nd dating to high-grade metamorphic terrains, providing an overview of the associated methodology. Data collected from selected shear zones throughout the Strangways Metamorphic Complex is presented and

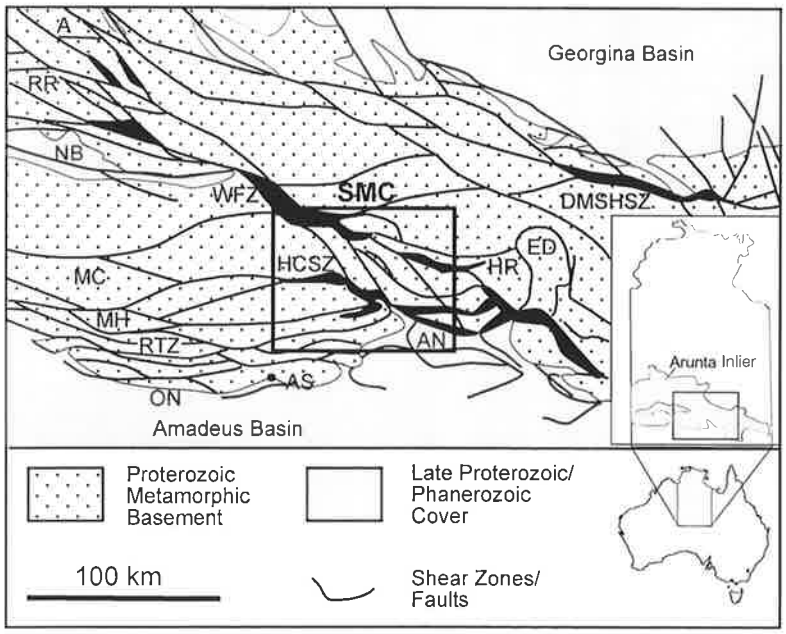

Figure 1.2. Distribution of major faults and other shear zones within part of the Arunta Inlier, and location of the Strangways Metamorphic Complex (SMC) (after Cartwright et al, 1999). Abbreviations: A-Anmatjira Ranges; AN-Arltunga Nappe Complex; AS-Alice Springs; DMSHSZ-Delny-Mt Sainthill Shear Zone; ED-Entia Dome; HCSZ-Harry Creek Shear Zone; HR-Harts Range; MC-Mt Chapple; MH-Mt Hay; NB-Ngalia Basin; ON-Ormiston Nappe Complex; RR-Reynolds Range; RTZ-Redbank Thrust Zone; WFZ-Woolanga Fault Zone.

discussed.

Chapter 4 is an investigation of the mineral chemistry and petrography of metapelitic units in the shear zones and assesses the thermobarometric information recorded in these rocks, with a view to determining the peak metamorphic conditions achieved and quantitatively constraining their trajectory through P-T space.

Chapter 5 focuses on the use of petrogenetic grids and pseudosections to determine the P-T paths of the shear zones, and presents a new petrogenetic grid applicable to common plagioclase-bearing metapelitic rocks in the chemical system NaCaKFMASH.

Chapter 6 investigates the thermobarometric and petrological evidence for the metamorphic evolution of metabasic rocks in the shear zones. This provides an independent confirmation of the P-T path data gathered from the metapelitic units.

Chapter 7 provides an assessment of the fluid flow regime during metamorphism and presents evidence from stable isotope and whole rock geochemistry in order to constrain the fluid source and the mechanics of the fluid flux.

Chapter 8 reviews the synorogenic sedimentary record from the adjacent Amadeus, Ngalia and Georgina Basins and attempts to correlate this data with evidence from the basement, in an effort to define the duration and architecture of the Alice Springs Orogeny.

Chapter 2

GEOLOGICAL OVERVIEW OF SHEAR ZONES IN THE STRANGWAYS METAMORPHIC COMPLEX

2.1 Introduction

The Arunta Inlier is an extensive polymetamorphic terrain comprised of variably deformed Palaeo- to Mesoproterozoic rocks that covers approximately 200,000 km^2 (Figure 2.1). Along the southern margin of the inlier the Palaeo-Mesoproterozoic complex is unconformably overlain by Neoproterozoic to mid-Palaeozoic basin sediments of the Amadeus Basin, and to the north the Arunta Inlier is bound by the Wiso, Georgina and Birrindudu Basins, the Granites-Tanami Block and Tennant Creek Block.

In the 1970's and early 1980's, the Arunta Inlier was the focus of an intensive study undertaken by the Australian Bureau of Mineral Resources (BMR), now known as the Australian Geological Survey Organisation (AGSO). This study established a working model for the tectono-stratigraphic evolution of the Arunta Inlier, based on the concept of 3 east-west trending tectonic provinces (the northern, central and southern provinces respectively) (Figure 2.1) and 3 litho-stratigraphic subdivisions defining an increasing degree of sedimentary reworking and maturity (Shaw et al, 1979; Shaw et al, 1984; Black et al, 1983; Stewart et al, 1984). The geological history of the Arunta Inlier was interpreted in terms of a series of five major high-grade tectono-metamorphic events during the Proterozoic followed much later by the Alice Springs Orogeny in the

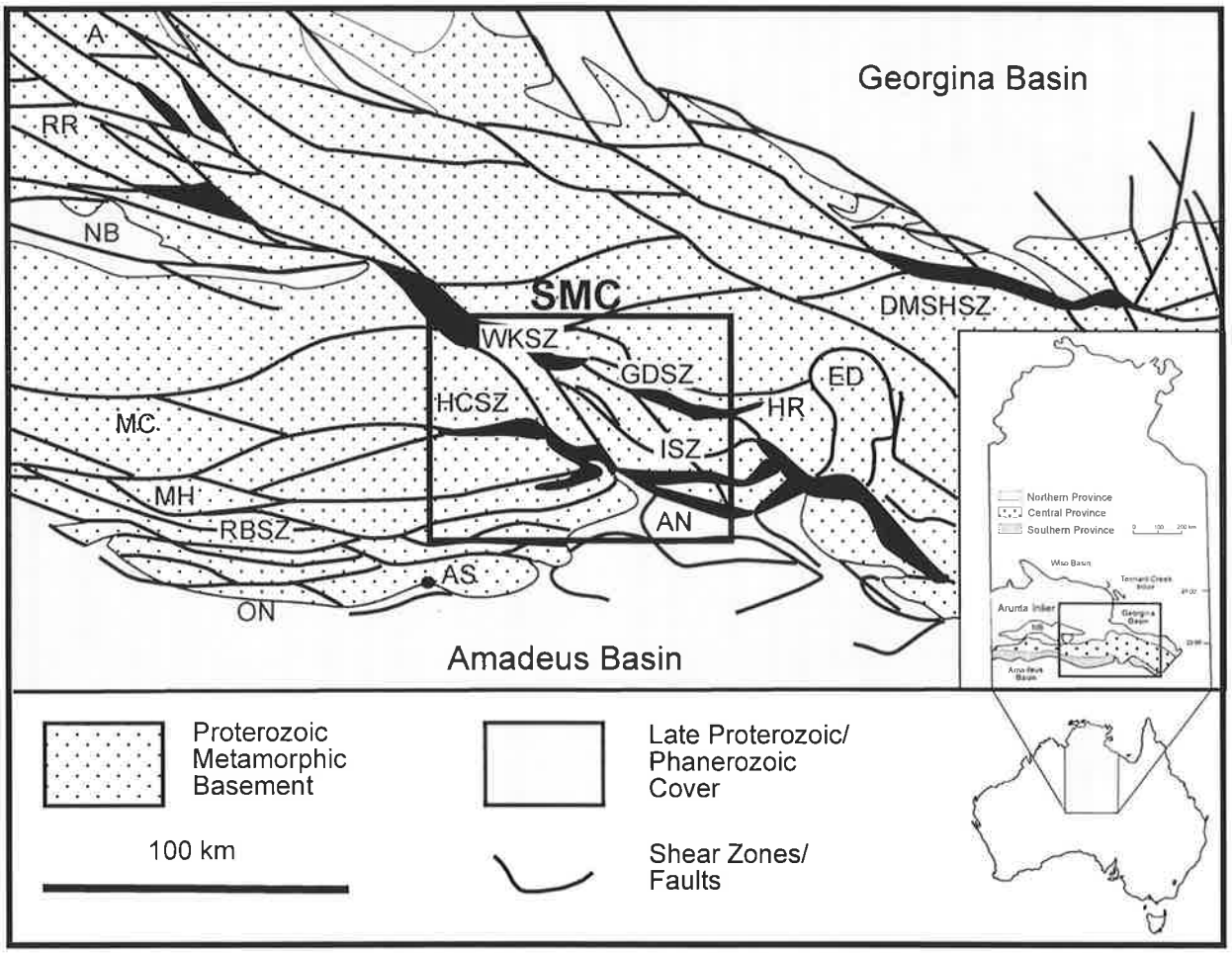

Figure 2.1. Location map indicating the position of the Arunta Inlier within the Australian Continent. Also shown are the distribution of major shear zones within the inlier and the location of the Strangways Metamorphic Complex (boxed area labelled SMC) (after Cartwright et al, 1999). Abbreviations: A-Anmatjira Ranges; AN-Arltunga Nappe Complex; AS-Alice Springs; DMSHSZ-Delny-Mt Sainthill Shear Zone; ED-Entia Dome; HCSZ-Harry Creek Shear Zone; HR-Harts Range; MC-Mt Chapple; MH-Mt Hay; NB-Naglia Basin; ON-Ormiston Nappe Complex; RR-Reynolds Range; RTZ- Redbank Thrust Zone; WFZ-Woolanga Fault Zone.

Age (Ma)	Northern Province		Central Province			Southern Province	
	Western Arunta Inlier (Mt Doreen region)	Reynolds-Anmatjira Range region	Mount Chappell region	Strangways Complex	Harts Range region	Alice Springs region	Chewings Range-Ormiston region
>2000	2000-2500 crust?	2000-2500 crust?	2000-2500 crust?	2000-2500 crust?	2000-2500 crust?	2000-2500 crust?	2000-2500 crust?
>1880	Deposition of Lander Rock beds		?				
>1818	Local low-P high-T metamorphism up to granulite facies-followed by felsic magmatism at 1880 Ma	Local low-P high-T (>700°C, 3-4 kbar) metamorphism	mafic and felsic magmatism?	High-T moderate P (>850°C, 6-7 kbar) metamorphism with an anticlockwise P-T path			
1800	Deposition of sediments (Reynolds Range Group)		Sedimentation?				
1760-1790	Felsic magmatism low- to medium grade metamorphism and deformation	Felsic-mafic magmatism, metamorphism & deformation (Local high-T (>700°C ~4 kar) metamorphism?)	High-T moderate P (>850°C, 6-9 kbar) metamorphism with an anticlockwise P-T path	High-PT metamorphism (>800°C, 5 kbar) clockwise P-T evolution?	Felsic-mafic magmatism - high-grade metamorphism	Felsic magmatism upper amphibolite facies metamorphism and deformation	
1760 - 1720		Felsic magmatism with Rare Earth enrichment?	Felsic magmatism & high-T metamorphism	High-PT metamorphism (>800°C, 9 kbar) anticlockwise P-T evolution, W-directed thrusting	Felsic-mafic magmatism	Upper? amphibolite facies metamorphism & deformation	
1670 - 1650	Intermediate-mafic magmatism	Felsic magmatism			↑	Felsic magmatism	Felsic magmatism
1610 - 1590				Deposition of precursors to the Mendip Metamorphics?		Deposition of Simpsons Gap & Chewings Range sediments, granitic magmatism.	
1590 - 1570	Voluminous felsic magmatism	Low-P, high-T (750°C, 5-6 kbar) metamorphism clock-wise P-T path, SW-directed thrusting	High grade metamorphism? (800oC; 7-8 kbar?)	(High grade metamorphism)?	Depositional of Irindina Supracrustal Assemblage in this interval		Amphibolite facies metamorphism, large-scale N-directed thrusting
~1450			Amphibolite grade (~650°C, 6-7 kbar) S-directed thrusts		↓		
~1200 - 1150			Pegmatite			Alkaline magmatism (Mordor Complex)	Felsic magmatism/pegmatites regional heating
>1000	Partial exhumation of basement rocks in the Arunta Inlier						
~900		minor mafic dykes	N-S & E-W trending mafic dykes	N-S trending mafic dykes			N-S & E-W trending mafic dykes

Table 2.1.Summary of tectonothermal events in the Arunta Inlier (after Hand et al, 1999a).

~850	Initial deposition of sediments in the Centralian Superbasin (later to separate into the Amadeus, Ngalia & Georgina Basins - basement includes granulites in the central Province.							
850 - 470	Reactivation of Proterozoic faults during extensional periods of basin formation in the Centralian Superbasin (?)							
~470 - 450				Granulite grade extensional ultramylonites of Norman, (1990) (?)	Larapinta Event Granulite & upper amphibolite facies metamorphism and mafic magmatism associated with N-S extension.			
~450	Onset of the Alice Springs Orogeny							
450 - 400	S-directed shear zones?	S-directed shear zones?	Greenschist facies S-directed shear zones	Amphibolite facies (600°C, 5-6 kbar) metamorphism & S-directed shear zones	Amphibolite facies (600°C, 5-6 kbar) metamorphism & S-directed shear zones	Greenschist facies S-directed shear zones?	Greenschist facies S-directed shear zones?	
400 - 300	Greenschist facies S-directed shear zones	Amphibolite facies (600°C, 6 kbar) metamorphism, N & S-directed shear zones Greenschist facies S-directed shear zones	Greenschist facies S-directed shear zones	Amphibolite facies (600°C, 6 kbar) - greenschist facies S-directed shear zones	Amphibolite facies (600°C, 6 kbar) - greenschist facies S-directed shear zones	Greenschist facies S-directed shear zones	Greenschist facies S-directed shear zones	

Palaeozoic (Table 2.1). The Alice Springs Orogeny was generally considered to be a greenschist facies event which led to the deformation, exhumation and metamorphism of Neoproterozoic to Palaeozoic sediments in the basins surrounding the inlier, and exhumed the Palaeo- to Mesoproterozoic basement complex of the Arunta Inlier from beneath these overlying sediments. As the geochronological database has expanded however, debate has arisen over the validity of various regional stratigraphic correlations, the timing of individual tectono-metamorphic episodes in the Proterozoic, and the magnitude and extent of influence of the Alice Springs Orogeny across the inlier (e.g. Collins and Teyssier, 1989a; Ding and James, 1989; Collins and Vernon, 1991; Hand et al, 1992; Hand et al, 1993; Collins and Vernon, 1993; Black and Shaw, 1995; Collins and Shaw, 1995; Vry et al, 1996).

The Arunta Inlier is transected on all scales by anastomosing E-W and NW-SE trending faults, schist belts and shear zones, which control its internal geometry and the current distribution of crustal blocks (Figure 2.1). Examples of the major shear zones include the Redbank Shear Zone (RBSZ), the Harry Creek Shear Zone (HCSZ), the Wallaby Knob Shear Zone, the Gough Dam Shear Zone and the Illogwa Shear Zone (Figure 2.2). It has been proposed that these zones coalesce and form the tectonic boundary between the central and southern provinces (Collins and Shaw, 1995). The shear zones generally dip north at steep to moderate angles (>35°) and juxtapose crustal blocks of differing metamorphic history. Movement on these crustal scale fault systems has differentially exhumed the region so that coeval geological records can be examined from different crustal levels. These shear zones are also primary sites for fluid movement, and have recrystallised new metamorphic mineral assemblages. While these are frequently greenschist facies assemblages and their growth is universally ascribed to the ASO, there are also numerous mid- to upper-amphibolite facies shear zones transecting the granulite facies basement rocks. The timing and significance of these amphibolite grade shear zones has been the subject of considerable debate (e.g. Collins and Teyssier, 1989b; Ding and James, 1985; James and Ding, 1988; Dunlap and Teyssier, 1995) due mainly to the similarities in structural style between the polymetamorphic basement and Amadeus Basin cover sequences, and the application of inappropriate geochronological systems to these high grade shear zone rocks which have thus failed to constrain the timing of

peak metamorphism in these rocks.

2.2 Shear Zones in the Strangways Metamorphic Complex

This study focuses on the Strangways Range and Winnecke areas (Figure 2.2 and 2.3) which contain granulite facies rocks of the Yambah, Utnalanama and Ongeva Granulites, the Anamarra Orthogneiss, Erontonga Metamorphics and Cadney Metamorphics which together comprise the Strangways Metamorphic Complex (Figure 2.2). These rocks are located in the southeast of the Arunta Inlier and form part of the central tectonic province along with the aluminous schists and amphibolites of the Harts Range Group and the Mt Hay-Mt Chapple region (Figure 2.1).

Up to seven discrete deformational events involving at least two tectonic phases have been recognised in the SMC as a result of detailed investigations by Goscombe (1989, 1991, 1992 a & b) in the Mt Pfitzner area, Norman (1991) and Norman and Clarke (1990) in the Ongeva and Anamarra areas, Lafrance et al (1995) in the Wuluma Hills, Allen (1979), Allen and Black (1979) and Allen and Stubbs (1982) in the Harry Creek Shear Zone, Iyer (1974) and Iyer et al (1976) in the Yambah Hills and Woodford (1974) and Woodford et al (1975) in the Woolanga area (Figure 2.2). These workers defined an initial granulite facies event (M1) at about 1750 - 1800 Ma on the basis of Rb-Sr isochrons produced by Iyer et al (1976), Black et al (1983) and Windrim and McCulloch (1986), and by U-Pb SHRIMP dating by Norman (1991), with evidence of a second overprinting granulite event (M2) observed in some localities, occurring at about 1700-1750 Ma (see review by Collins and Shaw, 1995; Black and Shaw, 1995; Allen and Stubbs, 1982). The second granulite facies event was accompanied by intense deformation creating meso- and mega-scale sheath and refolded fold patterns which characterise this part of the

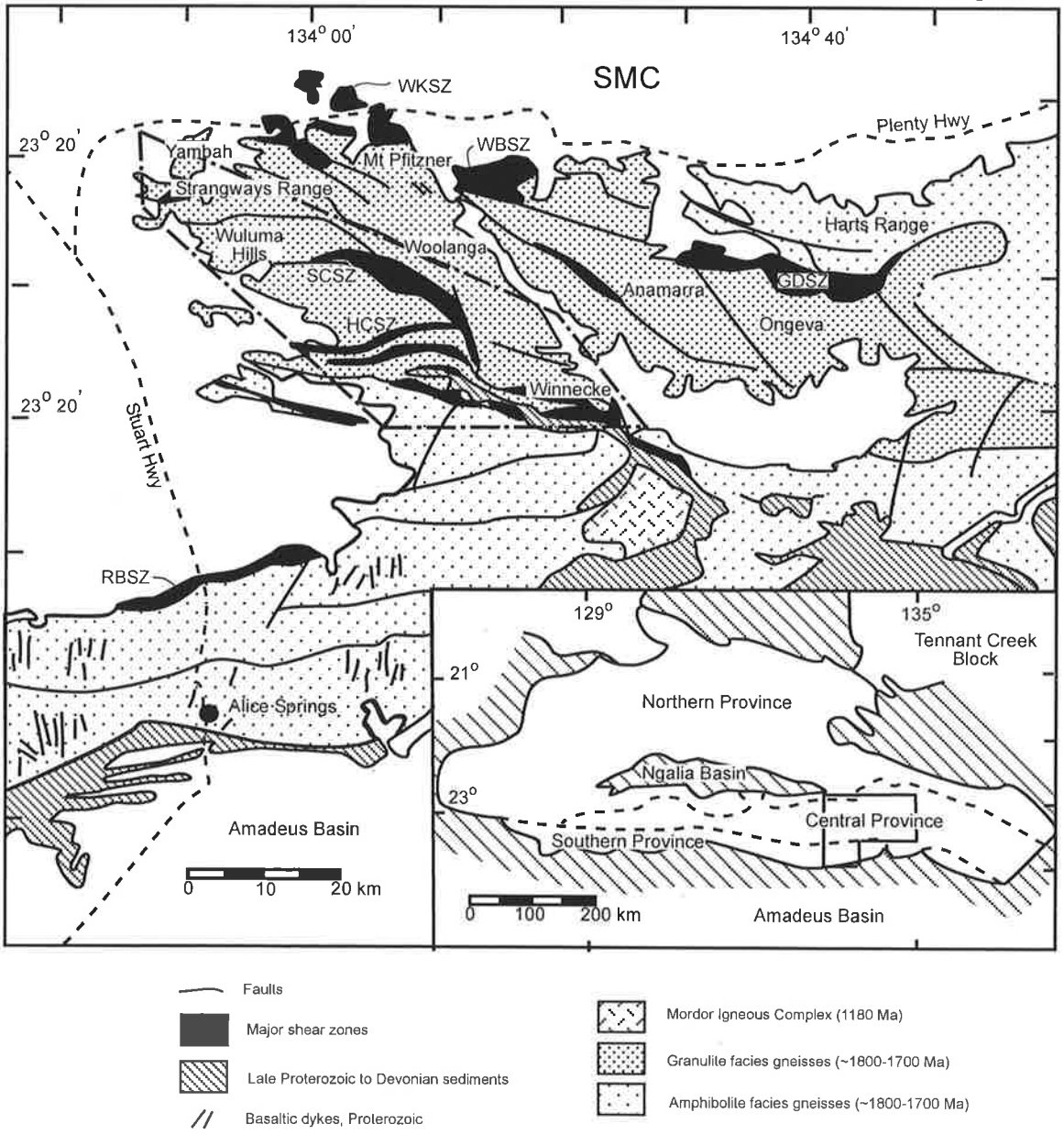

Figure 2.2. Regional geological features in the southeastern Arunta Inlier including part of the Strangways Metmorphic Complex. The study area is indicated by bounding dashed lines (adapted from Goscombe, 1992a).

Arunta Inlier and can be correlated across the Strangways Metamorphic Complex (Goscombe, 1989; Norman, 1991). Recent U-Pb SHRIMP dating of zircons from migmatites in the granulites suggest however, that M1 and M2 result from a single tectonothermal event at about 1720Ma (Möller et al, 1998; Ballèvre et al, 1999). Cross-cutting these regional granulite facies fabrics are two generations of granulite facies mylonites which are as yet undated (Goscombe, 1989; Norman, 1991). The older generation of mylonites appears to be related to compressional tectonism while the younger mylonites appear to have formed in an extensional regime.

Throughout the SMC, the youngest structural fabrics observed in the basement rocks are an E-W to NW-SE trending series of shear zones and schist belts which range in width from the metre-scale to kilometre-scale. These shear zones and schist belts cut all other fabrics and appear to correlate across the terrain. These fabrics include the D7/S7 of Goscombe (1989), the D5/S5 of Norman (1991) and the kyanite-gedrite stage of Warren (1983). Examples include the Gough Dam Schist Zone (Norman, 1991), the Wallaby Knob Schist Zone (Goscombe, 1989), the Yambah Schist Zone (Iyer, 1974), the Southern Cross Shear Zone (Shaw et al, 1979) and the Harry Creek Deformed Zone (Allen, 1979) (Figure 2.2). They are generally steeply N to NE dipping with lineations defined by the orientation of phyllosilicate minerals and quartz rodding plunging steeply to the NNE. Shear sense indicators, when observed, ubiquitously indicate south-directed thrusting (Goscombe, 1989; Norman, 1991; Collins and Teyssier, 1989a). Many of these shear zones contain only greenschist facies assemblages, however some assemblages include kyanite, gedrite, staurolite, garnet and sillimanite, suggesting some shear zones experienced mid- to upper-amphibolite facies conditions. Mid-amphibolite facies shear zones are generally found in the central and northern sections of the study area, while greenschist facies shear zones are found throughout (Figure 2.3). However greenschist facies assemblages generally occur as the peak metamorphic assemblage in southern shear zones, but as retrograde assemblages overprinting amphibolite assemblages in the northern and central shear zones. This suggests a regional metamorphic gradient exists in the SMC shear zones, with the lowest grade shear zones occurring within and adjacent to the Heavitree Quartzite and Bitter Springs Formation and increasing in grade northward to mid-amphibolite facies (Figure 2.3). The shear zones have developed from the relatively anhydrous granulite facies country rock, however the shear zone rocks contain hydrous retrograde mineral assemblages, indicating that the development of the shear zones involved at least one episode of regionally channelised fluid flow and associated metasomatism to facilitate the growth of retrograde hydrous

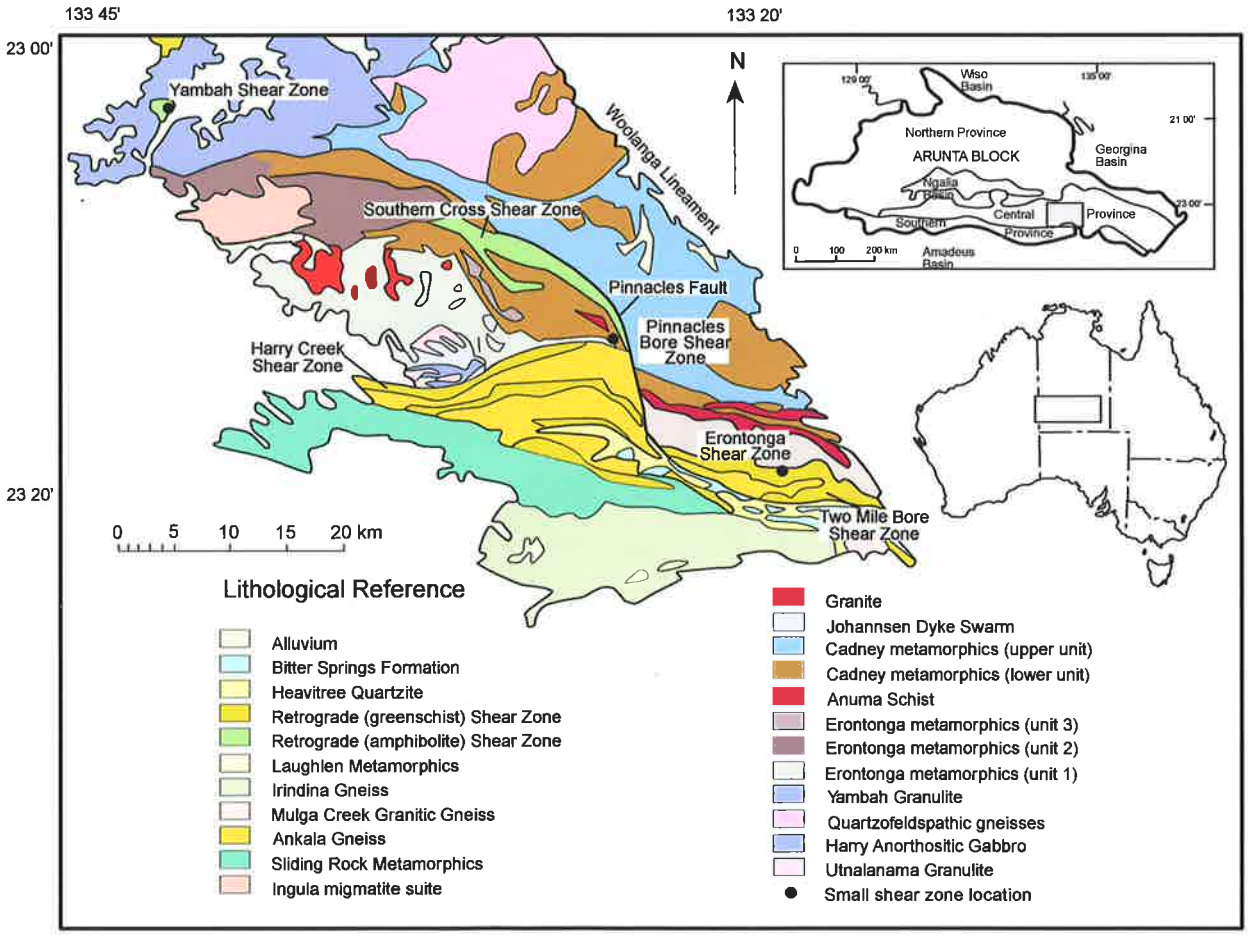

Figure 2.3. Generalised geology of the Strangways Metamorphic Complex indicating the distribution of mid-amphibolite and greenschist facies shear zones (adapted from D'Addario and Chan, 1982).

minerals. Despite the interest in the geological history of these shear zones, no detailed investigations of their metamorphic evolution or fluid flow regime have yet been undertaken.

2.3 The age of the shear zones

At the initiation of this study, efforts to date the shear zones had been made using the K-Ar, Ar-Ar and Rb-Sr isotopic systems (e.g. Stewart, 1971; Armstrong and Stewart, 1975; Iyer et al, 1976; Woodford et al, 1975; Allen and Stubbs, 1982; Windrim and McCulloch, 1986). The existing database was sparse and included a wide spread of ages for the shear zones ranging from about 1040 Ma to about 320Ma (Figure 2.4). Many of these dates were produced from the analysis of overprinting retrograde assemblages in granulites, rather than from the dating of totally recrystallised samples from the shear zones themselves (e.g. Allen and Stubbs, 1982; Windrim and McCulloch, 1986). Thus it is often unclear whether the sample material used actually relates to the same phase of deformation recorded in the shear zones. Furthermore, because the geochronometers used generally have closure temperatures lower than the metamorphic temperatures recorded by the dated mineral assemblages (i.e. $T_c < T_{max}$) (Dodson, 1973; Cliff, 1985), it is difficult to know if the dates produced relate to deformation associated with the development of the shear zones, or to periods of cooling unrelated to the deformation expressed in the shear zones (Collins and Shaw, 1995; Black and Shaw, 1995).

2.4 Description of key locations

In this study a number of shear zones distributed throughout the Strangways Metamorphic Complex, containing amphibolite facies rocks useful for geothermobarometry and geochronology have been selected for investigation.

2.4.1 The Yambah Shear Zone (G.R. 823498)

The Yambah Shear Zone (Figures 2.3 and 2.5) is an amphibolite facies schist zone which transects adjacent interlayered mafic, felsic and metapelitic granulites of the Strangways Range. The shear zone is located within a dry river valley which is about 2 kms wide, however the boundaries of the shear zone are completely obscured and the total outcrop width is only about 300 metres (Figure 2.6 a & b). The shear zone is composed predominantly of coarse-grained muscovite-biotite-quartz schists which may also be kyanite, staurolite and/or garnet-bearing. Mafic amphibolites and rarer calc silicate units also occur in the schist zone and are composed of hornblende-plagioclase-quartz ± (garnet, staurolite), chlorite-biotite-garnet and diopside-garnet-epidote assemblages respectively. The Yambah Shear Zone outcrops as two distinct areas, the northern and eastern zones, which are oriented orthogonal to each

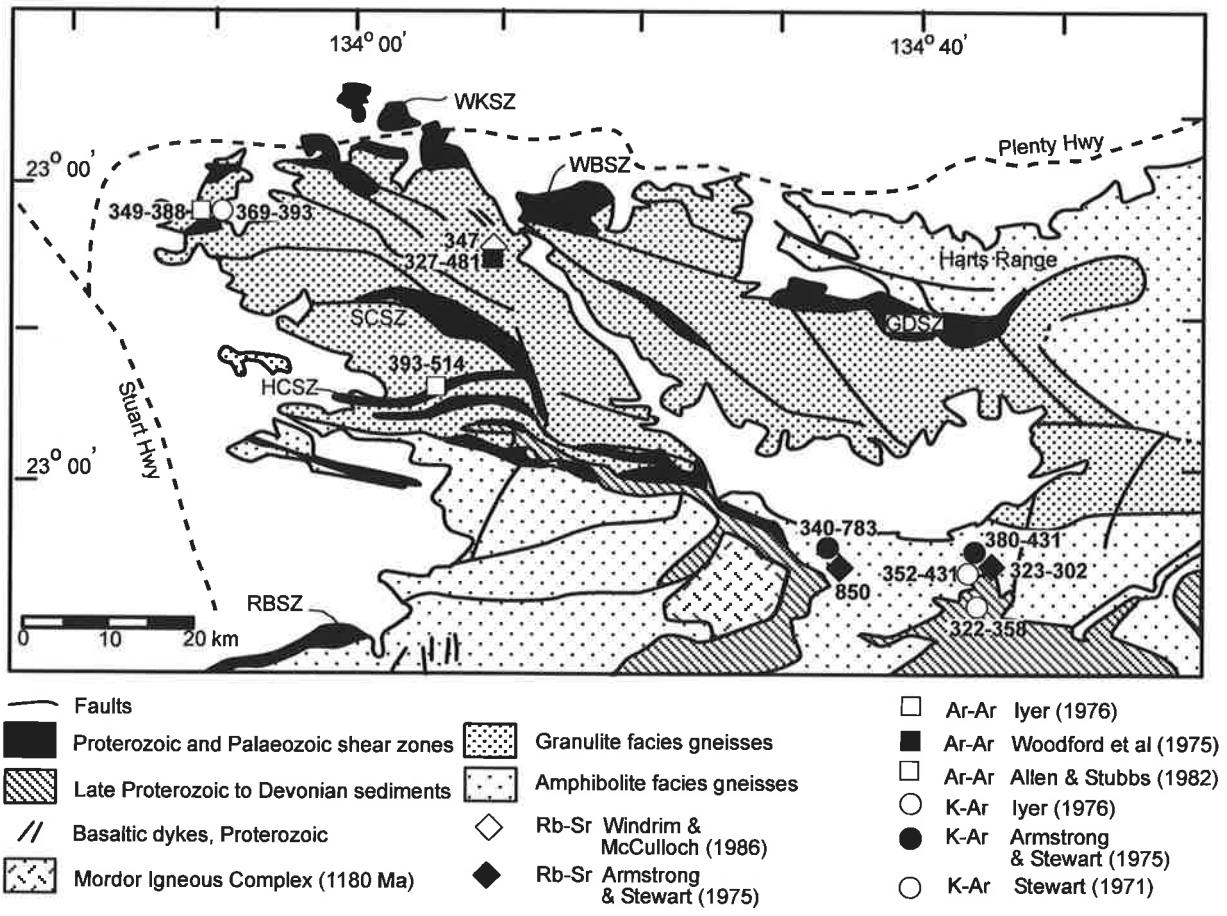

Figure 2.4. Existing Rb-Sr, Ar-Ar and K-Ar geochronological data for shear zone rocks in the Strangways Metamorphic Complex (adapted from Goscombe, 1992a).

other but separated by obscuring alluvium. The northern zone trends E-W approximately orthogonal to the compositional layering and structural fabrics in the adjacent Palaeoproterozoic granulite, whereas the eastern zone trends N-S and approximately parallel to the granulite fabrics and compositional layering. The schistosity in both zones is generally subvertical and in the northern zone varies between about 082/80°N and 102/70°S, with lineations plunging steeply eastward (i.e. L 65° → 108°; 85° → 108°) while the schistosity in the eastern zone varies between 166/80°E and 180/60°W, with lineations plunging down-dip. Conclusive kinematic indicators are not observed in the schists, and contacts between the schist zone and the granulites are obscured (Figure 2.6 c & d). However it is evident that the schists are derived from the adjacent granulites as individual granulite layers can be traced into their equivalent schist unit in parts of the northern schist zone (Iyer et al, 1976). There is no apparent offset in metamorphic grade in the granulites outcropping either side of the shear zone and so the net displacements across the shear zone are less than about 5 km parallel to the mineral elongation lineation.

2.4.2 The Pinnacles Bore Shear Zone (G.R. 310323)

The Pinnacles Bore Shear Zone (Figures 2.3 & 2.7) is a zone of kyanite-muscovite-biotite-quartz ± (garnet, staurolite)-bearing schists and scattered kyanite-quartz-bearing pods which forms part of an anastomosing system shear zones which transect the granulite facies rocks of the Erontonga Metamorphics and the SMC, and merge with the major NW trending Pinnacles Fault system (Figure 2.6 e, f & g). The

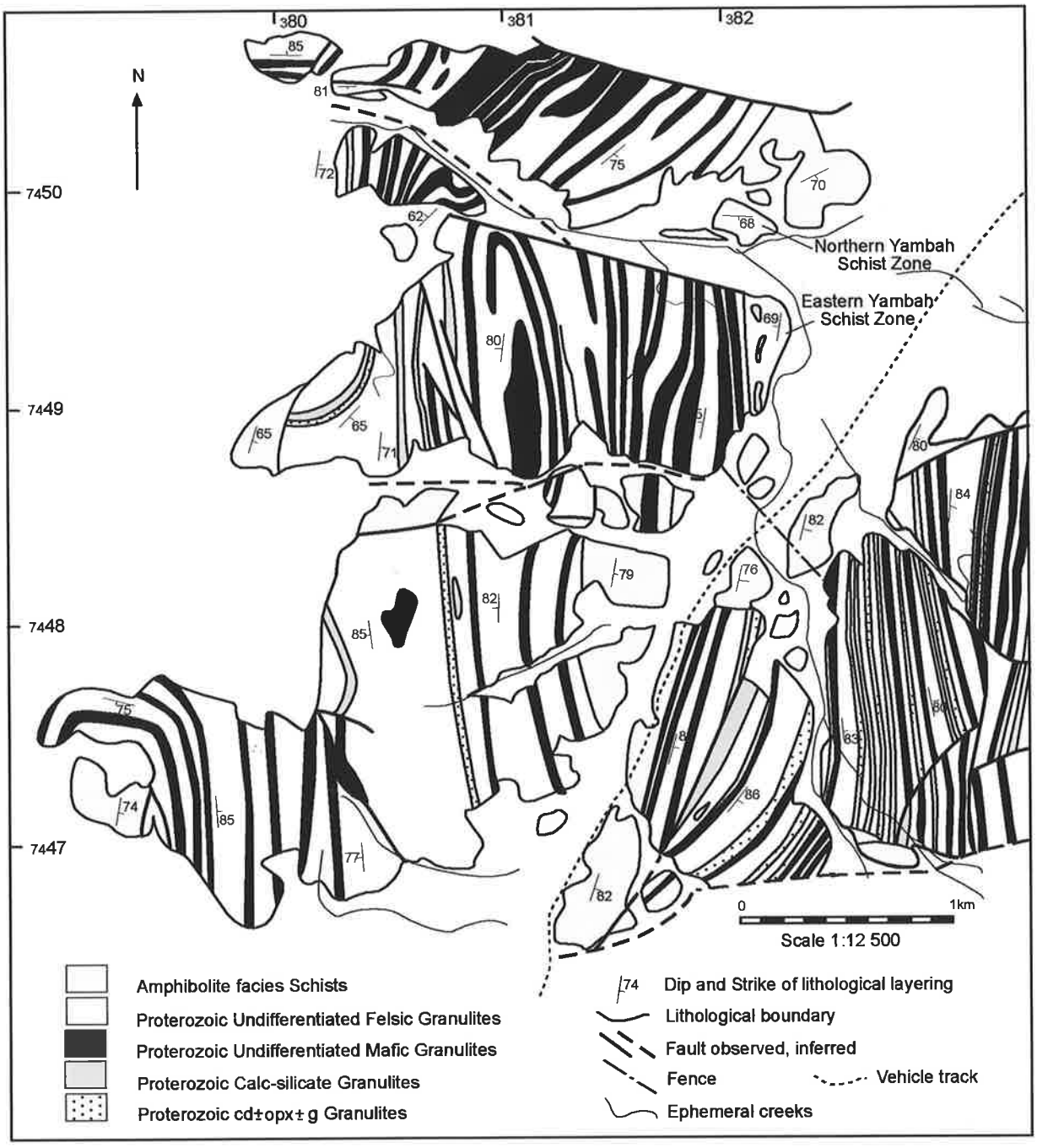

Figure 2.5. Generalised geology of the Yambah Schist Zone (adapted from Windrim, 1983).

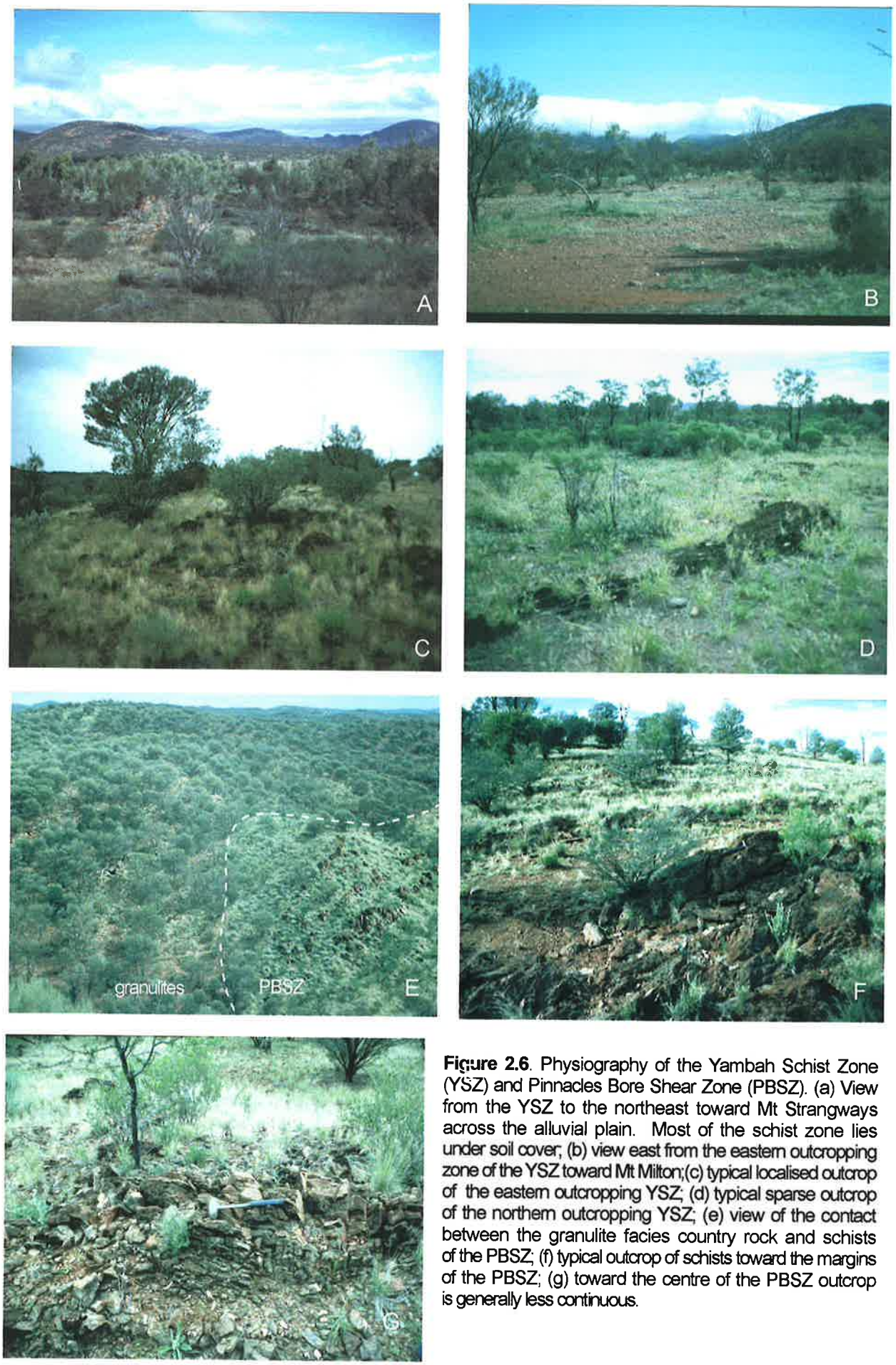

Figure 2.6. Physiography of the Yambah Schist Zone (YSZ) and Pinnacles Bore Shear Zone (PBSZ). (a) View from the YSZ to the northeast toward Mt Strangways across the alluvial plain. Most of the schist zone lies under soil cover; (b) view east from the eastern outcropping zone of the YSZ toward Mt Milton;(c) typical localised outcrop of the eastern outcropping YSZ; (d) typical sparse outcrop of the northern outcropping YSZ; (e) view of the contact between the granulite facies country rock and schists of the PBSZ; (f) typical outcrop of schists toward the margins of the PBSZ; (g) toward the centre of the PBSZ outcrop is generally less continuous.

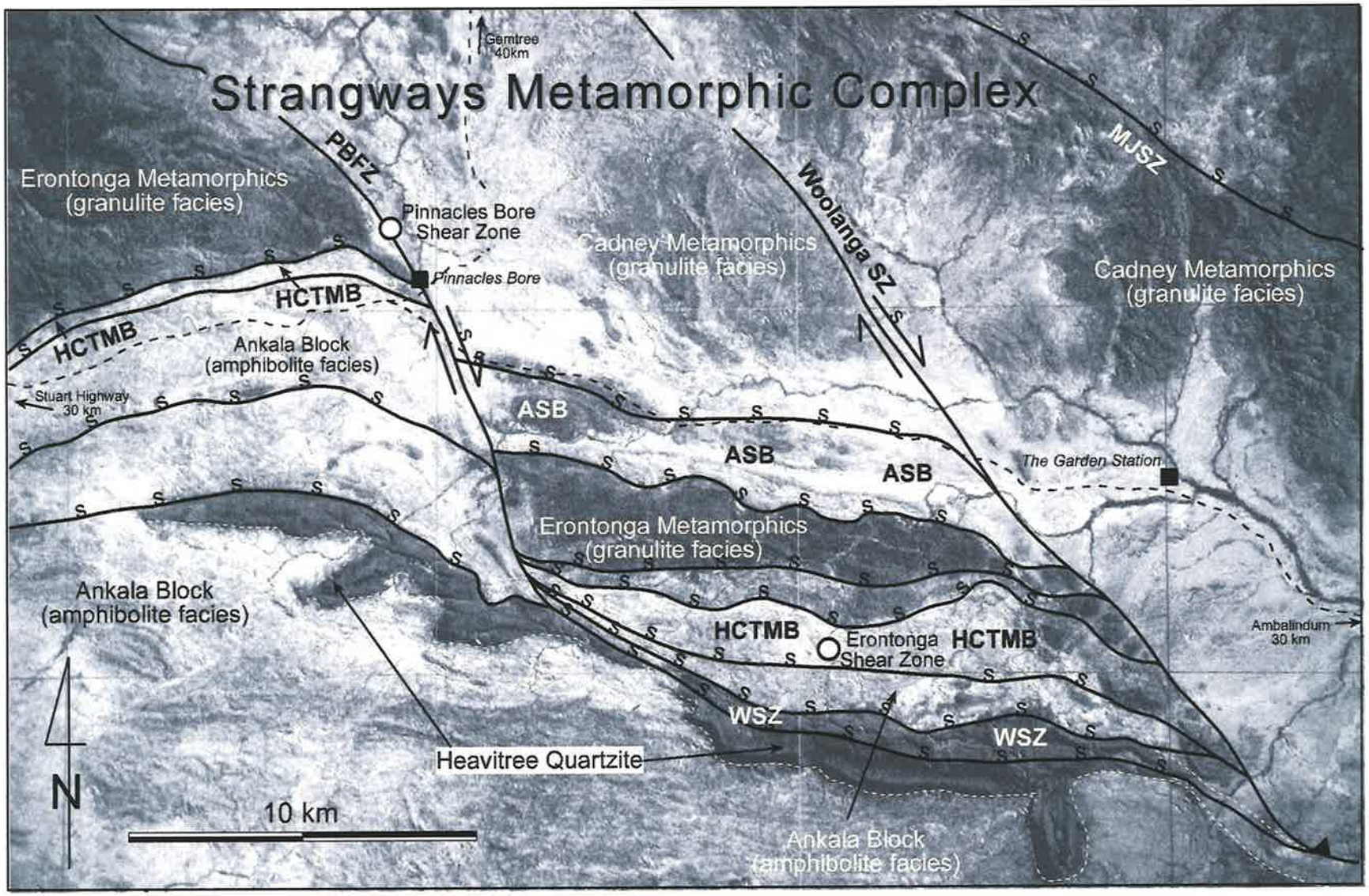

Figure 2.7. Generalised geology of the Winnecke Region in the southern Strangways Metamorphic Complex, showing the distribution of major amphibolite and greenschist facies shear zones that fomed during south-directed thrusting of the Strangways Metamorphic Complex, over the Neoproterozoic Heavitree Quartzite. Abbrev: HCTMB = Harry Creek-Two Mile Bore Shear Zone; PBFZ = Pinnacles Bore Fault Zone; WSZ = Winnecke Shear Zone; MJSZ = Mount Johnston Shear Zone; ASB = Anuma Schist Belt (after Hand et al, 1999a).

Pinnacles Fault system is composed primarily of greenschist facies shear zones which juxtapose granulite facies rocks of the Erontonga and lower Cadney Metamorphics to the east against granulites of the upper Cadney Metamorphics to the west. Rocks of the Erontonga Metamorphics also occur east of the Pinnacles Fault system, but lie further south than their western counterparts (Figure 2.7). The Pinnacles Bore Shear Zone cuts across granulite facies rocks of the Erontonga and lower Cadney Metamorphics forming part of the western section of the Pinnacles Fault system. The schistose fabric in the PBSZ is generally NW trending, dipping moderately to steeply NE. In the northern part of the shear zone, the fabric is oriented at about 125/45°NE but rotates to about 152/80°NE in the south, closer to the Pinnacles Fault system. Lineations defined by phyllosilicates, kyanite and occasionally staurolite plunge moderately to steeply toward NNW (~ 45°→340°). Kinematic indicators and the vergence of small-scale folds indicate east over west dextral movement, suggesting that the Pinnacles Fault System acted as a relay zone to accommodate disparate degrees of shortening in the Utranalama and Ankala Blocks to the west and the Winnecke Block to the east (Hand et al, 1999a) (Figure 2.7).

2.4.3 The Erontonga Shear Zone (G.R. 311226)

The Winnecke area (Figures 2.3 and 2.7) is transected by an extensive network of anastomosing E-W and NW-SE trending shear zones (Figure 2.8 a, b & c). In this region, shear zones and mylonite zones within the Neoproterozoic Heavitree Quartzite and the adjacent phyllonites form the main thrust between the Amadeus Basin cover sequences and the Palaeoproterozoic Arunta Basement, and are oriented E-W. The Heavitree Quartzite and the overlying Bitter Springs Formation form the basal Neoproterozoic units of the Amadeus Basin and comprise the footwall, while the Ankala Block and Erontonga Metamorphics form the hangingwall. The Winnecke area is bounded to the east and west by 2 major fault systems, the Woolanga Lineament and Pinnacles Fault respectively (Figures 2.3 and 2.7). East of the Woolanga Lineament, alluvium of the Hale Formation completely obscures the underlying geology.

In the Winnecke region, there are 3 major schists belts/shear zones termed the Winnecke Shear Zone (WSZ), the Harry Creek-Two Mile Bore Shear Zone (HC-TMBSZ) and the Anuma Schist. These major shear zones are diffuse, kilometre-wide schist belts which have focused south-directed thrusting. The Heavitree Quartzite (the basal unit of the Amadeus Basin sediments) hosts the WSZ along its northern margin and contact with the Arunta Basement, therefore this shear zone at least must have been active during the Alice Springs Orogeny. For most of its length the WSZ is oriented E-W and dips northward with quartz rodding plunging to the NNW (~092/48°N; L 46° →344°) except in the west where the zone swings northward and joins into the Pinnacles Fault. North of the WSZ is another major shear zone which appears to be contiguous with the

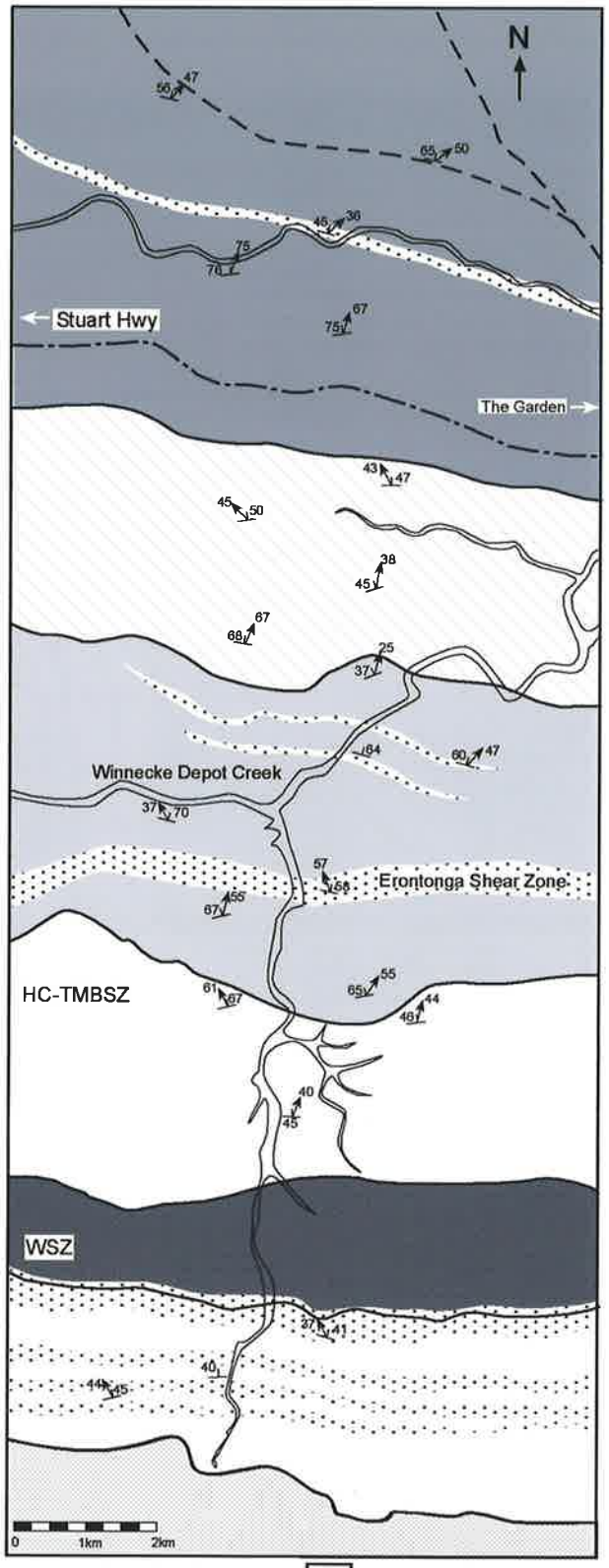

Figure 2.8. Generalised geology of the Winnecke area including location of the Erontonga Shear Zone. Abbrev: HC-TMBSZ-Harry Creek-Two Mile Bore Shear Zone; WSZ-Winnecke Shear Zone.

Figure 2.8. Physiography of the Winnecke area. (a) A series of metre-scale shear zones cross-cut this hillside in the northern Winnecke area, a feature common throughout the terrain; (b) contact between granulite facies country rock and a minor metre-scale shear zone in the Erontonga Metamorphics; (c) close up view of the contact observed in (b); (d) the central portion of the Erontonga Shear Zone outcrops as a low ridge of schist; (e) view of the transition from schists of the Erontonga Shear Zone to the surrounding granulites; (f) close up of the major unit of metapelitic schist in the Erontonga Shear Zone.

Harry Creek Deformed Zone, but offset across the Pinnacles Fault. Termed the Harry Creek-Two Mile Bore Shear Zone in this study, this is a diffuse zone about 2 kms wide composed of numerous anastomosing shear zones of varying intensity and ranging in width from the metre-scale to the hundred metre-scale. The HC-TMBSZ trends parallel to the WSZ and is oriented at about 095/49°N with a lineation defined by biotite, muscovite and quartz plunging toward NNW (L 44°→335°) in greenschist facies schists.

The Anuma Schist is about 1km wide and is the northern-most shear zone in the Winnecke region, effectively separating the granulite facies Erontonga and Cadney Metamorphics (Figures 2.6 & 2.7). It is also generally E-W trending although Emslie (1996) sub-divided the zone into northerly and southerly components on the basis of foliation and lineation orientations and strain intensity. The northern zone is intensely deformed with lineations plunging toward NNW (088/50°N; L 47°→345°) while lineations in the southern zone trend NNE (100/49°N; L 42°→020°). Porphyroclast systems are commonly symmetrical implying a degree of flattening. Rocks in this shear zone are mid to upper amphibolite facies grade with kyanite-staurolite-garnet and sillimanite-staurolite-bearing micaschists common. Also found scattered throughout the schist belt are numerous deformed metre-scale kyanite-quartz pods.

The Erontonga Shear Zone is a relatively narrow (~ 50 metres wide in outcrop) discrete shear zone which lies between the Anuma Schist and the HC-TMBSZ (Figure 2.7 & 2.8 d & f). This shear zone cuts the surrounding granulites of the Erontonga Metamorphics, which can be observed in outcrop either side of the shear zone (Figure 2.8 e), and is composed of mid-amphibolite facies mafic, quartzofeldspathic and metapelitic schists with quartz-feldspar-biotite-muscovite and garnet-staurolite-feldspar-biotite-muscovite-quartz assemblages. The ESZ has a very similar structural orientation as the WSZ, HC-TMBSZ and Anuma Schist, trending east-west and dipping steeply northward (~092/62°N) with lineations defined by quartz, kyanite, phyllosilicate minerals and occasional staurolite plunging NNW(~ 55°→320°) (Figure 2.7).

2.5 Summary

The Arunta Inlier is a polymetamorphic terrain primarily composed of intensely deformed rocks which have experienced up to 5 tectono-thermal events during the Proterozoic and have been subsequently overprinted in the Palaeozoic by the Alice Springs Orogeny. The youngest geological feature in the inlier is a series of E-W to NW-SE trending crustal-scale shear zones which transect the inlier, overprinting all other fabrics. The shear zone system is well represented in the Strangways Metamorphic Complex where individual amphibolite-facies shear zones cross-cut and offset granulite facies country rock. The current geochronological database for the SMC shear zones is small and limited to K-Ar, Ar-Ar and Rb-Sr dates which reflect cooling ages rather than crystallisation ages. The existing data suggests the ages of the shear zones could be between about 1040 Ma and 320 Ma and thus they could reflect the affects of either Proterozoic or Palaeozoic tectonism. This ambiguity highlights the need for additional comprehensive dating of the SMC shear zone rocks, using thermochronometers appropriate for mid-amphibolite facies metamorphic assemblages, which will be the subject of the next section. Detailed studies of the fluid flow regime and metamorphic evolution of these shear zones are also lacking, and these topics will constitute the focus of the majority of this study. A number of key localities identified for study in the SMC include the Yambah Shear Zone, the Pinnacles Bore Shear Zone and the Erontonga Shear Zone.

Chapter 3

Sm-Nd EVIDENCE FOR PALAEOZOIC POLYMETAMORPHISM IN THE STRANGWAYS METAMORPHIC COMPLEX

3.1 Introduction

Isotope geochronology can provide unique information on metamorphic processes, unravelling the P-T-t history of a metamorphic terrain by providing time constraints on development of key stages in structural and metamorphic evolution, which can provide clues on; kinematic and exhumation evolution; rates of heating and cooling; and the duration and style of metamorphic process associated with specific tectonic environments.

In the Strangways Metamorphic Complex, previous geochronological investigations have failed to satisfactorily constrain the timing of regional metamorphic episodes due to; the paucity of the database, the application of inappropriate isotopic systems to mid-amphibolite facies rocks, and a tendency to analyse overprinting retrograde assemblages in granulites rather than sampling totally recrystallised shear zone rocks (e.g. Iyer et al, 1976; Woodford et al, 1975; Allen and Stubbs, 1982; Windrim and McCulloch, 1986). Consequently previous geochronological work has resulted in a wide spread of ages for the shear zones, which has led to some controversy regarding the timing of the crustal scale amphibolite facies shear zones which both bound and dissect the SMC granulites (e.g. Collins and Shaw, 1995).

In order to resolve the problems concerning the age of the amphibolite facies shear zones which cross cut the SMC, a geochronological investigation of several of the shear zones was undertaken. Accurate ages will constrain the timing of metamorphism in these shear zones thereby clarifying their relationship to the surrounding granulite facies country rocks. The new data will contribute to the establishment of an accurate thermochronological database and assist in defining the tectonic environment in which metamorphism of the shear zones occurred, as well as aiding future investigations of the cooling rate of this particular metamorphic event.

3.2 Geochronology of shear zones in the Strangways Metamorphic Complex

Prior to initiation of this investigation, much of the information regarding the regional geological history in the SMC was derived from detailed structural and metamorphic studies (e.g. Allen, 1979; Goscombe, 1989; Norman, 1991; Warren, 1982; Ding and James, 1985; Teyssier, 1985) which have successfully determined the relative timing of successive metamorphic and deformation episodes but have not been closely coupled with geochronological studies, relying solely on existing local geochronological data and correlations from across the inlier to constrain the absolute timing of these events. While greenschist facies shear zones generally ascribed to the ASO have consistently returned K-Ar and Rb-Sr ages equivalent to the ASO in a number of studies (Armstrong and Stewart, 1975; Stewart, 1971), the amphibolite facies shear zones have remained problematic. Due to structural and kinematic similarities between assumed Proterozoic fabrics in the Arunta basement and fabrics found in the Amadeus Basin sediments affected by the Alice Springs Orogeny (e.g. Goscombe, 1989; Norman, 1991), workers have been unable to conclusively distinguish using field relations if these shear zones have Proterozoic or Palaeozoic origins (e.g. Norman, 1991; Collins and Shaw, 1995). As a result, workers were polarised into those advocating a primarily Proterozoic age for the high grade shear zones, with subsequent reactivation in the Palaeozoic due to the ASO at low grade conditions (Majoribanks and Black, 1974; Allen and Stubbs, 1982; Windrim and McCulloch, 1986; Black et al 1983; Shaw et al, 1984; Ding and James, 1985), and those suggesting that the effects of the ASO on the basement were more profound, including the creation or reactivation of shear zones at upper to mid-amphibolite facies (Teyssier, 1985; Collins and Teyssier, 1989a; Warren, 1983; Dunlap and Teyssier, 1995).

A small number of K-Ar, Ar-Ar and Rb-Sr ages exist from the amphibolite facies shear zones and retrogressed granulites in the SMC (e.g. Armstrong and Stewart, 1975; Iyer et al, 1976; Woodford et al, 1975; Allen and Stubbs, 1982;) but despite invariably producing Palaeozoic ages, the current database has failed to validate a Palaeozoic origin for the shear zones, since this data tended to be rejected as reflecting excess argon, argon loss or thermal resetting during later tectonothermal activity. As stated in Chapter 2, the underlying problem with most of the existing geochronological database in the Strangways Range area has been the application of isotopic systems with closure temperatures lower than the metamorphic temperatures experienced by the rocks and minerals used for dating (i.e. $T_{closure} < T_{max}$). The K-Ar and Rb-Sr isotopic systems are susceptible to resetting (George and Bartlett, 1996; Evans et al, 1995; Hickman and Glassley, 1984) and have maximum closure temperatures ranging from 500-350°C for most minerals (Cliff, 1985; Dodson and McLelland-Brown, 1985) therefore they are ineffective in determining crystallisation ages rather than cooling ages in rocks of amphibolite facies or

higher grade. Similarly while the use of Ar-Ar on hornblende may be effective to mid-amphibolite facies (Harrison, 1981) there are numerous examples of erroneous Ar-Ar hornblende ages caused through the presence of excess argon (e.g. Berger, 1975; Gaber et al, 1988; Maboko et al, 1991). In the case of amphibolite facies shear zone rocks, the added factor of pervasive and possibly punctuated fluid flow, coupled with intense deformation increases the likelihood of perturbation of these isotopic systems. A further problem with the existing database is the difficulty in correlating dates with observed tectonic fabrics, as overprinting retrograde assemblages from the surrounding granulites were often used to date overprinting events, including the timing of the shear zones (e.g. Allen and Stubbs, 1982; Windrim and McCulloch, 1986). As a result, the age of the mid-amphibolite facies shear zones in the SMC is still uncertain.

3.3 The use of Sm-Nd geochronology in dating amphibolite facies rocks

As outlined above, many of the methods previously used to date the SMC shear zones are inappropriate for amphibolite facies assemblages. A far more appropriate method for use on mid- to upper-amphibolite facies rocks are mineral isochrons using the Sm-Nd isotope system. Experimental and field-based studies have shown that the Sm-Nd system can be relatively immobile and insensitive to isotopic resetting via thermal perturbation (e.g. Cohen et al, 1988; Vance and O'Nions, 1990; Burton et al, 1995; Hensen and Zhou 1995 a & b; Becker, 1997; Ganguly et al, 1998), although examples do exist where the Sm-Nd system has been reset (e.g. McCulloch and Wasserburg, 1978; Black and McCulloch, 1987). Since the garnet point usually controls an Sm-Nd isochron due to its high Sm-Nd ratio, most available data relates to the behaviour of the Sm-Nd system in this mineral. Due to the number of variables which influence closure temperature, including grain size, cooling rate and mineral chemistry (Dodson, 1973; Cliff, 1985; Jenkin et al, 1995) and the added problems of contamination by REE rich inclusions such as monazite (e.g. Zhou and Hensen, 1995), opinions on the maximum effective closure temperature for Sm-Nd in garnet vary greatly, ranging from as low as 450-600°C (e.g. Humphries and Cliff, 1982; Mezger et al, 1992) up to about 850-900°C (e.g. Jagoutz, 1988; Cohen et al, 1988; Vance and O'Nions, 1990; Brueckner et al, 1996). However there is a growing consensus that the closure temperature of the Sm-Nd system is relatively high, approaching that of peak metamorphism experienced by granulites and upper amphibolite facies rocks (Jagoutz, 1988; Cohen et al, 1988; Getty et al, 1993; Vance and Holland, 1993; Burton et al, 1995;

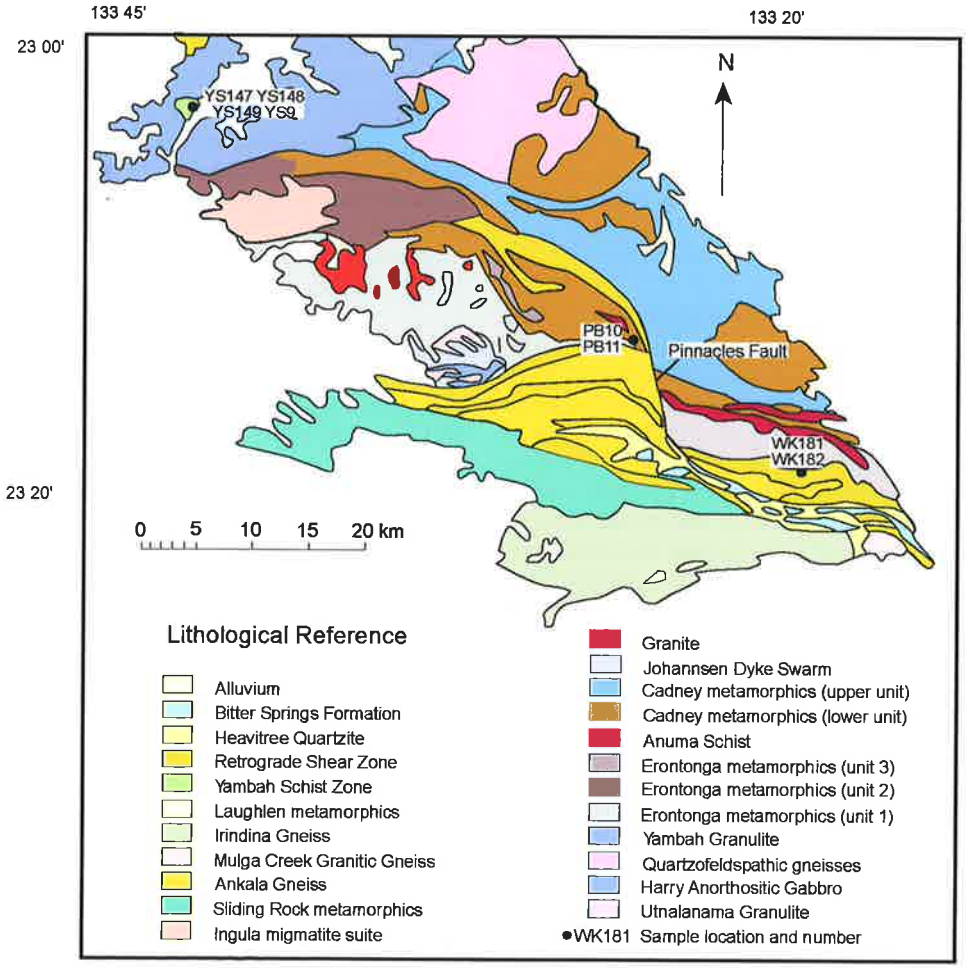

Figure 3.1. Generalised geology of the Strangways Metamorphic Complex indicating the location of amphibolite facies schists selected for Sm-Nd dating.

Brueckner et al, 1996; Becker, 1997), and temperatures of 600°C appear to be an absolute minimum estimate for the closure temperature of the Sm-Nd isotope system in garnets larger than about 1 mm (Burton and O'Nions, 1991; Mezger et al, 1992; Burton et al, 1995; Hensen and Zhou 1995a; Ganguly et al, 1998). Thermobarometry and phase equilibria studies (see chapters 4, 5 and 6) indicate that the mid-amphibolite facies shear zones rocks in the SMC reached peak metamorphic temperatures of about 600°C, thus the Sm-Nd system is appropriate for radiometric dating of these shear zone rocks, as it will provide dates which are crystallisation ages or ages reflecting conditions close to peak metamorphism, rather than cooling ages.

3.4 Sample selection

Ideally samples selected for geochronological analysis should also be useful for geothermobarometry and record simple clear textural relationships enabling the sample to be tightly constrained by independent structural and metamorphic observations to an appropriate stage in the regional geological history. The samples analysed in this study include two garnet-staurolite micaschists from the Erontonga Shear Zone (WK181 &WK182), two garnet-staurolite micaschists from the Pinnacles Bore Shear Zone (PB10 & PB11) and four mafic amphibolite gneisses from the Yambah Schist Zone (YS147, YS148, YS149 & YS9). Field locations of analysed samples are given in Figure 3.1 and Appendix 1. The samples have been selected on the basis of possessing mineralogical compositions suitable for Sm-Nd geochronology and (where possible) for geothermobarometry as well. The geographic extent of each of the shear zones is well defined and either side of these zones are anhydrous felsic and mafic granulites which represent the precursors of the shear zone rocks.

The samples selected are generally coarse-grained garnet-staurolite-biotite-quartz-muscovite ± (kyanite, feldspar, chlorite) schists or garnet-hornblende-plagioclase-quartz ± staurolite schists (see Appendix 1 for detailed petrography). Minerals chosen for analysis include garnet, staurolite, hornblende and biotite. Whole-rock analyses were also performed on each rock sample. Staurolite is not commonly used in Sm-Nd mineral isochrons but was selected in this study as it is a key mineral for petrological investigation of metamorphic conditions, having a limited range of thermal stability in most metapelites, and in these rocks defines the metamorphic fabric of interest. All samples were sectioned and checked petrographically, and chemically using a Cameca SX51 electron microprobe, for any signs of zonation or overgrowth rims and using back scatter electron imagery to detect the presence of microscopic REE enriched included phases such as monazite or allanite. All imaged included phases were either quartz or the oxides ilmenite and magnetite, except in the mafic amphibolite samples YS147, YS148, YS9 and YS149 which have significant amounts of fine-grained allanite adjacent to and/or included within hornblende. In all samples, phases generally show little or no major element zonation except for garnets in samples WK181, WK182 and PB10 which display bell shaped Mn profiles, which are interpreted as evidence of growth zoning typical of mid-amphibolite facies crystallisation (see § 4.3.1.2 for a detailed discussion). None of the phases were obviously rimmed except for garnets in PB11 which have unusual compositional profiles and apparent overgrowth rims which can be observed petrographically (see § 4.3.1.3). Petrography of the individual samples is discussed in greater detail in Appendix 1.

3.5 Analytical techniques

Hand trimmed rock samples (~ 2 kg samples) were initially coarsely crushed in a jaw crusher then milled to between 150 - 250 µm using a disc mill. Representative whole rock samples were obtained by splitting the milled bulk sample. Where possible coarse crushed garnet grains were hand picked and further crushed in a mortar and pestle, otherwise mineral separates were taken from sieved split samples of the bulk rock. Minerals were initially separated using a Franz Isodynamic magnetic separator and standard heavy liquid separation, then finished by hand picking under a binocular microscope to obtain inclusion free material. To remove surface contamination, minerals were washed several times in an ultrasonic bath in 1N HCl solution. After each interval the acid was discarded and replaced until the solvent remained clean, separates were then washed repeatedly in double-distilled water.

All mineral separates and whole rock samples were dissolved in steel jacketed, high pressure Teflon bombs using a HNO_3-HF acid mixture heated to 200°C for a period of 2-5 days after preliminary dissolution on an open hotplate. The samples were then evaporated and re-dissolved in 6N HCl for a further 24 hours in the high pressure bombs for conversion to chloride form. After total dissolution the mineral solutions were aliquoted for spiking with one half of the solution allocated to the isotopic composition (IC) component and the other half used for isotopic dilution (ID). The ID component was spiked with ^{85}Rb, ^{84}Sr and mixed ^{147}Sm -^{150}Nd tracers, and re-homogenised for a minimum 24 hours. All samples were then evaporated and re-dissolved in 1.5 ml of 2N HCl in preparation for cation exchange column extraction. Rb and Sr and Sm-Nd were separated using BioRad AG50W-X8 (200-400 mesh) resin columns, then Nd and Sm were separated in columns of Teflon powder impregnated with hydrogen di-2-ethylhexyl phosphate (HDEHP). In preparation for analysis, Nd and Sm were loaded onto double Ta-Re filaments with H_3PO_4.

Analysis was performed on a Finnigan MAT 261 single collector mass spectrometer at the University of Adelaide. All Nd ratios are corrected for within-run mass fractionation by normalisation to $^{146}Nd/^{144}Nd = 0.7129$. Within run precision from the mass

spectrometer which represents the minimum estimate of uncertainty is reported in Table 3.1. Total procedural Nd background contamination levels (blanks) were 0.2 ng/g respectively which in general is negligible by comparison with the typical >200ng of Nd dissolved and analysed. All regression calculations were calculated with a decay constant of 6.54×10^{-12} year^{-1} using the method of York (1969). All quoted errors are at 95% confidence interval, following the suggestions of Kullerud (1991). The long term reproducibility of the complete analytical procedure is measured by repeated analysis of an internal standard with the standard deviation for $^{143}Nd/^{144}Nd$ being 20 ppm. Machine performance was monitored by analyses of the international standard LaJolla which averages at 0.511830 ± 25 (n=25).

3.6 Results

Table 3.1 summarises the Sm-Nd isotopic data from which the isochrons shown in Figures 3.2, 3.3 & 3.4 are calculated. Results of the isochron calculations are presented in Table 3.2. The Sm-Nd mineral ages from the amphibolite facies assemblages of the Yambah Schist Zone, Pinnacles Bore Shear Zone and the Erontonga Shear Zone show that these assemblages crystallised in the Palaeozoic during the Devonian to mid-Carboniferous.

The four rocks sampled from the Yambah Schist produce a spread of Devonian ages from 401 Ma to 379 Ma but all are within error. The errors associated with these isochrons are relatively high, reflecting the small spread in the $^{147}Sm/^{144}Nd$ ratios. A three point isochron (garnet-hornblende-whole rock) from mafic amphibolite sample YS9 (Figure 3.2d) yielded an age of 380 ± 24 Ma with an MSWD of 1.709, while another mafic amphibolite YS149 from a nearby location produced an age of 401 ± 30 Ma with an MSWD of 3.378 also from a garnet-hornblende-whole rock isochron (Figure 3.2c). Two staurolite-bearing mafic amphibolites, YS147 and YS148, sampled in close proximity to each other, produced ages of 379 ± 31 Ma (MSWD = 0.406) and 380 ± 50 Ma (MSWD = 0.185) respectively from four point (garnet-staurolite-biotite-whole rock)

Samples	Sm (ppm)	Nd (ppm)	$^{147}Sm/^{144}Nd$	$^{143}Nd/^{144}Nd$	2σ
YS 147					
whole rock	9.9214	9.9460	0.1202	0.511535	0.000025
garnet	6.4820	40.7512	0.0962	0.511466	0.000025
hornblende	6.5680	16.0426	0.2476	0.511848	0.000024
staurolite	1.6820	9.3975	0.1083	0.511514	0.000036
YS148					
whole rock	8.5410	45.3438	0.1139	0.511495	0.000029
garnet	3.0050	15.1310	0.1201	0.511501	0.000020
hornblende	6.6530	22.7736	0.1769	0.511647	0.000015
staurolite	2.9880	17.7129	0.1019	0.511463	0.000028
YS149					
whole rock	3.7692	14.8699	0.1533	0.511502	0.000014
garnet	3.4150	16.3765	0.1261	0.511402	0.000028
hornblende	3.1649	7.6366	0.2507	0.511749	0.000015
YS9					
whole rock	4.2207	24.6002	0.1038	0.511419	0.000022
garnet	3.5753	18.2971	0.1182	0.511431	0.000030
hornblende	4.06197	8.9369	0.2749	0.511839	0.000016
WK181					
whole rock	1.84117	8.9824	0.1240	0.511392	0.000020
garnet	1.6139	2.5952	0.3762	0.511882	0.000028
staurolite	0.5186	2.1951	0.1429	0.511452	0.000028
biotite	1.6793	9.4616	0.1074	0.511334	0.000024
WK182					
whole rock	6.2103	33.5084	0.1121	0.511420	0.000036
garnet	1.7392	1.2406	0.8483	0.512984	0.000025
staurolite	1.5286	8.1762	0.1131	0.511412	0.000030
biotite	2.9855	16.4797	0.1096	0.511446	0.000022
PB10					
whole rock	6.3313	1.1230	0.1230	0.511377	0.000018
garnet	1.1040	2.4330	0.2746	0.511683	0.000025
staurolite	1.4860	7.4580	0.1206	0.511377	0.000020
biotite	3.0260	15.503	0.1181	0.511341	0.000018
PB11					
whole rock	5.1376	25.4679	0.1220	0.511460	0.000019
garnet	4.8317	13.8288	0.2113	0.512414	0.000019
staurolite	7.9424	45.1178	0.1065	0.511361	0.000015
biotite	3.2017	17.1598	0.1129	0.511359	0.000011
kyanite	3.6142	21.0627	0.1038	0.511320	0.000021

Table 3.1. Summary of Sm-Nd isotopic data for whole rock and pure mineral fractions from sampled shear zone rocks.

Sample	All points						Less Whole Rock		
	# of points	Age	±2σ	IR	±2σ	MSWD	Age	±2σ	MSWD
YS 147	4	379	31	0.511234	0.000032	0.406	381	32	0.736
YS 148	4	380	50	0.511207	0.000048	0.185	384	53	0.211
147&148	8	384	26	0.511214	0.000027	1.767	387	27	1.992
YS 149	3	401	30	0.511092	0.000038	3.378	425	38	0
YS 9	3	380	24	0.511154	0.000032	1.709	396	34	0
WK 181	4	312	18	0.511136	0.000024	3.091	314	19	5.909
WK 182	4	322	7	0.511197	0.000018	2.956	321	7	5.219
181&182	8	324	6	0.511161	0.000014	10.95	321	6.5	13.662
PB 10	4	317	27.6	0.511113	0.000028	3.12	321	28	5.057
PB 11	5	1578	36	0.510214	0.000031	14.632			
PB 11 (no g)	3	404	362	0.511062	0.000260	5.967			

Table 3.2. Results of Sm-Nd isochron calculations.

isochrons (Figures 3.2 a & b).

Usually garnet preferentially partitions Sm with respect to Nd resulting in a high $^{147}Sm/^{144}Nd$ ratio compared to most other common minerals (Faure, 1986). In the Yambah schist isochrons however, garnet has very low ratios compared to the general case where garnet is expected to have a ratio of about 0.5 or greater (Faure, 1986; Getty et al, 1993; Hensen and Zhou, 1995b; Mawby et al, 1999), tending to plot below hornblende, and in two instances (YS147 & YS149) even plotting below the whole rock points. In all the Yambah rocks analysed, hornblende has the highest $^{147}Sm/^{144}Nd$ ratios and effectively controls the slope of the isochrons. Garnet generally also has very low absolute levels of Sm and Nd, usually less than 5 ppm, whereas the Yambah Schist garnets appear enriched in Nd, with values ranging from 15 ppm to 40 ppm (see Table 3.1). The garnets of PB11 also have high levels of Nd at 13.8 ppm, but the $^{147}Sm/^{144}Nd$ ratio is not as low as in the Yambah rocks.

A possible explanation for this phenomenon, is the presence of sub-microscopic inclusions of REE enriched phases in the mineral separates samples, especially since acid leaching of the samples was not carried out (e.g. Zhou and Hensen, 1995). Contaminating inclusions of a mineral which is very Rare Earth Element (REE)-enriched such as apatite, allanite, titanite, zircon or monazite, would be capable of shifting the isotopic signature of garnet and

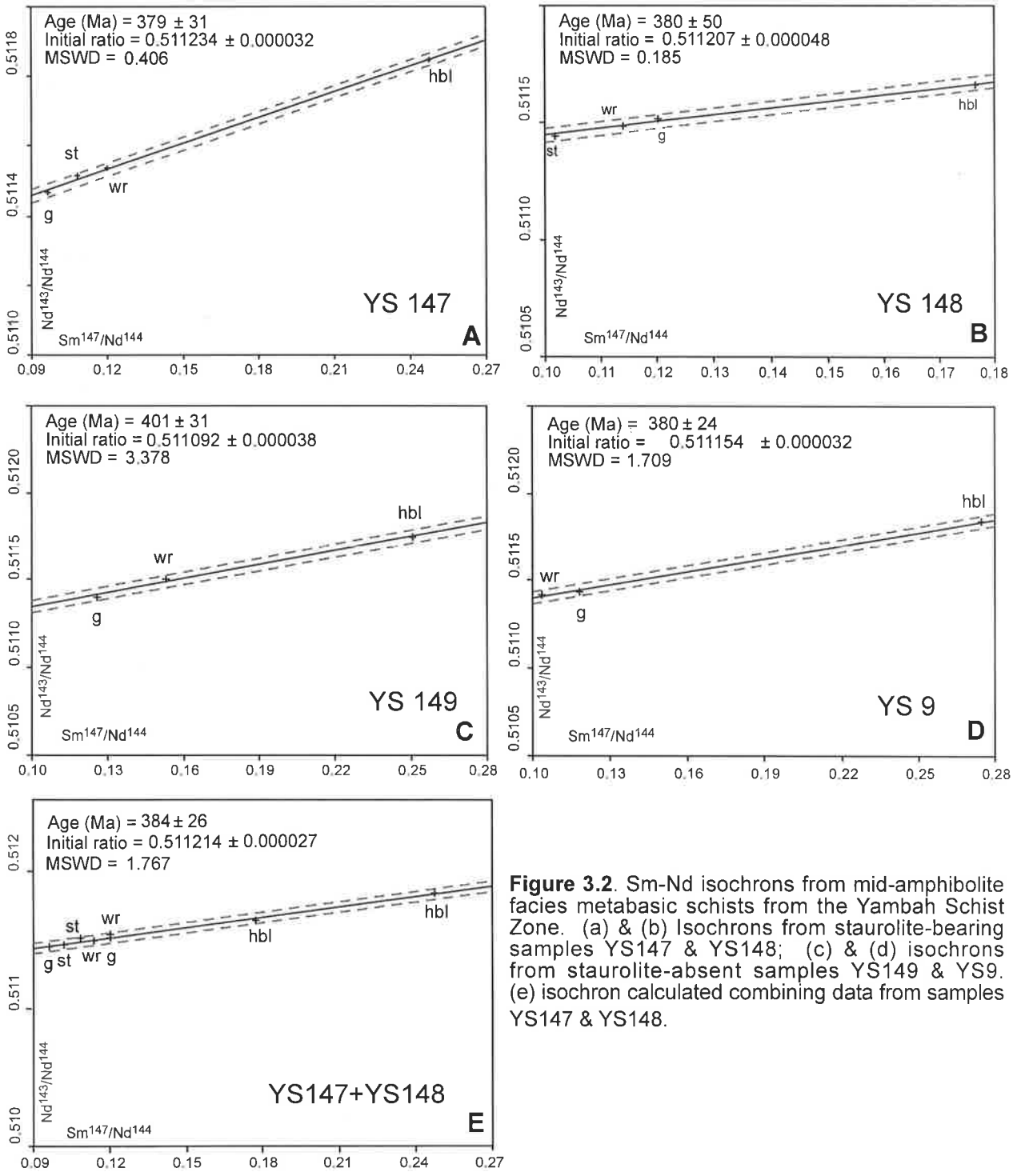

Figure 3.2. Sm-Nd isochrons from mid-amphibolite facies metabasic schists from the Yambah Schist Zone. (a) & (b) Isochrons from staurolite-bearing samples YS147 & YS148; (c) & (d) isochrons from staurolite-absent samples YS149 & YS9. (e) isochron calculated combining data from samples YS147 & YS148.

hornblende while being a volumetrically minute component in the analysed sample. In the case of the Yambah rocks, the contaminating inclusions must be preferentially enriched in Nd since the Sm levels in the analysed garnet and hornblende do not appear as greatly enhanced. Such behaviour is consistent with published Kd values for allanite, which has a greater affinity for Nd compared with Sm, but not for apatite which partitions Sm in preference to Nd, or zircon which have similar Kd for both Nd and Sm (Faure, 1986). Given that allanite is a common accessory mineral in the mafic schists from Yambah, and often occurs included within hornblende, it seems likely that there was some allanite contamination in the analysed garnet and hornblende fractions which has influenced their resultant $^{147}Sm/^{144}Nd$ ratios. In a study of the effects of contamination by REE-enriched phases on Sm-Nd garnet geochronology, Prince et al (2000) found that significant contamination need not adversely affect the accuracy of an age calculated using contaminated garnet, particularly if: 1) the Sm-Nd ratio of the contaminating material was close to that of the actual garnet Sm-Nd ratio or 2) the contaminating inclusions were isolated from diffusive exchange with the whole rock coincident with diffusive isolation of the garnet. Prince et al (2000) suggest that contamination by REE-enriched inclusions should be identifiable through the variation in Sm-Nd ratios of multiple separates. Although multiple separates from the same rock were not undertaken in this study, the similarity in the ages from samples YS147 and YS148 suggest that these ages are reliable and reproducible. If the data from these two rocks are combined they produce an eight point isochron of 384 ± 26 Ma (MSWD = 1.767) (Figure 3.2e), suggesting that any contamination has resulted in a negligible shift in the ages. In addition, the ages produced from the Yambah Schist Zone rocks are equivalent to a Sm-Nd isochron age of 381 ± 7 Ma from an amphibolite facies rock from the West Bore Shear Zone (Ballèvre et al, 2000). Although the behaviour of the Sm-Nd system in hornblende is poorly understood, hornblende-controlled Sm-Nd isochrons from upper amphibolite facies shear zones in the eastern Arunta Inlier (Mawby et al, 1999) produced ages equivalent to those from SHRIMP U-Pb monazite geochronology (Hand et al, 1999a), suggesting that the Sm-Nd system in hornblende is also quite robust.

Two samples from the Erontonga Shear Zone produced slightly younger ages from four point garnet-staurolite-biotite-whole rock isochrons with WK181 yielding an age of 312 ± 18 Ma, with an MSWD of 3.09 (Figure 3.3 a), and WK182 yielding 322 ± 7 Ma with an MSWD of 2.96 (Figure 3.3 b). These samples were collected only metres apart from within a single shear zone, and if the data are grouped, return an age of 324 ± 6 with an MSWD of 10.95 (Figure 3.3 c).

The two samples from the Pinnacles Bore Shear Zone produced particularly interesting results. PB10

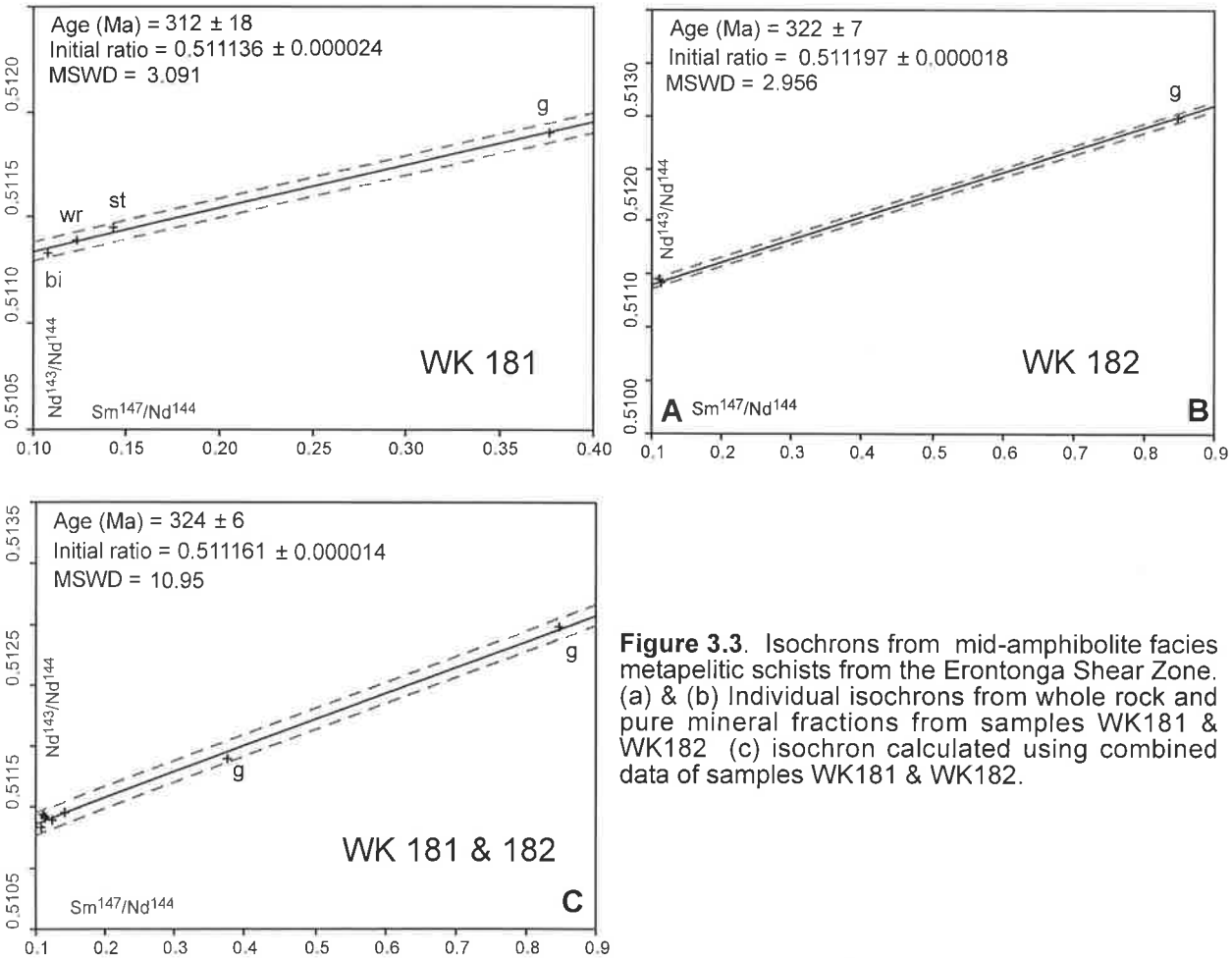

Figure 3.3. Isochrons from mid-amphibolite facies metapelitic schists from the Erontonga Shear Zone. (a) & (b) Individual isochrons from whole rock and pure mineral fractions from samples WK181 & WK182 (c) isochron calculated using combined data of samples WK181 & WK182.

returned an age of 317 ± 28 Ma with an MSWD of 3.12 from a four point isochron of garnet-staurolite-biotite-whole rock (Figure 3.4 a), which is consistent with the results from the Erontonga Shear Zone. In contrast sample PB11, with a similar mineralogy and sampled close to PB10, returned an age of 1578 ± 36 Ma with an MSWD of 14.63 from a five point isochron of garnet-staurolite-biotite-kyanite-whole rock (Figure 3.4 b). In the latter instance however, the garnet point which controls the distribution of the isochron may have been affected by the isotopic signature of inherited garnet cores (e.g. Getty et al, 1993; Brueckner et al, 1996; Stowell and Goldberg, 1997). In thin section the development of a rim of secondary generation garnet overgrowing older garnet cores can be seen (Figure 4.10). Although the 1578 ± 36 Ma isochron represents a mixing age, to some extent this age may be close to the actual age of the growth of the garnet cores, since the garnet cores have had about 1.3 Ga to accumulate radiogenic Nd and constitute >90% of the garnet volume. Therefore the garnet rims would need to be highly Sm-enriched to be able to shift the total garnet signature away from the inherent core garnet signature. If the garnet point is removed, the whole-rock point (which includes a component of the Proterozoic garnet), controls the isochron's slope and defines a mixing age of 995 ± 217 (MSWD = 11). If both the garnet and whole rock points are removed, a three point isochron defined by the fabric forming phases biotite-staurolite-kyanite produces a Palaeozoic age of 404 ± 362 with an MSWD of 5.967 (Figure 3.4 c). The error in this case is extreme, but again is reflecting the lack of spread in the data on the $^{147}Sm/^{144}Nd$ axis.

Given the polymetamorphic history of the SMC and the example above, it is reasonable to suspect that some minerals such as monazite, allanite and zircon might have been inherited from the granulite precursor rocks to the amphibolite facies shear zones. If this is the case, such phases are most likely to affect the whole rock point on the isochron, since the whole rock sample is not subjected to the same sieving, cleaning and hand picking process as the mineral separates. If the whole rock points are removed from these isochrons however, calculated ages and error values only alter marginally. YS9 and YS149 show the largest changes in their dates, now producing ages of 396 ± 34 Ma and 425 ± 38 Ma on 2 point garnet-hornblende isochrons, while YS147 and YS148 yield 381 ± 32 Ma (MSWD = 0.736) and 384 ± 53 Ma (MSWD = 0.211) respectively. WK181 yields 314 ± 19 Ma (MSWD = 5.909) and WK182 yields 321 ± 7 Ma (MSWD = 5.219), while PB10 gives 321 ± 28 Ma (MSWD = 5.057).

3.7 Discussion

Sm-Nd mineral isochron ages can represent either the timing of crystallisation of the mineral assemblage and therefore effectively date peak metamorphic conditions, or they may represent cooling ages,

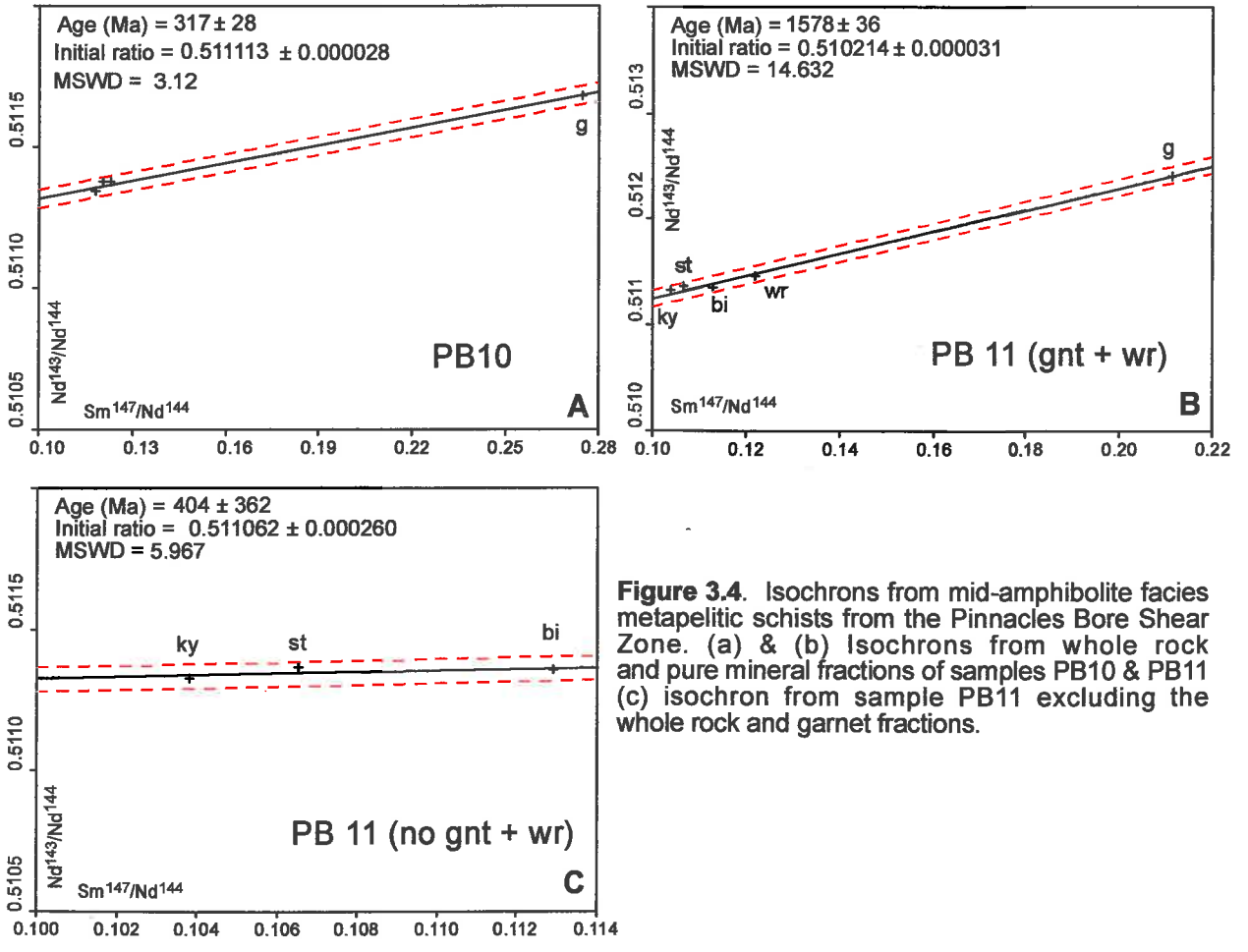

Figure 3.4. Isochrons from mid-amphibolite facies metapelitic schists from the Pinnacles Bore Shear Zone. (a) & (b) Isochrons from whole rock and pure mineral fractions of samples PB10 & PB11 (c) isochron from sample PB11 excluding the whole rock and garnet fractions.

reflecting the timing of cessation of diffusion of Sm and Nd. Geothermobarometric calculations indicate that the analysed SMC shear zone rocks formed under mid-amphibolite facies conditions of about 600°C and 6.0 kbar (see § 4.3 and 6.3), generally less than the minimum suggested closure temperature for Sm-Nd in garnet (e.g. Mezger et al, 1992; Burton et al, 1995). As such it is likely that the data presented here represent crystallisation ages rather than cooling ages, and indicates that the amphibolite facies assemblages defining these shear zones grew during the Devonian to mid Carboniferous, a period which is consistent with crystallisation during the Alice Springs Orogeny.

Although is apparent that the SMC shear zones analysed are of Alice Springs Orogeny-age (400-300 Ma), there is some spread in the data which is less easily resolved. While the Pinnacles Bore and Erontonga samples return very similar ages of ~320 Ma, the Yambah rocks appear to be on the order of about 60 m.y. older at ~380 - 400 Ma. Thermobarometry and phase equilibria studies on rocks from the Yambah, Pinnacles Bore and Erontonga Shear Zones (see Chapters 4, 5 and 6), including some of the dated rocks discussed above, indicate that the mid-amphibolite facies assemblages in all three shear zones represent fabrics which grew during clockwise prograde metamorphism at conditions of about 600°C and 6 kbars. Therefore the three shear zones experienced approximately the same peak metamorphic conditions and P-T path, but there appears to be an actual difference in the timing of activity in the shear zones, with rocks from the Yambah Shear Zone experiencing peak metamorphism about 60 m.y. before the Pinnacles Bore and Erontonga Shear Zone rocks (Figure 3.5). Thus the isotopic evidence from the Yambah, Pinnacles Bore and Erontonga Shear Zones implies that there were at least two prograde metamorphic episodes during the Alice Springs Orogeny, suggesting that this orogeny was a polymetamorphic event in the SMC.

The hypothesis of polymetamorphism during the ASO is supported by a growing database from shear zones elsewhere in the Arunta Inlier, which indicates that a similar trend in age distribution exists in shear zones in the north of the Strangways Range and to the west in the Reynolds Range area. In the Edwards Creek area, to the north of the Yambah Schist Zone and east of the Pinnacles Fault, Möller et al, (1999) recorded a U-Pb zircon age of 443 ± 6 Ma and U-Pb monazite age of about 385 Ma from a staurolite-bearing shear zone, while a post-kinematic amphibolite facies assemblage from the West Bore Shear Zone east of the Woolanga Lineament produced a Sm-Nd mineral isochron age of 381 ± 7 Ma (Ballèvre et al, 2000). Further to the north-west in the south-central Reynolds Range, Cartwright et al,

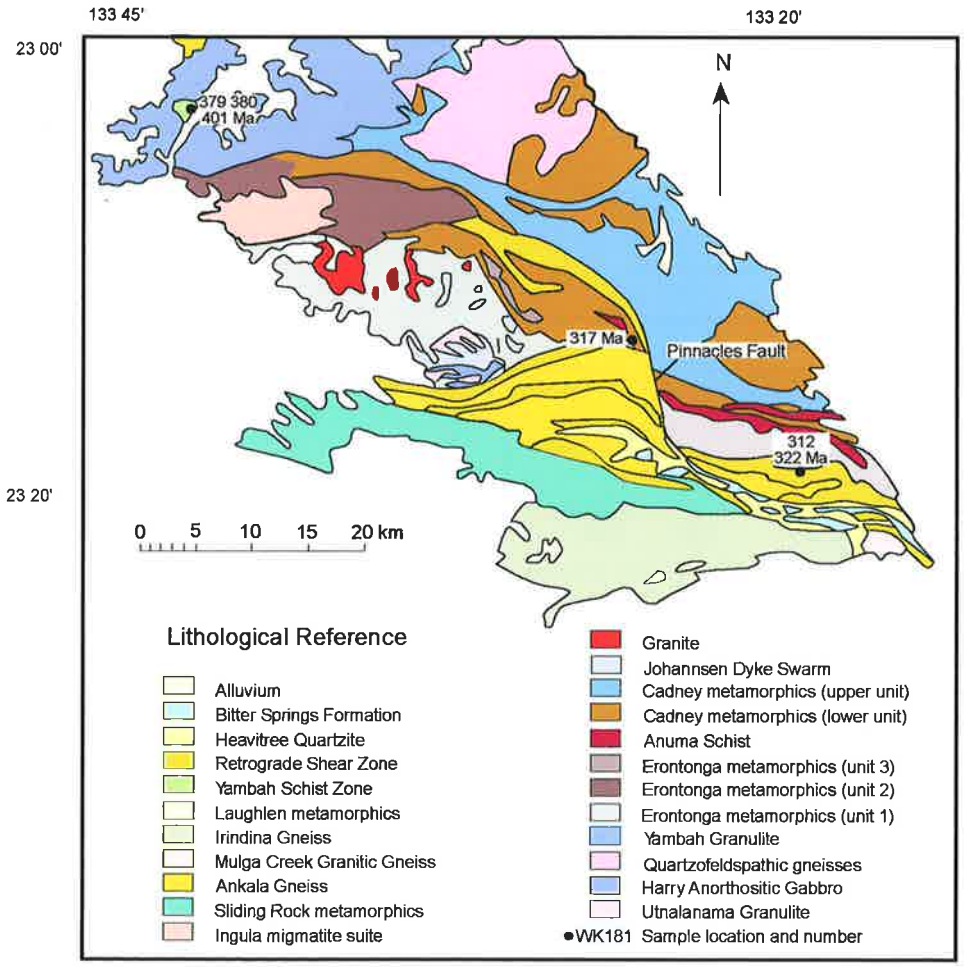

Figure 3.5. Generalised geology of the southern Strangways Metamorphic Complex indicating the distribution of Sm-Nd dates from the amphibolite facies shear zone rocks studied.

(1999) produced well defined and consistent Rb-Sr whole-rock and muscovite Ar-Ar ages of about 334 Ma from sheared granites and metapelites, and unpublished data from shear zone rocks in the southern and northern Reynolds Range, the Anmatjira Range and Redbank Shear Zone (Figure 3.6) indicate a northward decline in the age of ASO shear zones in this region (C. Read, Monash University, pers com June 2000).

The suggestion that the ASO was associated with atleast two prograde events provides a new perspective to some of the older existing data. While early K-Ar, Rb-Sr and Ar-Ar geochronological studies in the Strangways Range did record Palaeozoic ages from the higher grade shear zone rocks (e.g. Windrim and McCulloch, 1986; Iyer et al, 1976) these data were commonly considered inaccurate due an apparent wide spread in the Palaeozoic ages ranging from 510 to <330 Ma which did not fit well with ideas about the length and timing of the Alice Springs Orogeny (Allen & Stubbs, 1982; Iyer et al, 1976). This led many to question the reliability of the data and effectively dismiss it. However when viewed in the context of the hypothesis of polymetamorphic activity during the ASO, some of the older data may be credible. For example, Stewart (1971) recorded K-Ar muscovite ages of 327 - 358 Ma from the Heavitree Quartzite and Bitter Springs Formation in the Arltunga Nappe Complex, while adjacent basement rocks to the north of the nappe, returned slightly older K-Ar muscovite ages of 352 - 431 Ma (Figure 3.7). Two K-Ar biotite ages of 548 and 889 Ma appear dubious, and have not been recorded elsewhere, and may indeed result from excess argon. Further north, in the Harry Creek Deformed Zone, Allen and Stubbs (1982) using Ar-Ar on hornblende and biotite obtained a spread of ages from 393 - 514 Ma, with most results clustering about 430 Ma. Again two ages at 710 and 703 Ma (step heating and total degassing ages from the same sample) may be invalid, since no similar ages have been found elsewhere in the Arunta Inlier.

In the Woolanga Bore area, Woodford et al (1975) reported ages ranging from 327 - 481 Ma from Ar-Ar total degassing on hornblende and biotite, while at Yambah in the north-west, Iyer et al (1976) recorded hornblende and biotite Ar-Ar ages ranging from 349 - 388 Ma, and up to 393 Ma with K-Ar. While there is a significant overlap between these ages there does appear to be a general trend of increasing age which mimics the trend noted in the Sm/Nd data collected in this study (see Figure 3.7). Given that the K-Ar, Ar-Ar and Rb-Sr dates may reflect cooling ages, this data may imply that during the ASO the northern SMC was cooling before the southern SMC reached peak metamorphism.

Allen and Stubbs (1982) also recognised that much of the existing geochronological data indicated an earlier component to Alice Springs tectonism than the Early Devonian age generally ascribed to onset of this event, and subsequently divided the ASO into a series of 3 deformational events based on groupings of the available Palaeozoic geochronological data

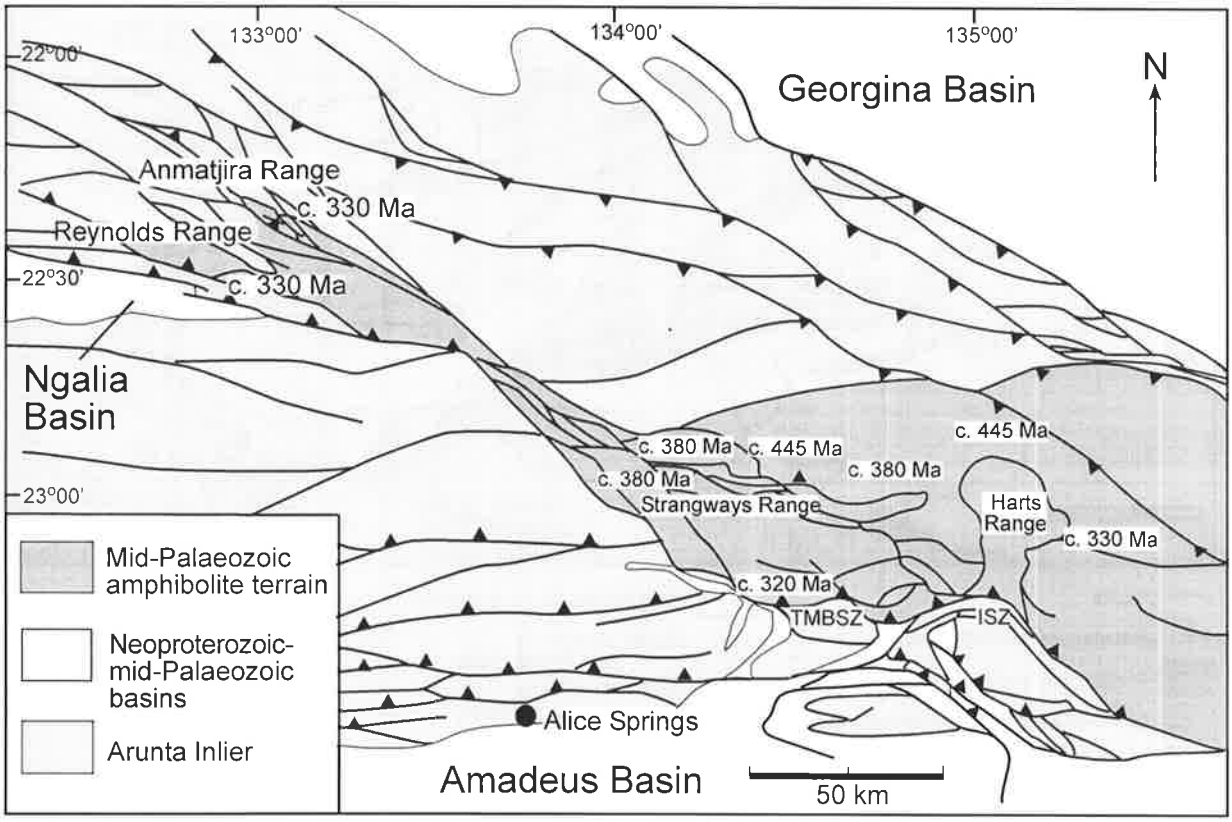

Figure 3.6. Variation in recent geochronological data across the southeastern Arunta Inlier. Data taken from: Ballevre et al (2000), Cartwright et al (1999), Mawby (2000), Moller et al (1999).

at 430 - 510 Ma, 370 - 400 Ma and <300Ma. These divisions are generally not spatially allied other than distinguishing between ages from basement rocks and Amadeus Basin cover rocks in the White Range Nappe (Figure 3.7) instead they primarily reflect the closure systematics of the geochronological systems used, however it is interesting to note that evidence for prolonged activity during the Alice Springs Orogeny has existed in the literature for some time but went apparently unrecognised.

The progression toward younger ages in the southern parts of the SMC and the northern parts of the Reynolds Range may in part be an artefact of the data, considering the variance in the closure systematics of the different isotopes and minerals used (i.e. generally Ar-Ar on biotite and hornblende in the northern high grade areas and in the Reynolds Range investigations, compared with Rb-Sr on white micas in the south and U-Pb and Sm-Nd in the central areas of the Strangways Range) or it may be providing information about differential timing of movement at different crustal levels in response to the Alice Spring Orogeny. This is a pertinent observation given that the large scale structural and metamorphic distribution of the inlier replicates this trend to some degree. In the Strangways, Harts and Reynolds Ranges, the ASO shear zones generally dip steeply north to northeast with steep north to northeast plunging lineations and a consistent south vergent thrusting movement (Goscombe, 1989; Collins and Teyssier, 1989a; Norman, 1991; Cartwright et al, 1999). ASO shear zone rocks are mid to upper amphibolite facies in the northern and central Strangways and Harts Ranges but metamorphic grade declines to lower greenschist facies southward toward the Arltunga Nappe Complex. North of the Reynolds Range and in the Delny-Mount Saint Hill Fault Zone area however, shear zones are southward dipping and have south over north movement (Freeman, 1986; Collins and Teyssier, 1989a) and the metamorphic grade begins to decline northward toward the unmetamorphosed mid-Neoproterozoic to mid-Palaeozoic sediments of the Georgina Basin (Shergold and Druce, 1980; Shergold, 1985). Thus the overall architecture of the ASO is that of a large scale 'pop-up' structure (Collins and Teyssier, 1989 b) (Figure 3.6) and the geochronological record of the progressive development of this structure may have been preserved in the shear zone rocks.

Thus at this stage, some geochronological evidence exists for the period of maximum expression of Alice Springs tectonism but conclusive constraints on the onset and cessation of this activity are lacking. This situation reiterates the necessity of further studies, particularly targetted thermochronological investigations throughout the Arunta Inlier, to

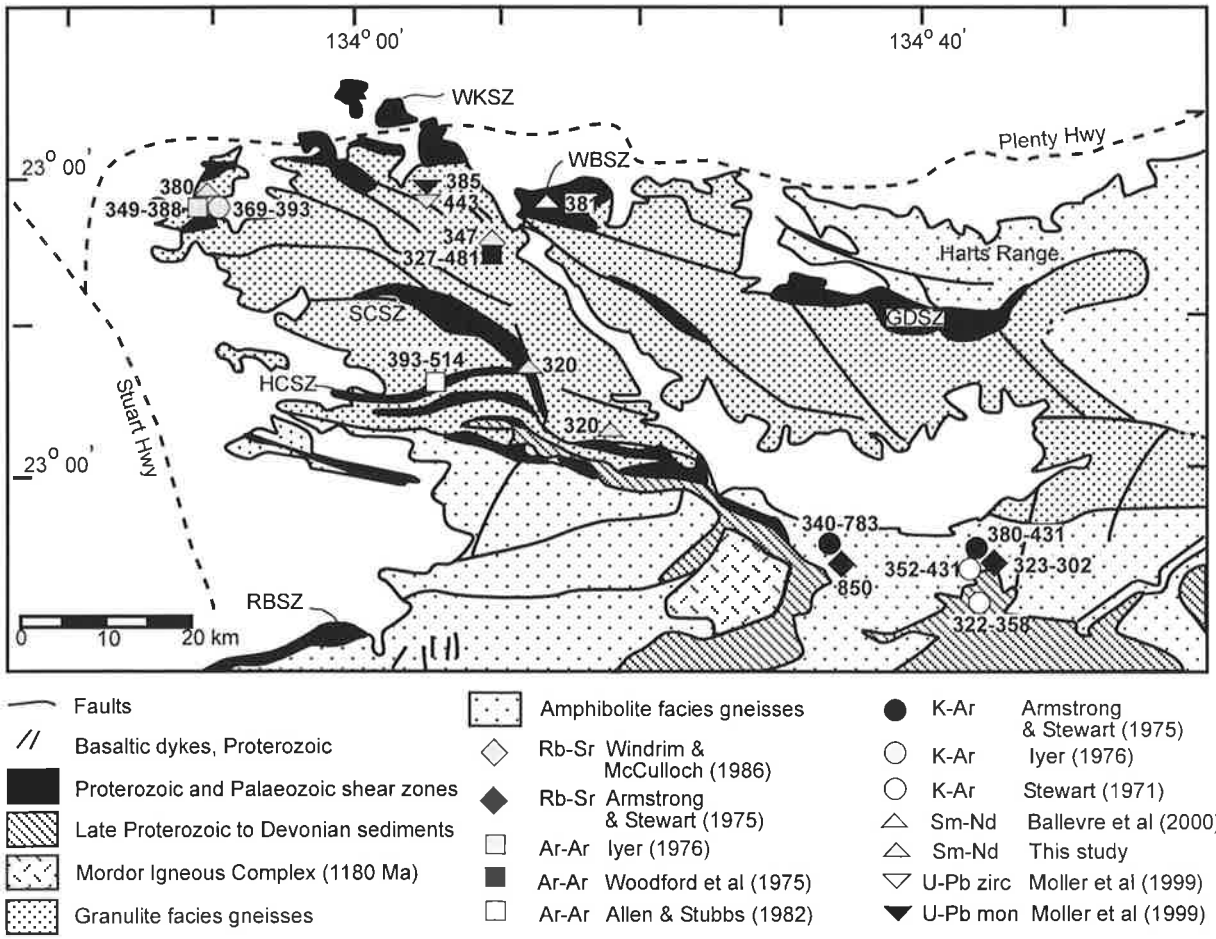

Figure 3.7. Expanded geochronological database for the Strangways Metamorphic Complex, including Rb-Sr, K-Ar and Ar-Ar data from the Arltunga and White Range Nappes, demonstrating the southward progression in younger ages.

characterise and delineate the duration and extent of this orogeny.

3.8 Summary

The amphibolite facies shear zones which transect the SMC show remarkable consistency in terms of their metamorphic character, and are clearly able to be correlated across the SMC and into the adjacent Harts Range (Collins and Teyssier, 1989a). Detailed structural analysis by previous authors in the SMC successfully delimited the relative timing of the various metamorphic and deformation events, but was unable to define the absolute timing of shearing and exhumation of the granulite terrain to its current crustal level. Early geochronological investigations failed to adequately constrain the age of shear zone fabrics because the isotopic systems used had closure temperatures below the crystallisation temperature of the rocks analysed, and therefore yielded mixing and cooling ages rather than crystallisation ages. Using the more robust Sm-Nd isotopic system with closure temperatures equivalent to or higher than the peak metamorphic conditions experienced by these rocks, mineral isochrons from three amphibolite facies shear zones distributed throughout the Strangways Range, have yielded Palaeozoic ages which are consistent with metamorphism during the ASO. These results, in conjunction with recent data based on U-Pb and Sm-Nd dating of high grade assemblages from the northern SMC, suggest that exhumation of the granulites along these shear zones occurred primarily during the Palaeozoic ASO and that metamorphism of the shear zones was at least diachronous, suggesting that the ASO was itself a long-lived polymetamorphic event spanning about 120 Ma (i.e. ~ 430 - 310 Ma).

Chapter 4

THERMOBAROMETRIC EVOLUTION OF MID-PALAEOZOIC METAPELITIC SCHISTS IN THE STRANGWAYS METAMORPHIC COMPLEX

4.1 Introduction

Despite being one of the best examples of intraplate orogenesis, as yet there has been little detailed description or analysis of the metamorphic rocks produced in the Arunta Inlier during the Alice Springs Orogeny, or the metamorphic environment in which they developed. In the southern Strangways Metamorphic Complex, Alice Springs Orogeny-aged shear zones within the basal unit of the Amadeus Basin sediments (i.e. the Heavitree Quartzite) (Figure 4.1) contain greenschist facies assemblages. Adjacent to these shear zones and throughout the southern part of the Winnecke area is a series of anastomosing greenschist facies shear zones, termed the Two Mile Bore Shear Zone (TMBSZ), which has a cumulative width of about 2 kms. To the north of the TMBSZ lies the Anuma Schist, a diffuse schist belt approximately 1 km wide which is composed predominantly of amphibolite facies schists. The Pinnacles Bore Shear Zone and Yambah Shear Zone in the central and northern SMC respectively are also dominated by mid-amphibolite facies assemblages, occassionally overprinted by retrograde greenschist facies assemblages.

Thus from the distribution of mineral assemblages in the shear zones (see §2.2) it appears that metamorphic grade generally increase northward through the SMC. However north of the SMC and in the Delny-Mt Sainthill area the metamorphic grade begins to decline northward toward the unmetamorphosed mid-Neoproterozoic to mid-Palaeozoic sediments of the Georgina Basin (Shaw et al, 1979; Goscombe, 1989; Scrimgeour and Raith, in press). This trend is mimicked structurally, with southern shear zones dipping moderately to steeply north to northeast with steep NNE-plunging lineations

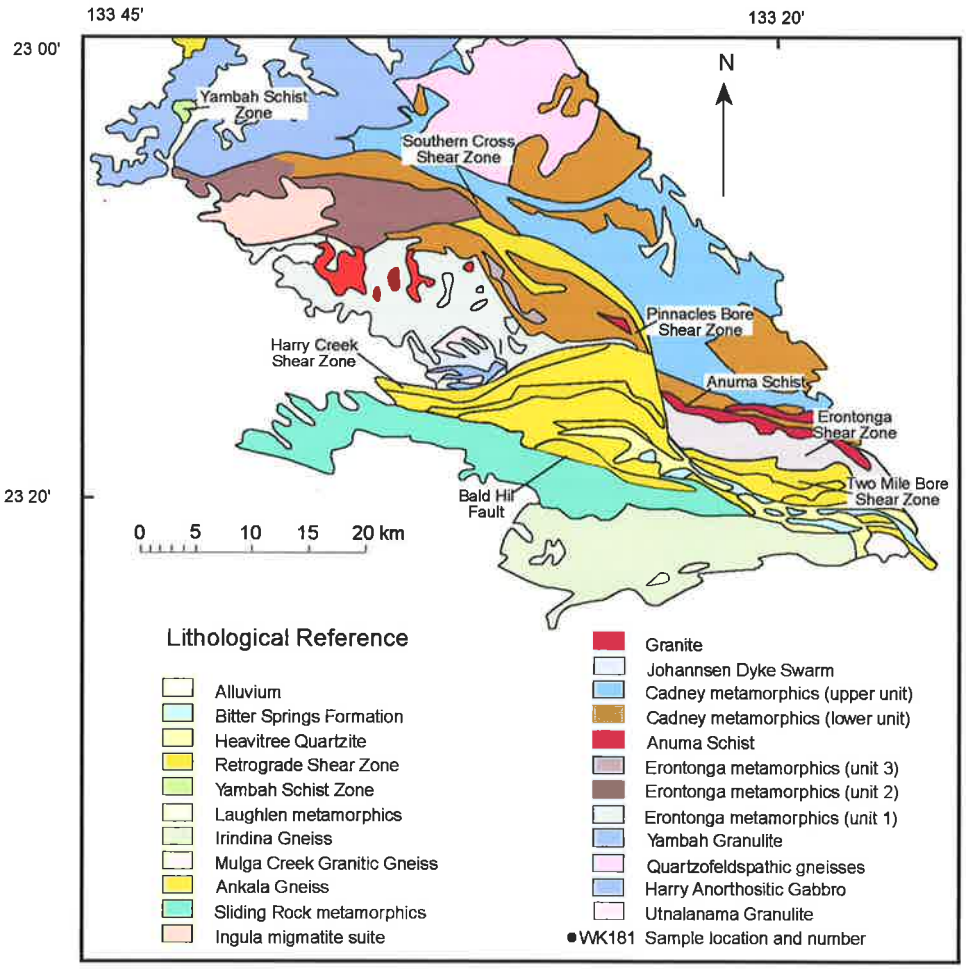

Figure 4.1. Generalised geology of the southern Strangways Metamophic Complex indicating the location of major shear zones of interest.

and kinematics providing a north over south sense of movement, while northern shear zones are southward dipping with a south over north sense of movement (Freeman, 1986; Collins and Teyssier, 1989a; Scrimgeour and Raith, in press). Although only a few of these shear zones have been dated, Sm-Nd isotopic data from the Strangways Metamorphic Complex indicates that amphibolite facies ASO shear zones in this area did not form contemporaneously (Figure 3.5), but developed over a prolonged time span on the order of about 100 m.y., with older shear zones located in the north (381 ± 7 Ma, Ballèvre et al, 2000; 443 ± 6 & ca. 385 Ma, Möller et al, 1999; ca. 380 Ma, Chapter 3) and younger shear zones in the south (312 ± 18 Ma and 322 ± 7 Ma, see Chapter 3). These dates suggest that the ASO was a polymetamorphic event. Thus ASO-age metamorphic rocks in the Strangways Ranges may record unique information about the development of this orogen through time.

Sm-Nd dates from two shear zones in the southern SMC, the Pinnacles Bore Shear Zone and the Erontonga Shear Zone (Figure 4.1) were obtained from amphibolite facies metasedimentary schists, while isotopic data from the Yambah Schist Zone were determined from metabasic lithologies. Each lithology is chemically and mineralogically distinct and in the following three chapters, they will be described and examined to determine the peak metamorphic conditions achieved and more importantly, the trajectory in P-T space taken by these rocks during orogenesis. While information about the P-T path taken by a metamorphic rock can be determined using a variety of methods including conventional geothermobarometry, the modelling of P-T paths from zoned minerals using the differential thermodynamics or Gibbs method (Spear et al, 1982; Spear and Selverstone, 1983; Spear and Rumble, 1986; Spear, 1988), and phase equilibria developed from petrogenetic grids, in this chapter only conventional geothermobarometry will be applied. In the following sections, the metamorphic mineral assemblages and mineral chemistry of metasedimentary lithologies from the Pinnacles Bore and Erontonga Shear Zones are described, and the metamorphic conditions and P-T paths recorded by these rocks will be investigated using information from geothermobarometry and chemical zoning in garnets.

4.2 Lithological observations from Pinnacles Bore and the Winnecke area.

In the Pinnacles Bore and Winnecke areas, granulite facies rocks are cut by and offset across a number of narrow (<100 m scale) discrete shear zones. These shear zones are composed mainly of metapelitic and felsic schists interlayered with subordinate metabasites. Granulite facies lithologies and shear zone rocks from the Pinnacles Bore area have a similar general appearance and mineralogy to granulites and shear zone rocks in the Winnecke area, and have been interpreted as analogous units separated spatially by late movement on the Pinnacles Fault (see Figures 4.1 and 2.7).

4.2.1 Petrography

Detailed petrography of individual selected samples is presented in Appendix 1. The metapelitic rocks in the shear zones are generally medium to coarse grained garnet-poor, two-mica schists. Typically mineral assemblages consist of quartz + muscovite + biotite ± (chlorite, kyanite) however locally units can be found with the assemblages quartz + muscovite + biotite ± (kyanite, staurolite, chlorite) or more rarely quartz + muscovite + biotite ± (kyanite, staurolite, garnet, chlorite). These assemblages indicate that the shear zone rocks achieved mid-amphibolite facies (kyanite-staurolite zone) conditions. In the Pinnacles Bore Shear Zone the more common two-mica metapelitic schists are occasionally interlayered with medium to coarse grained, plagioclase-bearing metapelitic schists containing the assemblage quartz + biotite + kyanite + plagioclase ± (staurolite, garnet). These plagioclase-bearing rocks often have a more gneissic appearance due to a lower proportion of phyllosilicates (Figure 4.2 a,b & c). Henceforth the terms metapelite and calcic metapelite will be used to distinguish the two-mica plagioclase-absent metapelitic schists from the plagioclase-bearing metapelitic schists.

Shear zones containing calcic metapelites are less common in the Winnecke area, and garnet-bearing examples are rarely found. However to the north of

Sample No.	g	st	ky	sill	bi	mu	plag	chl	q	ilm	mag	all	ap
PB10	P	P	-	-	P Ist,q	P Iq R	-	R	P Ist,bi	P Ig,st,bi,q	Ist,bi,q R	Ig,bi	Ig,q
PB215	P	P	-	-	P Ist	P R	-	R	P Ig,st	P Ist	Ist R	-	-
PB11	E P	P	P	R	P Ig	-	P	-	P Ig,st,ky	P Ig,st,ky	-	-	-
PB12	E P	P	P	R	P Ig,ky	-	P	R	P Ig,st,ky	P Ig,st,bi	R	-	-
PBS3	E P	-	P	-	P Ig	-	P	-	P Ig	P	-	-	-
WK71	P	P	-	-	P Ist	P R	-	R	P Ist	P Ig,st	R	Ibi	-
WK182	P	P	-	-	P Ist	P	-	-	P Ig,st	P Ig,st,bi	-	Ibi	-
CM19	E P	-	P Ig	P Ig R	P Ig	R	P R	-	P Ig R	P Ig	-	-	-
CM20	E P	-	P Ig	P R	P Ig	-	P Ig R	-	P R	P Ig	-	-	-

Table 4.1. Summary of general petrographic and textural relationships observed in selected metapelitic schists. Abbreviations: E = relic mineral from older assemblage; P = part of inferred peak assemblage; R = part of retrograde assemblage; Ix = inclusion within mineral denoted by lower case abbreviation.

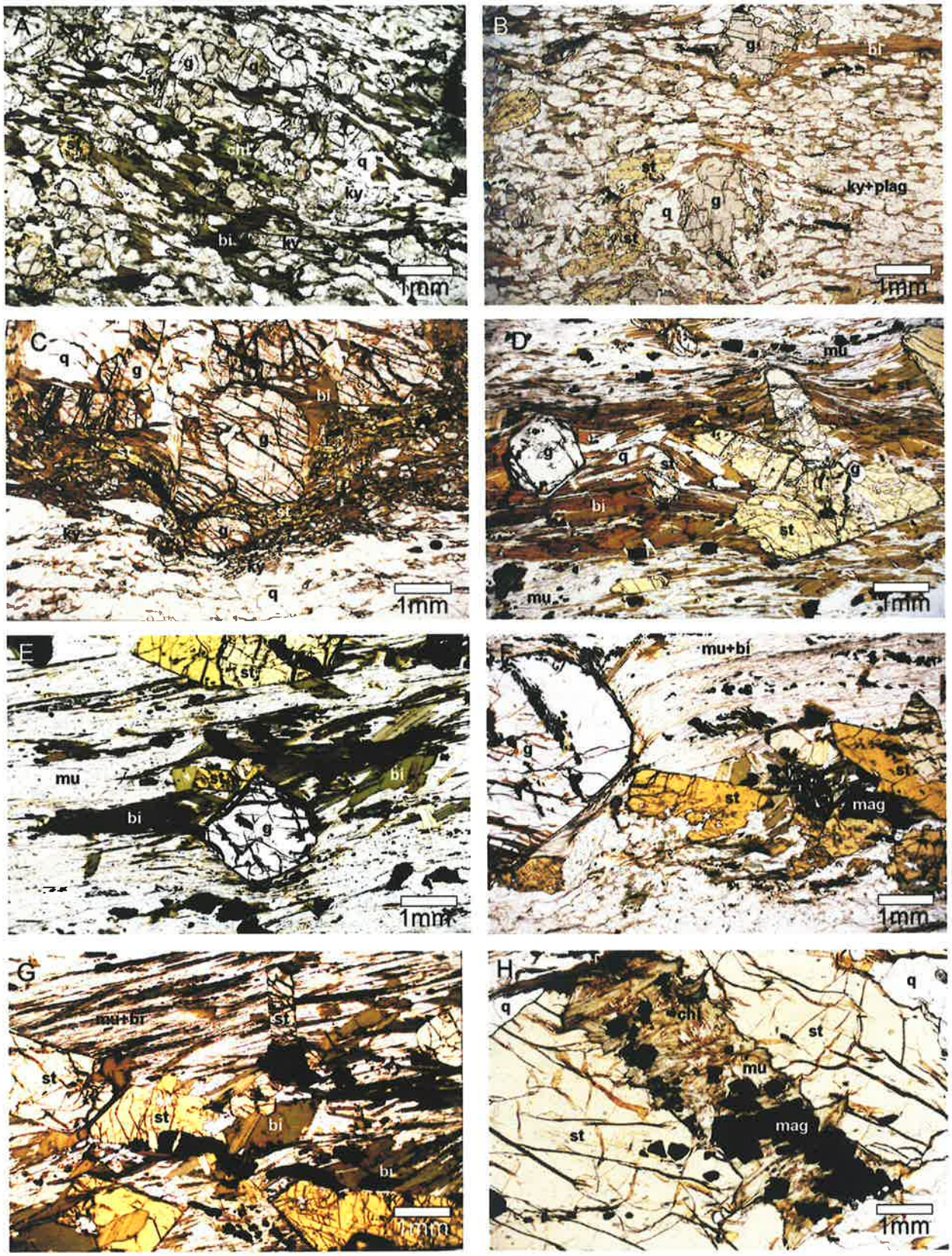

Figure 4.2. Representative examples of common mineral assemblages and textures in metapelitic schists from the Pinnacles Bore and Winnecke areas. (a) PB11: a g-st-ky-bi-q schist from Pinnacles Bore displaying the typical foliation of the calcic metapelites defined by oriented bi, st, ky & plag; (b) PB12: a calcic metapelite showing the matrix foliation wrapping garnet; (c) PB184: a calcic metapelite displaying some compositional layering. The foliation, defined by oriented ky, st & bi wraps garnet porphyroblasts; (d) PB215: a st-g-bi-mu schist with small garnet inclusions within st, & st overprinting the bi-mu foliation; (e) WK182: the bi-mu foliation wraps garnet porphyroblasts & (f) euhedral st overprints the matrix foliation; (g) WK71: the foliation also wraps garnet & is overprinted by euhedral st; (h) PB12: a broken staurolite grain with retrograde chlorite, muscovite & magnetite growing at the expense of staurolite.

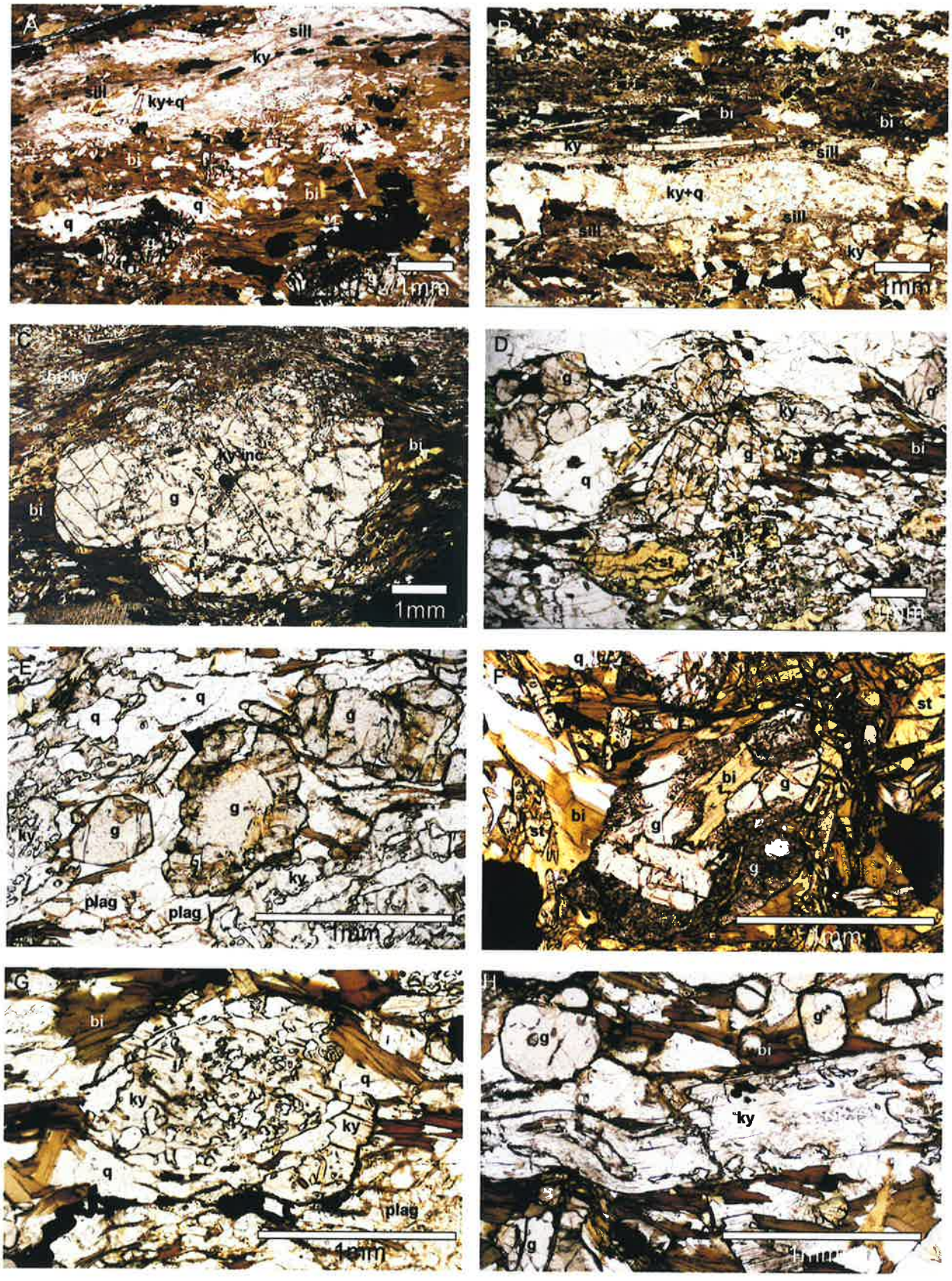

Figure 4.3. Photomicrographs of mineral assemblages and textures in metapelitic schists from the Pinnacles Bore and Winnecke areas. (a) PB246: a g-ky-bi-q schist with late sillimanite as one of the foliation defining minerals; (b) CM20 shows the typical fabric in g-ky-sill-bi-plag-q bearing metapelites from the Cadney Metamorphics; (c) a garnet porphyroblast in CM20 wrapped by the bi-ky fabric, contains numerous ky inclusions oriented orthogonal to the fabric; (d) PB11: a g-st-ky-bi-q schist appears to contain relic garnets overgrown by younger garnet rims; (e) PB12: older garnet cores rimmed by new garnet; (f) two stage garnet growth in PB184; (g) & (h) PB12: presence of coarse-grained resorbed, embayed and deformed blades of kyanite suggest growth of this mineral is syn-kinematic and relatively early in the heirarchy of mineral crystallisation.

the Anuma Schist belt and Erontonga Metamorphics which comprise the immediate Winnecke area, examples of these rocks are found in the Cadney Metamorphics (Figure 4.1). The calcic metapelites from shear zones in the Cadney Metamorphics are similar in appearance to those found in the Pinnacles Bore Shear Zone, however they lack staurolite and contain quartz + biotite + kyanite + plagioclase + sillimanite garnet assemblages. Table 4.1 presents a summary of the petrography of selected samples of metapelitic and calcic metapelitic schists, which are discussed in more detail in Appendix 1.2.

4.2.1.1 Plagioclase-absent metapelites

The foliation observed in these metapelitic schists is defined by biotite and muscovite as well as kyanite and staurolite (Figure 4.2 d-g). Garnet occurs as coarse, euhedral porphyroblasts wrapped by the fabric defining phases (Figure 4.2 d-f). Inclusions in garnet are commonly ilmenite and quartz with rarer biotite, and while generally not volumetrically large, these inclusions can often define a straight internal fabric which is slightly oblique to the external matrix foliation (Figure 4.2 f). Therefore texturally garnets appear pre- to syn-tectonic. The growth of staurolite appears to have initiated later in the crystallisation history as it is never seen included in garnet and occassionally overprints the fabric (Figure 4.2 d, f &g). Staurolite is coarse-grained and can form up to 15% of the rock. It generally only contains quartz and ilmenite as inclusions, but is often intergrown with biotite. These phases appear to form an equilibrium assemblage, with sharp grain boundaries and no evidence of reaction textures or other disequilibrium features other than the occasional presence of retrograde chlorite, which formed at the expense of staurolite in conjunction with retrograde muscovite and quartz (Figure 4.2 h).

4.2.1.2 Calcic metapelites

The foliation found in the calcic metapelitic schists and gneisses is generally defined by the preferred orientation of biotite, kyanite, staurolite and sillimanite where present, and in some examples by compositional layering on about the 5 mm scale (Figures 4.2 a-c & 4.3 a-c). Garnet is present as large euhedral to subhedral grains (2 - 10 mm) which appear to be pre- to syntectonic (Figures 4.2 c & 4.3 c). Texturally, some individual garnets appear to have rims developed on older cores (Figure 4.3 d-f) however there is no other evidence of a hiatus in the growth evolution of the garnets. Kyanite occurs generally as coarse (to 4mm) blades and is a ubiquitous phase, often lying parallel to the fabric and obviously deformed, but also occasionally cross-cutting the foliation (Figure 4.3 g & h). It may be embayed or resorbed and is sometimes surrounded by coarse-grained staurolite (Figure 4.4 d). Staurolite is present in the some of the Pinnacles Bore samples, but even in these cases, constitutes a minor phase forming up to about 7% of the rock. It generally occurs as moderate to coarse (2-3mm) tabular anhedral to subhedral poikiloblasts which commonly contain quartz and ilmenite inclusions. The growth of staurolite appears to have begun relatively late in the metamorphic history, as some grains overprint the fabric forming matrix phases and pre- to syn-tectonic garnet (Figure 4.4 a-c). Biotite occurs as fine to moderate grained laths in the matrix with larger grains sometimes observed in the pressure shadows of garnet and staurolite. Plagioclase is the only feldspar present and generally occurs throughout the matrix although it can be more concentrated in quartzofeldspathic-rich domains. It comprises up to 20% of the assemblage and commonly occurs either as moderate to coarse subhedral grains which may be porphyroblastic and wrapped by the fabric, or as smaller deformed elongate grains which may define part of the matrix fabric. Sillimanite is rarely present in the Pinnacles Bore samples, but very occasionally fine-grained fibrolite is observed growing randomly on the boundaries of garnet, quartz and plagioclase (Figure 4.4 e). In the Cadney Metamorphics samples, sillimanite is common and is also interpreted to grow later in the rock history as kyanite is generally the more common aluminosilicate included in garnet cores, whereas sillimanite tends to occur in the outer margins (Figure 4.4 f) . Additionally, fibrolitic sillimanite locally overgrows plagioclase (Figure 4.4 g & h).

4.2.2 Mineral Chemistry

Selected representative electron microprobe compositional data for garnet, staurolite, biotite, plagioclase, muscovite and chlorite are given in Appendix 2.1. Mineral analyses were performed on a Cameca SX51 Electron Microprobe at the Centre for Electron Microscopy and Microanalysis South Australia (CEMMSA) facility, University of Adelaide using an accelerating voltage of 15kV and 20nA current as standard operating conditions. Mineral analyses have been recalculated using the AX activity-composition computer program of Holland and Powell (1998a).

4.2.2.1 Mineral Chemistry of the metapelitic schists

Garnet in all the metapelitic samples is almandine-spessartine-rich with minor pyrope and grossular. Individual garnets are strongly zoned in their major element chemistry, but nonetheless core and rim analyses from different garnets tend to be similar (see Figure 4.5). The nature and significance of the chemical zoning in the garnets is discussed in detail below in section 4.3.1. *Staurolite* does not show any significant chemical zoning and the chemistry of staurolite within a sample is usually quite uniform with an XFe always lower than that of garnet (Figure 4.5). *Biotite* chemistry is also generally homogeneous with no systematic compositional differences within individual grains, however biotites from Pinnacles Bore display some variation in their XFe values based on their proximity to garnet and staurolite (e.g. samples PB10, PB215, PB12), and are overall more Fe-rich than those from the Erontonga Shear Zone samples. Pinnacles Bore biotites in contact with garnet have slightly higher XFe values (0.46-0.44) compared to those adjacent to both garnet and

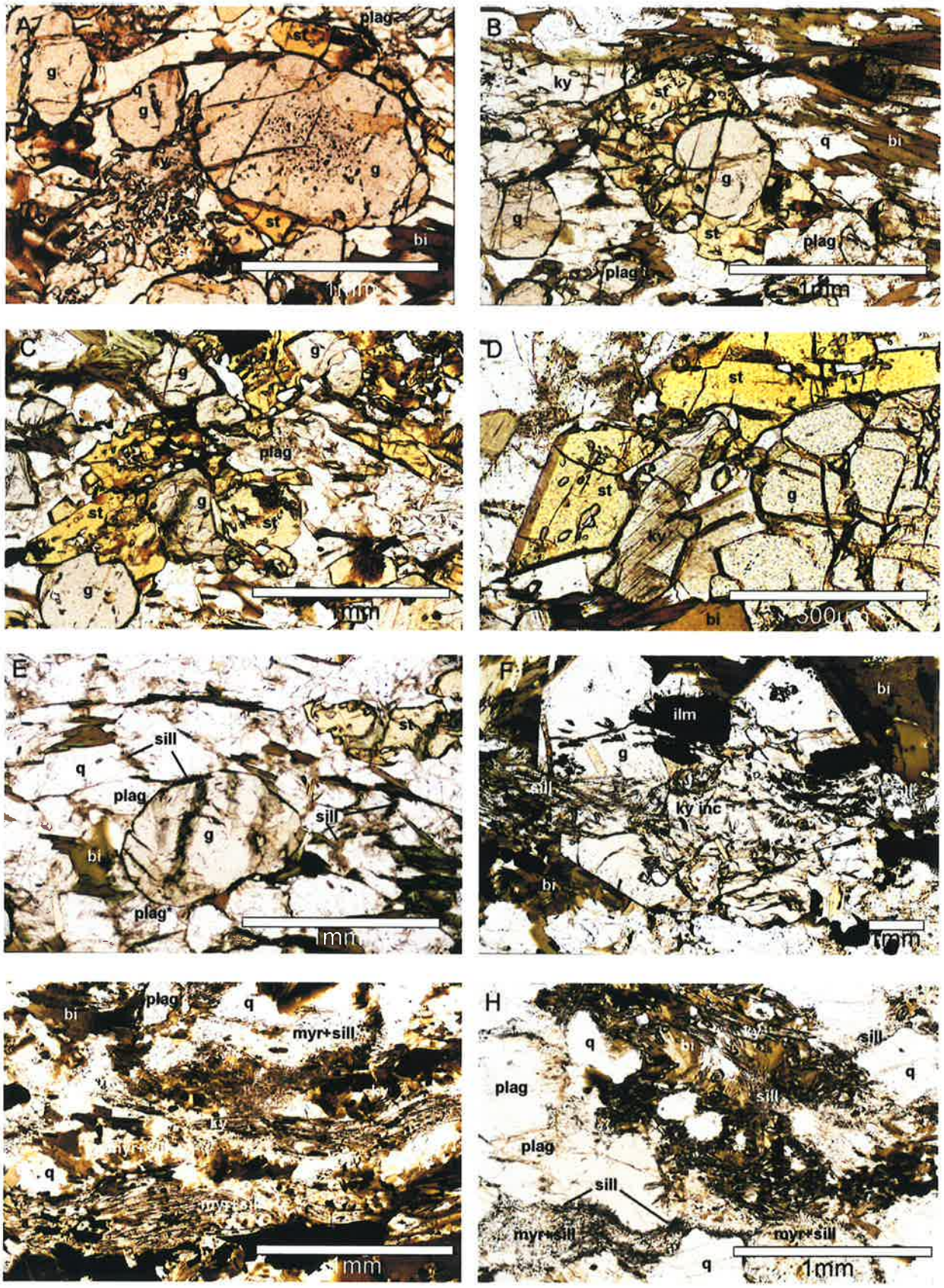

Figure 4.4. Photomicrographs of mineral assemblages and textures in metapelitic schists from the Pinnacles Bore and Winnecke areas. (a) PB11: zoned garnet & resorbed kyanite overgrown by late staurolite; (b) & (c) euhedral garnet surrounded by staurolite in PB11; (d) staurolite overgrowing kyanite in PB12; (e) PB11: fine grained acicular sillimanite growing along grain boundaries of quartz, plagioclase & garnet; (f) CM19: euhedral garnet porpyroblast with ky inclusions in its core oriented orthogonal to sillimanite inclusions in the garnet rim and to the external matrix fabric; (g) & (h) CM19: fine grained sillimanite growing in association with quartz & plagioclase after primary plagioclase.

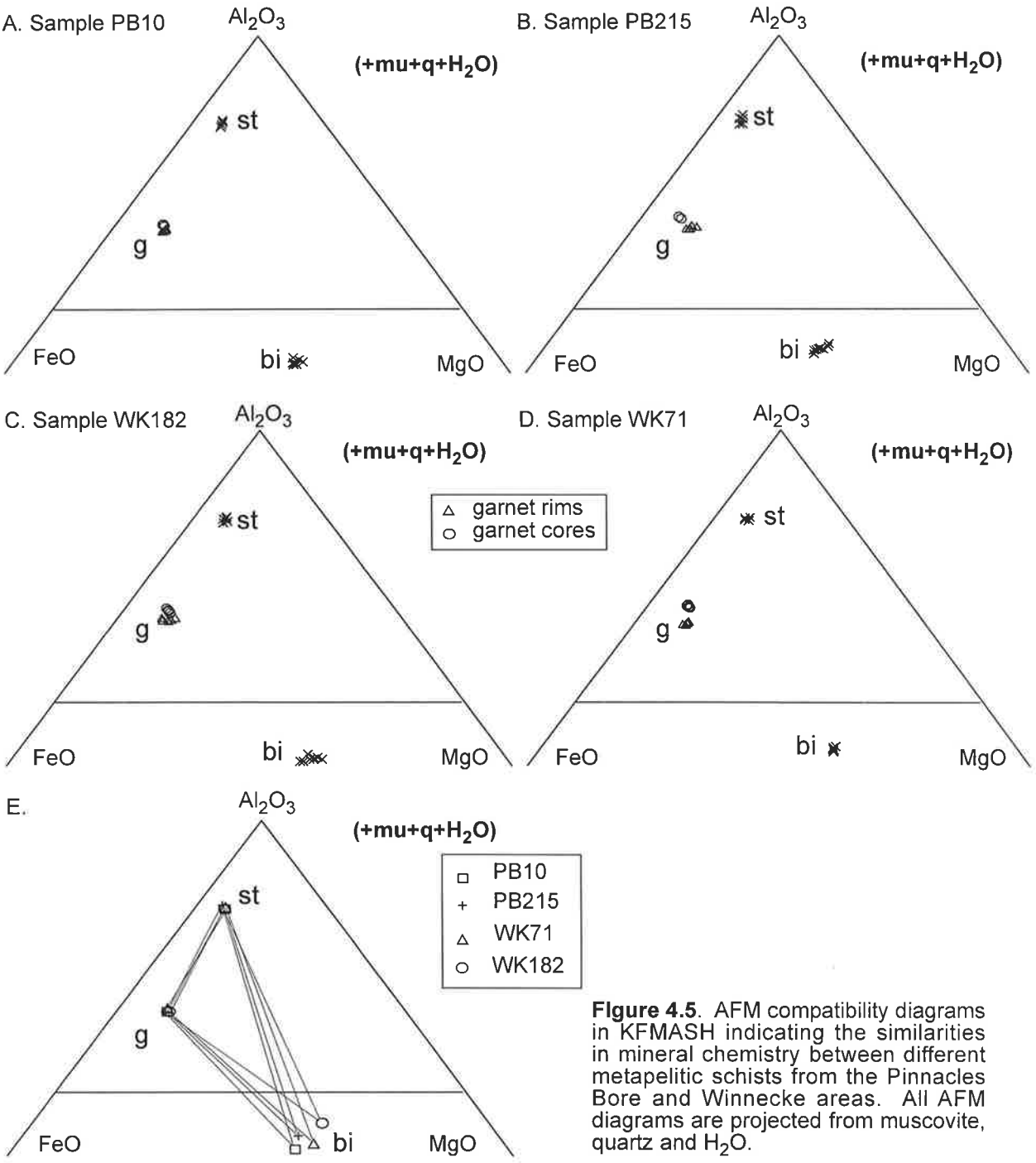

Figure 4.5. AFM compatibility diagrams in KFMASH indicating the similarities in mineral chemistry between different metapelitic schists from the Pinnacles Bore and Winnecke areas. All AFM diagrams are projected from muscovite, quartz and H_2O.

staurolite (0.39-0.44), while biotite grains not in contact with either phase consistently have an XFe of 0.43. *Muscovite* is generally compositionally homogeneous, however muscovites from Erontonga samples are slightly more sodic than Pinnacles Bore samples with paragonite components of about 0.23-0.29 and Al_{VI} of about 1.82-1.86 compared with paragonite at about 0.17-0.21 and Al_{VI} of about 1.80-1.83 respectively. Projected from muscovite, quartz and H_2O onto the Al_2O_3-FeO-MgO plane (Figure 4.5), average compositions of garnet, staurolite and biotite for PB10, PB215, WK71 and WK182 are quite similar, demonstrating the similarities in mineral chemistry and bulk chemistry between these rocks.

4.2.2.2 Mineral chemistry of the calcic metapelites

In all the samples analysed *garnet* is dominantly almandine (55 to 70%) and pyrope (13 to 23%) with a variable but significant spessartine component (from 5 to 20%), and minor grossular (3 to 10%). This chemical variation reflects both differences in bulk composition between samples, and compositional zoning within the individual garnets. The XFe of garnets varies from 0.71 to 0.80 however within samples this value is comparatively static, with individual crystals generally changing by only 0.03-0.05. Chemical zoning in garnet and plagioclase is discussed in more detail in section 4.3.1.3 below.

Staurolite does not display any significant chemical zoning, and has an XFe of 0.75-0.78. *Biotite* is generally chemically homogeneous with no systematic compositional differences noted within individual grains. Biotites from the Pinnacles Bore area are chemically quite similar having an XFe between 0.34-0.39 while biotite in Cadney Metamorphics samples tends to be more Fe-rich with XFe values of 0.40-0.44. *Plagioclase* in the Pinnacles Bore samples is predominantly albitic and zoned, with the albite content increasing toward the rim (rims of ab_{80} to cores of ab_{60}). In the Cadney Metamorphics samples, the same zonation trend is observed but the overall chemistry is more calcic with rim values of ab_{57} compared to core values of ab_{47}.

4.3 Metamorphic evolution of meta-sedimentary schists in the SMC

Since metamorphic rocks are commonly well equilibrated, evidence of previous equilibrium assemblages is often scant and may be confined to relic phases included within younger porphyroblastic minerals. This general lack of preservation of reaction textures and relic assemblages is exacerbated in high variance assemblages as mineralogical effects of varying P-T conditions are often buffered within continuous reactions, leading to changes in the modal proportions and solid solution chemistry of participating phases within multi-variant fields, rather than univariant changes in the mineral assemblage. In the following sections, the metamorphic conditions and P-T paths recorded by the metapelitic sequences from the Pinnacles Bore and the Winnecke-Two Mile Bore areas will be investigated using evidence from chemical zoning in garnets and conventional geothermobarometry. Calculated P-T pseudosections for these rocks and an interpretation of their P-T path from petrogenetic evidence is presented in Chapter 5.

4.3.1 Pressure-temperature paths from zoned garnets

Chemical zoning in metamorphic minerals in low and medium grade rocks, has been widely used to decipher the thermal history of regional metamorphism (see review by Tracy, 1982; Dempster, 1985; Bradshaw, 1991; Chakraborty and Ganguly, 1991; Vance and Holland, 1993; Spear, 1993). Chemically zoned minerals are created when changes in the external physical conditions of pressure, temperature and/or the local bulk composition of the rock causes chemical differentiation of either new material adding to the mineral (growth zoning) or differentiation of a pre-existing mineral via diffusion (diffusion zoning). Thus zoned minerals act as a chemical record of a rock's P-T-X history. While cation diffusion rates in many minerals are too swift to preserve chemical inhomogeneities developed during the rock's metamorphic evolution, slower diffusion rates in garnet can allow maintenance of internal chemical zoning to be preserved to upper amphibolite facies temperatures (Woodsworth, 1977; Cygan and Lasaga, 1985; Freer, 1981, Spear, 1993). Such garnets commonly display chemical zoning in their major element chemistry (i.e. Fe, Mg, Ca and Mn) and the abundances of these cations are frequently distributed in recognisable patterns interpreted to indicate a particular direction of movement through P-T space (e.g. prograde or retrograde metamorphism). Modelling of such chemical zoning in garnet, in concert with applicable Fe-Mg-Ca-Mn continuous reactions between garnet and adjacent phases, is commonly used to establish the general history of prograde and retrograde metamorphism for a given rock (e.g. Hollister, 1969; Selverstone et al, 1984; Dempster, 1985; St Onge, 1987; Whitney and Ghent, 1993).

In the past, evidence for zonation in minerals was determined by one dimensional traverses of quantitative spot analyses across a mineral of interest using an electron microprobe. However two dimensional X-ray images of the relative changes in elemental chemistry across a mineral are more effective in identifying inherent compositional variation than one dimensional quantitative profiles, as they very efficiently identify any minor chemical trends over the entire surface of the subject grain whether the variation be symmetrically or asymmetrically distributed (e.g. Chernoff and Carlson, 1997). These images produce scaled qualitative information on the chemical composition of the subject material, and once the distribution of key chemical variations within different phases in a rock have been identified from such images, quantitative spot analyses can then be performed.

As a first step in examining the metasedimentary schists from Pinnacles Bore and Winnecke, compositional mapping of selected samples was undertaken to identify and interpret the nature of any chemically zoned minerals, particularly garnet, and to enable accurate collection of quantitative data for subsequent geothermobarometry.

4.3.1.1 Methodology

Compositional images were collected using a Cameca SX51 electron microprobe at the Centre for Electron Microscopy and Microanalysis South Australia (CEMMSA), by moving the stage of the electron microprobe by a prescribed increment (usually in the range of 2 to 20 μm spacing) in a grid arrangement and collecting X-ray counts for a selected element on each of the available spectrometers, at each position. Analyses were made at an accelerating voltage of 15 kV and sample current of 500 nA with a dwell time of 10 ms. This data was then processed on a Sun workstation using the image analysis software VISILOG to produce a visual representation of the X-ray data. Each colour pixel represents a data point which has a discrete value for the concentration of the particular element at that spot. The data can also be rescaled in order to visually enhance minor variations in mineral composition in areas of interest.

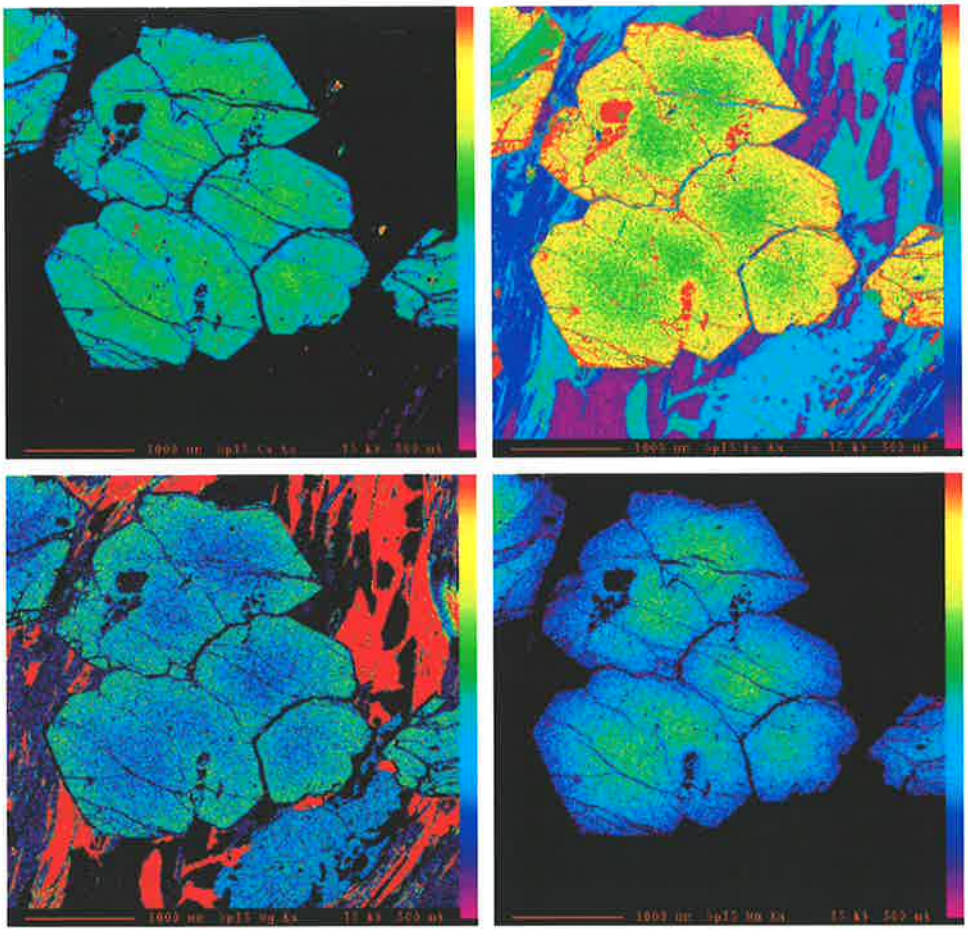

Figure 4.6. Qualitative compositional maps of garnets from the PBSZ: sample PB215, (a) Ca and (d) Mn decrease rimwards; (b) Fe & (c) Mg increase.

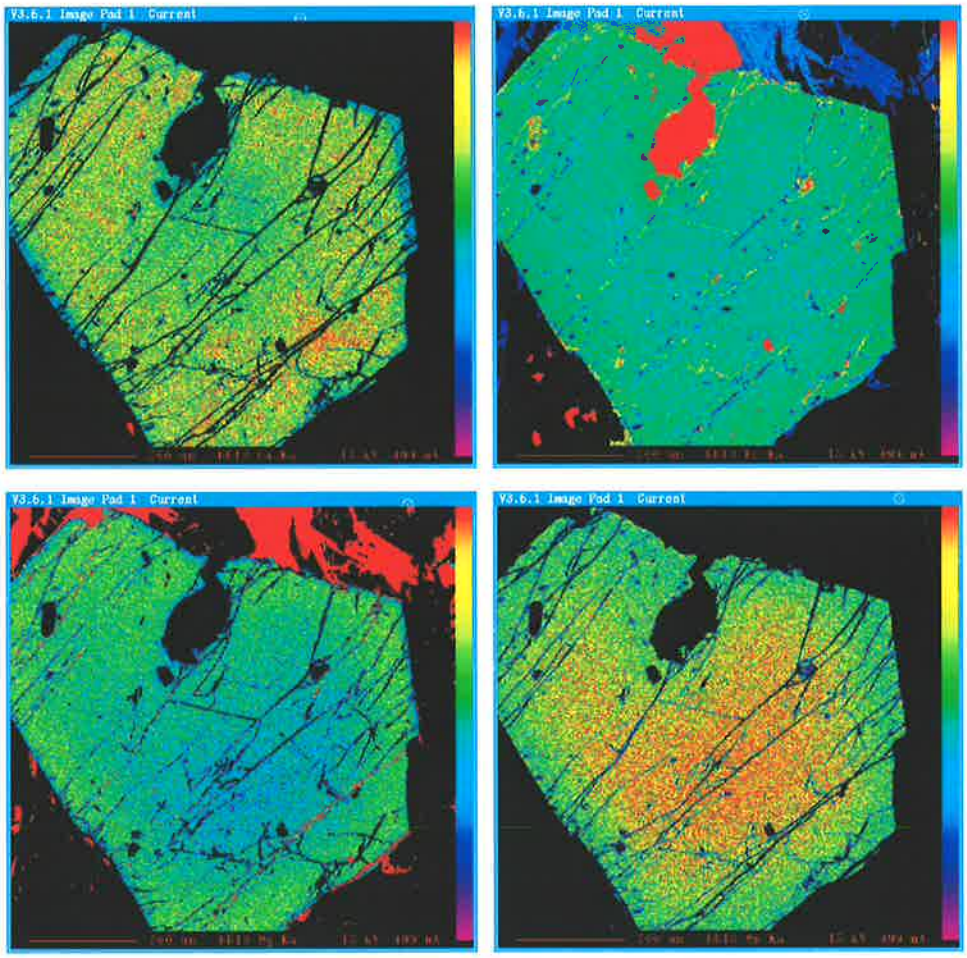

Figure 4.7. Qualitative compositional maps of a garnet from sample PB10 from the PBSZ. Garnets in this rock have zonation patterns generally associated with prograde metamorphism (e.g. Spear 1993). (a) Ca, (b) Fe and (c) Mg increase rimwards while (d) Mn decreases.

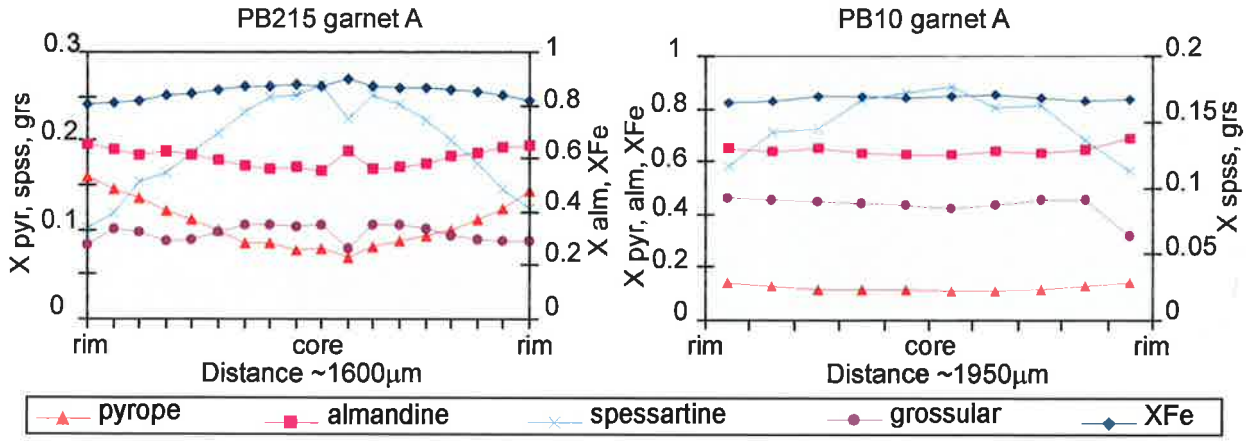

Figure 4.8. Quantitative traverses of garnets presented in Figures 4.6 and 4.7 from samples PB215 and PB10, showing the variation in the amounts of almandine, pyrope, spessartine, grossular and the XFe ratio across the garnet grains.

4.3.1.2 Compositional maps from metapelitic rocks

Pinnacles Bore Shear Zone

Two garnet + staurolite + biotite + muscovite + quartz schists (PB10 and PB215) from the Pinnacles Bore Shear Zone were selected for analysis, with several garnet porphyroblasts from each sample being chosen for compositional mapping. All images from both samples invariably show Mn concentrations declining concentrically toward the rim, while Mg and Fe increase (Figures 4.6 and 4.7) however PB215 garnets have decreasing Ca concentrations rimward while in PB10 garnets Ca increases in this direction. PB10 garnets also display very thin Mn enriched and Ca and Mg depleted rims (<100μm) around the margins of the grains (Figures 4.7 a,c & d) which are not present in PB215 garnets.

Linear traverses of spot quantitative analyses across the garnets show that the XFe (where XFe = Fe/Fe+Mg) of all the garnets decreases rimward (Figure 4.8), and confirms quantitatively the trends demonstrated in the images. While actual amounts of variation in the cation concentrations may not be large, they are still significant with core values of $Alm_{57}Py_9Spss_{24}Gr_{10}$ varying to $Alm_{66}Py_{16}Spss_{10}Gr_8$, at rims of PB215 garnets and values of $Alm_{63}Py_{11}Spss_{17}Gr_8$ in PB10 garnet cores varying to $Alm_{69}Py_{14}Spss_{11}Gr_9$ at their rims.

Winnecke

Compositional maps and quantitative linear traverses from two garnet + staurolite + biotite + muscovite + quartz schists (WK182 and WK71), sampled from two different shear zones in the Winnecke area, also indicate significant chemical zoning in these garnets (Figures 4.10 and 4.11). As in the Pinnacles Bore samples, Mn decreases concentrically rimward while Fe and Mg increase and the XFe decreases. Although Ca concentrations appear generally homogeneous across all the grains, there are some localised areas of Ca enrichment in WK182 garnets. All garnets display thin Ca depleted rims at their very outer margin, and some are similarly Mg depleted. Chemical variation in WK71 garnets ranges from $Alm_{67}Py_{13}Spss_{15}Gr_6$ at rims to $Alm_{51}Py_8Spss_{34}Gr_7$ in cores (Figure 4.9), while in WK182 garnets rim values of $Alm_{66}Py_{14}Spss_{15}Gr_6$ vary to about $Alm_{60}Py_{11}Spss_{22}Gr_7$ in cores (Figure 4.9).

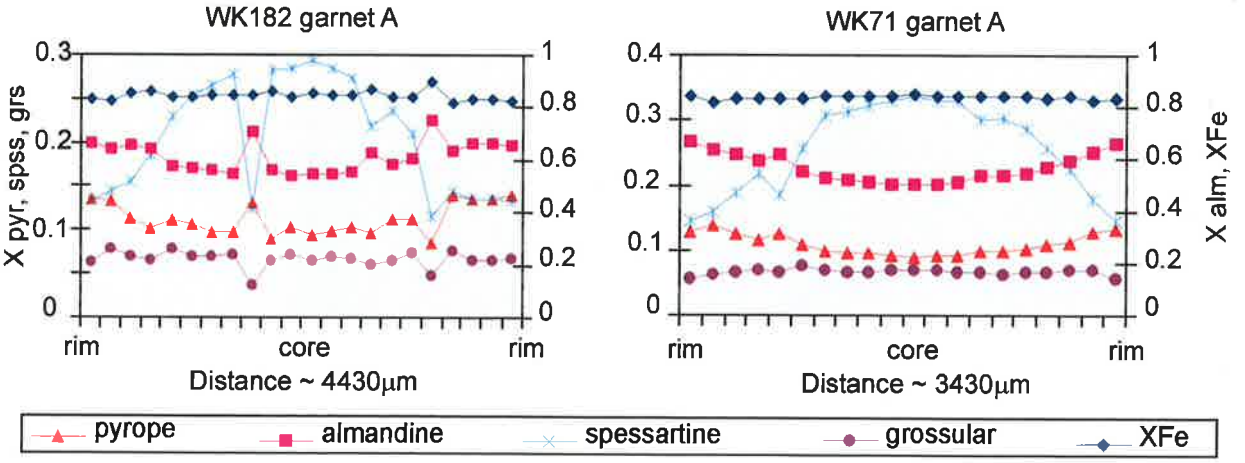

Figure 4.9. Quantitative traverses across garnets from samples WK182 and WK71 from shear zones in the Winnecke area indicating the variation in amounts of almandine, pyrope, spessartine, grossular and the XFe ratio across individual grains.

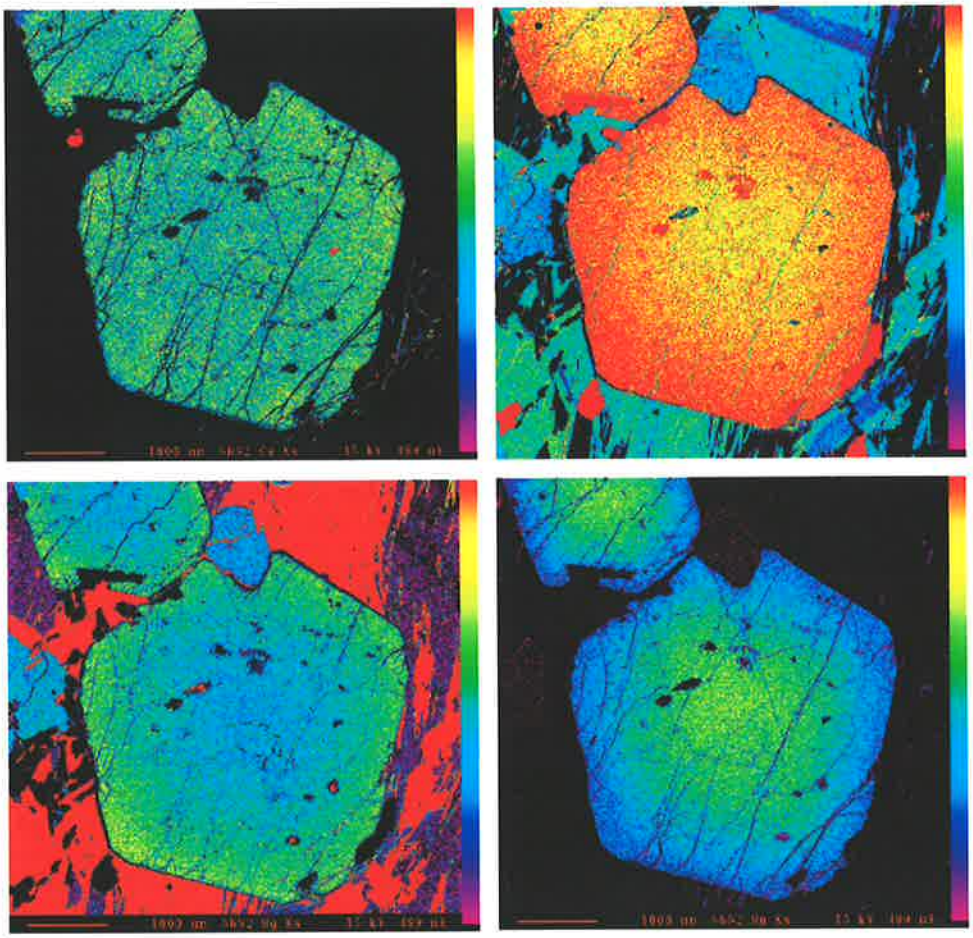

Figure 4.10. Qualitative compositional maps of a garnet from sample WK182, from the ESZ. (a) Ca, (b) Fe and (c) Mg increase rimwards while (d) Mn decreases.

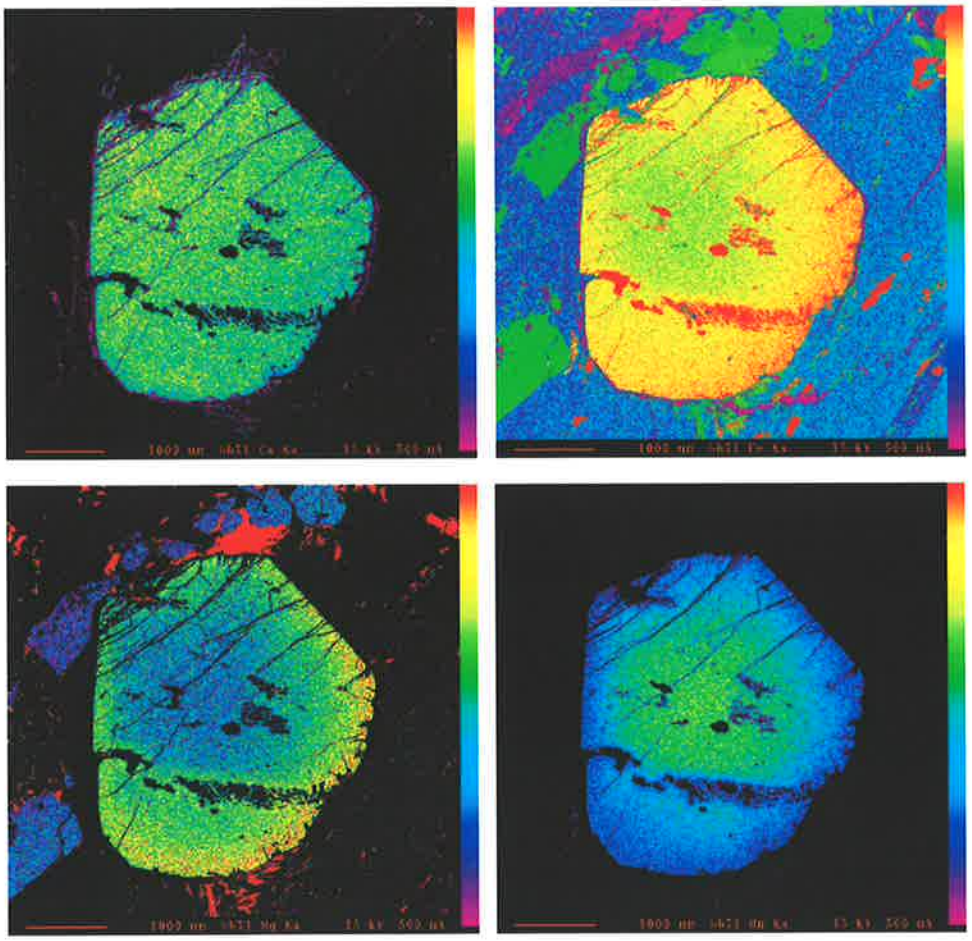

Figure 4.11. A similar trend is observed in these compositional maps of a garnet from sample WK71. Again (a) Ca, (b) Fe and (c) Mg increase rimwards while (d) Mn decreases.

Interpretation

The X-ray images and quantitative traverses produced from garnets from metapelitic rocks of the Pinnacles Bore and Winnecke areas consistently display zonation trends where Mn abundance decreases rimward producing bell shaped profiles, and correspondingly Fe, Mg and XMg increase (Figures 4.6-4.11). In general, bell shaped profiles of Mn in garnet crystals are interpreted to indicate prograde growth zoning, as Mn is concentrated in the growing garnet (e.g. Tracy, 1982; Chakraborty and Ganguly, 1991; Spear, 1993 and references therein). Coincident with the rimward decreases in Mn and Ca, most metapelites generally have rimward increases in Fe and Mg. Depending on the individual P-T path of the rock, the XFe may either increase or decrease (Delor et al, 1984; Dempster, 1985; Banno et al, 1986; St Onge, 1987; Vance and O'Nions, 1990; Spear, 1993; Chernoff and Carlson, 1997; Vance et al, 1998). However in a prograde environment, XFe generally decreases as garnet becomes progressively more magnesian with increasing temperature (Tracy, 1982; Spear, 1993). Thus the variations in major element chemistry in garnets from the Pinnacles Bore and Winnecke metapelites are interpreted to have resulted from garnet growth during prograde metamorphism. This suggests that for these rocks, analyses of mineral rims from the equilibrium assemblage will represent the respective mineral chemistries at or near that of peak metamorphism and consequently provide an estimate of the maximum P-T conditions experienced by the rock.

In addition to the prograde growth zoning trend, garnets from sample PB10 also display narrow rims with increased Mn and decreased Ca and Mg (Figure 4.7). Such reversals in the bell shaped trend associated with a prograde P-T path are common (e.g. Dempster, 1985; St Onge, 1987; Vance and O'Nions, 1990; Bradshaw, 1991; Nzenti, 1992; Ikeda, 1993). The mechanics producing 'reverse zoning' have been widely discussed (Grant and Weiblen, 1971; Kretz, 1973; De Bethune et al, 1975; Loomis, 1983; Tracy, 1982; Chakraborty and Ganguly, 1991) with two end member scenarios being used to explain this phenomenon namely, 1) zonation via garnet growth during retrograde metamorphism with Mn sourced from the break down of another phase or 2) via intracrystalline diffusion during retrogression where garnet is resorbed to produce biotite and/or chlorite and Mn is concentrated in the residual garnet. In the case of the PB10 garnets, the reverse zoned profiles are interpreted as evidence of the retrograde cooling path of the rock, created predominantly via intracrystalline diffusion within garnet.

4.3.1.3 Compositional maps from calcic metapelitic rocks

Pinnacles Bore Shear Zone

Compositional maps of three plagioclase-bearing metapelitic schists from Pinnacles Bore (PB11, PB12 and PBS3) indicate that chemically zoned garnets are also present in these rocks. The resultant maps from all three samples are not consistent with a simple growth zoning pattern, and delineate an apparent decoupling in the distribution of Ca with respect to Fe, Mg and Mn. While these latter three cations are generally smoothly distributed across the garnets with relatively minor variations toward grain margins, Ca contents are more variable, with relatively uniform regions cut by Ca-rich rims and linear domains which appear to be fractures within existing garnet porphyroclasts (Figures 4.12 - 4.14). Quantitative traverses across the garnets produce reasonably flat profiles for all the cations, with most variation occurring toward the rims (Figure 4.15). Detailed quantitative traverses across these enriched Ca rims however, show that almandine, spessartine and the XFe tend to increase rimward in concert with grossular while pyrope declines rimward. Overall, trends in the distribution of Ca in these zones of enrichment are generally quite closely mimicked by the other cations and the XFe ratio.

Interpretation

The overall trends in garnets from the calcic metapelites are more difficult to interpret than those of the plagioclase-absent schists. There is little evidence of any significant internal chemical zoning in the garnets from the calcic metapelites unlike those from the plagioclase-absent metapelites, with variations in Fe, Mg and Mn effectively confined to the Ca-rich zones. The Ca-rich zones, unlike the minor retrograde rims observed in the plagioclase free schists, are not confined to garnet margins but occur throughout the grains along what appear to be annealed fractures. This is interpreted to indicate that these zones arise from the subsequent growth of new or re-equilibrated garnet over existing older garnet porphyroclasts, rather than simple retrogression associated with a single period of metamorphism. Quantitative profiles of plagioclase show relatively homogeneous anorthite/albite compositions with a consistent trend toward anorthite depletion at plagioclase rims, particularly when adjacent to garnet, suggesting that garnet and plagioclase rim compositions are in equilibrium (Figure 4-16).

Homogeneous compositional profiles can occur during high temperature granulite facies metamorphism (e.g. Tracy, 1982; Mezger et al, 1992; Erambert and Austrheim, 1993; Becker, 1997) as a consequence of faster diffusive processes enabling cores of garnet porphyroblasts to maintain equilibrium with changes in the external matrix chemistry (Spear, 1993). It is possible that the cores of these garnets lack significant compositional zoning because they are relict high-temperature granulite facies garnets inherited from the Palaeoproterozoic precursor granulites from which the amphibolite facies schists developed. Thus the narrow Ca-rich rims are potentially the only portions of the garnets forming part of a Palaeozoic equilibrium assemblage with the external Alice Springs Orogeny generation matrix phases. This scenario might account for the older Sm-Nd age of 1578 ± 36 Ma produced from sample

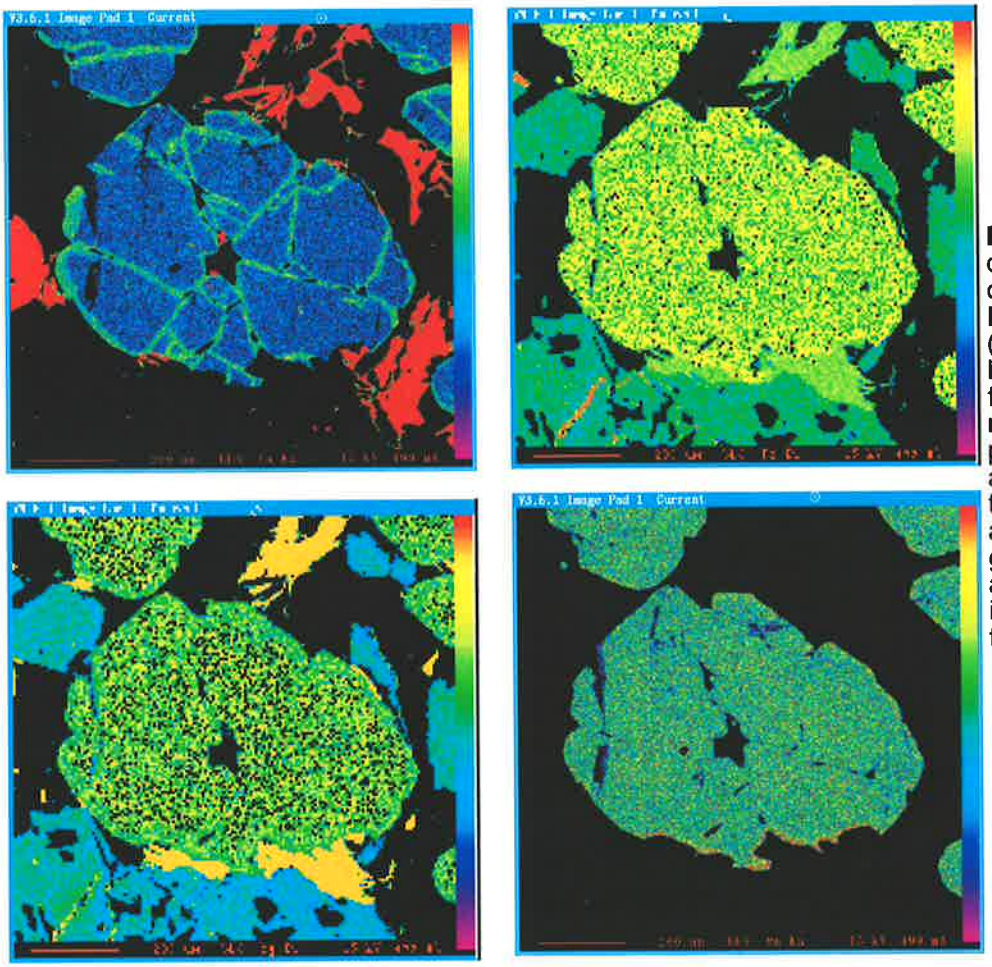

Figure 4.12. Qualitative compositional maps of a garnet from sample PB11 from the PBSZ. (a) Ca appears essentially homogeneous except for a narrow enriched margin around the garnet perimeter and within apparent fractures within the grain; (b) Fe, (c) Mg and (d) Mn are also homogeneous across the grain although Mg decreases in a narrow margin around the rim while Mn increases.

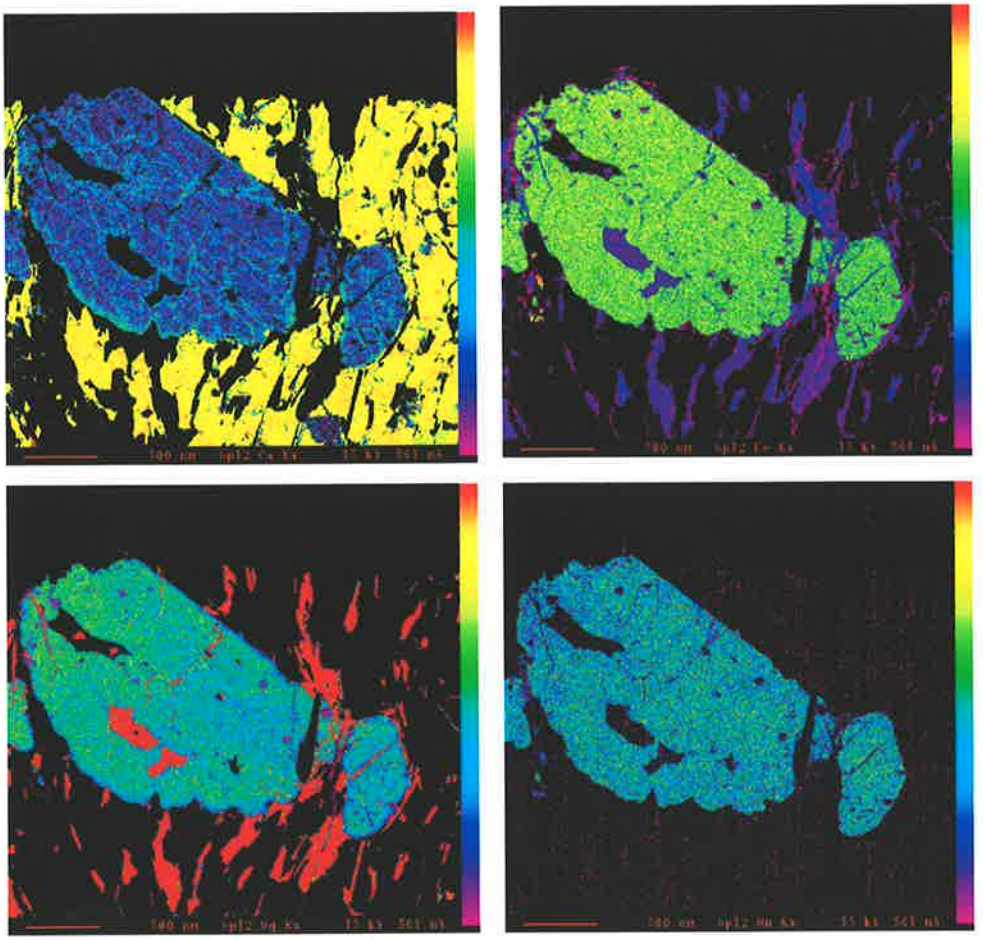

Figure 4.13. Sample PB12 from the PBSZ. (a) Ca; (b) Fe; (c) Mg; (d) Mn.

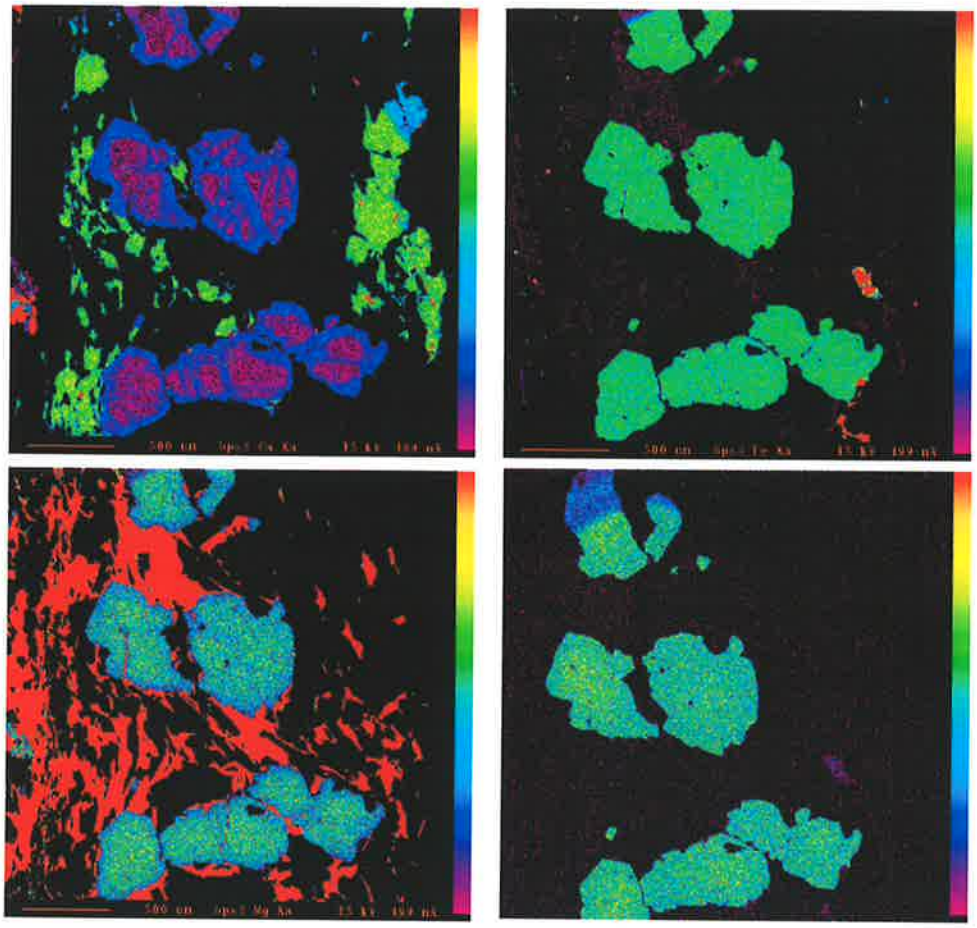

Figure 4.14. Qualitative compositional maps of garnets from sample PBS3, also clearly show the presence of Ca-rich domains around and within garnet grains as noted in PB11 and PB12. (a) Ca; (b) Fe; (c) Mg; (d) Mn.

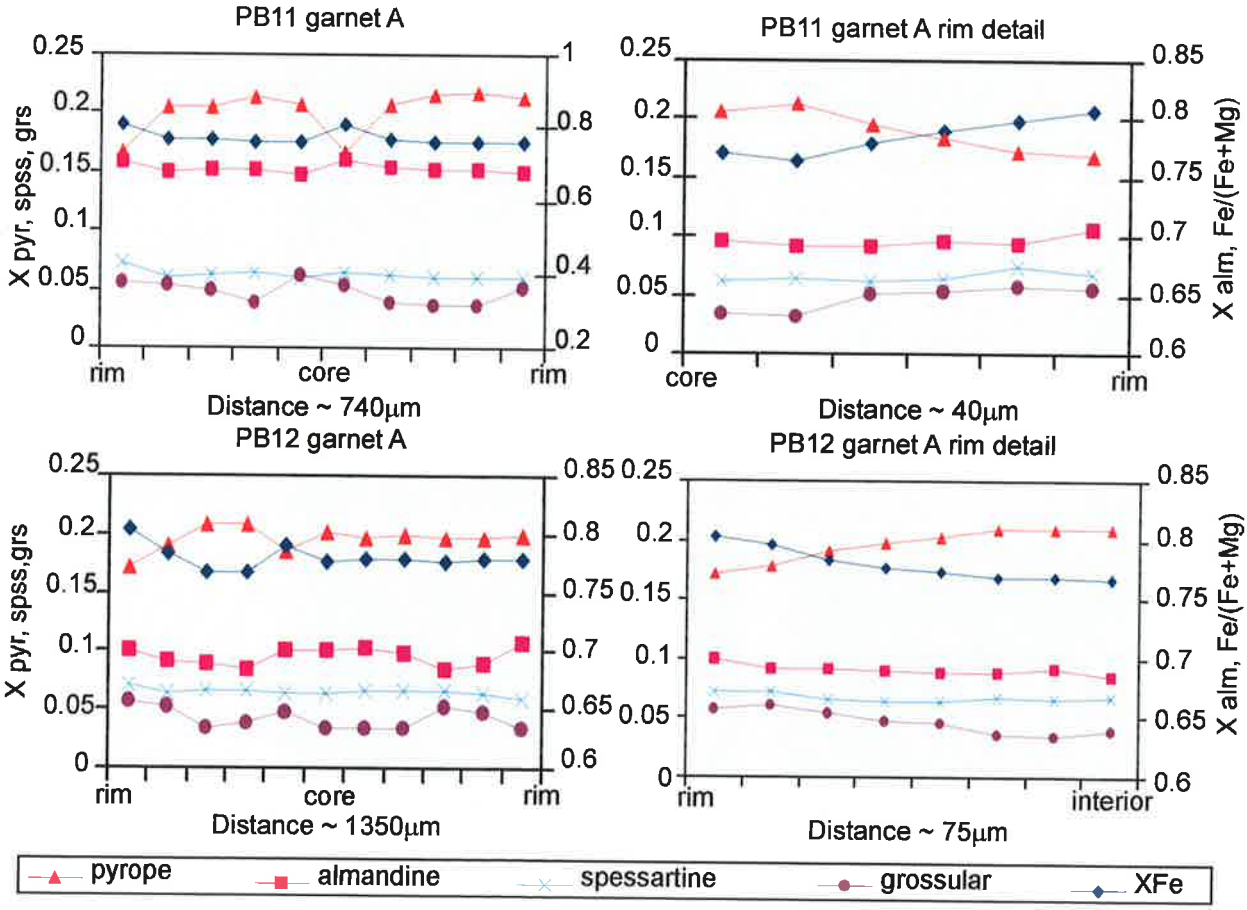

Figure 4.15. Quantitative traverses across garnets from PB11 and PB12 showing the variation in garnet composition overall and in detail across the Ca-enriched rims noted in the qualitative maps.

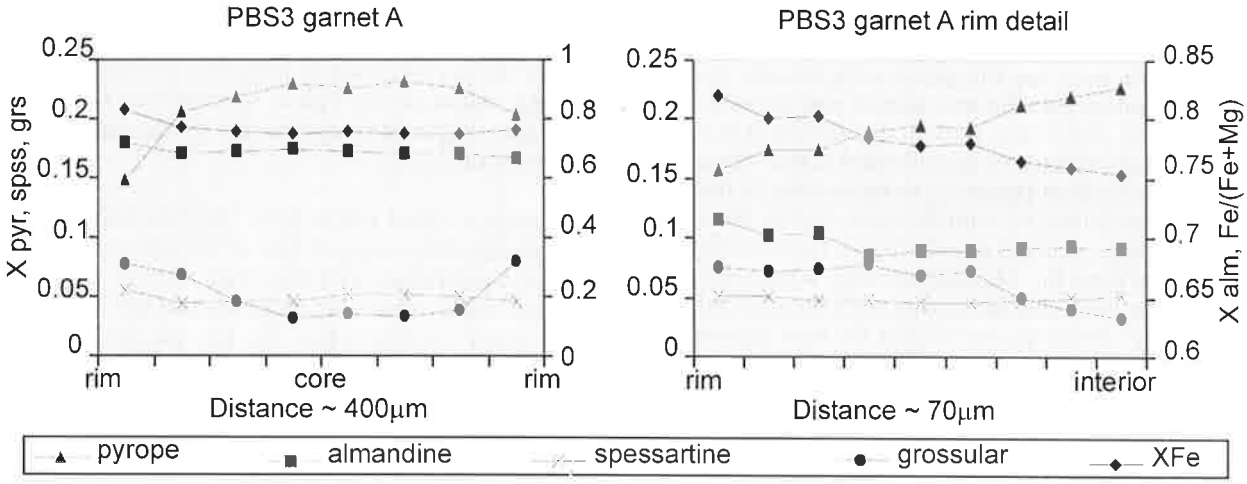

Figure 4.15 (cont). Quantitative traverses across a garnet from PBS3 showing the variation in garnet composition overall and in detail across the Ca-enriched rims noted in the qualitative maps.

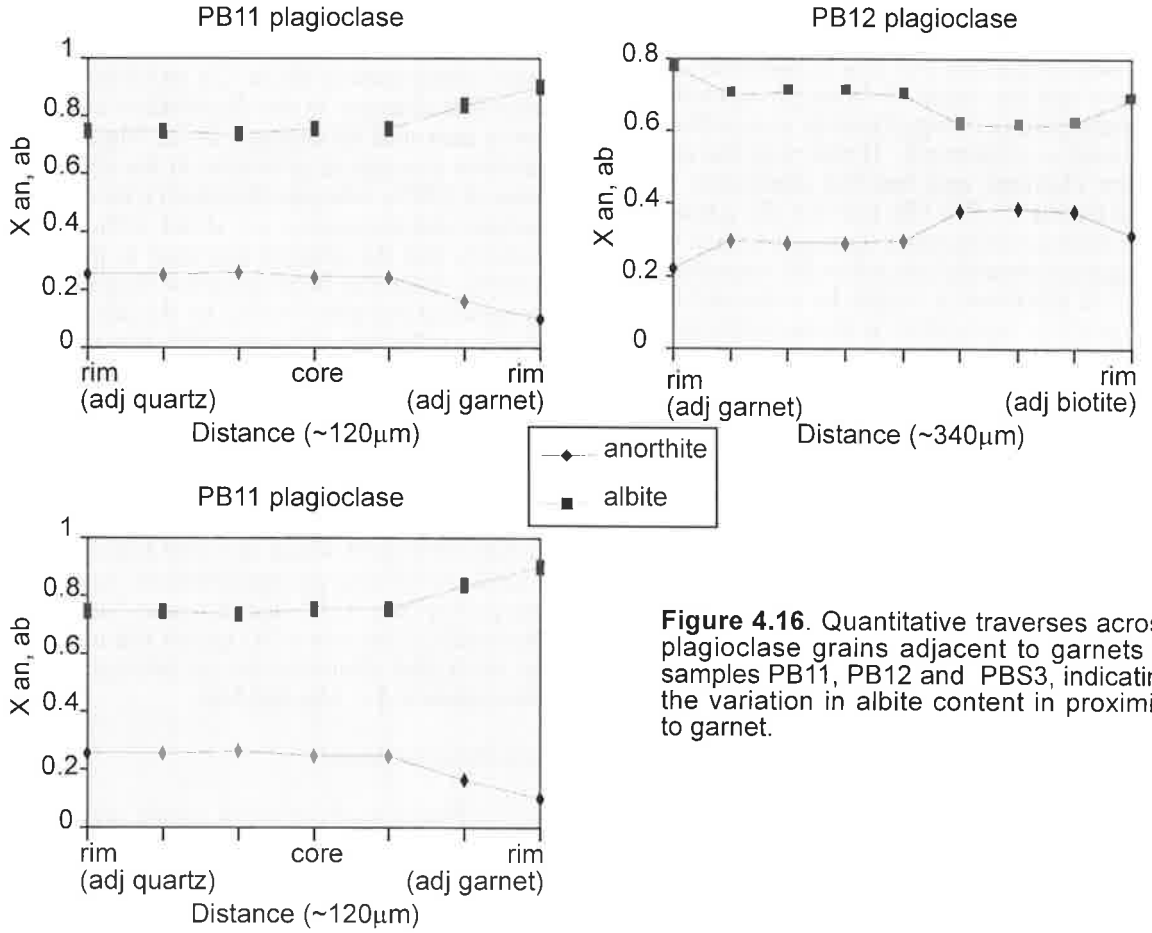

Figure 4.16. Quantitative traverses across plagioclase grains adjacent to garnets in samples PB11, PB12 and PBS3, indicating the variation in albite content in proximity to garnet.

PB11, as the relic cores volumetrically comprise most of the garnet grain and would dominate the mineral's radiogenic Nd signature unless the Sm content of the rim garnet was exceptionally high compared to the core. In this instance, the small amount of new garnet present in the rims and fractures, as indicated by the Ca-rich zones, may record only a minor portion of the ASO P-T path or may indicate that P-T conditions during this event were not amenable to the growth of volumetrically large amounts of garnet in these rocks.

Variations in Fe, Mg and the XFe across the Ca enriched zones (Figure 4.15) are consistent with a cooling path, however the growth of new garnet suggests that isomodes of garnet increased, and increases in Ca are often associated with increasing pressure although this can occur in a regime of either increasing or decreasing temperature (Bohlen and Liotta, 1986; Kohn and Spear, 1990; Spear et al, 1991; Eckert et al, 1993; Spear, 1993; Menard and Spear, 1993). There are a number of interpretations possible to account for the chemical zonation profiles expressed in the garnets from the Pinnacles Bore calcic metapelites, within the framework of the Ca enriched zones representing new garnet produced during the ASO. Firstly the observed variations in Fe, Mg, Mn and Ca within the rims may represent

chemical equilibrium during part of the ASO P-T path. Alternatively Ca may be decoupled from Fe, Mg and Mn such that the garnet core records its relic Ca distribution and the new garnet rim records a Ca distribution reflecting growth during the ASO, but Fe, Mg and Mn have re-equilibrated across the entire grain and the distribution of these cations in the rim reflects continued re-equilibration during the ASO cooling path. A final possibility is that Ca may be decoupled from Fe, Mg and Mn only within the new garnet rim, such that the garnet core records only its older relic chemistry but within the new garnet rim Ca records part of the early P-T path of garnet growth during the ASO while Fe, Mg and Mn have remained open to diffusion and re-equilibrated during the cooling path of ASO metamorphism.

Mineral assemblages in the ASO-aged shear zone rock are of mid-amphibolite facies suggesting that maximum temperatures during this orogeny did not reach much above about 600°C (see §4.2.1). Garnets in the Pinnacles Bore calcic metapelites are generally coarse-grained (~2 mm in diameter) and it is unlikely that the cores of these garnets would be able to completely or significantly re-equilibrate in such a cool environment. If this was the case, then major element and Sm-Nd chemistry (as evidenced by the ~1580 Ma age for the garnets) must have become completely decoupled, such that Sm-Nd in garnet remained closed to diffusion during the ASO. In addition, it might be expected that chemical profiles equivalent to those noted in the feldspar-absent metapelitic schists would also be observed in these rocks, which is not the case.

It is apparent that the calcic metapelites have a relatively calcium enriched bulk composition compared with the other metapelites, which probably reflects differences in the original bulk chemistry and mineralogy of the rocks' granulitic precursors, and interaction with subsequent metasomatic processes. The adjacent metapelitic granulites consist of two assemblages, either cordierite + orthopyroxene + biotite + quartz or cordierite + orthopyroxene + biotite + garnet + quartz, with the garnet-bearing varieties being generally less abundant. If the calcic metapelites are derived from the garnet-bearing granulites, it may be that the kinetics of garnet growth during the ASO was moderated by the presence of pre-existing granulite facies garnets. The presence of relic garnet may have effectively altered the bulk composition of the rock to preclude significant garnet growth during the ASO since much of the material required to produce new garnet was already locked up in the existing garnet porphyroclasts. In contrast, if the plagioclase-absent metapelites are derived from the garnet-absent granulites, then they did not have an intrinsic bulk composition amenable to garnet growth. However given that neither granulite assemblage is particularly Na or K rich and that they are anhydrous granulites it is likely that there was a significant metasomatic influence subsequent to granulite facies metamorphism which introduced Na and K (as a minimum) to the system and may have affected the bulk composition of the precursor metapelites. Therefore it may be that while garnet growth in the calcic metapelites was limited during the ASO, the bulk composition of the metapelites was amenable to voluminous garnet growth which enabled the preservation of prograde growth zoning patterns, while in the calcic metapelites the only newly grown garnet is represented by the narrow Ca enriched rims.

The compositional maps from the Pinnacles Bore calcic metapelites suggest that in the garnet rims Ca is not in equilibrium with the other cations, and that diffusion has to some extent diminished the variation in the other cations while Ca has maintained an original compositional distribution. This implies that Ca has become decoupled from equilibrium exchange with the other cations as a result of differing rates of diffusion. The phenomena of apparent disequilibrium in Ca is not uncommon (e.g. Crawford, 1977; Sakai et al, 1985; Chernoff and Carlson, 1997) and Fe, Mg and Mn are generally believed to be more mobile than Ca (Chakraborty and Ganguly, 1991; Spear, 1993; Schwandt et al, 1996; Becker, 1997). However inspection of the quantitative analyses taken across these Ca enriched zones indicates that changes in the distribution of the Ca content is mirrored by changes in Fe, Mg and Mn. The relative increase in grossular in the rims is on the order of 200%, whereas the relative increases in spessartine and almandine are about 33% and 3% respectively and the relative decrease in pyrope is about 25%. Thus the large apparent magnitude of the Ca enriched margins implied by the images may actually be a reflection of the overall low proportions of Ca present in these garnets compared with the other cations, so that the relative change in Ca is much greater across these areas than for any other cation and is exaggerated by scaling during the imaging process. If Ca has decoupled from Fe, Mg and Mn in the garnet rims, preserving an earlier part of the ASO P-T path while the distribution of the latter cations reflects re-equilibration during the cooling path of the ASO, then it seems fortuitous that the width of the new ASO garnet rim coincides neatly with the dimensions of retrograde re-equilibratation in Fe, Mg and Mn.

Cadney Metamorphics

Unlike the Pinnacles Bore rocks, calcic metapelites from the Cadney Metamorphics do not display Ca enrichment textures adjacent to rims or fractures in garnet, but instead appear to have relatively smooth chemical zonation across the garnet crystals, although they can be asymmetrically distributed (Figures 4.17 & 4.18). In garnets from sample 1088-20 a garnet-biotite-kyanite-plagioclase-quartz-sillimanite schist, (Figure 4.17) Mg concentration increases slightly rimward then at the grain margin decreases while Fe concentration continually increases with a slightly higher value at the rim. Mn and Ca decrease rimward with equivalent increases at the margin, however Ca is more erratic with very minor changes overall across the garnet. The XFe ratio decreases slightly and also increases at the very margin. These chemical trends in the compositional maps and traverses closely resemble those observed in garnets from the plagioclase-free schists which are interpreted as a

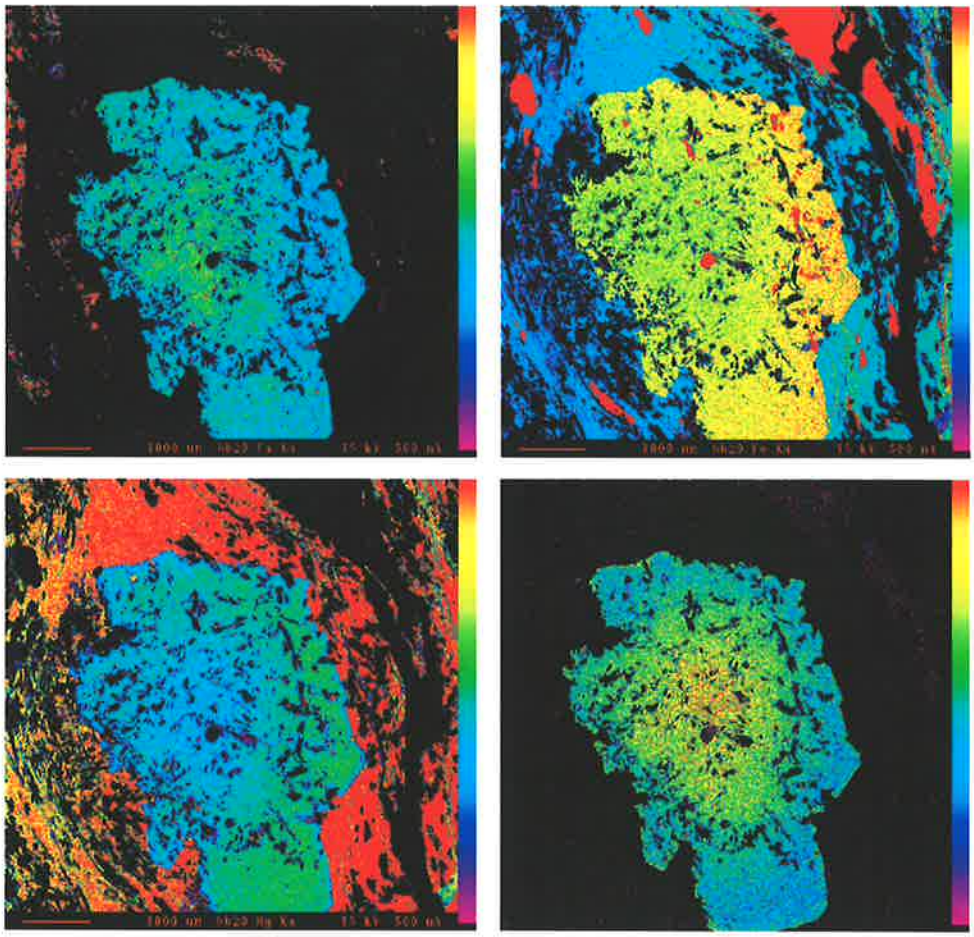

Figure 4.17. Qualitative compositional maps of garnet in sample CM20 from the Cadney Metamorphics. (a) Ca and (d) Mn decrease rimwards; (b) Fe and (c) Mg increase.

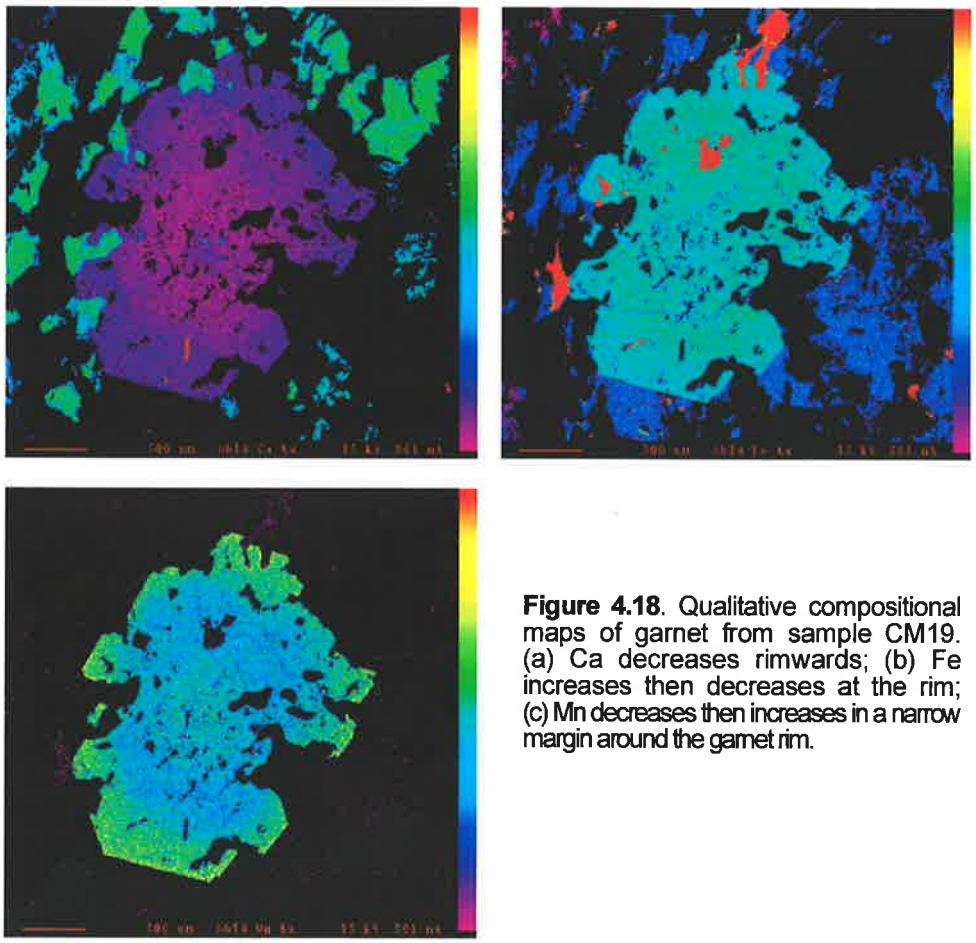

Figure 4.18. Qualitative compositional maps of garnet from sample CM19. (a) Ca decreases rimwards; (b) Fe increases then decreases at the rim; (c) Mn decreases then increases in a narrow margin around the garnet rim.

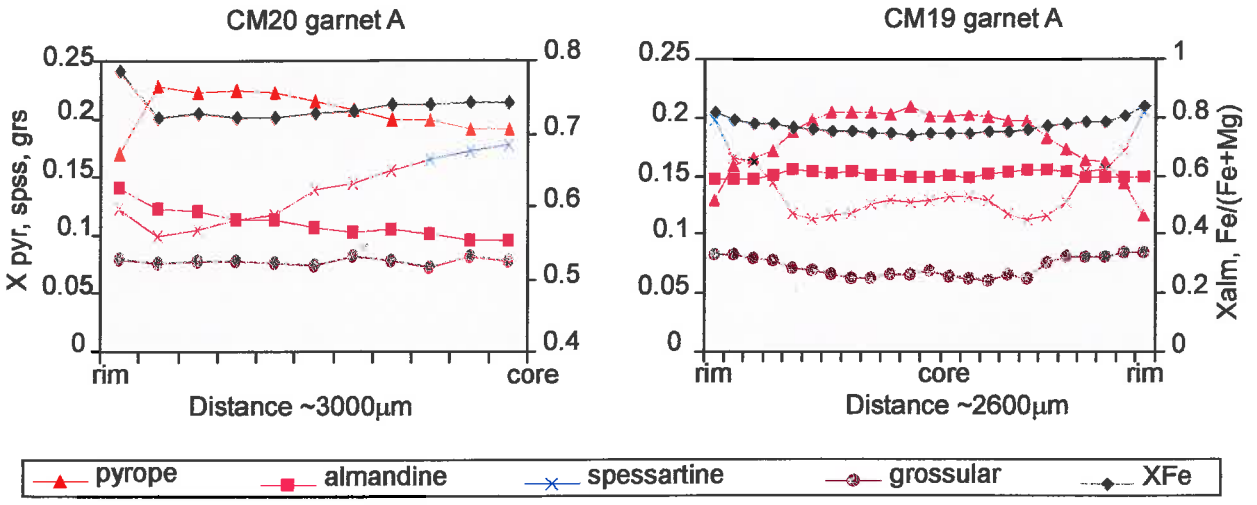

Figure 4.19. Quantitative traverses of garnets presented in Figures 4.14 and 4.15 from samples CM20 and CM19 showing the variation in almandine, pyrope, spessartine, grossular and the XFe ratio across the garnet grains. Note the pronounced 'humps' in the distribution of almandine, spessartine and grossular either side of the garnet core area.

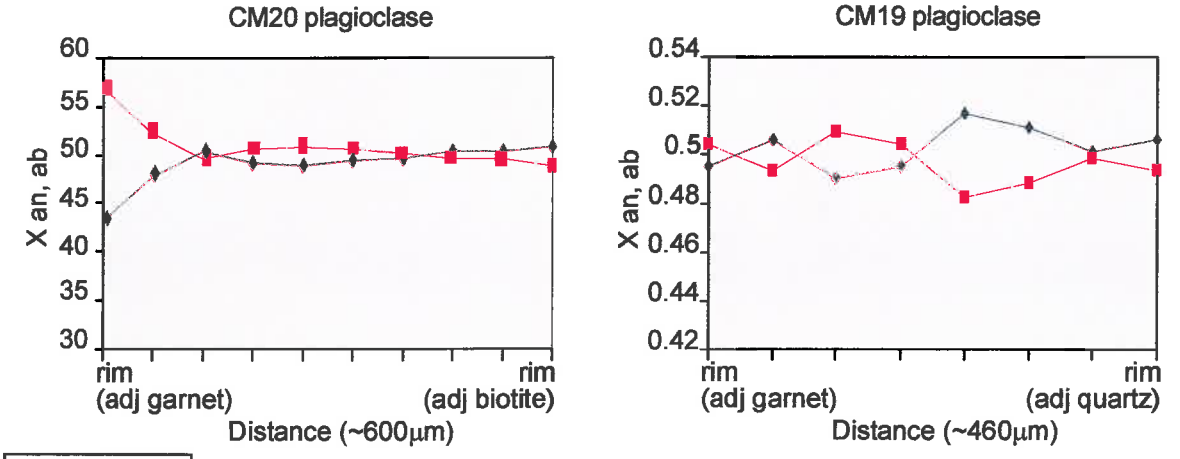

Figure 4.20. Quantitative traverses of plagioclase grains adjacent to garnets in samples CM20 and CM19 demonstrating the influence of garnet proximity on the variation in albite content.

growth zoning profiles with some retrogression recorded by the rim, and are in sharp contrast to the other plagioclase-bearing schists examined above which appear to have more complicated chemical distributions. Plagioclase is the only other phase in the assemblage which is significantly zoned. In the compositional maps (e.g. Fig 4.18 a), the interior of plagioclase grains are more calcic than the rims. Quantitative traverses across plagioclase confirm this and indicate that the level of Ca depletion in rims is quite narrow and allied to proximity to garnet (Fig 4.20). This is consistent with the observation of minor Ca enrichment at the very margins of the garnets.

Sample CM19, in hand sample appears almost identical to CM20 and yet produces quite different asymmetrically distributed chemical zonation maps (Figure 4.18). In CM19, Ca appears approximately homogeneous in the interior of garnets and then increases asymmetrically rimwards, Fe is also apparently homogeneous with a weak decrease at the rim. Mn generally decreases rimward then displays a reverse zoning trend with Mn increasing rimward. In sample CM20 the reverse zoning trend in Mn is interpreted as indicating retrograde conditions, however the Mn enriched rim in CM19 is much more developed. Linear traverses of spot quantitative analyses in garnets from CM19 provide more detail (Figure 4.19), and show Mn and Ca both decreasing slightly from the cores then, about halfway to the rim at an obvious point of inflection, beginning to increase. Mg generally decreases rimward however at the same inflection point a marked decrease in Mg concentration is observed. Fe initially increases across garnet cores and then begins to decrease at the rim after a significant increase in concentration at the same inflection point noted for the other cations. XFe always increases rimward but also shows a change in the rate of increase at these same inflection points. These inflection points are noteworthy as they are observed as pronounced 'humps' in the chemical profiles corresponding to the location of rim initiation seen in the maps. They suggest that the garnets in CM19 do not record a simple path of prograde growth, but a potentially complex trajectory through P-T space possibly including a period of later overgrowth on an older garnet core rather than simple retrograde re-equilibration. The potential change from relic core to new overgrowth garnet may be denoted by the inflection point in the profile

which is interpreted as a chemical step between the two separate garnet generations. To some extent the complex chemistry of the garnets is mimicked in plagioclase. As observed in the compositional maps from CM20, plagioclase in CM19 also shows Ca depletion at the rim compared with the interior (Figures 4.17a and 4.18a), however data from linear traverses (Figure 4.20) indicates that this is not a smooth trend as noted in plagioclase from CM20. Chemical profiles of the interiors of CM19 plagioclases are quite erratic and can vary significantly within and between individual grains. The only consistency is for Ca depletion of plagioclase rims, which is compatible with Ca trends observed in the rims of garnets.

Interpretation

Garnets from both Cadney Metamorphics samples share an irregular morphology with areas which are anhedral, and others with well developed crystal faces. The garnet cores and anhedral margins contain abundant kyanite inclusions while the euhedral margins have quite wide rims which are either inclusion free or contain comparatively fewer inclusions (e.g. Figures 4.3 c and 4.4 f). The presence or absence of inclusions is mirrored by the asymmetry in the chemical zonation patterns. This is particularly evident in Figure 4.18 c, where Mn decreases in the inclusion-rich core and rim portions of the garnet and increases in the inclusion-free garnet. The precursors from which the metapelitic shear zone schists developed are generally cordierite + biotite + quartz ± (feldspar, garnet, orthopyroxene, sillimanite) granulite gneisses, and the presence of sillimanite in the cores of garnets might be interpreted as indicating that they are inherited relic granulite garnets. However in the Cadney Metamorphics samples, randomly oriented kyanite inclusions are observed in the cores of both CM20 and CM19 garnets (Figures 4.3 c and 4.4 f) and in sample CM19, matrix sillimanite penetrates the rims of the garnet porphyroblasts and is continuous with the external fabric (Figure 4.4 f). This suggests that the garnets grew in an environment where initially only kyanite was stable, followed by the stable coexistence of both kyanite and sillimanite, and finally to the stability of sillimanite only. Throughout the Strangways Metamorphic Complex, Palaeozoic metapelitic schists usually have kyanite as the stable aluminosilicate mineral, but sillimanite rather than kyanite is generally recorded as the stable aluminosilicate mineral in Proterozoic SMC granulite-facies rocks (e.g. Iyer, 1974; Goscombe, 1992a & b; Norman, 1991). However at both Pinnacles Bore and the Yambah Schist Zone, rare fine-grained sillimanite occurs late in the reaction sequence in the ASO schists, overprinting the garnet-staurolite-biotite-kyanite-quartz assemblages in conjunction with the growth of muscovite (Figures 4.3 a, 4.4 e and 6.3 d & e), suggesting that metamorphic conditions during the ASO did move into the sillimanite field. In both shear zone samples from the Cadney Metamorphics, sillimanite is abundant in the matrix and appears to coexist with kyanite, although it appears to have continued to grow later than kyanite (Figures 4.3 b and 4.4 g & h). These observations are consistent with the interpretation of simple prograde zoning profiles in garnets from sample CM20, resulting from the development of these assemblages during progression along a clockwise path in P-T space. The complex chemical profiles observed in CM19 however are not as easily resolved.

It is likely that the samples from the Cadney Metamorphics have experienced a common P-T history, and that matrix phases in both samples reflect local metamorphic conditions associated with the ASO. Evidence from garnets in sample CM20 suggest they record simple prograde zoning associated with crystallisation during a single metamorphic event. This implies that diffusive processes have been more effective in eradicating the compositional step which identifies the hiatus between relic garnet cores (either Proterozoic or early ASO) and overgrown (later ASO) rims in sample CM19. Therefore, while the compositional maps and petrography give an indication of where the boundary between the new and relic garnet occurs in sample CM19, it is impossible to know whether quantitative spot analyses across this boundary reflect equilibrium at all. As such only quantitative analyses across the garnet rim up to this chemical step can be used with any confidence to investigate conditions associated with the latest stage of garnet growth.

4.3.1.4 Synopsis of Discussion on Compositional Maps

Garnets in the feldspar-absent metapelitic schists from Pinnacles Bore and Winnecke appear to display significantly different chemical zonation profiles from those of the calcic metapelites from the same or adjacent areas. Compositional images and quantitative traverses of garnets in metapelitic schists from Winnecke and Pinnacles Bore are interpreted to indicate prograde growth of garnet in these rocks. This implies that the metapelitic schists have totally re-equilibrated during the ASO and can thus be used with a reasonable degree of confidence for geothermobarometry. In contrast, garnets from calcic metapelites show complex compositional patterns, not generally indicative of classic growth or reverse zoning models. The complexity of garnet chemical profiles from calcic metapelites, suggests that their different initial bulk compositions and starting mineralogy, compared to those of the plagioclase-absent rocks, has significantly affected their response to a common P-T environment.

4.3.2 Metamorphic conditions from Conventional Geothermobarometry

In order to assess the pressure and temperature conditions associated with metamorphism of the metasedimentary schists in the Strangways Range during the ASO, a selection of conventional geothermobarometers, utilising various calibrations of Fe-Mg exchange between garnet and biotite (as presented in the computer program Thermobarometry V2.1 by Spear and Kohn, 1998), garnet-aluminosilicate-quartz-plagioclase and garnet-plagioclase-biotite-quartz equilibria, were applied

to assemblages which display textural equilirium in a number of samples from the study areas. In addition reactions between Fe and Mg endmember phases for garnet-biotite pairs were calculated using the computer program THERMOCALC V2.6 (calculation mode 3) (Powell and Holland, 1988) and a recent version of the internally consistent thermodynamic dataset of Holland and Powell, (1998b). An example of the output files produced by THERMOCALC for this type of calculation is presented in Appendix 3.2, and summaries of all thermobarometry results are tabulated in Appendix 4.

Calculations performed on rim assemblages from the plagioclase-absent metapelites use analyses from the margins of contacting equilibrium assemblage phases. In these rocks, garnets rarely contain useful included phases and those present are generally quartz, magnetite and ilmenite, therefore calculations on garnet cores are coupled with analyses from the cores of adjacent coarse grained biotite. Pressure estimates using standard geobarometers were not performed on the plagioclase-absent metapelites, as most existing geobarometers utilise plagioclase and/or an aluminosilicate phase.

The complex chemical profiles displayed by garnet and plagioclase in the calcic metapelites complicates the application of geothermobarometry to these rocks. The Pinnacles Bore samples have been interpreted to either contain relic Proterozoic garnets, or re-equilibrated Proterozoic garnets, with very narrow secondary Palaeozoic overgrowths. Therefore calculations on these rock utilise selected rim assemblages as well as interior analyses, measured within the Ca enriched zone close to the beginning of the zone, and core assemblages to try to determine if either interpretation is supported. The Cadney Metamorphics calcic metapelites have been interpreted as containing either relic Proterozoic or relic older Palaeozoic garnets, which have partially or completely re-equilibrated during the ASO. In these rocks, rim and core analyses of all the available phases have been used in calculations to assess this interpretation.

4.3.2.1 Results from the Pinnacles Bore Shear Zone

For the Pinnacles Bore samples, results from garnet-biotite pairs using cation exchange geothermometers and mode 3 in THERMOCALC are in close agreement, and consistently indicate that temperatures estimated from rim assemblages are higher than those from core assemblages (see Tables A4.1 and A4.2). Calculations from sample PB215 produced rim temperature estimates in the range of about 540-590°C, with core temperature estimates ranging beteween about 430-500°C. PB10 recorded a similar range of rim temperature estimates at about 570-595 °C, but higher core temperature estimates than PB215 ranging between about 520-560°C. These results are consistent with the interpretation made from the compositional maps that these garnets are growth zoned, and therefore rim assemblages will record peak or near peak metamorphic conditions.

4.3.2.2 Results from Winnecke

Calculations on the Winnecke samples also produced temperature estimates indicating higher rim temperatures than core temperatures. In sample WK71 estimates from garnet-biotite exchange thermometers and THERMOCALC for rim assemblages cluster around 520°C, while estimates from core assemblages vary slightly between the different methods of calculation (about 490°C for garnet-biotite geothermometry and 475°C from THERMOCALC) but are consistently lower than rim temperatures (Appendix 4, Table A4.3). Sample WK182 gave rim and core temperatures which were higher than equivalent assemblages from WK71, but maintained the same general trend of lower temperature cores compared with rim estimates (Appendix 4, Table A4.4). Garnet-biotite exchange thermometry gave temperatures of 550°C and 525°C for rim and core assemblages respectively, while equivalent THERMOCALC estimates were 570°C and 525°C. These results suggest that maximum temperatures achieved in this area were slightly lower than at Pinnacles Bore.

4.3.2.3 Results from Pinnacles Bore calcic metapelites

Quantitative analyses from the outermost and innermost portions of the Ca-rich rims of three samples from Pinnacles Bore (PB11, PB12 and PBS3) were used to estimate temperature and pressure conditions associated with the growth of the inferred ASO garnet rims. All the samples consistently produce higher temperature estimates from the internal margin of the Ca-rich rims (540-630°C) than from the garnet edge (520-570°C) (see Tables A4.5-A4.7). Pressure estimates for PB11, PB12 and PBS3 using the GASP and g-plag-bi-q barometers have a wide range (see Tables A4.5-A4.7) but estimates for the rims cluster around 6.0-6.3 kbar and are consistently higher than pressures recorded by the inner margins which cluster about 4.3-5.0 kbar. Geothermobarometry calculations performed using core analyses from all phases are also presented in Tables A4.5-A4.7. Results from geothermometry indicate that core conditions are approximately equivalent to rim calculations ranging between about 550-650°C, while geobarometry estimates for the cores are lower than for the rims by more than 1.0 kbar.

4.3.2.4 Results from the Cadney Metamorphics calcic metapelites

In CM20, core temperature estimates from Fe-Mg exchange thermometry on garnet-biotite pairs, are slightly higher than rim estimates, with averages ranging between 640°C to 790°C compared with 620°C to 690°C respectively, (see Table A4.8). These estimates are higher than the estimates given by all other samples from Pinnacles Bore and Winnecke, and are temperatures generally associated with upper amphibolite to granulite facies metamorphism rather than mid to upper amphibolite facies. CM19 rim estimates are slightly lower than those of CM20

ranging between 600°C and 690°C, but core estimates are much higher at about 730°C to 850°C (Appendix 4, Table A4.9). Given that prismatic sillimanite is part of the equilibrium assemblage, it is feasible that higher temperatures might be expected from these rocks, compared to the kyanite-only-bearing samples from elsewhere in the study area. However at the estimated temperatures the rock would have experienced fluid-absent partial melting. Since there is no evidence that the shear zone assemblages underwent partial melting, it is likely that the garnet and biotite core compositions used in these calculations are not in equilibrium. A more likely explanation is that the garnet cores have maintained a relic pre-ASO chemical signature which is not in equilibrium with that of the mid-amphibolite facies Palaeozoic biotite which defines the shear zone foliation.

Geobarometry results from the Cadney Metamorphics samples are also shown in Appendix 4, Tables A4.8-A4.9. Pressure estimates from CM19 rim analyses range from 4.6 to 5.7 kbars and are comparable to estimates from CM20 rim analyses which range between about 4.8 and 6.0 kbars. However core estimates from CM19 have a wide range (between about 4.0 to 7.2 kbar) which possibly reflects disequilibrium between garnet and biotite cores. CM20 core estimates between about 4.0 and 5.9 kbars. These results suggest a clockwise cooling path for CM19 and an anticlockwise burial with cooling path for CM20.

4.3.3 Geothermobarometry using THERMOCALC mode 2

While a range of conventional geobarometers are applicable to the calcic metapelites, the absence of an aluminosilicate and anorthitic plagioclase in the two-mica metapelitic schists presents major handicaps to evaluating the metamorphic pressure conditions experienced by these rocks, since this excludes the use of most existing geobarometers. Given the limited number of phases in the equilibrium assemblages of the two-mica metapelites, there are no useful standard geobarometers applicable to these rocks. However the software package THERMOCALC V2.6 (Powell and Holland, 1988), enables some quantitative calculation of pressure and temperature conditions via the 'average pressure calculation' (Average P) and the 'average pressure-temperature calculation' (Average PT) facilities in mode 2.

To perform the Average P and Averge PT calculations on a given rock, THERMOCALC requires a datafile identifying the suite phases present in the rock's equilibrium assemblage and the activities of these phases. THERMOCALC then identifies a series of possible reactions involving all the available endmembers in the dataset and constrains a set of independent reactions from this series. This independent set of reactions represents the minimum number of reactions needed to generate all the other possible reactions, creating a reaction surface in P-T-X space defined by the thermodynamic dataset inherent in the program (i.e. the internally consistent dataset of Holland and Powell, 1998b), within which the rock's assemblage lies. THERMOCALC then varies the activities of the phases, which are the least certain aspect of the thermodynamic data, to calculate an intersection point upon the reaction surface which is consistent with respect to the independent set of reactions (a least squares problem). Thus THERMOCALC uses a 'multiple equilibria' approach to constrain the equilibrium P-T conditions of the given mineral asemblage. In Average P calculations, a range of geologically reasonable temperatures selected by the operator, based on geological knowledge from other sources (e.g. petrography, field observations, geothermometry, phase diagrams) is given as a window over which the average pressures are calculated from the independent set of reactions. A number of statistical tests are applied to the data and the result is subjected to a chi squared (χ^2) test, expressed as a (σ fit) term which must be less than a calculated maximum term for the results to be accepted at a 95% level of confidence. THERMOCALC produces a diagnostic table as part of its output which can help identify inordinately influential data that might be suspect. A well constrained result can be achieved if an equilibrium assemblage is preserved, and provided sufficient independent reactions with favourable P-T slopes can be generated to adequately constrain the P-T-X surface. As such the best statistical results are usually generated from low variance assemblages. For a more detailed discussion on the use and mechanics of THERMOCALC, the reader is referred to Powell and Holland, (1988).

An example of a complete THERMOCALC output file for these types of calculations is presented in Appendix 3.2. All calculations were made using Thermocalc V2.6 with the dataset of April 20, 1996 (Holland and Powell, 1990) and end member activities applied were calculated using the software program AX by Holland and Powell, (1998a). An overview of the activity-composition models used to recalculate mineral analyses in AX is presented in Appendix 3.1 and representative analyses of minerals used in calculations are presented in Appendix 2.

4.3.3.1 Results from Pinnacles Bore Shear Zone metapelites

The results of THERMOCALC Average PT and Average P calculations for the Pinnacles Bore samples are presented in Tables A4.9 and A4.10. Average PT calculations made on rim assemblages from PB215 and PB10 include all available end members of the g-st-bi-mu-q-fluid equilibrium assemblage, and pass the statistical tests applied by THERMOCALC, with estimates of about 615°C and 7.5 kbar for PB215 and 640°C and 7.3 kbar for PB10. Core estimates for both samples were made using the assemblage g-bi-mu-q-fluid, since petrographic evidence suggests staurolite was not present during the initiation of garnet growth. As observed in the estimates from standard

geothermometry, PB215 again produced lower core temperatures compared to PB10 with average estimates of about 450°C and 5.6 kbar and 520°C and 6.4 kbar respectively, suggesting garnet growth may have initiated later in PB10. While temperature conditions calculated using the Average PT method vary slightly from those calculated from equivalent mineral data using standard Fe-Mg cation exchange thermometry (see §4.3.2.1), they are well within error and the temperature trends noted here are identical, suggesting metamorphism in an environment of increasing temperature. Unfortunately pressure estimates produced by the Average PT and Average P calculations have large associated errors, with most estimates from mineral cores being just within error of core estimates, reflecting the lack of pressure sensitive minerals such as the aluminosilicates or plagioclase. Regardless of this, the trend for core pressure estimates to be lower than rim estimates is clear, suggesting pressure was increasing with temperature during prograde metamorphism of the Pinnacles Bore Shear Zone.

4.3.3.2 Results from Winnecke

Average PT and Average P estimates for samples from the Winnecke-Two Mile Bore area are presented in Appendix 4, Tables A4.11 and A4.12. Again rim estimates for both WK182 and WK71 are higher than estimated core temperatures, with WK182 producing rim temperatures of about 605°C and pressures of about 7.2 kbar compared with core estimates of about 500°C and 5.9 kbar, while WK71 rim estimates are marginally higher at 630°C and 7.7 kbar compared with core estimates of about 460°C and 5.3 kbar. As noted in the Pinnacles Bore samples, the pressure estimates using both methods of calculation have large associated errors due to the high variance assemblage and lack of pressure sensitive phases. However the trend of these Average PT and Average P results are again consistent with data collected from standard geothermometry and compositional maps (see §4.3.1.4 and §4.3.2.2), indicating a rimwards increase in pressure and temperature conditions recorded by the participating phases, suggesting an up temperature and pressure trajectory through P-T space.

4.3.3.3 Results from Pinnacles Bore calcic metapelites

THERMOCALC Average PT calculations for the Pinnacles Bore calcic metapelites (Appendix 4, Tables A4.13-A4.15) produce very different results from those of standard Fe-Mg exchange thermometry discussed above. Average PT temperature estimates from samples PB11 and PB12 are quite well constrained with standard deviations generally less than about 40°C. However estimates from cores, rims and the internal margins of Ca enriched zones do not indicate cooling toward the rim, and are almost identical at about 640°C and well within error of each other. Pressure estimates are not as well constrained with standard deviations ranging from 1.1 to 1.8 kbar, however as observed from standard geobarometry calculations (§4.3.2.3; Appendix 4, Tables 4.13-A4.15), there is a general trend for pressure estimates to increase rimward compared to both core estimates and estimates from the interior of Ca-rich zones. Temperature and pressure estimates from PBS3 have larger errors of between 90°C and 120°C and 1.4 to 2.2 kbar, and temperature estimates are much lower than equivalent estimates from the other samples. In this rock, rim estimates are slightly cooler than those at the core with averages of about 470°C and 510°C respectively, but as observed in the other samples rim pressures are higher than core pressure estimates. THERMOCALC Average PT estimates are generally comparable to those from standard thermobarometry, except for sample PBS3 which gives lower pressure estimates using THERMOCALC in mode 2.

4.3.3.4 Results from Cadney Metamorphics calcic metapelites

Results of Average PT calculations from the Cadney Metamorphics are presented in Tables A4.16 and A4.17. In CM19, the Average PT temperature estimates for cores and rims are almost identical ranging between 600°C-635°C with standard deviations of less than 30°C, which is consistent with rim estimates from standard Fe-Mg thermometry. Associated pressures have standard deviations of about 0.5-0.7 kbar and range between 6.1-6.6 kbar with core estimates well within error of rim estimates. Similarly, THERMOCALC Average PT results from CM20 have rim and core temperatures within error at 618°C and 600°C respectively. Pressures are not well constrained for this sample, and again rim and core estimates are within error.

4.3.4 Discussion

Chemical zonation patterns in the garnets of the plagioclase-absent metapelites are interpreted as resulting from growth during prograde metamorphism as they ubiquitously display classic bell-shaped Mn, and inverted Mg and Fe profiles. Estimates of metamorphic conditions from cation exchange geothermometry and geothermobarometric calculation modes in THERMOCALC generally agree, and show consistent trends of increasing temperature and pressure when comparing core and rim assemblages, consonant with prograde metamorphism. Peak pressure and temperature estimates from rim analyses of a garnet-staurolite-biotite-muscovite-quartz equilibrium assemblage indicate maximum metamorphic conditions of about 580°C using Fe-Mg cation exchange thermometry on garnet-biotite pairs and about 600-630°C and 7-7.5 kbar using the mode 2 Average PT facility of THERMOCALC.

While the calcic metapelites from shear zones at Pinnacles Bore and in the Cadney Metamorphics appear coeval with feldspar-absent two-mica metapelitic schists both adjacent to them and from nearby shear zones when observed in the field, compositional maps and geochronology indicate that

these rocks may contain inherited garnet cores. Compositional maps and quantitative traverses of the garnets demonstrate the chemical complexity of these samples and highlight the inherent difficulties in applying geothermobarometry to the samples, given this complexity and the uncertainties in establishing equilibrium between phases. Estimates from geothermobarometry vary somewhat between methods, but suggest the rocks experienced conditions of about 600°C - 640°C and 6-7 kbar. However whether these estimates represent close to or peak metamorphic conditions is debatable as no clear interpretation of the P-T trajectory is possible from the zoning profiles observed in the garnets.

Given that the calcic metapelites from the Pinnacles Bore Shear Zone are interlayered with the feldspar-absent metapelites, it is unlikely they would have completely different geological histories. However while the plagioclase-absent two-mica metapelites invariably record simple prograde growth zoning and P-T conditions consistent with a clockwise P-T path, temperature and pressure estimates from the calcic metapelites do not clearly indicate a clockwise prograde path. From the chemical zonation patterns recorded in garnets from the calcic metapelites, it was interpreted that these garnets may have relic pre-ASO cores overgrown by thin ASO garnet rims as indicated by the presence of narrow Ca-enriched rims in the calcium compositional maps (Figures 4.12a, 4.13 a and 4.14a). In the Fe, Mg and Mn compositional maps little variation in the concentration of these cations was noted (Figures 4.12, 4.13 and 4.14), and the narrow rims observed in the Ca maps were not well defined, suggesting some decoupling of Ca from Fe, Mg and Mn. However chemical data from quantitative traverses across the Ca-enriched rims suggest that Fe, Mg and Mn did in fact vary in conjunction with Ca across the rims (Figure 4.15). The absolute concentration of Ca in garnets from the Pinnacles Bore calcic metapelites is very low so that small increases in the Ca content (i.e. on the order of ~ 1 wt%) resulted in very large proportional changes in Ca compared to those in Fe, Mg and Mn. Thus it is difficult to know whether the distribution of Fe, Mg, Mn and Ca in the Ca-enriched rims is in equlibrium or whether Ca has become decoupled, maintaining a profile from an earlier part of the ASO P-T path while Fe, Mg and Mn have re-equilibrated during the retrograde cooling path.

Temperature estimates from the Ca-enriched rim margins of the Pinnacles Bore garnets are lower than estimates from the rim interiors while pressure estimates increase between the rim interior and rim margin (Appendix 4, Table A4.5-A7) suggesting cooling with burial (i.e. a counterclockwise path) if it is assumed that Ca, Fe, Mg and Mn have maintained equilibrium. Given that the geobarometers used rely heavily on garnet-plagioclase equilibrium, it is possible that the pressure estimates for the calcic metapelites reflect disequilibrium between the garnet rim analyses and the plagioclase analyses used in the calculations. However regardless of the plagioclase analyses used, the general trend of increasing XFe and Ca concentration coincident with decreasing Mg observed in the compositional profiles of the rims of these garnets, is also consistent with a counterclockwise cooling path. The results of the temperature and pressure estimates are wholly consistent however with a scenario of decoupled Ca recording part of the prograde path while Fe, Mg and Mn have remained open to diffusion and have re-equilibrated during retrograde cooling.

The possibilty also exists that during the ASO Fe, Mg and Mn entirely re-equilibrated across the garnet cores as well as across the rims, and the changes in the rimward distribution of these cations reflects re-equilibration during the subsequent retrogressive path. In contrast, Ca may have maintained its original distribution in the relic cores and its ASO distribution across the Ca-enriched rims, thus resulting in geothermometers recording retrograde cooling while barometers may record conditions associated with prograde burial. Results from geothermometry indicate that core conditions are approximately equivalent to rim calculations, while geobarometry estimates for the cores are significantly lower than for the rims (Appendix 4), suggesting increasing temperature with burial consistent with a prograde path. These pressure and temperature estimates are geologically reasonable and consistent with the P-T paths recorded by the plagioclase-absent metapelites, however with maximum temperatures of only about 600°C during the ASO, it is unlikely that garnets of 2 mm diameter and greater would have been able to totally re-equilibrate. If the cores of the garnets were completely unequilibrated Proterozoic granulite relics then analyses chosen from matrix phases such as biotite would be in disequilibrium with the selected garnet core analyses and it would be reasonable to expect some unrealistically high estimates from geothermometry (as noted in the Cadney Metamorphics samples), as granulite garnet cores would have excessively high pyrope compositions for the amphibolite facies ferro-magnesian phases (Florence and Spear, 1991; Spear, 1993). That this is not the case is surprising and highlights a disturbing aspect of these results in the apparent sensibility of the Fe-Mg exchange thermometry and the Average PT estimates on the garnet cores, which are reasonably well constrained and convincingly pass the statistical tests imposed by THERMOCALC. Such information viewed in isolation, without the evidence of potential disequilibrium from compositional mapping, could be accepted at face value.

It seems unlikely that the calcic metapelites and the feldspar-absent metapelites from the Pinnacles Bore Shear Zone experienced entirely opposite P-T paths. It is more likely that due to the complex chemistry of garnets in the calcic metapelites, reflecting possible re-equilibration of Proterozoic porphyroclasts and the potential overgrowth of secondary Palaeozoic garnet, the compositions selected for calculations are not in equilibrium and the results are therefore questionable.

Thermobarometry results for the Cadney

Metamorphics calcic metapelites are also more difficult to interpret than results from the plagioclase-absent, two-mica metapelites. Compositional maps of garnets from these samples are quite complex (Figures 4.17 and 4.18) and suggest that the garnets may have older relic cores overgrown by younger secondary rims. Temperature estimates from Fe-Mg cation exchange thermometry on core analyses are very high (i.e. ~700-850°C) suggesting that there is chemical disequilibrium between garnet and biotite at least, and providing support for the interpretation of the preservation of relic garnet cores. However results from Average PT calculations with THERMOCALC on both core and rim assemblages are geologically reasonable and consistent with estimates from the two-mica metapelites at Pinnacles Bore and Winnecke. Such a large discrepancy is alarming but may demonstrate the advantage in using the 'multi-equilibria' approach of mode 2 Average PT calculations in THERMOCALC, rather than single equilibria thermometers such as gnt-bi Fe-Mg exchange thermometry. It appears that in the case of the Cadney Metamorphics calcic metapelites, disequilibrium between garnet and biotite has rendered Fe-Mg exchange thermometry ineffective. However as THERMOCALC uses the entire suite of end member phases present in a mineral assemblage to generate a series of independent reactions, from which it calculates a reaction envelope in P-T space (see §4.3.3), the corruption of the g-bi Fe-Mg equilibria is compensated for to some extent.

Although it is possible therefore that the THERMOCALC Average PT estimates are accurate, it is still difficult to interpret these results given the chemical complexity of garnets in the Cadney Metamorphics samples. It is likely that the samples from the Cadney Metamorphics have experienced a common P-T history, and that matrix phases in both samples reflect local metamorphic conditions associated with ASO metamorphism, while the complex chemical profiles preserved in garnet reflect the chemical signatures of inherited cores which have failed to completely re-equilibrate with the ambient Alice Springs Orogeny metamorphic conditions in which the rest of the assemblage has grown. Evidence from garnets in sample CM20 (Figures 4.17 and 4.19) suggest they record simple prograde zoning associated with crystallisation during a single metamorphic event. This implies that diffusive processes have been more effective in eradicating the compositional step which identifies the hiatus between relic garnet cores and overgrown rims in sample CM19 (Figures 4.18 and 4.19). Therefore, while the compositional maps and petrography give an indication of where the boundary between the new and potential relic garnet occurs in sample CM19, it is impossible to know whether quantitative spot analyses across this boundary reflect equilibrium at all.

If the garnet cores are older relic features, it is possible that they result from Proterozoic precursor granulite facies lithologies as is probably the case with the Pinnacles Bore Shear Zone calcic metapelites. However Sm-Nd dating of samples

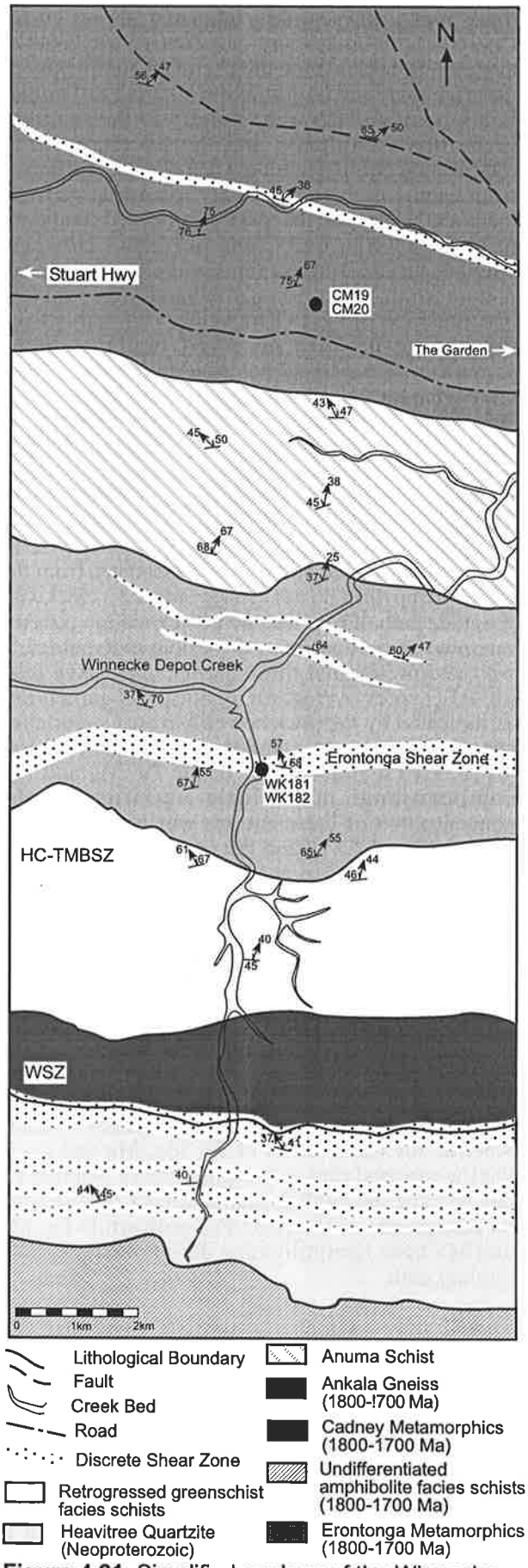

Figure 4.21. Simplified geology of the Winnecke area in the vicintiy of the Erontonga Shear Zone, showing the location of samples taken from the Cadney Metamorphics and the Erontonga Shear Zone.

from the Erontonga, Pinnacles Bore and Yambah Shear Zones have demonstrated that peak assemblages in these shear zones are diachronous with older (ca. 380 Ma) shear zones occurring to the north and younger (ca. 320 Ma) shear zones to the south (see Chapter 3). These data suggest that peak metamorphism during the ASO was separated temporally by up to at least 60 m.y., and hence that individual shear zones did not experience identical trajectories in P-T space. The shear zone from which the Cadney Metamorphics samples were collected is located north of the Winnecke area, and lies in a central portion of the SMC (Figure 4.1 and 4.21). No shear zones from this part of the SMC have been dated as yet, and thus a number of possibilities exist for the timing of these shear zones. Firstly the central shear zones may have experienced crystallisation during a single metamorphic progression at either ca. 380 or ca. 320 Ma, or at some distinct intermediate time. Alternatively shear zone rocks from this location may have experienced polymetamorphism during the ASO resulting in initial crystallisation during the onset of the ASO metamorphic cycle at about 380Ma, followed by overprinting or complete recrystallisation during the subsequent 320 Ma pulse. Thus without dating the Cadney Metamorphics shear zone rocks it is impossible to determine whether the garnets preserve inherited cores and if so, what age the garnet cores may be. As a consequence it is also difficult to interpret the significance of the calculated P-T estimates for the Cadney Metamorphics calcic metapelites.

4.4 Conclusion

The metasedimentary schists from ASO-aged shear zones in the Pinnacles Bore and Winnecke areas in the southern Strangways Metamorphic Complex are typical of many commonly observed metapelites in that they consist of high variance mineral assemblages which are well equilibrated, displaying little in the way of reaction textures or useful relict phases. As a result quantitative information about the P-T path taken by these rocks using geothermobarometry is limited to chemical zonation trends in equilibrium minerals. In the plagioclase-absent two-mica metapelitic schists from the Pinnacles Bore and Erontonga Shear Zones, chemical zonation patterns in garnets are interpreted to result from prograde growth zoning. Conventional thermometry using gnt-bi Fe-Mg cation exchange equilibria and Average PT calculations using THERMOCALC on core and rim analyses of minerals which appear to be in textural equilibrium indicate peak metamorphic conditions of 600-640°C and 6-7 kbar were achieved during a clockwise prograde P-T path. In the field, calcic metapelites from a shear zone within the Cadney Metamorphics and from the Pinnacles Bore Shear Zone appear coeval with adjacent shear zone plagioclase-absent two-mica metapelitic schists. However compositional maps and Sm-Nd data indicates that these rocks may contain inherited garnet cores. P-T estimates on rim assemblages vary somewhat between methods, but suggest the rocks achieved conditions of about 600°C - 640°C and 6-7 kbar. Whether these estimates represent close to or peak metamorphic conditions is debateable as no clear interpretation of the P-T trajectory is possible from the zoning profiles observed in the garnets. Given that evidence from adjacent and interbedded metapelites of different bulk composition invariably indicate a clockwise trajectory, it is suggested that the calcic metapelites also experienced this type of path.

Chapter 5

PRESSURE-TEMPERATURE PATHS FROM METAPELITIC SHEAR ZONE ASSEMBLAGES IN THE SMC USING P-T PSEUDOSECTIONS

5.1 Introduction

A fundamental objective of metamorphic petrology is to decipher the mechanisms and controls on the metamorphic evolution of orogenic belts, using the information contained in metamorphic rocks. An important step in investigating orogenesis is the determination of the peak metamorphic conditions experienced by the rocks being studied. However this data is an intrinsically static feature, pinpointing a rock's location in pressure-temperature (P-T) space at a particular stage in its evolution, but ignoring the path it took in order to arrive at that maximum pressure and temperature, or how it was subsequently returned to the Earth's surface. Thus in isolation this data provides little insight into the process of metamorphism or the tectonic environment in which metamorphism occurred. Although the peak metamorphic conditions experienced by Alice Springs Orogeny-aged metapelitic rocks from the Pinnacles Bore and Erontonga Shear zones in the southern SMC have been examined using thermobarometry (Chapter 4), the P-T evolution of these metapelites has not been investigated in detail. An assessment of the P-T paths taken by these rocks is particularly important, given that some of the metapelites contain garnet which preserves prograde chemical zonation patterns, and these garnets have been dated in order to constrain the timing of peak metamorphism in the shear zones (Chapter 3).

The trajectory of a metamorphic rock through P-T space is much more informative in deducing the rock's metamorphic evolution and in constraining the controlling tectono-thermal environment. There are three methods commonly used to model the pressure-temperature path taken by a metamorphic rock; (1) conventional geothermobarometry, (2) the differential thermodynamics or 'Gibbs' method (Spear et al, 1982; Spear and Selverstone, 1983; Spear et al, 1984; Spear and Rumble, 1986; Spear, 1988; Crowley, 1990), and (3) phase equilibria developed from petrogenetic grids and calculated P-T pseudosections.

Conventional geothermobarometers use cation-exchange and phase equilibria to calculate the equilibrium pressure and temperature for a suite of phases in a rock which constitute an equilibrium assemblage. These calculations only quantify a point along the rock's P-T path taken by the rock, so to constrain the P-T path further, the rock must preserve relic assemblages which are suitable for such calculations. However while rocks can fail to completely re-equilibrate during their metamorphic evolution they will rarely maintain a complete mineralogical record of their prograde and retrograde path. Frequently relic minerals which are preserved occur in reaction textures, as inclusions or other disequilibrium features and therefore may not be conclusively identified as part of an equilibrium assemblage. The metapelitic schists from the Strangways Metamorphic Complex are generally composed of high variance assemblages, and are texturally well equilibrated with little or no evidence of reaction textures or preserved relic assemblages. Some of the metapelitic schists contain porphyroblastic chemically zoned garnet, however the garnets do not contain inclusions suitable for geothermobarometry. As a result conventional geothermobarometry is of limited use in constraining the P-T path of these rocks.

To model a rock's movement through P-T space, the differential thermodynamics or 'Gibbs' method uses incremental changes in the chemical composition of a chemically zoned phase(s) which forms part of a preserved equilibrium assemblage (Spear, 1988; Spear and Selverstone, 1983; Spear et al, 1984; Spear, 1998). In order to describe a unique path in P-T space however, at least one other phase is required to be present in order to compositionally 'fix' a minimum of one component (Crowley, 1990; Spear, 1998). Garnet is commonly used as the zoned phase and in this instance there may be up to 4 components (i.e. Fe, Mg, Mn, Ca) which are free to vary as a function of the P-T environment. Another phase which also contains one of these 4 components must be added to the calculations in order to fix one of the components. If present, plagioclase is a useful choice as the second phase, as this will accurately describe the variation of calcium and hence provide constraints on the rock's pressure path, since calcium exchange between grossular-anorthite is particularly pressure-sensitive (Spear and Selverstone, 1983; Spear et al, 1991; Spear, 1998). The 'Gibbs' method is therefore ideal for use on assemblages which contain chemically zoned, porphyroblastic phases with numerous inclusions of useful relic minerals, which are interpreted to be in equilibrium with the composition of the zoned porphyroblast at that point in its P-T trajectory (e.g. Spear and Selverstone, 1983; Selverstone et al, 1984; Kohn et al, 1992; Menard and Spear, 1993). Other zoned matrix minerals (rather than inclusions) could also potentially be used in conjunction with the zoned porphyroblastic phase, however this is complicated by the need to accurately identify which parts of the respective zoned minerals were in chemical equilibrium, if ever (Selverstone et al, 1984; Spear and Rumble, 1986;

Crowley, 1990; Spear et al, 1991; Florence and Spear, 1991; Kohn et al, 1992; Menard and Spear, 1993). As mentioned above, porphyroblastic garnets in the southern Strangways Metamorphic Complex mid-Palaeozoic shear zone rocks are generally inclusion-free or contain inclusions such as ilmenite, magnetite and quartz which are of little value when considering cation exchange equilibria in garnet. In addition, compositional zoning in accompanying phases such as staurolite or plagioclase is often either lacking or inconsistent (§4.3.1) and thus difficult to correlate with zonation trends in the adjacent garnet. As a result the southern Strangways Metamorphic Complex shear zone rocks are also not well suited to this method of investigation.

The use of P-T pseudosections calculated for the specific bulk composition of a rock can be advantageous in the absence of well-preserved relic equilibrium assemblages, richly-included porphyroblasts, or for rocks with high-variance assemblages where variation in the ambient P-T environment is accommodated by continuous reactions regulating changes in existing mineral chemistry rather than growth of new phases. P-T pseudosections define all the possible stable assemblages within selected P-T space that the given rock can develop, and can predict the chemistry and modal proportions of those minerals at any given pressure and temperature. Thus using the chemical zonation profile from a single phase, an incomplete relic assemblage or hierarchy of mineral growth in an equilibrium assemblage the rock's trajectory in P-T space can be reconstructed.

In this chapter a new petrogenetic grid in the system NaCaKFMASH applicable to plagioclase-bearing metapelitic rocks is presented, and the metamorphic conditions and P-T paths recorded by metapelitic shear zone rocks from the Pinnacles Bore and Winnecke areas will be investigated using evidence from calculated P-T pseudosections derived from the KFMASH and the NaCaKFMASH model systems. All the phase diagrams presented here have been calculated using the computer program THERMOCALC V2.6 (Powell and Holland, 1988) and a recent version of the internally consistent thermodynamic dataset of Holland and Powell (1998b), as utilised in the geothermobarometry calculations in sections 4.3.2 and 4.3.3.

5.2 Petrogenetic Grids and P-T Pseudosections

Petrogenetic grids are a powerful tool for investigating the metamorphic evolution of rocks as they describe the potential changes in a rock's equilibrium mineral assemblage as it moves through P-T-X space. However as petrogenetic grids only describe the distribution of univariant (i.e. discontinuous) reactions which apply to all bulk compositions within the model chemical system, their utility is generally limited to rocks with low variance assemblages displaying evidence of crossing univariant reactions (i.e. rocks which have 'seen' one or more univariants). In the case of high variance assemblages, dedicated P-T pseudosections calculated for a prescribed bulk composition are more useful as they can display and predict all the reactions, reaction fields, mineral mode and compositional isopleths relevant to a rock of that specific composition in all parts of P-T-X space (e.g. Vance and Holland, 1993; Xu et al ,1994; Stüwe and Powell, 1995; Mahar et al, 1997; Vance and Mahar, 1998).

Real rocks are chemically complex, yet current information and understanding of the thermodynamic properties of even the most common rock-forming minerals is limited to simple models of major component mineral end-members. As a result petrogenetic grids and P-T pseudosections are generally constructed using a simplified chemical system which describes the main compositional features of the rock's major minerals, but ignores it's minor components. The K_2O-FeO-MgO-Al_2O_3-SiO_2-H_2O (KFMASH) model chemical system is most commonly used to investigate metapelitic rocks (e.g. Grant, 1985; Clarke et al, 1989; Spear and Cheney, 1989; Powell and Holland, 1990; Xu et al, 1994; Carrington and Harley, 1995) with additional components such as CaO, NaO, MnO and TiO_2 being added as required (e.g. Vance and Holland, 1993; Droop and Harte, 1995; Clarke et al, 1989; Mahar et al, 1997; Worley and Powell, 1998a). KFMASH grids are generally constructed with muscovite, quartz and H_2O (+ mu + q + H_2O) in excess since this assumption is generally a valid assumption for most sub-solidus metapelites and allows graphical simplification of the calculated grid and pseudosections. As the KFMASH model system contains six components, according to the phase rule;

$$P = C - F + 2$$

where; P is the number of phases (i.e. minerals), C is the number of components (e.g. oxides) and F is the number of thermodynamic degrees of freedom (e.g. pressure, temperature, composition of one or more phases), a muscovite-biotite-staurolite-garnet-aluminosilicate-quartz-H_2O assemblage would be univariant, meaning that only one variable (e.g. pressure or temperature) is free to change without altering the assemblage. A muscovite-biotite-staurolite-garnet-quartz-H_2O assemblage would be divariant, meaning that two variables are able to change without altering the assemblage. Whereas the equilibrium P-T conditions of a univariant assemblage will be tightly constrained as they must lie somewhere along a single reaction line in the P-T space defined by the petrogenetic grid, the conditions appropriate to a divariant assemblage will fall within a field in which any two variables of pressure, temperature or mineral composition are free to alter independently. As such low variance assemblages are preferable for investigating conditions of metamorphism. The methodology for calculating phase diagrams using THERMOCALC has been discussed by a number of authors (e.g. Powell and Holland, 1985; Guirard et al, 1990; Will et al, 1990; Stüwe and Powell, 1995; Worley and Powell, 1998b) but for a detailed review and worked examples of this procedure the reader is referred to Powell (1998).

5.3 Petrogenetic evidence for the P-T evolution of plagioclase-absent metapelites from the Pinnacles Bore and Erontonga Shear Zones.

The mineral assemblages and textural features observed in the Pinnacles Bore and Winnecke plagioclase-absent metapelitic schists can be adequately described in the chemical system K_2O-FeO-MgO-Al_2O_3-SiO_2-H_2O (KFMASH). A petrogenetic grid modelled in this system, presented in Figure 5.1 displays the stable invariant and univariant equilibria involving the phases muscovite, biotite, garnet, staurolite, cordierite, chloritoid, kyanite, sillimanite, andalusite, chlorite, quartz and H_2O. Although individual mineral chemistry varies somewhat between samples, in general the Pinnacles Bore and Winnecke metapelites are chemically quite similar and display almost identical phase relations which can be modelled in KFMASH using a bulk chemistry of A:F:M:K = 44:24:16:16. A P-T pseudosection for this bulk composition is presented in Figure 5.2a. From petrographic observations (see §4.2.1) it is apparent that these rocks have all passed through the staurolite-garnet-biotite (+ muscovite + quartz + H_2O) divariant field and that most of the rocks contain this equilibrium assemblage. However textural evidence suggests that initiation of garnet growth preceded that of staurolite, while staurolite continued to grow after garnet growth ceased, as garnet is commonly wrapped by matrix biotite and muscovite while staurolite is sometimes observed overprinting the fabric (Figure 4.2). This suggests that the rocks passed either up temperature through the chlorite + garnet + biotite (+ muscovite + quartz + H_2O) divariant or down pressure through the garnet + biotite (+ muscovite + quartz + H_2O) trivariant prior to onset of staurolite growth in the staurolite + garnet + biotite (+ muscovite + quartz + H_2O) divariant (Figure 5.2a). Unfortunately no evidence of a relic assemblage containing chlorite remains, and the garnet porphyroblasts contain no chlorite, biotite or muscovite inclusions which might indicate one path or the other. However chemical zonation in the garnets inevitably results in a decrease in the XFe ratio from core to rim (see §4.3.1). Figure 5.2b indicates that in the staurolite + garnet + biotite (+ muscovite + quartz + H_2O) divariant field, isopleths of XFe in garnet decrease with increasing pressure and temperature, and isopleths of XFe in staurolite are subparallel to those of garnet. Therefore the rocks must have moved from the chlorite + garnet + biotite (+ muscovite + quartz + H_2O) divariant across the staurolite isograd into the staurolite + garnet + biotite (+ muscovite + quartz + H_2O) divariant, in order to produce the zonation trends observed in the real garnets. While zonation in staurolite is not observed and thus a unique path can't be determined, it is apparent that the rocks must have moved in a manner that produced decreasing XFe ratios in garnet coincident with garnet growth and with increasing modal proportion of staurolite until late in the trajectory. Figure 5.2c indicates that isomodes of garnet increase with increasing pressure and temperature subparallel to isopleths of XFe. Staurolite modes in the staurolite + garnet + biotite (+ muscovite + quartz + H_2O) divariant occur at a low angle to those of garnet and in the opposite direction, increasing down pressure, while in the staurolite + biotite (+ muscovite + quartz + H_2O)

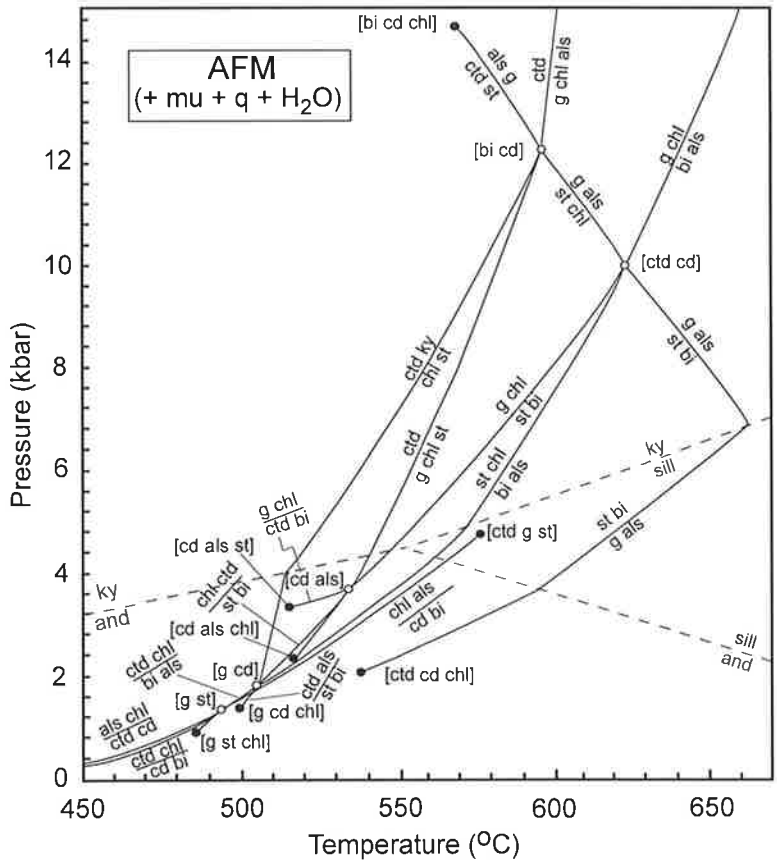

Figure 5.1. A petrogenetic grid for metapelitic rocks in the chemical system KFMASH, incorporating the following phases; and, bi, cd, chl, ctd, g, ky, mu, q, sill, st & H_2O. (After Powell, 1998).

trivariant field staurolite isomodes are steeper and increase down pressure. The continuation of staurolite growth after cessation of garnet growth, and the presence of minor retrograde rims on some of the garnets suggests that the rocks' path crossed back through higher XFe isopleths and into the staurolite + biotite (+ muscovite + quartz + H_2O) trivariant.

The growth of retrograde chlorite in equilibrium with biotite and muscovite and at the expense of staurolite suggests the rocks moved from the staurolite + biotite (+ muscovite + quartz + H_2O) trivariant into either the staurolite + biotite + chlorite (+ muscovite + quartz + H_2O) divariant, or the biotite + chlorite (+ muscovite + quartz + H_2O) trivariant. At the boundary between these two fields, the modal proportion of staurolite approaches zero, however chlorite modal proportions are at about 15%. At the chlorite-in boundary of the staurolite + biotite + chlorite (+ muscovite + quartz + H_2O) divariant however proportions of staurolite are about 8% while chlorite proportions approach zero. Given that retrograde chlorite forms a maximum of about 1% of these rocks and staurolite forms about 10%, it appears that the metapelites may have just entered into the staurolite + biotite + chlorite (+ muscovite + quartz + H_2O) divariant field and/or the biotite + chlorite (+ muscovite + quartz + H_2O) trivariant before reaction ceased. Unfortunately mode and XFe isopleths for chlorite are sub-parallel to the field boundaries and thus there is no constraint on where within these fields the rocks lie. If the modal proportion of staurolite reflects equilibrium during the retrograde stages of the P-T path, then Figure 5.2c suggests conditions of about 4-4.5 kbar and 560°C are appropriate.

The observations discussed above suggest the most probable trajectory for the ASO-aged shear zones in the southern SMC, is a clockwise prograde path (Figure 5.2d) passing up P and T through the chlorite + garnet + biotite (+ muscovite + quartz + H_2O) field into the staurolite + garnet + biotite (+ muscovite + quartz + H_2O) field where maximum metamorphic conditions were experienced, then cooling and decompression through the staurolite + biotite (+ muscovite + quartz + H_2O) trivariant and into the

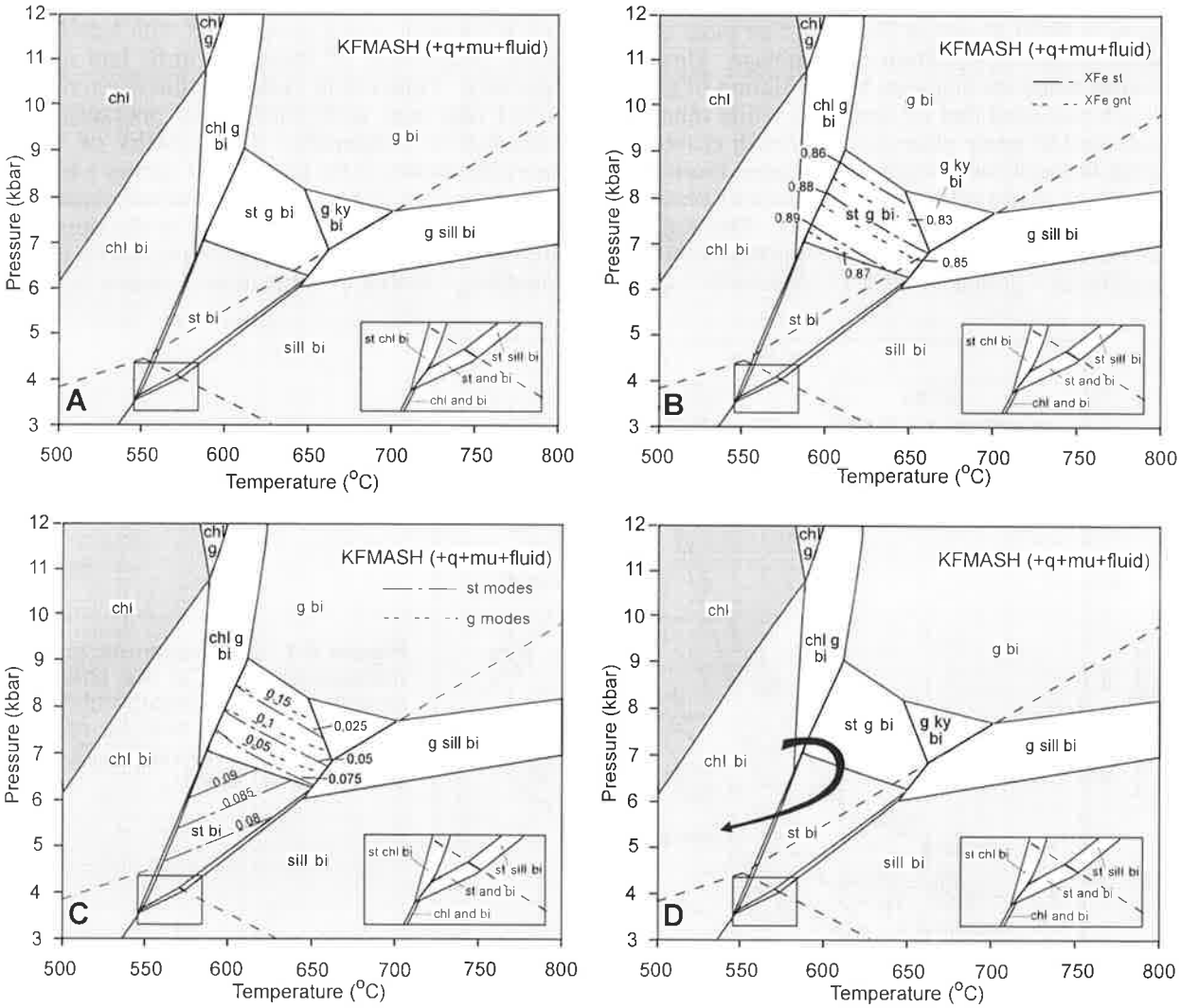

Figure 5.2. (a) A pseudosection calculated in KFMASH for the bulk composition A:F:M:K = 44:24:16:16 suitable for plagioclase-absent metapelites from the Pinnacles Bore and Winnecke areas; (b) the distribution of XFe isopleths in garnet and staurolite in the g-st trivariant field; (c) the distribution of garnet and staurolite mineral modes within the g-st trivariant field; (d) the inferred P-T path taken by the metapelitic schists.

staurolite + biotite + chlorite (+ muscovite + quartz + H_2O) or biotite + chlorite (+ muscovite + quartz + H_2O) chl+bi (+mu+q+H_2O) fields. This path is also consistent with the observation of kyanite as a common phase in the calcic metapelites, as this trajectory occurs entirely within the stability field of kyanite.

5.4 Petrogenetic evidence for the P-T evolution of the plagioclase-absent metapelites

The plagioclase-bearing, muscovite-poor schists of Pinnacles Bore and the Cadney Metamorphics, have a more sodic and calcic and less potassic bulk composition than the adjacent feldspar-absent, two-mica metapelites. As a result, the growth of plagioclase feldspar and biotite was stabilised in these rocks, while muscovite was not produced for much of their metamorphic evolution. Thus most existing petrogenetic grids applicable to metapelitic rocks are inadequate for interpreting the P-T evolution of these rocks, as the grids are commonly modelled in the KFMASH system for muscovite-saturated bulk compositions, and do not include equilibria involving plagioclase as an active phase. In order to investigate the full reaction history of the Pinnacles Bore and Cadney Metamorphic schists, a new petrogenetic grid modelled in the NaCaKFMASH chemical system including these features and P-T pseudosections produced for bulk compositions appropriate for these rocks have been calculated.

The subsystem CaKFMASH and NaKFMASH grids (Figures 5.3 and 5.4) have been used to calculate the full system NaCaKFMASH grid (Figure 5.5a & b) using a restricted set of phases (garnet, staurolite, chlorite, biotite, muscovite, chloritoid, cordierite, plagioclase, quartz, kyanite, sillimanite, andalusite, and water as a pure fluid phase). In the subsystem grids, plagioclase has been treated as its appropriate endmember phase anorthite or albite, with grossular being the only other Ca-bearing phase included and muscovite the only other Na-bearing phase. The compositional parameters of these minerals and their end-member activities are presented in Appendix 5, and incorporate both the FeMg-1 and (Fe,Mg)SiAl-2 substitutions in biotite, muscovite and chlorite, the FeMg-1 substitution in chloritoid, cordierite, garnet and staurolite and the CaAlNa-1Si-1 solid solution in muscovite and plagioclase. The activity-composition relationships for plagioclase (equivalent to model 4 of Holland and Powell, 1992) and muscovite are identical to those used by Worley and Powell (1998a) who provide a detailed discussion on the non-ideal mixing models developed for Na2O-CaO mixing in these two minerals. All thermodynamic data of the mineral end-members involved in calculations are included in the internally consistent thermodynamic dataset of Holland and Powell (1998b).

Not all of the phases selected for inclusion in the grids are observed in the Strangways Metamorphic Complex shear zones, however they were added to reflect the common major variations observed in metapelitic rocks, and their inclusion also enables some degree of direct comparison between the commonly employed KFMASH system and the

Invariant Point	Phases	P(kbar)	T(oC)	x(st)	x(ctd)	x(g)	z(g)	x(chl)	y(chl)	x(bi)	y(bi)	x(mu)	y(mu)	k(mu)	x(cd)	h(cd)
KFMASH	(+ mu+q+fluid)															
[bi cd]	g, st, chl, ctd, als	12.21	594.9	0.865	0.662	0.830		0.436	0.556			0.701	0.793			
[ctd cd]	g, st, chl, als, bi	9.97	622.1	0.819		0.772		0.363	0.565	0.385	0.356	0.620	0.822			
[cd als]	g, st, chl, ctd, bi	3.67	534.4	0.982	0.935	0.973		0.831	0.611	0.854	0.453	0.933	0.882			
[g cd]	st, chl, ctd, als, bi	1.80	505.6	0.986	0.943			0.841	0.634	0.866	0.503	0.937	0.915			
[g st]	cd, chl, ctd, als, bi	1.33	493.9	0.957	0.875				0.635	0.896	0.506	0.952	0.919		0.849	0.537
CaKFMASH	(+ q + fluid)															
[bi cd]	an, g, st, chl, ctd, als	7.3	551.7	0.906	0.726	0.665	0.271	0.487	0.616			0.736	0.943			
[ctd cd]	an, g, st, chl, als, bi	6.2	592.2	0.852		0.698	0.169	0.3880	0.601	0.421	0.431	0.641	0.9390			
[cd als]	an, g, st, chl, ctd, bi	2.49	517.1	0.985	0.941	0.897	0.084	0.839	0.625	0.863	0.484	0.936	0.952			
[g an cd]	st, chl, ctd, als, bi	1.8	505.6	0.986	0.943			0.8410	0.634	0.866	0.503	0.937	0.957			
[g an st]	cd, chl, ctd, als, bi	1.33	493.9	0.957	0.875				0.635	0.896	0.506	0.952	0.959		0.850	0.537
NaKFMASH	(+ q + fluid)															
[bi cd]	ab, g, st, chl, ctd, als	12.21	594.9	0.865	0.662	0.83	0.436		0.5560			0.7010	0.897	0.003		
[ctd cd]	ab, g, st, chl, als, bi	7.47	642.4	0.773		0.714		0.305	0.5750	0.334	0.391	0.545	0.924	0.54		
[cd als]	ab, g, st, chl, ctd, bi	1.65	509.8	0.995	0.979	0.992		0.937	0.621	0.948	0.479	0.976	0.951	0.765		
[g ab cd]	st, chl, ctd, als, bi	1.29	502.2	0.994	0.976			0.928	0.626	0.941	0.491	0.973	0.954	0.776		

Table 5.1. Summary of the stable invariant points and solid solution substitutions in participating minerals in the KFMASH, CaKFMASH and NaKFMASH subsystems.

NaCaKFMASH	Phases (+ q + fluid)	P (kbar)	T(°C)
[bi cd]	plag, g, st, chl, ctd, als	8.15	560.1
[ctd cd]	plag, g, st, chl, als, bi	6.84	613.8
[cd als]	plag, g, st, chl, ctd, bi	1.77	509.2
[g cd]	plag, st, chl, ctd, als, bi	1.49	503.7

Table 5.2. In the NaCaKFMASH system, univariants end at invariant points in the NaKFMASH and CaKFMASH subsystems. Along the univariants, plagioclase models I1 and C1 exchange at the P-T points indicated in the table.

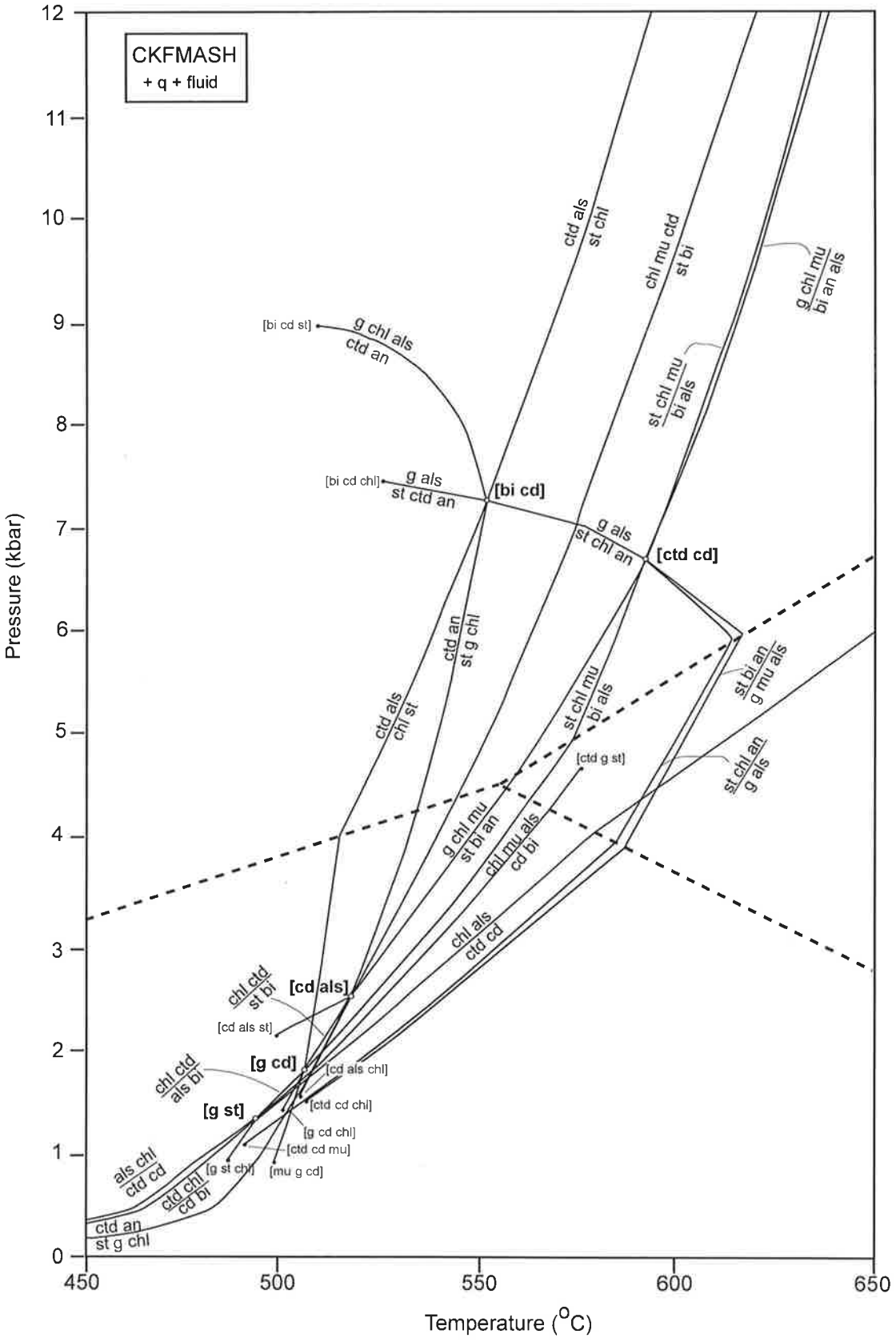

Figure 5.3. A petrogenetic grid for the chemical system CaFMASH incorporating the phases an, and, bi, cd, chl, ctd, g, ky, mu, sill, st with q & H_2O in excess.

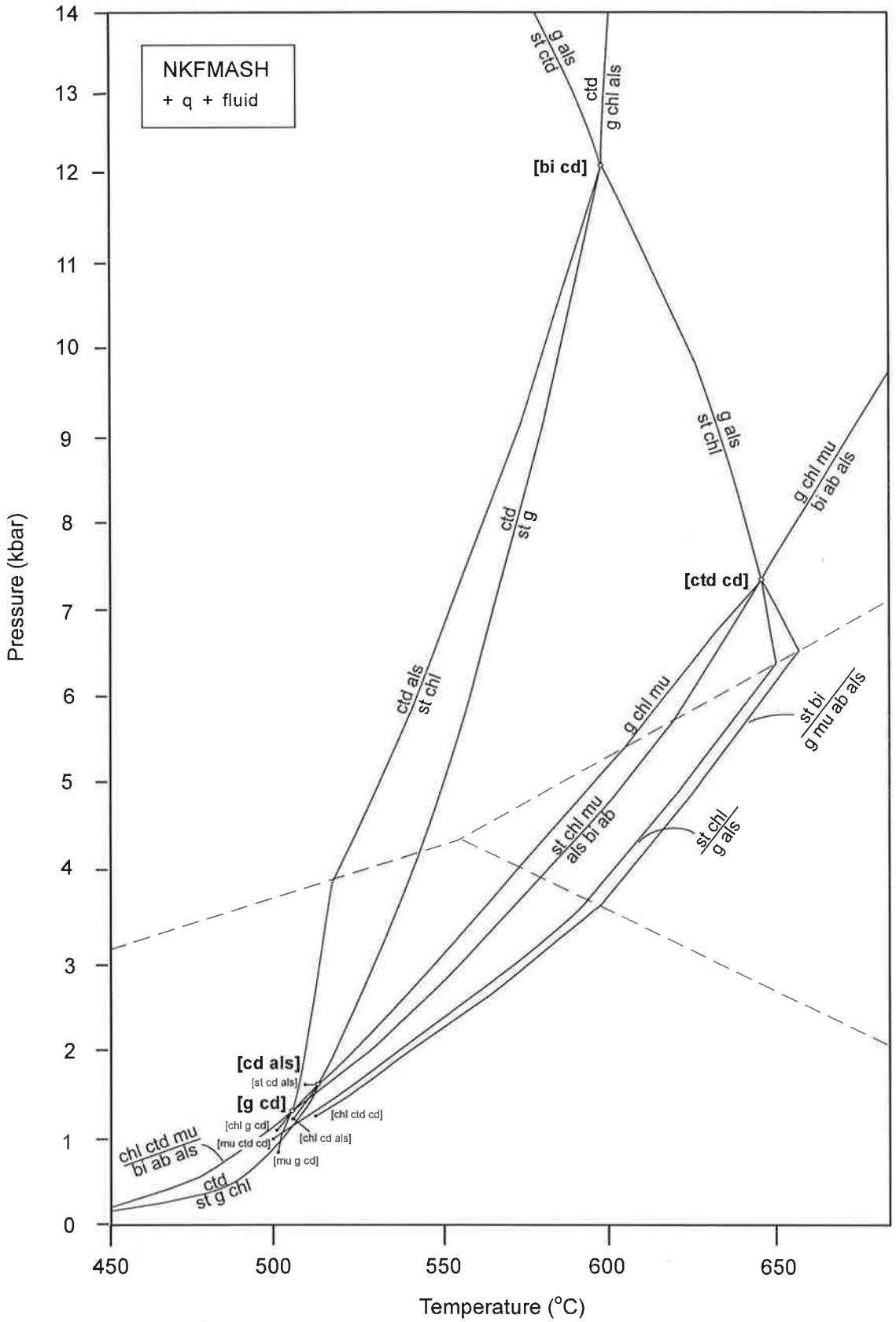

Figure 5.4. A petrogenetic grid calculated in the NaKFMASH chemical system using the phases ab, and, bi, cd, chl, ctd, g, ky, mu, sill, st with q & H_2O in excess.

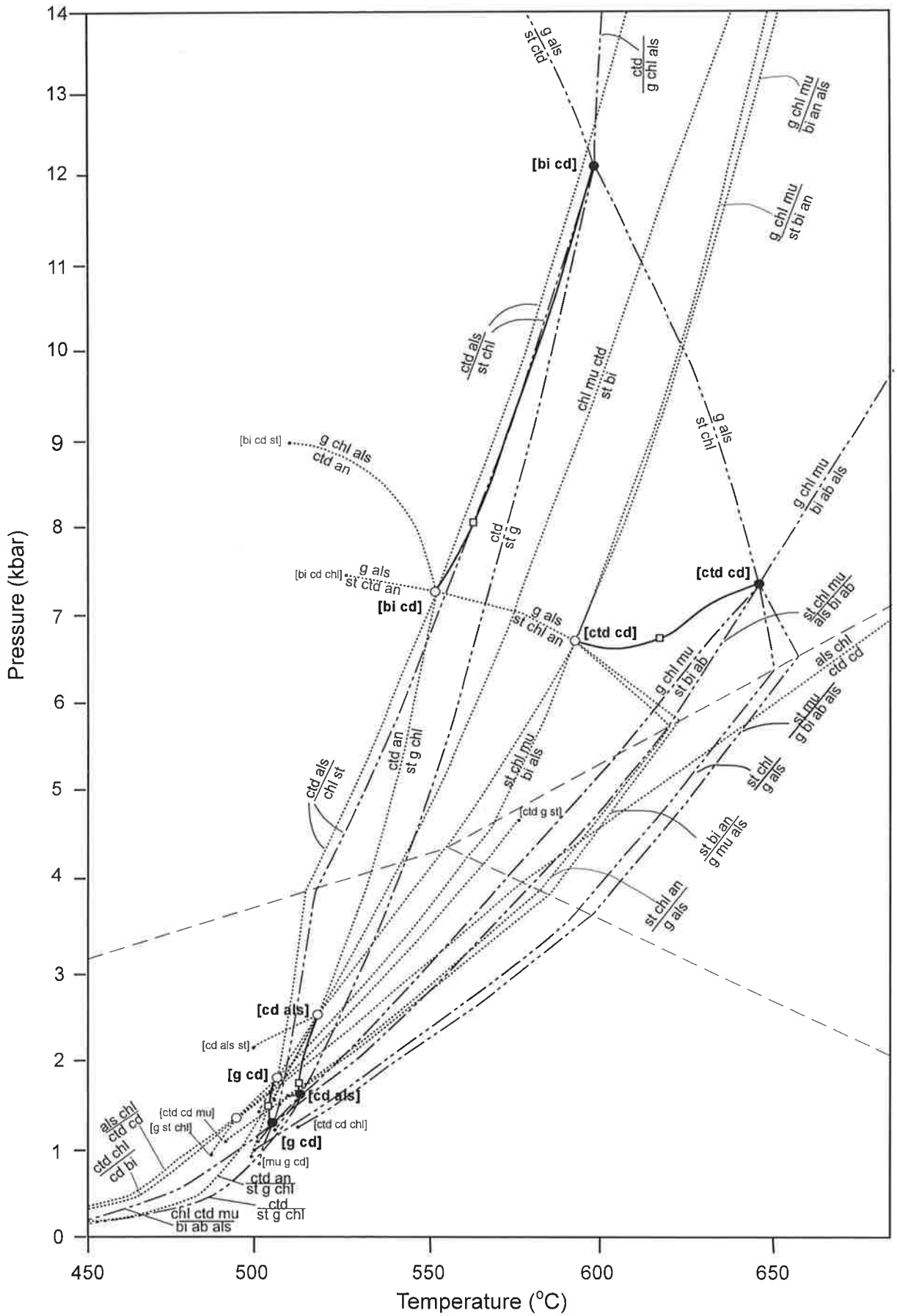

Figure 5.5a. Petrogenetic grid for the NaCaKFMASH system. CaKFMASH and NaKFMASH invariant points are marked by unfilled and filled circles respectively. Solid lines represent NaCaKFMASH univariant reactions, while CaKFMASH univareinats are denoted by dotted lines and dashed lines indicate NaKFMASH univariants. Transition points for the plagioclase models are indicated by unfilled squares on NaCaKFMASH univariants.

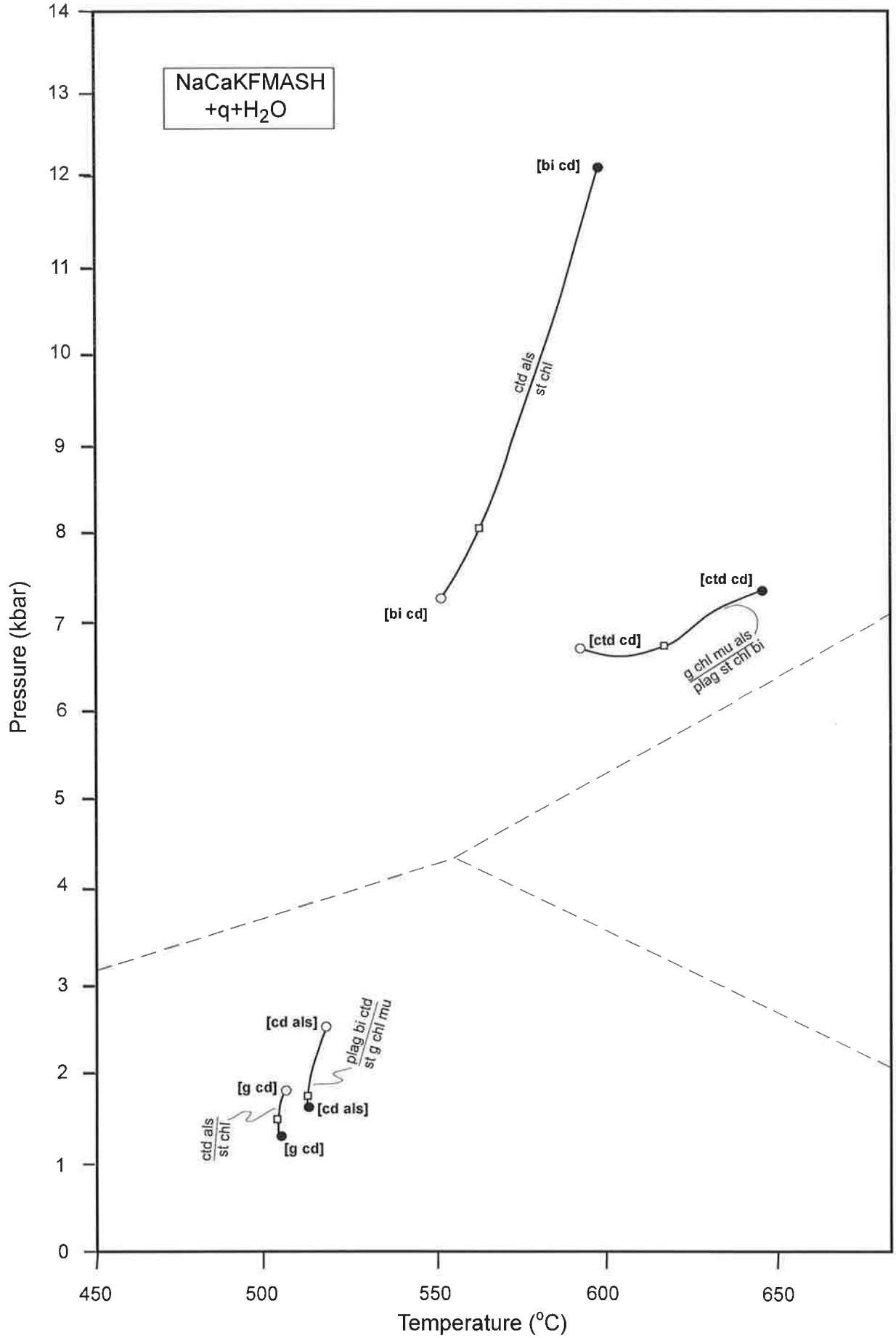

Figure 5.5b. Petrogenetic grid for the NaCaKFMASH chemical system without the underlying NaKFMASH and CaKFMASH subsystems. Univariant reactions end at invariant points in the underlying subsystems. Unfilled circles represent the CaKFMASH subsystem and filled circles indicate the NaKFMASH subsystem.

expanded NaCaKFMASH system used here. This latter feature is desirable since although petrologists concentrate on the use of two-mica bearing, plagioclase-absent metapelites in elucidating metamorphic histories (due to the desire to remain within the KFMASH system and therefore use generally lower variance assemblages), many metapelites do contain plagioclase and are not muscovite-saturated. Plagioclase-bearing metapelitic rocks have generally not been widely used for petrogenetic investigation since the inclusion of plagioclase necessitates the use of an 8 component model system. Thus although an extra phase (plagioclase) has been included, a divariant assemblage in KFMASH will become trivariant in NaCaKFMASH and consequently more difficult to constrain. Direct comparison between the KFMASH system and the NaCaKFMASH system not only enables the influence of the growth of plagioclase upon the stability of other common phases to be monitored, but also allows correlation of P-T information recorded in feldspar-absent two-mica metapelites with that recorded in chemically distinct and independent calcic metapelitic lithologies from within the same terrain.

5.3.1 The CaKFMASH and NaKFMASH subsystem grids

In order to extend the KFMASH system (as used in §5.3) into the full NaCaKFMASH grid the intermediate CaKFMASH and NaKFMASH subsystem grids were first calculated using pure anorthite and albite respectively as the appropriate feldspar species, although these are uncommon in natural assemblages. In both subsystems the calculated stable invariant points are identical to that of the KFMASH system although displaced in P-T space. The only exception is the [g st] invariant which in NaKFMASH is metastable. Calculated

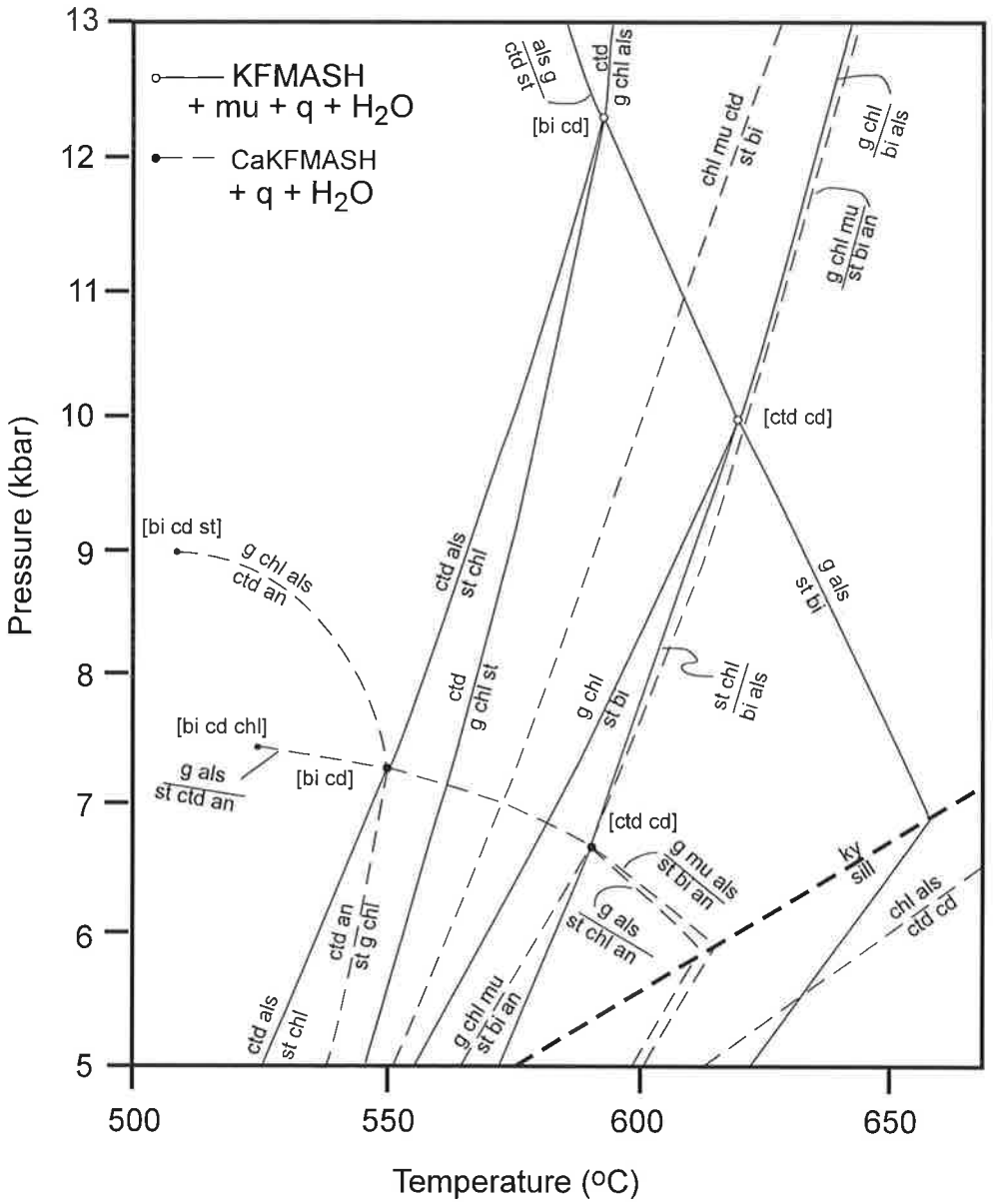

Figure 5.6. Detail of part of the KFMASH and CaKFMASH systems demonstrating how the CaKFMASH grid is connected to the subsystem grid via [g an] univariant reactions which link through the stable invariant points common to both systems.

results for stable invariant equilibria and cation substitutions used to describe solid solutions in participating minerals are presented in Tables 5.1 and 5.2. A number of degenerate reactions and singularities occur in the CaKFMASH and NaKFMASH subsystems and in the NaCaKFMASH, full system due to the restricted number of phases available for K, Na and Ca substitutions. Worley and Powell (1998a) provide an excellent discussion on the mechanics of calculating a full system petrogenetic grid from subsystem grids and the difficulties encountered as a result of degeneracies and singularities, hence only a brief account will be presented here.

In CaKFMASH, the calculated stable invariants are linked to the KFMASH subsystem by the degenerate [g an] univariants, as grossular is the only other phase able to exchange Ca with anorthite (Figure 5.6). An example of this is the [ctd cd] invariant in CaKFMASH which is linked to the [ctd cd] invariant in KFMASH by the degenerate [g an] univariant reaction st + chl + mu bi + ky. In Figure 5.6 this is demonstrated by the [g an] univariant passing through both the KFMASH and CaKFMASH [ctd cd] invariants. This degeneracy exists because the phases taking place in the reaction (i.e. st, chl, bi,

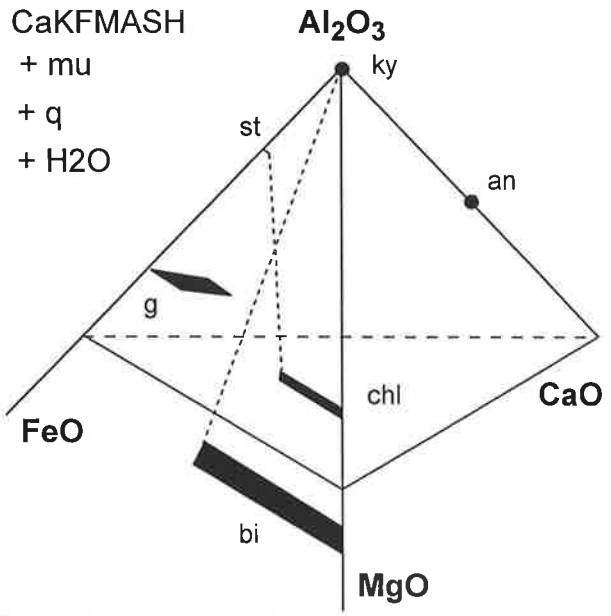

Figure 5.7. A compositional tetrahedron defined by CaO-FeO-MgO-Al_2O_3 with mu, q & H2O in excess, demonstrating the concept of degenerate reactions. In the reaction st +chl = bi + ky, all particpating phases lie on the FeO-MgO-Al2O3 plane of the tetrahedron, thus the reaction effectively occurs within the FMASH subsystem.

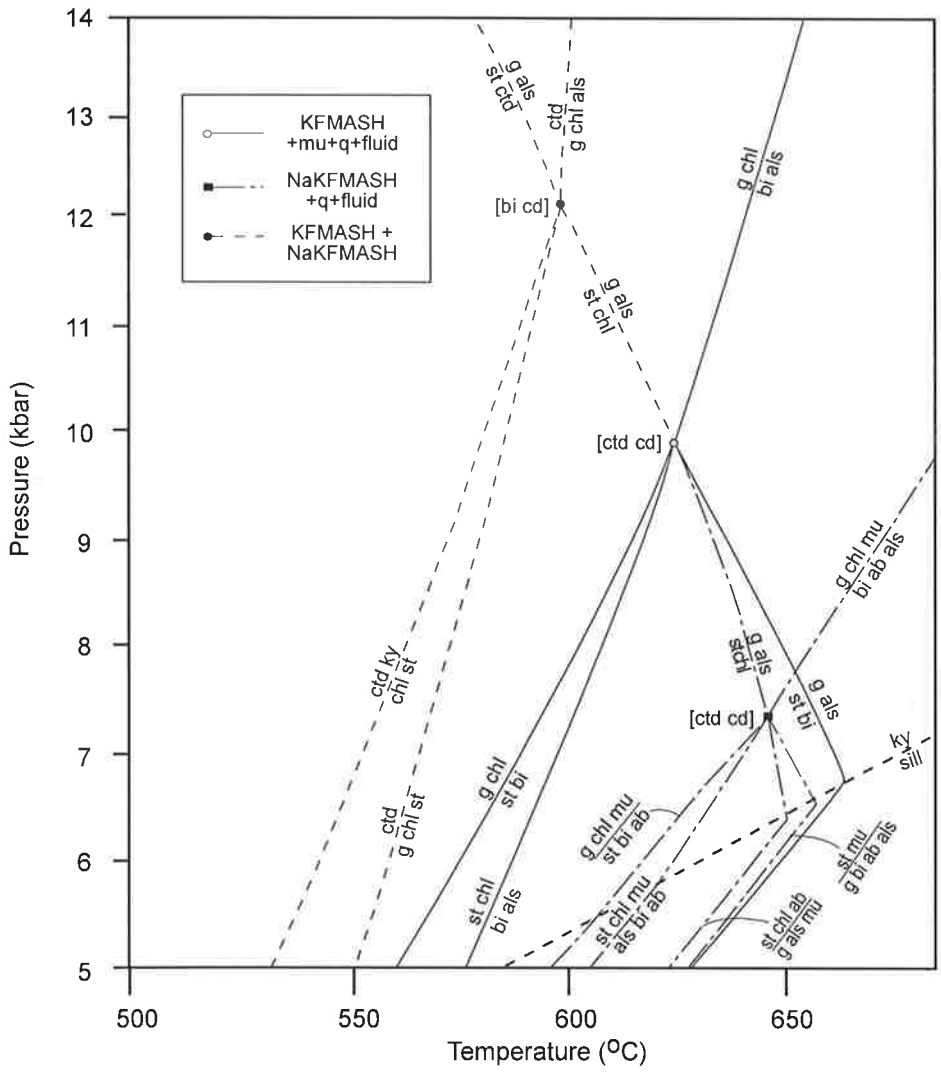

Figure 5.8. Detail of part of the KFMASH and NAKFMASH petrogenetic grids demonstrating how they are linked via degenerate [bi mu ab] univariant reactions.

ky) are coplanar, lying within the Al_2O_3-FeO-MgO plane of the CaO-Al_2O_3-FeO-MgO tetrahedron (with muscovite, quartz and H_2O in excess) (see Figure 5.7). Therefore the reaction can be written in terms of these Al_2O_3-FeO-MgO phases only, indicating that the reaction is effectively a subsystem reaction. While the calcium-bearing phases garnet and anorthite are not required to write the equation, the garnet structure includes Ca, Fe and Mg in solid solution and therefore still maintains chemical equilibrium with the reacting assemblage.

In a similar fashion, the NaKFMASH stable invariants are linked via the degenerate [bi mu ab] univariants (Figure 5.8). These [bi mu ab] reactions are degenerate with respect to muscovite as this is the only phase able to exchange Na with albite, but are also degenerate with respect to biotite as this is the only phase able to exchange K with muscovite. Regardless, the [mu] equilibria still involve biotite in the equilibrium assemblage because although its modal proportions are fixed by the amount of potassium present in the system, biotite is still free to interact in the reaction via Fe-Mg and tschermaks substitutions. Therefore these reactions can be effectively described in the FMASH subsystem and participating biotite compositions can still be calculated. Similarly, [an] reactions degenerate with respect to garnet also still involve garnet via substitutions in the FMASH subsystem. As a result of these degeneracies, there are effectively no new stable invariant points possible in the CaKFMASH or NaKFMASH systems. Thus the expansion of the KFMASH grid into these higher systems does not greatly affect the topology of either of the resultant petrogenetic grids.

A singularity occurs in CaKFMASH along the [ctd cd] [bi] univariant which is equivalent to the [bi cd] [ctd] univariant, and along the [ctd cd] [st] univariant a singularity exists in both the CaKFMASH and NaKFMASH subsystems. Singularities can occur when phases involving solid solutions take part in a univariant reaction. Since minerals with solid solutions may change their compositions at different rates in response to the changing P-T environment, a compositional colinearity or coplanarity can develop at some point along a univariant, that is the univariant becomes a degenerate reaction. As a result the topology of the reaction changes across this colinearity or coplanarity and one or more solid solution phases may consequently alter from product to reactant or vice versa. As an example, in the CaKFMASH subsystem the [ctd cd] [bi] univariant reaction st + chl + an g + ky, at low P/high T can be represented on a CaO-Al_2O_3-FeO-MgO tetrahedron with quartz and H_2O in excess by a g-ky tie-line piercing a st-chl-an plane (Figure 5.9a). With increasing pressure and decreasing temperature, garnet becomes more calcic and loses magnesium at a rate greater than the accompanying loss of magnesium in staurolite. Eventually g-st-ky-an become compositionally coplanar (Figure 5.9b). At this point the reaction can be written st + an = g + ky and is represented by the crossing of the st-an and g-ky tie-lines with the st-an-g-ky plane, as such

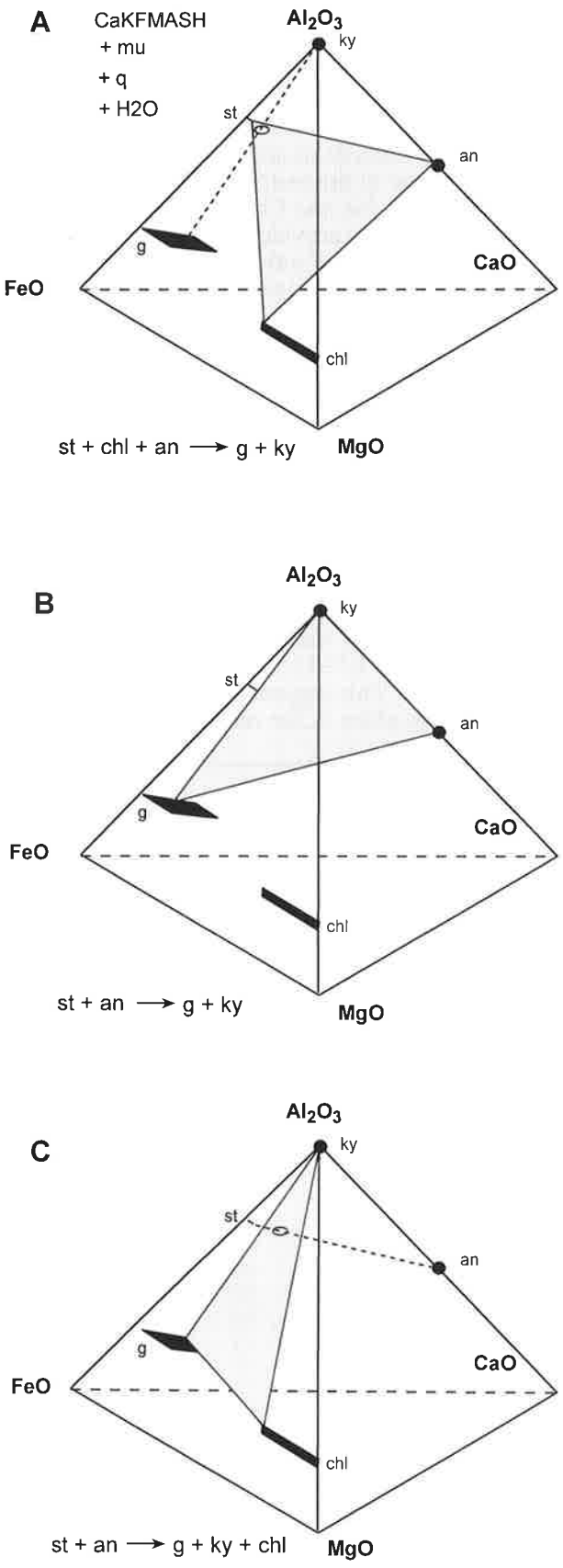

Figure 5.9. CaO-FeO-MgO-Al_2O_3 compositional tetrahedra with quartz and H_2O in excess, indicating how a compositional coplanarity exists between g-st-ky-an due to changing g and st compositions with increasing pressure and decreasing temperature.

it does not involve chlorite. With further increase in pressure and decrease in temperature garnet continues to decrease its Mg content (and increase in Ca) at a faster rate than staurolite and the coplanarity is broken. The reaction now becomes st + an = g + ky + chl and is represented as a st-an tie-line piercing a g-chl-ky plane (Figure 5.9c).

5.3.2 The NaCaKFMASH grid

The full system NaCaKFMASH grid involving the phases muscovite, biotite, garnet, staurolite, cordierite, chloritoid, kyanite, sillimanite, andalusite, chlorite, quartz, plagioclase and H_2O is shown in Figures 5.5 a & b. Compared to the subsystem grids, the NaCaKFMASH grid appears quite simple, containing no new invariant points and only a small number of univariant reactions linking the stable invariant points calculated in the subsystems. These univariant reactions effectively track the CaAlNa-1Si-1 substitution in plagioclase between the pure albite- and pure anorthite-bearing invariants of the subsystems (Figure 5.5 b). Whereas in the subsystem calculations these endmembers were used to model plagioclase involvement, in the full system non-ideal but continuous Na_2O-CaO mixing in plagioclase is assumed, using the activity-composition models (C1 and I1) employed by Worley and Powell (1998a). The point along the univariants at which stability of the C1 and I1 models swap are marked on the grid as open squares. Note the trend toward C1 (sodic) plagioclase at the lower temperature end of the univariants and I1 (calcic) at the upper temperature end. As observed in the CaKFMASH and NaKFMASH subsystems, a number of degeneracies and singularities also exist in the NaCaKFMASH full system. The degeneracies again relate to the limited number of phases available to take part in Na, Ca and K cation exchange. The singularities involve muscovite and biotite changing reaction sides on the univariant reaction mu + ctd + als bi + st + chl which links the subsystem [g cd] invariants, and plagioclase and garnet changing sides on the reaction plag + ctd + ky = g + st + chl which links the [bi cd] subsystem invariants. In both cases the relevant phases 'swap sides' of the reaction numerous times over the range of a few degrees in temperature, suggesting that the composition of the phases is very close to a coplanarity over much of the length of the reaction.

The trend toward fewer stable invariant points and

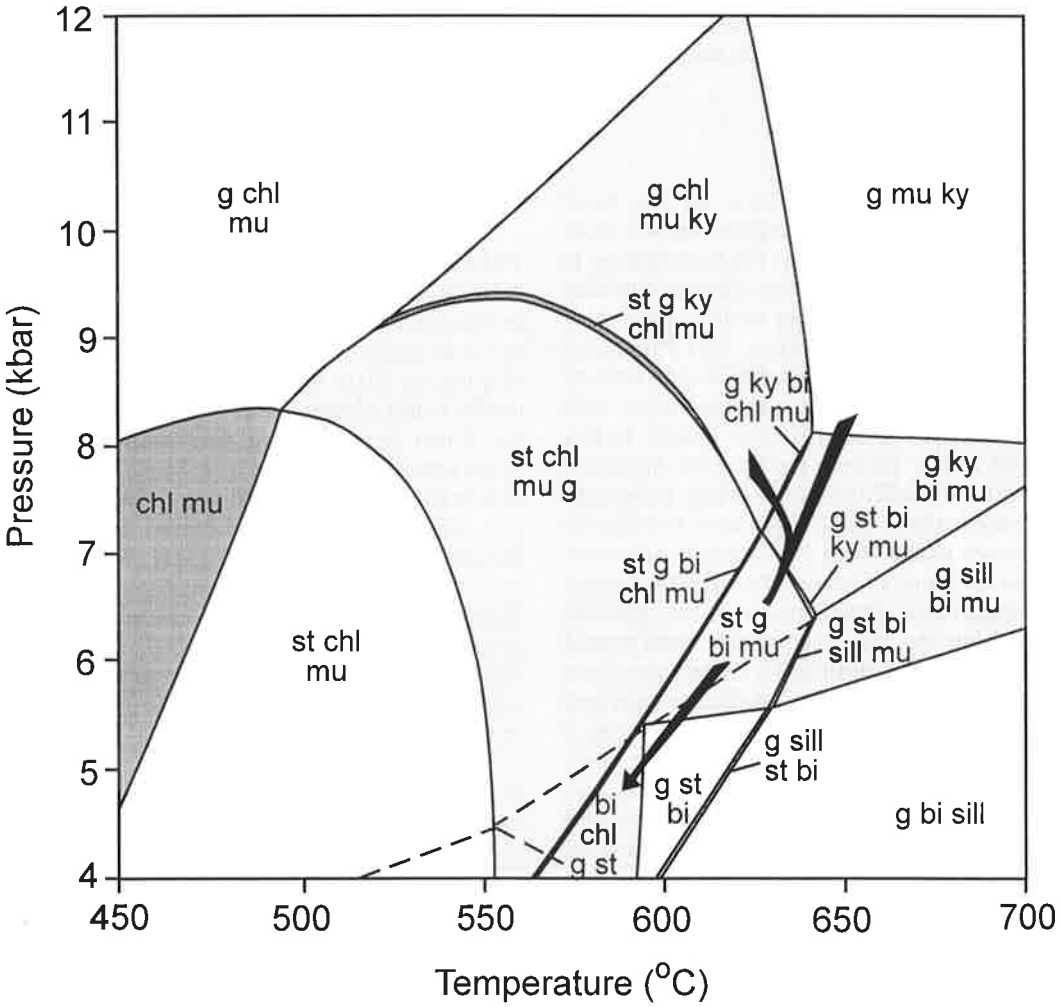

Figure 5.10. Pressure-temperature pseudosection constructed for a metapelitic rock of bulk composition A:F:M:K:C:N = 44.44 : 24.05 : 10.3 : 3.03 : 7.27 : 10.91, with plagioclase, quartz and H_2O in excess. The bifurcated black arrow indicates the possible paths taken by the Yambah Schist Zone metabasites.

univariant reactions in more chemically complex petrogenetic grids is not unreasonable nor unexpected. A general observation made in natural rock systems is for continuous reactions within and between minerals capable of solid solution to dominate reaction sequences, producing numerically few, chemically complex minerals in high variance assemblages, rather than predominantly discontinuous reactions producing numerous new minerals and subsequently low variance assemblages. The trend toward high variance assemblages in natural rocks, highlights an advantage of calculated grids over qualitative petrologically derived ones. Petrogenetic grids calculated from integrated thermodynamic datasets not only contain information on all the invariant and univariant reactions for every possible bulk composition in the modelled system, but also on the manner of chemical and modal variation of phases during continuous reactions in multi-variant fields, which comprise the bulk of P-T space. Consequently rocks composed of high variance assemblages and displaying evidence of chemical disequilibrium such as chemical zonation, are potentially useful for inferring metamorphic trajectories. The calculation of P-T pseudosections specific to the bulk composition of the selected samples provides explicit representation of the assemblages formed and reactions 'seen' by a given rock, as well as the composition and modal proportion of each participating phase as the rock tracks through P-T space.

5.3.3 Results

A P-T pseudosection appropriate to the bulk composition of the metapelitic samples studied from Pinnacles Bore and the Cadney Metamorphics is presented in Figure 5.10, and demonstrates the way in which the mineralogy of these rocks would vary with changing physical conditions. The Pinnacles Bore and Cadney Metamorphics ASO-aged schists generally consist of high variance assemblages with the lowest variance assemblages found being trivariant. The major phases rarely host included minerals useful in defining an earlier prograde assemblage, nor is there any evidence of retrograde reaction textures aside from the growth of minor chlorite at the expense of staurolite. Furthermore, unlike the plagioclase-absent metapelites, garnets from these schists do not have easily interpreted chemical zoning profiles defining a simple prograde evolution which can be easily modelled within one divariant field. Instead, the relative timing of major mineral growth potentially provides the only constraints on the P-T evolution of these schists, and suggests movement through a succession of tri- and quadrivariant fields via a series of continuous reactions.

Textural evidence suggests that while kyanite, garnet, biotite, staurolite and quartz do occur as an equilibrium assemblage in these rocks, the growth of staurolite was initiated somewhat later than the other phases. Since these rocks do not contain significant amounts of platy or acicular minerals aside from minor biotite, they have not all developed a strong foliation, therefore evidence of the crystallisation sequence is limited. However there are examples of coarse-grained kyanite and porphyroblastic garnet being overprinted by staurolite (Figure 4.4b), of embayed kyanite, and of minor retrograde chlorite growing at the margins of staurolite possibly at the expense of garnet (see Figures 4.3 and 4.4). These observations suggest the rocks followed a path beginning in either the g-chl-mu-ky-q-H_2O trivariant or g-mu-ky-q-H_2O quadrivariant, moving down pressure into the g-ky-bi-mu-q-H_2O trivariant, through the very narrow g st ky bi mu-q-H_2O divariant and g-st-bi-mu-q-H_2O trivariant, where growth of staurolite is first stabilised, through the g-st-bi-q-H_2O quadrivariant and into the g-st-chl-bi-q-H_2O trivariant where retrograde chlorite growth is stabilised while garnet is consumed and staurolite becomes more Fe rich. Muscovite is present for much of the high temperature-high pressure part of this trajectory, but is being consumed continuously during the down pressure path through the g-ky-bi-mu-q-H_2O trivariant, forming less than 3% of the rock by the time staurolite growth is commenced with entry into the g-st-ky-bi-mu-q-H_2O divariant. While muscovite is not observed in the calcic metapelites, it is present as a minor phase (~1%) in CM19, suggesting that it may have completely reacted out in the other samples. This P-T path describes either isothermal decompression with some retrogressive cooling late in the path, or a clockwise trajectory in P-T space consistent with that implied for the plagioclase-absent metapelites from the same terrain.

5.4 Conclusion

The Pinnacles Bore-Winnecke ASO-aged metapelitic schists are typical of many commonly observed metapelites in that they are composed of high variance mineral assemblages which are well equilibrated, displaying little in the way of reaction textures or useful relict phases. The construction of a P-T path for such rocks using univariant equilibria in petrogenetic grids, on the basis of petrographic interpretation is difficult given the lack of identifiable pre- and post-peak equilibrium assemblages, and the prevalence of mineralogical change in response to continuous rather than discontinuous reactions. However well developed chemical zonation in porphyroblastic garnet combined with petrographic interpretation of sequential mineral growth can enable some inferences to be about the general trajectory of these rocks in P-T space.

In the Pinnacles Bore-Winnecke plagioclase-absent metapelites, chemical zonation patterns in the garnets are interpreted as resulting from growth during prograde metamorphism as they ubiquitously display classic bell-shaped Mn, and inverted Mg and Fe profiles. Estimates of metamorphic conditions using cation exchange geothermometry and geothermobarometric calculation modes in THERMOCALC generally closely agree, and inevitably show consistent trends of increasing temperature and pressure when comparing core and rim assemblages, also consonant with prograde

metamorphism. The use of P-T pseudosections calculated for an appropriate bulk composition suggest the rocks moved along a clockwise P-T path probably from the chlorite + garnet + biotite (+ muscovite + quartz + H_2O) divariant field across the staurolite isograd into the staurolite + garnet + biotite (+ muscovite + quartz + H_2O) divariant. They achieved peak metamorphic conditions within this field, at about 600-620°C and 6.5 kbar at ~ 320 Ma, then progressed along a retrograde exhumation and cooling path through the staurolite + biotite (+ muscovite + quartz + H_2O) trivariant and into the staurolite + chlorite + biotite (+ muscovite + quartz + H_2O) divariant or chlorite + biotite (+ muscovite + quartz + H_2O) trivariant.

When observed in the field and in section, the calcic metapelites from shear zones at Pinnacles Bore and in the Cadney Metamorphics appear coeval with feldspar-absent two-mica metapelitic schists occurring adjacent to them and in nearby shear zones. However compositional maps (§4.3.1) suggest that these rocks may contain inherited garnet cores. The chemical complexity of the calcic metapelites, as demonstrated in the compositional maps and quantitative traverses of the garnets, highlights the inherent difficulties in applying geothermobarometry to these samples, given the uncertainties in determining equilibration between phases. It also creates difficulties in selecting an appropropriate bulk composition for calculating pseudosections, as it is apparent that some of the garnet present is effectively chemically isolated from the reacting portion of the rock volume (e.g. Stüwe, 1997). Estimates from geothermobarometry on rim assemblages vary somewhat between methods, but suggest the rocks achieved conditions of about 600°C - 640°C and 6-7 kbar. However whether these estimates represent peak or close to peak metamorphic conditions is debatable, as no clear interpretation of the P-T trajectory is possible from the zoning profiles observed in the garnets. Petrogenetic assessment of these rocks is complicated by the presence of plagioclase and lack of muscovite, requiring the use of a petrogenetic grid calculated in the NaCaKFMASH system. From a pseudosection calculated using an appropriate bulk composition, and the apparent hierarchy of mineral growth observed petrographically, a path of isothermal decompression followed by retrograde cooling, or a clockwise P-T path is inferred. A clockwise trajectory for the calcic metapelites is consistent with evidence for a clockwise P-T path for adjacent and interbedded metapelites of different bulk composition.

Chapter 6

METAMORPHIC EVOLUTION OF PALAEOZOIC METABASITES IN THE YAMBAH SCHIST ZONE, N.W. STRANGWAYS METAMORPHIC COMPLEX

6.1 Introduction

The Yambah Schist Zone, located in the northwest of the study area, records the oldest Sm-Nd ages of the shear zones investigated in this study (i.e. ~380-400 Ma) (see §3.6). This age data, in conjunction with a Sm-Nd age of 381 ± 7 Ma from a prograde garnet-bearing mafic amphibolite from the West Bore Shear Zone (Ballèvre et al, 2000) and a U-Pb age of about 385 Ma from monazite in a staurolite-bearing shear zone rock from Edwards Creek (Möller et al, 1999) (Figure 3.7) suggests that these northern shear zones were active, and achieved peak metamorphism approximately 60 m.y. earlier than shear zones in the southern Strangways Metamorphic Complex such as the Pinnacle Bore Shear Zone and the Erontonga Shear Zone.

Although the area containing the Yambah Schist Zone has been the focus of a number of studies (e.g. Shaw et al, 1979; Iyer, 1974; Iyer et al, 1976; Windrim, 1983; Windrim and McCulloch, 1986), much of their work has focused on describing and interpreting the geological evolution of the Palaeoproterozoic granulite facies country rocks, which enclose the Yambah Schist Zone. In comparison information about the rocks which define the Yambah Schist Zone is scant, with few detailed descriptions of the lithologies present or an assessment of their metamorphic evolution.

This chapter concentrates on describing the metabasic rocks found in the Yambah Schist Zone, investigating the metamorphic conditions which created them, and determining their path through P-T space.

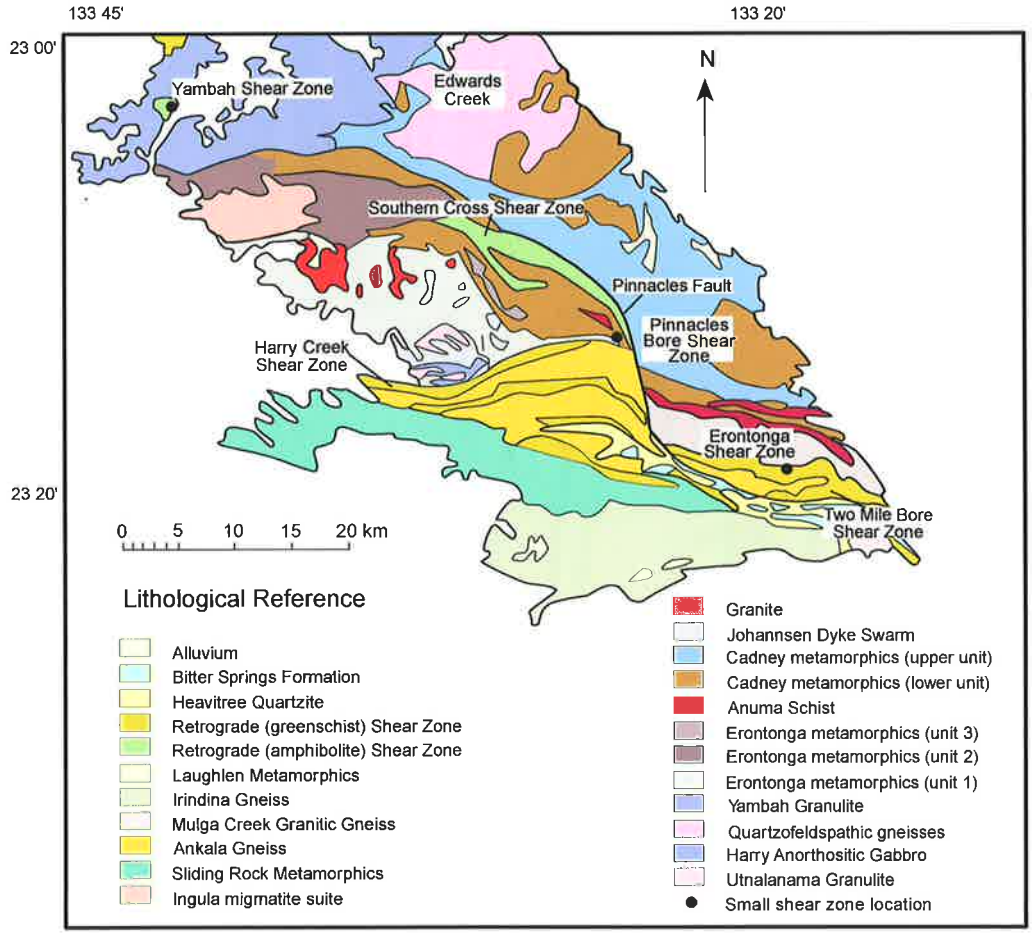

Figure 6.1. Location map of the southern Strangways Metamorphic Complex indicating the position of the Yambah Schist Zone, Edwards Creek area and other significant shear zones in the terrain.

6.2 Lithological observations in the Yambah Schist Zone

The Yambah Schist Zone (Figures 6.1 & 6.2) is a discrete unit consisting of interlayered mafic, metapelitic and quartzofeldspathic schists and discontinuous subordinate calc silicate bodies, which cross-cut the surrounding mafic, ultramafic and felsic Proterozoic granulite facies country rock. The shear zone rocks have been metamorphosed to mid-amphibolite facies and are typically medium to coarse grained. Detailed petrography of selected samples is presented in Appendix 1. In the area sampled, the Yambah Shear Zone outcrops as two distinct areas which have their fabrics oriented orthogonal to each other but are separated by obscuring alluvium. Fabrics in the northern outcrop zone trends E-W approximately orthogonal to the compositional layering and structural fabrics in the host granulite, while in the eastern outcrop zone the foliation trends N-S, approximately parallel to the granulite fabrics (see §2.4.1). Metapelitic schists in the Yambah Schist Zone contain the assemblage quartz + biotite + kyanite ± (muscovite, staurolite), with kyanite commonly occurring as lenticular or euhedral bladed porphyroblasts up to 2 cm in length within a quartz + biotite + muscovite matrix. When present, staurolite occurs generally as porphyroblasts up to 1 cm long, however the Yambah Schist is renown for a number of small but spectacular metapelitic units which contain euhedral staurolite crystals up to 5 cm in

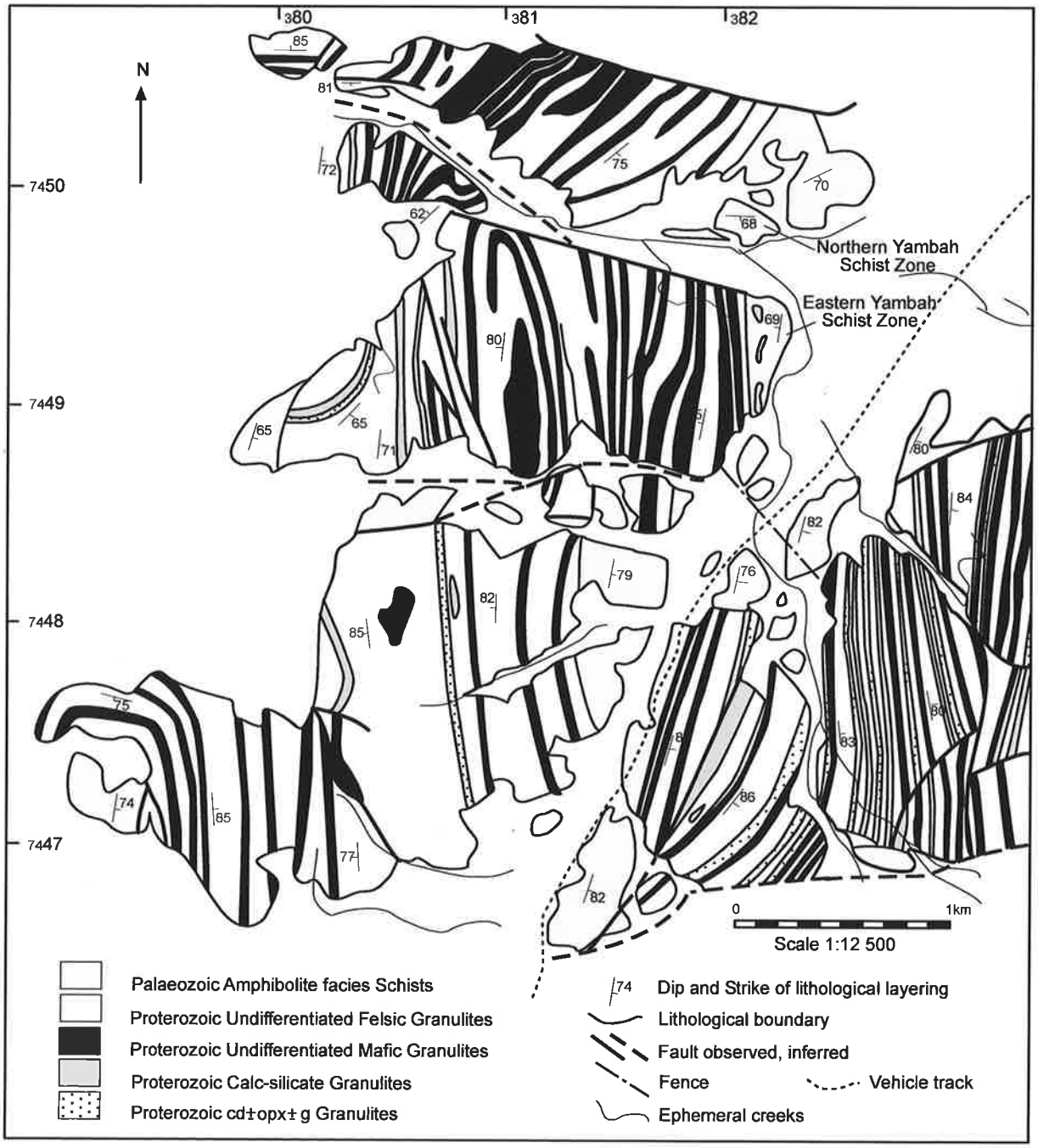

Figure 6.2. Generalised geology of the Yambah Schist Zone. (Adapted from Windrim, 1983).

length.

The assemblages found in the metapelites are at best trivariant in KFMASH and are consequently stable over a large range of P-T space (e.g. Worley and Powell, 1998b) for moderate Fe and Al bulk compositions and particularly for bulk compositions which plot above the chlorite-garnet tieline in AFM. In addition, garnet was not found in the metapelites during this investigation, and thus the metapelites are less useful for study using phase equilibria or standard geothermobarometry than the mafic amphibolites found at Yambah. However the presence of staurolite and almost ubiquitous presence of kyanite in these rocks, coupled with the rare occurrence of sillimanite (Figure 6.3 a-e) suggests the maximum temperature achieved by these rocks must be near the kyanite-sillimanite univariant.

The metabasic amphibolites of the Yambah Schist are noteworthy as they occasionally have the uncommon assemblages of hornblende + staurolite + plagioclase + quartz + ilmenite ± garnet or hornblende + quartz + plagioclase + kyanite as well as the more common, classic amphibolite facies assemblage of hornblende + plagioclase + quartz ± garnet. The aluminous staurolite-bearing metabasites often preserve evidence of incomplete reactions which provide some information about the metamorphic history of the rocks, and were thus targeted for study.

6.2.1 Petrography

Despite the complex polymetamorphic history of their multiply deformed granulite facies precursors, the metabasites in the Yambah Schist Zone record an apparently simple chemical and microstructural history. They have a simple schistose fabric defined by the preferred orientation of hornblende, quartz and staurolite (where present) (Figure 6.3 f-h), and it appears that the granulite facies phases which existed in the precursor rocks have been completely recrystallised to a stable amphibolite facies assemblage.

The majority of mafic schists outcropping consist of the typical amphibolite assemblage hornblende + quartz + plagioclase ± garnet. Variation in the number of phases present in the amphibolites probably reflects differences in bulk composition with more Fe- and Ca-rich samples producing more garnet and plagioclase. Staurolite-bearing amphibolites are rarer and appear to reflect local variation in alumina levels within the mafic units (Figure 6.3 f-h). In these schists, garnet and staurolite coexist, but their morphology and textural relationship can vary between samples. Staurolite can occur as coarse embayed, poikiloblastic grains seen in contact with garnet and as inclusions within garnet, suggesting that it may have preceded the growth of garnet (Figure 6.4 a-c). In some samples it also occurs in contact with hornblende, plagioclase and quartz in apparent equilibrium (Figure 6.4 d & e), but frequently small (0.5 mm) relict corroded angular staurolite grains are observed within moats of quartz and plagioclase, separating it from hornblende and garnet (Figure 6.4 f-h). These textures are interpreted as evidence for the reaction:

$$\text{staurolite} + \text{hornblende} \longrightarrow \text{garnet} + \text{plagioclase} + \text{quartz} \quad (6.1)$$

Similar reaction textures have been reported by Arnold et al (1995) in mafic amphibolites in the adjacent Harts Range approximately 80 kms to the east of the Strangways Metamorphic Complex.

6.2.2 Mineral Chemistry

Detailed petrographic descriptions of individual samples from the YSZ are presented in Appendix 1.2.5, and selected representative electron microprobe analyses for garnet, staurolite, hornblende and plagioclase from each sample are presented in Appendix 2. Mineral analyses were performed on a Cameca SX51 Electron Microprobe at the Centre for Electron Microscopy and Microanalysis South Australia (CEMMSA) facility, University of Adelaide using an accelerating voltage of 15 kV and 20 nA current as standard operating conditions. Mineral analyses have been recalculated using the AX activity-composition computer program of Holland and Powell (1998) and the activity-compositions relations used by this program are tabulated in Appendix 3.1.

Hornblende is the dominant mineral in the mafic schists comprising up to 40% of the rock. It occurs as moderate to coarse elongate subhedral grains with a preferred orientation defining the schistose foliation of the rocks, and contains abundant inclusions of quartz, ilmenite and allanite, which is commonly surrounded by radiation damage haloes. The general composition is that of alumino-tschermakite to tschermakite according to the nomenclature of Leake (1978). Values of Al^{VI} range between 0.86 and 1.15 and XMg ranges between 0.54 to 0.62, but within samples, hornblende chemistry is quite homogeneous. Representative analyses of hornblende are presented in Appendix 2, with ferric recalculation performed according to the method of Holland and Blundy (1994) which is similar to that Spear and Kimball (1984) and Robinson et al (1982).

Garnet in the mafic schists commonly occurs as euhedral porphyroblasts ranging in size from 1 to 5 mm. It frequently has numerous inclusions of quartz, ilmenite and less commonly allanite which can produce a poikiloblastic appearance in coarser garnets, but small garnets are generally inclusion poor. In some samples, garnet has developed an elongate anhedral form, commonly associated with the reaction textures discussed in section 7.2.1. The garnets are dominantly almandine (65% to 68%) with lesser pyrope (18% to 23%), and minor spessartine (2% to 4%) and grossular (7% to 12%). The XFe ranges from 0.74 to 0.79, and is always greater than that of accompanying hornblende and staurolite. Concentric zoning in the major cations and the XFe is observed in garnets from all the samples and is discussed to detail below in section 6.3.2.

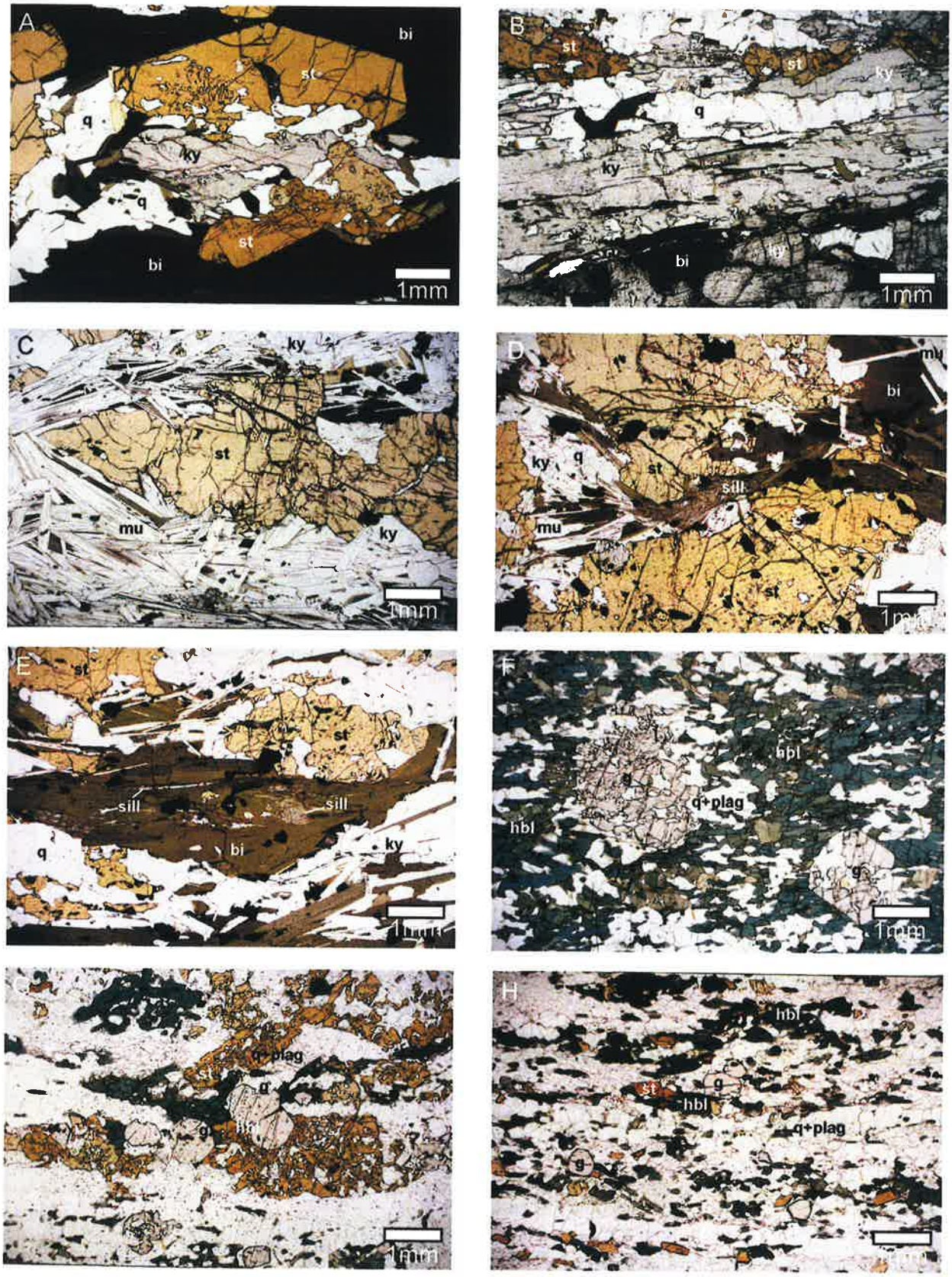

Figure 6.3. Representative mineral assemblages and textures in metapelitic and mafic amphibolites from the Yambah Schist Zone. (a) Sample YB30: typical coarse grained st-ky-bi-mu-q schist; (b) YB23: a fine grained, ky-rich st-ky-bi-q schist; (c) YB19: a st-ky-bi-mu-q schist with mu dominating the matrix. (d) YB31: late acicular sillimanite with biotite in the matrix. (e) YB31:foliation defining sillimanite; (f) YB149: a typical garnet-bearing mafic amphibolite with the fabric defined by the preferred orientation of hbl and q; (g) YS148: a staurolite-bearing mafic amphibolite. In this view garnet is partially enclosed by staurolite and appears to be in equilibrium with staurolite; (h) YS147:a st-bearing mafic amphibolite. This sample does not record the disequilibrium textures observed in some other examples of these rocks (e.g. Figure 6.4 b&c).

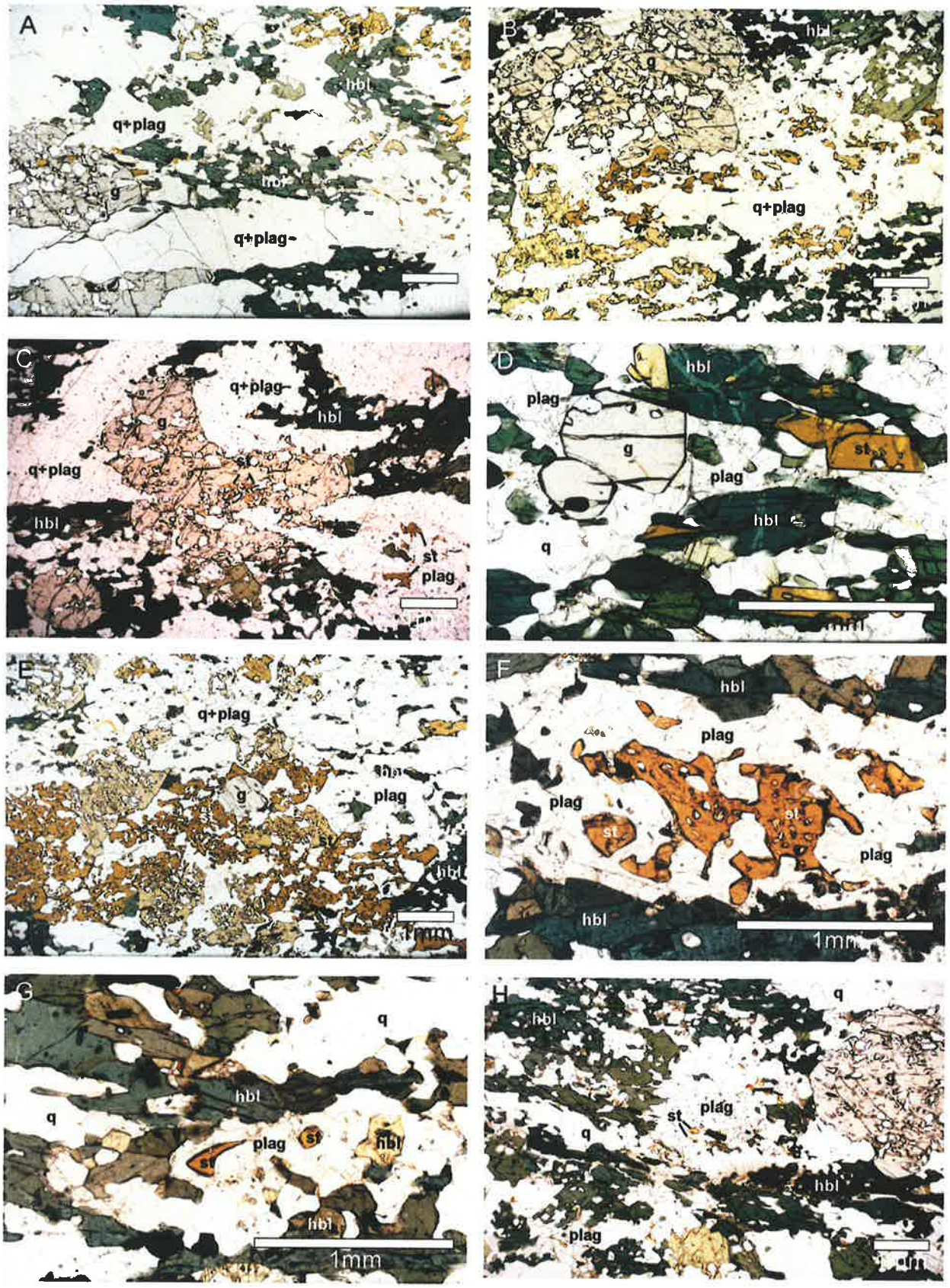

Figure 6.4. Representative mineral assemblages and textures in mafic amphibolites from the Yambah Schist Zone. (a) YS148: foliation defined by st and hbl and q ribbons. Note the embayed and poikiloblastic appearance of st; (b) YS148: garnet partially enclosing staurolite, and small relic grains of staurolite enclosed within plagioclase; (c) YS148: staurolite inclusions within garnet and plagioclase. This observation suggests that garnet growth was relatively late & occurred at the expense of staurolite; (d) YS147: apparent textural equilibrium between garnet, hornblende, staurolite and plagioclase; (e) YS147: garnet partially surrounded by poikiloblastic staurolite; (f), (g) & (h) YS148: relic staurolite surrounded by a moat of plagioclase. This observation suggests plagioclase grew at the expense of staurolite.

Staurolite occurs either as small (~0.5 mm) euhedral crystals, or coarser (to 2 mm) sub- to anhedral poikiloblastic grains. Where present in reaction textures, it occurs as small (<0.5 mm) anhedral corroded remnants surrounded by quartz and plagioclase. Staurolite does not exhibit any significant zonation and although XFe values between samples vary greatly, within samples the chemistry is quite homogeneous, generally ranging from 0.69 to 0.77 or 0.42-0.45. ZnO is a minor component, present at less than about 0.03 wt%.

Plagioclase, when present, is a major mineral and can comprise up to about 30% of the rock. It is dominantly anorthitic but can be compositionally

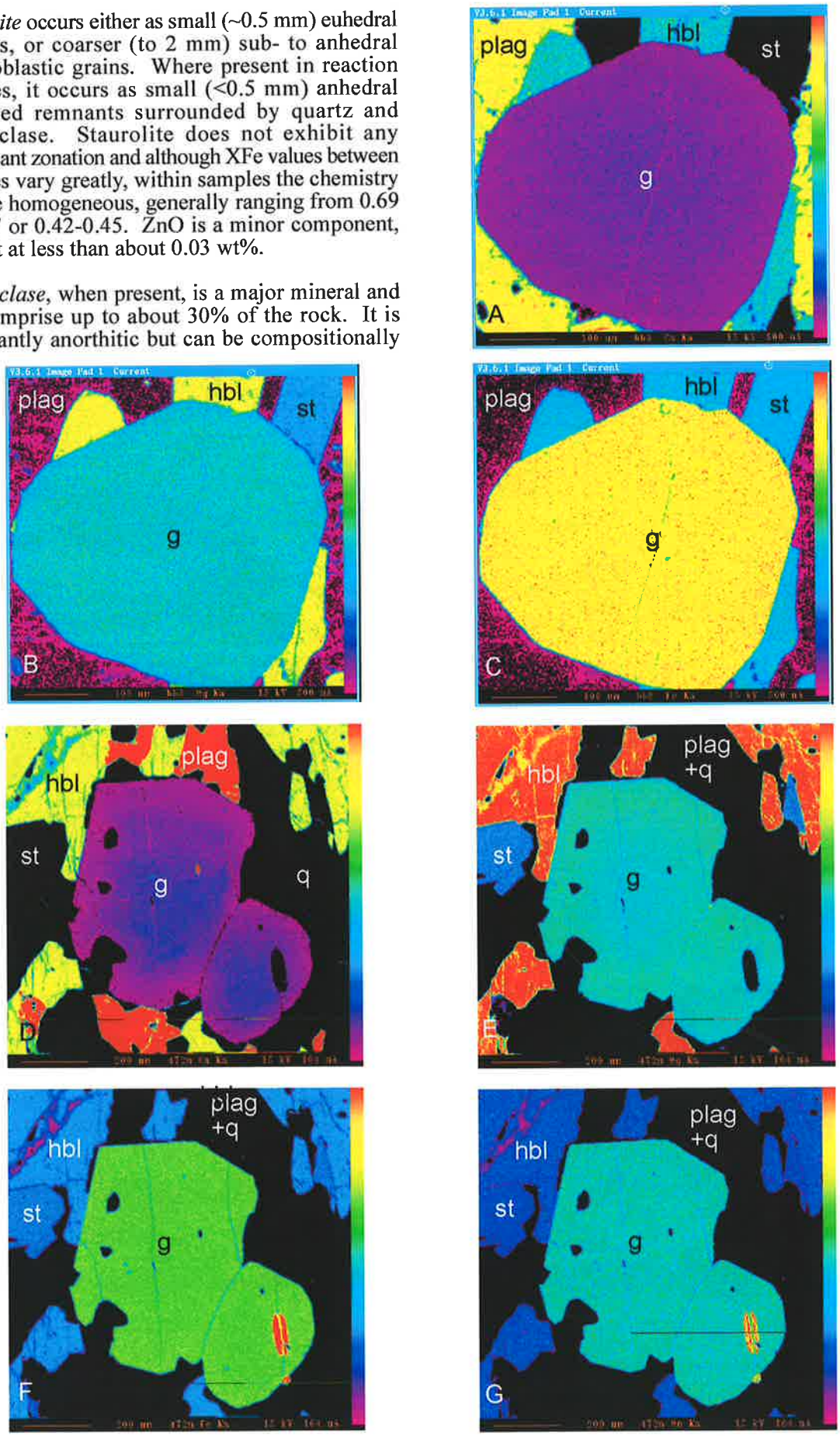

Figure 6.5. Qualitative compositional maps of garnets in a st-bearing mafic amphibolite (sample YS147). Note in (a) & (d) the consistent decrease in Ca rimwards, whereas (e) Mg increases rimwards while in (b) Mg appears homogeneous; (c) & (f) Fe and (g) Mn also appear homogeneous.

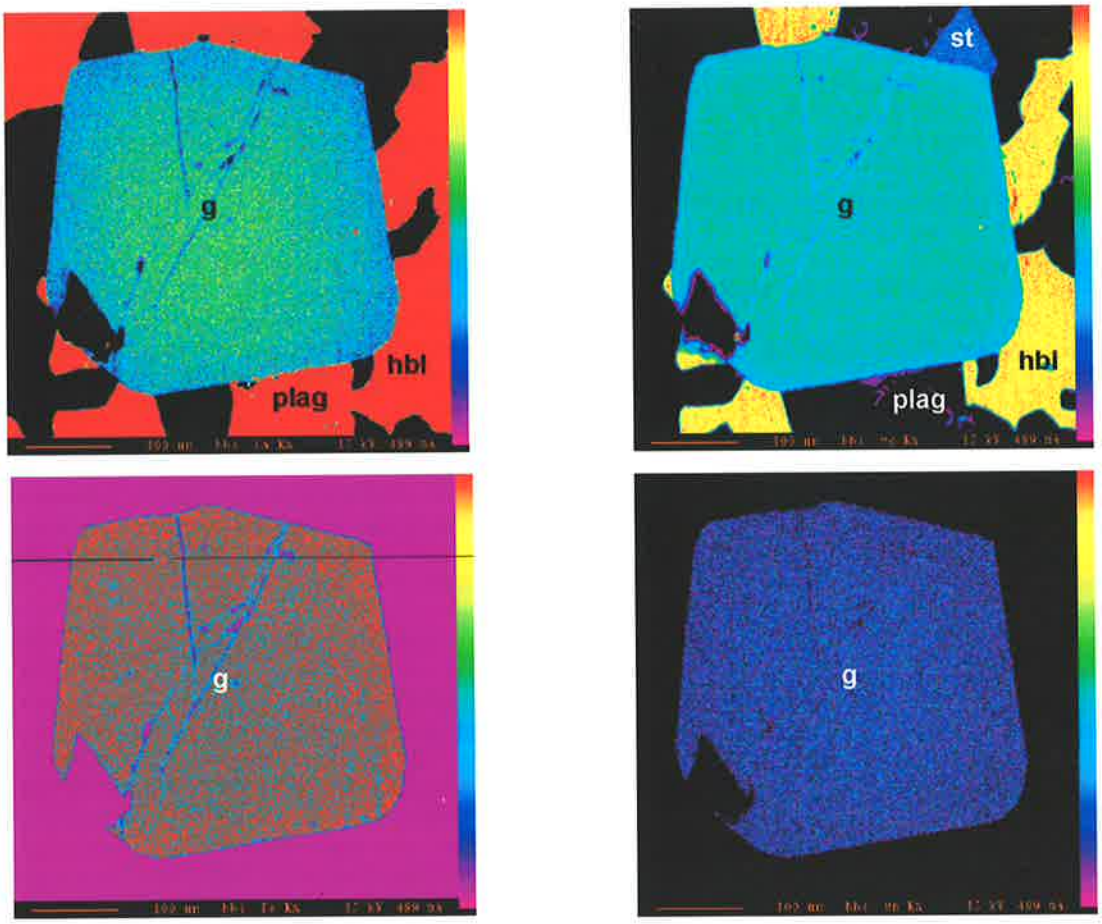

Figure 6.6. Qualitative compositional maps of garnet from st-bearing mafic amphibolite YS147. (a) Ca decreases rimwards while (b) Mg remains homogeneous except for a minor decrease at the garnet's margin; (c) Fe and (d) Mn appear homogeneous across the garnet. Adjacent hornblende, staurolite and plagioclase appear unzoned.

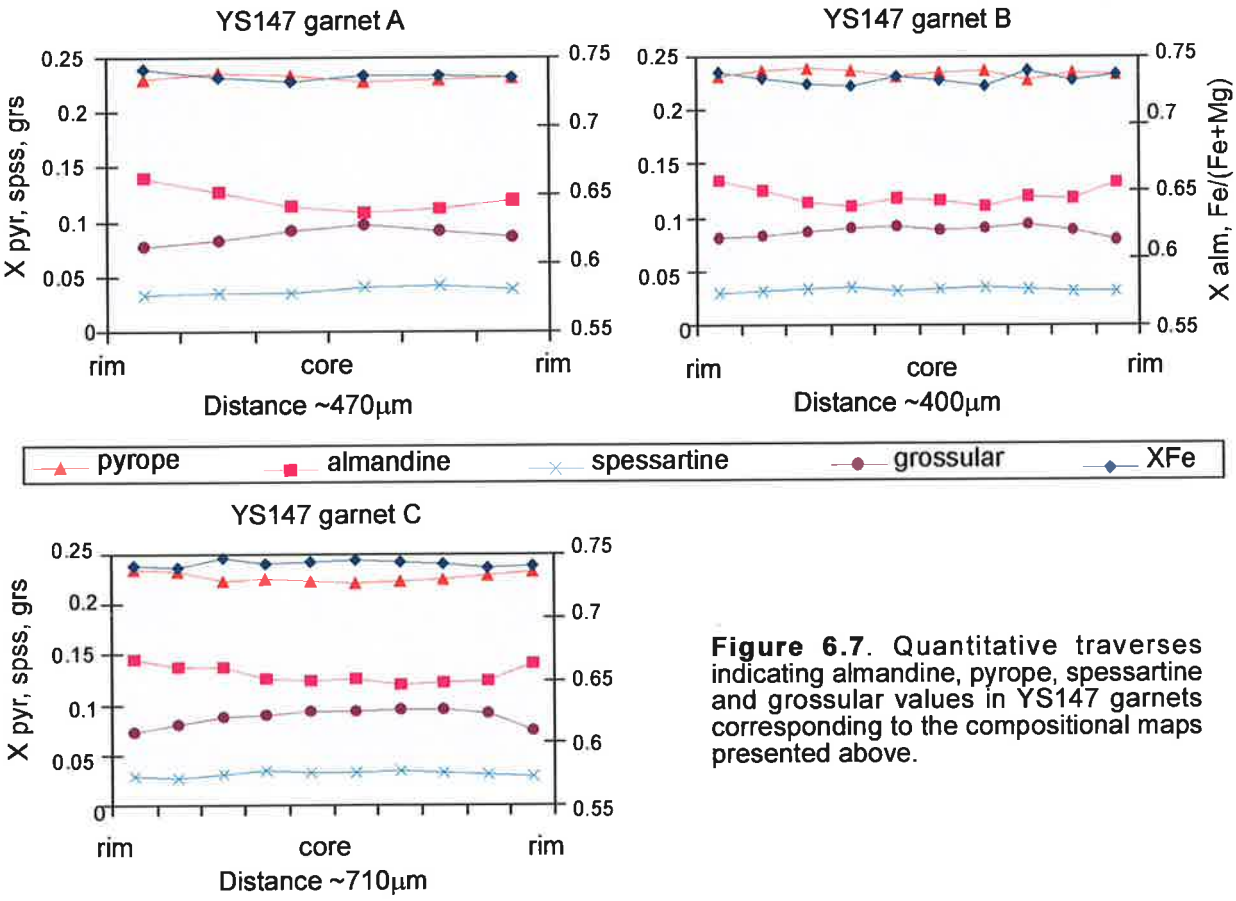

Figure 6.7. Quantitative traverses indicating almandine, pyrope, spessartine and grossular values in YS147 garnets corresponding to the compositional maps presented above.

zoned ranging from about $An_{85}Ab_{15}$ at the rim to $An_{92}Ab_8$ in cores of individual mineral grains. As a matrix mineral it commonly occurs as fine to moderate sized subhedral grains which tend toward a equigranular granoblastic texture. Where it occurs in conjunction with quartz as moats surrounding relic corroded staurolite or hornblende, it tends to be coarser grained and anhedral.

6.3 Physical conditions of metamorphism

6.3.1 Compositional mapping and P-T paths from zoned garnets

Mafic schists from the Yambah Schist Zone record Alice Springs Orogeny Sm-Nd ages (see §3.6) and appear have completely recrystallised during the ASO. Compositional mapping of five metabasites was undertaken to establish whether any phases in these rocks maintained chemical zonation profiles which might provide information on their metamorphic evolution. The selected samples included two staurolite-bearing amphibolites (YS147 and YS148) and two garnet-bearing amphibolites (YS9 and YS149). These were analysed using a Cameca SX51 electron microprobe to produce multiple qualitative compositional maps of Ca, Fe, Mg and Mn content in garnet and adjacent phases. Detailed discussions on the rationale for using this approach and the methodology adopted are presented in sections 4.3.1 and 4.3.1.1 respectively.

6.3.1.1 Results

Images from YS147, centred around small (~1 mm) euhedral garnets in contact with hornblende, staurolite, plagioclase and quartz, produced inconsistent results. In all cases the only mineral which displays any evidence of chemical zonation is garnet, however there is significant variation in the manner in which garnet is chemically inhomogeneous. In all cases, Ca decreases toward the rims of garnets, while Mn remains constantly distributed. However in one crystal (see Figure 6.5 b & c and Figure 6.6) Mg and Fe are apparently homogeneous, while in another (Figure 6.5 e) Mg increases rimward in contrast to Ca. Linear traverses of quantitative spot analyses support these trends (Figure 6.7) and indicate that the XFe of garnets are also quite variable.

By comparison, garnets from YS148 gave consistent results except for displaying variability in the distribution of Fe. Again garnet is the only chemically inhomogeneous phase, with all the garnets analysed having rimward decreases in Ca and Mn while Mg increases rimward (Figures 6.8 and 6.9). Fe appears essentially homogeneous across garnet porphyroblasts (Figures 6.8 and 6.9). Linear traverses of spot analyses are consistent with these observations and

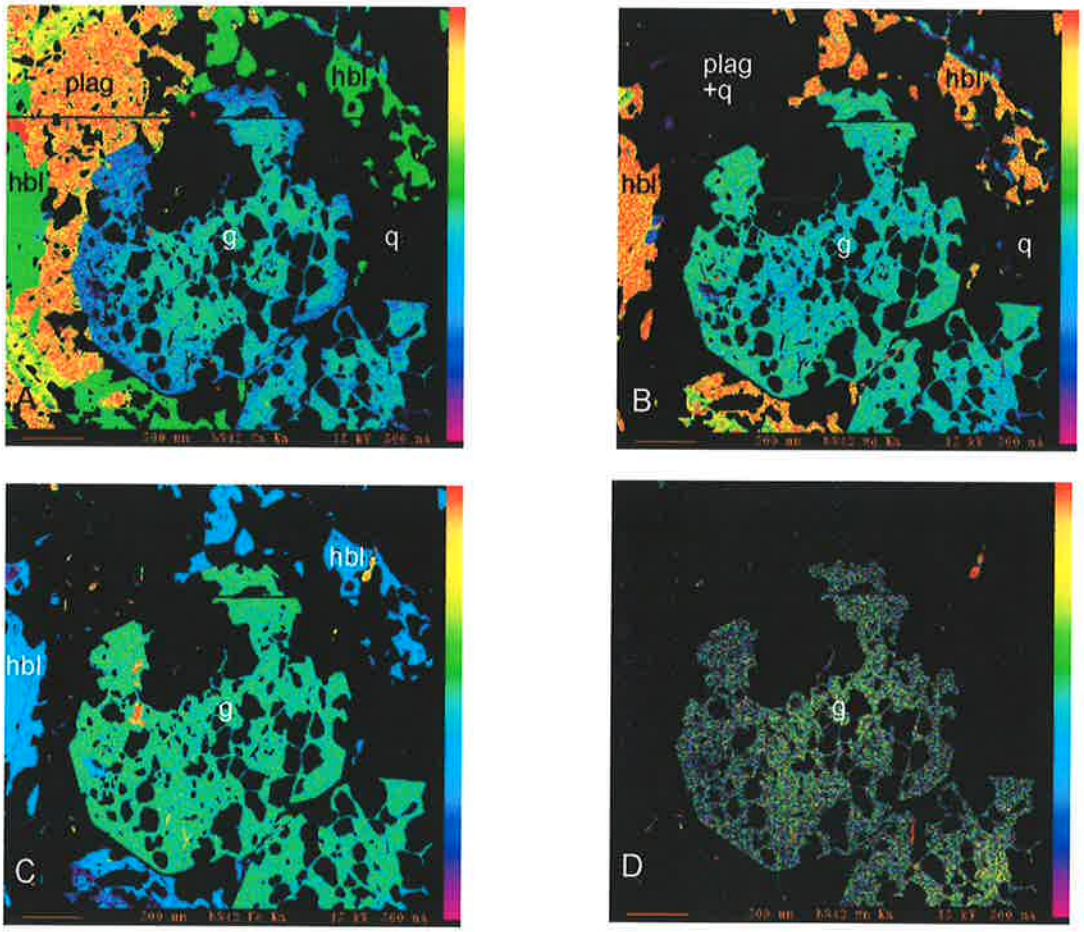

Figure 6.8. Qualitative compositional maps of a garnet in st-bearing mafic amphibolite schist YS148. (a) Ca and (d) Mn decrease rimwards while (b) Mg increases toward the garnet rim and (c) Fe appears essentially homogeneous in distribution. These trends suggest prograde growth zoning.

show XFe decreasing slightly in all the garnets (Figure 6.10).

Garnets from the garnet-bearing, staurolite-absent mafic schist YS149 are also consistently zoned, with Ca increasing and Mn decreasing rimward, while Fe and Mg remain homogeneous. One example (Figure 6.12) is an exception with Mg decreasing in a thin margin at the rim, suggesting some minor retrogressive re-equilibration. Calcium in the garnets appears patchily distributed compared with the other measured elements which are concentrically distributed, and in Figure 6.12 in particular this cation appears to be distributed in concentrated linear

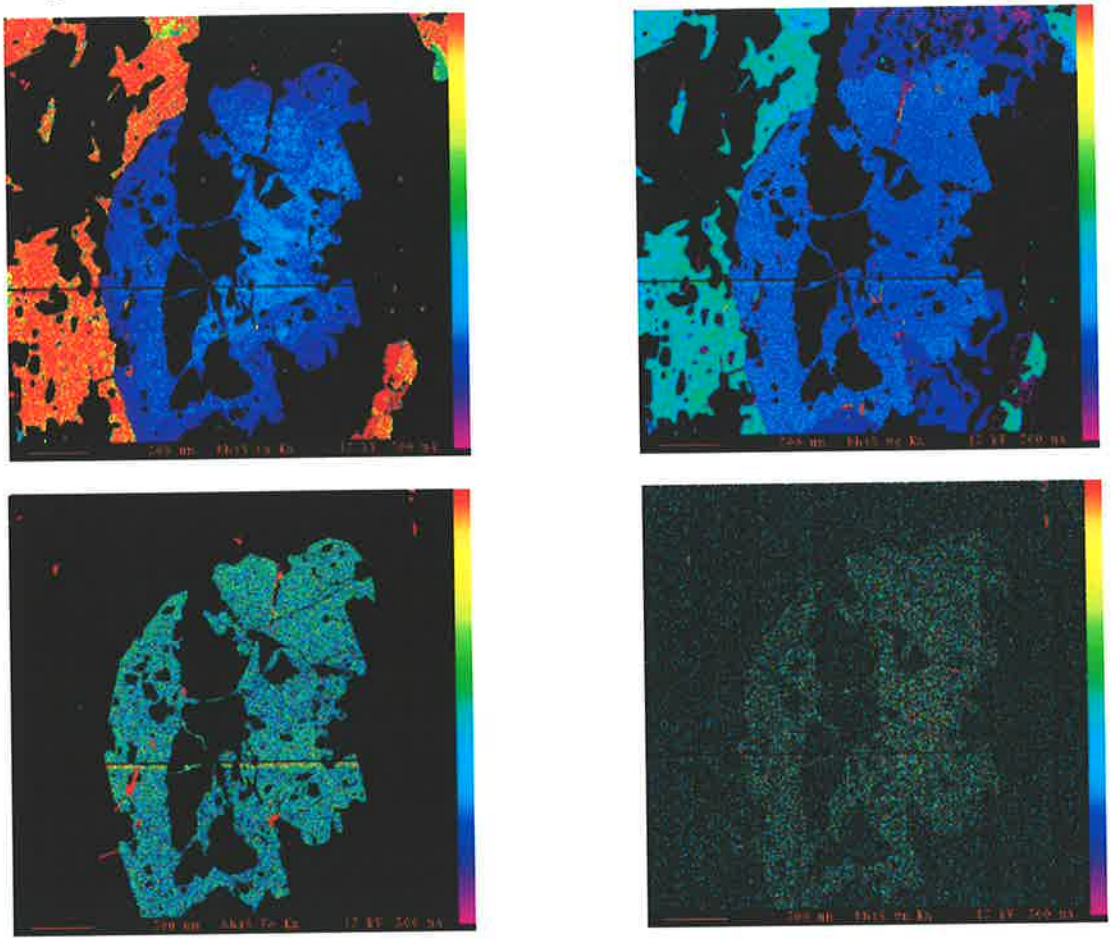

Figure 6.9. Qualitative compositional maps of a garnet in st-bearing mafic amphibolite schist YS148. (a) Ca and (d) Mn decrease rimwards while (b) Mg increases toward the garnet rim and (c) Fe appears essentially homogeneous in distribution. These trends suggest prograde growth zoning.

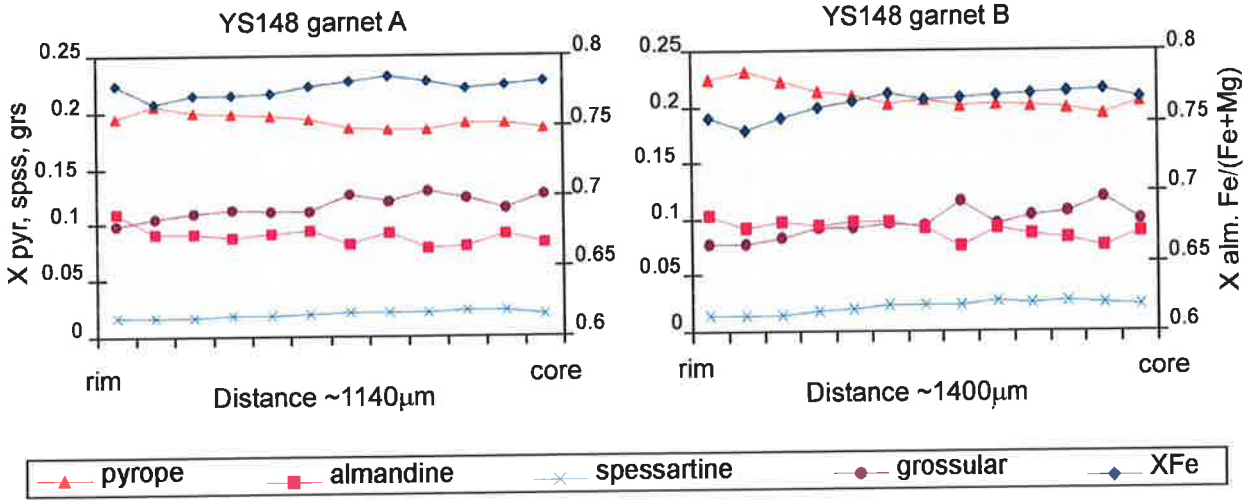

Figure 6.10. Quantitative traverses of garnets from sample YS148 indicating the amounts of almandine, pyrope, spessartine and grossular present and corresponding to the compositional maps presented in Figures 6.8 and 6.9.

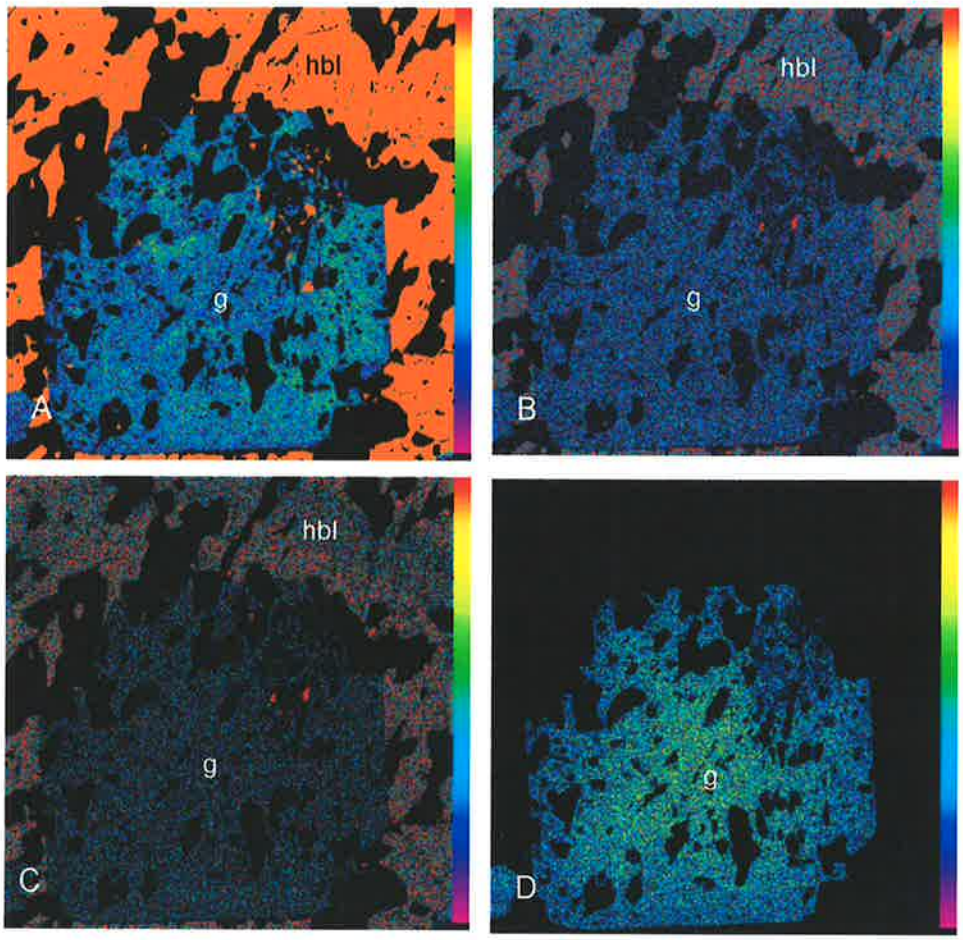

Figure 6.11.Qualitative compositional maps of a garnet from sample YS149 a mafic amphibolite schist, showing the zonation pattern typical for this rock. (a) Ca increases rimward; (b) Mg and (c) Fe appear homogeneous while (d) Mn decreases.

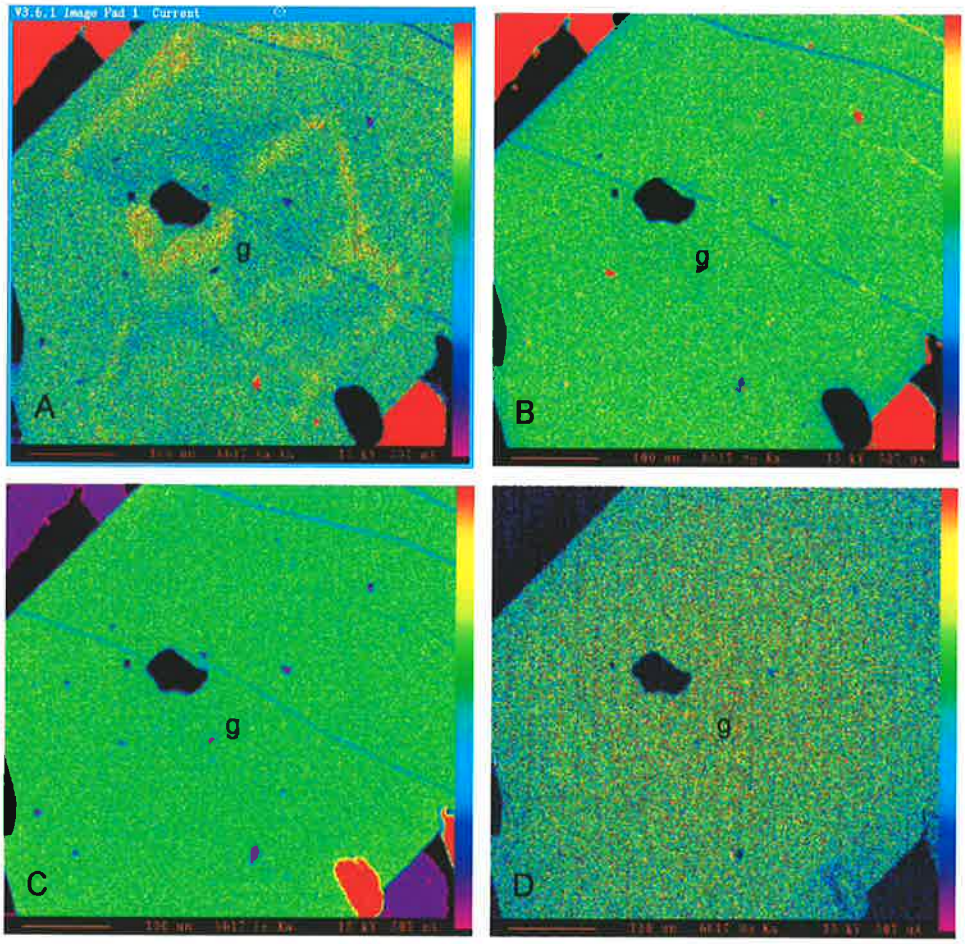

Figure 6.12. Qualitative compositional maps of a garnet from sample YS149 a mafic amphibolite schist, showing a unique zonation pattern for this rock. (a) internally this garnet displays linear increases in Ca which may represent the relic signature of earlier smaller garnets; (b) Mg is homogeneous except for a narrow rim with decreased Mg; (c) Fe appears homogeneous while (d) Mn decreases.

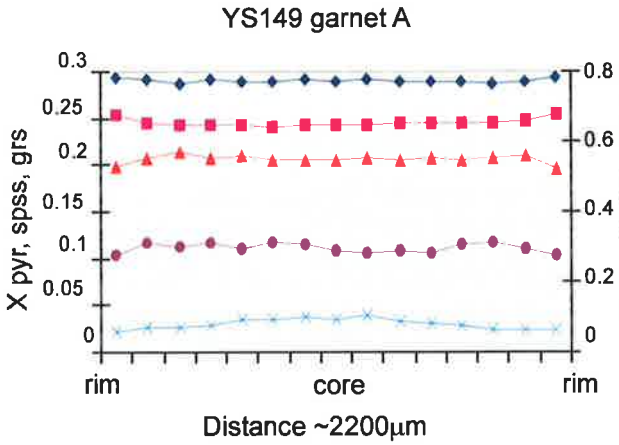

Figure 6.13. Quantitative traverse of the garnet from sample YS149 also shown in the compositional maps in Figure 6.11, indicating the amounts of almandine, pyrope, spessartine and grossular present.

zones parallel to existing crystal faces. This suggests that the garnet has maintained the original Ca signature of numerous early nucleated garnets which predated the present larger garnet (e.g. Daniel and Spear, 1998).

In YS9 compositional maps consistently show concentrically zoned garnets with Ca and Mn declining smoothly from core to rim, while Fe and Mg both increase in abundance in this direction (see Figure 6.14).

6.3.1.2 Discussion

Although there are some apparent disparities in garnet zoning profiles from the mafic schists, these are not difficult to explain. The lack of zoning in sample YS147 suggests either 1) the garnets grew under constant P-T conditions, 2) they grew in a changing P-T regime but in a direction approximately parallel to Fe, Mg and Mn isopleths and subparallel to Ca isopleths in P-T space, or 3) that due to their small size garnets in this rock have been unable to effectively isolate their cores from rehomogenisation via diffusion. This latter scenario is probably the

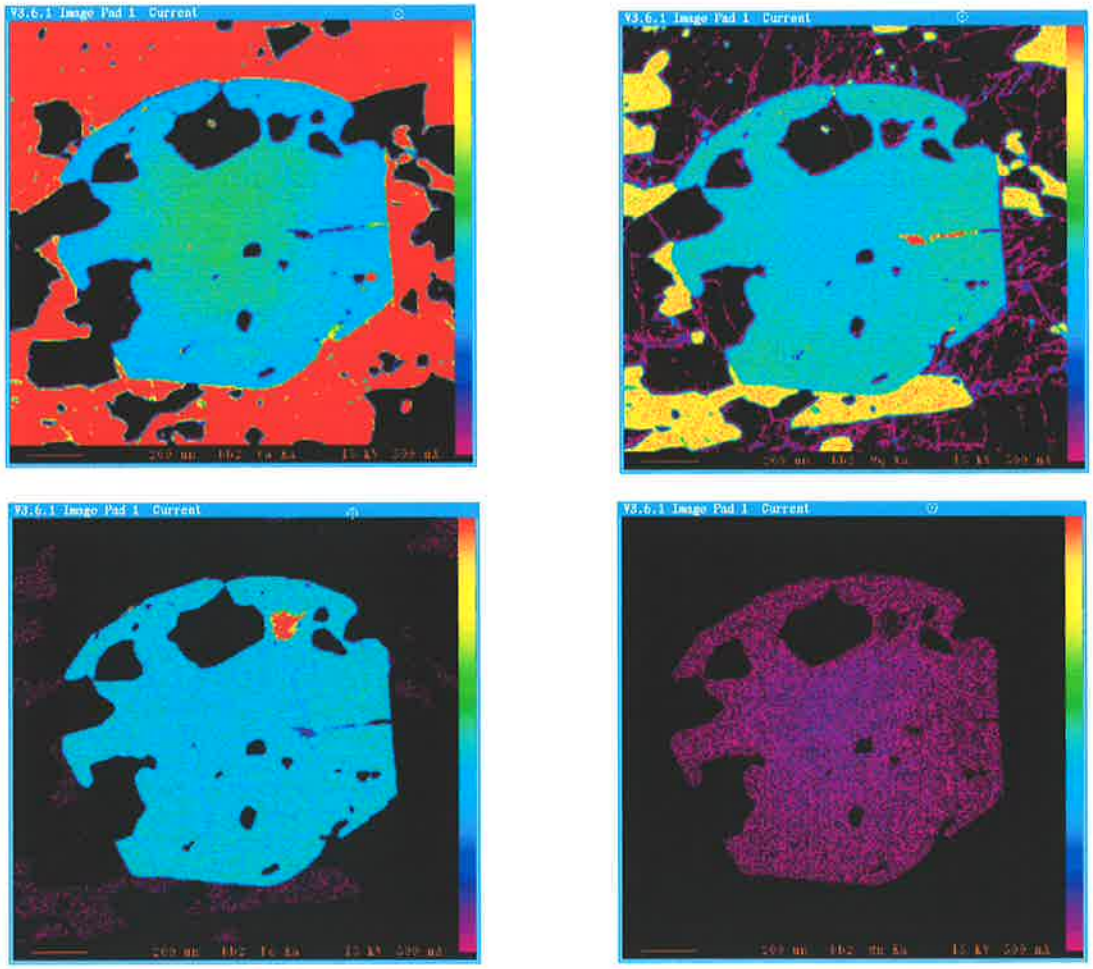

Figure 6.14. Qualitative compositional maps of a garnet from sample YS9 a mafic amphibolite schist. (a) Ca and (d) Mn decrease rimwards while both (b) Mg and (c) Fe increase suggesting this garnet has grown during prograde metamorphism.

most likely explanation, as the garnets in this sample are on the order of 1 mm in diameter compared with the other samples which are up to 4 mm in diameter. Aside from this sample however, trends in garnet zonation in the metabasites are quite consistent.

In general, all the samples show Mn to be either homogeneous or decreasing toward the rim, Mg and Fe either homogeneous or increasing toward the rim, and the XFe either reasonably constant or decreasing rimward. Homogeneity in these cations may reflect factors such as diffusion kinetics and the influence of grain size, but where zonation is recorded, then the trends in these cations and in the XFe ratio are consistent with an interpretation of growth zoning profiles. A detailed discussion on the characterisation of growth and reverse zoning profiles in garnet is presented in section 4.3.1, and observed zonation trends in these garnets, particularly in those of YS9, are consistent with the growth of garnet during prograde metamorphism.

Except for sample YS149, garnets from all the samples have grossular contents which decrease with garnet growth. Isopleth diagrams from the Kohn and Spear (1990) garnet-hornblende geobarometers based on the reactions:

(Mg eqn)

$$6an + 3tr \longrightarrow 2gr + py + 3tsch + 6q \quad (6.2)$$

and

(Fe eqn)

$$6an + 3Fe\text{-}act \longrightarrow 2gr + alm + 3Fe\text{-}tsch + 18q \quad (6.3)$$

show that isopleths of lnKd values for these two equations are nearly horizontal, and that with increasing pressure, Mg and Fe in garnet generally increase (Figure 6.15 a & b). However the relationship between grossular-pyrope and grossular-almandine in the Kd equations means that the lnKd value is more sensitive to relative changes in grossular. Thus Mg and Fe in garnet may be increasing but relatively small decreases in Ca may lead to smaller values of lnKd. In this instance the path may be up temperature but down pressure. Isopleths of lnKd for Fe-Mg partitioning from the Graham and Powell (1984) garnet-hornblende thermometer based on the reaction:

$$1/4\ Fe\text{-}parg + 1/3\ py \longrightarrow 1/4\ parg + 1/3\ alm \quad (6.4)$$

indicate that Mg in garnet and Fe in hornblende generally increase with increasing temperature (Figure 6.15 c). A decrease in XCa in garnet coincident with constant pyrope and almandine content, implies garnet growth parallel to an lnK isopleth which must also be down temperature (Figure 6.15 c). However given the slope of the isopleths in Figure 6.15c, any decrease in grossular

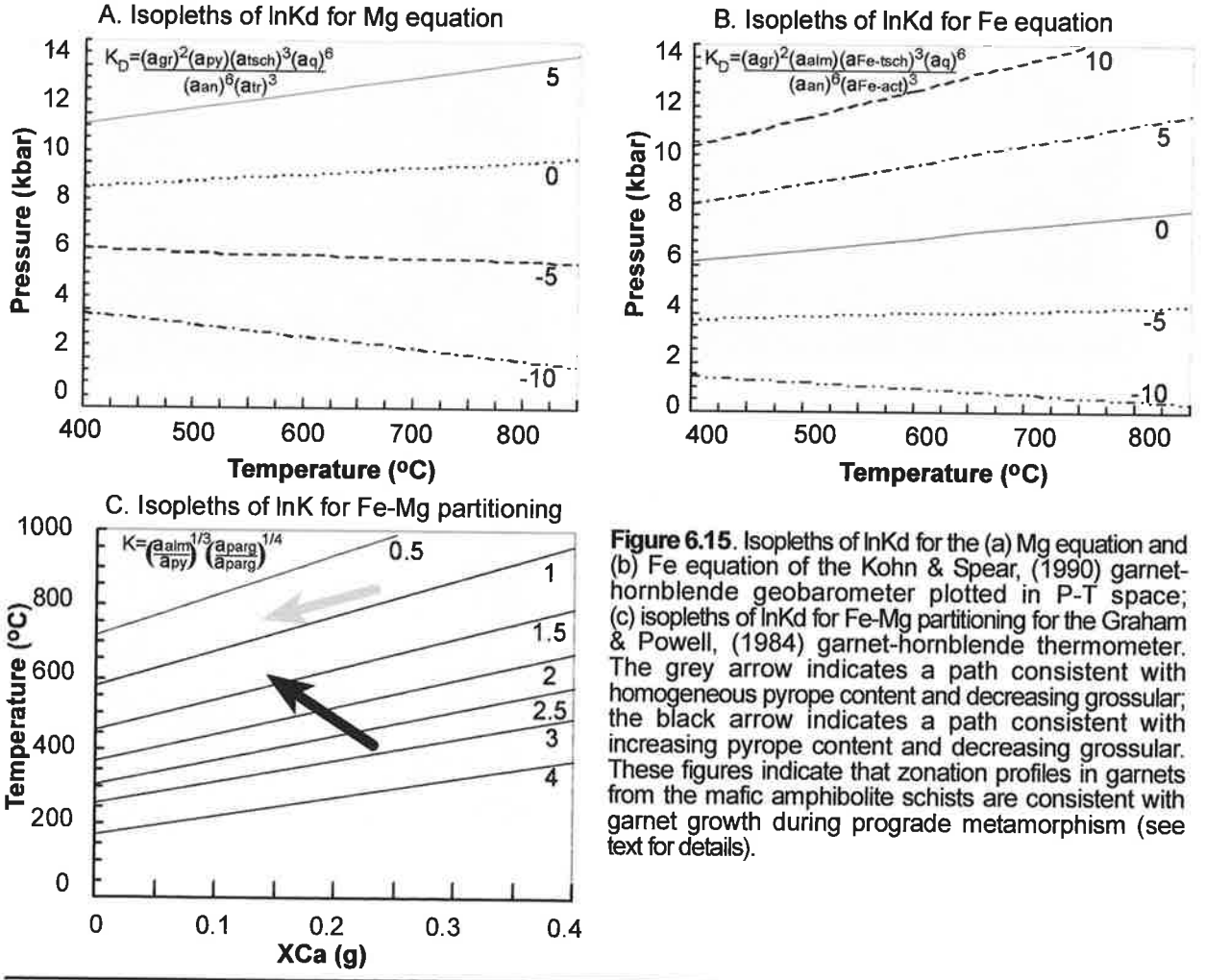

Figure 6.15. Isopleths of lnKd for the (a) Mg equation and (b) Fe equation of the Kohn & Spear, (1990) garnet-hornblende geobarometer plotted in P-T space; (c) isopleths of lnKd for Fe-Mg partitioning for the Graham & Powell, (1984) garnet-hornblende thermometer. The grey arrow indicates a path consistent with homogeneous pyrope content and decreasing grossular; the black arrow indicates a path consistent with increasing pyrope content and decreasing grossular. These figures indicate that zonation profiles in garnets from the mafic amphibolite schists are consistent with garnet growth during prograde metamorphism (see text for details).

content coupled with an increase in pyrope, must cross lnK isopleths and therefore be up temperature. This suggests that a garnet in a mafic amphibolite with a zonation profile of increasing Mg and decreasing Ca with garnet growth records a path of heating with either burial or decompression. This is consistent with the interpretation made above that the patterns of Mg, Fe and Mn distribution in garnets from the Yambah Schist Zone record growth zoning.

6.3.2 Conventional Geothermobarometry

Given the high variance of common assemblages in mafic amphibolites in general, it is understandable that they can be difficult to constrain in P-T space petrographically. However from the mineral assemblages discussed above, the Yambah Schist Zone rocks must lie within a portion of P-T space which is bound by the staurolite-in isograd, the clinopyroxene and orthopyroxene-in isograds and the kyanite-sillimanite univariant. To constrain the P-T conditions of metamorphism further a number of different approaches can be taken. Geothermobarometry using calibrated thermometers and barometers based on equilibrium reactions is one method. However while a number of potentially useful equilibria (such as GRIPS, GRAIL, GRAIP, and various Fe-Mg exchange thermometers for different mineral pairs) exist for use on amphibolites, a lack of rutile and the typically small number of phases present in metabasic rocks from the Yambah Schist Zone, severely restricts the range of applicable thermometers and barometers.

6.3.2.1 Results of geothermobarometry on the metabasites

Results of geothermometry calculations are presented in Tables 6.1 to 6.3. Two calibrations of Fe-Mg cation exchange in garnet-hornblende pairs have been used to constrain peak temperatures recorded by the Yambah metabasites. The Graham and Powell, (1984) g-hbl thermometer produced reasonably consistent results, with estimates ranging between 526°C and 553°C, while the Perchuk et al, (1985) calibration for the equivalent equilibria produced slightly higher estimates ranging between 565°C and 615°C. The Holland and Blundy, (1994) amphibole-plagioclase thermometers produced unreasonably high temperatures (in excess of 700°C) for all samples, however the chemistry of plagioclase in these samples is at the extreme range recommended for these thermometers and this may explain the anomalous results. There was no significant difference in temperature estimates between rims and cores of garnets. Attempts at estimating pressure conditions using the Kohn and Spear, (1989) and Kohn and Spear, (1990) g-hbl-plag-q barometers met with little success, producing a scattered range of pressure estimates on the order of 2 - 4 kbar, however the chemistry of plagioclase in these samples is also outside the calibrated ranges of the barometers. Results of these calculations are presented in Table 6.1 and in Figure 6.16, which demonstrate that while the g-hbl temperature estimates are acceptable, when combined with the unreasonably low barometric estimates, they place the metabasites well below the

g-hbl	YS147	YS147	YS148	YS149
X(Fe) hbl	0.392	0.396	0.433	0.398
X(Fe) gnt	0.735	0.737	0.759	0.773
ln Kd	1.459	1.454	1.416	1.638
T (°C) G&P	537	537	553	526
T (°C) P	605	605	615	565

Table 6.1. Temperature estimates on Yambah metabasites using Fe-Mg partitioning for g-hbl. Abbrev: G&P=Graham & Powell (1984); P= Perchuk et al (1985).

hbl-plag	YS147	YS147	YS148
X(Fe) hbl	0.392	0.396	0.433
X(ab) plag	0.11	0.11	0.1
T(°C) H&B 1	828	828	829
T(°C) H&B 2	736	736	722

Table 6.2. Temperature estimates on Yambah metabasites using hbl-plag pairs at 5 kbars. Abbrev: H&B1=Holland & Blundy (1990) ed-tr thermometer; H&B2=Holland & Blundy (1990) ed-ri thermometer.

g-hbl-plag-q	YS 147 a			YS 147b			YS 148		
T (°C)	550	600	650	550	600	650	550	600	650
K&S 1	2.31	1.86	1.40	2.40	2.0	1.60	1.83	1.37	0.92
K&S 2	3.77	3.53	3.29	3.80	3.6	3.40	3.50	3.30	3.00
K&S 3	2.11	2.37	2.63	2.97	3.3	3.59	2.29	2.54	2.8
K&S 4	2.30	2.20	2.10	2.92	2.9	2.83	2.10	1.98	1.87

Table 6.3. Pressure estimates on metabasic amphibolites using the Kohn & Spear (1989) g-hbl-plag-q barometers. Abbrev: K&S1=parg-Fe model 1 barometer; K&S2=parg-Mg model 1 barometer; K&S3=parg-Fe model 2 barometer; K&S4=parg-Mg model 2 barometer.

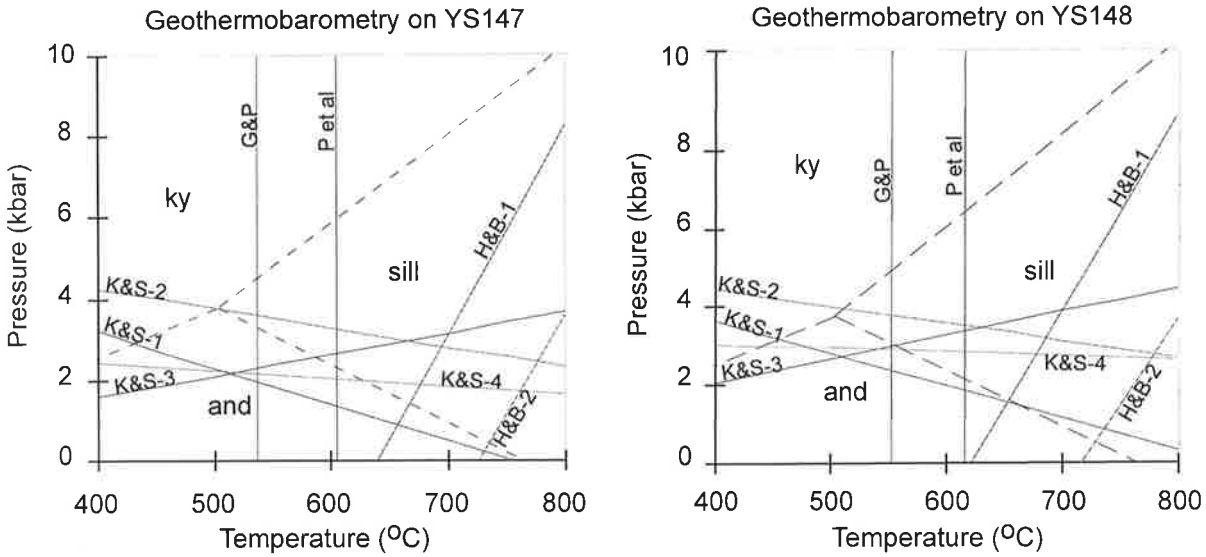

Figure 6.16. Estimates for peak metamorphic conditions using the independently calibrated thermobarometers. Although some temperature estimates appear reasonable, the pressure estimates are too low, placing the rocks outside of the kyanite-stable field. Abbrev: G&P=Graham & Powell (1984); H&B1= Holland & Blundy (1990) ed-tr thermometer; H&B2=Holland & Blundy (1990) ed-ri thermometer; K&S1= Kohn & Spear (1989) parg-Fe model 1 barometer; K&S2=parg-Mg model 1 barometer; K&S3=parg-Fe model 2 barometer; K&S4=parg-Mg model 2 barometer; P= Perchuk et al (1985).

kyanite field, which is at odds with the presence of kyanite in the interlayered aluminous schists. The limited success of these equilibria probably reflects the inherent complexities of composition, solid solution and thermodynamics associated with amphiboles and plagioclase, and the fact that plagioclase compositions used were generally outside or at the limit of the thermobarometers' calibration. This situation is exacerbated in this instance by the high variance nature of the stable assemblage in these mafic schists which restricts the total number of equilibria available for calculation.

6.3.3 Average P-T calculations using THERMOCALC

The results of average pressure and temperature estimates for adjacent mineral rims calculated using the computer programme THERMOCALC V2.6 are presented in Tables 6.4 and 6.5. Due to the absence of plagioclase in YS149, THERMOCALC was unable to determine complete reaction sets for this rock and thus no results are presented. Average pressure and temperature estimates using all available end members in the reaction sets (see Table 6.4) for YS147 and YS148 failed statistical tests imposed by the program expressed as a 'σ fit' value. However review of the individual end-member statistics indicated that pargasite and tschermakite appear to have a controlling influence upon the calculations as they consistently produced high values for the (e*) statistic (see Appendix 3.2 for an example of the complete statistical output of THERMOCALC Average PT calculations). Subsequent removal of these phases as end-members available for calculation of a reaction set, resulted in statistically acceptable estimates and a significant improvement in the associated errors (Tables 6.5). For an $X(H_2O)=1.0$, metamorphic conditions were estimated to be around 630°C and 5.2 kbar. These pressure estimates appear to be more geologically reasonable than those gained from conventional cation exchange geobarometry (section 6.3.2.1 above) and while they place the rock just into the sillimanite field, they are within error of the kyanite field.

Given the presence of unusual aluminous and hydrous phases in the metabasic schists, and the presence of intercalated calc silicate units within the Yambah Schist Zone, there is considerable evidence suggesting a significant alteration of the bulk chemistry of the schists compared with the surrounding granulites via the introduction of a fluid phase. The metasomatism of these rocks also implies that any such fluid phase present in the system was not a pure H_2O fluid. Average PT calculations were thus performed for a range of $X(H_2O)$ to examine the influence of a fluid phase of varying composition. Direct modelling of the fluid chemistry was not undertaken, however by introducing varying $X(CO_2)$ in a H_2O-CO_2 fluid, some assessment could be made of the dependency of the mineral assemblage on the fluid composition. Reducing the $X(H_2O)$ of the fluid resulted in temperature estimates steadily declining while pressures were either unaffected or declined marginally (see Table 6.6), however all the estimates still placed the rocks just into the sillimanite field.

Average pressure calculations using THERMOCALC were then made over the temperature range of 590-650°C constrained on the basis of temperature estimates from cation exchange geothermometry and THERMOCALC Average PT calculations, at varying $X(H_2O)$. Results of these calculations are presented in Table 6.7. Invariably the pressures estimated over the selected temperature range placed the rocks below the kyanite field into the sillimanite field, however many of the higher temperature/higher pressure estimates fall close to the kyanite-sillimanite univariant and are within error of the kyanite field.

YS147	Average PT calculations								
mineral assemblage	rim data g-st-hbl-plag-q-fluid								
T (ºC)	618	622	632	629	630	643	644	642	641
sd (T)	92	94	111	109	106	117	110	114	111
P (kbar)	4.7	4.8	5	5	5.1	5.5	5.5	4.9	4.8
sd (P)	3.5	3.6	4.2	4.2	4.1	4.4	4.2	4.5	4.4
σ fit	3.12	3.16	3.62	3.63	3.52	3.72	3.62	3.59	3.52
σ fit (max)	1.54	1.54	1.54	1.54	1.54	1.54	1.54	1.54	1.54
X(H2O)	1.0	1.0	1.0	1.0	1.0	1.0	1.0	1.0	1.0

YS148	Average PT calculations								
mineral assemblage	rim data g-st-hbl-plag-q-fluid								
T (ºC)	643	642	620	644	641	639	639	640	643
sd (T)	120	116	113	118	123	117	123	124	124
P (kbar)	5.2	6	5.3	5.7	5.4	5.2	5.2	5.3	4.9
sd (P)	4.4	4.2	4.2	4.3	4.5	4.4	4.6	4.6	4.9
σ fit	3.65	3.6	3.59	3.65	3.77	3.69	3.85	3.85	3.69
σ fit (max)	1.54	1.54	1.54	1.54	1.54	1.54	1.54	1.54	1.54
X(H2O)	1.0	1.0	1.0	1.0	1.0	1.0	1.0	1.0	1.0

Table 6.4. Results of THERMOCALC average PT calculations using the complete assemblage of g-st-hbl-plag-q-fluid. For 95% confidence (σ fit) should be less than (σ fit max). Both samples failed the statistical test.

YS147	Average PT calculations								
mineral assemblage	rim data without pargasite & tschermakite end members								
T (ºC)	616	620	631	627	629	644	643	641	639
sd (T)	42	38	35	40	37	44	38	41	42
P (kbar)	4.8	4.9	5.1	5	5.2	5.6	5.6	5.4	5.4
sd (P)	1.7	1.5	1.4	1.5	1.4	1.7	1.5	1.7	1.7
σ fit	1.44	1.29	1.15	1.32	1.24	1.4	1.27	1.33	1.34
σ fit (max)	1.73	1.73	1.73	1.73	1.73	1.73	1.73	1.73	1.73
X(H2O)	1.0	1.0	1.0	1.0	1.0	1.0	1.0	1.0	1.0

YS148	Average PT calculations								
mineral assemblage	rim data without pargasite & tschermakite end members								
T (ºC)	644	643	620	646	643	639	641	640	640
sd (T)	40	32	31	33	33	32	32	34	46
P (kbar)	5.3	6.2	5.4	5.9	5.5	5.3	5.4	5.3	5.3
sd (P)	1.5	1.2	1.2	1.2	1.2	1.2	1.2	1.3	1.7
σ fit	1.23	0.83	0.46	1.01	1	0.88	0.99	1.07	1.42
σ fit (max)	1.73	1.73	1.73	1.73	1.73	1.73	1.73	1.73	1.73
X(H2O)	1.0	1.0	1.0	1.0	1.0	1.0	1.0	1.0	1.0

Table 6.5. Results of THERMOCALC average PT calculations using the same data as above minus the pargasite and tschermakite end memeberscomplete assemblage. For 95% confidence (σ fit) should be less than (σ fit max). Both samples pass the statistical test. Temperature estimates are little affected by the removal of the two end members, but pressure estimates increase slightly and errors are significantly reduced.

YS147	Average PT calculations							
mineral assemblage	rim data without pargasite & tschermakite end members							
T (°C)	639	634	629	624	638	633	628	623
sd (T)	34	33	33	32	35	34	34	33
P (kbar)	5.6	5.5	5.5	5.5	5.5	5.5	5.4	5.4
sd (P)	1.4	1.4	1.4	1.4	1.5	1.4	1.4	1.4
σ fit	1.1	1.1	1.09	1.09	1.14	1.13	1.13	1.12
σ fit (max)	1.61	1.61	1.61	1.61	1.61	1.61	1.61	1.61
X(H2O)	1.0	0.9	0.8	0.7	1.0	0.9	0.8	0.7

YS148	Average PT calculations							
mineral assemblage	rim data g-st-hbl-plag-q-fluid				without pargasite & tschermakite			
T (°C)	648	642	637	632	644	638	633	628
sd (T)	62	61	60	59	33	32	32	31
P (kbar)	5.8	5.7	5.7	5.6	6	6	5.9	5.9
sd (P)	2.5	2.5	2.5	2.5	1.4	1.3	1.3	1.3
σ fit	1.86	1.85	1.85	1.84	0.92	0.92	0.9	0.9
σ fit (max)	1.54	1.54	1.54	1.54	1.61	1.61	1.61	1.61
X(H2O)	1.0	0.9	0.8	0.7	1.0	0.9	0.8	0.7

Table 6.6. Results of THERMOCALC average PT calculations testing the effect of varying $X(H_2O)$ on the same data used for Tables 6.4 & 6.5. Pressure estimates are little affected by changes in $X(H_2O)$ however temperature estimates generally decrease with decreses in $X(H_2O)$.

147av	Ave PT w/out pargasite or tschermakite gives 639°C±34 & 5.6±1.4 kbar							
Ave P X(H2O)	T(°C)	590	600	610	620	630	640	650
1	P (kbar)	4.1	4.4	4.7	5	5.2	5.5	5.8
	sd (P)	1.13	1.3	0.96	0.91	0.92	0.92	0.92
	σ fit	1.3	1.2	1.1	1	1	0.9	1
	σ fit (max)	1.73	1.73	1.73	1.73	1.73	1.73	1.73
0.9	P (kbar)	4.2	4.5	4.8	5.1	5.4	5.7	6
	sd (P)	1.07	0.98	0.92	0.9	0.91	0.91	0.92
	σ fit	1.2	1.1	1	1	0.9	0.9	1
	σ fit (max)	1.73	1.73	1.73	1.73	1.73	1.73	1.73
0.8	P (kbar)	4.4	4.7	5	5.3	5.5	5.8	6.1
	sd (P)	1	0.93	0.91	0.92	0.93	0.94	0.97
	σ fit	1.1	1	1	0.9	0.9	1	1
	σ fit (max)	1.73	1.73	1.73	1.73	1.73	1.73	1.73
0.7	P (kbar)	4.5	4.8	5.1	5.4	5.7	6	6.2
	sd (P)	0.96	0.9	0.9	0.92	0.92	0.94	1.1
	σ fit	1.1	1	1	0.9	0.9	1	1.1
	σ fit (max)	1.73	1.73	1.73	1.73	1.73	1.73	1.73

Table 6.7. The effect of varying $X(H_2O)$ on THERMOCALC average P calculations over a selected temperature range. It appears that an impure fluid composition may have stabilised the mineral assemblage at lower temperatures and higher pressures than calculated by thermobarometry.

148av	Ave PT w/out pargasite or tschermakite gives 644°C±33 & 6.0±1.4 kbar							
Ave P X(H2O)	T(°C)	590	600	610	620	630	640	650
1	P (kbar)	4.6	4.9	5.1	5.4	5.7	5.9	6.2
	sd (P)	1.17	1.06	1.01	1.02	1.03	1.04	1.05
	σ fit	1.2	1.1	1	0.9	0.8	0.8	0.8
	σ fit (max)	1.73	1.73	1.73	1.73	1.73	1.73	1.73
0.9	P (kbar)	4.7	5	5.2	5.5	5.8	6	6.3
	sd (P)	1.1	1	1	1.01	1.03	1.04	1.05
	σ fit	1.1	0.9	0.9	0.8	0.8	0.8	0.8
	σ fit (max)	1.73	1.73	1.73	1.73	1.73	1.73	1.73
0.8	P (kbar)	4.7	4.9	5.2	5.5	5.8	6.1	6.3
	sd (P)	1.06	0.98	0.99	1	1.01	1.03	1.04
	σ fit	1.1	1	0.9	0.9	0.8	0.8	0.9
	σ fit (max)	1.73	1.73	1.73	1.73	1.73	1.73	1.73
0.7	P (kbar)	4.8	5	5.3	5.6	5.9	6.2	6.4
	sd (P)	1.01	0.98	0.98	1	1.01	1.02	1.04
	σ fit	1.1	1	1	0.8	0.8	0.8	0.9
	σ fit (max)	1.73	1.73	1.73	1.73	1.73	1.73	1.73

Table 6.7. (continued.)

Values for the 'σ fit' statistic and standard deviations are lowest for pressure estimates calculated at an assumed temperature range of 620°C-640°C, also implying that the higher temperature estimates are closer to actual values. Decreasing the $X(H_2O)$ of the fluid phase results in significant increases in the pressure estimates at any given temperature, but also produces some accompanying decreases in associated errors and improving statistical fit parameters at lower fixed temperatures. Given that Fe-Mg exchange thermometry (which is independent of a fluid phase) places the temperature of metamorphism at around 600°C, and decreasing the $X(H_2O)$ value lowers temperature estimates and raises pressure estimates calculated by THERMOCALC, it seems plausible that the fluid phase has helped to stabilise the existing mineral assemblage at lower T and higher P (i.e. further into the kyanite field) than calculated. Thus although the fluid used here is a simple linear mixing of CO_2-H_2O, these results imply that the stability of the mineral assemblage may have been influenced by the fluid composition.

6.3.4 Petrogenetic evidence for the P-T evolution of metabasic schists from the Yambah Schist Zone

Due to the generally high variance nature of most mafic amphibolite facies assemblages compared with metapelitic rocks, most existing petrogenetic grids have been developed for metapelitic rocks in subsets of the chemical system MnCaKFMASH (e.g. Carrington and Harley, 1995; Spear and Cheney, 1989; Powell and Holland, 1990, Xu et al, 1994, Droop and Harte, 1995), and thus relatively few petrogenetic grids exist for metabasites (e.g. Abbott, 1982, Frey et al, 1991; Will et al, 1990). Furthermore, the existing mafic grids rarely include aluminous phases such as kyanite, sillimanite, staurolite (exceptions are Froese and Hall, 1983; Spear and Rumble, 1986; Arnold et al, 1995; Arnold et al, 2000) and tend to concentrate on discontinuous reactions within the chosen chemical system rather than addressing the continuous reactions which are more applicable to most rocks. Arnold et al, (2000) have produced a theoretical grid for aluminous mafic rocks from equilibrium thermodynamic calculations carried out using the computer program THERMOCALC (Powell and Holland, 1988) (see Figure 6.17). The petrogenetic grid of Arnold et al, (2000) is aimed at determining phase relations in kyanite- and staurolite- bearing amphibolites and the continuous reactions which influence them.

Mafic amphibolites with staurolite and/or kyanite-bearing assemblages have commonly been interpreted as evidence of high pressure metamorphism (e.g. Spear, 1982; Selverstone et al, 1984, Grew and Sandiford, 1985; Helms et al, 1987; Ward, 1984; Cooper, 1980) since they generally occur in amphibolite facies metamorphic terranes at pressures greater than about 6 kbar. Calculated stability fields for staurolite and kyanite-bearing mafic amphibolites modelled in CaNaFMASH by Arnold et al, (2000) support the interpretation of higher pressure genesis for these rocks, indicating that these assemblages

generally occur at pressures above 5.5 kbar (Figure 6.17). These conditions correspond to common Barrovian style metamorphism, thus the rarity of these assemblages probably reflects a small window of P-T-X space, with predominantly bulk compositional factors (particularly Al and XFe contents) controlling their stability (Arnold et al, 2000). As such staurolite and/or kyanite-bearing mafic amphibolites have rarely been used for calculating metamorphic pressure and temperature conditions beyond asserting the interpretation of a high pressure environment. The petrogenetic grid of Arnold et al (2000) is therefore particularly useful as it explores the phase equilibria relating to these rocks and demonstrates the sensitivity of the stable staurolite and/or kyanite-bearing assemblages to small bulk compositional variations in Al and Fe content. Thus although such assemblages are relatively rare, the advent of the Arnold et al, (2000) petrogenetic grid enables them to be used to more thoroughly constrain the ambient conditions of metamorphism.

The st-g-hbl-plag-q assemblages from the Yambah Schist Zone are trivariant within the NaCaFMASH chemical system. While they do not preserve textural evidence consistent with crossing any of the univariant reactions on the petrogenetic grid (see Figure 6.17), the reaction textures noted above in section 6.2.1 suggest that staurolite has been present in some samples prior to the growth of garnet, and that these rocks underwent the reaction:

hornblende + staurolite ⟶
garnet + plagioclase + quartz (6.1)

This reaction suggests that the Yambah mafic amphibolites moved up temperature through a quadrivariant st-hbl-plag-q field into a trivariant st-g-hbl-plag-q field (e.g. Figure 6.18) and then must have undergone cooling and decompression to exist at the current surface. The lack of any apparent retrogressive phases limits investigation of the exhumation path taken by these rocks. However it is obvious from the local presence of relatively late stage sillimanite overprinting kyanite in adjacent metapelites, that the rocks underwent a broadly clockwise P-T evolution.

Attempts were made to more closely define the

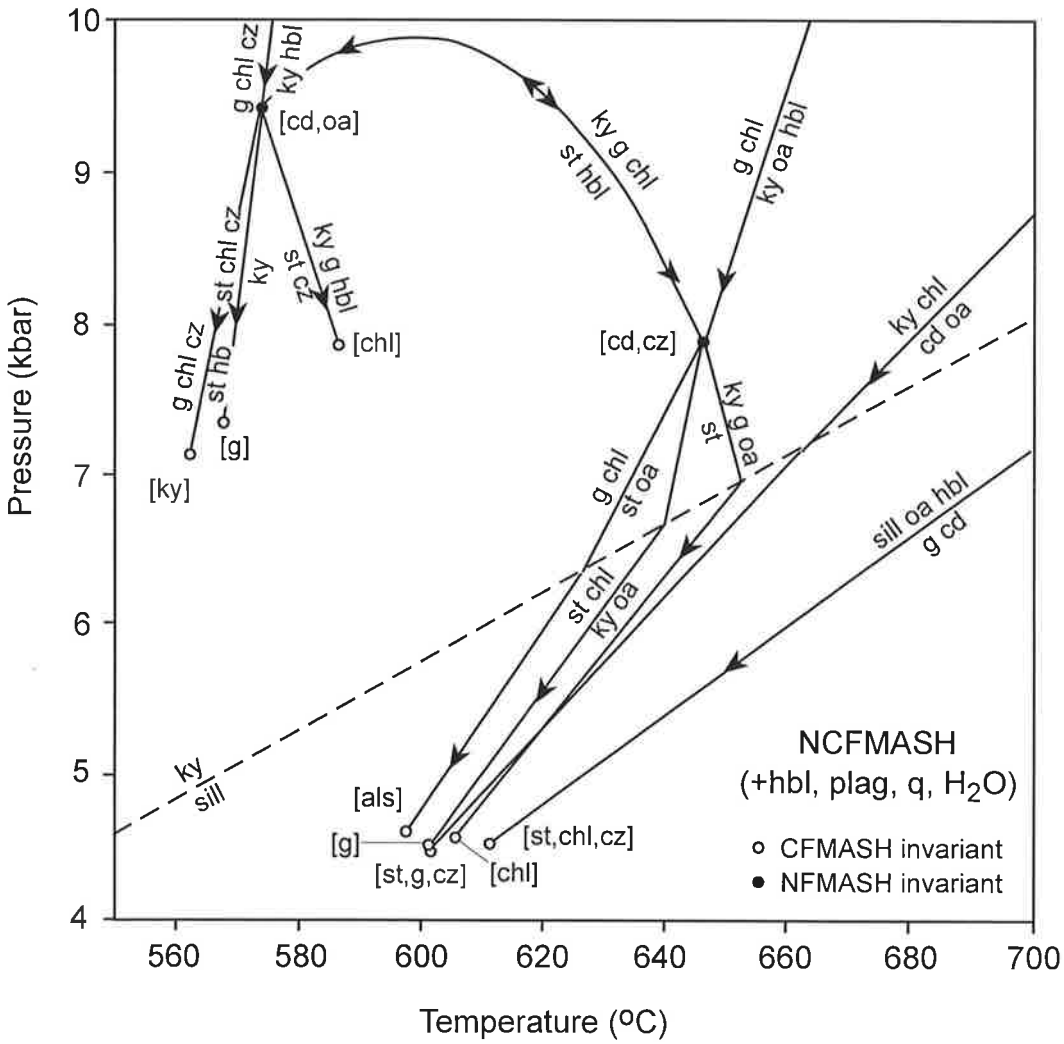

Figure 6.17. Petrogenetic grid for the chemical system NaCaFMASH including the minerals cordierite, orthoamphibole, garnet, chlorite, clinozoisite, kyanite, sillimanite and andalusite with hornblende, quartz, plagioclase and H_2O in excess. The direction of arrows on univariant lines indicates the direction of increasing anorthite content in plagioclase. (After Arnold et al, 2000.)

metamorphic history of the Yambah mafic amphibolites using a pseudosection constructed for the staurolite-bearing samples. Representative bulk compositions were derived using electron microprobe analyses of the minerals and point counting to establish modal proportions. While these calculated bulk compositions fell within the range of compositions suitable for crystallisation of aluminous phases in mafic rocks as discussed by Arnold et al, (2000), the resultant pseudosections (e.g Figure 6.19 c) either did not stabilise a staurolite-garnet trivariant field or placed the staurolite-garnet trivariant at considerably lower pressures (well below that of the kyanite-sillimanite univariant) than expected, given the presence of staurolite in these rocks and kyanite in the adjacent lithologies. Furthermore although calculated modal proportions of the minerals were similar to those in the actual rocks, calculated mineral chemistries differed significantly.

After calculating a number of pseudosections over a range of bulk compositions, it became apparent that the amount of sodium in the bulk composition was a critical factor in stabilising the position of the relevant staurolite-garnet trivariant field. To investigate this observation further, bulk sodium contents were varied with the other cations (Al, Fe, Mg, Ca) being recalculated to maintain their relative ratios (Figures 6.19 a-d). Increasing the bulk sodium content resulted in staurolite being stabilised at higher (and more geologically reasonable) pressures, approaching those calculated by Arnold et al, (2000). However while calculated modal proportions of minerals were not unduly affected by varying the bulk sodium content, calculated mineral chemistries (particularly of hornblende and plagioclase) were affected and no longer approached that of the actual minerals in the rocks. It was found that in bulk compositions with Na less than about 4 mol %, the staurolite-garnet trivariant field would inevitably plot below the kyanite-sillimanite univariant and move up the temperature axis toward higher temperatures, regardless of the relative proportions of Al:Mg:Fe:Ca. As the mafic amphibolites from Yambah tend to have bulk sodium contents of about 2 mol %, (c.f. the average mafic bulk composition used by Arnold et al, (2000) with Na >5 mol %) the resultant pseudosections always produced staurolite-bearing assemblages at unreasonably low pressures and elevated temperatures.

In general terms, the addition of sodium to the bulk composition results in the calculated anorthite content of plagioclase declining from about An $_{0.85 - 0.70}$ to

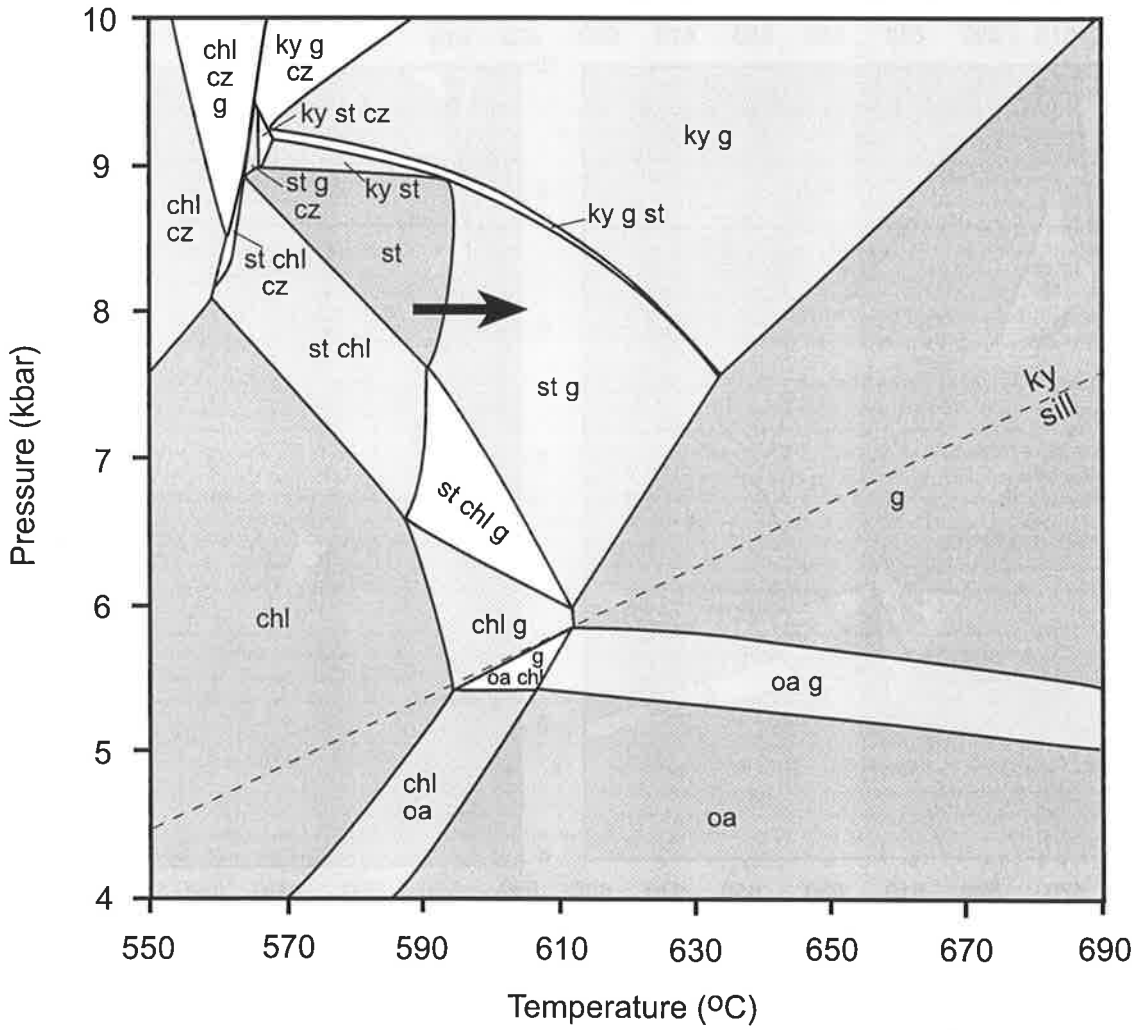

Figure 6.18. P-T pseudosection for a moderately aluminous amphibolite calculated for a bulk composition of A:C:M:F:N = 26: 26.73: 20.87: 20.87: 5.53. (After Arnold et al, 2000). The black arrow indicates the path implied by the reaction of hornblende and staurolite to produce garnet

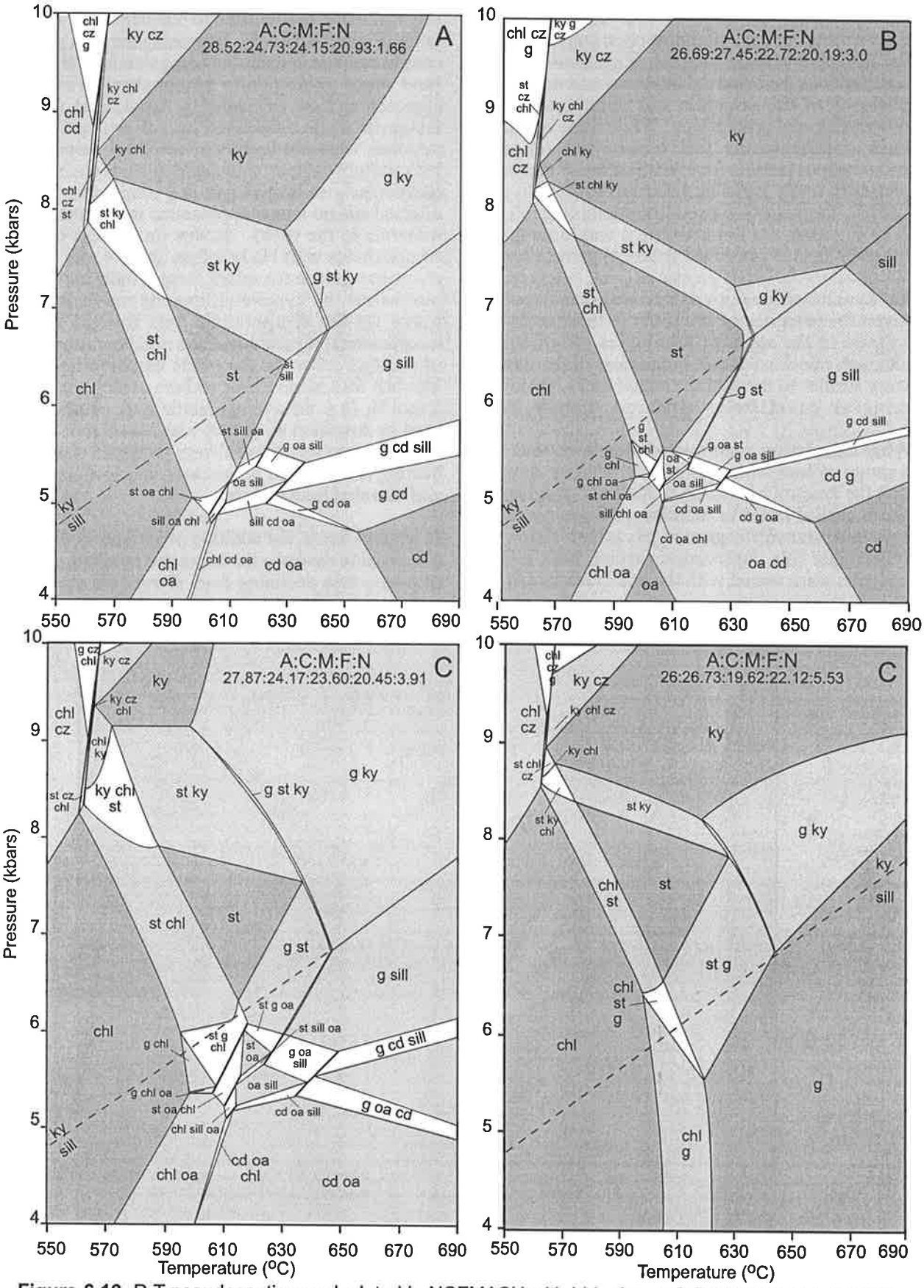

Figure 6.19. P-T pseudosections calculated in NCFMASH with hbl, plag, q & fluid in excess, for bulk compositions (BC) with varying amounts of Na to examine the effect of XNa on field topology. (a) Calculated for a bulk composition appropriate for the st-bearing metabasites from Yambah, but does not stabilise a g-st trivariant; (b) a low Na composition derived from the moderately Al- & Fe-rich amphibolite composition C of Arnold et al (2000), with XFe at 0.47, the g-st field lies within the sill field; (c) a more sodic version of the BC used in (a) recalculated to unity. Note that a g-st field has stabilised and straddles the ky-sill univariant; (d) a more sodic version of the BC used in pseudosection (b). In this case the g-st field has moved partially into the ky stable field.

about An 0.35 and 0.50, while calculated hornblende becomes more Ca enriched and Na depleted. Coincidentally calculated XFe ratios increase slightly in Fe-bearing phases, by up to 10%. Therefore the amount of sodium present appears to be preferentially partitioned into plagioclase, thereby reducing the proportion of anorthite in that phase and producing a flow-on effect influencing the exchange of calcium between all other calcium-bearing phases. This consequently affects calculated mineral chemistry, but the topology of the pseudosection and calculated modal proportions of stable minerals remains essentially unaffected. This observation suggests that either the plagioclase of the Yambah metabasic rocks is anomalously calcic or the thermodynamic data and activity composition relations used to model hornblende and plagioclase do not adequately model actual minerals in bulk compositional ranges appropriate to mafic amphibolites in the Yambah Schist Zone.

A review of the literature demonstrates that plagioclase chemistry varies widely in mafic amphibolites (Table 6.8). While plagioclase generally becomes increasingly anorthitic with increasing metamorphic grade and can display some systematic relationships with coexisting hornblende chemistry (Laird, 1980; Spear, 1980; Spear, 1981), solid-solutions in both minerals are non-ideal and are apparently influenced by associated mineral and whole rock compositions. Plagioclase solid solutions are complicated by the peristerite, Huttenlocher and Bøggild miscibility gaps and, of particular importance in amphibolite facies metabasites, the Voll gap between ~An_{40}-An_{90}. In many staurolite-bearing metabasites, plagioclase tends to be either moderately anorthitic (~An 30 - 60) (e.g. Sharma and McRae, 1981; Stout, 1972; Spear, 1977; Spear, 1978; Spear, 1980) or predominantly anorthitic (~An_{70} to >An_{90}) (e.g. Gibson, 1979; Ward, 1984; Schumacher and Robinson, 1987; Helms et al, 1987), reflecting the influence of the Voll gap. The distribution coefficient (K_D) for the partitioning of Ca and Na between plagioclase and hornblende in these rocks is extremely variable (see Table 6.8) with albitic plagioclase producing low K_D values, and anorthitic plagioclase resulting in K_D values an order of magnitude higher. Although the mafic amphibolites tabulated in table 6.8 are estimated to have experienced similar temperature conditions, the wide range in K_D values in these rocks indicate that the K_D is not independent of mineral composition, suggesting that the distribution of Na-Ca between hornblende and plagioclase in the rocks is highly non-ideal, consistent with the observations made in more common staurolite-absent mafic amphibolites. Thus while the Yambah plagioclases are particularly anorthitic, they are not unusually so.

In the Arnold et al, (2000) petrogenetic grid, sodium is contained solely within plagioclase and hornblende, and in real rocks the Na-Ca ratio between hornblende and plagioclase is sensitive to bulk composition and controls the resultant chemistry of these phases.

Reference Sample No.	plagioclase no. of cations		hornblende no. of cations		Kd	XAn	T (oC)
	Ca	Na	Ca M4	Na M4			
Selverstone							
Z 3M	0.33	0.687	1.66	0.182	0.053	0.324	500-600
Z 3N	0.295	0.719	1.648	0.195	0.049	0.291	
FH 1M	0.325	0.671	1.593	0.253	0.077	0.326	
FH 1P	0.334	0.69	1.639	0.209	0.062	0.326	
Helms							
L 100	0.89	0.102	1.585	0.093	0.512	0.897	540-620
L 112d	0.961	0.033	1.665	0.05	0.875	0.967	
L 112n	0.956	0.056	1.618	0.067	0.707	0.945	
L 75	0.661	0.334	1.551	0.152	0.194	0.664	
Humphries							
kdh 5-105	0.297	0.704	1.66	0.18	0.046	0.297	600-625
g 5b	0.459	0.55	1.645	0.189	0.096	0.455	
va 12a	0.412	0.588	1.58	0.223	0.099	0.412	
Arnold							
hr 91-8	0.89	0.07	1.61	0.27	2.132	0.927	570-710
853-16	0.61	0.36	1.75	0.21	0.203	0.629	
85-72	0.83	0.13	1.66	0.28	1.077	0.865	
950-077	0.36	0.29	1.58	0.39	0.306	0.554	

Table 6.8. Summary of varation in the chemistry of plagioclase in mafic amphibolites from a range of localities. Abbrev: Selverstone = Selverstone et al (1984); Helms = Helms et al (1987); Humphries = Humphries (1993); Arnold = Arnold et al, 2000.

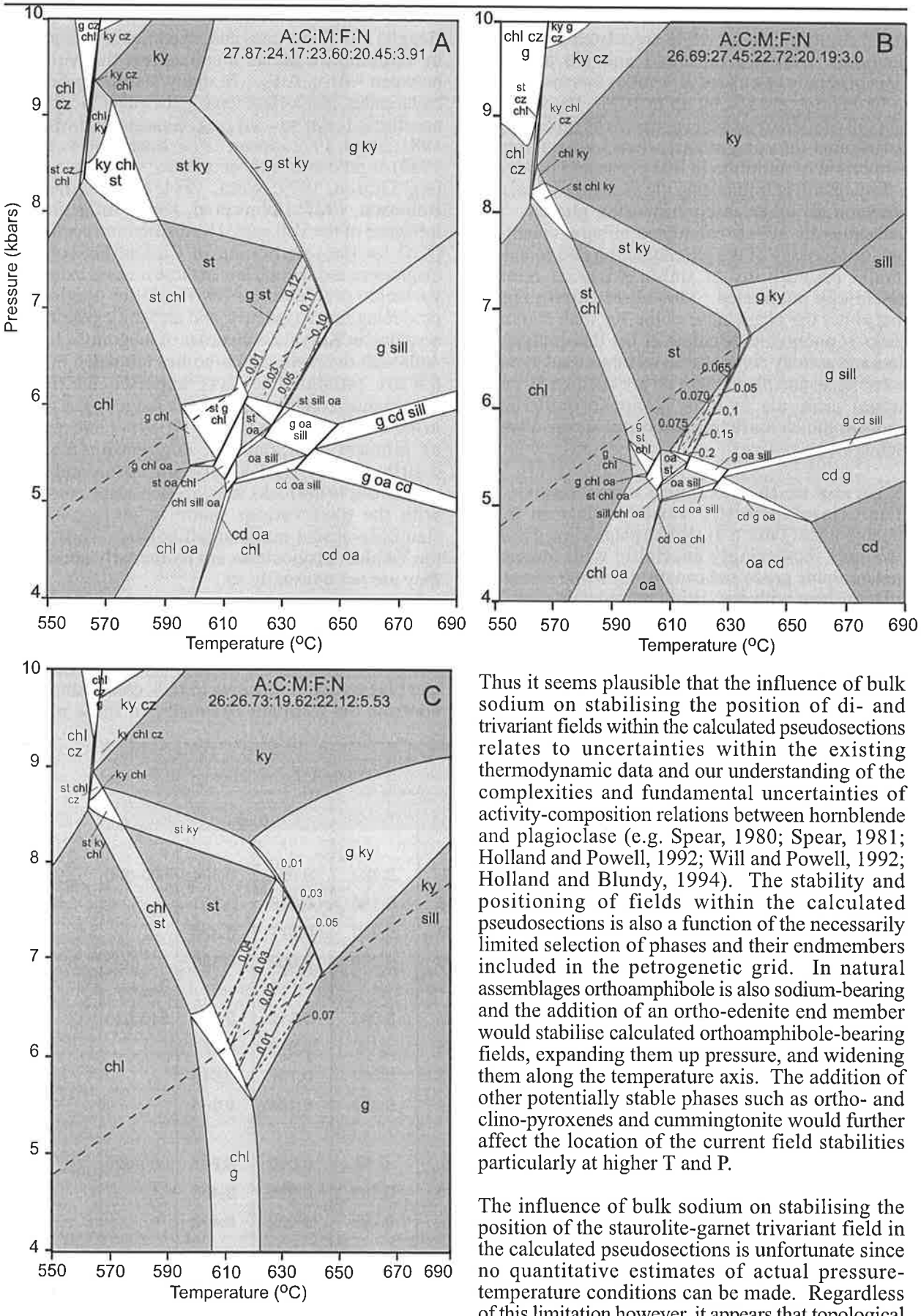

Figure 6.20. Mineral isomodes for staurolite and garnet in the st-g trivariant field. Pseudosection (a) is the same as Figure 6.19 (d) while (b) and (c) are equivalent to (b) and (d) in Figure 6.19 respectively. Note that the orientation of isomodes is consistent with the growth of garnet and decrease in staurolite with increasing temperature in the st-g field.

Thus it seems plausible that the influence of bulk sodium on stabilising the position of di- and trivariant fields within the calculated pseudosections relates to uncertainties within the existing thermodynamic data and our understanding of the complexities and fundamental uncertainties of activity-composition relations between hornblende and plagioclase (e.g. Spear, 1980; Spear, 1981; Holland and Powell, 1992; Will and Powell, 1992; Holland and Blundy, 1994). The stability and positioning of fields within the calculated pseudosections is also a function of the necessarily limited selection of phases and their endmembers included in the petrogenetic grid. In natural assemblages orthoamphibole is also sodium-bearing and the addition of an ortho-edenite end member would stabilise calculated orthoamphibole-bearing fields, expanding them up pressure, and widening them along the temperature axis. The addition of other potentially stable phases such as ortho- and clino-pyroxenes and cummingtonite would further affect the location of the current field stabilities particularly at higher T and P.

The influence of bulk sodium on stabilising the position of the staurolite-garnet trivariant field in the calculated pseudosections is unfortunate since no quantitative estimates of actual pressure-temperature conditions can be made. Regardless of this limitation however, it appears that topological relationships are little affected. In all the calculated pseudosections produced, the inferred P-T path of the Yambah metabasites is through the st-hbl-plag-q-H_2O quadrivariant into the st-g-hbl-plag-q-H_2O trivariant, and then into the g-hbl-plag-q-H_2O quadrivariant. This path is consistent with

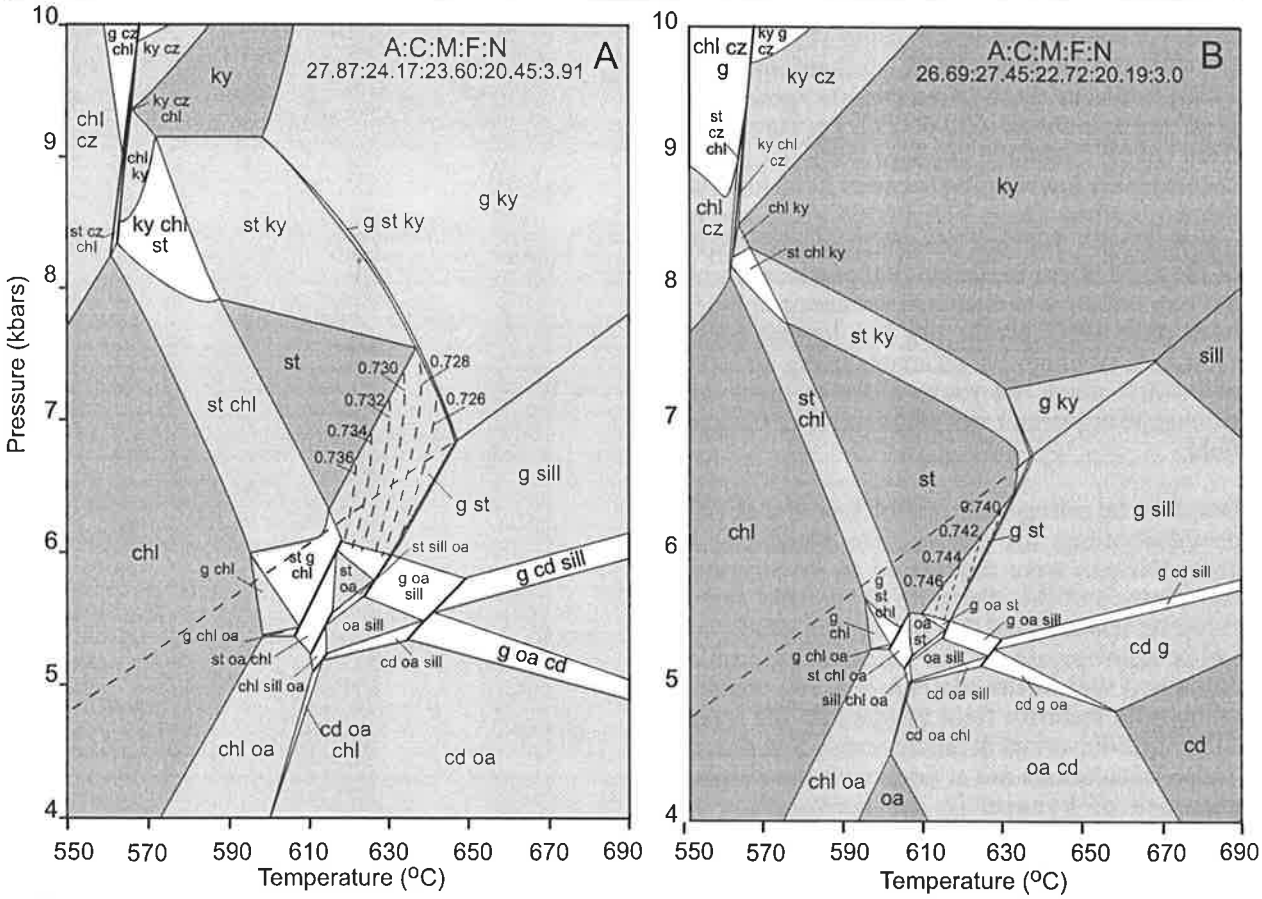

Figure 6.21. Isopleths of X(Fe) in garnet in the st-g trivariant field. Pseudosection (a) is equivalent to Figure 6.19 (d) while (b) and (c) are equivalent to (b) and (d) in Figure 6.19 respectively. Note that X(Fe) isopleths are oriented sub-parallel to the pressure axis such that an up-temperature path will tend to grow garnet with a decreasing X(Fe) ratio.

increasing temperature, and is supported by modal proportion data which indicates that the growth of garnet at the expense of staurolite through the st-g-hbl-plag-q-H_2O trivariant field is achieved via an up-temperature path (Figure 6.20). In addition, any up-temperature path, regardless of whether the rock moves isobarically, up or down pressure will result in a path either parallel to XFe isopleths or in decreasing the XFe ratio in garnet (Figure 6.21), consistent with the garnet zonation profiles discussed in section 6.3.1.2. Thus the available pseudosection data, while not quantitatively reliable, indicates that the metabasites in the Yambah Schist Zone have experienced up-temperature metamorphism, probably associated with decompression through P-T space.

6.4 Conclusions

In the Yambah Schist Zone metapelitic rocks consist of high variance assemblages which are ineffective for geothermobarometry and petrogenetic investigations. Adjacent interlayered metabasites locally contain hbl-plag-q±g, but some examples contain the relatively rare assemblage st-hbl-plag-q±g and record informative reaction textures resulting from the growth of garnet at the expense of staurolite. As such, these lower variance metabasic schists are more appropriate for studying the ambient metamorphic environment during the ASO. Chemical zonation patterns in garnets from the metabasites show small changes across individual grains which are interpreted as resulting from the growth of garnet during prograde metamorphism. Temperature estimates from geothermobarometry are slightly lower than those

from Average PT calculations using THERMOCALC (Powell and Holland, 1988; Holland and Powell, 1990) however there is reasonable agreement for peak temperatures of ~600-640°C. Pressure estimates from cation exchange geobarometry are generally unreasonably low ranging between 2-3.5 kbar, while those obtained from THERMOCALC are more reasonable at ~ 5-6 kbar. Manipulation of the X(H2O) of the fluid phase indicated that pressure estimates are very sensitive to chemical variations in the fluid, with pure H2O producing the lowest pressure estimates. Average PT estimates using an X(H2O) of 0.8-0.7 place the rocks close to the kyanite-sillimanite univariant and within error of the kyanite field.

Based on the petrogenetic grid of Arnold et al, (2000), pseudosections for appropriate metabasic bulk compositions were calculated to investigate the significance of the staurolite breakdown textures. However it was found that the tri- and quadrivariant fields appropriate to the mineral assemblages contained within the metabasites, lay within the sillimanite stability field or straddle the kyanite-sillimanite univariant at unreasonably low pressures. These calculations are at odds with the ubiquitous presence of kyanite in the surrounding ASO metapelites. Further assessment indicates that the position of the appropriate tri- and quadrivariant fields in P-T space is directly linked to the amount of sodium present in the bulk composition used to calculate the pseudosections. This may reflect inadequacies in the activity-composition relations used to model cation exchange between hornblende and plagioclase. As a result, the quantitative position of the fields in P-T space and calculated chemistry of these phases may not be directly applicable to the natural assemblages at Yambah. While varying the bulk sodium content effects the position of fields within P-T space, it appears to have little effect upon topological relationships. The pseudosections, in conjunction with textural information, indicate that the rocks from the Yambah Schist Zone have moved along an up temperature path in P-T space from the st+hbl+plag+q+H_2O trivariant to the st+g+hbl+plag+q+H_2O divariant and then down pressure into the g+hbl+plag+q+H_2O trivariant, consistent with heating during decompression.

Sm-Nd dating of the Yambah metabasites indicate that they experienced peak metamorphism at about 380 Ma while undertaking a clockwise trajectory in P-T space. The age of this metamorphism contrasts with the prograde metamorphism (600-640°C and 6 kbar) recorded for the Pinnacles Bore and Winnecke regions at about 320 Ma. Thus it appears that there are at least two episodes of prograde metamorphism during the ASO in the Strangways Metamorphic Complex, separated by an interval of about 60 m.y.

Chapter 7

FLUID FLOW, METASOMATISM AND STABLE ISOTOPE ALTERATION IN ASO SHEAR ZONES

7.1 Introduction

Mid-crustal ductile shear zones are zones of pervasive mineralogical, chemical and isotopic alteration, which can extend over large distances. Such large-scale alteration is not adequately explained by diffusive mass transfer (Dipple and Ferry, 1992a; Fletcher and Hofmann, 1974; Bickle and McKenzie, 1987; Etheridge et al, 1984; Rumble, 1989), and thus shear zones must act as conduits for the movement of large volumes of fluid. Indeed, the close relationship between the distribution of shear zones and zones of metasomatism suggests that the progression of metamorphic reactions, deformation and fluid flow are contemporaneous and self perpetuating processes (Beach, 1980; Etheridge et al, 1983; McCaig, 1984; Fourcade et al, 1989; Oliver et al, 1990; Oliver, 1996; McCaig, 1997).

The Strangways Metamorphic Complex is an excellent locality to explore fluid-rock interactions that occurred during the ASO, as it is a Proterozoic granulite facies terrain cut by a large number of anastomosing Palaeozoic amphibolite facies shear zones. The shear zones contain hydrous amphibolite facies assemblages, implying the localised infiltration of a water-rich fluid along the shear zones during deformation associated with the ASO. Geothermobarometry and petrogenetic evidence (see Chapters 4, 5 & 6) suggest that these amphibolite facies assemblages developed at peak conditions of about 600-640°C and 6-7 kbars (~20 km depth in the crust). Mineralogical differences between the granulites and the shear zone rocks, such as the growth of potassic phases in metabasic shear zone rocks, and the common occurrence of kyanite-rich veins, also suggest that some changes in whole-rock geochemistry may have occurred. Therefore, an important aspect of understanding the metamorphic environment in which these Palaeozoic assemblages grew includes an investigation of the source and transport environment of the fluid which facilitated mineral recrystallisation in these shear zones.

In many instances, fluids permeating shear zones in response to regional metamorphism have been derived from devolatilisation of a local rock mass during prograde metamorphism, a process which is capable of producing large volumes of fluid (Connelly and Thompson, 1989; Graham et al, 1997; Marquer and Burkhard, 1992), or from magmatic waters derived from the intrusion of syn-metamorphic igneous bodies (Burnham, 1979; Fleck and Criss, 1985; Kerrich, 1988). Environments in which subduction, thrusting or nappe stacking have occurred are particularly amenable to the production of large volumes of metamorphic fluids, which are derived from the underlying sequences as they are heated through burial and the emplacement of the overlying thrust sheets. Fluid movement in these systems is often mediated by an interconnected network of ductile faults, effectively channelling fluid flow through the rock mass via permeability contrasts, leading to metasomatism of the hangingwall rocks (Oliver, 1996; McCaig, 1997). This scenario is often invoked to explain sources and transport mechanisms for fluid circulation in high grade terrains (e.g. Lobato et al, 1983; Jamtveit et al, 1990; Selverstone et al, 1991; Crespo-Blanc et al, 1995; Marquer and Burkhard, 1992). However a growing body of evidence suggests that meteoric fluids are also able to infiltrate to significant depths in the crust, or may be recycled without flowing from surface to depth (e.g. dehydration of earlier hydrothermally altered rocks) (Wickham and Taylor, 1985; Sheppard, 1986; McCaig et al, 1990; Frost and Bucher, 1994; Morrison, 1994; Cartwright and Buick, 1999). A significant problem arises however when considering retrograde shear zones in relatively anhydrous granulite facies terrains, particularly in the absence of intrusive bodies. In this scenario a water-rich fluid must have been able to access the rocks in order to facilitate the recrystallisation of granulite facies assemblages to lower grade hydrous assemblages. The fluid is unlikely to have been generated in large amounts from the surrounding granulites, particularly in the absence of melt generation, implying the influx of an exotic fluid to enable retrograde recrystallisation. This conundrum is exacerbated in the Strangways Metamorphic Complex since the terrain experienced granulite facies metamorphism during the Proterozoic, but the shear zones experienced prograde amphibolite facies metamorphism during the Palaeozoic. Thus while the shear zones are lower grade (i.e. 'retrograde') with respect to the surrounding granulite country rocks, they are not related to the retrograde path of the Proterozoic granulite facies event.

Characterisation of the infiltrating fluid and the manner in which it interacted with the shear zone rocks can be examined using whole-rock geochemistry and stable isotope analysis. Stable isotopes can be quite robust to resetting, and whole-rock stable isotope signatures may only reset after interaction with a significant fluid flux (e.g. Hoernes and Hoffer, 1995; Jiang et al, 1988; Cartwright et al, 1993; Farquhar et al, 1996). In addition, fluid interaction may also affect the bulk composition of a host rock via the mass transfer of major and trace

elements. Therefore the largest shifts in isotopic signatures are likely to be in shear zone rocks which are mineralogically distinct from their precursor.

This chapter examines the metamorphic fluid flow regime experienced by the Alice Springs Orogeny-age shear zones using stable isotope data and whole rock geochemistry. Since this study focuses on investigating the Alice Springs Orogeny-age shear zones, only shear zones which have been constrained both geochronologically and petrologically were targeted for study. Results from P-T calculations and Sm-Nd dating of shear zones in the SMC indicate that shear zones in the northern SMC (e.g. the Yambah Schist Zone) underwent prograde metamorphism at about 380 - 400 Ma, while shear zones in the southern part of the SMC (e.g. the Erontonga Shear Zone) experienced similar peak conditions during prograde metamorphism about 60-80 m.y. later at around 320 Ma. As a result the Yambah Schist Zone and Erontonga Shear Zone were both selected for reconnaissance stable isotope studies in order to assess the fluid flow regimes which existed during these two periods of prograde metamorphism.

7.2 Shear Zones descriptions and sampling strategy

Samples were selected from the major rock types present adjacent to and within the Yambah Schist Zone and the Erontonga Shear Zone, including

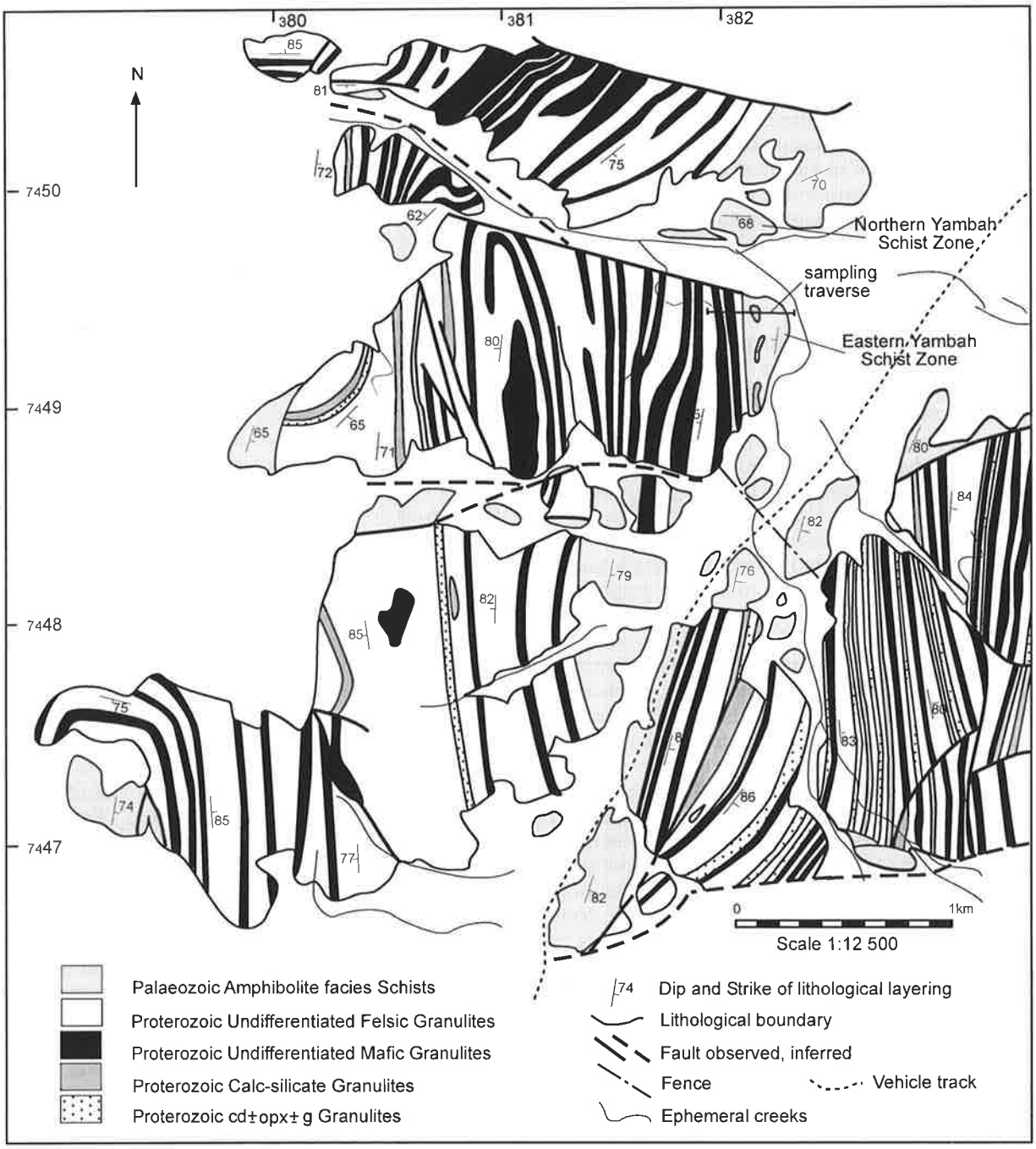

Figure 7.1. Simplified geology of the Yambah Schist Zone , indicating locations of the northern and eastern schist zones and the traverse used for sampling (adapted from Windrim, 1983).

mafic, quartzofeldspathic and aluminous metapelitic gneisses and schists. Although there are marbles and calc silicates scattered throughout the Strangways Metamorphic Complex, there are few associated with the metapelites and metabasites used for calculating metamorphic conditions in the selected shear zones. Therefore, carbon isotope studies were not able to be performed in conjunction with oxygen isotope studies. Unfortunately contacts between the Yambah and Erontonga Shear Zones and their unaffected granulite facies host rock are commonly obscured by scree or do not crop out, and the Yambah Schist Zone in particular has quite difffuse boundaries. The shear zones are generally oriented parallel to sub-parallel to lithological contacts and fabrics in the surrounding granulites, and contain metabasic, metapelitic and felsic schists interlayered on the metre to ten metre scale. As a result, the individual schist units can rarely be traced into unaffected precursor granulite and thus the specific precursors to the sheared and metasomatised rocks are often unknown.

7.2.1 The Yambah Schist Zone

In the Yambah Schist Zone there are two distinct areas of outcropping schists (termed the northern and eastern zones), which are spatially separated by an area of obscuring alluvium (Figure 7.1). The shear zone rocks are derived from adjacent interlayered mafic, ultramafic, felsic and metapelitic granulites of the Strangways Metamorphic Complex (SMC). However, contacts between the granulites and the shear zone do not outcrop and the diffuse nature of the shear zone further hinders systematic sampling in a measured traverse. The granulites are laterally heterogeneous with individual units commonly measuring less than 10 metres in width. Rocks within the shear zone are also heterogeneously distributed with mafic, felsic and metapelitic schists interlayered on a 5-10 metre scale. The mafic granulites are generally medium to coarse grained gneissic rocks with a granoblastic polygonal texture. Assemblages in the mafic granulites consist of plag + opx + cpx + mag + ilm ± (hbl, bi, all, q). Felsic granulites are generally medium to coarse-grained gneissic rocks composed of q + plag + opx + bi + ilm + mag ± (ksp, g, ap), while the more aluminous metapelitic granulites have q + opx + cd + bi + ilm + mag ± (g, ksp, plag, sill, ap) assemblages.

In the field at Yambah, a metasomatic influence is implied by the growth of biotite and kyanite in the mafic schists, as well as the presence of quartz-kyanite pods within the schist zones. In both zones, biotite is the more common mica, however in the northern zone muscovite is less common than in the eastern zone, where it is a major phase in the rocks. In addition, the eastern zone is marked by small isolated lenses of very coarse-grained biotite-kyanite-rich and hornblende-kyanite-rich schists, and almost monomineralic pods of very coarse-grained kyanite and quartz. Mafic amphibolites in the shear zones are commonly foliated hbl + plag ± (q, ep, chl, bi, sph, rut) + mag + ilm-bearing rocks. Quartzofeldspathic rocks are generally well-foliated

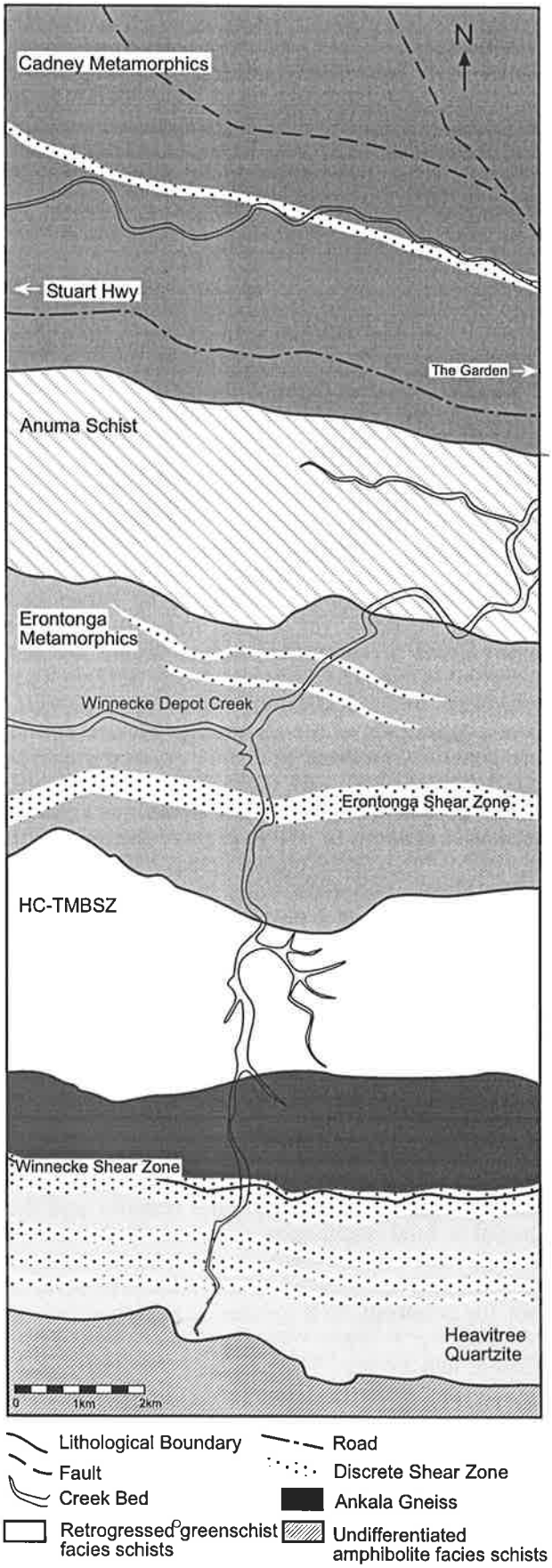

Figure 7.2. Simplified geology of the Winnecke area indicating the location of the Erontonga Shear Zone (adapted from Emslie, 1996).

plag + q + bi ± (mu, ksp, mag) + ilm + ap schists. The metapelitic schists are more aluminous having ky + bi + st + plag + q ± (g, sill, mu, chl) assemblages. A more detailed description of the mineralogy of some of the Yambah schists is given in section 6.2.1 and Appendix 1.25. As the eastern schist zone appears to be more affected by metasomatism, sampling was concentrated here.

7.2.2 The Erontonga Shear Zone

The Erontonga Shear Zone in the Winnecke area is smaller than the Yambah Schist Zone with a total outcropping width of about 50 metres (Figure 7.2). It also contains interlayered mafic, metapelitic and felsic schists but generally appears to have less voluminous growth of coarse micas and the other unusual metasomatic assemblages seen at Yambah including the monomineralic pods. The shear zone is oriented parallel to lithological layering and deformation fabrics observed in the adjacent granulites and contacts between the shear zone and surrounding rocks are obscured by scree and alluvium. Therefore, the original unsheared granulite equivalents of individual schist layers are not identifiable, but the schists are clearly derived from granulites of the Erontonga Metamorphics suite. Mafic granulites of the Erontonga Metamorphics are generally medium to coarse grained gneisses consisting of plag + opx + cpx + mag + ilm ± (hbl, bi, q, sp) assemblages. Felsic granulites are also generally medium to coarse-grained gneisses with q + opx + bi + ilm + mag ± (plag, ksp, g, ap, zr) assemblages, and metapelitic granulites have q + opx + cd + bi + ilm + mag ± (g, ksp, plag, sill, ap, sp) assemblages. Mafic amphibolites from the shear zone contain hbl + plag + q ± (g, cz, ap) assemblages, while felsic shear zone rocks contain bi + q ± (mu, ky, fsp, ap) and metapelitic schists contain bi + q ± mu, ky, g, st, fsp, ap) assemblages.

7.3 Stable Isotope Geochemistry

The interaction of CO_2- and H_2O-rich fluids with rocks commonly results in the growth of new mineral assemblages, metasomatic mass transfer and the partial or total rehomogenisation of stable isotope values. On a centimetre to metre scale isotopic resetting may be mediated by advection or dispersion, but for resetting on a greater scale advection is required (e.g. Rumble, 1989; Ferry and Dipple, 1991; Dipple and Ferry, 1992a; Cartwright and Buick, 1995). In the case of oxygen isotopes, the direction and magnitude of isotopic alteration in the rocks (i.e. either relative enrichment or depletion in ^{18}O) can provide information on the source of the infiltrating fluid, the flow direction with respect to the ambient thermal gradient and the time-integrated fluid flux (e.g. McCaig et al, 1990; Baumgartner and Ferry, 1991; Dipple and Ferry, 1992 a & b; Van Haren et al, 1996; Cartwright and Buick, 1999). Since the exchange of oxygen isotopes between a fluid and rock is temperature sensitive, the analysis of oxygen isotope ratios in coexisting minerals can also be used for geothermometry and to determine the degree of equilibration and the scale over which isotopic equilibration has occurred (Valley, 1986; Gregory, 1990; Matthews, 1994; Zheng, 1993a). Thus stable isotopes are a useful source of information for investigating metamorphic P-T-X_{fluid} regimes and hence the tectono-metamorphic histories of orogenic belts.

7.3.1 Methodology

Whole rock samples for stable isotope analyses are powders derived from the crushing of ~3-5 kg of material, while pure mineral samples were separated from coarsely crushed and sieved hand specimens using a Franz Isodynamic separator and by hand picking. Stable isotope ratios were measured at Monash University on a Finnigan MAT 252 mass spectrometer, and were analysed following the method of Clayton and Mayeda (1963) but using chlorine trifluoride (ClF_3) as the oxidising reagent. Oxygen isotope values are expressed in conventional 'delta' (δ) notation relative to V-SMOW. Internal and international standards analysed during the same period as the study samples returned values within 0.2‰ of their accepted values. The long term average $\delta^{18}O$ value for the NBS28 quartz standard at the Monash laboratory is 9.55 ± 0.11‰. Errors on individual analyses are within ± 0.2‰.

7.3.2 Results from the Yambah Shear Zone

Granulites from the Strangways Metamorphic Complex in the vicinity of the Yambah Schist Zone have $\delta^{18}O$ values ranging between about 2.8‰ and 6.2‰ (Table 7.1 and Figure 7.3; n=23). The mafic granulites have a large spread of values but tend to have the lowest average value at about 4.3‰, while the felsic granulites have a smaller range of between 4.5‰ and 6.2‰ but a slightly larger average value of around 5‰. Mafic amphibolites from the Yambah Shear Zone also have widely distributed $\delta^{18}O$ values, ranging between about 4‰ and 9.3‰ (n=11). Although values in the mafic amphibolites can overlap with the upper ranges of the mafic granulites, the data does suggest a trend toward higher $\delta^{18}O$ values with an average shift of about +2‰ and a maximum shift of about +5‰. In comparison, felsic schists from the shear zone have a very large spread of values ranging from 4.5‰ to 11.9‰ (n=9), suggesting average increases of only around +1.6‰ but maximum shifts of up to +6.9‰ (Figure 7.3). Figure 7.4 shows the trend toward higher $\delta^{18}O$ values in the shear zone rocks more clearly. In this figure values are plotted as a transect from pristine granulites of the Strangways Metamorphic Complex (SMC) into and across the shear zone. The granulites adjacent to the shear zone have $\delta^{18}O$ values of between 3‰ and 5‰ and, while some of the shear zone rocks have equivalent values, most are higher. The largest shifts are found in very coarse-grained staurolite-biotite-muscovite schists and hornblende-biotite-kyanite schists (e.g. YS30, YS31, YS19).

Sample	Description	$\delta^{18}O$ values								density
		WR	qtz	bi	chl	g	hbl	opx	mu	(kg/m^3)
Mafic schists										
YS10	g-chl schist	4			2.9	3.5				
YS148	g-st-bearing amphibolite	7.1	7.5				5			
YS149	g-bearing amphibolite	6.1	7.2				4.7			
YB32	hbl-plag-q amphibolite	6.7								2.92
YB33	g-bearing amphibolite	6.6								2.9
YS145	g-chl schist	4.8								
YB1	hbl-plag-q amphibolite	6.4								
YB2	hbl-plag-q amphibolite	6.6								3.1
YB3	g-st-bearing amphibolite	7.1								
YB4	g-bearing amphibolite	5.9								
YB15	g-st-bearing amphibolite	6.6								
YB20	ky blow w/in hbl-bi-ky schist	6.9								
YB22	hbl-bi-ky schist	9.3								2.73
YB24	retrogressed ultramafic	5.6								
YB25	retrogressed ultramafic	4.9								
Felsic schists										
YB8	bi-rich schist	8.7	9.5	6.3						2.69
YB19	ky-rich micaschist	7.2	8.7	5.5						3.04
YB30	micaschist	9.1	10.1	6.4						3.02
YB31	micaschist	11.9	10.7	5.8						3.07
A1	micaschist		8.7	1.5					4.3	
A18	st-ky schist		10.2	5.1						
A22	micaschist		13.2	7.7					11	
A90	micaschist		6.9	-0.1						
A99	st-ky schist			4.2					6.2	
A128	bi-rich schist		6.6	-0.4					7	
YS2	bi ky fsp q schist	7.1								
YS8	ky-rich micaschist	4.2								
YS11	bi mu ky schist	4.8								
YS11A	bi mu ky schist	5.3								
YS146	st-ky schist	6.5								
YS146A	ky bearing micaschist	4.5								
YS150	micaschist w very coarse st	5.3								
YS151	micaschist w very coarse st	4.5								
YB18	coarse bi ky schist	5.9								2.86
YB6	(subcrop) bi-rich schist	7.8								2.96
YB7	v coarse micaschist	4.6								2.88
YB27	micaschist	5.9								2.4
YB28	quartzofeldspathic schist	7.1								
YB29	ky bearing micaschist	5.6								3.02

Table 7.1. Summary of $\delta^{18}O$ data from whole rock and pure mineral separates from selected rock samples from the Yambah Schist Zone.

Sample	Description	$\delta^{18}O$ values								density
		WR	qtz	bi	chl	g	hbl	opx	mu	(kg/m^3)
Granulites										
YB10	felsic granulite	4.7	5.9					2.2		2.8
A129	felsic granulite		5.1	0				2.5		
YB11	felsic granulite	4.7								3.12
YB13	felsic granulite	4.5								2.57
YB14	felsic granulite	5								2.74
YB21	ultramafic granulite	3.5								
35895	felsic granulite	4.7								
39227a	felsic granulite	4.8								
39575	felsic granulite	5.2								
35924	felsic granulite	5.8								
35889	metapelitic granulite	4.7								
39573	metapelitic granulite	6.2								
YB9	mafic granulite	3.7								3.11
39922	mafic granulite	2.8								
39227b	mafic granulite	3.3								
39226	mafic granulite	4								
35925	mafic granulite	4.2								
35890	mafic granulite	4.3								
35847	mafic granulite	4.6								
35926	mafic granulite	4.9								
39959	mafic granulite	5.2								
39949	mafic granulite	5.3								
35901	mafic granulite	5.4								

Table 7.1 (continued).

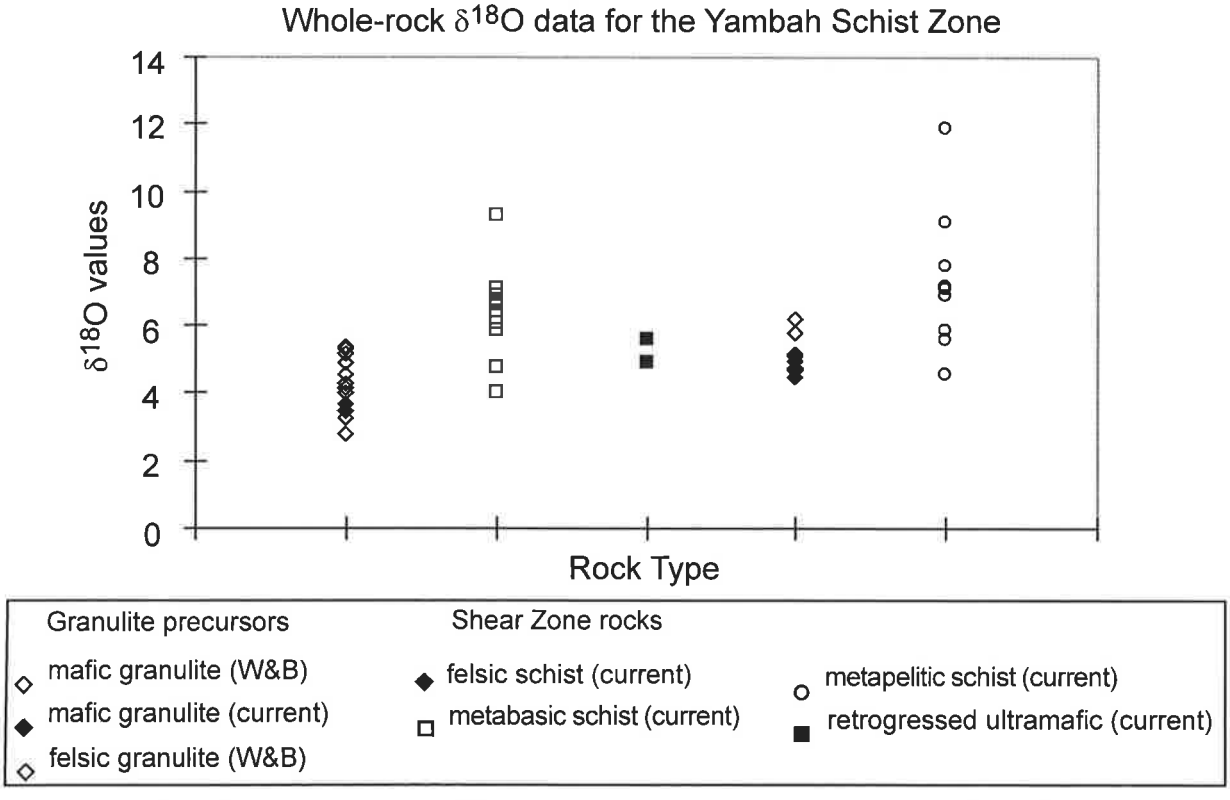

Figure 7.3. Variation in whole-rock $\delta 1^8O$ values in different rock types from the Yambah Schist Zone. Abbrev: W&B = Wilson & Baski, (1983).

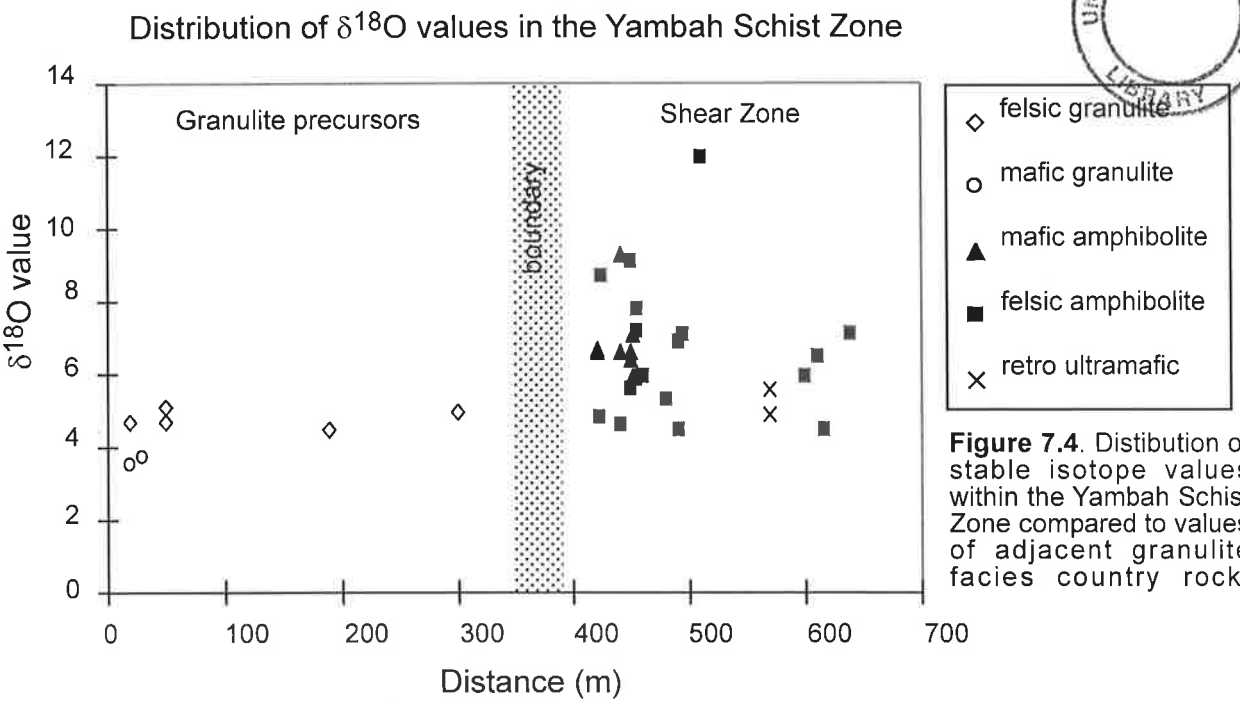

Figure 7.4. Distibution of stable isotope values within the Yambah Schist Zone compared to values of adjacent granulite facies country rock.

7.3.3 Results from the Erontonga Shear Zone

Granulites in the Erontonga Metamorphics have a similar range of $\delta^{18}O$ values to the SMC granulites with most mafic and felsic granulites ranging between about 2‰ and 7‰ (Table 7.2 and Figure 7.5). Mafic granulites have an average $\delta^{18}O$ value of about 3.6‰, felsic granulites have an average of about 5.1‰ and metapelitic granulites have an average of about 3.8‰. Rocks from within the selected shear zone tend to have higher $\delta^{18}O$ values than the granulites, ranging between about 8‰ and 12‰ with an average value of about 9.9‰. These figures indicate average isotopic shifts in the mafic rocks of about +5.7‰, average shifts in the felsic rocks of about 4.6‰, and average shifts in the metapelitic rocks of about +6.3‰, however maximum isotopic shifts are on the order of about +7‰ (see Figures 7.5 & 7.6). As noted in the Yambah Shear Zone, the largest isotopic shifts in the Winnecke Shear Zone are present in the micaceous shear zone rocks. Thus general trends in $\delta^{18}O$ data from the Winnecke Shear Zone are similar to those noted in the Yambah data.

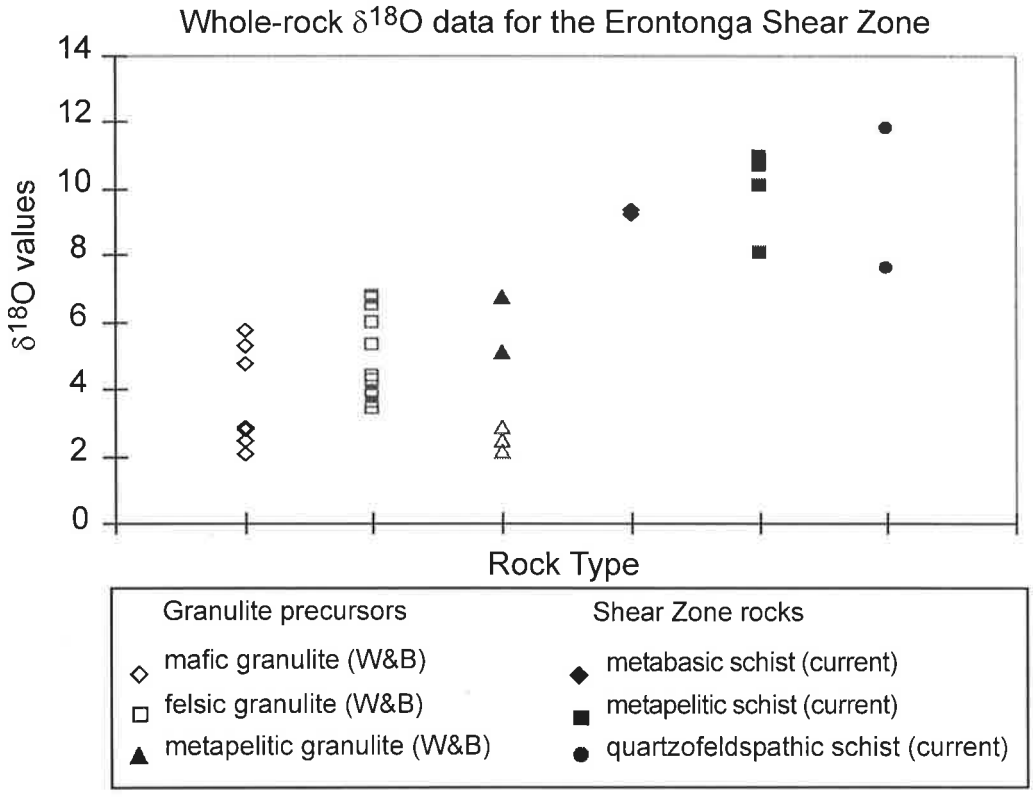

Figure 7.5. Variation in oxygen isotope values in rocks from the Erontonga Shear Zone area. Abbrev: W&B + Wilson and Baksi, (1983).

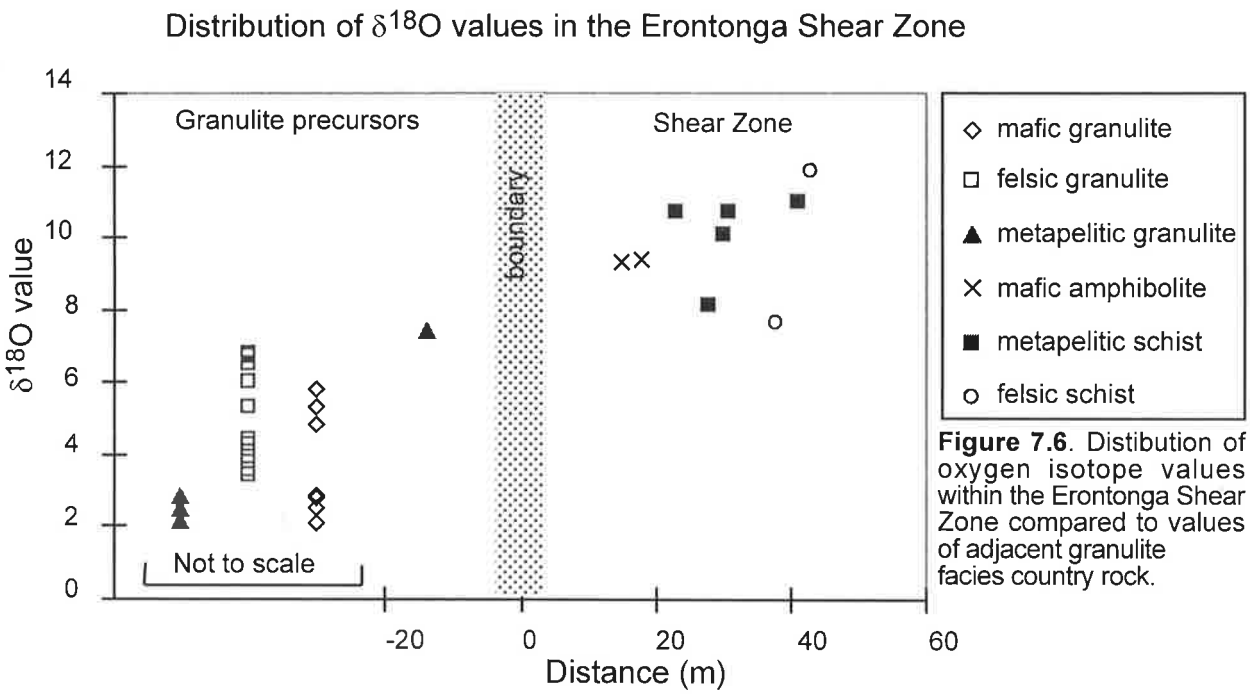

Figure 7.6. Distibution of oxygen isotope values within the Erontonga Shear Zone compared to values of adjacent granulite facies country rock.

7.3.4 Mineral Fractionations

The extent of equilibrium achieved between a rock mass and an introduced homogeneous fluid can be investigated by comparing the degree of homogeneity in the whole-rock and mineral $\delta^{18}O$ values from different fluid-affected rock types. Any given mineral having equilibrated with a homogeneous fluid at a given temperature, will have the same $\delta^{18}O$ value independent of the type of rock it occurs in (Faure, 1986; Rumble, 1982). Thus all quartz grains (for example) regardless of whether they occur in a metapelitic, felsic or mafic schist, should have homogeneous $\delta^{18}O$ values if they have completely re-equilibrated with the same homogeneous fluid under the same conditions. Similarly, the overall effect of the interaction of a pervasive homogeneous fluid with a variety of lithologies will be to minimise chemical differences within and between those rock units.

A δ-δ graph (Gregory, 1990; Gregory and Criss, 1986; Criss et al, 1987) for quartz-biotite pairs (Figure 7.8) from the Yambah Schist Zone shows that fractionation between quartz and biotite (i.e. $\delta^{18}O$ q-bi values) are variable, with samples plotting in a scattered array across the 400°C to 700°C isotherms. Assuming that the mineral separates were pure and did not contain any contaminants, that the individual minerals separated for analysis were not isotopically zoned and that all the mineral grains within a separated sample had identical $\delta^{18}O$ values, then the scattered distribution of the $\delta^{18}O$ q-bi values suggests disequilibrium exists between the minerals (Gregory et al, 1989; Kohn and Valley, 1998; Fourcade et al, 1989). During cooling along a retrograde path, some minerals (particularly feldspars) commonly continue to re-equilibrate with incoming fluids while minerals more resistant to isotopic exchange at low temperatures (e.g. quartz) undergo no or limited isotopic exchange (Gregory and Criss, 1986; Fourcade

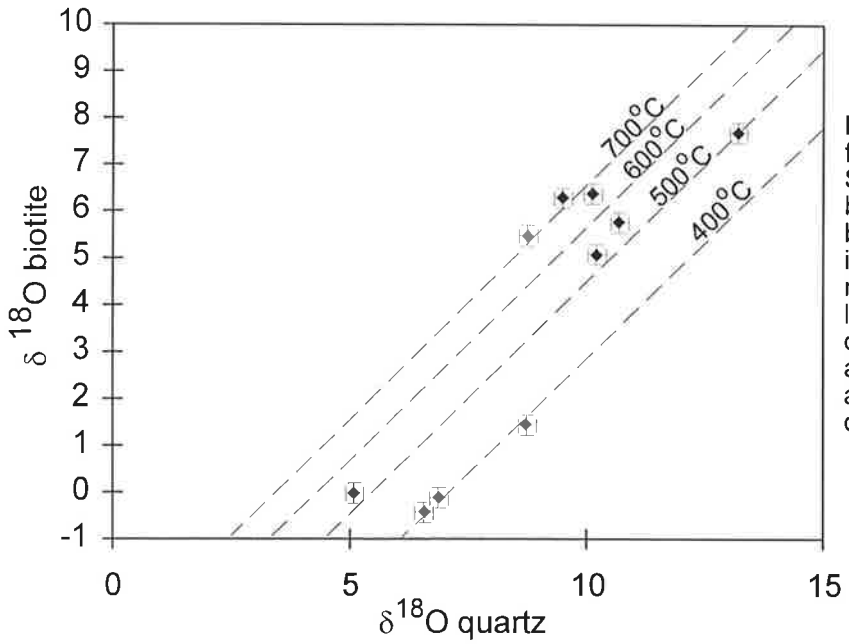

Figure 7.7. A Δ q-bi plot for schists from the Yambah Schist Zone. If isotopic equilibrium had been maintained between these minerals then individual fractionation values might vary but would tend to lie along an isotherm. In this case the values are scattered across an array of isotherms arguing that isotopic equilibrium can not be assumed.

Sample	Description	δ^{18}O values	density (kg/m^3)
Mafic amphibolites			
WK55	layered mafic gneiss	9.3	2.9
WK56	micaceous amphibolite	9.4	2.6
Metapelitic schists			
WK57	micaschist	10.7	3.5
WK58	st-g micaschist	8.1	3
WK59	st-g micaschist	10.1	2.9
WK59a	st-g micaschist	10.7	2.7
WK61	micaschist	11	2.8
Felsic schists			
WK60	bi-q-fsp schist	7.6	3.1
WK62	bi-q-fsp schist	11.8	2.7
Mafic granulites			
39495	mafic granulite	2.5	
39476	mafic granulite	2.8	
39375	mafic granulite	1.3	
39559	mafic granulite	4.8	
39560	mafic granulite	5.8	
39556	mafic granulite	2.1	
39505	mafic granulite	2.9	
39504	mafic granulite	2.9	
39562	mafic granulite	5.3	
felsic granulites			
37442	Siliceous granulite	3.9	
37440	Siliceous granulite	4.4	
37487	Siliceous granulite	6	
metapelitic granulites			
WK52	g-sill granulite	7.4	2.9
39396	cd granulite	2.5	
39561	cd granulite	2.2	
39452	cd granulite	2.9	

Table 7.2. δ^{18}O data for selected samples from the Erontonga Shear Zone.

et al, 1989; Giletti, 1986; Giletti et al, 1978). Examination of whole-rock data from Yambah and Winnecke (Tables 7.1 and 7.2) shows that δ^{18}O values of the shear zone rocks are heterogeneous, however whole-rock and quartz δ^{18}O values in the schists are rarely the same as the δ^{18}O signatures of the granulites, commonly showing shifts toward higher values. This suggests that there has been an overall shift in the oxygen isotope values of the schists, toward heavier values during ASO metamorphism, but that either 1) the schists have

Sample	Description	δ^{18}O values
Winnecke Shear Zone		
BHN-2	micaschist adjacent to HTQ	9
BHN-4	chl-rich schist	7.6
BHN-5	bi-fsp-q schist	11
BHN-6	mafic schist w mu overprint	9.4
Winnecke anthophyllite shear zone		
PAW-1	cd granulite	7.9
PAW-2	cd granulite	5.1
PAW-3	ky-anth schist	4.9
PAW-6	bi schist	3.1
PAW-7	mu-bi-plag-q mylonite	6
PAW-9	bi-plag-q mylonite	5.8
PAW-10	ky-anth schist	6.3
PAW-11	b-rich schist	8.6
PAW-12	mafic amphibolite	3.4
PAW-13	cd-g granulite	6.8
PAW-20	bi schist with mu overprint	6.2
Utranalama anthophyllite shear zone		
MRN-11	cd granulite	3.8
MRN-12	anth-ky-bi schist	6.3
MRN-13	cd-g granulite	5.3
MRN-14	bi schist	5.4
MRN-16	anth-g-ky protomylonite	5.4
MRN-17	cd-g mylonite	5.1

Table 7.3. δ^{18}O data from selected minor shear zones in the Winnecke and Pinnacles Bore areas.

not achieved complete isotopic equilibrium with a homogeneous infiltrating fluid or 2) the schists achieved equilibrium with an isotopically heavy fluid during the earlier stages of ASO metamorphism but subsequently interacted and partially re-equilibrated with a different, isotopically lighter fluid during their retrograde path (e.g. Kohn and Valley, 1998; Cartwright et al, 1996).

The greatest shifts in δ^{18}O values (up to about 6‰) are seen in the most micaceous schists, which may reflect their greater permeability and hence greater ability to interact with the fluid, particularly when compared to the mafic amphibolite schists which contain no or very minor amounts of phyllosilicate minerals. This implies that the observed heterogeneity in whole rock and mineral δ^{18}O values may reflect the partitioning of fluid flow within the shear zone through permeability contrasts (e.g. Etheridge et al, 1983; Fourcade et al 1989; Oliver, 1996; McCaig, 1997). Alternatively, some minerals within the schists may not have completely recrystallised and may preserve their original granulite δ^{18}O signature (e.g. Cartwright et al, 1993) although

there is no evidence of preserved relict minerals in these shear zone rocks. If the lower $\delta^{18}O$ values do result from re-equilibration during cooling from peak metamorphic conditions during the ASO, then it would be expected that some mineralogical evidence for this retrogression should be observed in the rocks. However there is also very little evidence of retrograde reaction or significant growth of retrograde minerals in the schists. As such, isotopic inhomogeneities in the basement shear zones are interpreted as evidence for incomplete equilibration between the rocks and the fluid.

7.3.5 Stable isotope data from other shear zones in the Winnecke area

A major retrograde shear zone (here called the Winnecke Shear Zone) about 500 metres in width, consisting of greenschist facies chlorite-muscovite and biotite-muscovite bearing schists of the Arunta Basement, lies immediately adjacent to the Heavitree Quartzite in the Bald Hill-Winnecke area (Figure 7.2). This structure constitutes the main thrust separating the southern footwall containing the Heavitree Quartzite and Bitter Springs Formation, and the northern hangingwall, which includes the granulite facies Erontonga Metamorphics. The rocks in this shear zone have potentially experienced the greatest fluid flux in the area, as this zone has experienced large vertical movements and represents a fundamental structural boundary between the basal Amadeus Basin sediments and the overthrust Arunta Basement. Samples of schists and phyllonites immediately adjacent to the Heavitree Quartzite in this location record $\delta^{18}O$ values of between 7.6‰ and 11‰ (see Table 7.3), similar to the higher $\delta^{18}O$ values recorded in some schists from the Yambah and Erontonga shear zones. This suggests that the greenschist facies schists may have equilibrated with a similar fluid from a similar source as the higher grade schists in the Yambah and Erontonga shear zones. This evidence supports the hypothesis that the isotopic inhomogeneities observed at Yambah and Erontonga result from incomplete equilibration with an infiltrating isotopically heavy fluid during early stages of ASO metamorphism, rather than from an episode of subsequent retrograde re-equilibration with another fluid.

Also found throughout the Pinnacles Bore and Winnecke areas are narrow (i.e. ~ 10-20 metres wide) anthophyllite-bearing and garnet-cordierite-bearing shear zones and mylonites that are commonly mineralogically similar to the host granulites, generally mica-poor, and are not substantially retrogressed. These shear zones have not been dated and may have developed prior to the ASO. Alternatively, they may have undergone limited reaction during the ASO but due to the paucity of a fluid phase, failed to recrystallise a new equilibrium assemblage (e.g. Hoernes and Hoffer, 1985). These rocks record $\delta^{18}O$ values ranging between about 3‰ and 6.8‰ (Table 7.3), which are essentially the same as that of the precursor granulites. This evidence is consistent with the observation that oxygen isotopes are quite robust, resetting only after substantial fluid interaction, and supports the interpretation that the heavier $\delta^{18}O$ values recorded by schists from the Yambah and Erontonga shear zones result from interaction with an ASO fluid.

7.4 Whole-rock Geochemistry

Mineralogical differences between the shear zone rocks and host granulites in the SMC reflects fundamental differences in the ambient metamorphic environments which existed during crystallisation of the respective assemblages. However, in the field the large volumes of biotite and muscovite present in the shear zone schists suggests that mineralogical differences may also reflect significant changes in bulk chemistry resulting from mass-transfer via infiltrating fluids. Such large-scale major element metasomatism is considered to require much larger volumes of fluid than would be required to only reset stable isotope values (e.g. Cartwright and Oliver, 1994; Cartwright and Buick, 1995; Spear, 1993). Moreover, if the magnitude of elemental addition or loss via metasomatism can be quantified through mass balance calculations, then some assessment of the interacting fluid regime can be made, including calculation of the size and direction of flow of the fluid flux.

7.4.1 Mass balance calculations

In order to assess the differences in whole-rock geochemistry between the Palaeoproterozoic granulite-facies host rocks and the Alice Springs Orogeny-age amphibolite facies shear zone rocks, some quantification of the net mass change between the rocks must be made. However this is not a simple process of directly comparing the mass of each element present in the precursor rock with the same element's mass in the altered equivalent, since the mineralogical changes inherent in the metasomatic process may also have effected a change in rock volume (Gresens, 1967; Grant, 1986; Baumgartner and Olsen, 1995). As such, the total mass per unit volume of the altered and unaltered rock samples must be used to calculate the net mass change between the unaltered and altered rocks. The Gresens method (Gresens, 1967) compares the major and trace element concentrations of altered samples and their unaltered precursors by using rock densities and the concentrations of identified immobile elements in both the unaltered and altered samples, to calculate quantitative changes in element concentration and rock volume. Elements such as Al, Ti, Zr, Y, V and the Rare Earth Elements (REE) are often assumed to be immobile (e.g. MacLean and Kranidiotis, 1987; O'Hara, 1988; Selverstone et al, 1991; Dipple and Ferry, 1992b; McCaig, 1997). However these elements may not be ubiquitously immobile in all metamorphic circumstances. The isocon plot (Grant, 1986) enables some interpretation of the mobility of elements in rocks by graphically comparing elemental concentrations in a metasomatically altered rock of interest and an equivalent unaltered precursor. Any immobile elements in the altered rock will have identical mass ratios to the unaltered rock and hence will define a

straight line (an isocon) through the origin. The relative change (i.e. addition or depletion) of a mobile element's concentration is then graphically represented by that element's displacement from the isocon (Grant, 1986). An alternative method of determining immobility is through the use of bivariate plots. In this instance concentrations of two potentially immobile elements in a suite of rock samples are plotted against each other. If the selected element pair are immobile then they will plot as a straight line array with a line of best fit passing through the origin (MacLean and Kranidiotis, 1987; Barrett and MacLean, 1994). If one element is immobile whereas the other is not, then a line of best fit will tend to plot parallel to the immobile element axis and intesect the axis of the mobile element. Once the immobile element(s) in a rock have been determined, elemental gains and losses in the sheared rocks can be quantitatively calculated using the method of Gresens (1967).

In order to investigate element immobility in the granulite precursors and the altered schists from the Yambah Schist Zone and the Erontonga Shear Zone, the elemental concentrations of individual sheared samples were first plotted against that of either their corresponding original granulite or the elemental concentrations of an equivalent average granulite as isocon plots (Grant, 1986). Then, to verify the results of the isocons, a series of bivariate plots of potential immobile elements including Al, Ti, Cr, Ni, Zn, Zr were constructed. The geochemical data used in this investigation is a compilation of published data from the literature, unpublished data provided by the Australian Geological Survey Organisation (AGSO) and unpublished new data. Details of new and published whole-rock geochemical data is tabulated in Appendix 6. However, due to current confidentiality agreements data sourced from the AGSO geochemical database can not be reproduced. All new chemical determinations were made using a Phillips PW 1480 XRF

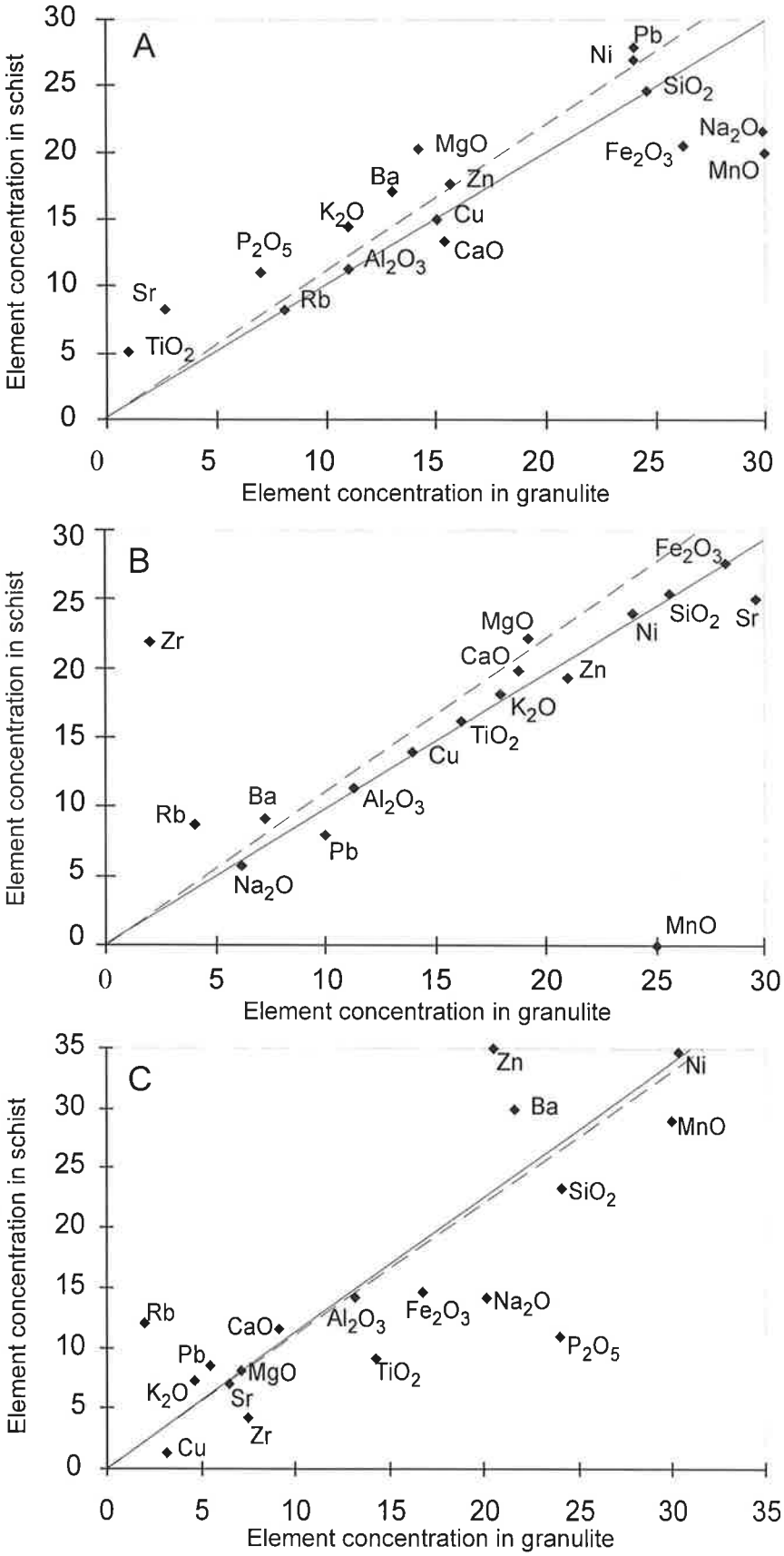

Figure 7.8. Plots of element concentrations in unaltered granulite precursors versus equivalent altered shear zone rocks. Element concentrations in ppm or wt% have been scaled by multiplying or dividing by a common factor (see Appendix 6.2 for details). Data is from Iyer (1974). Constant mass (solid line) & constant volume (broken line) reference lines have been added. (a) felsic granulite A91 v felsic schist A93; (b) felsic granulite A129 v felsic schist A128; (c) mafic granulite A92 v mafic amphibolite A89.

Spectrometer, with an analysis package calibrated against several international and local Standard Reference Materials. A dual-anode (Sc-Mo) X-ray tube was used, operating at 40 kV and 75 mA. Trace element analyses were determined on pellets of powdered material, while major elements were determined on disks of fused sample. Matrix corrections were made using either the Compton Scatter peak or mass absorption coefficients calculated from the major element data.

7.4.2 Element mobility in the Yambah Schist Zone rocks

As the eastern shear zone is oriented approximately parallel to the compositional layering and fabrics observed in the surrounding granulites, the specific precursors to the schists in this shear zone can not be identified. However the northern shear zone trends orthogonal to the fabrics in the granulites, and Iyer (1974) was able to locate a small outcrop where an unaltered mafic granulite and two felsic granulite units could be tracked into the shear zone and be directly correlated with their equivalent altered schists. No stable isotope data exists for these samples, however whole-rock geochemical data is presented in Appendix 6.

Figure 7.8 a-c shows plots of elemental concentration in the original granulite precursor rock compared to the equivalent altered schist. According to the method of Grant (1986), an isocon is defined by suite of immobile elements describing a straight line through the origin. Elements plotting above the isocon line are enriched in the altered rock while elements falling below the isocon are depleted. The geochemical datasets for the three rock pairs from the northern Yambah Schist Zone are limited and do not include analysis on a full suite of trace and Rare Earth elements (such as Y and Nb) which are generally considered less sensitive to remobilisation (Rollinson, 1993). However it is apparent that the potential immobile elements included in the chemical datasets such as Al, Ti, Cr, Ni, Zn and Zr, do not describe clearly defined isocons in these plots. In the case of samples A91 & A93 (one of the felsic rock pairs from Iyer, 1974: Figure 7.8 a) the distribution of Al, Ti and Ni may constitute a poorly defined isocon, however the common occurrence of kyanite-quartz pods within the Yambah Schist Zone, and the lack of consistency in immobile elements with the other felsic pair is suspicious.

Since in the eastern shear zone there is no way of confirming altered and unaltered equivalents, whole rock geochemical data for felsic, mafic and metapelitic granulite country rock from the Strangways Metamorphic Complex in the vicinity of the Yambah Schist Zone has been compiled from a variety of sources and used to calculate average compositions for these rock types (see Appendix 6.1). Examination of the isocon diagrams for the felsic schists (Appendix 6.2.1) shows that the potential immobile elements included in the datasets for these rocks do not generally plot as well defined isocons. In two cases, samples A22 and YB6 (Appendix 6.2.1) Al, Ti, Cr, Ni, Zn and Zr have totally random distributions while in the other plots (see Appendix 6.2.1) isocons can not be constrained using more than two elements, and the elements which define the isocons are inconsistent between samples. Potential immobile elements from the metapelites and metabasites also fail to plot as well constrained isocons (see Appendix 6.2.2 and 6.2.3). In every case the elements Al, Ti, Cr, Ni, Zn and Zr are randomly distributed and no isocon can be identified.

Bivariate plots of Al, Ti, Cr, Ni, Zn and Zr from the felsic, metapelitic and metabasic rocks are presented in Appendix 6.3. In general, the data plot as a scattered array and do not define linear trends. Aluminium in the mafics and felsics is an exception to this since when plotted against Ni, Zn, Ti and Cr in the mafics (Appendix 6.3.2), and against Ti and Zn in the felsic rocks (Appendix 6.3.1), it does define linear trends. However the linear trends in these plots intersect the Al axis rather than the origin, suggesting that Al concentrations in the granulite precursors have been homogenised at some time. Data points from the shear zone rocks do not generally lie within the linear trends defined by the granulite data suggesting that Al has been mobile in the shear zone rocks. The linear trends in the Al plots suggest that Ti and Zn in the felsic granulites or Ni, Zn, Ti or Cr in the mafic granulites were more conserved than Al, however these elements are not necessarily immobile since if this was the case then plots comparing them to each other would produce straight lines through the origin.

Thus no immobile elements have been conclusively determined from analysing precursor granulites and altered schists from the Yambah Schist Zone. The inability to determine any elemental immobility in these rocks may arise from a number of factors including; geochemical heterogeneity in the original source rocks and/or the inappropriate use of an average precursor for geochemical comparison, incomplete re-equilibration with the metasomatising fluid, and the use of inconsistent data sources which have not included a full suite of trace and REE data.

7.4.3 Element mobility in the Erontonga Shear Zone rocks

Shear zones in the Winnecke area are derived from granulites of the Erontonga Metamorphics. However since the shear zones trend approximately parallel to the gneissic fabric and lithological layering in the granulites, it is rarely possible to conclusively establish the granulite precursor to the individual schists in the shear zones. As such, the whole rock geochemistry of schists from the Erontonga Shear Zone are compared to average compositions of felsic, mafic and metapelitic granulites from the Erontonga Metamorphics (see Appendix 6.1). As mentioned above (§7.4.1) the geochemical dataset used in this study has been accumulated from a number of sources which do not all include analysis of a full range of trace and Rare Earth elements. As such, the number of potential immobile elements analysed is quite

limited, and probably only includes Al, Ti, Cr, Ni and Zr.

The geochemistry and mineralogy of metapelitic granulites in the Erontonga Metamorphics varies somewhat, therefore these granulites have been divided into three major groups (Appendix 6.1). The first two groups have quite similar bulk geochemistry, but different mineralogy with one group consisting of an opx + cd + plag + bi + q assemblage, while the other consists of opx + gnt + sill +bi + q plag. The third group has lower SiO_2 and Al_2O_3 concentrations, elevated Fe_2O_3, MnO and CaO concentrations and particularly high MgO concentrations compared to the other two groups. These 'magnesian' metapelitic rocks have Mg-opx + plag + q + bi ± g assemblages. In general, the geochemistry of the metapelitic schists in the Erontonga Shear Zone mostly closely approximates that of the magnesian metapelites. However as the precursors can not be conclusively identified in the field, the schists were compared to all three metapelitic granulite groups.

Isocon diagrams of the metapelitic schists compared to the average garnet-sillimanite-bearing granulite are shown in Appendix 6.2.7. The metapelitic schists are compared to the cd-rich granulites in Appendix 6.2.6 and to the 'magnesian' metapelitic granulites in Appendix 6.2.8. Regardless of the granulite precursor used however, in general the potential immobile elements plot as a scattered array and do not define a well constrained isocon passing through the origin.

Similarly, there are no well defined isocons result from the isocon diagrams for the felsic and mafic schists from the Erontonga Shear Zone (Appendix 6.2.4 and 6.2.5) as Al, Ti, Cr, Ni and Zr again plot as a scattered array across the diagrams.

Bivariate plots of Al, Ti, Cr, Ni and Zr in the Erontonga Shear Zone mafic, felsic and metapelitic rocks also failed to distinguish any elemental immobility (see Appendix 6.3). In most cases, the available data plotted as scattered arrays across the bivariate diagrams. As noted in the Yambah Schist Zone bivariate plots however, plots of Al versus Ti in the metapelitic rocks (Appendix 6.3.6), Al versus Ti and Zr in the felsic rocks (Appendix 6.3.5), and Al versus Ti, Zr, Cr and Ni (Appendix 6.3.4) in the mafic rocks did define linear trends intersecting the Al axis rather than the origin. This is interpreted to indicate that Al concentrations in the respective granulites have been homogenized at some time, and that the other element included in the plot may have been more conserved. In the Zr versus Ti bivariate plot for the felsic rocks, a linear trend intersecting the Zr axis is also observed (Appendix 6.3.5), suggesting that Ti may be more conserved than Zr. In all cases however the shear zone rocks do not tend to lie within the linear arrays defined by the granulites, suggesting that Al and the other elements have been mobile within the shear zones. None of the bivariate plots produced straight line arrays intersecting the origin, which would indicate possible immobility of both elements. As such no immobile elements have been conclusively identified in rocks from the Erontonga Shear Zone.

7.4.4 Discussion

In order to perform mass balance calculations using the Gresens method, a known unaltered precursor to the altered rock and elemental immobility must be established. From the geochemical data available for the Yambah Schist Zone and the Erontonga Shear Zone however, isocons were not able to be clearly defined. Bivariate plots of the potential immobile elements were also constructed to determine if any pair of elements defined a straight line through the origin. Such a plot would indicate conservation of these elements. However bivariate plots of Al, Cr, Ni, Ti, Zn and Zr generally displayed scattered distributions. The only plots which suggested some degree of conservation were the Zr vs Ti plot for the Erontonga felsic rocks and some of the bivariate plots involving Al for both the Yambah and Erontonga rocks. In these cases elements such as Ti and Zr appear to be less mobilised than Al but not necessarily immobile.

Since no immobile elements can be confidently identified from the available geochemical datasets and the specific precursors to the shear zone rocks are not known, mass balance calculations using the Gresens method could not be undertaken. Without a quantitative measure of the net loss or addition of material between the precursor granulites and the resulting altered schists, calculations describing the magnitude and direction of the fluid flux also could not be undertaken for these rocks.

7.5 Assessing the Fluid Regime

Mineralogical evidence and stable isotope studies indicate that Alice Springs Orogeny-age shear zones in the Strangways Metamorphic Complex were infiltrated by fluids that influenced the stability of their mineral assemblages and fundamentally altered their stable isotope signatures. The stable isotope data allows a number of aspects of the fluid flow regime to be constrained.

7.5.1 The Fluid Source

The shear zones that cut the granulites have acted as fluid conduits subsequent to Proterozoic granulite facies metamorphism, facilitating recrystallisation of the affected rocks to amphibolite facies during prograde metamorphism assoicated with the ASO. The heterogeneity in $\delta^{18}O$ values across the Yambah Shear Zone rocks suggests incomplete isotopic equilibration of the schists with the infiltrating fluid and channelised flow within the shear zones, with variations in $\delta^{18}O$ values between micaschists and metabasites also reflecting factors such as differences in mineralogy, relative permeabilities and initial $\delta^{18}O$ values. Regardless of the heterogeneity in $\delta^{18}O$ values however, there is a consistent shift toward higher values in all the shear zone rocks, with a potential maximum shift of about +6‰.

Given that there are no known igneous bodies of Alice Springs Orogeny age in the Strangways Metamorphic Complex, there are three major potential sources for the fluid which created this isotopic shift. These are 1) dehydration fluids released from the surrounding granulite country rock 2) introduction of meteoric and/or basinal fluids directly into the pre-existing shear zones during growth faulting associated with formation of the Amadeus Basin which is inferred to have covered the SMC prior to the ASO, and 3) formation/metamorphic fluids associated with dewatering of Amadeus Basin lithologies during burial via compression during the ASO in an open system environment. In the following section the attributes of these potential sources will be discussed.

7.5.1.1 Devolatilization of the Granulites

Frost and Bucher (1994) and Newton (1989) provide excellent reviews of petrological evidence for sources of deep crustal fluids, in which they discuss the interaction, transport and maintenance of fluids in the deep crust. One possibility discussed therein is the production of fluid locally derived from further dehydration of a granulite terrain. Felsic granulites of the Strangways Metamorphic Complex and Erontonga Metamorphics are generally anhydrous, consisting primarily of pyroxene-cordierite-sillimanite-garnet assemblages with very minor amounts of biotite. Similarly, the only hydrous mineral commonly found in the mafic granulites is hornblende. Therefore, it is unlikely that significant fluid fluxes could be derived from these rocks via further dehydration, which would require an overprinting episode of granulite facies metamorphism during the ASO. There is no petrological or geochronolgical data from the Strangways Metamorphic Complex which supports the existence of Alice Springs Orogeny granulites. In addition, the isotopic signatures of felsic and mafic granulites in the SMC are generally low, with average $\delta^{18}O$ values of about 4.7‰ and 3.8‰ respectively (see Table 7.1).

With the available stable isotope data it is difficult to model the appropriate oxygen isotope signature of a fluid derived from the granulites. However, equilibrium fractionation calculations using anorthite of 4.7‰ as a proxy for the granulite whole-rock source, show that a fluid derived from this rock at 600°C would have a $\delta^{18}O$ value of about 3.8‰, using the fractionation data of Zheng (1993a) (Table 7.4). Fractionation calculations between this fluid and modelled rock compositions equivalent to those found in the Yambah and Winnecke Shear Zones (Table 7.7), indicate that at 600°C the interacting rocks would reach maximum $\delta^{18}O$ values of only about 5.9‰. General predictions on stable isotope variation from modelling of fluid-rock interaction over thermal gradients show that fluid flow in a down-temperature regime will lead to increases in rock $\delta^{18}O$ values if the fluid is in equilibrium with the rocks along the flow path (Dipple and Ferry, 1992b). However calculations performed using the above mentioned parameters indicate that while equilibrium in a lower temperature regime would generally produce higher values in the rocks, the maximum increase in $\delta^{18}O$ values is only on the order of about +0.9‰ per 100°C (Table 7.4).

Therefore, a fluid derived from the granulites would not be capable of producing the maximum shifts observed in the adjacent schists. Furthermore, any fluid trapped within these rocks at higher crustal levels and subsequently held in situ at granulite facies conditions is likely to have been consumed by reaction with the rock (Frost and Bucher, 1994) or, surviving this process, to have completely re-equilibrated with the surrounding granulites thereby attaining similarly low $\delta^{18}O$ values. Therefore, this evidence suggests that the shear zone rocks interacted with an influx of an isotopically distinct high $\delta^{18}O$ exotic fluid.

7.5.1.2 Direct introduction of a meteoric or basinal fluid to the shear zones

In the absence of any magmatic fluid sources in the SMC, the only other potential source for an externally derived fluid which might have interacted with the shear zone rocks are basinal fluids associated with the evolution of the Amadeus Basin. Formation/basin waters can be quite variable in their $\delta^{18}O$ signatures (see Sheppard, 1986 and references therein), but the majority have $\delta^{18}O$ values intermediate between seawater and the meteoric water line, with average seawater since about 2500Ma having a $\delta^{18}O$ value of 0-3‰, and meteoric waters ranging between about -10 and 0‰ (Sheppard, 1986). Most formation/basin waters have $\delta^{18}O$ values below 5‰, but maximum values up to 8-9‰ have been recorded (see Sheppard, 1986 and references therein). This movement toward heavier isotopic ratios is mainly due to increasing isotopic equilibration between the formation waters and detrital minerals comprising the host sediment during diagenesis (Sheppard, 1986).
Discriminating between formation waters and metamorphic waters can be difficult since major

Fractionation factor for anorthite-water	$\delta^{18}O$ of water in equilibrium with anorthite @ 4.7‰		
	400°C	500°C	600°C
Matsushita et al, 1979 (400-500°C)	5.19	4.39	4.70
Matsushita et al, 1979 (500-800°C)	-	5.34	4.96
Bottinga and Javoy, 1973 (500-800°C)	-	3.74	4.70
O'Neil & Taylor, 1967 (350-800°C)	6.18	5.03	4.25
Zheng, 1993	4.89	4.13	3.75

Table 7.4. Summary of water-rock fractionation calculations, indicating the variation in $\delta^{18}O$ values of pure water in equilibrium with anorthite over a range of temperatures.

fluid-rock interactions occur during diagenesis and low-grade metamorphism. During burial, initial fluids are derived from compaction of the sedimentary sequence and expulsion of pore fluids. With increasing temperature, fluids are then released via the reaction of clay minerals to micas and the subsequent crystallisation of other less hydrous phases during prograde metamorphism (Sheppard, 1986; Faure, 1986; Marquer and Burkhard, 1992). During these processes, the $\delta^{18}O$ values for formation waters tends to increase (Sheppard, 1986), but since fractionation factors are greater at lower temperatures (i.e. ln $1/T^2$ hence approaches 1 with increasing temperature, (Faure, 1986; Bottinga and Javoy, 1975), the greatest isotopic shifts tend to occur early in a cycle of prograde metamorphism. Therefore higher grade metamorphism may not significantly change isotopic signatures, and waters derived from this process may have similar $\delta^{18}O$ values as if expulsed at significantly lower temperatures.

In the case of the shear zones sampled in the SMC, an isotopically light meteoric or basinal fluid interacting directly with the shear zone rocks would have been interacting with an isotopically light host rock. This assumes that the shear zone rocks had maintained a signature similar to their granulite precursors or if the rocks had interacted with an external fluid during retrogression and/or exhumation, that such a fluid was also isotopically light. The assumption that the shear zone rocks still retained the isotopic signatures of the granulite precursors is probably valid as there only appears to be evidence for one episode of fluid-rock interaction recorded in each of the Yambah Schist Zone and the Erontonga Shear Zone (see §7.3.5). If the basinal fluid was directly introduced into the shear zones during growth faulting of the Amadeus Basin, it may have evolved toward a heavier signature during fractionation with burial, but it would not have been capable of shifting the shear zone rocks' $\delta^{18}O$ values up to the heavy values observed since it would have been equilibrating with and bufferred by isotopically light host rocks. The outcome might be different however if an open system existed, permitting continuous flow of formation/metamorphic waters from the adjacent sedimentary pile through the shear zones.

7.5.1.3 Dewatering of the Amadeus Basin sediments

In the vicinity of the Yambah and Winnecke Shear Zones, the only other rocks with high $\delta^{18}O$ values are the Heavitree Quartzite and the Bitter Springs Formation, which constitute the basal units of the Amadeus Basin sediments. Cartwright et al (1994) recorded $\delta^{18}O$ values of 13.2 - 16.9‰ in the quartzites and phyllites of the Heavitree Formation and 23.4 - 27.7‰ in dolomites of the Bitter Springs Formation (Table 7.5), and found that the pervasive syntectonic veins in these rock units had near-equivalent $\delta^{18}O$ values. From their study of the veins Cartwright et al, (1994) not only demonstrated that these syntectonic veins were produced from locally derived fluids under greenschist facies conditions, but there was no evidence of any other external fluids interacting with these rocks.

Fluid-rock $\delta^{18}O$ fractionation calculations were performed to determine the equilibrium $\delta^{18}O$ signature of a pure-water fluid produced from a quartzite with an equivalent range of $\delta^{18}O$ values as those recorded by Cartwright et al, (1994) for the Heavitree Quartzite over a temperature range of 300°C to 600°C (see Table 7.6). The Heavitree Quartzite was selected for modelling calculations as the range of $\delta^{18}O$ values for this unit is lower than the phyllites and thus provides a guide to the minimum effects that an exotic fluid with a higher $\delta^{18}O$ range might have had upon the shear zone rocks. In addition, the calculation of fluid-rock fractionation relations is greatly simplified in a monmineralic system compared to the more complex mineralogy of the phyllites, although the phllites are more likely to readily devolatilise. The resultant fluid values were then used to determine the equilibrium $\delta^{18}O$ values for various modelled rock compositions in order to assess if a fluid derived from the Heavitree Quartzite was able to produce the large positive isotopic shifts observed in the basement shear zones (see Table 7.6). Results of these calculations indicate that an equilibrium fluid derived from the Heavitree Quartzite at temperatures between 400°C and 600°C would have minimum $\delta^{18}O$ values ranging between about 9‰ and 11.9‰, and maximum values of 9.5‰ to 15.2‰ with the higher values being produced at higher temperatures (Table 7.5). As fractionation factors approach unity with increasing temperature (Faure, 1986; Bottinga

Heavitree Formation samples (Cartwright et al, 1994)		$\delta^{18}O$ values
Quartzites		
F21A	Heavitree Quartzite	14.1
F21B	Heavitree Quartzite	13.6
F21E	Heavitree Quartzite	15.4
F22A	Heavitree Quartzite	16.8
F27	Heavitree Quartzite	14.5
Phyllites		
F21F		15.6
F21H		16.9
F21L		16.2
F21N		16.4
F23		15.7
F24		16.6
Basement		
B1		7
B2		6.6

Table 7.5. Summary of $\delta^{18}O$ data for the Heavitree Quartzite and associated Amadeus Basin sediments. Data compiled from Cartwright et al (1994).

Fractionation factor for quartz-water	$\delta^{18}O$ of water in equilibrium with a pure quartzite with $\delta^{18}O$ of 13.6				$\delta^{18}O$ of water in equilibrium with a pure quartzite with $\delta^{18}O$ of 16.9			
	300°C	400°C	500°C	600°C	300°C	400°C	500°C	600°C
Clayton et al, 1972 (200-500°C)	6.6	9.5	11.3	-	9.9	12.8	14.6	-
Clayton et al, 1972 (500-750°C)	-	-	11.3	12.2	-	-	14.6	15.5
Shiro and Sakai, 1972 (195-573°C)	5.3	8.3	10.2	-	8.6	11.6	13.5	-
Matsushita et al, 1978 & 1979 (250-500°C)	6.7	9.5	11.3	-	9.9	12.8	14.6	-
Matsushita et al, 1978 & 1979 (500-800°C)	-	-	11.2	12.0	-	-	14.5	15.3
Zheng, 1993	6.5	9.0	10.5	11.5	9.8	12.3	13.8	14.7
Bottinga and Javoy, 1973 (500-800°C)	-	-	10.4	11.9	-	-	13.7	15.2
Average	6.3	9.1	11.0	11.9	9.5	12.4	14.3	15.2

Table 7.6. Summary of quartz-water fractionation calculations used to derive the $\delta^{18}O$ signature of a pure H_2O fluid in equilibrium with a pure quartzite of a given isotopic value over a range of temperatures.

and Javoy, 1975), an introduced fluid with this range of $\delta^{18}O$ values is capable of producing the maximum shifts in $\delta^{18}O$ values observed in the shear zone rocks under either isothermal or prograde conditions. For example, a fluid derived from a quartzite of 13.6‰ at 400°C would have an equilibrium ^{18}O value of about 9‰. Interaction between this fluid and the modelled metapelitic compositions under isothermal conditions would result in these rocks having equilibrium $\delta^{18}O$ values of about 11.4‰, while at 500°C and 600°C their $\delta^{18}O$ values would be about 11‰ and 10.7-10.9‰ respectively. A fluid derived from the same quartzite at 500°C would have an equilibrium $\delta^{18}O$ value of about 11‰, and modelled metapelites in equilibrium with this fluid at the same temperature would have a $\delta^{18}O$ value of about 13-13.2‰, whereas at 600°C these same rocks would have a value of 12.7-12.9‰. So fluids with this range of $\delta^{18}O$ values would be able to produced the shifts observed in the shear zone rocks under either isothermal conditions or prograde conditions if temperature increases along the fluid path were on the order of 100-200°C. Since the Heavitree Quartzite and the adjacent phyllites have very similar $\delta^{18}O$ values, the devolatilisation of the phyllites would also result in the release of fluids with appropriately high $\delta^{18}O$ values.

Although Sm-Nd dating of the Yambah Schist Zone and the Erontonga Shear Zone indicates peak metamorphism in these shear zones occurred at about 380 Ma and 320 Ma respectively, these dates do not necessarily fix the timing of the fluid-rock interaction. Since introduction of the fluid into the shear zone must have occurred either prior to or during growth of the amphibolites facies assemblages in the shear zone rocks, these Sm-Nd dates only effectively provide a minimum age for the timing of the fluid flux which need not have infiltrated the two shear zones contemporaneously.

7.5.2 The Tectono-metamorphic Environment and Mechanisms of Fluid Flow

From the evidence presented above, it appears likely that the fluids which infiltrated the ASO-age shear zones in the Strangways Metamorphic Complex have been sourced from prograde dewatering of the basal sedimentary units of the Amadeus Basin and that the fluid's passage through the basement rocks has been channelled within the shear zones. This implies that the fluids have migrated either laterally or toward deeper crustal levels through the shear zones. Generally fluids are considered to move from depth toward the surface or laterally, as movement along pressure and/or thermal gradients are obvious and easily explained mechanisms for fluid transport (e.g. Etheridge et al, 1983; Baumgartner and Ferry, 1991; Dipple and Ferry, 1992b; Walther, 1994; Ferry, 1994). However mechanisms for the infiltration of fluids to deeper crustal levels are still contraversial (e.g. Valley, 1986; Wood and Walther, 1986; Newton, 1989; Frost and Bucher, 1994; Oliver, 1996; Graham et al, 1997; Cartwright et al, 1999). The most common scenarios for this style of fluid flow are generally subduction and compressional

Shear Zone Rock	$\delta^{18}O$ of rock in equilibrium with water of 3.8‰			$\delta^{18}O$ of rock in equilibrium with water derived from: a quartzite of 13.6‰			a quartzite of 16.9‰	
mafics	400°C	500°C	600°C	400°C	500°C	600°C	500°C	600°C
YS149	-	5.67	5.33	10.07	12.89	13.44	16.19	16.75
YS148	-	5.59	5.32	9.75	12.61	13.02	15.91	16.33
YS147	-	6.09	5.91	10.53	12.75	12.88	16.05	16.18
YB9	-	5.84	5.70	9.88	12.64	12.95	15.95	16.25
YS10	-	4.54	4.85	8.05	12.98	14.25	16.29	17.55
metapelites								
WK182	-	3.15	3.78	9.10	11.59	13.16	14.89	16.47
WK71	-	3.01	3.93	9.04	11.37	13.24	14.70	16.58
YB30	4.98	4.50	4.21	11.45	13.19	14.36	16.49	16.26
YB26	5.97	5.54	5.23	11.39	13.00	14.1	16.3	16.00

Table 7.7. Summary of fractionation calculations demonstrating the variation in modelled oxygen isotope values of mafic amphibolites and metapelitic schists in equilibrium with water of differing isotopic origin.

environments where the subducted slab or underthrust sequences of a terrain are heated via burial and undergo prograde dewatering (e.g. Lobato et al, 1983; McCaig, 1984; Jamtveit et al, 1990; Selverstone et al, 1991; Crespo-Blanc et al, 1995; Marquer and Burkhard, 1992).

Superficially it seems that this is a likely explanation for the mode of fluid transport in the Strangeways Metamorphic Complex shear zones. The Alice Springs Orogeny is undeniably a compressional event and kinematic evidence clearly and consistently indicates a reverse sense of shear on these structures. Therefore it is possible that parts of the Amadeus Basin were buried under thrust sheets composed of Arunta basement, and certainly in the Winnecke area the Heavitree Quartzite structurally underlies basement rocks in the hangingwall of the Harry Creek-Two Mile Bore Shear Zone (Figures 7.9 and 7.10). However the geometry of the shear zones is not really consistent with the creation and emplacement of large nappe complexes or indicative

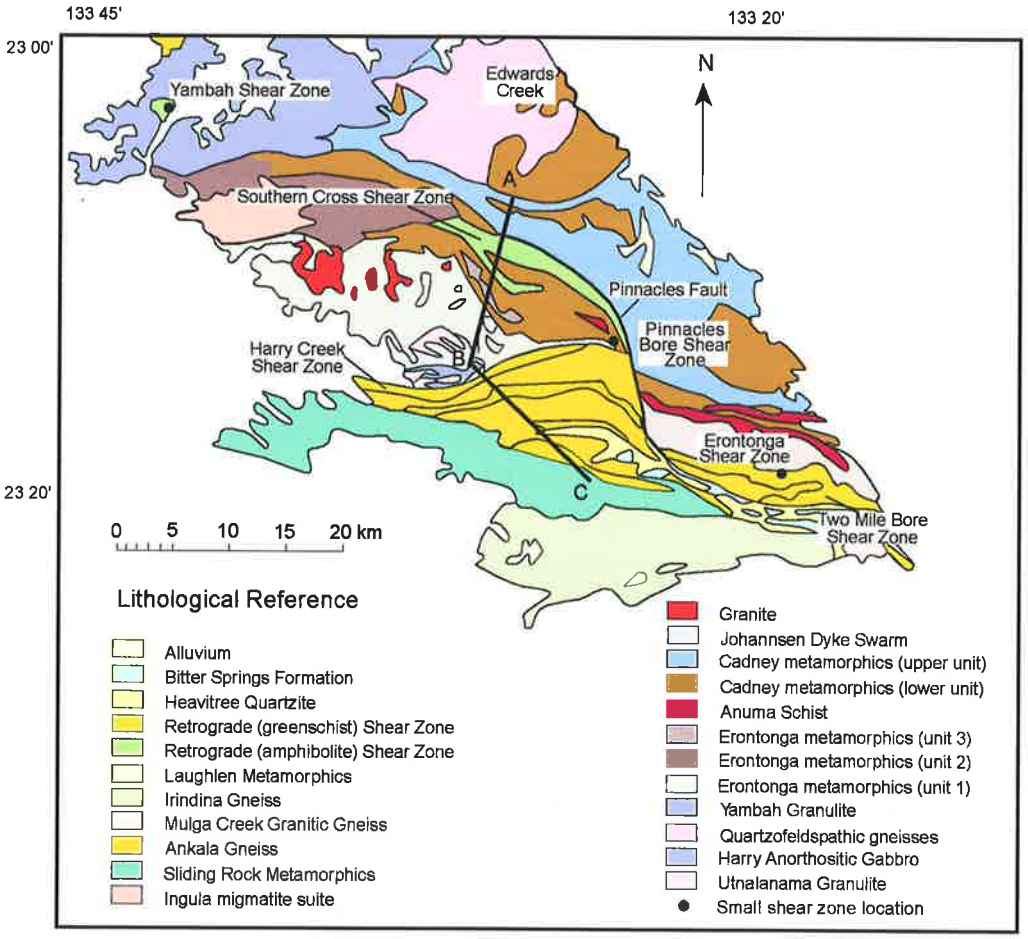

Figure 7.9. Simplified geology of the southern Strangways Metamorphic Complex. The Heavitree Quartzite structurally underlies the basementrocks which occur to the north of the Winnecke and Two Mile Bore Shear Zones.

of large-scale horizontal shortening (e.g. Flöttman and Hand, 1999), as the shear zones are relatively steeply dipping (i.e. > 35°) and tend to steepen to a near-vertical orientation in the northern part of the area (e.g. the Yambah Shear Zone) (Figure 7.9 and 7.10). This geometry would make it difficult to substantially underthrust the sediments.

The fundamental difficulty then is to discover a mechanism that transports the Amadeus Basin sediments to greater depth in the crust without invoking nappe-stacking or significant overthrusting. Another method for achieving this situation is to deposit the sediments in an extensional environment, where down-faulted regions in parts of the basin produce deeper local depo-centres, which are buried by further deposition and subsequent compression. In the Strangways Metamorphic Complex area, the Heavitree Quartzite is observed in the footwall of the Harry Creek-Two Mile Bore Shear Zone in the Winnecke area, but also occurs in the hanging wall in the vicinity of the Southern Cross Bore, further north near Edwards Creek and to the northwest near Woolanga Bore (Figure 7.9). These outcrops are separated by more than 20 kms of basement outcrop including 3-4 kms cumulative width of shear zones which show a regional variation in metamorphic grade and pressure from 2-3 kbar to about 6 kbar, yet they are currently at the same structural level. The shear zones which separate the quartzite outcrops are steep to moderately north dipping with a reverse sense of movement. Therefore it seems inescapable that prior to exhumation along these shear zones during the ASO, the quartzite units resided at different structural levels. This implies that prior to initiation of the ASO, the northern Strangways Range area was down-faulted so that the northern quartzite units resided at greater depth than the quartzite units found in the Winnecke area. Using microstructural analysis of recrystallised quartz in shear zone rocks from the Heavitree Quartzite in the Winnecke area, Emslie (1996) suggested that this unit had experienced metamorphism at temperatures of about 400°C and adjacent chlorite-biotite schists produced pressure estimates of about 3 kbar (Palamountain, 1996). Thus it is possible that parts of the Heavitree Quartzite and Bitter Springs Formation deposited over the central and northern Strangways Range were locally buried to even greater depths as a result of normal faulting during pre-ASO extensional tectonism, however exhumation and erosion during the ASO has since eradicated these rocks.

This supposition is supported by evidence from the Harts Range Metamorphic Complex located approximately 100 kms east of the Strangways Range, where geochronology on detrital zircons in granulite facies rocks shows that the precursor sediments to these granulites were deposited in the late Neoproterozoic (I. Buick et al, in press; Miller et al, 1998) and were metamorphosed to granulite facies during the Early Ordovician (Miller et al, 1997; Miller et al, 1998; Hand et al, 1999b; Mawby et al, 1999) prior to inversion of the Amadeus Basin during compressional tectonism associated with the ASO. High-grade Early Ordovician structural fabrics preserved in the Irindina Supracrustal Assemblage suggest regional extension was occurring at this time, oriented in a north-south to northeast-southwest direction (Mawby et al, 1999; Hand et al, 1999b). This is consistent with evidence from the sedimentary record of the Amadeus and Georgina Basins which were connected as part of an Early Ordovican seaway which spanned central Australia, linking oceanic masses to the east and west (Webby, 1978; Walley and Cook, 1991; Romine et al, 1994). At this time deposition of the Late Cambrian to Mid-Ordovician Larapinta Group was underway. Isopach data from the Larapinta Group indicate that these units were deposited into a narrow asymmetric intracratonic trough with its depocentre located over the current southeastern Arunta Inlier, oriented in a northwest-southeast direction and shallowing to the west (Figure 7.11) (Wells et al, 1970; Smith, 1972; Lindsay and Owen, 1993; Hand et al, 1999a & b; Mawby et al, 1999). Thus the sedimentary record provides evidence for persistent and continuing extension deepening toward the east - southeast, which is also the direction of increasing metamorphic grade. Geothermobarometry on Early Ordovician granulites in the Harts Range region indicate they experienced at least 25 km of subsidence in response to this

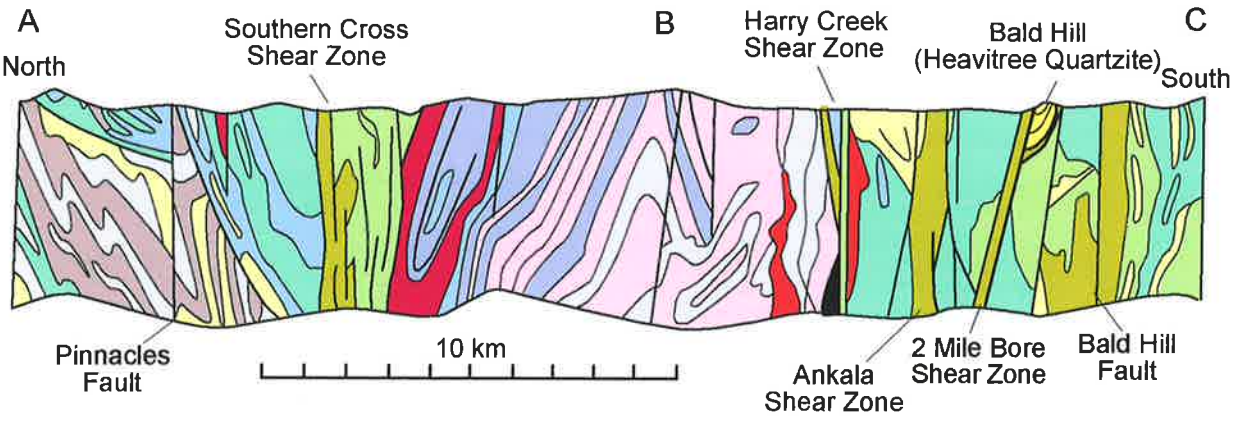

Figure 7.10. A cross section throught the southern Strangways Metamorphic Complex (see location on Figure 7.9). Note that most major faults and shear zones dip steeply northward to sub-vertical, suggesting that thrusting on these structures did not result in the creation of large basement cored nappes or large-scale horizontal shortening. (Adapted from D'Addario and Chan, 1982).

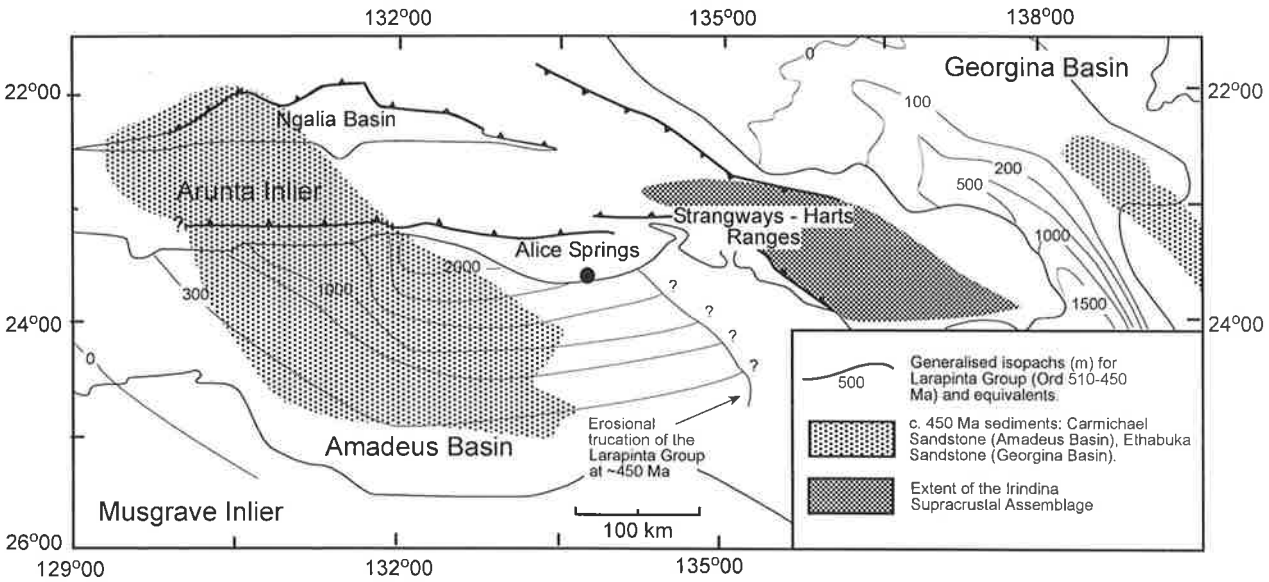

Figure 7.11. Map indicating the generaldistribution of isopacs for the mainly Ordovician Larapinta Group and equivalent sedimentary units in the Georgina Basin. The isopac data suggests sediments were deposting into a narrow NW-SE oriented trough with a depocentre located over the current SE Arunta Inlier. (after Hand et al, 1999a).

extensional event which has been termed the Larapinta Event (Hand et al, 1999a; Hand et al, 1999b; Mawby et al, 1999; Miller et al, 1999). Thus it is possible that as a result of extension during the Larapinta Event, and potential further burial during the ASO, parts of the Heavitree Quartzite and the Bitter Springs Formation were buried to the depths recorded by the ASO-aged amphibolite facies shear zones. As such fluid flow may have occurred laterally into the shear zones rather than to greater depth against a pressure gradient.

This interpretation is also consistent with fluid flow evidence from the Reynolds Range which lies about 150 kms west of the SMC (Figure 2.1). In the Reynolds Range area, shear zones of similar age and crustal level to those in the Strangways Metamorphic Complex, have interacted with meteoric/surficial fluids rather than metamorphic fluids (Cartwright and Buick, 1999; Read and Cartwright, 1999a; Read and Cartwright, 1999b). In a scenario of Neoproterozoic asymmetric rifting shallowing toward the west, it would be expected that surface-derived fluids would exert a greater influence on shallower buried basement rocks in the west, than on eastern basement rocks overlain by thicker sediments. Therefore it is more likely that evidence for meteoric fluid infiltration would be found in western shear zones than in deeper parts of the basin such as the Strangways and Harts Range Metamorphic Complexes where a metamorphic fluid influx is observed.

Sm-Nd and U-Pb dating from shear zones in the Strangways Metamorphic Complex (Chapter 3; Ballevre et al, 2000; Moller et al, 1999) indicates that some northern ASO-aged shear zones are older than southern ASO-aged shear zones by up to ca. 100 m.y. Given that the infiltrating fluid was derived from the prograde dewatering of sediments in the Amadeus Basin, then infiltration of the fluid into the shear zones must have occurred at some time during the Alice Springs Orogeny. In order to facilitate the growth of amphibolite facies assemblages in the shear zones, infiltration must have occurred during the prograde path either prior to, or coincident with, peak metamorphism in the shear zones. As such, Sm-Nd dates from the shear zones provide a minimum age on the timing of the fluid influx. If local depo-centres in the north of the SMC were deeper than in the south, and/or if northern parts of the cover sequences were more deeply buried during regional extension in the Ordovician, then the dewatering of sediments and migration of fluids into the northern shear zones may have preceeded fluid mobility and interaction in the south. Potentially then, the timing of peak metamorphism in the shear zones may have been controlled by the timing of the fluid influx, as well as the ambient PT environment.

7.6 Conclusions

In the Strangways Metamorphic Complex stable isotope studies show that Alice Springs Orogeny-aged mid-amphibolite facies shear zones hosted by granulite facies basement rocks have been hydrated through the infiltration of an externally derived, relatively isotopically heavy fluid. Fractionation calculations suggest that fluids produced from the devolatilization of pelitic units within the Heavitree Quartzite, the basal unit of the Amadeus Basin sediments, during prograde metamorphism associated with the ASO, would be capable of creating the observed shifts in the oxygen isotope signatures observed in the basement shear zone rocks. Although the Strangways Metamorphic Complex underwent convergent deformation during the ASO and the ASO-aged shear zones have a reverse sense of movement, the geometry of the shear zones is not consistent with the large-scale underthrusting of cover sequences. Thus nappe-stacking is unlikely

to have provided the mechanism for the infiltration of the basinal fluids into the shear zones at mid-crustal depths. Outcrops of the Heavitree Quartzite are found in the Winnecke area south of the Harry Creek-Two Mile Bore Shear Zone and about 20 - 30 kms to the north. These outcrops are separated by about 3 - 4 kms cumulative width of shear zones which show a progressive increase in metamorphic grade and pressure from about 2-3 kbar in the southern SMC to about 6 kbar in the north. This implies that northern outcrops of the Heavitree Quartzite resided at greater depths than southern outcrops prior to convergent deformation, and suggests that basal units of the Amadeus Basin may have been buried to, or near to, mid-crustal depths enabling lateral fluid flow rather than fluid flow against temperature and pressure gradients. The infiltration of the fluid must have occurred during the Alice Springs Orogeny prior to or coincident with peak metamorphism in the shear zones. Thus Sm-Nd dates constraining the timing of peak metamorphism of the shear zones provide a minimum age on the timing of the fluid influx. If Amadeus Basin sediments were buried to deeper crustal levels in the north of the SMC than in the south, then sediment dewatering and migration of fluids into the northern shear zones may have occurred earlier here than in the south. This provides a potential mechanism for the differences in the timing of prograde metamorphism between the northern and southern shear zones.

Chapter 8

METAMORPHIC, GEOCHRONOLOGICAL & SEDIMENTOLOGICAL EVIDENCE FOR THE ARCHITECTURE OF THE ALICE SPRINGS OROGENY

8.1 Introduction

The results of this study show that the ASO had a more complex evolution, and a wider ranging effect upon the Strangways Metamorphic Complex than previously thought. Sm-Nd geochronology shows that mid-amphibolite facies metamorphic assemblages in shear zones in the Strangways Metamorphic Complex record ASO ages and that peak metamorphism in these shear zone rocks is diachronous, with shear zones becoming younger toward the south of the area. The oldest ages from the northern-most shear zone in the SMC indicate activity from about 440-450 Ma (Ballèvre et al, 2000; Möller et al, 1999) which confirms that basement-involvement during the ASO was initiated closely on cessation of an episode of intraplate extensional tectonism associated with the recently recognised Ordovician Larapinta Event (Hand et al, 1999a; Mawby et al, 1999). Geothermobarometry and information from phase diagrams presented in Chapters 4, 5 and 6 indicate that the metamorphic evolution of the ASO generally followed clockwise paths in the Strangways Metamorphic Complex and had a pervasive effect on basement rocks, with pressure and temperature conditions increasing northward from the Amadeus Basin and reaching to at least mid-amphibolite facies in the Strangways Range. The timing, duration, conditions and extent of both the Larapinta Event and the Alice Springs Orogeny are still poorly constrained and resolution of these issues will require further work to be undertaken in the Arunta Inlier.

There are three possible sources of evidence for constraining the timing and duration of orogenesis namely; (1) mineral growth ages, (2) cooling ages and (3) the deposition of synorogenic sediments. Mineral ages may only reflect the local peak to post-peak metamorphic environment since the first expressions of deformation such as cold brittle structural features, the growth of illite and other minerals during diagenesis and very low grade metamorphism will be destroyed and/or overprinted by successive growth of higher grade minerals and ductile features on the prograde path. Cooling ages reflect the local post-peak metamorphic environment via retrograde recrystallisation and homogenisation of isotopic systems, and thus provide constraints on the decline and cessation of orogenesis. While isotopic dating of metamorphic minerals is particularly important when trying to investigate orogenesis especially in polymetamorphic terrains, potentially the most useful method for studying large-scale tectonic processes is the record of synorogenic sedimentation, as this may provide the sole constraint on the initiation of uplift as well as information on the progression of deformation throughout the duration of a tectonic episode. Thus over the timespan of an orogenic event, evidence from mineral growth ages, cooling ages and the deposition of synorogenic sediments should go through a period where they can be directly correlated.

Early in the development of an orogen, the sedimentary record is decoupled from isotopic mineral ages, since the generation of topography will relatively quickly result in an increase in the deposition of associated sediments. However any isotopic re-equilibration occurring at this time will be subsequently overprinted during progressive prograde metamorphism. During mid-orogenesis, mineral ages reflecting local peak and near-peak metamorphic conditions and the sedimentary record are coupled for a period. With the waning of orogenic processes mineral ages and the sedimentary record potetnially decouple, as the isotopic systems with higher closure temperatures cease diffusion and are effectively 'frozen-in'. Thus the individual metamorphic, structural and isotopic records of a rock will not in isolation provide many constraints on the duration of an orogenic event, since these records simply reflect the thermal and deformational conditions that the individual rock experienced during its residence in the local system. The sedimentological record however can provide a time integrated record which may potentially exceed the duration of time that a single rock resides in the system. Therefore combining evidence from the sedimentary record with data from the structural, isotopic and metamorphic records is a powerful means to investigating large scale features of an orogen, such as its timing and duration. One of the problems in investigating orogenesis in plate margin environments however, is the loss of much of the preserved sedimentological record into adjacent marine basins. However in an intraplate setting such as the Alice Springs Orogeny, this material may remain partially preserved in an intraplate basin.

A well preserved record of intraplate sedimentation and tectonics spanning much of the Neoproterozoic and Palaeozoic exists within the current sedimentary basins of central and northern Australia. (Figure 8.1) In this chapter evidence from synorogenic sediments will be presented and correlated with thermochronological evidence to further constrain the timing of tectonism associated with the ASO.

8.2 Brief Overview of the development of the Amadeus Basin

The Amadeus Basin is located in the centre of the Australian continent and separates the basement rocks of the Musgrave and Arunta Inliers. Throughout its history the basin has been located in an intracratonic environment, although for much of its development an epicontinental seaway has linked the basin to major oceanic regions in the east and west (Webby, 1978; Walley et al, 1991; Lindsay and Korsch, 1991). During the Neoproterozoic, much of central Australia, including the current Amadeus Basin area and the basement rocks of the Musgrave and Arunta Inliers, was covered by a single large depositional system referred to as the Centralian Superbasin (Webby, 1978; Walter and Gorter, 1994; Walter et al, 1995). Deposition in this system was punctuated by episodic periods of erosion and changes in sub-basin distribution, resulting in local unconformities and disconformities (Jones, 1972; Shaw, 1991; Oaks et al, 1991) but was essentially constant until the Late Devonian-Early Carboniferous (i.e. between about 900-350 Ma). The only major disruption during this time was to the southern part of the Superbasin when the late Neoproterozoic to Early Cambrian Petermann Orogeny (Forman and Shaw, 1973; Camacho et al, 1997) led to the exhumation of the Mesoproterozoic basement of the Musgrave Inlier, consequently separating the Officer Basin from the rest of the Superbasin. After this orogeny, the depositional area of the Superbasin expanded northward to include the areas which constitute the present Georgina and Wiso Basins, and south of the Musgrave Inlier deposition expanded southward in the Officer Basin (Walley et al, 1991). Sedimentation in the Superbasin continued essentially uninterrupted in a largely extensional environment with sediments accumulating in the centre of the basin which is the area now occupied by the northern Amadeus Basin and Arunta Inlier (Sandiford and Hand, 1998). This belt of sedimentation apparently extended west into the Canning Basin and east into the Georgina and Warburton Basins respectively, in a shallow marine setting which connected to oceanic regions to the west and east throughout much of the Cambrian and Ordovician (Walley et al, 1991; Walter et al, 1995). During the Early Ordovician, the pattern of marine sedimentation appears to have been controlled by rifting that was associated with intense deformation and high-grade lower- to mid-crustal metamorphism during the Larapinta Event (Mawby et al, 1999; Hand et al, 1999a). Exhumation of the Arunta Inlier during the ASO resulted in the segmentation of the remaining Centralian Superbasin into the preserved remnant Amadeus, Ngalia, Georgina and Wiso Basins which exist today (Walley et al, 1991; Jones, 1991; Walter et al, 1995). These basins continued to fill with synorogenic sediments during the Alice Springs Orogeny, providing a local record of ASO activity.

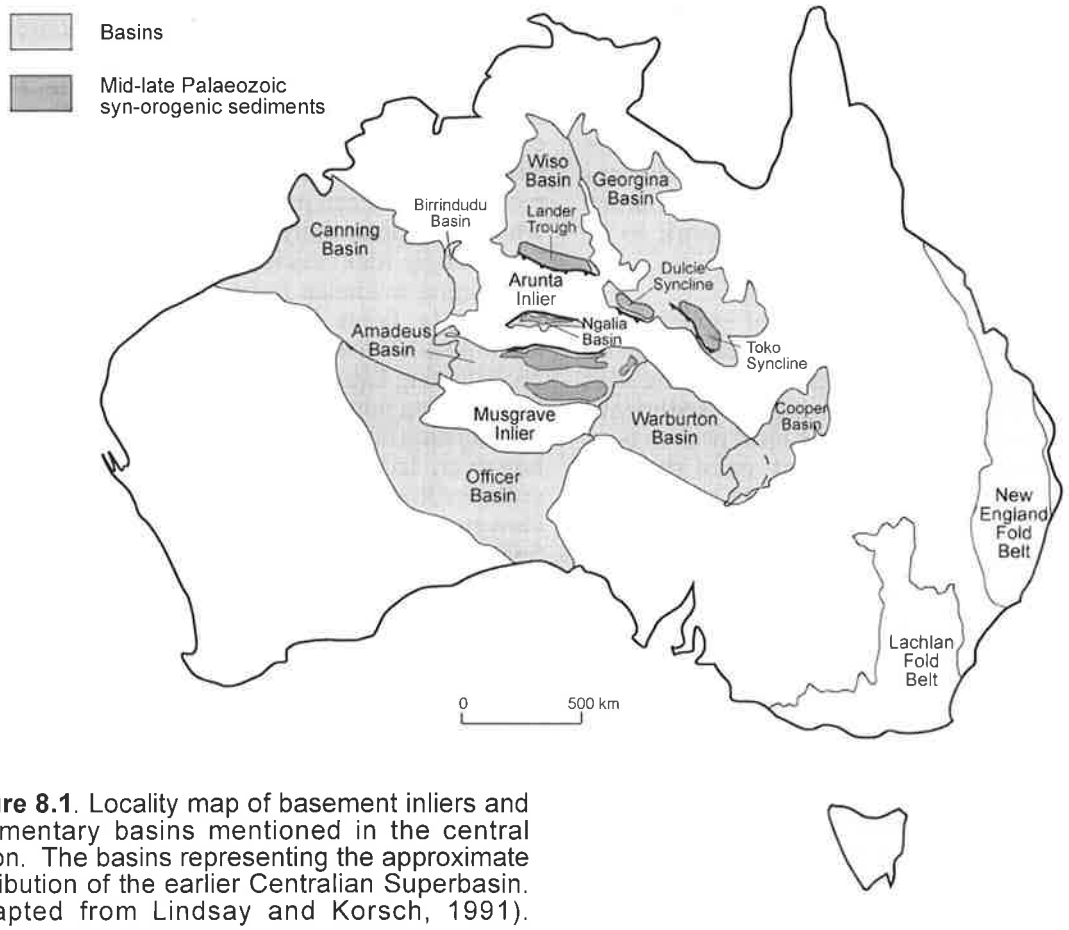

Figure 8.1. Locality map of basement inliers and sedimentary basins mentioned in the central region. The basins representing the approximate distribution of the earlier Centralian Superbasin. (Adapted from Lindsay and Korsch, 1991).

8.3 Synorogenic Sedimentological Evidence of the ASO

The Alice Springs Orogeny has primarily been identified and defined in terms of its effect upon the sediments of the Amadeus Basin and to a much lesser extent the Ngalia and Georgina Basins (e.g. Forman et al, 1967; Wells et al, 1970; Jones, 1972; Smith, 1972; Wells and Moss, 1983; Lindsay and Korsch, 1991; Shaw, 1991). In addition, radiometric dating of retrograde metamorphism in the Arunta Inlier has also aided in constraining the absolute timing of the orogeny (e.g. Black et al, 1980; Shaw et al, 1984; Stewart et al, 1984). The complex tectonic nature of the Amadeus, Georgina and Ngalia Basins has resulted in significant local variation in the distribution of sequences and their relationships to over- and underlying sedimentary units. As a result there is a degree of diversity between various definitions of what constitutes the Alice Springs Orogeny. For example, some authors confine the Alice Springs Orogeny to the event which led to deposition and deformation of the Early Devonian Pertnjara Group (e.g. Forman, 1966; Wells et al, 1970; Cook, 1971; Jones, 1972) and consider the various movements which preceded the orogeny (e.g. the Rodingan, Pertnjara and various unnamed local movements) as disconnected epeirogenic movements (Table 8.1). Other interpretations extend the term ASO to encompass all Palaeozoic convergent deformation including these earlier movements (e.g. Forman et al, 1967; Bradshaw and Evans, 1988). Many workers however define the ASO as a episode of cover and basement interaction and thus limit the ASO to a period between the onset of the Pertnjara Movement (ca. 400 Ma) and about 300 Ma on the basis of isotopic evidence (e.g. Black et al, 1980; Shaw et al, 1984; Stewart et al, 1984; Lindsay and Korsch, 1991; Shaw, 1991). Recent isotopic studies from the Arunta Inlier however, provide evidence for widespread basement-involved convergent deformation reaching as far back as ca. 450 Ma (Ballèvre et al, 2000; Möller et al, 1999; Mawby et al, 1999; Hand et al, 1999b; Scrimgeour and Raith, in press) supporting the view that convergent movement on deep seated basement structures, at least in the south-eastern Arunta Inlier, may have initiated in the mid to late Ordovician. Thus the isotopic data suggests that the ASO was a long-lived event. The sedimentary record in the adjacent Amadeus, Ngalia and Georgina Basins also has a long history, yet in the literature, local unconformities and deformation in the basins, such as the Rodingan and Pertnjara Movements, are generally referred to

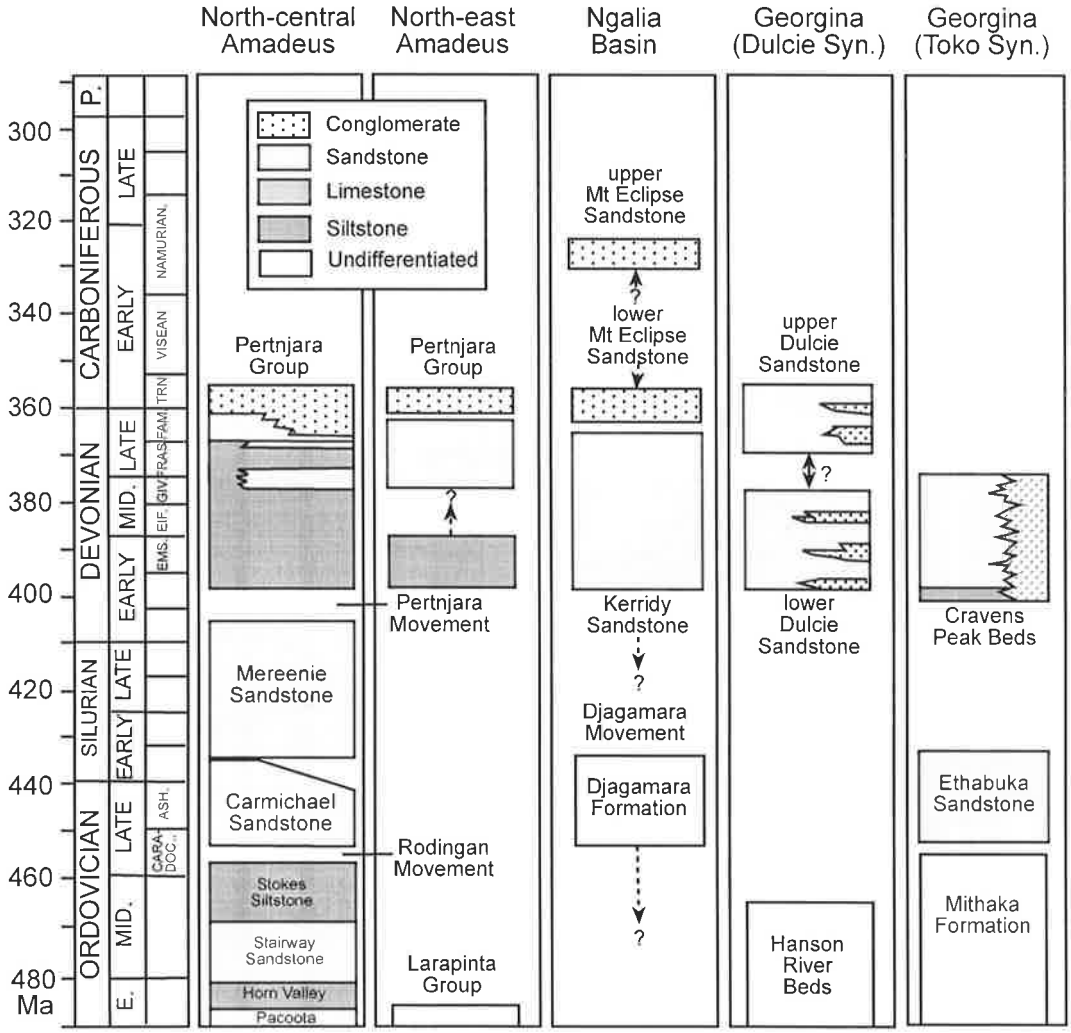

Table 8.1. Stratigraphic overview of Palaeozoic sedimentation in parts of the Amadeus, Ngalia and Georgina Basins.

only as epeirogenic movements although they probably reflect basin response to the initiation of orogenesis. In the next section a brief description of the stratigraphy and sedimentary styles of the Amadeus, Ngalia and Georgina Basins will be presented, followed by a discussion on correlations between the isotopic data and the sedimentological record.

8.3.1 The Rodingan Movement

While the Late Cambrian Pacoota Sandstone and Early Ordovician Horn Valley Siltstone of the Larapinta Group (see Table 8.1) are of marine origin, an increase in carbonate and clastic sedimentation in the upper Stairway Sandstone and Stokes Siltstone (particularly in the upper Stokes Siltstone where there is an absence of marine fossils) reflects increasingly shallow conditions and suggests the emergence of some relief adjacent to the basin (Kennard and Nicoll, 1986; Walley et al, 1991). Overlying the Stokes Siltstone is the Late Ordovician Carmichael Sandstone which shows evidence of a deltaic depositional environment representing a significant change in sedimentary style and the pattern of sedimentation. In the northern Amadeus Basin, a major unconformity exists at the base of the Carmichael Sandstone, and the unit is generally recognised as indicating a change in the tectonic regime (Wells et al, 1970; Lindsay and Korsch, 1991; Shaw, 1991; Mawby et al, 1999) although authors differ over its stratigraphic assignment. Shaw (1991) for example treat the Carmichael Sandstone as a separate individual sequence, whereas Owen (in Kennard and Nicoll, 1986), Lindsay and Korsch (1991) and Lindsay and Owen (1993) consider it a member of the predominantly Silurian Mereenie Sandstone, and Oaks et al (1991) include both the Carmichael Sandstone and the Mereenie Sandstone within the Larapinta Group. Much of this confusion appears to arise from variations in the local style of contact between the Stokes Siltstone and the Carmichael Sandstone, and between the Carmichael and Mereenie Sandstones. Contacts between these units are generally gradational and conformable toward the western and central parts of the basin but appear unconformable in the northeast (Laurie et al,1991; Nicoll et al, 1991; Oaks et al, 1991; Lindsay and Owen, 1993).

According to Wells et al (1970), the unconformity and the change in sedimentation from the Stokes Siltstone to the coarse clastics found within the Carmichael Sandstone, and a major erosional period between deposition of the Carmichael Sandstone and the overlying Mereenie Sandstone are representative of initiation and cessation of the Rodingan Movement. This movement was responsible for significant uplift and erosion of older sediments, particularly in the northeastern of the Amadeus Basin where between 1000 m and 3000 m of material including the Pacoota Sandstone was completely removed, prior to deposition of the Mereenie Sandstone. This erosion becomes less

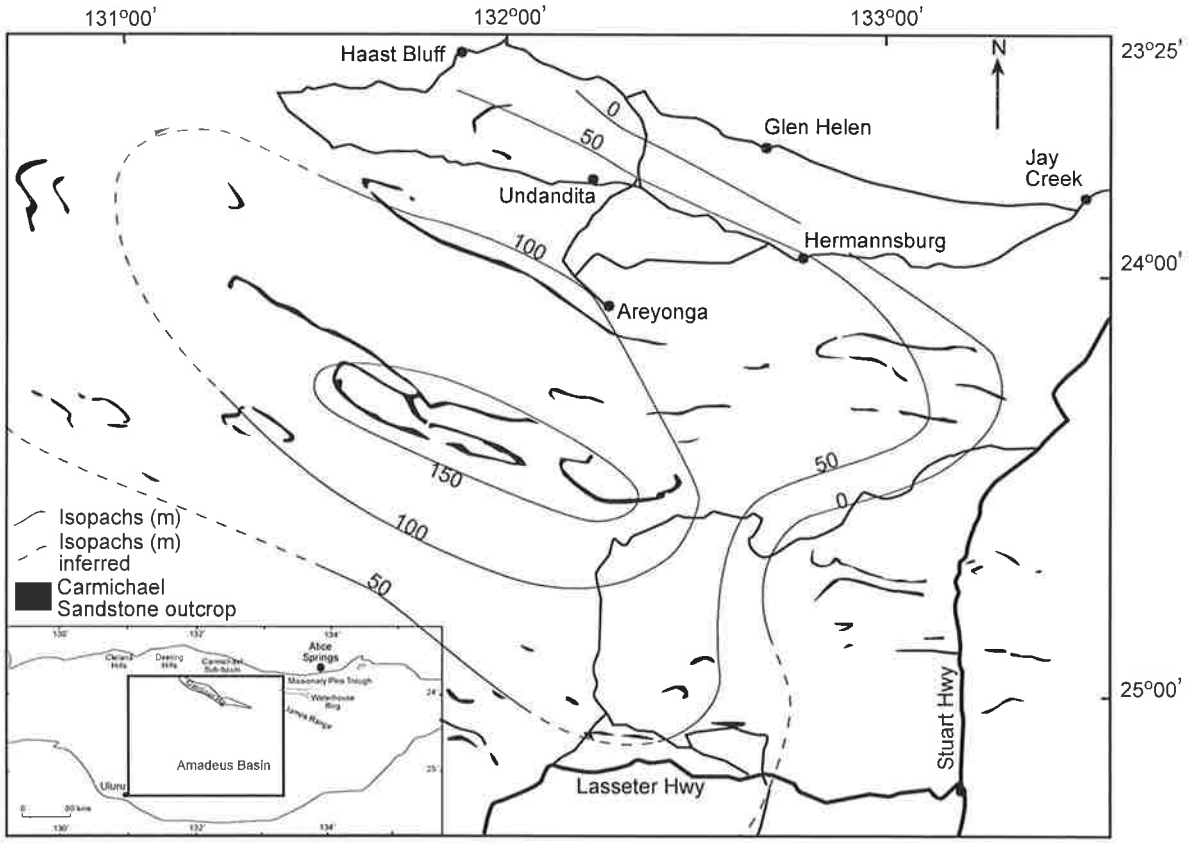

Figure 8.2. Isopach map of the Late Ordovician to Silurian Carmichael Sandstone, including location of major outcrops in the northern-central Amadeus Basin. (Adapted from Liindsay and Owen, 1993).

severe and then ultimately conformable with westward progression toward the Missionary Plain and Carmichael Sub-basin areas (Wells et al, 1970; Shaw and Wells, 1983; Oaks et al, 1991; Nicoll et al, 1991) (Figure 8.3). The age of initiation of the Rodingan Movement is not well constrained, but is believed to be Caradocian (i.e. 450-460 Ma) on the basis of fossil fish fragments found in the base of the Carmichael Sandstone (Shergold et al, 1991), and from the presence of reworked earlier Ordovician conodont fragments within the unit, which indicates the erosion of exposed older sediments (Walley et al, 1991; Nicoll et al, 1991). The distribution of the Carmichael Sandstone is not fully known and this has led to some confusion over its stratigraphic position and possible sources of the material (e.g. Owen in Kennard and Nicoll, 1986; Walley et al, 1991; Shaw, 1991; Shaw et al 1991). What is known is that the sediments were deposited in an elongate depression trending NW-SE (see Figure 8.2) and onlapped highs created by the Rodingan Movement, in the northeast and possibly southwest of the basin (Lindsay and Owen, 1993). Given that the Rodingan Movement exposed underlying Ordovician sequences in the north-eastern Amadeus Basin, it seems plausible that this may have been a source area for the conodont fragments found in the Carmichael Sandstone.

In the Ngalia Basin (see Table 8.1) the Rodingan Movement is correlated with an unconformity known as the Djagamara Movement, occurring between the Ordovician Djagamara Formation and the Ordovician or Devonian Kerridy Sandstone. Age constraints on the Djagamara Formation and the Kerridy Sandstone are poor due to a paucity of fossil evidence, however a K-Ar age of 447 Ma from glauconite in the upper parts of the Djagamara Formation (Cooper et al, 1971) provides a potential minimum age constraint for this unit, which has been correlated with the Larapinta Group sandstones (Cooper et al, 1971; Wells and Moss, 1983). The Kerridy Sandstone does not closely resemble any of the mid-Palaeozoic units from the Amadeus or surrounding basins and could be equivalent to the Carmichael Sandstone, the Mereenie Sandstone or the lower to middle parts of the Pertnjara Group, although it is probably coeval with the Carmichael and/or Mereenie Sandstones (Wells and Moss, 1983; Deckelman and Davidson, 1994; Walley et al, 1991). The full distribution of the Kerridy Sandstone is also unknown due to extensive erosion of the unit during the Kerridy Movement prior to deposition of the Late Devonian - Early Carboniferous Mt Eclipse Sandstone, however it is considered a fluvio-deltaic sequence (Wells et al, 1972: Deckelman and Davidson, 1994) which thins westward (Wells et al, 1972). The Djagamara Movement was most intense in the western part of the basin recording a period of diastrophism and folding which probably occurred during the Silurian (Wells and Moss, 1983).

In the Georgina Basin (see Table 8.1) a similar relationship exists whereby the Lower to Mid-Ordovician rocks of the Ethabuka Sandstone are unconformably overlain by the Mid-Devonian (Emsian-Eifelian) Craven Peak Beds (Jones, 1972; Draper, 1980; Shergold, 1985). Some ambiguity exists over the stratigraphic assignment of the Ethabuka Sandstone with early workers assigning it as the lowest unit of the Cravens Peak Beds (despite the significant unconformity which marks its upper contact with the Cravens Peak Beds) while later authors classified it as the youngest unit in the Toko Group, (e.g. Smith, 1972; Draper, 1980; Lodwick and Lindsay, 1990 and references therein). This uncertainty is due to the paucity of information about the Ethabuka Sandstone which is mainly collected from drillhole data (Shergold and Druce, 1980). It is generally correlated with the upper Stokes Siltstone and Carmichael Sandstone however as it contains Ordovician fossils and conformably overlays the Ordovician Mithaka Formation (Draper, 1980; Shergold and Druce, 1980; Lodwick and Lindsay, 1990; Cook and Totterdell, 1991), while the Cravens Peak Beds have been correlated with the Mereenie Sandstone and the Pertnjara Group (Gilbert-Tomlinson, 1965; Draper, 1976; Turner et al, 1981; Lodwick and Lindsay, 1990). Thus the unconformity which separates these sequences can probably be correlated with the Rodingan Movement in the Amadeus Basin.

Overlying the Carmichael Sandstone is the Mereenie

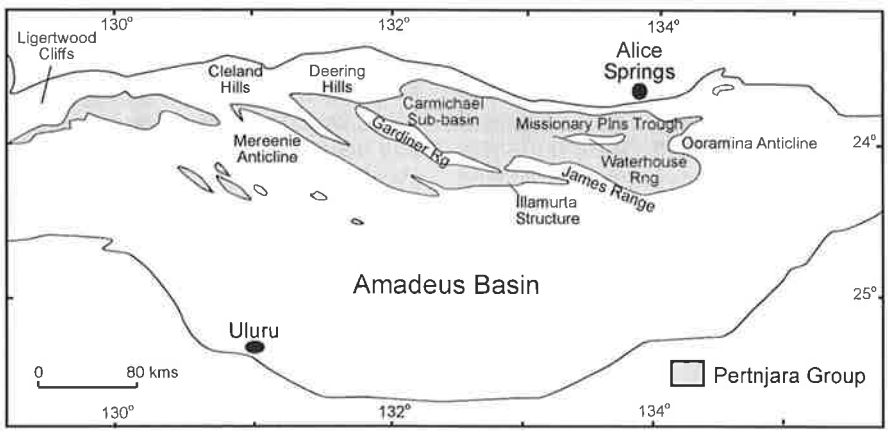

Figure 8.3. Locality map indicating the distibribution of the Pertnjara Group in the northern Amadeus Basin and salient structures mentioned in the text.

Sandstone, an areally extensive unit dominated by mature aeolian sands and minor fluvial material which suggests it was derived from low relief sedimentary units adjacent to the basin margins (Wells et al 1970; Oaks et al, 1991; Walley et al, 1991). The age of the Mereenie Sandstone is poorly constrained due to a lack of fossil remains in the unit, however it is generally believed to be Silurian to Early Devonian although it could be as old as latest Ordovician (Kennard and Nicoll, 1986; Young, 1985; Li et al, 1991; Shaw, 1991). The accumulation of this unit is interpreted as indicating a period of relative tectonic stability in the Amadeus Basin (Nicoll et al 1991; Jones, 1991; Shaw et al 1995) which may have spanned a period of up to 40 Ma. Equivalent sequences have not yet been conclusively identified in the adjacent basins although the Kerridy Sandstone in the Ngalia Basin and Cravens Peak Beds in the Georgina Basin have been variably correlated with the Mereenie Sandstone (Wells and Moss, 1983; Lodwick and Lindsay, 1990; Walley et al, 1991).

8.3.2 The Pertnjara Movement.

The aeolian sands of the Mereenie Sandstone were overtaken by playa and lacustrine sediments of the Pertnjara Group during the Emsian (397-388 Ma) (Kennard and Nicoll, 1986; Young et al, 1987; Walley et al 1991; Shergold et al, 1991) (Table 8.1). The change in depositional environment from that of the Mereenie Sandstone and the creation of the depocentre into which the Parke Siltstone was deposited is generally equated with onset of the Pertnjara Movement, the first of a number of movements observed in the sedimentological record resulting in regional and/or localised epicratonic uplift which were associated with the Alice Springs Orogeny (Kennard and Nicoll,1986; Walley et al 1991; Jones, 1991). However Jones (1991) noted that the Harajica Sandstone Member, which was deposited in response to uplift during deposition of the Parke Siltstone, overlies the Deering Siltstone and N'Dahla Members. Fossil evidence from the Harajica Sandstone indicates a Givetian to Early Frasnian age for the Pertnjara Movement (~375-385 Ma). The Henbury Movement and a number of other unnamed movements are also observed in the Amadeus Basin, generally as local unconformities within the Pertnjara Group and are often invoked to explain the lack of sedimentation over local structural features. Further studies have shown however that these local events frequently have a more regional character. The Henbury Movement for example was originally defined as an uplift event which eroded part of the Parke Siltstone off the Illamurta Structure (located in the north-central Amadeus Basin to the south of the Gardiner Range) (Figure 8.3) prior to deposition of the Hermannsburg Sandstone and appeared to be a localised phenomenon (Cook, 1971; Jones, 1972) however its definition was later extended to include uplift prior to and during deposition of the Hermannsburg Sandstone (Wells, 1976: Bradshaw and Evans, 1988) and, along with the Pertnjara Movement, was later equated with major uplift and the erosional interval which preceded deposition of the Mt Eclipse Sandstone in the Ngalia Basin (Wells and Moss, 1983; Jones, 1991).

During deposition of the Pertnjara Group, depocentres progressively shifted north in response to localised uplift and rapid erosion until the Fammenian (~ 370-360 Ma), by which time sedimentation was restricted to localised northern depocentres in the northern Amadeus Basin and extreme southern depocentres in the southern Amadeus Basin (Walley et al, 1991). Upper units in the Pertnjara Group become increasingly conglomeritic and in succeeding sedimentary units clastic material was sourced from progressively older underlying sedimentary rocks, until finally from about the 900m interval until the top of the Brewer Conglomerate, basement clasts from the Arunta Inlier appear and increase in distribution (Jones, 1972; Jones, 1991). The rapid influx of material derived from the exhuming Arunta basement and deposited as the Brewer Conglomerate was attributed to the Brewer Movement which was defined as a major regional uplift phase which also created an unconformable contact between the Hermannsburg Sandstone and the Brewer Conglomerate in the north-east of the basin (Bradshaw and Evans, 1988). Spores from the Undandita Member at the top of the Brewer Conglomerate indicate this unit is Late Devonian (Fammenian ~375-360 Ma) in age (Playford et al, 1976). Maturation studies from the same unit indicate further cover of 1-1.5 km thickness existed above the presently preserved youngest sediments (Jones, 1991), however the lack of granulite facies basement clasts within the Brewer Conglomerate (Bradshaw and Evans, 1988), suggest that a significant thickness of material was yet to have been removed from above the exhuming basement rocks of the Arunta Block. Estimates of the total volume of basement clast-bearing Brewer Conglomerate and associated sediments suggest about 5 kms of uplift of the Arunta Block (Jones, 1991). The Brewer Conglomerate is the youngest preserved sedimentary sequence in the Amadeus Basin but folding of this formation and its upper member the Undandita Member (Forman, 1966; Jones, 1991; Shaw, 1991) indicates that deformation continued into the Carboniferous, therefore information about the final stages of the ASO must come from sedimentary evidence in the adjacent Ngalia and Georgina basins.

Throughout the Ngalia Basin, an unconformity exists between the Kerridy Sandstone and the overlying Mt Eclipse Sandstone (the Kerridy Movement) which has been correlated with the Pertnjara Movement (Wells et al, 1968; Benbow et al, 1983; Wells and Moss, 1983) and the Henbury Movement (Jones, 1991) in the Amadeus Basin. In the north of the basin, significant relief may have been created during this movement as some of the underlying sediments were removed creating angular unconformities between the Latest Famennian to Late Carboniferous Mt Eclipse Sandstone and the underlying Kerridy Sandstone, Djagamara Formation and the mid-Cambrian Bloodwood Formation (Wells and Moss, 1983). The Mt Eclipse Sandstone is a thick (~2400 m) and laterally extensive arkosic sandstone unit

with interbedded pebble and boulder conglomerates which has been equated with the mid to upper Pertnjara Group. It was subsequently deformed and eroded during the Mt Eclipse Orogeny, which is ubiquitously correlated with the Alice Springs Orogeny's deformation of the Brewer Conglomerate (e.g. Wells and Moss, 1983; Lambeck, 1984; Jones, 1991). Fossils located in the upper part of the Mt Eclipse Sandstone (White, 1983) indicate that Mt Eclipse Orogeny was no older than Late Carboniferous and therefore post-dates the deposition of basement clasts in the Late Devonian Brewer Conglomerate. The Mt Eclipse Sandstone was derived from the north (Wells and Moss, 1983) however there is no record of any basement clasts within the Mt Eclipse Sandstone, thus although the topography created here during the Kerridy/Pertnjara Movement may have been significant, basement rocks of the northern Arunta Block had not yet been exposed at a time when movement in the south had exhumed parts of the basement there (Figure 2/1). Interestingly, no material was apparently shed into the Ngalia Basin from the rear of the highlands on its southern margin which provided copious basement-sourced sediments to the Amadeus Basin. Given that there are sillimanite and kyanite bearing ASO age (c. 334 Ma) shear zones in the eastern Reynolds Range (Cartwright and Buick, 1999; Read and Cartwright, 1999b), it is possible that up to 15-20 kms of sediment was still to be removed by the mid-Carboniferous.

Also coeval with the Pertnjara Group in the Amadeus Basin were the fluvial-lacustrine sediments of the Cravens Peak Beds in the Toko Syncline, and the Dulcie Sandstone in the Dulcie Syncline of the Georgina Basin (Gilbert-Tomlinson, 1965; Draper, 1976; Turner et al, 1981) (see Figure 8.1). Both the Cravens Peak Beds and Dulcie Sandstone contain pebble conglomerates (Smith, 1972) and have been correlated with the Mereenie Sandstone and Pertnjara Group of the Amadeus Basin (Young et al, 1987; Young, 1988; Shaw, 1991) although the presence of fish fossils in the Dulice Sandstone, Cravens Peak Beds (Gilbert-Tomlinson, 1965) and Pertnjara Group (Young et al, 1987; Young, 1988) suggests this correlation is more likely. Palaeocurrent data from the Dulcie Sandstone indicates that sediments in this unit were sourced from the southwest off the Arunta Inlier (P. Haines, University of Tasmania, pers comm July 2000). Both the Cravens Peak Beds and the Dulcie Sandstone have unconformable contacts with their locally underlying Ordovician sequences, and these unconformities may be correlated with the Pertnjara Movement. Gilbert-Tomlinson (1965) identified a hiatus during the deposition of both units which may be a response to gentle epeirogenic movements, possibly related to the many movements noted within the Pertnjara Group. The basal unit of the Cravens Peak Beds are marine limestones suggesting that the Georgina Basin maintained contact with a larger oceanic region to the east (Walley et al, 1991). This is supported by the distribution of palaeodrainage (Jones, 1972) and the dispersal of similar fish fossils found within units of the Amadeus and Georgina Basins and throughout eastern Australia during the mid to late Devonian (Gilbert-Tomlinson, 1965; Turner et al, 1981; Young et al, 1987; Young, 1988; Shergold et al, 1991). On the basis of the fish fossils identified by Gilbert-Tomlinson (1965), the youngest known rocks in the Georgina Basin to be affected by the Alice Springs Orogeny are Upper Devonian (Frasnian-Famennian).

Numerous correlatives of sedimentary sequences, erosional and depositional hiatus and folding events exist across the Amadeus, Georgina and Ngalia Basins, particularly of the regionally significant Rodingan, Pertnjara and Brewer Movements. Clearly then the sedimentological record indicates that fairly widespread orogenic activity occurred throughout the Centralian Basin and its derivatives, from about the Late Ordovician until at least the Late Carboniferous. However the youngest Amadeus Basin sequences are older than the youngest shear zone rocks from the Strangways Range (~ 310-320 Ma) which, at that time, were still located at about 20kms depth in the crust and were undergoing prograde mid-amphibolite facies deformation. The youngest sediments affected by the ASO in the Ngalia and Georgina Basins are only Late Carboniferous, and while they contain conglomeritic interbeds, these units do not host basement clasts. Maturation studies from the upper Brewer Conglomerate indicate only a further 1-2 kms of sediment was ever deposited over this unit, and no granulite clasts derived from the extensive granulite terrains in the Arunta Inlier, have been recorded. Therefore after about the mid to late Carboniferous, a large part of the sediment record assoicated with denudation of the Arunta Inlier, is missing from the basins adjacent to the Inlier, as there is no record of the denudation which exhumed these younger shear zones through about 20 km of overburden, arguably the most intense phase of tectonism during the ASO (Li et al, 1991). One possible explanation for the absence of sediment, as indicated by maturation studies, is that the basins adjacent to the Alice Springs Orogen filled up and sediments were transported further afield. Given that the Georgina Basin and Amadeus Basins were sporadically linked to a larger ocean mass to the east throughout the Ordovician, Devonian and Carboniferous (Gilbert-Tomlinson, 1965; Draper, 1976; Veevers, 1984; Cook and Totterdell, 1991; Walley et al, 1991), it is plausible that this sediment was carried southeastward and deposited into the Warburton-Cooper Basin area or further southeastward toward the present Tasman and Lachlan Fold Belts (Figure 8.1).

In the Amadeus Basin, sedimentary sequences deformed by the ASO are overlain by thin undeformed Permian sediments of the Crown Point Formation, Buck Formation and other unnamed rocks (Wells et al, 1970; Bradshaw and Evans, 1988). These units occur mainly at the margins of the basin and are poorly exposed generally, thus fossil evidence for their age is sparse and palynological evidence ranges between late Carboniferous (~300 Ma) to Lower Permian. The best preserved fossil evidence suggests a Sakmarian age (~270-275 Ma) (Wells et al, 1970). In the Georgina Basin rare unnamed

pebble deposits unconformably overlying the Cravens Peak Beds were thought to be Permian glacial deposits however fossil evidence indicates that these sediments are Triassic (Smith, 1972). The Mt Eclipse Sandstone in the Ngalia Basin is unconformably overlain by thin Cainozoic units of middle Eocene age (Wells and Moss, 1983). Although there is some doubt about the age of the oldest Crown Point Formation units, these undeformed younger sediments indicate that by the Sakmarian and possibly as early as the Late Carboniferous, orogenesis in central Australia had ceased according to the sedimentary record. Consequently information on the later stages of the Alice Springs Orogeny may only be available from isotopic information in the form of cooling ages from metamorphic minerals. This situation highlights the notion discussed above, that although the sedimentary record is potentially the most useful single means of investigating orogenesis, it is limited by the need for all the synorogenic sediments to remain accessible. Thus if the process of orogenesis, and the Alice Springs Orogeny specifically, is to be adequately defined and characterised, all pertinent information including isotopic, structural and metamorphic evidence from the basement as well as from the sedimentological record needs to be considered.

8.4 Correlating the sedimentary record and evidence from the Arunta basement

Although the ASO is generally considered to be an episode of north-south directed compression, the overall geometry of the mid-Palaeozoic structures indicate that it was a transpressional system, with a sinistral strike-slip component (NE-SW directed stress) to the deformation (Harrison, 1980; Bradshaw and Evans, 1988; Collins and Teyssier, 1989b; Scrimgeour and Raith, in press). The dominant ASO structural features in the Arunta basement are the extensive arrays of anastomosing shear zones which are both E-W and NW-SE trending. While many structures in the basins are E-W trending, the NW-SE trend of some basement shear zones is mimicked to an extent by the distribution of features such as the Hugh River High, the Goyder Structure and the Casey Bore uplift and local depocentres in the Amadeus Basin (Bradshaw and Evans, 1988; Nicoll et al, 1991; Lindsay and Korsch, 1991; Oaks et al, 1991) and the orientation of the Dulcie and Toko Synclines in the Georgina Basin (Lodwick and Lindsay, 1990; Harrison, 1980) (Figure 8.1). The timing of the Rodingan Movement would appear to be coeval with the oldest ASO basement ages from the Bruna Detachment Zone in the Harts Range in the eastern Arunta Inlier (Mawby et al, 1999; Hand et al, 1999b), the Entire Point Shear Zone (Scrimgeour and Raith, in press), and other shear zones from the northeastern Strangways Range (Ballèvre et al, 1998; Möller et al, 1999), suggesting that it is directly related to local basement-involved deformation. The distribution of the Carmichael Sandstone within the Amadeus Basin in this same general NW-SE orientation also suggests that early movement on these structures may be connected with the deposition of this sedimentary unit and the Rodingan Movement generally. Although the provenance of the Carmichael Sandstone is not conclusively known, significant exhumation occurred in the northeast of the Amadeus Basin in response the Rodingan Movement, exposing Ordovician sediments to erosion in a region immediately south of areas of the Arunta Inlier in which mid-Ordovician deformation ages

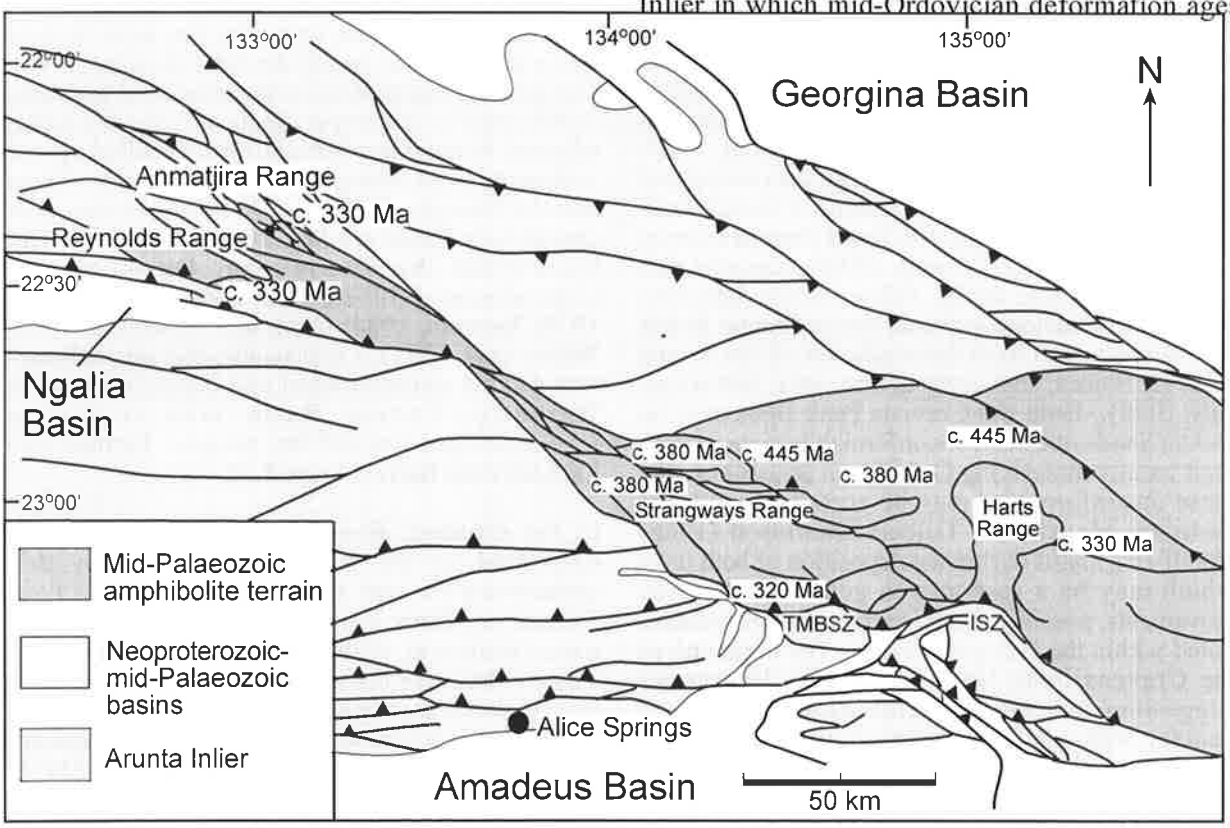

Figure 8.4. Map showing the distribution of ASO-aged amphibolite facies metamorphism, defined by the location of the Reynolds, Harts and Strangways Ranges.

have been found (eg. Hand et al, 1999b; Mawby et al, 1999; Scrimgeour and Raith, in press). These sediments may have been the source of the reworked Ordovician conodont fragments found in the Carmichael Sandstone. Thus it appears that the shallowing depositional environment noted in the Stokes Siltstone and deposition of the Carmichael Sandstone may mark the end of the extensional Early Ordovician Larapinta Event (Hand et al, 1999b; Mawby et al, 1999) and heralds the onset of transpressional tectonism associated with the ASO.

Ages constraining peak metamorphism from high grade ASO shear zones in the Arunta basement range from the Late Ordovician (ca. 450 Ma) through to the Late Carboniferous (ca. 315 Ma) (Figure 3.7) and are therefore contemporaneous with deposition of the Carmichael and Mereenie Sandstones, the Pertnjara Group and their correlatives in the Ngalia and Georgina Basins as well as the deformational and erosional events noted within them (Table 8.1). Similarly Rb-Sr, K-Ar and Ar-Ar dates from the Redbank Shear Zone, Arltunga Nappe Complex, Woolanga Bore, Yambah Schist Zone, the Harry Creek Deformed Zone and Harts Range also fall within this period (Stewart, 1970; Armstrong and Stewart, 1975; Woodford et al, 1975; Iyer et al, 1976; Allen and Stubbs, 1982; Mortimer et al, 1987; Cooper et al, 1988; Shaw and Black, 1991; Dunlap et al, 1995; Dunlap and Teyssier, 1995; Foden et al, 1995; Mawby, 2000). It appears from the Rb-Sr, K-Ar and Ar-Ar data that ASO tectonism began to wane by about 320-300 Ma (Shaw et al, 1984; Dunlap and Teyssier, 1995), however in the Strangways, Harts and Reynolds Ranges some of the high grade shear zones were still undergoing mid-amphibolite facies metamorphism at depths 20 kms at about 330-320 Ma (this study; Mawby, 2000; Cartwright and Buick, 1999), so it is likely that much of this part of the Arunta Inlier was still at considerable depth in the Late Carboniferous. This suggests the distribution of deformation and exhumation became highly focused at this time, and concentrated in a narrow NW-SE trending corridor defined by the locations of the Reynolds, Strangways and Harts Ranges (Figure 8.4). As such the large-scale form of the orogen is fan-shaped. The data also indicates that the southeastern Arunta area at least, resided at depth throughout most of the orogenic cycle, since shear zones in this region record peak metamorphic conditions throughout a period spanning about 130 m.y. (~ 450-320 Ma), an interpretation consistent with the hypothesis of Warren (1983). This suggests that the overall orogenic strain rates must have increased through the mid-Carboniferous in order to exhume the southeastern Arunta area to its current structural level.

As there is no record of the final periods of orogenesis which exhumed the SMC granulites preserved in the basins, and it is unlikely that the synorogenic sediments resulting from this period of exhumation were ever actually deposited there as maturation studies indicate there was little additional sediment (Jones, 1991), isotopic evidence from the Reynolds, Strangways and Harts Ranges is probably the only source of information on the latter stage of the ASO. Unfortunately the thermochronological data for much of the inlier is still quite scant and often difficult to interpret as it has frequently been collected from high grade polymetamorphic rocks which have had numerous episodes of isotopic resetting (e.g. Allen and Stubbs, 1982; Windrim and McCulloch, 1986). Moreover the geochronological systems used to produce the data generally have had closure temperatures lower than the peak conditions encountered by the rocks, plus the samples used have often been poorly constrained structurally and their metamorphic grade and history is also often poorly defined. Thus it often impossible to know what the thermochronological data represent as they are effectively cooling ages which are unlinked to any structural or metamorphic feature which might place them at a particular point in P-T space. As such many cooling ages cannot be correlated with any particular baric location on a exhumation path, and therefore may not actually describe the exhumation history of the rocks. This point is made quite clear in the detailed reviews and interpretation of the existing data by Dunlap and Teyssier (1995), Dunlap et al (1995) and Hand et al (1999b). Problems with the existing thermochronological data are also highlighted by the presence of Rb-Sr, K-Ar and Ar-Ar cooling ages which are older than or equivalent to the dates produced from peak ASO assemblages in the high grade shear zones (Figure 3.7).

Hand et al (1999b) and Mawby (2000) also noted that cooling ages in the northern parts of the Harts Range tended to be significantly younger that those in the southern areas, and suggested that this trend might reflect the influence of a local heat source. They suggested the large influx of pegmatites which occurred at about 340-330 Ma in the Harts Range, might be allied to the intrusion of an unidentified larger underlying magmatic body, rather than arising solely from decompression melting of the surrounding country rocks. The thermal consequences of the emplacement of such a body at about 330-340 Ma are intriguing, potentially triggering lithospheric weakening of this region, which resulted in the dramatic focusing of deformation and exhumation in the southeastern Arunta Inlier at about 320 Ma.

8.5 Conclusion

This study coupled with other recent work, has clearly shown that in the SMC the expression of the Alice Springs Orogeny was thermally complex, with basement-involved deformation occurring over a period greater than 100 m.y. from ca. 450 Ma (Ballèvre et al, 2000; Möller et al, 1998; Möller et al, 1999) until ca. 310-320 Ma. Isotopic and sedimentological evidence indicates that the first movements associated with the ASO occurred in the Late Ordovician involving both the basement and cover sequences throughout the Centralian Basin. In the southeastern Arunta Inlier the earliest movement appears to have occurred on shear zones in the central part of the inlier and then progressively shifted north and south toward the adjacent basins. It appears that intense deformation and exhumation

may have been initiated earlier in the southern part of the inlier (i.e. south of the Ngalia Basin) compared to the north. The overall distribution of the orogen is a fan-shape (Figure 8.4) with the greatest exhumation occurring along the central zone but concentrated in the southeastern portion of the Inlier north of the Arltunga Nappe Complex. This is evident from the distribution of metamorphic grade across the orogen and is consistent with the large scale structural style of the orogen. The southern parts of the orogen are dominated by south-directed thrusting on steep north dipping shear zones with lineations plunging steeply to the NE, but toward the central core of the orogen the trend of shear zones become very steep to vertical until in the northern parts of the orogen shear zones verge northward (Figures 3.6 and 7.10). Initial orogenic activity began at about 450 Ma (Ballèvre et al, 2000; Möller et al, 1998; Möller et al, 1999; Mawby et al, 1999; Scrimgeour and Raith, in press) and is expressed in the Amadeus Basin by deformation of the sediments during the Rodingan Movement. Orogenic activity began to wane throughout much of the inlier by about 320-300 Ma, however in the southeastern portion of the inlier exhumation of the basement was beginning at about this time. The cessation of the ASO is not well constrained as there is no preserved sedimentary record of this period and the existing thermochronological database is scant and imprecise aside from localised detailed studies (e.g. Dunlap et al, 1995).

An underlying theme throughout this discussion has been the need for a holistic approach to be used when unravelling the evolution of the Alice Springs Orogeny or indeed when investigating orogenesis generally. However when attempting to correlate information from different geological disciplines it has become apparent that many of the difficulties in understanding the ASO arise from the differing definitions of what constitutes the orogeny. Does the ASO constitute all the Palaeozoic compressional movements in the Amadeus Basin and is the movement valid when occurring in isolation or only when allied with basement involvement? If so then the ASO appears to span a total period of about 150-170 Ma. Should it refer strictly to the prograde metamorphism and deformation of the Amadeus Basin sediments? Or should the ASO be restricted to the phase of deformation which resulted in the exhumation of the high grade basement areas of the Reynolds Range, Strangways and Harts Ranges which so fundamentally define the character of this episode of orogenesis in the Arunta Inlier?

8.6 Future Work

To date most of the studies instigated in the Arunta Inlier have concentrated on elucidating the Proterozoic evolution of the inlier, and only recently has attention turned toward its Palaeozoic development. This is particularly evident when one considers that until recently the extent of basement-involved deformation during the Palaeozoic tectonism was effectively unconstrained by high temperature thermochronology, and the Larapinta Event, a major Palaeozoic extensional event associated with regional granulite facies metamorphism, has just been identified (Mawby et al, 1999; Mawby, 2000). Although a significant start has now been made toward unravelling the history of the Alice Springs Orogeny in areas such as the SMC, further multidisciplinary research would enhance the current understanding of this event and that of the Palaeozoic history of the Arunta Inlier generally. Some aspects which require attention include:

1) The paucity of baseline geochronological and metamorphic data. At present there is a sparse database of accurate thermochronology performed on the high grade shear zones which record Palaeozoic influences. As such the extent and duration of the Early Ordovician extensional Larapinta Event (Hand et al, 1999a; Mawby et al, 1999) has not been constrained and the extent of the ASO is still poorly defined in different parts of the Arunta Inlier. High precision thermochronology of metamorphic minerals in the shear zones in conjunction with detailed structural analysis and metamorphic petrology is required in order to; characterise, define and distinguish the temporal and spatial extent of the Larapinta Event and Alice Springs Orogeny; to establish whether there is a discernible periodicity to ASO movement on the shear zones particularly in the central SMC and; to link them with observed sedimentological features in the adjacent basins.

2) Modelling of the amount and distribution of the overburden removed from above the inlier and a comparison with the distribution and thickness of sediments in the basins. A better understanding of the size and distribution of material removed from above the basement and how it was deposited in the basins would provide first order information on the overall architecture of the orogen. This would provide an appreciation of where the most exhumation occurred and how exhumation and deformation were linked, as well as an insight into where the creation of topography was occurring and hence where lithospheric loading was concentrated. Correlation between how much material was removed and deposited throughout the ASO would also give some independent assessment of the exhumation/cooling rates across the orogen.

3) The loss of the Late to post-Carboniferous synorogenic sediments from the adjacent basins restricts the investigation of the latter stages of the ASO and hence our knowledge of the lithosphere's response to loading at a point when exhumation became most pronounced and focused into a NW-SE trending corridor. This in turn affects our ability to accurately model the tectonic regime which created the orogen. It also poses the question of where the sediments went, which may have interesting consequences for provenance studies in eastern Australia.

4) A unifying model which not only describes

the lengthy evolution of the thick-skinned ASO and the adjacent basins in an intracratonic setting, but also provides a mechanism for change to a more intense and localised expression of tectonism in the southeastern Arunta Inlier, as well as the inversion from an extensional environment to a compressional environment.

REFERENCES

Abbott Jr, R.N. (1982). A petrogenetic grid for medium and high grade metabasites. *American Mineralogist*, 67: 865-876.

Allen, A.R. (1979). The Metamorphic Evolution of the Arunta Block in the Harry Creek area, southeastern Strangways Range, Northern Territory. Unpublished PhD Thesis, University of Queensland.

Allen, A.R. and Black, L.P. (1979). The Harry Creek Deformed Zone, a retrograde schist zone of the Arunta Block, central Australia. *Journal of the Geological Society of Australia*, 26: 17-28.

Allen, A.R. and Stubbs, D. (1982). An $^{40}Ar/^{39}Ar$ study of a polymetamorphic complex in the Arunta Block, central Australia. *Contributions to Mineralogy and Petrology*, 79: 319-332.

Armstrong, R.L. and Stewart, A.J. (1975). Rubidium-Strontium dates and erroneous Argon in the Arltunga Nappe Complex, Northern Territory. *Journal of the Geological Society of Australia*, 22 (1): 103-115.

Arnold, J., Sandiford, M. and Wetherley, S. (1995). Metamorphic events in the eastern Arunta Inlier, Part 1. Metamorphic petrology. *Precambrian Research*, 71: 183-205.

Arnold, J., Powell, R. and Sandiford, M. (2000). Amphibolites with staurolite and other aluminous minerals: calculated mineral equilibria in NCFMASH. *Journal of Metamorphic Geology*, 18 (1): 23-40.

Ballèvre, M., Möller, A. and Hensen, B. (2000). Exhumation of the lower crust during crustal shortening: an Alice Springs (380 Ma) age for a prograde amphibolite-facies shear zone in the Strangways Metamorphic Complex, (central Australia). *Journal of Metamorphic Geology*, 18: 737-747.

Ballèvre, M., Hensen, B.J. and Möller, A. (1999). Part 2. Granulite-facies rocks from the Strangways Metamorphic Complex and crosscutting amphibolite-facies shear zones. In: Hand, M., Mawby, J., Miller, J., Ballevre, M., Hensen, B., Moller, A., and Buick, I. Tectonothermal evolution of the Harts and Strangways Range Region, eastern Arunta Inlier, central Australia. Specialist Group in Geochemistry, Mineralogy and Petrology Field Guide No. 4., Geological Society of Australia.

Banno, S., Sakai, C. and Higashino, T. (1986). Pressure-temperature trajectory of the Sanbagawa metamorphism deduced from garnet zoning. *Lithos*, 19: 51-63.

Barrett, T.J. and MacLean, W.H. (1994). Mass changes in hydrothermal alteration zones associated with VMS deposits of the Noranda area. *Exploration and Mining Geology*, 3(2); 131-160.

Baumgartner, L.P. and Ferry, J.M. (1991). A model for coupled fluid-flow and mixed-volatile mineral reactions with applications to regional metamorphism. *Contributions to Mineralogy and Petrology*, 106: 273-285.

Baumgartner, L.P. and Olsen, S.N. (1995). A least-squares approach to mass transport calculations using the isocon method. *Economic Geology*, 90: 1261-1270.

Beach, A. (1980). Retrogressive metamorphic processes in shear zones with special reference to the Lewisian complex. *Journal of Structural Geology*, 2: 257-263.

Becker, H. (1997). Sm-Nd ages and cooling history of high-temperature garnet peridotite massifs and high-pressure granulites from lower Austria. *Contributions to Mineralogy and Petrology*, 127: 224-236.

Benbow, D.D., Davidson, J. and Mulready, J. (1983). Recent exploration developments in the Ngalia Basin, Northern Territory. *APEA Journal*, 23 (1): 182-191.

Berger, G.W. (1975). Ar/Ar step heating of thermally overprinted biotite, hornblende and potassium feldspar from Eldorado, Colorado. *Earth and Planetary Science Letters*, 26: 387-408.

Berman, R.G. (1990). Mixing properties of Ca-Mg-Fe-Mn garnets. *American Mineralogist*, 75: 328-344.

Bickle, M.J. and McKenzie, D. (1987). The transport of heat and matter by fluids during metamorphism. *Contributions to Mineralogy and Petrology*, 95: 384-392.

Black, L.P and McCulloch, M.T. (1987). The Rayner Complex of East Antarctica: complex isotopic systematics within a Proterozoic mobile belt. *Journal of Metamorphic Petrology*, 5: 1-26.

Black, L.P. and Shaw, R.D. (1992). U-Pb zircon chronology of prograde Proterozoic events in the Central and Southern Provinces of the Arunta Block, central Australia. *Australian Journal of Earth Science*, 39: 153-171.

Black, L.P., and Shaw, R.D. (1995). An assessment based on U-Pb zircon data, of Rb-Sr dating in the Arunta Inlier. *Precambrian Research*, 71: 3-15.

Black, L.P., Shaw, R.D. and Offe, L.A. (1980). The age of the Stuart dyke swarm and its bearing on the onset of late Precambrian sedimentation in central Australia. *Journal of the Geological Society of Australia*, 27: 151-155.

Black, L.P., Shaw, R.D. and Stewart, A.J. (1983). Rb-Sr geochronology of Proterozoic events in the Arunta Inlier, central Australia. *BMR Journal of Australian Geology & Geophysics*, 8: 129-137.

Bohlen, S.R. and Liotta, J.J. (1986). A barometer for garnet amphibolites and garnet granulites. *Journal of Petrology*, 27 (5): 1025-1034.

Bottinga, Y. and Javoy, M. (1973). Comments on oxygen isotope geothermometry. *Earth and Planetary Science Letters*, 20: 250-265.

Bottinga, Y. and Javoy, M. (1975). Oxygen isotope partitioning among the minerals in igneous and metamorphic rocks. *Reviews in Geophysics and Space Physics*, 13 (2): 401-418.

Bradshaw, J.Y. (1991). Zoned garnets in metapelites in western Fiordland, southwest New Zealand: polychronic crystallisation and insight into the nature and extent of Early Cretaceous regional metamorphism. *New Zealand Journal of Geology and Geophysics*, 34: 261-270.

Bradshaw, J.D. and Evans, P.R. (1988). Palaeozoic tectonics, Amadeus Basin, central Australia. *APEA Journal*, 28: 267-282.

Brueckner, H.K., Blusztajn, J. and Bakun-Czubarow, N. (1996). Trace element and Sm-Nd 'age' zoning in garnets from peridotites of the Caledonian and Variscan Mountains and tectonic implications. *Journal of Metamorphic Geology*, 14; 61-73.

Buick, I.S., Miller, J.A., Williams, I.S. and Cartwright, I. (in press). Ordovician high grade metamorphism of a newly recognised Late Neoproterozoic terrane in the northern Harts Range, central Australia. *Journal of Metamorphic Geology.*

Burnham, C.W. (1979). Magmas and hydrothermal fluids. In: 'Geochemistry of Hydrothermal Ore Deposits.' (Ed. H.L. Barnes) pp71-136. (Wiley: New York).

Burton, K.W. and O'Nions, R.K. (1991). High-resolution garnet chronometry and the rates of metamorphic processes. *Earth and Planetary Science Letters*, 107: 649-671.

Burton, K.W., Kohn, M.J., Cohen, A.S. and O'Nions, R.K. (1995). The relative diffusivities of Pb, Nd, Sr and O in garnet. *Earth and Planetary Science Letters*, 133: 199-211.

Camacho, A., Compston, W., McCulloch, M. and McDougall, I. (1997) Timing and exhumation of eclogite facies shear zones, Musgrave Block, central Australia. *Journal of Metamorphic Geology*, 15: 735-751.

Carrington, D.P. and Harley, S.L. (1995). Partial melting and phase relations in high-grade metapelites: an experimental petrogenetic grid in the KFMASH system. *Contributions to Mineralogy and Petrology*, 120: 270-291.

Cartwright, I. and Buick, I.S. (1995). Formation of wollastonite-bearing marbles during late regional metamorphic channelled fluid flow in the Upper Calcsilicate Unit of the Reynolds Range Group, central Australia. *Journal of Metamorphic Geology*, 13: 397-417.

Cartwright, I. and Buick, I.S. (1999). The flow of surface-derived fluids through Alice Springs age middle-crust ductile shear zones, Reynolds Range, central Australia. *Journal of Metamorphic Geology*, 17: 397-414.

Cartwright, I. and Oliver, N.H.S. (1994). Fluid flow during contact metamorphism: Mary Kathleen, Queensland, Australia. *Journal of Petrology*, 35: 1493-1519.

Cartwright, I., Valley, J.W. and Hazelwood, A-M. (1993). Resetting of oxybarometers and oxygen isotope ratios in granulite facies orthogneisses during cooling and shearing, Adirondack Mountains, New York. *Contributions to Mineralogy and Petrology*, 113: 208-225.

Cartwright, I., Power, W.L., Oliver, N.H.S., Valenta, R.K. and McLatchie, G.S. (1994). Fluid migration and vein formation during deformation and greenschist facies metamorphism at Ormiston Gorge, central Australia. *Journal Metamorphic Geology*, 12: 373-386.

Cartwright, I., Buick, I.S., and Vry, J.K. (1996). Polyphase metamorphic fluid flow in the Lower Calcsilicate Unit, Reynolds Range, central Australia. *Precambrian Research*, 77: 211-229.

Cartwright, I. , Buick, I.S., Foster, D.A. and Lambert, D.D. (1999). Alice Springs age shear zones from

the southeastern Reynolds Range, central Australia. *Australian Journal of Earth Science*, 46: 355-363.

Chakraborty, S. and Ganguly, J. (1991). Compositional zoning and cation diffusion in garnets. In : 'Diffusion, Atomic ordering and Mass Transport.' (Ed. J. Ganguly) *Advances in Physical Geochemistry*, 8: 120-175.

Chernoff, C.B. and Carlson, W.D. (1997). Disequilibrium for Ca during growth of pelitic garnet. *Journal of Metamorphic Geology*, 15: 421-438.

Clarke, G.L., Powell. R. and Guiraud, M. (1989). Low pressure facies metapelitic assemblages and corona textures from MacRobertson Land, east Antarctica: The importance of Fe_2O_3 and TiO_2 in accounting for spinel-bearing assemblages. *Journal of Metamorphic Geology*, 7, (3): 323-335.

Clayton, R.N. and Mayeda, T.K. (1963). The use of bromine pentafluoride in the extraction of oxygen from oxides and silicates for isotopic analysis. *Geochimica et Cosmochimica Acta*, 27: 43-52.

Clayton, R.N., O'Neil, J.R. and Mayeda, T.K. (1972). Oxygen isotope exchange between quartz and water. *Journal of Geophysical Research*, 77: 3057-3067.

Cliff R.A. (1985). Isotopic dating in metamorphic belts. *Journal of the Geological Society of London*, 142: 97-110.

Cohen, A.S., O'Nions, R.K., Siegenthaler, R. and Griffin, W.L. (1988). Chronology of the pressure temperature history recorded by a granulite terrain. *Contributions to Mineralogy and Petrology*, 98: 303-311.

Collins, W.J. and Teyssier, C. (1989a). Crustal scale ductile fault systems in the Arunta Inlier, central Australia, discussion. *Tectonophysics*, 158: 67-70.

Collins, W.J. and Teyssier, C. (1989b). Crustal scale ductile fault systems in the Arunta Inlier, central Australia. *Tectonophysics*, 158: 49-66.

Collins, W.J. and Vernon, R.H. (1991). Orogeny associated with anticlockwise P-T-t paths: Evidence from low-P, high-T metamorphic terrains in the Arunta Inlier, central Australia. *Geology*, 19: 835-838.

Collins, W.J. and Vernon, R.H. (1993). How well established is isobaric cooling in Proterozoic orogenic belts? An example from the Arunta Inlier, central Australia - Comment. *Geology*, 21: 953-954.

Collins, W.J. and Shaw, R.D. (1995).Geochronological constraints on orogenic events in the Arunta Inlier, a review. *Precambrian Research*, 71: 315-346.

Connelly, J.A. and Thompson, A.B. (1989). Fluid and enthalpy production during regional metamorphism. *Contribution to Mineralogy and Petrology*, 102: 347-366.

Cook, P.J. (1971). Illamurta Diapiric Complex. *American Association of Petroleum Geologists Bulletin*, 55 (1): 64-79.

Cook, P.J. and Totterdell, J.M. (1991). 'Palaeogeographic Atlas of Australia Volume 2: Ordovician.' Bureau Mineral Resouces: Canberra.

Cooper, A.F. (1980). Retrograde alteration of chromian kyanite in metachert and amphibolite whiteschist from the Southern Alps, New Zealand, with implications for uplift on the Alpine Fault. *Contributions to Mineralogy and Petrology*, 75: 153-164.

Cooper, J.A, Wells, A.T. and Nicholas, T. (1971). Dating of glauconite from the Ngalia Basin, Northern Territory, Australia. *Journal of the Geology Society of Australia*, 18 (2): 97-106.

Cooper, J.A., Mortimer, G.E. and James, P.R. (1988). Rate of Arunta Inlier evolution at the eastern margin of the Entia Dome, central Australia. *Precambrian Research*, 40/41: 217-231.

Crawford, M.L. (1977). Calcium zoning in almandine garnet, Wissahickon Formation, Philadelphia, Pennsylvania. *Canadian Mineralogist*, 15: 243-249.

Crespo-Blanc, A., Masson, H., Sharp, Z., Cosca, M. and Hunziker, J. (1995). A stable and $^{40}Ar/^{39}Ar$ isotope study of a major thrust in the Helvetic nappes (Swiss Alps): Evidence for fluid flow and constraints on nappe kinematics. *Geological Society of America Bulletin*, 107 (10): 1129-1144.

Criss, R.E., Gregory, R.T. and Taylor, H.P. (1987). Kinetic theory of oxygen isotope exchange between minerals and water. *Geochimica et Cosmochimica Acta*, 51: 1099-1108.

Crowley, P.D. (1990). Metamorphism within the Çokkul synform: evidence for detachment faulting within the metamorphic infrastructure of the Norwegian Caledonides (6730N). *Journal of Metamorphic Geology*, 8: 615-628.

Cygan, R.T. and Lasaga, A.C. (1982). Crystal growth and the formation of chemical zoning in garnets. *Contributions to Mineralogy and Petrology*, 79: 187-200.

D'Addario, G.W. and Chan, R.A. (Eds.), (1982).

Geology of the Strangways Range Region Northern Territory. Australian Bureau of Mineral Resources: Australia 1:100 000 Geological Map Series: Canberra.

Daniel, C.G. and Spear, F.S. (1998). Three dimensional patterns of garnet nucleation and growth. *Geology*, 26 (6): 503-506.

De Bethune, P., Laduron, D. and Bocquet, J. (1975). Diffusion processes in resorbed garnets. *Contributions to Mineralogy and Petrology*, 50: 197-204.

Deckelman, J.A. and Davidson, J.K. (1994). A closer look at the petroleum potential of the Ngalia Basin, Northern Territory. *PESA Journal*, 22: 92-100.

Delor, C.P., Burg, J.P. and Leyreloup, A.F. (1984). Staurolite producing reactions and geothermo-barometry of a high pressure thermal aureole in the French Massif Central. *Journal of Metamorphic Geology*, 2 (1): 55-72.

Dempster, T.J. (1985). Garnet zoning and metamorphism of the Barrovian type area, Scotland. *Contributions to Mineralogy and Petrology*, 89: 30-38.

Ding, P. and James, P.R. (1985). Structural evolution of the Harts Range area and its implication for the development of the Arunta Block, central Australia. *Precambrian Research*, 27: 251-276.

Ding, P. and James, P.R. (1989). Crustal scale ductile fault systems in the Arunta Inlier, central Australia. Reply. *Tectonophysics*, 158: 71-73.

Dipple, G.M. and Ferry, J.M. (1992a). Metasomatism and fluid flow in ductile fault zones. *Contributions to Mineralogy and Petrology*, 112: 149-164.

Dipple, G.M. and Ferry, J.M. (1992b). Fluid flow and stable isotopic alteration in rocks at elevated temperatures with applications to metamorphism. *Geochimica et Cosmochimica Acta*, 56: 3539-3550.

Dirks, P.H.G.M., Hand, M. and Powell, R. (1991). The P-T-deformation path for a mid-Proterozoic, low pressure terrane; the Reynolds Range, central Australia. *Journal of Metamorphic Geology*, 9 (5): 641-661.

Dodson, M.H. (1973). Closure temperature in cooling geochronological and petrological systems. *Contributions to Mineralogy and Petrology*, 40: 259-274.

Dodson, M.H. and McLelland-Brown, E. (1985). Isotope and palaeomagnetic evidence for cooling, uplift and erosion. *Geological Society of London Memoirs*, 10: 315-325.

Draper, J.J. (1976). The Devonian rocks of the Toko Syncline, western Queensland. *Bureau of Mineral Resources, Geology and Geophysics Record*, 1976/29.

Draper, J.J. (1980). Ethabuka Sandstone, a new Ordovician unit in the Georgina Basin, and a redefinition of the Toko Group. *Queensland Government Mining Journal*, 81 (947): 469-475.

Droop, G.T.R. and Harte, B. (1995). The effect of Mn on the phase relations of medium-grade pelites: Constraints from natural assemblages on petrogenetic grid topology. *Journal of Petrology*, 36 (6): 1549-1578.

Dunlap, J.W. and Teyssier, C. (1995). Palaeozoic deformation and isotopic disturbance in the southeastern Arunta Block, central Australia. *Precambrian Research*, 71: 229-250.

Dunlap, W.J., Teyssier, C., McDougall, I. and Baldwin, S. (1995). Thermal and structural evolution of the intracratonic Arltunga Nappe Complex, central Australia. *Tectonics*, 14 (5): 1182-1204.

Eckert, J. Jnr. and Newton, R.C. (1993). Palaeopressures of south Indian two-pyroxene garnet granulites from thermochemically calibrated CMAS barometers. *Journal of Metamorphic Geology*, 11: 845-854.

Emslie, J. (1996). The structural evolution of the Winnecke Domain, Northern Territory, with a focus on the kinematic evolution of 'retrograde' shear zones involving Amadeus Basin sediments and areas north. Unpublished Honours Thesis, University of Adelaide.

Erambert, M. and Austrheim, H. (1993). The effect of fluid and deformation on zoning and inclusion patterns in poly-metamorphic garnets. *Contributions to Mineralogy and Petrology*, 115: 204-214.

Etheridge, M.A., Wall, V.J. and Vernon, R.H. (1983). The role of the fluid phase during regional metamorphism and deformation. *Journal of Metamorphic Geology*, 1: 205-226.

Etheridge, M.A., Wall, V.J., Cox, S.F. and Vernon, R.H. (1984). High fluid pressures during regional metamorphism and deformation: Implications for mass transfer and deformation mechanisms. *Journal of Geophysical Research*, 89B (6): 4344-4358.

Eugster, H.P., Albee, A.L., Bence, A.E., Thompson, J.B., Jr and Waldbaum, D.R. (1972). The two phase region and excess mixing properties of paragonite-muscovite crystalline solutions. *Journal of Petrology*, 13: 147 - 179.

Evans, J.A., Millar, I.L. and Noble, S.R. (1995).

Hydration during uplift is reecorded by reset Rb Sr whole-rock ages. *Journal of the Geological Society of London*, 152: 209-212.

Farquhar, J., Chacko, T. and Ellis, D.J. (1996). Preservation of oxygen isotope compositions in granulites from Northwestern Canada and Enderby Land, Antarctica: implications for high temperature isotopic thermometry. *Contributions to Mineralogy and Petrology*, 125: 213-224.

Faure, G. (1986). 'Principles of Isotope Geology.' 2nd Ed. (John Wiley and Sons: New York).

Ferry, J.M. (1994). Overview of the petrological record of fluid flow during regional metamorphism in northern New England. *American Journal of Science*, 294: 905-88.

Ferry, J.M. and Dipple, G.M. (1991). Fluid flow, mineral reactions and metasomatism. *Geology*, 19: 211-214.

Ferry, J.M. and Spear, F.S. (1978). Experimental calibration of the partitioning of Fe and Mg between biotite and garnet. *Contributions to Mineralogy and Petrology*, 66: 113-117.

Fleck, R.J. and Criss, R.E. (1985). Strontium and oxygen isotopic variations in Mesozoic and Tertiary plutons of central Idaho. *Contributions to Mineralogy and Petrology*, 90: 291-308.

Fletcher, R.C. and Hofmann, A.W. (1974). Simple models of diffusion and combined diffusion infiltration metasomatism. In: 'Geochemical transport and kinetics' (Carnegie Institute Wash Pub 634) (Eds. A.W. Hofmann, B.J. Giletti, H.S. Yoder and R.A. Yund Jr) pp 243-259. Carnegie Institute: Washington.

Florence, F.P. and Spear, F.S. (1991). Effects of diffusional modification of garnet growth zoning on P-T path calculations. *Contributions to Mineralogy and Petrology*, 107: 487-500.

Flöttman, T and Hand, M. (1999). Folded basement cored tectonic wedges along the northern edge of the Amadeus Basin, central Australia: evaluation of orogenic shortening. *Journal of Structural Geology*, 21: 399-412.

Foden, J., Mawby, J., Kelley, S., Turner, S. and Bruce, D. (1995). Metamorphic events in the eastern Arunta Inlier: Part 2, Nd-Sr-Ar isotopic constraints. *Precambrian Research*, 71: 207 -227.

Forman, D.J. (1966). The geology of the south western margin of the Amadeus Basin, central Australia. *Bureau of Mineral Resources Report*, 87: 54 pp.

Forman, D.J., Milligan, E.N. and McCarthy W.R. (1967). Regional geology and structure of the northeast margin of the Amadeus Basin, Northern Territory. *Bureau of Mineral Resources Report*, 103: 77 pp.

Forman, D.J. and Shaw, R.D. (1973). Deformation of the crust and mantle in central Australia. *Bureau of Mineral Resources Bulletin*, 144: 20 pp.

Fourcade, S., Marquer, D. and Javoy M. (1989). $^{18}O/^{16}O$ variations and fluid circulations in a deep shear zone: The case of the Alpine ultramylonites from the Aar massif (Central Alps, Switzerland). *Chemical Geology*, 77: 119 -131.

Freeman, M.J. (1986). Huckitta SF53-11 1:250 000 Geological Map Series Explanatory Notes. Northern Territory Geological Survey: Darwin.

Freer, R. (1981). Diffusion in silicate minerals and glasses: a data digest and guide to the literature. *Contributions to Mineralogy and Petrology*, 76: 440-454.

Frey, M., de Capitani, C. and Liou, J.G. (1991). A new petrogenetic grid for low-grade metabasites. *Journal of Metamorphic Geology*, 9 (4): 497-509.

Froese, E. and Hall, R.D., (1983). A reaction grid for potassium-poor pelitic and mafic rocks. *Current Research, Part A*, Geological Survey of Canada, Paper 83-1A: 121-124.

Frost, B.R. and Bucher, K. (1994). Is water responsible for geophysical anomalies in the deep continental crust? A petrological perspective. *Tectonophysics*, 231: 293-309.

Gaber, L.J., Foland, K.A. and Corbato, C.E. (1988). On the significance of argon release from biotite and amphibole during Ar-Ar vacuum heating.. *Geochimica et Cosmochimica Acta*, 52: 2457-2465.

Ganguly, J. and Saxena, S.K. (1984). Mixing properties of aluminosilicate garnets: constraints from natural and experimental data, and applications to geothermobarometry. *American Mineralogist*, 69: 88-97.

Ganguly, J., Tirone, M. and Hervig, R.L. (1998). Diffusion kinetics of Samarium and Neodymium in garnet, and a method for determining cooling rates of rocks. *Science*, 281: 805-807.

George, M.T. and Bartlett, J.M. (1996). Rejuventaion of Rb-Sr mica ages during shearing on the northwestern margin of the Nanga Parbat Haramosh massif. *Tectonophysics*, 260: 167-185.

Getty. S.R. and Gromet, I.P. (1992). Geochronological constraints on ductile deformation, crustal

extension and doming about a basement-cover boundary, New England Appalachians. *American Journal of Science*, 292: 359-397.

Getty, S.R., Selverstone, J., Wernicke, B.P., Jacobsen, S.B., Aliberti, E. and Lux, D.R. (1993). Sm-Nd dating of multiple garnet growthevents in an arc-continent collision zone, northwestern US Cordillera. *Contributions to Mineralogy and Petrology*, 115: 45-57.

Gibson, G., (1979). Margarite in kyanite- and corundum-bearing anorthosite, amphibolite and hornblendite from central Fiordland, New Zealand. *Contributions to Mineralogy and Petrology*, 68: 171-179.

Gilbert-Tomlinson, J. (1965). A new record of *Bothriolepsis* in the Northern Territory of Australia. *Bureau of Mineral Resources Bulletin*, 80: 191-215.

Giletti, B.J. (1986). Diffusion effects on oxygen isotope temperatures of slowly cooled igneous and metamorphic rocks. *Earth and Planetary Science Letters*, 77: 218-228.

Giletti, B.J., Semet, M.P. and Yund, R.A. (1978). Studies in diffusion III: Oxygen in feldspars, an ion microprobe determination. *Geochimica et Cosmochimica Acta*, 42: 45-57.

Goscombe, B. (1989). Stucture and metamorphism of the northeast Strangways Range, N.T. Unpublished PhD Thesis, University of Melbourne.

Goscombe, B. (1991). Intense non-coaxial shear and the development of mega-scale sheath folds in the Arunta Block, central Australia. *Journal of Structural Geology*, 13: 299-318.

Goscombe, B. (1992a). High-grade reworking of central Australian granulites, Part I. Structural evolution. *Tectonophysics*, 204: 361-399.

Goscombe, B. (1992b). High-grade reworking of central Australian granulites: metamorphic evolution of the Arunta Complex. *Journal of Petrology*, 33: 917-962.

Graham, C.M. and Powell, R. (1984). A garnet-hornblende geothermometer: calibration, testing and application to the Pelona Schist, Southern California. *Journal of Metamorphic Geology*, 2: 13-21.

Graham, C.M., Skelton, A.D.L., Bickle, M. and Cole, C. (1997). Chapter 8. Lithological, structural and deformation controls on fluid flow during regional metamorphism. In: 'Deformation-enhanced Fluid Transport in the Earth's Crust and Mantle.' (Ed. M.B. Holness). Chapman and Hall: London

Grant, J.A. (1985). Phase equilibria in low-pressure partial melting of rocks. *American Journal of Science*, 285: 409-435.

Grant, J.A. (1986). The Isocon diagram- a simple solution to Gresens' equation for metasomatic alteration. *Economic Geology*, 81: 1976-1982.

Grant, J.A. and Weiblen, P.W. (1971). Retrograde zoning in garnet near the second sillimanite isograd. *American Journal of Science*, 270: 281-296.

Gregory, R.T. (1990). Mineral pairs as stable isotopic monitors of fluid-rock interaction in the lithosphere. In: 'Proceedings of the conference on stable isotopes and fluid processes in mineralization.' (Eds. H.K. Herbert and S.E. Ho). University of Western Australia: Perth.

Gregory, R.T. and Criss, R.E. (1986). Isotope exchange in open and closed systems. In: 'Stable Isotopes in High Temperature Geological Processes.' (Eds. J.W. Valley, H.P. Taylor and J.R. O'Neil). *Reviews in Mineralogy*, 16: 91 -127. (Mineralogical Society of America: Washington DC)

Gregory, R.T., Criss, R.E. and Taylor, H.P. (1989). Oxygen isotope exchange kinetics of mineral pairs in closed and open systems; applications to problems of hydrothermal alteration of igneous rocks and Precambrian Iron Formations. *Chemical Geology*, 75: 1-42.

Gresens, R.L. (1967). Composition-volume relationships of metasomatism. *Chemical Geology*, 2: 47-65.

Grew, E.S and Sandiford, M. (1985). Staurolite in a garnet-hornblende-biotite schist from the Lanterman Range, northern Victoria Land, Antarctica. *Neues Jahrbuch für Mineralogie Monatschefte*, 9: 396-410

Guirard, M., Holland, T.J.B. and Powell, R. (1990). Calculated mineral equilibria in the greenschist-blueschist-eclogite facies in Na2O-FeO-MgO-Al_2O_3-SiO_2-H_2O: methods, results and geological applications. *Contributions to Mineralogy and Petrology*, 104: 85-98.

Hand, M., Dirks, P.H.G.M., Powell, R. and Buick, I.S. (1992). How well established is isobaric cooling in Proterozoic orogenic belts? An example from the Arunta Inlier, central Australia. *Geology*, 21: 954-955.

Hand, M., Dirks, P.H.G.M., Powell, R. and Buick, I.S. (1993). How well established is isobaric cooling in Proterozoic orogenic belts? An example from the Arunta Inlier, central Australia - Reply. *Geology*, 20: 649-652.

Hand, M., Mawby, J., Miller, J., Ballevre, M., Hensen,

B., Moller, A., and Buick, I. (1999a). 'Tectonothermal evolution of the Harts and Strangways Range Region, eastern Arunta Inlier, central Australia.' Specialist Group in Geochemistry, Mineralogy and Petrology Field Guide No. 4., Geological Society of Australia.

Hand, M., Mawby, J., Kinny, P. and Foden, J. (1999b). U-Pb ages from the Harts Range, central Australia: evidence for early Ordovician extension and constraints on Carboniferous metamorphism. *Journal of the Geological Society of London*, 156: 715-730.

Harrison, P.L. (1980). The Toomba Fault and the western margin of the Toko Syncline, Georgina Basin, Queensland and Northern Territory. *Bureau of Mineral Resources Journal of Australian Geology and Geophysics*, 5: 201-214.

Harrison, T.M. (1981). The diffusion of ^{40}Ar in hornblende. *Contributions to Mineralogy and Petrology*, 78: 324-331.

Helms, T.S., McSween, H.Y., Labotka, T.C. and Jarosewich E. (1987). Petrology of a Georgia Blue Ridge amphibolite unit with hornblende +gedrite+ kyanite + staurolite. *American Mineralogist*, 72: 1086 - 1096.

Hensen, B.J. and Zhou, B. (1995a). Retention of isotopic memory in garnets partially broken down during overprinting granulite facies metamorphism; implications for Sm-Nd closure temperature. *Geology*, 23 (3): 225-228.

Hensen, B.J. and Zhou, B. (1995b). A pan-African granulite facies metamorphic episode in Prydz bay, Antarctica: evidence for Sm-Nd garnet dating. *Australian Journal of Earth Science*, 42: 249-258.

Hickman, M.H. and Glassley, W.E. (1984). The role of metamorphic fluid transport in the Rb-Sr isotopic resetting of shear zones; evidence form Nordre Stromfjord, West Greenland. *Contributions to Mineralogy and Petrology*, 87: 265-281.

Hodges, K.V. and Spear, F.S. (1982). Geothermometry, geobarometry and the Al_2SiO_5 triple point at Mt. Moosilauke, New Hampshire. *American Mineralogist*, **67**: 1118-1134.

Hodges, K.V. and Crowley, P.D. (1985). Error estimation and empirical geothermobarometry for pelitic systems. *American Mineralogist*, 70: 702-709.

Hoernes, S. and Hoffer, E. (1995). Stable isotope evidence for fluid-present and fluid-absent metamorphism in metapelites from the Damara orogen, Namibia. *Contributions to Mineralogy and Petrology*, 90: 322-30.

Hoisch, T.D. (1990). Empirical calibration of six geobarometers for the mineral assemblage quartz +muscovite+biotite+plagioclase+garnet. *Contributions to Mineraogy and Petrology*, 104: 225-234.

Holland, T and Blundy, J. (1994). Non-ideal interactions in calcic amphiboles and their bearing on amphibole-plagioclase thermometry. *Contributions to Mineralogy and Petrology*, 116: 433-447.

Holland, T.J.B. and Powell, R. (1990). An enlarged and updated internally consistent thermodynamic dataset with uncertainties and correlations: the system K_2O-Na_2O-CaO-MgO-MnO-FeO-Fe_2O_3-Al_2O_3-TiO_2-SiO_2-C-H_2-O_2. *Journal of Metamorphic Geology*, 8: 89-124.

Holland, T.J.B. and Powell, R. (1992). Plagioclase feldspars: activity-composition relations based on Darken's Quadratic Formalism and Landau Theory. *American Mineralogist*, 77: 53-61.

Holland, T.J.B. and Powell, R. (1998a). AX: A program to calculate activities of mineral endmembers from chemical analyses. (Windows '95 GUI version) [computer program]. Available distributor: T.J.B. Holland, Cambridge Earth Sciences.URL:http://www.esc.cam.ac.uk/staff/holland

Holland, T.J.B. and Powell, R. (1998b). An internally consistent thermodynamic dataset for phases of petrological interest. *Journal of Metamorphic Geology*, 16: 309-343.

Holland, T., Baker, J. and Powell, R. (1998). Mixing properties and activity-composition relationship of chlorite in the system MgO-FeO-Al_2O_3-SiO_2-H_2O. *European Journal of Mineralogy*, 10: 395-406.

Hollister, L.S. (1969). Contact metamorphism in the Kwoiek area of British Columbia: an end member of the metamorphic process. *Geological Society of America Bulletin*, 80: 2465-2494.

Humphries, F.J. and Cliff, R.A. (1982). Sm-Nd dating and the cooling history of Scourian granulites, Scotland. *Nature*, 295: 515-517.

Ikeda, T. (1993). Compositional zoning patterns of garnet during prograde metamorphism from the Yanai district, Ryoke metamorphic belt, southwest Japan. *Lithos*, 30: 109-121.

Indares, A. and Martignole, J. (1985). Biotite-garnet geothermometry in the granulite facies: the influence of Ti and Al in biotite. *American Mineralogist*, 70: 272-278.

Iyer, S.S. (1974). Granulites and associated schists from the northern Strangways Range, central Australia: Geochemical and isotopic studies. Unpublished PhD thesis, University of

Queeensland.

Iyer, S.S., Woodford, P.J. and Wilson, A.F. (1976). Rb-Sr isotopic studies of a polymetamorphic granulite terrane, Strangways Range, central Australia. *Lithos*, 9: 211-224.

Jagoutz, E. (1988). Nd and Sm systematics in an ecolgite xenolith from Tanzania: Evidence for frozen mineral equilibria in the continental lithosphere. *Geochimica et Cosmochimica Acta*, 52: 1285-1293.

James, P.R. and Ding, P. (1988). "Caterpillar tectonics" in the Harts Range area, a kinship between two sequential Proterozoic extension collision orogenic belts within the eastern Arunta Inlier of central Australia. *Precambrian Research*, 40-41: 199-216.

Jenkin, G.R.T., Rogers, G., Falick, A.E. and Farrow, C.M. (1995) Rb-Sr closure temperature in bi-mineralic rocks; a mode effect and test for different diffusion models. *Chemical Geology*, 122: 227-240.

Jamtveit, B., Bucher-Nurminen,K. and Austrheim, H. (1990). Fluid controlled eclogitization of granulites in deep crustal shear zones, Bergen Arcs, Western Norway. *Contributions to Mineralogy and Petrology*, 104: 184-193.

Jiang, J., Clayton, R.N. and Newton, R.C. (1988). Fluids in granulite facies metamorphism: a comparative oxygen isotope study on the South India and Adirondack high-grade terrains. *Journal of Geology*, 96: 517-33.

Jones, B.G. (1972). Upper Devonian to Lower Carboniferous stratigraphy of the Pertnjara Group, Amadeus Basin, central Australia. *Journal of the Geological Society of Australia*, 19 (2): 229 -249.

Jones, B.J. (1991). Fluvial and lacustrine facies in the Middle to Late Devonian Pertnjara Group, Amadeus Basin, Northern Territory, and their relationship to tectonic events and climate. In: 'Geological and Geophysical Studies in the Amadeus Basin, central Australia.' (Eds. R.J. Korsch and J.M. Kennard). *Australian Bureau of Mineral Resources Bulletin*, 236: 333-348.

Kennard, J.M. and Nicoll, R.S. (1986). Late Proterozoic and Early Palaeozoic depositional facies of the northern Amadeus Basin, central Australia. *12th International Sedimentological Congress*: Field Excursion 25B

Kerrich, R, (1988). Detatchment zones of Cordilleran metamorphic core complexes: thermal, fluid and metasomatic regimes. *Geologische Rundschau*, 77: 157-182.

Kleemann, U. and Reinhardt, J. (1994). Garnet-biotite thermometry revisited; the effect of Al_{VI} and Ti in biotite. *European Journal of Mineralogy*, 6: 925-941.

Kohn, M.J. and Spear, F.S. (1989). Empirical calibration of geobarometers for the assemblage garnet-hornblende-plagioclase-quartz. *American Mineralogist*, 74: 77-84.

Kohn, M.J. and Spear, F.S. (1990). Two new geobarometers for garnet amphibolites, with applications to southeastern Vermont. *American Mineralogist*, 75: 89-96.

Kohn, M.J., Orange, D.L., Spear, F.S., Rumble III, D. and Harrison, T.M. (1992). Pressure, temperature and structural evolution of west central New Hampshire: hot thrusts over cold basement. *Journal of Petrology*, 33 (3): 521 -556.

Kohn, M.J. and Valley, J.W. (1998). Obtaining equilibrium oxygen isotope fractionations from rocks: theory and examples. *Contributions to Mineralogy and Petrology*, 132: 209-224.

Kretz, R. (1973). Kinetics of the crystallization of garnet at two localities near Yellowknife. *Canadian Mineralogist*, 12: 1-20.

Kullerud, L. (1991). On the calculation of isochrons. *Chemical Geology (Isotope Geoscience Section)*, 87: 115-124

Lafrance, B., Clarke, G.L., Collins, W.J. and Williams, I.S. (1995). The emplacement of the Wuluma Granite: melt generation and migration along steeply dipping extensional fractures at the close of the Late Strangways orogenic event, Arunta Block, central Australia. *Precambrian Research*, 72: 43-67.

Laird, J. (1988). Phase equilibria in mafic schist from Vermont. *Journal of Petrology*, 21: 1-37.

Lambeck, K. (1984). Structure and evolution of the Amadeus, Officer and Ngalia Basins of central Australia. *Australian Journal of Earth Science*, 31: 25-48.

Laurie, J.R., Nicoll, R.S. and Shergold, J.H. (1991). Ordovician siliclastics and carbonates of the Amadeus Basin, Northern Territory. Guidebook for Field Excursion 2. Sixth International Symposium on the Ordovician System. *Bureau of Mineral Resources Geology and Geophysics Record* 1991/49.

Leake, B.E. (1978). Nomenclature of amphiboles. *American Mineralogist*, 63: 1023-1052.

Li, Z.X., Powell, C.McA. and Morris, D.G. (1991). New palaeomagnetic results from the Amadeus Basin and their implications for stratigraphy and tectonics. In Geological and Geophysical Studies in the Amadeus Basin, central Australia. (eds Korsch, R.J. and Kennard, J.M.) *Australian Bureau of Mineral Resources Bulletin*, 236: 349-

360.

Lindsay, J.F. and Korsch, R.J. (1991). The evolution of the Amadeus Basin, central Australia. In: 'Geological and Geophysical Studies in the Amadeus Basin, central Australia'. (Eds R.J. Korsch and J.M. Kennard). *Australian Bureau of Mineral Resources Bulletin*, 236: 7-32.

Lindsay, J.F. and Owen, M. (1993). Plate 20: Ordovician to Devonian formations of the Amadeus Basin (1:1 000 000) In: 'Geological Atlas of the Amadeus Basin'. (Ed.) J.F. Lindsay. Australian Geological Survey Organisation: Canberra.

Lobato, L.M., Forman, J.M.A., Fuzikawa, K., Fyfe, W.S. and Kerrich, R. (1983). Uranium in overthrust Archean Basement, Bahia, Brazil. *Canadian Mineralogist*, 21: 647-654.

Lodwick, W.R. and Lindsay, J.F. (1990). Southern Georgina Basin: a new perspective. *APEA Journal*, 30 (1) : 137-148.

Loomis, T.P. (1983). Compositional zoning of crystal: a record of growth and reaction history. In: 'Kinetic and equilibrium in mineral reactions'. (Ed.) S.K. Saxena. *Advances in Physical Geochemistry*, 3: 1-60.

Maboko, M.A.H., McDougall, I., Zeitler, P.K. and FitzGerald, J.D. (1991). Discordant Ar-Ar ages from the Musgrave Ranges, central Australia: Implications for the significanceof hornblende Ar-Ar spectra. *Chemical Geology (Isotope Geoscience)*, 86: 139-160.

MacLean, W.H. and Kranidiotis, P. (1987). Immobile elements as monitors of mass transfer in hydrothermal alteration: Phelps Dodge massive sulfide deposit, Matagami, Quebec. *Economic Geology*, 82: 951-962.

Mahar, E., Baker, J.M., Powell, R., Holland, T.J.B. and Howell, N. (1997). The effect of Mn on mineral stability in metapelites. *Journal of Metamorphic Geology*, 15: 223-238.

Majoribanks, R.W. and Black, L.P. (1974). The geology and geochronology of the Arunta Complex, north of Ormiston Gorge, central Australia. *Journal of the Geoloogical Society of Australia*, 21: 291-299.

Marquer, D. and Burkhard, M. (1992). Fluid circulation, progressive deformation and mass transfer processes in the upper crust: the example of basement-cover relationships in the External Crystalline Massifs, Switzerland. *Journal of Structural Geology*, 14 (8/9): 1047-1057.

Matthews, A. (1994). Oxygen isotope geothermometers for metamorphic rocks. *Journal of Metamorphic Geology*, 12: 211-219.

Matsushita, Y., Goldsmith, J.R. and Clayton, R.N. (1978). Mechanisms of hydrothermal crystallisation at 250oC and 15 kbars. *Geochimica et Cosmochimica Acta*, 42: 173-183.

Matsushita, Y., Goldsmith, J.R. and Clayton, R.N. (1979). Oxygen isotope fractionation in the system quartz-albite-anorthite-water. *Geochimica et Cosmochimica Acta*, 43: 1131-1140.

Mawby, J., Hand, M. and Foden, J. (1999). Sm-Nd evidence for high-grade Ordovician metamorphism in the Arunta Block, central Australia. *Journal of Metamorphic Geology*, 17: 653-668.

Mawby, J. (2000). Metamorphic and geological constraints on Palaeozoic tectonism in the eastern Arunta Inlier. Unpublished PhD Thesis, University of Adelaide.

McCaig, A.M. (1984). Fluid-rock interaction in some shear zones from the Pyrenees. *Journal of Metamorphic Geology*, 2: 129-141.

McCaig, A.M. (1997). Chapter 9. The geochemistry of volatile fluid flow in shear zones. In: 'Deformation-enhanced Fluid Transport in the Earth's Crust and Mantle'. (Ed.) M.B. Holness. Chapman and Hall; London.

McCaig, A.M., Wickham, S.M. and Taylor, H.P. (1990). Deep fluid circulation in alpine shear zones, Pyrenees, France: Field and oxygen isotope studies. *Contributions to Mineralogy and Petrology*, 106: 41-60.

McCulloch, M.T. and Wasserburg, G.J. (1978). Sm-Nd and Rb-Sr chronology of continental crust formation. *Science*, 200: 1003-1011.

Menard, T. and Spear, F.S. (1993). Metamorphism of calcic pelitic schists, Strafford Dome, Vermont: Compositional zoning and reaction history. *Journal of Petrology*, 34 (5): 977-1005.

Mezger, K., Essene, E.J. and Halliday, A.N. (1992). Closure temperature of the Sm-Nd system in metamorphic garnets. *Earth and Planetary Science Letters*, 113: 397 - 409

Miller, J.A., Cartwright, I. and Buick, I.S. (1997). High grade metamorphism in the Harts Range. Petrology and P-T constraints from Mallee Bore, northern Harts Range, central Australia. *Journal of Metamorphic Geology*, 15: 613-629.

Miller, J.A., Buick, I.S., Williams, I.S. and Cartwright, I. (1998). Re-evaluating the metamorphic and tectonic history of the eastern Arunta Block, central Australia. *Geological Society of Australia Abstracts*, 49: 316.

Miller, J., Mawby, J., Hand, M., Buick, I.S. and Williams, I.S. (1999). The Larapinta Event: Ordovician metamorphism in the eastern Arunta

Inlier. *Geological Society of Australia Abstracts*, 54: 67.

Möller, A., Hensen, B.J. and Armstrong, R.A. (1998). Dating high-grade metamorphism: SHRIMP results on zircons from melts and TIMS U-Pb monazite data for the Strangways Metamorphic Complex, Arunta Inlier. *Geological Society of Australia Abstracts*, 49: 319.

Möller, A., Williams, I.S., Jackson, S. and Hensen, B.S. (1999). Palaeozoic deformation and mineral growth in the Strangways Metamorphic Complex: in-situ dating of zircon and monazite in a staurolite - corundum bearing shear zone. *Geological Society of Australia Abstracts*, 54: 71.

Morrison, J. (1994). Meteroic water-rock interaction in the lower plate of the Whipple Mountain metamorphic core complex, California. *Journal of Metamorphic Geology*, 12: 827-840.

Mortimer, G.E., Cooper, J.A., and James, P.R. (1987). U-Pb and Rb-Sr geochronology and geological evolution of the Harts Range Ruby Mine area of the Arunta Inlier, central Australia. *Lithos*, 20: 445-467.

Newton, R.C. (1989). Metamorphic fluids in the deep crust. *Annual Reviews in Earth and Planetary Science*, 17: 385-412.

Newton, R.C. and Haselton, H.T. (1981). Thermodynamics of the garnet-plagioclase Al_2SiO_5 - quartz geobarometer. In:'Thermodynamics of minerals and melts'. (Eds. R.C. Newton, A. Navrotsky and B.J. Wood) pp. 131 -147. Springer-Verlag: New York.

Nicoll, R.S., Gorter, J.D and Owen, M. (1991). Ordovician sediments in the Waterhouse Range Anticline, Amadeus Basin, central Australia: their interpretation and tectonic implications. In: 'Geological and Geophysical Studies in the Amadeus Basin, central Australia'. (Eds. R.J. Korsch and J.M. Kennard). *Australian Bureau of Mineral Resources Bulletin*, 236: 277-284.

Norman, A.R. (1991). The structural and metamorphic evolution of the central Arunta Block: evidence from the Strangways Metamorphic Complex and the Harts Range Group, central Australia. Unpublished PhD Thesis, Macquarie University.

Norman, A.R. and Clarke, G.L. (1990). A barometric response to late compression in the Strangways Metamorphic Complex, central Australia: *Journal of Structural Geology*, 12: 667-684.

Nzenti, J.P. (1992). Prograde and retrograde garnet zoning at high pressure and temperature in metapelitic and grenatite rocks from Yaounde (Cameroon Pan-African north-equatorial fold belt). *Journal of African Earth Sciences*, 15 (1): 73-79.

Oaks, Jr., R.Q., Deckelman, J.A., Conrad, K.T., Hamp, L.T., Phillips, J.O. and Stewart, A.J. (1991). Sedimentation and tectonics in the northeastern and central Amadeus Basin, central Australia. In: 'Geological and Geophysical Studies in the Amadeus Basin, central Australia'. (Eds. R.J. Korsch and J.M. Kennard) *Australian Bureau of Mineral Resources Bulletin*, 236: 73-90.

O'Hara, K. (1988). Fluid flow and volume loss during mylonitization: an origin for phyllonite in an overthrust setting, North Carolina, U.S.A. *Tectonophysics*, 156: 21-36.

Oliver, N.H.S. (1996). Review and classification of structural controls on fluid flow during regional metamorphism. *Journal Metamorphic Geology*, 14: 477-492.

Oliver, N.H.S., Valenta, R. and Wall, V.J. (1990). The effect of heterogeneous stress and strain on metamorphic fluid flow, Mary Kathleen, Australia, and a model for large-scale fluid circulation. *Journal Metamorphic Geology*, 8: 311-331.

O'Neil, J.R. and Taylor, H.P. Jr (1967). The oxygen isotope and cation exchange chemistry of feldspars. *American Mineralogist*, 52: 1414 -1437.

Palamountain, R. (1996). Metamorphic petrology of the Winnecke Domain, central Australia: P-T-t constraints on the granulite to lower amphibolite facies terrane. Unpublished Honours Thesis, University of Adelaide.

Patiño Douce, A.E., Johnston, A.D. and Rice, J.M. (1993). Octahedral excess mixing properties in biotite: a working model with applications to geobarometry and geothermometry. *American Mineralogist*, 78: 113-131.

Perchuk, L.L (1991). Derivation of a thermodynamically consistent set of geothermometers geobarometers for metamorphic and magmatic rocks. In: 'Progress in metamorphic and magmatic petrology: A memeorial volume in honour of D.S. Khorzhinsky'. (Ed. L.L. Perchuk) pp 93-112. Cambridge University Press: Cambridge.

Perchuk, L.L. and Lavrent'eva, I.V. (1983). Experimental investigation of exchange equilibria in the system cordierite-garnet-biotite. In: 'Kinetics and equilibrium in mineral reactions.' (Ed S.K. Saxena) Adv. Phys. Geochem., 3: 199-239.

Perchuk, L.L., Aranovich, L.Y., Podlesskii, K.K., Lavrent'eva, I.V., Gerasimov, V.Y., Fed'Kin, V.V., Kitsul, V.I., Karasakov, L.P. and Berdnikov, N.V. (1985). Precambrian granulites of the Aldan shield, eastern Siberia, USSR. *Journal of*

Metamorphic Geology, 3: 265-310.

Playford, G., Jones, B.G. and Kemp, E.M. (1976). Palynological evidence for the age of the synorogenic Brewer Conglomerate, Amadeus Basin, central Australia. *Alcheringa*, 1: 235-243.

Powell, R. (1998). Calculating phase diagrams involving solid solutions via non-linear equations, with examples using THERMOCALC. *Journal of Metamorphic Geology*, 16: 577-588.

Powell, R. and Holland, T.J.B. (1985). An internally consistent thermodynamic data set with uncertainties and correlations: 1. Methods and a worked example. *Journal of Metamorphic Geology*, 3: 327-342.

Powell, R. and Holland, T.J.B. (1988). An internally consistent thermodynamic data set with uncertainties and correlations: 3. Applications to geobarometry, worked examples and a computer program. *Journal of Metamorphic Geology*, 6: 173-204.

Powell, R. and Holland, T.J.B. (1990). Calculated mineral equilibria in the pelite system KFMASH (K_2O-FeO-MgO-Al_2O_3-SiO_2-H_2O). *American Mineralogist*, 75: 367-380.

Powell, R., Holland, T. and Worley, B. (1998). Calculating phase diagrams involving solid solutions via non-linear equations, with examples using THERMOCALC. *Journal of Metamorphic Geology*, 16 (4): 577-588.

Prince, C.I., Kosler, J., Vance, D. and Gunther, D. (2000). Comparison of laser ablation ICP-MS and isotope dilution REE analyses-implications for Sm-Nd garnet geochronology. *Chemical Geology*, 168: 255-274.

Read, C.M. and Cartwright, I. (1999a). Fluid-rock interaction within shear zones of the Arunta Inlier, central Australia: implications for tectonics. *Specialist Group in Tectonics and Structural Geology, Halls Gap Conference Abstract Volume*, XX: pp 211-212.

Read, C.M. and Cartwright, I. (1999b). Meteroic fluid infiltration during Palaeozoic exhumation of the Proterozoic Yalbadjandi shear zone, central Australia. *Geological Society of Australia Abstract*, 54: 86-87.

Reche, J. and Martinez, F.J. (1996). GPT: an excel spreadsheet for thermobarometic calculations in metapelitic rocks. *Computers in Geosciences*, 22 (7): 775-784.

Robinson, P., Spear, F.S., Schumacher, J.C., Laird, J., Klein, C., Evans, B.W. and Doolan, B.L. (1982). Phase relations of metamorphic amphiboles: natural occurrence and theory. In: 'Amphiboles: Petrology and experimental phase relations.' (Eds. D.R. Veblen and P.H. Ribbe). *Reviews in Mineralogy*, 9B. pp 1-211.

Rollinson, H. (1993). 'Using geochemical data: evaluation, presentation, interpretation.' pp 352. Longman: Singapore.

Romine, K.K., Southgate, P.N., Kennard, J.M. and Jackson, M.J. (1994). The Ordovician to Silurian phase of the Canning basin WA: Structure and sequence evolution. In: (Eds. P.G. Purcell and R.R. Purcell) 'The sedimentary basins of Western Australia.' *Proceedings of the 4th Petroleum Exploration Society of Australia (PESA) Symposium Perth*: 851-864.

Rumble, D., III (1982) Chapter 8. Stable Isotope fractionation during metamorphic devolatilization reactions. In: 'Characterization of Metamorphism through Mineral Equilibria.' (Ed. J.M. Ferry). *Reviews in Mineralogy*, 10: 327-354.

Rumble, D., III (1989). Evidences of fluid flow during regional metamorphism. *European Journal of Mineralogy*, 1:731-737.

Sakai, C., Banno, S., Toriumi, M. and Higashiro, T. (1985). Growth history of garnet in pelitic schists of the Sanbagawa metamorphic terrain in central Shikoku. *Lithos*, 18: 81-95.

Sandiford, M. and Hand, M. (1998). Controls on the locus of intraplate deformation in central Australia. *Earth and Planetary Science Letters*, 162: 97-110.

Schumacher, J.C. and Robinson, P. (1987). Mineral chemistry and metasomatic growth of Aluminous enclaves in gedrite - corderite gneiss from Southwestern New Hampshire, USA. *Journal of Petrology*, 28 (6): 1033-1073.

Schwandt, C.S., Cygan, R.T. and Westrich, H.R. (1996). Ca self-diffusion in grossular garnet. *American Mineralogist*, 81: 448-451.

Scrimgeour, I. and Raith, J.G. (in press). High grade reworking of Proterozoic granulites during Ordovician intraplate transpression, eastern Arunta Inlier, central Australia. In: 'Polytectonism and reactivation mechanisms in metamorphic belts.' (Eds J. Miller, I. Buick, M. Hand, and R.E. Holdsworth) Geological Society of London Special Publication.

Selverstone, J., Spear, F.S., Franz, G. and Morteani, G. (1984). High-pressure metamorphism in the SW Tauern Window, Austria: P-T paths from hornblende-kyanite-staurolite schists. *Journal of Petrology*, 25 (2): 501-531.

Selverstone, J., Morteani, G. and Staude, J.-M. (1991). Fluid channelling during ductile shearing: transformation of granodiorite into aluminous schist in the tauern Window, Eastern Alps. *Journal of Metamorphic Geology*, 9: 419-431.

Sharma, R.S., and McRae, N.D., (1981). Paragenetic

relations in gedrite-cordierite-staurolite-biotite sillimanite-kyanite gneisses at Ajitpura, Rajasthan, India. *Contributions to Mineralogy and Petrology*, 78: 48-60.

Shaw, R.D. (1991). The tectonic development of the Amadeus Basin, central Australia. In: 'Geological and Geophysical Studies in the Amadeus Basin, central Australia'. (Eds. R.J. Korsch and J.M. Kennard) *Australian Bureau of Mineral Resources Bulletin*, 236: 73-90.

Shaw, R.D. and Black, L.P. (1991). The history and tectonic implications of the Redbank Thrust Zone, central Australia, based on structural, metamorphic and Rb-Sr isotopic evidence. *Australian Journal of Earth Science*, 38: 307-332.

Shaw, R.D. and Wells, A.T. (1983). Alice Springs, Northern Territory 1:250 000 Geological Series. Australian Bureau of Mineral Resource Explanatory Notes Sheet SF/53-14 (2nd Edn).

Shaw, R.D., Langworthy, A.P., Offe, L.A., Stewart, A.J., Allen, A.R. and Senior, B.R. (1979). Geological report on 1:100,000-scale mapping of the southeastern Arunta Block, Northern Territory. *Australian Bureau of Mineral Resources Record* 1979/47, BMR microform MF133.

Shaw, R.D., Stewart, A.J. and Black, L.P. (1984). The Arunta Inlier: a complex ensialic mobile belt in central Australia. Part 2: tectonic history. *Australian Journal of Earth Science*, 31: 457-484.

Shaw, R.D., Etheridge, M.A. and Lambeck, K. (1991). Development of the late Proterozoic t mid-Palaeozoic, intracratonic Amadeus Basin in central Australia: a key to understanding tectonic forces in plate tectonics. *Tectonics*, 10 (4); 688-721.

Sheppard, S.M.F (1986). Chapter 6. Characterization and isotopic variations in natural waters. In: 'Stable Isotopes in High Temperature Geological Processes.' (Eds. J.W. Valley, H.P. Taylor, and J.R. O'Neil). *Reviews in Mineralogy*, 16: 165-183.

Shergold, J.H. (1985). Report 251: 'Notes to accompany the Hay River-Mount Whelan special 1:250 000 Geological Sheet, Southern Georgina Basin'. Bureau of Mineral Resources: Canberra.

Shergold, J.H. and Druce, E.C. (1980). Upper Proterozoic and Lower Palaeozoic rocks of the Georgina Basin. In: 'The Geology and Geophysics of Northeastern Australia.' (Eds. R.A. Henderson and P.J Stephenson), pp 149-174.

Shergold, J.H., Elphinstone, R., Laurie, J.R., Nicoll, R.S., Walter, M.R., Young, G.C. and Zang, W. (1991). Late Palaeozoic and early Palaeozoic palaeontology and biostratigraphy of the Amadeus Basin. In: 'Geological and Geophysical Studies in the Amadeus Basin, central Australia.' (Eds. R.J. Korsch and J.M. Kennard) *Australian Bureau of Mineral Resources Bulletin*, 236: 97-111.

Shiro, Y. and Sakai, H. (1972). Calculation of the reduced partition function ratios of α, β-quartz and calcite. *Bull. Chem. Soc. Japan*, 45: 2355-2359.

Smith, K.G. (1972). Stratigraphy of the Georgina Basin. *Australian Bureau of Mineral Resources Bulletin*, 111: 156pp

Spear, F.S. (1977). Phase equilibria of amphibolites from the Post Pond Volcanics, Vermont. *Carnegie Institution of Washington Yearbook*, 76: 613-6 619.

Spear, F.S. (1978). Petrogenetic grid for amphibolites from the Post Pond and Ammonoosuc Volcanics, Vermont. *Carnegie Institution of Washington Yearbook*, 77: 805-808.

Spear, F.S. (1980). The gedrite-anthophyillite solvus and the composition limits of orthoamphibole from the Post Pond Volcanics, Vermont. *American Mineralogist*, 65: 1103-1118.

Spear, F.S. (1981). An experimental study of hornblende stability and compositional variation in amphibolite. *American Journal of Science*, 281: 697-734.

Spear, F.S. (1982). Phase equilibria of amphibolites from the Post Pond Volcanics, Mt Cube Quadrangle, Vermont. *Journal of Petrology*, 23 (3): 383-426.

Spear, F.S. (1988). The Gibbs method and Duhem's Theorem: the quantitative relationships among P, T, chemical potential, phase compostion and reaction progress in igneous and metamorphic systems. *Contributions to Mineralogy and Petrology*, 99: 249-256.

Spear, F.S. (1993). 'Metamorphic phase equilibria and Pressure-Temperature-Time Paths.' Mineralogical Society of America: Washington.

Spear, F.S. and Cheney, J.T. (1989). A petrogenetic grid for pelitic schists in the system SiO_2-Al_2O_3 FeO-MgO-K_2O-H_2O. *Contributions to Mineralogy and Petrology*, 101: 149-164.

Spear, F.S. and Kimball, K.L. (1984). RECAMP -A FORTRAN IV program for estimating Fe^{3+} contents in amphiboles. *Computers in Geology*, 10: 317-325.

Spear, F.S. and Kohn, M.J. (1998). Program Thermobarometry (Mac Version 2.1.)[computer program]. Available distributor: F.S. Spear,

Institute. URL: http://www.geo.rpi.edu/facstaff/spear

Spear, F.S. and Rumble III, D. (1986). Pressure, temperature and structural evolution of the Orfordville Belt, West-Central New Hampshire. *Journal of Petrology*, 27: 1071-1093.

Spear, F.S. and Selverstone, J. (1983). Quantitativ P-T paths from minerals: Theory and tectonic applications. *Contributions to Mineralogy and Petrology*, 83: 348-357.

Spear, F.S., Ferry, J.M. and Rumble III, D. (1982). Analytical formulation of phase equilibria: the Gibbs method. In: 'Characterisation of metamorphism through mineral equilibria'. (Ed. J.M. Ferry). *Reviews in Mineralogy*, 10: 105-152 152.

Spear, F.S., Kohn, M.J., Florence, F.P. and Menard, T. (1991). A model for garnet and plagioclase growth in pelitic schists: implications for thermobarometry and P-T path determinations. *Journal of Metamorphic Geology*, 8: 683-696.

Spear, F.S., Selverstone, J., Hickmott, D., Crowley, P. and Hodges, K.V. (1984). P-T paths from garnet zoning: A new technique for deciphering tectonic processes in crystalline terranes. *Geology*, 12: 87-90.

Stewart, A.J. (1971). Potassium-Argon dates from the Arltunga Nappe Complex, Northern Territory. *Journal of the Geological Society of Australia*, 17 (2): 205-211.

Stewart, A.J., Shaw, R.D. and Black, L.P. (1984). The Arunta Inlier: a complex ensialic mobile belt in central Australia. Part 1: stratigraphy, correlations and origin. *Australian Journal of Earth Science*, 31: 445-455.

St Onge, M.R. (1987). Zoned poikiloblastic garnets: P-T paths and syn-metamorphic uplift through 30 km of structural depth, Wopmay Orogen, Canada. *Journal of Petrology*, 28 (1): 1-21.

Stowell, H.H. and Goldberg, S.A. (1997). Sm-Nd garnet dating of polyphase metamorphism: northern Coast Mountains, south-eastern Alaska, USA. *Journal of Metamorphic Geology*, 15; 439-450.

Stüwe, K (1997). Effective bulk composition changes due to cooling: a model predicting complexities in retrograde reaction textures. *Contributions to Mineralogy and Petrology*, 129: 43-52.

Stüwe, K. and Powell, R. (1995). PT paths from modal proportions: application to the Koralm Complex, Eastern Alps. *Contributions to Mineralogy Petrology*, 119: 83-93.

Teyssier, C. (1985). A crustal thrust system in an intracratonic tectonic enviroment. *Journal of Structural Geology*, 7 (6): 689-700.

Tracy, R.J. (1982). Compositonal zoning and inclusions in metamorphic minerals. In: 'Characterization of Metamorphism through Mineral Equilibria. (Ed. J.M. Ferry). *Reviews in Mineralogy*, 10: 355-397.

Turner, S., Jones, P.J. and Draper, J.J. (1981). Early Devonian thelodonts (Agnatha) from the Toko Syncline, western Queensland, and a review of other Australian discoveries. *Australian Bureau of Mineral Resources Journal of Australia Geology and Geophysics*, 6: 51-69.

Valley, J.W. (1986). Chapter 13. Stable isotope geochemistry of metamorphic rocks. In: "Stable Isotopes in High Temperature Geological Processes." (Eds. J.W.Valley, H.P. Taylor and J.R. O'Neil) *Reviews in Mineralogy*, 16: 445-489.

Van Haren, J.L.M., Ague, J.J. and Rye, D.M. (1996). Oxygen isotope record of fluid infiltration and mass transfer during regional metamorphism of pelitic schist, Connecticut, USA. *Geochimica et Cosmochimica Acta*, 60 (18): 3487-3504.

Vance, D. and O'Nions, R.K. (1990). Isotopic chronometry of zoned garnets: growth kinetics and metamorphic histories. *Earth and Planetary Science Letters*, 97: 227-240.

Vance, D. and Holland, T. (1993). A detailed isotopic and petrological study of a single garnet from the Gassetts Schist, Vermont. *Contributions to Mineralogy and Petrology*, 114: 101-118.

Vance, D. and Mahar, E (1998). Pressure-temperature paths from P-T psseudosections and zoned garnets: potential, limitations and examples from the Zanskar Himalaya, NW India. *Contributions to Mineralogy and Petrology*, 132: 225-245.

Vance, D., Strachan, R.A. and Jones, K.A. (1998). Extensional versus compressional settings for metamorphism: Garnet chronometry and pressure-temperature-time histories in the Moine Supergroup, northwest Scotland. *Geology*, 26 (10): 927-930.

Veevers, J.J. (1984). 'Phanerozoic earth history of Australia'. Clarendon Press: Oxford. 418pp.

Vry, J., Compston, W. and Cartwright, I.. (1996). SHRIMP II dating of zircons and monazites: reassessing the timing of high-grade metamorphism and fluid flow in the Reynolds Range, northen Arunta Block, Australia. *Journal of Metamorphic Geology*, 14: 566-587.

Walley, A.M., Cook, P.J., Bradshaw, J., Brakel, A.T., Kennard, J.M., Lindsay, J.F., Nicholl, R.S., Olissoff, S., Owen, M., Shergold, J.H., Totterdell, J.M. and Young, G.C. (1991). The Palaeozoic palaeogeography of the Amadeus Basin region.

In: 'Geological and geophysical studies in the Amadeus Basin, central Australia'. (Eds. R.J. Korsch and J.M. Kennard). *Australian Bureau of Mineral Resources, Geology and Geophysics Bulletin*, 236: 155-169.

Walter, M.R. and Gorter, J.D. (1994). The Neoproterozoic Centralian Superbasin in Western Australia: the Savoy and Officer Basins. In: 'The Sedimentary Basins of Western Australia.' (Eds. P.G Purcell and R.R. Purcell). Proceedings of Petroleum Exploration Society of Australia (PESA) Symposium, pp 851-864.

Walter, M.R., Veevers, J.J., Calver, C.R. and Grey, K. (1995). Neoproterozoic stratigraphy of the Centralian Superbasin, Australia. *Precambrian Research*, 73: 173-195.

Walther, J.V. (1994). Fluid-rock reactions during metamorphism at mid-crustal conditions. *Journal of Geology*, 102: 559-570.

Ward, C.M., (1984). Magnesium staurolite and green chromium staurolite from Fiordland, New Zealand. *American Mineralogist*, 69: 531-540.

Warren, R.G. (1982). Metamorphic paragenesis in part of the Arunta Complex, Northern Territory. Unpublished PhD Thesis, University of NSW.

Warren, R.G. (1983). Metamorphic and tectonic evolution of granulites, Arunta Block, central Australia. *Nature*, 305: 300-303.

Webby, B.D. (1978). History of the Ordovician continental platform shelf margin of Australia. *Journal of the Geological Society of Australia*, 25: 41-63.

Wells, A.T. and Moss, F.J. (1983). The Ngalia Basin, Northern Territory: stratigraphy and structure. *Australian Bureau of Mineral Resources Bulletin*, 212: 88 pp

Wells, A.T., Evans, T.G. and Nicholas, T. (1968). The geology of the central part of the Ngalia Basin, Northern Territory. Australian Bureau of Mineral Resources Record, 1968/38: (unpublished).

Wells, A.T., Forman, D.J., Ranford, L.C. and Cook, P.J. (1970). Geology of the Amadeus Basin, central Australia. *Australian Bureau of Mineral Resources Bulletin*, 100: pp 222

Wells, A.T., Moss, F.J. and Sabitay, A. (1972). The Ngalia Basin, Northern Territory-recent geological and geophysical information upgrade petroleum prospects. APEA Journal: 12: 144-151.

White, M.E. (1983). Appendix 6: Plant fossils from the Mt Eclipse Sandstone. In: 'The Ngalia Basin, Northern Territory: stratigraphy and structure'. (Eds. A.T. Wells and F.J Moss) *Australian Bureau of Mineral Resources Bulletin*, 212: 85-86.

Whitney, D.L. and Ghent, E.D. (1993). Prograde reactions and garnet zoning reversals in staurolite schist, British Columbia: significance for thermobarometric interpretations. *Journal of Metamorphic Geology*, 11: 779-788.

Will, T.M., and Powell, R. (1990). Activity composition relationships in multicomponent amphiboles: An application of Darken's quadratic formalism. *American Mineralogist*, 77: 954-966.

Wickham, S.M. and Taylor, H.P. (1985). Stable isotopic evidence for large-scale seawater infiltration in a regional metamorphic terrane; the Trois Seigneurs Massif, Pyrenees, France. *Contributions to Mineralogy and Petrology*, 91: 122-137.

Will, T.M., Powell, R. and Holland, T.J.B. (1990). A calculated petrogenetic grid for ultramafic rocks in the system CaO-FeO-MgO-Al_2O_3 SiO_2-CO_2-H_2O at low pressures. *Contributions to Mineralogy and Petrology*, 105: 347-358.

Wilson, A.F. and Baksi, A.K. (1983). Widespread ^{18}O depletion in some Precambrian granulites of Australia. *Precambrian Reasearch*, 23: 33 -56.

Windrim, D.P. (1983). Chemical and thermal evolution of Stragways Granulites, central Australia. Unpublished PhD thesis, Australian National University.

Windrim, D.P. and McCulloch, M.T. (1986). Nd and Sr isotopic systematics of central Australian granulites: chronology of crustal development and constraints on the evolution of lower continental crust. *Contributions to Mineralogy and Petrology*, 94: 289-303.

Wood, B.J. and Walther, J.V. (1986). Fluid flow during metamorphism and its implications for fluid-rock ratios. In: 'Fluid-Rock Interactions During Metamorphism'. (Eds. J.V. Walther and B.J. Wood). *Advances in Physical Geochemistry*, 5: 89-108.

Woodford, P.J. (1974). Polymetamorphism in granulites from the north-eastern Strangways Range, central Australia. Unpublished PhD Thesis, University of Queensland.

Woodford, P.J., Mateen, A., Green, D.C. and Wilson, A.F. (1975). $^{40}Ar/^{39}Ar$ geochronology of a high grade polymetamorphic terrain, northeastern Strangways Range, central Australia. *Precambrian Research*, 2: 375-396.

Woodsworth, G.J. (1977). Homogenization of zoned garnet from pelitic schists. *Canadian Mineralogist*, 15: 230-242.

Worley, B. and Powell, R. (1998a). Singularities in NCKFMASH (Na_2O-CaO-K_2O-FeO-MgO Al_2O_3-SiO_2-H_2O. *Journal of Metamorphic Geology*, 16: 169-188.

Worley, B. and Powell, R. (1998b). Making movies: phase diagrams changing in pressure, temperature, composition and time. In: 'What Drives Metamorphism and Metamorphic Reactions?' (Eds. P.J. Treloar and P.J. O'Brien). *Geological Society of London Special Publication*, 138: 269-280.

Xu, G., Will, T.M. and Powell, R. (1994). A calculated petrogenetic grid for the system K_2O -FeO-MgO-Al_2O_3-SiO_2-H_2O, with particular reference to contact-metamorphosed pelites. *Journal of Metamorphic Geology*, 12: 99-119.

York, D. (1969). Least squares fitting of a straight line with correlated errors. *Earth and Planetary Science Letters*, 5: 320-324.

Young, G.C. (1985). New discoveries of Devonian vertebrates from the Amadeus Basin, central Australia. *Australian Bureau of Mineral Resources Journal of Australian Geology and Geophysics*, 9: 239-254.

Young, G.C. (1988). New occurrences of phyllolepid placoderms from the Devonian of central Australia. *Australian Bureau of Mineral Resources Journal of Australian Geology and Geophysics*, 10: 363-376.

Young, G.C., Turner, S., Owen, M., Nicoll, R.S., Laurie, J.R. and Gorter, J.D. (1987). A new Devonian fish fauna, and revision of post Ordovician stratigraphy in the Ross River Syncline, Amadeus Basin, central Australia. *Australian Bureau of Mineral Resources Journal of Australian Geology and Geophysics*, 10: 233-242.

Young, D.N., Fanning, C.M., Shaw, R.D., Edgoose, C.J., Blake, D.H., Page, R.W. and Camacho, A. (1995). U-Pb zircon dating of tectonomagmatic events in the northen Arunta Inlier, central Australia. *Precambrian Research*, 71: 45-68.

Zheng, Y.-F. (1993a). Calculation of oxygen isotope fractionation in hydroxyl-bearing silicates. *Earth and Planetary Science Letters*, 120; 247-263.

Zheng, Y.-F. (1993b). Calculation of oxygen isotope fractionation in anhydrous silicates. *Geochimica et Cosmochimca Acta*, 57; 1079-1091.

Zhou, B. and Hensen, B.J. (1995). Inherited Sm/Nd isotope components presered in monazite inclusions within garnets in leucogneiss from East Antarctica and implications for closure temperature studies. *Chemical Geology (Isotope Geoscience Section)*, 121 317-326.

Appendix 1

SAMPLE LOCALITY LIST AND DETAILED PETROGRAPHY OF SELECTED SAMPLES

Table A1.1. List of samples discussed in this thesis. All samples listed are stored at the Department of Geology and Geophysics, University of Adelaide, and are preceeded with the Accession No. A1028-.

Sample Number	Easting	Northing	Locality	1:50 00 map sheet	Sample use
BHN2	415504	7425204	Ankala Gneiss	Angkarla	stable isotopes
BHN4	415509	7425226	North of Bald Hill	Angkarla	stable isotopes
BHN5	415515	7425422		Angkarla	stable isotopes
BHN6	415511	7425528		Angkarla	stable isotopes
CM19	431500	7426940	Cadney	Laughlen	petrography/petrology
CM20	431504	7426944	Metamorphics	Laughlen	petrography/petrology
MRN11	417146	7431701	lower	Pfitzner	stable isotopes
MRN12	417144	7431705	Cadney	Pfitzner	stable isotopes
MRN13	417160	7431715	Metamorphics	Pfitzner	stable isotopes
MRN14	417158	7431718	North of road	Pfitzner	stable isotopes
MRN16	417162	7431727	to Arltunga	Pfitzner	stable isotopes
MRN17	417166	7431730		Pfitzner	stable isotopes
PAW1	427872	7422055		Laughlen	stable isotopes
PAW2	427870	7422053		Laughlen	stable isotopes
PAW3	427867	7422048		Laughlen	stable isotopes
PAW6	427810	7421985	Erontonga	Laughlen	stable isotopes
PAW7	427805	7421980	Metamorphics	Laughlen	stable isotopes
PAW9	427690	7421658	West of Patsy's	Laughlen	stable isotopes
PAW10	427694	7421655	Bore	Laughlen	stable isotopes
PAW11	427580	7421342		Laughlen	stable isotopes
PAW12	427136	7420625		Laughlen	stable isotopes
PAW13	424421	7422420		Laughlen	stable isotopes
PAW20	424441	7422005		Laughlen	stable isotopes
PB10	418807	7431764		Pfitzner	Sm-Nd; petrography/petrology
PB11	418810	7431760		Pfitzner	Sm-Nd; petrography/petrology
PB12	418854	7431750	Pinnacles Bore	Pfitzner	Sm-Nd; petrography/petrology
PB184	418918	7431766	Shear Zone	Pfitzner	petrography
PB246	418830	7431757		Pfitzner	petrography
PBS3	417165	7431983		Pfitzner	Sm-Nd; petrography/petrology
YB1	382250	7449697		Yambah	stable isotopes
YB2	382250	7449697		Yambah	stable isotopes; geochemistry
YB3	382251	7449697		Yambah	stable isotopes
YB4	382252	7449698		Yambah	stable isotopes
YB6	382232	7449772	Yambah Schist	Yambah	stable isotopes; geochemistry
YB7	382220	7449790	Zone	Yambah	stable isotopes
YB8	382215	7449801		Yambah	stable isotopes; geochemistry
YB9	381834	7449830		Yambah	petrography
YB10	382215	7449804		Yambah	stable isotopes; geochemistry
YB11	381850	7449758		Yambah	stable isotopes; geochemistry
YB12	381850	7449758		Yambah	stable isotopes; geochemistry
YB13	381912	7449772		Yambah	stable isotopes; geochemistry
YB14	382022	7449795		Yambah	stable isotopes; geochemistry
YB15	382210	7449805		Yambah	stable isotopes
YB18	382225	7449775		Yambah	stable isotopes
YB19	382235	7449762		Yambah	stable isotopes; geochemistry
YB20	382284	7449653		Yambah	stable isotopes
YB21	381820	7449840		Yambah	stable isotopes
YB22	382245	7449794		Yambah	stable isotopes; geochemistry
YB23	382264	7449693		Yambah	stable isotopes
YB24	382373	7449704		Yambah	stable isotopes
YB25	382373	7449704		Yambah	stable isotopes
YB27	382375	7449680		Yambah	stable isotopes

Sample Number	Easting	Northing	Locality	1:50 00 map sheet	Sample use
YB29	382252	7449268	Yambah Schist Zone	Yambah	stable isotopes
YB30	382252	7449268		Yambah	stable isotopes; geochemistry
YB31	382307	7449548		Yambah	stable isotopes; geochemistry
YB32	382222	7449507		Yambah	stable isotopes; geochemistry
YB33	382222	7449507		Yambah	stable isotopes
YS2	4382252	7449268	Yambah Schist Zone	Yambah	stable isotopes
YS8	4382252	7449268		Yambah	stable isotopes
YS9	4382250	7449697		Yambah	stable isotopes
YS10	4382215	7449801		Yambah	stable isotopes; geochemistry
YS11	4382252	7449268		Yambah	stable isotopes
YS11A	4382252	7449268		Yambah	stable isotopes
YS145	4382215	7449801		Yambah	stable isotopes
YS146	4382250	7449697		Yambah	stable isotopes
YS147	4382250	7449697		Yambah	Sm-Nd; petrography/petrology
YS148	4382250	7449697		Yambah	Sm-Nd; petrography/petrology stable isotopes; geochemistry
YS149	4382250	7449697		Yambah	Sm-Nd; petrography/petrology stable isotopes; geochemistry
YS150	4382252	7449268		Yambah	stable isotopes
YS151	4382252	7449268		Yambah	stable isotopes
WK52	431096	7422633	Winnecke-Depot Creek	Laughlen	stable isotopes; geochemistry
WK55	431097	7422610		Laughlen	stable isotopes; geochemistry
WK56	431097	7422608		Laughlen	stable isotopes; geochemistry
WK57	431099	7422606		Laughlen	stable isotopes; geochemistry
WK58	431096	7422603		Laughlen	stable isotopes; geochemistry
WK59	431096	7422598		Laughlen	stable isotopes; geochemistry
WK59A	431096	7422598		Laughlen	stable isotopes; geochemistry
WK60	431102	7422593		Laughlen	stable isotopes; geochemistry
WK61	431105	7422588		Laughlen	stable isotopes; geochemistry
WK62	431105	7422590		Laughlen	stable isotopes; geochemistry
WK71	431110	7422750		Laughlen	petrography/petrology
WK181	431100	7422604		Laughlen	Sm-Nd; petrography/petrology; stable isotopes
WK182	431103	7422602		Laughlen	Sm-Nd; petrography/petrology; stable isotopes

A1.2. Detailed petrography of selected samples from shear zones in the Strangways Metamorphic Complex.

A1.2.1 Petrographic descriptions of metapelites from the Winnecke area.

WK182

This is a coarse-grained metapelitic rock sampled from a shear zone in the Winnecke area. It has a strongly developed foliation defined by muscovite (~40%) and biotite (~25%) which constitute the bulk of the rock. This fabric wraps coarse (2-5mm) euhedral porphyroblastic garnet which forms about 10% of the rock. The garnet is not optically zoned and displays no textural evidence of secondary rims or other disequilibrium features. It is predominantly almandine garnet (58% core to 64% rim) with a significant spessartine component (22% core to 14% rim) and lesser pyrope (12% core to 15% rim) and grossular (8% core to 7% rim). The XFe of garnet varies from 0.81-0.84. Inclusions in garnet are commonly either ilmenite or quartz but are not volumetrically large. Staurolite, biotite and muscovite are never seen included in garnet. Where present, inclusions in garnet can form linear trails which are usually slightly oblique to the external matrix fabric. These observations suggest garnet growth initiated early in the crystallisation history of this assemblage. Staurolite occurs as coarse (~4 mm) euhedral grains which are commonly twinned and comprise about 15% of the rock. It has an XFe of about 0.77-0.79. Biotite, ilmenite and quartz are common inclusions in staurolite which on occasion can be poikiloblastic. Staurolite growth appears to have begun late in the crystallisation history as individual examples are deformed and are observed to be wrapped by the matrix fabric however other examples clearly overprint the fabric. Biotite occurs as both fine laths and as coarser (2-3 mm) grains disseminated throughout

the matrix, however there is no systematic chemical variation between the two forms which have an XFe of 0.40-0.41. Occasionally biotite is observed with tiny radiation haloes surrounding inclusions of allanite. Muscovite comprises the bulk of the rock, occurring as fine grained laths with a paragonite content of about 0.26-0.29 and AlVI of 1.84-1.86. Quartz is present mainly as small anhedral grains filling voids between the larger ferro-magnesian phases. Ilmenite is present as inclusions in garnet, staurolite and biotite, and throughout the rock as a minor matrix phase. No chlorite is observed in this rock.

WK 71

Another strongly foliated metapelite from the Winnecke area, this rock is generally finer grained than WK182. Again garnet is present as coarse (~5 mm) euhedral porphyroblasts which are wrapped by the fabric, defined by the phyllosilicate phases. The garnet is dominantly almandine but with a significant spessartine component. It is strongly zoned with 51% almandine at the core increasing to 66% at the rim, lesser spessartine (33% core to 15% rim) and minor pyrope (9% core to 13% rim) and grossular (7% core to 5% rim). The XFe ranges between 0.83-0.85. In this rock the major ferro-magnesian phases are less prevalent and garnet defines only about 8% of the rock, with staurolite comprising about 10% and biotite about 20%. Garnet has volumetrically few inclusions, and these are ubiquitously ilmenite which define linear trails oblique to the matrix foliation. Staurolite occurs as coarse (~3 mm) euhedral to subhedral grains which are commonly twinned and contain poikiloblastic cores rich with ilmenite and quartz inclusions. It has an XFe of about 0.77 to 0.78. As observed in WK182, garnet growth appears to begin early in the crystallisation history while staurolite is observed both overprinting and being wrapped by the foliation. Biotite is present as small laths throughout the matrix and as inclusions in staurolite, and as coarser (~ 2-3 mm) grains in contact with staurolite and garnet and disseminated throughout the matrix. There is no apparent chemical distinction between biotite forms which have an XFe of about 0.38-0.40 and an AlVI of about 0.34-0.37. Individual coarser biotite grains can contain tiny inclusions of allanite. Muscovite has a paragonite content of about 0.28-0.30, and AlVI is 1.85-1.86. It dominates the matrix and along with biotite defines the foliation, comprising about 50% of the total rock. Muscovite occurs mainly as fine grained laths in the matrix but in some isolated domains, as randomly oriented fine laths which form part of a retrograde assemblage with magnetite and chlorite. Minor chlorite occurs as small laths in conjunction with retrograde muscovite and has an XFe of about 0.34. It grows in conjunction with magnetite at the expense of staurolite. Quartz is present as a minor phase forming about 5% of the rock either as void filling anhedral grains as part of the peak assemblage or as part of the retrograde assemblage domains of dynamically recrystallised quartz with numerous sub-grain boundaries approaching a granoblastic texture. Ilmenite is present as inclusions in garnet and staurolite, and throughout the rock as a minor matrix phase.

A1.2.2 Petrographic descriptions of calcic pelites from the Cadney Metamorphics

CM 19

In hand specimen this rock has a gneissic appearance, with the fabric defined by 4-5 mm scale compositional layering with quartzofeldspathic and biotite rich domains. However in section the fabric is seen to be defined strongly by the preferred orientation of biotite and fine grained to fibrolitic sillimanite. Garnet accounts for about 5% of the rock and appears to be essentially syntectonic. Present as 2-3mm euhedral to subhedral porphyroblasts, garnet contains numerous inclusions of quartz, kyanite, sillimanite ilmenite and biotite. In most instances, kyanite is the predominant aluminosilicate inclusion in the garnet cores and is generally randomly oriented along with any other phases present, however the fabric defined by fine grained sillimanite and minor kyanite can be seen extending directly from the matrix into th outer margins of the garnet. There is no apparent break in garnet growth between these sets of inclusions. Garnet has some compositional zoning with rim compositions of $alm_{60}py_{13}sps_{20}gr_8$ and core compositions of $alm_{60}py_{20}sps_{13}gr_7$, while XFe values of 0.82 at the rim decrease to 0.75 at the core. Biotite forms about 25% of the rock and although concentrated in biotite rich layers, it is disseminated throughout the rock as medium grained laths. This form of biotite is chemically homogeneous with an XFe of 0.42-0.44 and Al_{VI} of 0.35-0.37. Very fine grained biotite is also present growing in conjunction with fine grained sillimanite in randomly oriented masses which may possibly represent pseudomorphs of an earlier phase and is not observed in contact with garnet. Plagioclase is present as subhedral moderate to coarse (2-3mm) grains generally concentrated in quartzofeldspathic rich layers. It is observed in contact with all other phases and constitutes about 25% of the rock. It commonly appears with fibrolitic sillimanite growing on its boundaries and/or reacting to form fibrolite plus very fine grained quartz and plagioclase which can appear myrmekitic. Primary plagioclase core compositions are approximately $ab_{50}an_{50}$ but can have either endmember greater by up to 1%. Plagioclase rims however are always more albitic at about $ab_{52}an_{48}$. Kyanite (~10%) is present as fine grained poikiloblasts included in garnet and throughout the matrix. It appears in contact with sillimanite and can often form part of the sillimanite rich domains, however it tends to be most abundant in low strain domains. Kyanite is interpreted as crystallising ealier than sillimanite as it is more common as inclusions in the interior of garnets, however there is no clear evidence of a hierarchy of growth. Sillmanite is more prevalent than kyanite (~15%)

present as fine grained prisms and fibrolite in sillimanite rich layers generally adjacent to and within biotite rich domains. It is also observed as coarser prisms up to 1mm in length. Quartz forms about 20% of the rock most abundantly in the quartzofeldspathic domains. It generally occurs as medium subhedral grains throughout the matrix but can also be observed in myremkite or as very fine grains in association with plagioclase and sometimes fibrolite growing at the expense of primary plagioclase. Rare muscovite (<1%) is seen adjacent to garnet and ilmenite. It has Al_{VI} of 0.75-0.77 and a very low paragonite content at about 0.08-0.09.

CM 20

CM20 is a strongly foliated calcic metapelitic schist where biotite, as the dominant mineral forming about 45% of the rock, and fine grained to fibrolitic sillimanite (~10%) define the schistose fabric. In this rock garnet (~5%) occurs as coarse (up to 10mm) subhedral to euhedral porphyroblasts which appear to be syntectonic. Although the foliation is perturbed by the garnet and coarser biotite is observed growing in the pressure shadows of garnet, this fabric does not appear strongly developed and kyanite, ilmenite, plagioclase and biotite inclusions are observed to be randomly oriented in garnet suggesting that it may have initiated growth early in the rock's crystallisation history, rather than being porphyroclastic. Garnet rim compositions are $alm_{59}py_{23}sps_{10}gr_8$ with core compositions of $alm_{55}py_{19}sps_{18}gr_8$. XFe values of 0.71at the rim increase to 0.74 at the core. Kyanite (~10%) occurs as moderate to coarse (up to 2mm) poikiloblastic blades disseminated throughout the rock, although it is more concentrated in quartzofeldspathic rich domains. Sillimanite (~15%) is present as fibrolitic to fine grained prisms and also as less common coarse prisms to 2mm in length. These coarser grains often appear to incorporate an impurity which can be seen as pleochroic pink to colourless cores. Massed fine grained sillmanite tends to form thin layers and is commonly associated with biotite rich domains in the rock. Kyanite and sillimanite appear to coexist contemporaneously and are observed in contact, although sillimanite is interpreted to begin growth later than kyanite since sillimanite isn't observed as inclusions in garnet. Fibrolitic sillmanite is also occassionally observed growing in random orientations and the sillimanite fabric can be occassionally be observed deflecting around coarser kyanite. Biotite occurs as fine to moderate sized laths and chemically is quite homogeneous with an XFe of 0.40-0.43 and Al_{VI} of 0.34-0.37. Plagioclase (~15%) generally occurs as moderate to coarse (2mm) subhedral grains disseminated throughout the matrix and can be wrapped by the biotite fabric. The chemistry of plagioclase is strongly influenced by it's proximity to garnet, with rims adjacent to garnet recording higher albitic compositions at ab_{57} an_{43} than rim analysis not adjacent to garnet at $ab_{47}an_{52}$. Core analyses are also variable depending on proximity to garnet but generally have approximately equivalent albite and anorthite values, ranging from $ab_{51}an_{49}$ to $ab_{48}an_{52}$. As observed in CM19 plagioclase appears to be reacting to myrmekite and fibrolite, although this texture is less well developed than in the that sample. Quartz occurs as a fine grained matrix phase and in narrow quartz rich domains.

A1.2.3. Petrographic descriptions of metapelites from Pinacles Bore

PB 10

A coarse grained metapelitic rock sampled from a shear zone in the Pinnacles Bore area, PB10 has only a moderately developed foliation due to the fairly low proportions of phyllosilicate minerals. This fabric wraps coarse (2-5 mm) euhedral porphyroblastic garnet but is also occasionally overprinted by garnet, which forms about 5% of the rock. It is predominantly almandine garnet (62% core to 69% rim) with a large spessartine component (18% core to 11% rim) and lesser pyrope (11% core to 14% rim) and grossular (9% core to 6% rim). XFe of garnet ranges from 0.82-0.85. Inclusions within garnet are generally ilmenite or very tiny allanite and apatite visible only with an electron microprobe. Included phases are not volumetrically large and do not define any fabric. Staurolite occurs as coarse (3-4 mm) euhedral to subhedral grains which can be twinned. While some grains are euhedral and appear to overgrow the fabric, others are broken and deformed. It is the most abundant phase, comprising about 50% of the rock. Staurolite has an XFe of about 0.77-0.79, and has numerous inclusions of ilmenite, magnetite and quartz, plus lesser amounts of biotite and tourmaline. These observations suggest garnet and staurolite are syn-tectonic and have been present throughout the development of this equilibrium assemblage. Biotite occurs mainly as coarse (2-3 mm) grains but also as fine grained laths disseminated throughout the matrix. It forms about 15% of the rock and is the major fabric defining phase. While there is no systematic chemical variation between the two forms of biotite or within individual grains, some chemical distinction is possible on the basis of proximity to garnet and staurolite. Biotite which is in contact with garnet only has the higher XFe at about 0.46-0.49, while those in contact with both staurolite and garnet have an XFe of 0.39-0.44 and those in contact with neither have an XFe of 0.43. Small quartz inclusions can be found in biotite and occasionally tiny radiation haloes surrounding inclusions of allanite are seen. Muscovite comprises only about 7% of the rock, occurring as fine to medium grained laths with a paragonite content of about 0.17-0.20 and Al_{VI} of 1.80-1.83. Along with biotite it defines the rock fabric, commonly in biotite-muscovite rich domains. It can also occur intergrown with chlorite as part of a retrograde assemblage. Quartz forms about 23% of the rock and is present mainly as medium to coarse anhedral grains filling voids between

the other phases. Quartz grains are generally deformed with serriate boundaries and well-developed sub-grain boundaries. They commonly contain numerous inclusions of muscovite, biotite, apatite and tourmaline. Ilmenite and magnetite are present as inclusions in garnet, staurolite, biotite, and quartz and throughout the rock as minor matrix phases. Chlorite is present as a minor phase forming part of a retrograde assemblage. It is usually observed filling voids between broken staurolite grains or individual staurolite grains or between staurolite and garnet, suggesting its growing at the expense of these minerals.

PB 215

Together, muscovite (about 45%) and biotite (about 20%) constitute the bulk of this rock and thus this metapelitic schist is more strongly foliated than sample PB10. Garnet is also more prevalent, at about 10% of the rock, occurring as medium grained (2-3 mm) euhedral porphyroblasts which are wrapped by the fabric. The garnet is strongly zoned with 59% almandine at the core increasing to 66% at the rim, spessartine at 22% at the core down to 10% at the rim, minor pyrope at 6.9% core up to 16% rim and grossular 7% at the core to 8% at the rim. The XFe ranges between 0.88 at the core down to 0.80 at the rim. Garnet has very few inclusions, and these are ubiquitously fine grained ilmenite which occasionally define linear trails slightly oblique to the matrix foliation. Staurolite occurs as coarse (~3 mm) euhedral to subhedral prisms which are often twinned and can contain ilmenite, magnetite, quartz and rare biotite inclusions, often resulting in a poikiloblastic appearance. It has an XFe of about 0.79 to 0.80. As observed in some of the Winnecke samples, in PB215 garnet growth appears to begin early in the crystallisation history while staurolite is observed both overprinting and being wrapped by the foliation. Biotite is present as small laths throughout the matrix, as rare inclusions in staurolite, and as coarser (~ 2 mm) grains disseminated throughout the rock. There is no apparent chemical distinction between biotite forms which have an XFe however chemistry does vary depending on the adjacent minerals. As noted in PB10, biotites adjacent to garnet have slightly higher XFe values (0.42-0.44) than those adjacent to garnet and staurolite (0.40-0.42) and those not in contact with either of these phases (XFe of 0.43). Biotite grains can contain muscovite, magnetite and ilmenite inclusions and rare tiny inclusions of allanite. Muscovite occurs mainly as fine grained laths in the matrix with a paragonite content of about 0.19-0.21, and Al^{VI} is 1.80-1.83 but in some isolated areas it is also present as randomly oriented fine laths which form part of a retrograde assemblage with chlorite. Rare chlorite occurs as small laths in conjunction with retrograde muscovite and has an XFe of about 0.40. It is usually seen growing at the expense of staurolite. Quartz forms about 10% of the rock either as void filling anhedral grains or as domains of quartz ribbons. It is commonly deformed with serriate boundaries and extensive sub-grain boundary development. Ilmenite and magnetite are present as inclusions, and throughout the rock as minor matrix phases.

A1.2.4 Petrographic descriptions of calcic metapelites from Pinnacles Bore

PB 11

This calcium bearing pelitic rock was sampled from the same shear zone as sample PB10, but by comparison has a much more weakly developed fabric due to the lower proportion of phyllosilicate minerals. In this rock the fabric is predominantly defined by the preferred orientation of elongate minerals such as biotite, staurolite and kyanite and deformed elongate plagioclase and quartz, but also by ~ 5mm-10mm scale compositional layering of quartz and plagioclase rich domains compared with ferro-magnesian mineral rich domains. Garnet forms about 15% of this rock and is generally confined to thin layers which are also rich in staurolite, kyanite and biotite. It occurs as moderate (~2mm) subhedral grains with occasional inclusions of quartz and ilmenite and rare biotite. The relationship between garnet and fabric development is not clear cut as the fabric is weak and does not conclusively wrap any of the coarser phases, however evidence can be found for garnet perturbing the orientation of biotite in particular. Garnet is predominantly almandine (70% rim to 68% core) with a significant pyrope component (18% rim to 22% core) and lesser spessartine (7% rim to 6% core) and grossular (6% rim to 4% core). While there is no conclusive evidence for two stage garnet growth such as highly included cores and clean rims or marked abrupt changes in the chemistry across grains, some individuals do appear to have minor overgrowth rims. Kyanite forms about 10% of the rock, occurring as coarse 2-4mm subhedral poikiloblastic blades commonly with quartz and ilmenite inclusions. Blades of kyanite are often observed to be deformed and bent, however they can also lie randomly oriented with respect to the fabric particularly in low strain areas. Staurolite constitutes about 7% of the rock occurring as moderate to coarse (2-3mm) anhedral to subhedral poikiloblasts with quartz and ilmenite inclusions. It has a lower XFe at 0.76 to 0.78, than garnet rims at 0.80 although garnet cores can be as low as 0.76. Staurolite, kyanite and garnet are all seen in contact with each other and the matrix phases of biotite, quartz and plagioclase. Biotite is the only mica present and forms only about 12% of the rock, predominantly as medium grained laths disseminated throughout the matrix and more sparsely through the quartzofeldspathic rich domains. Chemically it appears fairly homogeneous with an XFe of 0.35-0.37 and an Al^{VI} of 0.37 to 0.39. Quartz (~35%) and plagioclase (~20%) together constitute the bulk of the rock. They are observed forming quartz-feldspar rich domains within the rock and as matrix phases in the ferro-magnesian rich domains. Plagioclase is predominantly albitic (0.70 at cores to 0.80 at rims) and occurs as medium to coarse grains, generally deformed with their elongate axis parallel to the foliation.

However in low strain areas they are often coarser grained (to 1mm) and equigranular with triple point boundaries. In the ferro-magnesian rich domains, quartz occurs as a void filling mineral between other grain boundaries, and is generally fine to medium grained and sub- to anhedral. In the quartz rich domains it appears to have undergone some dynamic recrystallisation with finer subhedral grains annealing to form coarse (~2mm) anhedral grains with pronounced subgrain boundaries and serriate edges. Rare tiny fibrolite can also be observed in this rock growing in random orientation on plagioclase and garnet.

PB 12

This calcic metapelite is similar to PB11 but has a slightly greater abundance of biotite imparting a more schistose appearance due to a more strongly defined foliation. Again the fabric is predominantly defined by the preferred orietation of biotite and elongate plagioclase and quartz and to a lesser extent staurolite and kyanite. Due to the relatively low proportion of biotite however, relationships between fabric developement and the coarser phases such as garnet, kyanite and staurolite are often ambiguous. Some compositional layering is present with quartzofeldspathic rich versus ferro-magnesian mineral rich domains on the ~ 5mm scale observed, however the layering is less well defined than that in PB11 and doesnt impart a gneissic texture. Garnet is prevalent forming about 20% of the rock as subhedral to anhedral grains ranging up to about 2 mm in size. They are mainly almandine (68% rim to 70% core) garnets, with lesser pyrope (21% rim to 19% core), spessartine (6% rim to 7% core) and grossular (5% rim to 3% core). The XFe of the garnets vary from 0.76 at the rim to 0.78 at the core. The timing of garnet development is difficult to establish conclusively but it appears to be an early phase. Inclusions are not common in the garnet but examples of quartz, ilmenite and rare biotite are observed, and in areas of greater biotite proportion, the fabric can be seen to deflect about garnet. Kyanite, present as 2-4mm long poikiloblastic and occassionally embayed blades, are often seen to be bent and growing about garnet grains. Quartz and biotite occur as inclusions within kyanite but staurolite is never seen within kyanite. Staurolite occurs as coarse subhedral to anhedral poikiloblastic and embayed grains up to 3mm long with common inclusions of quartz and ilmenite. It has an XFe of about 0.75-0.77. Again the relationship of staurolite growth to fabric development is unclear, however it is seen to grow around kyanite and garnet suggesting it develops later in the crystallisation history. Biotite is present as fine to moderate sized laths, often with ilmenite inclusions, and defines the schistosity in the rock. Biotite rim and core analyses are generally consistent with XFe values of about 0.38-0.39, however occassionally analyses immediately adjacent to garnet have higher $Fe3^{+}$ values, and consequently lower XFe values of about 0.32-0.34, suggesting fine scale exchange with local garnet rims. Plagioclase is the only feldpar present. It is predominantly albitic (0.76 rims to 0.62 cores) forming moderate suhedral grains with their elongate axis parallel to the fabric. It is particularly abundant in the quartzofeldspathic domains. Quartz occurs as a void filling matrix phase in the ferro-magnesian rich domains and as moderate sized deformed and elongated grains in the quartzofeldspathic rich domains. Occassionally coarser quartz grains are observed where smaller grains in the quartz rich domains are annealing and which themselves are approching a granoblastic texture with plagioclase. Minor chlorite is present as retrograde mineral growing at the expense of staurolite, observed as fine grained laths randomly oriented with respect to the foliation. While the major rock forming minerals all appear in contact with each other without evidence of disequilibrium, the observations made above suggest a hierarchy of growth with garnet developing early, followed by growth of kyanite and then staurolite. Biotite, quartz and plagioclase appear to have grown throughout.

PBS 3

PBS3 differs from in PB11 and PB12 in its lack of staurolite and more felsic composition, and finer grained appearance. In this rock quartz (~45%) and plagioclase (~15%) are the dominant minerals and the fabric is defined mainly by the preferred orientation of biotite and the development of ~ 5mm scale compositional layering, similar to that observed in the other calcic metapelites. Garnet is again almandine (67% rim to 68% core) with subordinate pyrope (18% rim to 23% core) and minor spessartine (9% rim to 5% core) and grossular (10% rim to 3% core), with an XFe of 0.78 at the rim to 0.74 at the core. It composes about 15% of the rock, occuring as euhedral to subhedral grains up to 1mm with rare quartz and biotite inclusions. Kyanite is present as fine grained euhedral crystals or subhedral blades up to 1mm in length. Kyanite forms about 10% of the rock and tends to be concentrated within narrow garnet- kyanite- and biotite-rich layers. Biotite, forming 15% of the rock, is the predominant fabric forming mineral occurring as fine grained laths with an XFe of 0.32-0.34. Although also concentrated in layers, it is more widely disseminated through the rock than garnet and kyanite. Plagioclase (Ab_{72} at the rim to Ab_{63} at the core) occurs as fine to moderate subhedral grains throughout the rock, with the elongate axis of grains oriented parallel to the foliation. Quartz is observed as highly deformed fine to moderate grains with serriate edges and sub grain boundaries. It is present throughout the rock but often forms quartz fibbons and is the dominant mineral in the quartzofeldspathic domains. All the minerals present are observed in intimate association and there are no reaction textures or other disequilibrium features, suggesting these minerals constitute an equilibrium assemblage.

A1.2.5. Petrographic descriptions of mafic schists from the Yambah Schist Zone

YS 9

YS 9 is a mafic schist with the classic amphibolite assemblage of garnet-hornblende-plagioclase-quartz. Garnet comprises about 10% of the rock, as small to moderate euhedral grains up to 2mm in size. It is often inclusion free but can contain significant quartz inclusions as well as lesser ilmenite and rare allanite. Hornblende is present as subhedral elongate 1-2mm laths and is the main fabric defining phase, along with well developed quartz ribbons. It forms about 40% of the rock proportionally, and commonly contains quartz and ilmenite and allanite inclusions which have radiation damage haloes. Although staurolite is not observed in this sample, there are small domains of quartz and plagioclase which have inclusions on tiny hornblende scattered through them. These may be equivalent to the corroded relic staurolite seen in other samples such as YS148. Plagioclase (20% of the rock) and quartz (25%) are fine to moderate grained and generally have a granoblastic texture aside from those areas which host the relic hornblende, which tend to be anhedral.

YS 10

This coarse grained chlorite-biotite-garnet schist was sampled about 30 metres along strike from the garnet bearing amphibolites, adjacent to a calc silicate unit. Its has an unusual mineralogy compared to all other lithologies in the Schist Zone and as its contacts with adjacent units are obscured such that in the field its precursor is not obvious. Garnet in this rock occurs as large (to 12mm) euhedral porphyroblasts often with perfect crystal faces, forming about 30% of the rock. It is dominantly almandine (70% rim to 67% core) and pyrope (23% rim to 18% core) with minor spessartine (1% rim to 9% core) and grossular (5% rim to 8% core) and an XFe of 0.75 at the rim to 0.79 in cores. Within the garnet are numerous ilmenite, quartz, allanite, clinozoisite and zoisite inclusions which indicate that the rock is derived from a mafic precursor. These inclusions commonly define curved inclusion trails in the garnet and the matrix fabric wraps the porphyrobalsts, suggesting garnet is pre- to syntectonic. Small zircon inclusions are also found in garnet but are concentrated toward the rims, suggesting late growth of this phase. Chlorite is the dominant phase in the rock, comprising about 40% of the rock, and along with biotite, at about 25% of the rock, defines the strong fabric. It is classified as repidolite with an XFe of 0.26 to 0.30. Chlorite and biotite are intimately intergrown, occurring as medium to coarse grained laths. Biotite has an XFe of 0.27 to 0.32 and an octahedral Al value of 0.30-0.34. Quartz is a minor component of the rock at about 2%. It occurs in the matrix as medium to coarse subhedral grains with ilmenite, biotite and chlorite inclusions. Ilmenite is also a minor mineral comprising to 3% of the rock, occurring as either medium subhedral equigranular grains or fine needle-like grains throughout the matrix and as inclusions in garnet. As observed in the other mafic rocks from Yambah allanite is an abundant accessory phase throughout the matrix, along with lesser monazite/zircon?, zoisite and clinozoisite. The unique mineralogy and abundance of late monazite suggests that this rock has experienced significant metasomatism.

YS 147

This mafic amphibolite is texturally very different to YS9, YS148 and YS149 being finer grained and considerably more quartzofeldspathic in composition. Garnets (about 5% of the rock) are small (to 1mm) euhedral grains with very few quartz and ilmenite inclusions and often have perfect crystal faces. They are chemically zoned with rims of 67% almandine, 23% pyrope, 2% spessartine and 7% grossular with an XFe of 0.74 to cores of 65% almandine, 22% pyrope, 3% spessartine and 9% grossular with XFe of 0.75. It is seen in contact with all other phases including staurolite (proportionally about 7%) which is observed as fine (to 1mm) euhedral to subhedral prisms, oriented parallel to the schistose fabric, with minor quartz inclusions. Staurolite is chemically homogeneous with an XFe of 0.69-0.70. There is no evidence of disequilibrium or the reaction textures observed in other samples involving staurolite. The fabric is defined by the preferred orientation of elongate fine grained hornblende (25%) and well developed quartz ribbons. Hornblende is classified as alumino-tschermakite according to Leake, (1978) with an Al_{VI} of 1.04-1.07 and XMg of 0.60 to 0.62. The bulk of the rock is comprised of plagioclase (28%) and quartz (35%) which tend to form a fine grained equigranular matrix (apart from the quartz ribbon domains), and approach a granoblastic polygonal texture. Plagioclase is also chemically zoned ranging from an_{85} at the rim to an_{90} in the core. Allanite inclusions in hornblende and is some staurolite are observed but this mineral is less abundant in this rock than in most of the other Yambah samples.

YS 148

In this staurolite and garnet bearing mafic amphibolite, garnet forms about 15% of the rock, occuring as coarse (to 4mm) subhedral grains rich with included quartz which can produce a poikiloblastic and somewhat amoeboid appearance. Other included phase are ilmenite and rarer allanite. Garnet is chemically zoned and predominantly almandine (68% rim to 66% core) with lesser pyrope (21% rim to 18% at the core) and minor spessartine (2% rim to 3% core) and grossular (9% rim to 12% core), the XFe ranges from

0.77 to 0.79. Comprising about 30% of the rock, hornblende is observed as moderate to coarse subhedral elongate grains defining the schistose fabric, or as anhedral grains extending along grain boundaries between quartz and plagioclase producing a shapeless poikiloblastic appearance. It is has numerous allanite and quartz inclusions. The chemistry of hornblende classifies it as alumino-tschermakite, with an Al_{VI} of 1.10-1.15 and XMg of 0.54 to 0.58. Staurolite is a minor component at about 10%, occuring as anhedral poikiloblastic grains up to 2mm in size, with numerous quartz inclusions and lesser hornblende and ilmenite inclusions. It has a homogeneous composition with an XFe of 0.42 to 0.45. Although staurolite, hornblende and garnet are seen in contact without evidence of disequilibrium, there are areas where relic corroded staurolite is separated from hornblende by domains of quartz and plagioclase. Here minor plagioclase appears to be growing at the expense of staurolite as tiny remnants of staurolite can occur within plagioclase. Inclusion-free plagioclase occurs throughout the rock often in association with quartz as moderate subhedral to equigranular grains. It forms about 10% of the rock, and along with quartz (about 35%) tends toward a granoblastic polygonal texture suggesting these phases have undergone some recrystallisation and annealing. Plagioclase is also zoned ranging from an_{85} at rims to an_{90} in cores.

YS149

This mafic amphibolite is has coarse (to 4mm) euhedral garnet porphyroblasts (about 15% of the rock) with numerous quartz inclusion producing a poikiloblastic appearance. It commonly has perfect crystal faces and appears to be syntectonic but late with respect to fabric development, as it can contain rare hornblende and ilmenite inclusions, but also appears to overprint the hornblende fabric which does not deflect around it. Also, in some instances quartz inclusions within garnet are elongate and are oriented parallel to the external matrix fabric. Garnet compositions vary across the grains from $alm_{67}py_{19}sp_{2}gr_{10}$ with an XFe of 0.78 at the rims to $alm_{65}py_{21}sp_{4}gr_{11}$ and an XFe of 0.77 at the core. Hornblende is the dominant mineral comprising about 45% of the rock proportionally. It occurs as moderate to coarse elongate grains which defined the well developed schistosity. With an Al_{VI} of 0.86-0.90 and an XMg of 0.58 to 0.60, it plots across the boundary of tschermakite to tshermakitic hornblende in the nomenclature of Leake (1978). Hornblende is commonly included with quartz and ilmenite, and lesser apatite and allanite which is often surrounded by a halo from radiation damage. Quartz forms about 35% of the rock occurring as moderate void filling anhedral grains or, in quartz rich domains, as low strain equigranular and polygonal grains suggesting some degree of recrystallisaion and annealing. No plagioclase is observed in this sample.

Appendix 2

MINERAL CHEMISTRY

This appendix contains representative mineral chemistry analyses for samples used in thermobarometric and petrogenetic calculations. Analyses were erformed on a Cameca SX51 Electron Microprobe at CEMMSA, University of Adelaide, using an acceleration voltage of 15kV. Analyses have been recalculated using the AX computer program of Holland and Powell, (1998).

A 2.1 Plagioclase-absent metapelitic schists from the Pinnacles Bore Shear Zone.

Sample	PB215	core analyses										
Mineral	g	g	g	st	st	st	bi	bi	bi	mu	mu	mu
SiO2	36.25	36.66	36.8	27.42	27.39	27.86	36.46	36.55	35.8	48.09	48.11	48.08
TiO2	0.17	0.08	0.06	0.54	0.49	0.5	1.12	1.3	1.21	0.42	0.42	0.43
Al2O3	19.75	20.63	20.51	51.88	51.74	54.26	18.08	18.3	17.99	34.74	34.51	34.97
Cr2O3	0.02	0	0.01	0.04	0.08	0.06	0.05	0.03	0.02	0.02	0.01	0.02
FeO	25.70	27.43	30.63	14.33	14.62	12.17	15.58	16.7	15.46	2.42	2.52	2.36
MnO	10.97	9.37	5.41	0.26	0.23	0.25	0.08	0.07	0.07	0.01	0.01	0
MgO	1.87	2.27	3.32	2.21	2.04	1.77	12.87	12.02	12.48	0.61	0.65	0.58
CaO	3.48	3.21	2.88	0.01	0	0	0.05	0.07	0.06	0.01	0.02	0.01
Na2O	0.02	0	0	0	0	0	0.33	0.29	0.39	1.42	1.42	1.41
K2O	0	0.01	0.01	0	0.01	0.03	8.62	7.83	8.66	8.57	8.56	8.58
Totals	98.23	99.66	99.63	96.69	96.6	96.9	94.25	93.17	93.49	96.32	96.24	96.45
Oxygens	12	12	12	46	46	46	11	11	11	11	11	11
Si	2.992	2.973	2.967	7.74	7.75	7.742	2.745	2.772	2.728	3.147	3.152	3.141
Ti	0.011	0.005	0.004	0.115	0.104	0.104	0.063	0.074	0.069	0.021	0.021	0.021
Al	1.922	1.972	1.95	17.266	17.259	17.775	1.605	1.636	1.616	2.68	2.666	2.693
Cr	0.001	0	0.001	0.009	0.018	0.013	0.003	0.002	0.002	0.001	0.001	0.001
Fe3	0.074	0.073	0.125	0	0	0	0.09	0.059	0.077	0.004	0.006	0.002
Fe2	1.692	1.779	1.927	3.383	3.46	2.828	0.944	0.993	0.985	0.128	0.132	0.127
Mn	0.767	0.644	0.37	0.062	0.055	0.059	0.005	0.004	0.005	0.001	0.001	0
Mg	0.23	0.274	0.399	0.93	0.86	0.733	1.444	1.358	1.417	0.059	0.063	0.056
Ca	0.308	0.279	0.249	0.003	0	0	0.004	0.006	0.005	0.001	0.001	0.001
Na	0.003	0	0	0	0	0	0.048	0.043	0.058	0.18	0.18	0.179
K	0	0.001	0.001	0	0.004	0.011	0.829	0.758	0.843	0.716	0.716	0.716
Sum	8	8	7.992	29.508	29.509	29.265	7.781	7.706	7.805	6.938	6.939	6.937

Sample	PB215	rim analyses										
Mineral	g	g	g	st	st	st	bi	bi	bi	mu	mu	ilm
SiO2	36.86	36.62	36.96	27.66	28.13	27.84	36.15	36.81	37.26	48.71	47.77	0.07
TiO2	0.04	0.05	0.03	0.44	0.48	0.51	1.29	1.31	1.29	0.34	0.44	42.54
Al2O3	20.32	20.77	20.86	52.69	52.86	54.05	17.82	18.27	18.76	34.63	35.21	0.04
Cr2O3	0	0.02	0.01	0.04	0.01	0.05	0.06	0.02	0.01	0.01	0.01	17.39
FeO	30.97	31.53	30.18	13.75	14.29	12.4	16.84	16.03	16.22	1.96	2.28	36.31
MnO	5.21	4.52	5.01	0.27	0.27	0.22	0.03	0.07	0.05	0.02	0	1.21
MgO	3.44	3.37	3.54	1.94	1.74	1.77	12.43	11.86	11.96	0.74	0.5	0.43
CaO	2.93	2.85	3.04	0	0	0.01	0.07	0.06	0.07	0.02	0.01	0.03
Na2O	0	0	0	0	0	0	0.36	0.28	0.31	1.26	1.55	0
K2O	0.02	0	0.01	0.01	0.02	0.02	8.18	7.87	8.09	8.25	8.68	0
Totals	99.79	99.73	99.64	96.8	97.8	96.87	93.23	93.4	94.03	96.62	96.46	98.02
Oxygens	12	12	12	46	46	46	11	11	11	11	11	3
Si	2.963	2.946	2.968	7.766	7.83	7.747	2.744	2.785	2.795	3.167	3.124	0.002
Ti	0.002	0.003	0.002	0.093	0.1	0.107	0.074	0.075	0.073	0.017	0.022	0.828
Al	1.926	1.97	1.975	17.441	17.347	17.732	1.595	1.63	1.659	2.654	2.715	0.001
Cr	0	0.001	0.001	0.009	0.002	0.011	0.004	0.001	0.001	0.001	0.001	0.001
Fe3	0.198	0.13	0.085	0	0	0	0.11	0.051	0	0.033	0	0.338
Fe2	1.862	1.991	1.942	3.229	3.327	2.886	0.966	1.009	1.018	0.106	0.125	0.786
Mn	0.355	0.308	0.341	0.064	0.064	0.052	0.002	0.004	0.003	0.001	0	0.027
Mg	0.412	0.404	0.424	0.812	0.722	0.734	1.406	1.338	1.337	0.072	0.049	0.017
Ca	0.252	0.246	0.262	0	0	0.003	0.006	0.005	0.006	0.001	0.001	0.001
Na	0	0	0	0	0	0	0.053	0.041	0.045	0.159	0.197	0
K	0.002	0	0.001	0.004	0.007	0.007	0.793	0.761	0.775	0.685	0.725	0
Sum	7.973	8	8	29.418	29.399	29.278	7.751	7.7	7.712	6.895	6.957	2

Sample	PB10	rim analyses										
Mineral	g	g	g	st	st	st	bi	bi	bi	mu	mu	mu
SiO2	37.02	36.91	36.89	27.82	28.15	27.60	36.22	37.20	36.59	46.2	46.62	45.99
TiO2	0.02	0.02	0.05	0.58	0.65	0.5	1.51	2.25	1.8	0.32	0.22	0.33
Al2O3	20.74	20.94	20.74	52.68	53.22	52.33	19.27	18.99	18.94	34.48	34.54	34.18
Cr2O3	0	0.01	0.02	0.03	0.05	0.02	0.04	0.04	0.03	0.03	0.03	0.04
FeO	31.8	29.98	29.97	13.4	13.24	13.97	16.2	15.88	16.24	2.54	2.67	2.81
MnO	4.91	4.68	5.91	0.31	0.31	0.29	0.07	0.08	0.09	0.01	0.01	0.03
MgO	3.35	3.3	3.25	2.12	2.03	2.26	11.96	11.88	11.99	0.63	0.54	0.71
CaO	2.15	3.53	3.15	0.01	0.01	0.01	0.08	0.03	0.04	0.01	0.02	0.01
Na2O	0.02	0.07	0.02	0.01	0.01	0.02	0.4	0.41	0.4	1.45	1.5	1.46
K2O	0.01	0	0	0.01	0.01	0.01	8.69	8.66	8.62	9.32	9.27	9.34
Totals	100.02	99.44	100.00	96.97	97.68	97.01	94.45	95.43	94.75	95	95.43	94.91
Oxygens	12	12	12	46	46	46	11	11	11	11	11	11
Si	2.974	2.968	2.959	7.786	7.808	7.749	2.723	2.757	2.739	3.093	3.106	3.089
Ti	0.001	0.001	0.003	0.122	0.136	0.106	0.085	0.125	0.101	0.016	0.011	0.017
Al	1.964	1.985	1.962	17.382	17.403	17.32	1.708	1.659	1.672	2.721	2.713	2.706
Cr	0	0.001	0.001	0.007	0.011	0.004	0.002	0.002	0.002	0.002	0.002	0.002
Fe3	0.09	0.087	0.115	0	0	0	0.007	0	0.01	0	0	0
Fe2	2.047	1.929	1.895	3.136	3.071	3.28	1.011	0.984	1.006	0.142	0.149	0.158
Mn	0.334	0.319	0.402	0.073	0.073	0.069	0.004	0.005	0.006	0.001	0.001	0.002
Mg	0.401	0.395	0.389	0.884	0.839	0.946	1.34	1.312	1.338	0.063	0.054	0.071
Ca	0.185	0.304	0.271	0.003	0.003	0.003	0.006	0.002	0.003	0.001	0.001	0.001
Na	0.003	0.011	0.003	0.005	0.005	0.011	0.058	0.059	0.058	0.188	0.194	0.19
K	0.001	0	0	0.004	0.004	0.004	0.834	0.82	0.824	0.797	0.789	0.801
Sum	8	8	8	29.402	29.353	29.491	7.78	7.726	7.759	7.023	7.017	7.036

Sample	PB10	core analyses									
Min	g	g	bi	bi	bi	st	st	st	mu	mu	mu
SiO2	37.06	37.03	36.48	36.89	36.55	27.63	28.15	27.45	46.16	45.48	46.32
TiO2	0.06	0.07	1.5	1.39	1.54	0.49	0.46	0.43	0.31	0.35	0.33
Al2O3	19.81	20.68	18.83	19.37	18.75	52.57	53.23	52.26	34.96	34.53	34.87
Cr2O3	0.03	0	0.04	0.03	0.03	0	0	0.04	0.03	0.06	0.02
FeO	29.13	29.32	16.74	15.58	15.99	14.13	13.5	14.38	2.22	2.49	2.53
MnO	7.02	7.47	0.05	0.05	0.07	0.39	0.31	0.31	0	0.01	0.03
MgO	2.91	2.87	12.23	12.65	12.36	2.23	2.11	2.3	0.6	0.59	0.56
CaO	2.92	3	0.06	0.03	0.04	0.01	0	0.02	0.01	0	0.03
Na2O	0.07	0.07	0.34	0.44	0.4	0	0	0.01	1.45	1.42	1.56
K2O	0.02	0.01	8.61	8.74	8.42	0	0.02	0.02	9.18	9.22	9.15
Totals	99.03	100.52	94.89	95.18	94.15	97.45	97.78	97.22	94.93	94.16	95.41
Oxygens	12	12	11	11	11	46	46	46	11	11	11
Si	2.962	2.964	2.733	2.739	2.744	7.729	7.808	7.71	3.083	3.072	3.085
Ti	0.002	0.004	0.085	0.078	0.087	0.103	0.096	0.091	0.016	0.018	0.017
Al	1.919	1.951	1.663	1.696	1.659	17.337	17.407	17.305	2.753	2.75	2.738
Cr	0	0	0.002	0.002	0.002	0	0	0.009	0.002	0.003	0.001
Fe3	0.165	0.124	0.016	0.005	0.021	0	0	0	0	0	0
Fe2	1.837	1.838	1.031	0.962	0.993	3.306	3.132	3.378	0.124	0.141	0.141
Mn	0.489	0.506	0.003	0.003	0.004	0.092	0.073	0.074	0	0.001	0.002
Mg	0.356	0.342	1.366	1.4	1.383	0.93	0.872	0.963	0.06	0.059	0.056
Ca	0.257	0.257	0.005	0.002	0.003	0.003	0	0.006	0.001	0	0.002
Na	0.011	0.011	0.049	0.063	0.058	0	0	0.005	0.188	0.186	0.201
K	0.002	0.001	0.824	0.829	0.807	0	0.007	0.007	0.783	0.795	0.778
Sum	8	8	7.778	7.778	7.761	29.5	29.396	29.548	7.009	7.024	7.019

A 2.2 Plagioclase-bearing metapelitic schists from the Pinnacles Bore Shear Zone.

Sample	PB11	rim analyses											
Mineral	g	g	g	fsp	fsp	fsp	st	st	st	bi	bi	bi	ilhem
SiO2	37.7	37.52	36.74	64.38	66.81	60.69	27.96	28.68	28.23	37.11	37.33	37.56	2.35
TiO2	0	0.02	0.02	0.01	0	0.03	0.61	0.58	0.63	1.41	1.63	1.86	56.6
Al2O3	20.63	20.96	21	23.07	20.64	23.5	52.79	52.9	52.69	18.42	17.98	17.54	0.88
Cr2O3	0.01	0	0.01	0.04	0	0.02	0.07	0.06	0.08	0.05	0.07	0.09	0
FeO	31.85	32.86	32.24	0.19	0.26	0.42	13.16	13.44	12.88	13.54	14.36	14.62	32.39
MnO	3.51	3.19	3.46	0.02	0	0	0.18	0.19	0.18	0.02	0.03	0.04	0.51
MgO	3.92	4.06	4.17	0	0.04	0.11	2.3	2.18	2.42	13.59	13.52	13.44	0.24
CaO	1.87	1.97	1.56	4.73	1.79	5.67	0.01	0	0.02	0.09	0.06	0.03	0.13
Na2O	0.02	0.07	0.03	8.49	8.88	7.42	0.04	0.07	0.01	0.52	0.51	0.5	0.07
K2O	0.04	0.02	0	0.05	1.11	0.21	0.01	0.01	0.01	8.36	8.47	8.58	0.2
Totals	99.55	100.67	99.38	100.98	99.53	98.07	97.13	98.11	97.15	93.82	93.97	94.27	93.37
Oxygens	12	12	12	8	8	8	46	46	46	11	11	11	3
Si	3.028	2.983	2.958	2.812	2.941	2.742	7.799	7.92	7.858	2.77	2.788	2.803	0.059
Ti	0	0.001	0.001	0	0	0.001	0.128	0.12	0.132	0.079	0.092	0.104	1.068
Al	1.954	1.964	1.993	1.188	1.071	1.252	17.359	17.222	17.292	1.621	1.583	1.543	0.026
Cr	0.001	0	0.001	0.001	0	0.001	0.015	0.013	0.018	0.003	0.004	0.005	0
Fe3	0	0.081	0.092	0.006	0.008	0.014	0	0	0	0.049	0.025	0.009	0
Fe2	2.14	2.095	2.079	0	0	0	3.07	3.104	2.999	0.834	0.869	0.903	0.679
Mn	0.239	0.215	0.236	0.001	0	0	0.043	0.044	0.042	0.001	0.002	0.003	0.011
Mg	0.469	0.481	0.5	0	0.003	0.007	0.956	0.897	1.004	1.512	1.505	1.495	0.009
Ca	0.161	0.168	0.135	0.221	0.084	0.275	0.003	0	0.006	0.007	0.005	0.002	0.003
Na	0.003	0.011	0.005	0.719	0.758	0.65	0.022	0.037	0.005	0.075	0.074	0.072	0.003
K	0.004	0.002	0	0.003	0.062	0.012	0.004	0.004	0.004	0.797	0.808	0.818	0.006
Sum	7.998	8	8	4.951	4.929	4.954	29.398	29.362	29.36	7.75	7.755	7.758	1.865

Samples	PB11	core analysis										
Mineral	g	g	g	bi	bi	bi	st	st	st	fsp	fsp	fsp
SiO2	37.02	37.37	38.01	37.34	37.45	38.05	27.32	27.52	28.67	60.39	60.52	60.44
TiO2	0.05	0.01	0.02	1.63	1.74	1.02	0.63	0.59	0.71	0	0	0
Al2O3	21.14	20.96	21.00	17.98	18.07	18.08	52.55	52.71	52.78	24.08	23.73	23.9
Cr2O3	0.09	0.04	0	0.07	0.02	0.11	0.09	0.05	0.13	0	0	0
FeO	31.89	31.79	30.9	14.85	13.74	13.75	14.24	14.17	12.51	0.01	0.06	0.06
MnO	3.08	2.81	2.66	0.03	0.04	0.1	0.2	0.21	0.16	0.05	0.01	0.01
MgO	5.32	5.26	5.18	13.52	13.55	14.43	2.3	2.37	2.46	0	0	0
CaO	1.23	1.66	2.18	0.06	0.05	0	0	0	0.01	5.88	6.03	6.02
Na2O	0.01	0.03	0.03	0.51	0.58	0.56	0	0.02	0.01	7.84	7.85	7.7
K2O	0.01	0.02	0.25	8.47	9.02	8.52	0.01	0	0	0.06	0.02	0.02
Totals	99.84	99.95	100.23	93.97	94.27	94.63	97.34	97.64	97.44	98.31	98.22	98.15
	12	12	12	11	11	11	46	46	46	8	8	8
Si	2.944	2.973	3.001	2.789	2.791	2.813	7.657	7.683	7.936	2.724	2.733	2.73
Ti	0.003	0.001	0.001	0.092	0.098	0.057	0.133	0.124	0.148	0	0	0
Al	1.982	1.966	1.955	1.583	1.588	1.576	17.363	17.348	17.224	1.281	1.263	1.272
Cr	0.006	0.003	0	0.004	0.001	0.006	0.02	0.011	0.028	0	0	0
Fe3	0.122	0.091	0.069	0.025	0	0	0	0	0	0	0.002	0.002
Fe2	1.999	2.006	1.971	0.868	0.856	0.85	3.338	3.308	2.896	0	0	0
Mn	0.207	0.189	0.178	0.002	0.003	0.006	0.047	0.05	0.038	0.002	0	0
Mg	0.63	0.624	0.61	1.505	1.505	1.59	0.961	0.986	1.015	0	0	0
Ca	0.105	0.142	0.185	0.005	0.004	0	0	0	0.003	0.284	0.292	0.291
Na	0.002	0.005	0.004	0.074	0.084	0.08	0	0.011	0.005	0.686	0.687	0.674
K	0.001	0.002	0.025	0.808	0.859	0.804	0.004	0	0	0.003	0.001	0.001
Sum	8	8	8	7.754	7.788	7.782	29.521	29.52	29.293	4.98	4.979	4.971

Sample	PB11 interior analyses		
Mineral	g	g	g
SiO2	37.87	37.21	37.64
TiO2	0.01	0.02	0.02
Al2O3	21.08	20.68	20.87
Cr2O3	0.01	0.06	0.01
FeO	32.11	32.55	32.4
MnO	2.82	2.83	2.92
MgO	4.7	5.32	5.02
CaO	1.69	1.1	1.38
Na2O	0	0	0.01
K2O	0.01	0	0.01
Totals	100.44	99.97	100.41
	12	12	12
Si	3.003	2.966	2.986
Ti	0.001	0.001	0.001
Al	1.971	1.943	1.952
Cr	0.001	0.004	0.001
Fe3	0.023	0.12	0.075
Fe2	2.113	2.05	2.075
Mn	0.189	0.191	0.196
Mg	0.555	0.632	0.594
Ca	0.144	0.094	0.117
Na	0	0	0.002
K	0.001	0	0.001
Sum	8	8	8

Sample	PB12	core analyses				
Mineral	g	g	bi	bi	fsp	fsp
SiO2	37.6	37.61	37.39	37.63	60.52	62.37
TiO2	0.04	0.02	1.25	1.57	0	0.01
Al2O3	21.22	20.98	18.01	18.03	22.99	23.14
Cr2O3	0.04	0	0.04	0.08	0	0.02
FeO	32.20	32.30	14.87	14.3	0.09	0.21
MnO	2.84	3.1	0.04	0.06	0.01	0
MgO	5.34	4.89	13.15	13.11	0	0.01
CaO	1.27	1.36	0.01	0.02	5.64	4.94
Na2O	0	0.02	0.51	0.5	7.83	8.39
K2O	0.01	0.01	8.56	8.52	0.04	0.05
Totals	100.57	100.29	93.84	93.83	97.12	99.14
	12	12	11	11	8	8
Si	2.971	2.988	2.806	2.814	2.759	2.781
Ti	0.002	0.001	0.071	0.088	0	0
Al	1.977	1.965	1.593	1.59	1.236	1.216
Cr	0.002	0	0.002	0.005	0	0.001
Fe3	0.075	0.062	0	0	0.003	0.007
Fe2	2.045	2.077	0.933	0.894	0	0
Mn	0.19	0.209	0.003	0.004	0	0
Mg	0.629	0.579	1.471	1.461	0	0.001
Ca	0.108	0.116	0.001	0.002	0.276	0.236
Na	0	0.003	0.074	0.073	0.692	0.725
K	0.001	0.001	0.82	0.814	0.002	0.003
Sum	8	8	7.773	7.744	4.969	4.971

Sample	PB12	rim analyses										
Mineral	g	g	g	st	st	st	bi	bi	bi	fsp	fsp	fsp
SiO2	37.41	37.74	37.71	28.07	28.08	28.09	37.3	37.65	37.86	60.39	61.36	61.42
TiO2	0	0.02	0	0.59	0.55	0.52	1.53	1.54	1.82	0.11	0.01	0
Al2O3	20.84	20.66	20.88	53.03	53.1	53.17	18.08	18.05	17.70	21.40	23.75	23.07
Cr2O3	0	0	0	0.03	0.04	0.05	0.07	0.1	0.09	0	0	0.01
FeO	30.55	31.95	31.64	13.7	13.42	13.15	14.64	14.31	14.93	1.91	0.28	0.18
MnO	2.99	3.03	3.19	0.19	0.2	0.21	0.05	0.05	0.07	0	0.02	0.02
MgO	4.58	4.08	4.33	2.35	2.39	2.42	13.59	13.6	13.77	1.2	0	0
CaO1.88		1.83	1.99	0	0.01	0.01	0.01	0	0.02	3.81	5.4	5.46
Na2O	0.04	0.07	0	0	0.01	0.01	0.46	0.46	0.44	7.3	8.04	7.87
K2O	0	0.18	0	0	0.01	0.01	8.43	8.58	8.23	0.9	0.04	0.12
Totals	98.29	99.56	100.19	97.96	97.81	97.64	94.17	94.44	94.94	97.02	98.9	98.15
	12	12	12	46	46	46	11	11	11	8	8	8
Si	3.02	3.026	3.004	7.779	7.785	7.791	2.781	2.799	2.795	2.755	2.747	2.769
Ti	0	0.001	0	0.123	0.115	0.108	0.086	0.086	0.101	0.004	0	0
Al	1.984	1.953	1.961	17.329	17.356	17.385	1.589	1.582	1.54	1.17	1.254	1.226
Cr	0	0	0	0.007	0.009	0.011	0.004	0.006	0.005	0	0	0
Fe3	0	0.022	0.03	0	0	0	0.041	0.006	0.072	0.067	0.009	0.006
Fe2	2.063	2.118	2.105	3.176	3.112	3.05	0.867	0.889	0.841	0	0	0
Mn	0.204	0.206	0.215	0.045	0.047	0.049	0.003	0.003	0.004	0	0.001	0.001
Mg	0.551	0.488	0.514	0.972	0.988	1	1.51	1.507	1.515	0.083	0	0
Ca	0.163	0.157	0.17	0	0.003	0.003	0.001	0	0.002	0.189	0.259	0.264
Na	0.006	0.011	0	0	0.005	0.005	0.066	0.066	0.063	0.657	0.698	0.688
K	0	0.018	0	0	0.004	0.004	0.803	0.815	0.776	0.053	0.002	0.007
Sum	7.991	8	8	29.43	29.422	29.407	7.751	7.759	7.715	4.978	4.971	4.962

Sample	PB12	interior analyses	
Mineral	g	g	g
SiO2	37.46	37.74	37.21
TiO2	0.01	0	0.01
Al2O3	20.92	20.88	20.78
Cr2O3	0	0	0.05
FeO	31.53	31.71	32.54
MnO	2.72	2.74	2.81
MgO	5.29	5.09	4.92
CaO	1.2	1.48	1.65
Na2O	0.02	0.01	0.02
K2O	0.03	0.01	0.01
Totals	99.17	99.66	100
	12	12	12
Si	2.997	3.008	2.967
Ti	0.001	0	0.001
Al	1.973	1.962	1.953
Cr	0	0	0.003
Fe3	0.038	0.024	0.113
Fe2	2.067	2.087	2.044
Mn	0.184	0.185	0.19
Mg	0.631	0.605	0.585
Ca	0.103	0.126	0.141
Na	0.003	0.002	0.003
K	0.003	0.001	0.001
Sum	8	8	8

Sample	PBS3	interior analyses		
Mineral	g	g	g	g
SiO2	37.32	37.22	37.54	37.36
TiO2	0.01	0	0.03	0.01
Al2O3	20.95	20.7	20.74	20.8
Cr2O3	0.01	0	0	0
FeO	31.16	32.00	31.75	31.64
MnO	2.2	2.37	1.98	2.18
MgO	5.51	5.78	4.89	5.39
CaO	1.98	1.13	2.55	1.89
Na2O	0.06	0	0	0.02
K2O	0	0	0.01	0
Totals	99.2	99.2	99.47	99.29
	12	12	12	12
Si	2.977	2.975	2.997	2.983
Ti	0.001	0	0.002	0.001
Al	1.97	1.951	1.952	1.958
Cr	0	0	0	0
Fe3	0.083	0.098	0.05	0.077
Fe2	1.986	2.03	2.064	2.027
Mn	0.149	0.16	0.134	0.148
Mg	0.655	0.688	0.581	0.642
Ca	0.169	0.097	0.218	0.161
Na	0.009	0	0	0.003
K	0	0	0.001	0
Sum	8	8	8	8

Sample	PBS3	rim analyses								
Mineral	g	g	g	bi	bi	bi	bi	fsp	fsp	fsp
SiO2	37.91	38.05	37.54	38.18	38.15	38.68	37.97	60.94	60.63	60.38
TiO2	0.02	0.02	0.02	1.32	1.36	1.21	1.23	0	0	0.01
Al2O3	21.09	21.32	20.93	17.42	17.33	18.21	17.25	22.71	24.55	23.66
Cr2O3	0.04	0.03	0.02	0	0	0	0	0.02	0.01	0.02
FeO	32.15	31.7	31.9	13.31	13.47	13.82	13.99	0.67	0.13	0.31
MnO	2.08	2.15	2.61	0.03	0.01	0.01	0.04	0.04	0	0.01
MgO	4.56	4.57	4.34	14.99	15.23	14.67	15.1	0.02	0.02	0.03
CaO	2.66	2.61	2.61	0.02	0.04	0.01	0.03	5.55	6.85	6.29
Na2O	0	0	0	0.42	0.38	0.41	0.42	7.99	7.36	7.32
K2O	0	0	0.01	8.5	8.58	8.57	8.72	0.06	0.05	0.36
Totals	100.28	100.46	100.08	95.19	94.58	95.6	94.74	98.00	99.6	98.38
	12	12	12	11	11	11	11	8	8	8
Si	3.005	3.007	2.993	2.805	2.815	2.824	2.806	2.76	2.704	2.728
Ti	0.001	0.001	0.001	0.073	0.075	0.066	0.068	0	0	0
Al	1.971	1.987	1.967	1.509	1.508	1.567	1.502	1.213	1.291	1.26
Cr	0.002	0.002	0.001	0	0	0	0	0.001	0	0.001
Fe3	0.013	0	0.025	0.075	0.042	0	0.062	0.023	0.004	0.01
Fe2	2.103	2.096	2.106	0.796	0.785	0.843	0.796	0	0	0
Mn	0.139	0.144	0.176	0.002	0.001	0.001	0.002	0.002	0	0.001
Mg	0.539	0.539	0.515	1.641	1.675	1.596	1.663	0.001	0.002	0.002
Ca	0.226	0.221	0.223	0.002	0.004	0.001	0.002	0.27	0.327	0.305
Na	0	0	0	0.059	0.055	0.058	0.06	0.702	0.637	0.641
K	0	0	0.001	0.797	0.809	0.799	0.823	0.004	0.003	0.021
Sum	8	7.997	8.009	7.758	7.767	7.755	7.784	4.974	4.968	4.967

Sample	PBS3	core analyses							
Mineral	g	g	bi	bi	bi	fsp	fsp	fsp	fsp
SiO2	37.84	37.74	38.78	38.21	38.41	59.64	59.75	59.99	59.19
TiO2	0.02	0.02	1.15	1.32	1.42	0.01	0.02	0.02	0
Al2O3	21.23	21.17	18.24	17.72	17.49	24.37	24.51	24.14	24.47
Cr2O3	0.03	0.01	0.02	0.01	0	0	0	0	0.01
FeO	31.39	32.09	13.91	14.11	13.89	0.17	0.28	0.11	0.11
MnO	2.49	2.41	0.02	0.02	0.03	0.02	0.01	0.05	0
MgO	5.94	5.9	15.11	15.12	15.19	0	0	0.01	0
CaO	1.15	1.3	0.01	0.02	0.01	6.97	6.95	6.98	6.98
Na2O	0	0	0.45	0.38	0.35	7.22	7.23	7.32	7.1
K2O	0	0	8.4	8.45	8.67	0.18	0.03	0.48	0.03
Totals	100.09	100.64	96.09	95.36	95.46	98.59	98.77	99.09	97.89
	12	12	11	11	11	8	8	8	8
Si	2.988	2.97	2.809	2.798	2.811	2.693	2.69	2.7	2.688
Ti	0.001	0.001	0.063	0.073	0.078	0	0.001	0.001	0
Al	1.977	1.964	1.558	1.53	1.509	1.297	1.301	1.281	1.31
Cr	0.002	0.001	0.001	0.001	0	0	0	0	0
Fe3	0.042	0.093	0.056	0.064	0.051	0.006	0.009	0.004	0.004
Fe2	2.027	2.009	0.781	0.793	0.793	0	0	0	0
Mn	0.167	0.161	0.001	0.001	0.002	0.001	0	0.002	0
Mg	0.699	0.692	1.631	1.65	1.656	0	0	0	0
Ca	0.097	0.11	0.001	0.002	0.001	0.337	0.335	0.337	0.34
Na	0	0	0.063	0.054	0.05	0.632	0.631	0.639	0.625
K	0	0	0.777	0.79	0.811	0.01	0.002	0.028	0.001
Sum	8	8	7.741	7.754	7.762	4.976	4.969	4.991	4.968

A 2.3 Plagioclase-absent metapelitic schists from the Winnecke area.

Sample	WK182 core analyses									
Mineral	g	g	g	st	st	bi	bi	bi	mu	mu
SiO2	36.46	36.27	36.80	27.90	28.21	37.22	36.47	36.46	48.21	47.13
TiO2	0.02	0.07	0.1	0.47	0.48	1.28	1.36	1.39	0.29	0.29
Al2O3	20.46	20.41	20.56	52.61	52.52	17.98	17.69	17.61	35.29	35.14
Cr2O3	0.04	0	0.02	0.04	0.04	0	0	0	0.02	0.02
FeO	27.95	28.47	24.34	14.34	14.37	16.08	16.33	15.91	2.36	2.26
MnO	9.32	8.85	12.61	0.39	0.32	0.12	0.11	0.15	0.01	0.01
MgO	2.93	2.99	2.3	2.21	2.34	13.05	13.08	12.93	0.59	0.59
CaO	2.24	2.4	2.26	0	0	0.01	0	0.02	0.01	0
Na2O	0.06	0	0.1	0.01	0	0.42	0.41	0.37	1.97	2.01
K2O	0	0	0	0.01	0.01	8.8	8.99	8.92	7.83	7.94
Totals	99.48	99.46	99.09	97.98	98.29	94.97	94.45	93.77	96.55	95.4
	12	12	12	46	46	11	11	11	11	11
Si	2.953	2.939	2.999	7.768	7.824	2.78	2.75	2.766	3.137	3.111
Ti	0.001	0.004	0.006	0.098	0.1	0.072	0.077	0.079	0.014	0.014
Al	1.953	1.95	1.975	17.268	17.174	1.584	1.572	1.575	2.707	2.734
Cr	0.003	0	0.001	0.009	0.009	0	0	0	0.001	0.001
Fe3	0.145	0.163	0.029	0	0	0.01	0.049	0.013	0.002	0
Fe2	1.748	1.766	1.626	3.339	3.333	0.993	0.975	0.995	0.124	0.125
Mn	0.639	0.607	0.87	0.092	0.075	0.008	0.007	0.01	0.001	0.001
Mg	0.354	0.361	0.279	0.917	0.967	1.453	1.47	1.462	0.057	0.058
Ca	0.194	0.209	0.197	0	0	0.001	0	0.002	0.001	0
Na	0.009	0	0.016	0.005	0	0.061	0.06	0.054	0.249	0.257
K	0	0	0	0.004	0.004	0.84	0.866	0.864	0.651	0.669
Sum	8	8	8	29.5	29.486	7.801	7.825	7.82	6.943	6.97

Sample	WK182 rim analyses											
Mineral	g	g	g	st	st	st	bi	bi	bi	mu	mu	mu
SiO2	37.26	37.55	36.66	27.89	28.23	28.17	36.68	36.95	36.90	47.17	48.52	48.97
TiO2	0.04	0.04	0.04	0.48	0.53	0.51	1.32	1.35	1.37	0.26	0.29	0.3
Al2O3	20.88	20.64	20.67	52.77	52.77	52.74	17.71	17.85	17.91	35.55	35.13	35.61
Cr2O3	0	0.03	0	0.05	0	0.02	0	0.02	0.02	0	0.02	0.02
FeO	30.94	29.03	30.01	14.18	14.16	14.12	15.42	15.41	15.3	1.99	2.27	2.32
MnO	5.87	6.38	6.29	0.36	0.35	0.34	0.09	0.08	0.1	0.03	0.01	0.02
MgO	3.38	3.5	3.53	2.21	2.28	2.27	13.02	12.95	13.12	0.56	0.58	0.61
CaO	2.16	2.63	2.33	0	0.01	0.01	0	0.02	0.03	0	0	0.01
Na2O	0.05	0.06	0.06	0	0	0	0.36	0.35	0.33	2.09	1.94	1.97
K2O	0	0.01	0.03	0.01	0.01	0.01	9.08	8.58	8.52	7.96	7.74	7.81
Totals	100.58	99.87	99.62	97.95	98.34	98.19	93.69	93.57	93.61	95.62	96.51	97.65
	12	12	12	46	46	46	11	11	11	11	11	11
Si	2.975	3.011	2.951	7.759	7.817	7.811	2.779	2.791	2.783	3.103	3.154	3.147
Ti	0.002	0.002	0.002	0.1	0.11	0.106	0.075	0.077	0.078	0.013	0.014	0.014
Al	1.965	1.951	1.961	17.308	17.226	17.241	1.582	1.59	1.593	2.757	2.692	2.698
Cr	0	0.002	0	0.011	0	0.004	0	0.001	0.001	0	0.001	0.001
Fe3	0.088	0.032	0.145	0	0	0	0	0	0.011	0	0	0
Fe2	1.978	1.915	1.875	3.299	3.279	3.274	0.977	0.974	0.953	0.109	0.123	0.125
Mn	0.397	0.433	0.429	0.085	0.082	0.08	0.006	0.005	0.006	0.002	0.001	0.001
Mg	0.402	0.418	0.423	0.916	0.941	0.938	1.47	1.458	1.475	0.055	0.056	0.058
Ca	0.185	0.226	0.201	0	0.003	0.003	0	0.002	0.002	0	0	0.001
Na	0.008	0.009	0.009	0	0	0	0.053	0.051	0.048	0.267	0.245	0.245
K	0	0.001	0.003	0.004	0.004	0.004	0.879	0.828	0.821	0.669	0.643	0.641
Sum	8	8	8	29.483	29.462	29.462	7.821	7.776	7.771	6.974	6.929	6.932

Sample	WK71	rim analyses										
Mineral	g	g	g	bi	bi	bi	st	st	st	mu	mu	mu
SiO2	37.29	37.21	37.15	36.61	37.15	37.32	27.96	28.00	27.83	47.51	47.66	47.5
TiO2	0.02	0.01	0.02	1.46	1.45	1.45	0.51	0.51	0.49	0.17	0.23	0.29
Al2O3	20.76	20.73	20.75	18.14	19.24	19.07	52.6	52.6	52.37	35.5	35.6	35.35
Cr2O3	0.01	0.01	0.01	0.02	0.06	0.04	0.1	0.1	0.05	0.01	0.04	0.02
FeO	28.04	29.55	29.79	15.52	14.94	14.89	13.48	13.48	13.76	2.25	2.48	2.25
MnO	7.34	6.15	6.84	0.08	0.05	0.06	0.33	0.33	0.36		0.01	0.02
MgO	3.34	3.42	3.38	12.84	12.84	12.85	2.23	2.23	2.26	0.56	0.61	0.6
CaO	2.28	1.95	2.11	0.08	0.04	0.05	0.01	0.01	0.01	0	0.02	0
Na2O	0.01	0.01	0.02	0.35	0.4	0.39	0	0	0	2.05	2.08	1.99
K2O	0.01	0.01	0.01	8.15	8.08	8.38	0.01	0	0	7.75	7.83	7.7
				93.25		94.5						
Totals	99.10	99.05	100.08	93.26	94.26	94.51	97.23	97.26	97.13	95.81	96.57	95.72
	12	12	12	11	11	11	46	46	46	11	11	11
Si	3.007	3.012	3.009	2.767	2.764	2.773	7.808	7.816	7.794	3.116	3.107	3.117
Ti	0.001	0.001	0.001	0.083	0.081	0.081	0.107	0.107	0.103	0.008	0.011	0.014
Al	1.984	1.978	1.982	1.616	1.688	1.671	17.318	17.31	17.29	2.745	2.736	2.735
Cr	0.001	0.001	0.001	0.001	0.004	0.002	0.022	0.022	0.011	0.001	0.002	0.001
Fe3	0.001	0.005	0.003	0.043	0	0	0	0	0	0	0.011	0.003
Fe2	1.9	1.994	1.947	0.933	0.93	0.925	3.148	3.147	3.223	0.123	0.123	0.119
Mn	0.504	0.422	0.462	0.005	0.003	0.004	0.078	0.078	0.085	0	0.001	0.001
Mg	0.404	0.413	0.408	1.446	1.424	1.423	0.928	0.928	0.943	0.055	0.059	0.059
Ca	0.198	0.169	0.183	0.006	0.003	0.004	0.003	0.003	0.003	0	0.001	0
Na	0	0.002	0	0.051	0.058	0.056	0	0	0	0.261	0.263	0.253
K	0	0.001	0	0.787	0.768	0.795	0.004	0	0	0.649	0.652	0.645
Sum	7.999	7.997	7.997	7.739	7.722	7.735	29.416	29.411	29.452	6.958	6.965	6.948

Sample	WK71	core analyses										
Min	g	g	g	bi	bi	bi	st	st	st	mu	mu	mu
SiO2	36.98	36.56	36.77	36.82	37.33	36.61	27.68	27.94	27.70	47.42	47.47	47.46
TiO2	0.19	0.45	0.42	1.38	1.43	1.46	0.48	0.49	0.48	0.3	0.35	0.27
Al2O3	20.52	20.45	20.48	18.23	18.89	18.14	52.25	52.84	52.15	35.4	35.8	35.79
Cr2O3	0.06	0.07	0.06	0	0.04	0.02	0	0.1	0	0	0.04	0.08
FeO	23.79	23.27	23.08	15.45	15.1	15.52	14.03	13.49	14.03	2.36	2.38	2.49
MnO	12.67	14.35	13.51	0.1	0.03	0.08	0.43	0.36	0.38	0	0	0
MgO	2.53	2.32	2.37	13.29	12.79	12.84	2.28	2.24	2.29	0.59	0.58	0.48
CaO	2.29	2.36	2.32	0.02	0.07	0.08	0	0	0.01	0.01	0.01	0.01
Na2O	0.01	0.01	0.01	0.42	0.35	0.35	0	0	0	1.98	2.13	2.26
K2O	0.02	0.01	0.01	8.68	8.35	8.15	0	0	0	7.77	7.82	7.76
Totals	99.06	99.85	99.03	94.39	94.39	93.25	97.15	97.46	97.04	95.84	96.58	96.61
	12	12	12	11	11	11	46	46	46	11	11	11
Si	3.013	2.995	3.004	2.758	2.78	2.767	7.765	7.784	7.778	3.111	3.094	3.095
Ti	0.006	0.022	0.014	0.078	0.08	0.083	0.101	0.103	0.101	0.015	0.017	0.013
Al	1.971	1.975	1.973	1.61	1.658	1.616	17.28	17.356	17.263	2.738	2.751	2.752
Cr	0.002	0.002	0.002	0	0.002	0.001	0	0.022	0	0	0.002	0.004
Fe3	0	0.004	0.002	0.026	0	0.043	0	0	0	0.007	0.003	0
Fe2	1.621	1.522	1.572	0.938	0.94	0.933	3.292	3.143	3.295	0.121	0.126	0.136
Mn	0.874	0.996	0.935	0.006	0.002	0.005	0.102	0.085	0.09	0	0	0
Mg	0.307	0.271	0.289	1.483	1.419	1.446	0.954	0.931	0.958	0.058	0.056	0.047
Ca	0.2	0.207	0.203	0.002	0.006	0.006	0	0	0.003	0.001	0.001	0.001
Na	0	0.002	0.002	0.061	0.051	0.051	0	0	0	0.252	0.269	0.286
K	0.001	0.001	0.001	0.83	0.794	0.787	0	0	0	0.651	0.651	0.646
Sum	7.995	7.995	7.995	7.792	7.732	7.739	29.494	29.424	29.489	6.953	6.971	6.98

A 2.4 Plagioclase-bearing metapelitic schists from the Cadney Metamorphics.

Sample	CM19	rim analyses										
Mineral	g	g	g	g	fsp	fsp	fsp	fsp	bi	bi	bi	bi
SiO2	37.45	37.18	37.67	37.48	55.74	56.79	56.54	56.9	36.36	36.39	36.76	36.76
TiO2	0	0.02	0	0.04	0.06	0.2	0.06	0.05	1.94	1.93	2.07	1.74
Al2O3	20.79	20.81	20.92	20.95	27.24	26.18	27.14	26.17	18	18.18	17.98	18.08
Cr2O3	0	0.01	0	0.01	0.01	0	0.02	0.02	0.05	0.02	0.05	0.04
FeO	27.49	27.61	27.86	26.74	0.17	0.2	0.22	0.14	16.03	15.95	15.96	16.21
MnO	7.45	7.06	7.13	8.89	0.07	0	0.02	0.03	0.12	0.14	0.16	0.08
MgO	3.67	3.63	3.78	3.31	0	0	0.01	0.01	11.89	11.58	12.43	12.33
CaO	3.1	2.95	3.13	2.91	10.12	9.05	9.95	9.16	0.01	0.02	0.02	0.02
Na2O	0	0	0	0	5.55	6.63	5.52	6.06	0.17	0.18	0.16	0.16
K2O	0	0	0	0.01	0.04	0.06	0.06	0.06	9.21	9.16	9.33	9.18
Totals	99.95	99.27	100.49	100.34	99.00	99.11	99.54	98.6	93.79	93.56	94.93	94.61
	12	12	12	12	8	8	8	8	11	11	11	11
Si	2.994	2.993	2.994	2.993	2.531	2.577	2.532	2.588	2.762	2.768	2.758	2.766
Ti	0	0.001	0	0.002	0	0	0.002	0	0.111	0.11	0.117	0.098
Al	1.96	1.975	1.96	1.972	1.458	1.401	1.459	1.403	1.612	1.63	1.59	1.604
Cr	0	0.001	0	0.001	0	0	0	0	0.003	0.001	0.003	0.002
Fe3	0.051	0.036	0.052	0.037	0.006	0.007	0.008	0.002	0	0	0	0
Fe2	1.787	1.823	1.8	1.749	0	0	0	0	1.018	1.015	1.001	1.02
Mn	0.505	0.481	0.48	0.601	0.003	0	0.001	0	0.008	0.009	0.01	0.005
Mg	0.437	0.435	0.448	0.394	0	0	0.001	0.001	1.346	1.313	1.39	1.383
Ca	0.266	0.255	0.267	0.249	0.492	0.44	0.486	0.446	0.001	0.002	0.002	0.002
Na	0	0	0	0	0.489	0.584	0.488	0.534	0.025	0.027	0.023	0.023
K	0	0	0	0.001	0.002	0.003	0.003	0.003	0.893	0.89	0.894	0.882
Sum	8	8	8	8	4.982	5.012	4.979	4.978	7.779	7.764	7.788	7.785

Sample	CM19	core analyses					
Mineral	g	g	bi	bi	fsp	mu	ilhem
SiO2	37.31	37.61	36.08	36.27	55.61	45.32	0.02
TiO2	0.06	0.01	2.13	1.8	0.07	0.36	12.47
Al2O3	20.44	20.81	17.79	17.86	27.22	32.85	0.15
Cr2O3	0	0.02	0.06	0.04	0	0	0.14
FeO	26.62	28.12	15.75	16.22	0.09	3.56	84.56
MnO	5.84	5.28	0.14	0.09	0	0	0.2
MgO	5.01	5.24	12.05	12.26	0	0.89	0.07
CaO	3.58	2.35	0	0	10.24	0.03	0.03
Na2O	0	0	0.13	0.19	5.36	0.57	0
K2O	0	0.01	9.33	9.27	0.06	9.83	0
Totals	98.86	99.46	93.47	94.01	98.65	93.42	97.64
	12	12	11	11	8	11	3
Si	2.989	2.996	2.752	2.754	2.531	3.098	0.001
Ti	0.004	0.001	0.122	0.103	0.002	0.019	0.252
Al	1.931	1.954	1.6	1.598	1.461	2.648	0.005
Cr	0	0.001	0.004	0.002	0	0	0.003
Fe3	0.083	0.052	0	0	0.003	0.081	1.488
Fe2	1.691	1.816	1.005	1.03	0	0.114	0.244
Mn	0.396	0.356	0.009	0.006	0	0	0.005
Mg	0.598	0.622	1.37	1.387	0	0.091	0.003
Ca	0.308	0.201	0	0	0.499	0.002	0.001
Na	0	0	0.019	0.028	0.473	0.076	0
K	0	0.001	0.909	0.899	0.003	0.858	0
Sum	8	8	7.788	7.807	4.973	6.986	2

Sample	CM20	core analyses								
Mineral	g	g	g	bi	bi	bi	fsp	fsp	fsp	ilhem
SiO2	37.96	38.02	37.77	36.8	36.79	36.74	56.09	58.35	55.30	0.01
TiO2	0	0.02	0.09	1.02	1.77	1.59	0	0.01	0	12.11
Al2O3	21.2	21.18	20.97	17.89	17.68	17.68	27.17	26.18	27.36	0.08
Cr2O3	0	0	0	0	0.02	0.02	0.02	0	0.02	0.09
FeO	28.33	24.9	25.04	16.77	15.38	15.83	0.11	0.12	0.07	78.01
MnO	5.21	8.16	7.93	0.01	0.08	0.08	0.01	0	0	0.04
MgO	4.71	4.89	4.89	12.72	12.85	12.73	0.01	0	0	0.02
CaO	2.83	2.78	2.72	0.03	0.02	0.02	9.97	8.75	10.47	0.02
Na2O	0	0	0	0.2	0.22	0.21	5.63	6.38	5.34	0
K2O	0.01	0	0	8.88	9.03	8.98	0.06	0.05	0.06	0.01
Totals	100.26	99.95	99.68	94.33	93.85	93.89	99.07	99.84	98.62	97.88
	12	12	12	11	11	11	8	8	8	3
Si	3.004	3.011	3.003	2.773	2.779	2.779	2.541	2.612	2.521	0
Ti	0	0.001	0.005	0.058	0.101	0.09	0	0	0	0.244
Al	1.978	1.977	1.966	1.589	1.575	1.576	1.451	1.381	1.47	0.003
Cr	0	0	0	0	0.001	0.001	0.001	0	0.001	0.002
Fe3	0.016	0	0.018	0.067	0	0.009	0.004	0.004	0.002	1.507
Fe2	1.857	1.649	1.663	0.982	0.972	0.991	0	0	0	0.241
Mn	0.349	0.547	0.534	0.001	0.005	0.005	0	0	0	0.001
Mg	0.555	0.577	0.579	1.428	1.447	1.435	0.001	0	0	0.001
Ca	0.24	0.236	0.232	0.002	0.002	0.002	0.484	0.42	0.511	0.001
Na	0	0	0	0.029	0.032	0.031	0.495	0.554	0.472	0
K	0.001	0	0	0.854	0.871	0.867	0.003	0.003	0.003	0
Sum	8	7.999	8	7.784	7.784	7.787	4.98	4.974	4.981	2

Sample	CM20	rim analyses										
Mineral	g	g	g	g	bi	bi	bi	bi	fsp	fsp	fsp	ilhem
SiO2	37.87	37.96	37.82	38.02	37.82	36.69	36.98	37.18	56.05	55.74	56.58	0.01
TiO2	0	0	0	0.08	1.39	1.4	1.51	1.61	0.03	0	0	12.07
Al2O3	21.04	21.2	20.92	20.96	18.14	17.67	17.91	17.87	27.26	27.24	26.6	0.1
Cr2O3	0.02	0	0.01	0	0.01	0.01	0.01	0.03	0.04	0.01	0	0.13
FeO	28.09	28.33	28.33	27.71	15.84	16.30	15.67	15.18	0.01	0.17	0.26	85.1
MnO	5.6	5.21	5.42	5.34	0.09	0.08	0.04	0.11	0	0.07	0.03	0.02
MgO	4.36	4.71	4.55	5.07	13.22	12.61	12.81	12.95	0	0	0	0.01
CaO	2.68	2.83	2.83	3.11	0	0.02	0	0.04	10.07	10.12	9.59	0.04
Na2O	0	0	0	0.01	0.22	0.21	0.19	0.21	5.66	5.55	5.88	0
K2O	0.01	0.01	0.01	0	8.97	8.92	9.05	9.04	0.09	0.04	0.04	0
Totals	99.67	100.26	99.89	100.29	95.71	93.92	94.18	94.23	99.21	98.94	98.98	97.48
	12	12	12	12	11	11	11	11	8	8	8	3
Si	3.018	3.004	3.008	3.001	2.796	2.778	2.784	2.791	2.537	2.531	2.564	0
Ti	0	0	0	0.005	0.077	0.08	0.085	0.091	0.001	0	0	0.244
Al	1.977	1.978	1.962	1.951	1.581	1.578	1.59	1.582	1.455	1.458	1.421	0.003
Cr	0.001	0	0.001	0	0.001	0.001	0.001	0.002	0.001	0	0	0.003
Fe3	0	0.016	0.027	0.038	0	0.019	0	0	0	0.006	0.009	1.505
Fe2	1.872	1.857	1.854	1.786	0.979	1.011	0.987	0.953	0	0	0	0.243
Mn	0.378	0.349	0.365	0.357	0.006	0.005	0.003	0.007	0	0.003	0.001	0
Mg	0.518	0.555	0.539	0.596	1.457	1.423	1.437	1.449	0	0	0	0
Ca	0.229	0.24	0.241	0.263	0	0.002	0	0.003	0.488	0.492	0.466	0.001
Na	0	0	0	0.002	0.032	0.031	0.028	0.031	0.497	0.489	0.517	0
K	0.001	0.001	0.001	0	0.847	0.863	0.87	0.867	0.005	0.002	0.002	0
Sum	7.994	8	7.998	8	7.775	7.79	7.784	7.775	4.985	4.982	4.98	2

A 2.4 Metabasic schists from the Yambah Schist Zone.

Sample	YS147 rim analyses										
Mineral	g	g	g	g	st	st	st	st	hbl	hbl	hbl
SiO2	38.00	37.94	37.89	38.36	27.53	27.56	27.86	27.61	42.35	42.39	42.07
TiO2	0.02	0.02	0	0.03	0.61	0.61	0.55	0.66	0.4	0.4	0.44
Al2O3	21.27	21.28	21.19	21.25	51.78	51.67	51.98	52.14	16.62	16.42	17.18
Cr2O3	0.01	0.09	0	0.01	0.08	0.13	0.16	0	0.1	0	0.06
FeO	30.97	30.66	30.96	30.35	14.56	14.43	13.94	13.94	16.62	16.42	15.7
MnO	1.33	1.34	1.36	1.28	0.06	0.04	0.06	0.14	0.18	0.08	0.11
MgO	6.17	6.05	5.92	5.95	3.35	3.29	3.38	3.47	10.09	10.27	10.01
CaO	2.82	2.65	2.75	2.68	0	0	0.01	0.01	10.19	10.28	10.29
Na2O	0.04	0.02	0	0	0	0	0.04	0	1.57	1.44	1.48
K2O	0	0.01	0	0	0	0.01	0	0.01	0.21	0.16	0.27
Totals	100.63	100.06	100.07	99.91	97.97	97.74	97.98	97.98	98.33	97.86	97.61
	12	12	12	12	46	46	46	46	23	23	23
Si	2.968	2.982	2.981	3.008	7.681	7.703	7.746	7.68	6.207	6.217	6.134
Ti	0.001	0.001	0	0.002	0.128	0.128	0.115	0.138	0.044	0.044	0.048
Al	1.959	1.972	1.965	1.965	17.033	17.026	17.037	17.097	2.872	2.839	2.953
Cr	0.001	0.006	0	0.001	0.018	0.029	0.035	0	0.012	0	0.007
Fe3	0.108	0.061	0.073	0.015	0	0	0	0	0.488	0.515	0.503
Fe2	1.915	1.954	1.964	2.004	3.398	3.373	3.241	3.243	1.373	1.358	1.411
Mn	0.088	0.089	0.091	0.085	0.014	0.009	0.014	0.033	0.022	0.01	0.014
Mg	0.718	0.709	0.694	0.695	1.394	1.37	1.4	1.438	2.204	2.245	2.175
Ca	0.236	0.223	0.232	0.225	0	0	0.003	0.003	1.6	1.615	1.608
Na	0.006	0.003	0	0	0	0	0.022	0	0.446	0.409	0.418
K	0	0.001	0	0	0	0.004	0	0.004	0.039	0.03	0.05
Sum	8	8	8	8	29.666	29.643	29.614	29.636	15.306	15.282	15.321

Sample	YS147 rim analyses					
Mineral	hbl	fsp	fsp	fsp	fsp	ilm
SiO2	41.58	46.04	46.76	46.23	46.16	0.04
TiO2	0.46	0	0	0	0.03	22.12
Al2O3	16.59	34.45	33.71	34.16	34.4	0.11
Cr2O3	0	0	0	0	0.02	0.13
FeO	15.13	0.28	0.12	0.08	0.09	71.09
MnO	0.17	0.01	0.03	0	0	0.23
MgO	9.72	0.07	0.02	0	0.01	0.23
CaO	10.5	17.96	17.33	17.8	17.92	0.01
Na2O	1.57	1.17	1.43	1.26	1.19	0
K2O	0.26	0.02	0.27	0	0.02	0
Totals	95.98	100	99.67	99.53	99.84	93.96
	23	8	8	8	8	3
Si	6.168	2.119	2.157	2.135	2.126	0.001
Ti	0.051	0	0	0	0.001	0.433
Al	2.901	1.869	1.833	1.86	1.868	0.003
Cr	0	0	0	0	0.001	0.003
Fe3	0.489	0.01	0.004	0.003	0.003	1.127
Fe2	1.387	0	0	0	0	0.419
Mn	0.021	0	0.001	0	0	0.005
Mg	2.149	0.005	0.001	0	0.001	0.009
Ca	1.669	0.886	0.856	0.881	0.884	0
Na	0.452	0.104	0.128	0.113	0.106	0
K	0.049	0.001	0.016	0	0.001	0
Sum	15.336	4.994	4.997	4.991	4.991	2

Sample	YS148 rim analyses										
Mineral	g	g	g	g	st	st	st	st	hbl	hbl	hbl
SiO2	37.67	37.62	37.50	37.53	27.13	27.29	27.42	27.19	41.57	40.95	40.81
TiO2	0	0.02	0	0.02	0.75	0.61	0.62	0.7	0.39	0.37	0.41
Al2O3	21.03	21.14	21.18	20.99	52.20	51.64	51.79	51.4	16.91	17.44	16.45
Cr2O3	0	0.07	0.06	0.05	0.13	0.03	0.01	0.02	0	0	0.06
FeO	32.19	31.32	31.15	31.91	14.57	14.06	13.83	14.5	15.82	17.37	16.43
MnO	0.67	0.87	0.71	0.76	0.04	0.02	0.07	0.04	0.05	0.07	0.09
MgO	5.5	5.43	5.93	5.49	2.44	3.1	2.93	3.09	9.64	8.69	9.07
CaO	2.74	3.5	2.69	2.95	0.02	0.01	0	0	10.32	10.68	10.42
Na2O	0.03	0	0.04	0.04	0.03	0	0	0	1.45	1.33	1.36
K2O	0.01	0.02	0	0	0	0.01	0	0.01	0.23	0.32	0.23
Totals	99.84	99.99	99.26	99.74	97.31	96.77	96.67	96.95	96.38	97.22	95.33
	12	12	12	12	46	46	46	46	23	23	23
Si	2.979	2.968	2.971	2.97	7.621	7.689	7.721	7.667	6.145	6.047	6.123
Ti	0	0.001	0	0.001	0.158	0.129	0.131	0.148	0.043	0.041	0.046
Al	1.961	1.966	1.978	1.958	17.287	17.153	17.192	17.088	2.947	3.036	2.91
Cr	0	0.004	0.004	0.003	0.029	0.007	0.002	0.004	0	0	0.007
Fe3	0.086	0.094	0.081	0.102	0	0	0	0	0.509	0.585	0.583
Fe2	2.043	1.972	1.983	2.011	3.423	3.313	3.257	3.42	1.446	1.56	1.479
Mn	0.045	0.058	0.048	0.051	0.01	0.005	0.017	0.01	0.006	0.009	0.011
Mg	0.648	0.638	0.7	0.648	1.021	1.302	1.231	1.299	2.124	1.912	2.028
Ca	0.232	0.296	0.228	0.25	0.006	0.003	0	0	1.634	1.69	1.675
Na	0.005	0	0.006	0.006	0.016	0	0	0	0.416	0.381	0.396
K	0.001	0.002	0	0	0	0.004	0	0.004	0.043	0.06	0.044
Sum	8	8	8	8	29.571	29.604	29.551	29.64	15.314	15.322	15.301

Sample	YS148 rim analyses						
Mineral	hbl	plag	plag	plag	plag	ilm	ilm
SiO2	40.02	46.34	45.6	45.55	45.96	0.77	0.36
TiO2	0.44	0	0	0.03	0	48.97	47.06
Al2O3	17.03	34.03	34.88	34.59	34.44	0.36	0.09
Cr2O3	0	0	0.03	0.01	0.01	0	0
FeO	16.91	0.04	0.08	0.09	0.11	38.86	40.84
MnO	0.02	0.01	0.02	0.03	0	2.02	0.2
MgO	8.71	0.02	0.01	0	0.01	0.17	0.36
CaO	9.86	17.88	18.03	18.04	17.44	0.15	0.18
Na2O	1.41	1.28	1.05	1.08	1.3	0	0
K2O	0.39	0.01	0.03	0.01	0.01	0.01	0.02
		99.61	99.73	99.43	99.28	91.31	89.11
Totals	94.79	99.61	99.73	99.43	99.28	91.31	89.11
	23	8	8	8	8	3	3
Si	6.062	2.139	2.104	2.108	2.126	0.021	0.01
Ti	0.05	0	0	0.001	0	1	0.995
Al	3.041	1.851	1.897	1.888	1.878	0.012	0.003
Cr	0	0	0.001	0	0	0	0
Fe3	0.516	0.002	0.003	0.003	0.004	0	0
Fe2	1.626	0	0	0	0	0.883	0.96
Mn	0.003	0	0.001	0.001	0	0.046	0.005
Mg	1.966	0.001	0.001	0	0.001	0.007	0.015
Ca	1.6	0.884	0.891	0.895	0.864	0.004	0.005
Na	0.414	0.115	0.094	0.097	0.117	0	0
K	0.075	0.001	0.002	0.001	0.001	0	0.001
Sum	15.354	4.993	4.993	4.994	4.991	1.973	1.994

Appendix 3

MINERAL RECALCULATION USING AX AND EXAMPLES OF THERMOCALC OUTPUTS

A3.1. Activity models and recalculation schemes used in the computer program AX.

In order to perform thermobarometric calculations on any given rock sample, the THERMOCALC program (Powell et al, 1998) requires mineral chemistry data from the selected sample to be entered in the form of mineral end member activities. In this thesis, the conversion of mineral analyses in the form of oxide weight percent to activities of mineral end members has been performed using the computer program AX (Holland and Powell, 1998). The AX program also performs standard mineral recalculations and ferric iron estimation. In each mineral output, AX lists the activity-composition models used to recalculate end member activities and the ferric iron treatment adopted, as well as propogating errors from the microprobe data through to the final calculated activities. THERMOCALC and AX can be downloaded from Tim Holland's web site at:

http://www.esc.cam.ac.uk/astaff/holland/index.html

The models used to recalculate the various minerals used in P-T calculations in this thesis are listed below.

Mineral	**Ferric scheme**	**Activity models**
garnet	8 cations for 12 oxygens	2 site mixing + regular solution. Gammas: gr.py = 41.4 - 0.0188T, py.alm = 2.5, py.andr = 73, alm.andr = 60, spss.andr = 60 (kJ)
staurolite	All ferrous	4 site ideal Fe-Mg mixing.
biotite	M1+M2+M3+T = 6.9 for 11 oxygens, Max. Fe^{3+}/Fe^{2+} = 0.15	Al-M1 ordered, site mixing model + macroscopic RS gammas; (ann, phl, east, obi) ωpa=9, ωpe=10, ωpo=3, ωoa=6, ωae=-1, ωoe=10 (kJ). Eugster et al, (1972). *Journal of Petrology*, 13: 147-179.
muscovite	Tet + oct cations = 6.05 for 11 oxygens	Holland & Powell, (1998) model + non ideal mu-cel-fcel -pa interactions
chlorite	10 cations for 14 oxygens. Max. Fe^{3+}/Fe^{2+}= 0.30	Holland, Baker & Powell, (1998). *European Journal of Mineralogy*, 10: 395-406.
plagioclase	All ferric	Holland & Powell, (1992). *American Mineralogist*, 77: 53-61. (model 1, I1 structure)
ilmenite -haematite	2 cations for 3 oxygens	2 site ideal mixing
hornblende	Average of max. & min. constraints. See Holland & Blundy, (1994).	Non-ideal mixing model for Ca-amphiboles. See Holland & Blundy, (1994).

A3.2 Average P and Average PT calculations using THERMOCALC.

```
THERMOCALC v2.6, © Roger Powell and Tim Holland (no copro version)
THERMOCALC v2.6, © Roger Powell and Tim Holland  running at 12.40 on Mon 27
Aug,1999
```

Average P-T

```
calculation type :
     0 = table of thermodynamic data of end-members
     1 = phase diagram calculations
     2 = average pressure-temperature calculations
     3 = calculations on all reactions between end-members
control code  : 2
data filename : suffix to 'th d' : pb11a
reading phase info from this file ...
phl  ann  east  mst  fst  gr  py  alm  spss  an  ab
q  ky  H2O  CO2
output filename : suffix to 'th opb11a' : (nothing input)
(thermodynamic dataset produced at 16.38 on Sat 5 Nov, 1996)

standard default uncertainties on activities ? yes

spss is unnecessary and so is excluded
ab is unnecessary and so is excluded
CO2 is unnecessary and so is excluded
type of rock calculation:
       1 : average P
       2 : average T
       3 : average PT
code : 3

           phl      ann     east      mst      fst      gr      py      alm
    a    0.144   0.0387   0.0321 0.00296   0.3460.000100 0.00640    0.329
 sd(a)  0.0333   0.0153   0.0130 0.00209   0.0692 8.18e-5 0.00382   0.0493

            an       q      ky     H2O
    a    0.453    1.00    1.00
 sd(a)  0.0407       0       0

these data ok ? yes
rock was fluid-bearing ? yes
PT window within which average PT is expected to lie
T low,high ,P low,high :  200 800 2 8
fluid is just H2O ? yes

Reactions must be reasonably linear within the window;
allowed angle change of reaction per kbar (try 1) : 1
reactions :
|0|0|XX|X|0000|0X|000000000000------00000000000000|0X

an independent set of reactions has been calculated

print the independent set of reactions and their thermodynamics ? yes

rock

               phl      ann     east      mst      fst      gr      py      alm
a            0.144   0.0387   0.0321 0.00296   0.3460.000100 0.00640    0.329
sd(a)/a    0.23103  0.39412  0.40426 0.70549  0.20000 0.81839 0.59683  0.15000

               an       q      ky     H2O
a            0.453    1.00    1.00    1.00
sd(a)/a    0.15000       0       0

reactions
1)  6mst + 23gr + 48q = 8py + 69an + 12H2O
2)  6mst + 75an = 25gr + 8py + 96ky + 12H2O
3)  6fst + 23gr + 48q = 8alm + 69an + 12H2O
4)  3phl + 4gr + 12ky = 3east + py + 12an
5)  2phl + ann + 4gr + 12ky = 3east + alm + 12an
```

```
calculations (for x(H2O) = 1.0)
        P(T)   sd(P)       a   sd(a)         b        c     ln_K sd(ln_K)
1        4.1    1.01  802.88   36.22  -3.08585  147.442  151.723   22.409
2        2.5    0.98-1244.37   36.92   3.60918 -163.339 -176.345   24.205
3        2.7    0.96 1467.35   17.80  -3.69154  145.196  154.674   21.548
4        4.3    0.97  252.83    8.17  -0.63080   27.947   17.785    4.033
5        4.5    0.97  205.52    8.20  -0.61684   27.660   23.038    3.977

rock : average PT (for x(H2O) = 1.0)


svd1 ... svd2 ... svd3 ...
Single end-member diagnostic information

avP, avT, sd's, cor, fit are result of doubling the uncertainty on ln a :
a ln a is suspect if any are v different from lsq values.
e* are ln a residuals normalised to ln a uncertainties :
large absolute values, say >2.5, point to suspect info.
hat are the diagonal elements of the hat matrix :
large values, say >0.42, point to influential data.
For 95% confidence, fit (= sd(fit)) < 1.61
however a larger value may be OK - look at the diagnostics!

          avP    sd    avT    sd   cor   fit
     lsq  5.8   2.5    651    55 0.230  2.22

            P  sd(P)      T  sd(T)     cor     fit      e*    hat
     phl 5.75   2.38    657     53   0.218    2.11    0.86   0.03
     ann 5.71   2.43    644     55   0.241    2.15    0.81   0.05
    east 5.48   1.88    654     41   0.223    1.66   -2.34   0.01
     mst 5.73   2.35    644     52   0.234    2.08    1.12   0.03
     fst 5.76   2.64    648     78   0.378    2.22   -0.06   0.39
      gr 7.00   4.17    649     54   0.061    2.17   -0.47   0.74
      py 5.80   2.38    656     53   0.227    2.11   -1.19   0.03
     alm 5.90   2.58    657     69   0.329    2.21   -0.25   0.28
      an 6.18   3.15    650     55   0.150    2.20    0.26   0.22
       q 5.79   2.51    651     55   0.230    2.22       0      0
      ky 5.79   2.51    651     55   0.230    2.22       0      0
     H2O 5.79   2.51    651     55   0.230    2.22       0      0


T = 651¡C, sd = 55,
P = 5.8 kbars, sd = 2.5, cor = 0.230, f = 2.22


more calculations with this rock ? yes


************************************
```

Average P

```
type of rock calculation:
       1 : average P
       2 : average T
       3 : average PT
code : 1

           phl     ann    east     mst     fst      gr      py     alm
     a   0.144  0.0387  0.0321 0.00296  0.3460.000100 0.00640   0.329
 sd(a)  0.0333  0.0153  0.0130 0.00209  0.0692 8.18e-5 0.00382  0.0493

            an       q      ky     H2O
     a   0.453    1.00    1.00
 sd(a)  0.0680       0       0

these data ok ? yes
rock was fluid-bearing ? yes
P window within which average P is expected to lie low,high :  4 7
T range over which average P to be calculated low,high :  500 680
T window : 500 <-> 680¡C :T interval : 20
fluid is just H2O ? yes
```

```
Reactions must be reasonably linear within the window;
allowed angle change of reaction per kbar (try 1) : 1
reactions :
|0|0|X0|00|0|0000|000000|00000000000000000000000000000000|000000XX000000
00000000X0X

an independent set of reactions has been calculated

print the independent set of reactions and their thermodynamics ? yes

rock

              phl     ann    east     mst     fst      gr      py     alm
a           0.144  0.0387  0.0321 0.00296  0.3460.000100 0.00640   0.329
sd(a)/a   0.23103 0.39412 0.40426 0.70549 0.20000 0.81839 0.59683 0.15000

              an       q      ky     H2O
a          0.453    1.00    1.00    1.00
sd(a)/a  0.15000       0       0

reactions
1)  6mst + 23gr + 48q = 8py + 69an + 12H2O
2)  24east + 6fst + 171an = 16phl + 8ann + 57gr + 192ky + 12H2O
3)  8ann + 6mst + 23gr + 48q = 8phl + 8alm + 69an + 12H2O
4)  8east + 6fst + 57an = 8ann + 4mst + 19gr + 64ky + 4H2O
5)  3ann + 4gr + 2py + 12ky = 3east + 3alm + 12an

calculations  at T = 590¡C (for x(H2O) = 1.0)
       P(T)   sd(P)       a   sd(a)         b         c     ln_K sd(ln_K)
1       5.2    1.11  789.32   36.22  -3.07614   148.448   151.723   22.409
2       5.3    1.03-2206.11   74.50   7.89872  -384.219  -357.702   54.343
3       5.2    1.12  415.37   36.54  -2.96984   146.131   193.753   22.229
4       6.1    1.07  -39.74   33.56   2.15422  -128.036  -145.287   18.566
5       5.8    1.18  110.16    8.37  -0.58741    26.995    33.546    4.296

average pressures (for x(H2O) = 1.0)

av P at 500¡C,
av P at 520¡C,
av P at 540¡C,
av P at 560¡C,
av P at 580¡C,
av P at 600¡C,

 diagnostics - svd1 ... svd2 ...

Single end-member diagnostic information

av, sd, fit are result of doubling the uncertainty on ln a :
a ln a is suspect if any are v different from lsq values.
e* are ln a residuals normalised to ln a uncertainties :
large absolute values, say >2.5, point to suspect info.
hat are the diagonal elements of the hat matrix :
large values, say >0.42, point to influential data.
For 95% confidence, fit (= sd(fit)) < 1.54;
however a larger value may be OK - look at the diagnostics!

         av    sd   fit
lsq    5.32  2.27  2.20

             P     sd    fit     e*   hat
     phl   5.26   2.24   2.17   -0.5  0.00
     ann   5.30   2.13   2.07   -1.3  0.00
    east   5.04   1.91   1.84    2.2  0.01
     mst   5.34   2.09   2.03   -1.4  0.00
     fst   5.12   2.13   2.05    1.4  0.01
      gr   6.82   3.79   2.14    0.6  0.72
      py   5.30   2.23   2.17    0.8  0.00
     alm   5.20   2.22   2.14   -0.9  0.01
      an   5.81   2.87   2.18   -0.3  0.22
       q   5.32   2.27   2.20      0     0
```

```
      ky    5.32    2.27    2.20       0      0
     H2O    5.32    2.27    2.20       0      0
av P at 620¡C,
av P at 640¡C,
av P at 660¡C,
av P at 680¡C,


T¡C      500    520    540    560    580    600    620    640    660    680
av P     4.8    4.9    5.0    5.1    5.2    5.3    5.5    5.6    5.8    5.9
sd      3.64   3.31   3.00   2.72   2.47   2.27   2.13   2.09   2.13   2.26
f        4.0    3.6    3.2    2.8    2.5    2.2    2.0    1.9    1.9    2.0


more calculations with this rock ? no
more rock calculations ? no
all done ? yes
```

Appendix 4

THERMOBAROMETRY

Table A4.1. Results of g-bi thermometry calculations on sample PB215.

g-bi	PB215			Geothermometry					
	rim data								
XFe gnt	0.827	0.827	0.827	0.825	0.821	0.819	0.831	0.833	0.828
XFe bi	0.422	0.398	0.434	0.415	0.428	0.432	0.432	0.43	0.422
T (°C)									
H&S	557.9	536.7	573.1	559.5	588.4	598.6	569	565	563.5
P&L	553.5	541.8	566.5	555.3	570.1	575.9	560.4	557.1	556.9
I&M (b)	548.7	545.9	564.2	565.4	598.5	607	575	573.6	571
F&S	554.9	535.7	570.2	557.8	586.9	596.4	569	563	562
PD et al	561.7	539.4	576.9	565.2	592.6	607.7	579.8	571.2	570
K&R	559.1	548.5	567.7	561.6	578.5	583.5	567.3	564.3	563.7
ave	556.0	541.3	569.8	560.8	585.8	594.9	570.1	565.7	564.5

g-bi	PB215			THERMOCALC V2.6					
	rim data								
XFe gnt	0.827	0.827	0.827	0.821	0.819	0.831	0.833	0.828	
XFe bi	0.422	0.398	0.434	0.428	0.432	0.432	0.43	0.422	
Pressure (kbar)	T (°C)								average
5.6	556	541	576	565	607	565	567	569	568
5.9	557	542	578	567	609	567	569	570	570
6.2	559	544	579	569	610	568	571	572	572
6.5	560	545	581	570	612	570	572	574	573
6.8	562	547	582	572	614	572	574	575	575
7.1	564	548	584	573	615	573	575	577	576

g-bi	PB215		Geothermometry	
	core data			
XFe gnt	0.88	0.88	0.825	
XFe bi	0.415	0.422	0.43	0.422
T (°C)				
H&S	450.9	458.3	492.8	485
P&L	484.7	489.4	513	508.2
I&M (b)	467	474.2	504	497
F&S	445.4	453	488.9	481
PD et al	451.7	459.6		
K&R	492.5	497.7	521	515.7
average	465.4	472	502.7	495.9

g-bi	PB215	THERMOCALC V2.6		
	core data			
		0.88	0.825	0.821
XFe bi	0.415	0.422	0.43	0.422
Pressure (kbar)	T (°C)			
5.6	426	434	480	473
5.9	427	435	481	475
6.2	429	437	482	476
6.5	430	438	484	477
6.8	431	439	485	479
7.1	432	440	487	480
average	429.2	437	483.2	476.7

Table A4.2. Results of g-bi thermometry calculations on sample PB10.

g-bi	PB10			Geothermometry					
	rim data				core data				
XFe gnt	0.823	0.83	0.83	0.826	0.827	0.843	0.843	0.836	0.838
XFe bi	0.43	0.431	0.428	0.429	0.43	0.407	0.418	0.429	0.419
T (°C)									
H&S	588.2	573.1	574.8	578	577.7	515.8	527.9	546	539.5
P&L	569.4	560.8	559.4	564.4	563	528.4	535.6	551.7	542.4
I&M (b)	594.2	579.2	570.1	563.7	578.4	521.8	531.3	516.7	543
F&S	587.1	571.3	575.5	575.6	576.6	512.5	524.7	543.3	536.2
PD et al	594.1	578.3	572.6	572.7	578.7	520.7	529.2	540.5	540.8
K&R	576.1	558.1	567.5	567.5	570.1	535.1	541.2	549.3	548
ave	584.9	570.1	570.0	570.3	574.1	522.4	531.7	541.3	541.7

g-bi	PB10			THERMOCALC V2.6					
	rim data				core data				
XFe gnt	0.823	0.83	0.83	0.826	0.827	0.843	0.843	0.836	0.838
XFe bi	0.43	0.431	0.428	0.429	0.43	0.407	0.418	0.429	0.419
Pressure (kbar)	T (°C)								
5.6	587	573	586	578	582	502	522	550	536
5.9	588	574	588	579	584	504	523	551	538
6.2	590	576	590	581	585	505	524	553	539
6.5	592	578	591	582	587	507	526	554	541
6.8	593	579	593	584	588	508	527	556	542
7.1	595	581	594	586	590	510	529	557	544

Table A4.3. Results of g-bi thermometry calculations on sample WK71.

g-bi	WK71			Geothermometry		
	rim data			core data		
XFe g	0.825	0.828	0.827	0.849	0.841	0.845
XFe bi	0.3939	0.3944	0.392	0.387	0.393	0.392
T (°C)						
H&S	529.5	519.1	521.4	476.1	496.4	488.7
P&L	541.3	537.2	537.6	508.2	521.3	516.4
I&M (b)	521.4	504.6	511.7	473.9	490.4	483.2
F&S	523.3	513.5	515.6	464.4	485.8	477.5
PD et al	531.7	513.7	520	468.6	489.8	481.7
K&R	541.4	533.5	536.1	504	517.7	512.6

g-bi	WK71			THERMOCALC V2.6		
	rim data			core data		
XFe g	0.825	0.828	0.827	0.849	0.841	0.845
XFe bi	0.3939	0.3944	0.392	0.387	0.393	0.392
Pressure (kbar)	T (°C)					
5.6	519	521	514	458	486	473
5.9	520	523	516	460	488	475
6.2	522	524	517	461	489	476
6.5	523	526	519	462	490	478
6.8	525	527	520	463	492	479
7.1	526	529	522	465	493	480

Table A4.4. Results of g-bi thermometry calculations on sample WK182.

g-bi	WK182		Geothermometry					
	rim data							
XFe g	0.813	0.8129	0.8131	0.8192	0.82	0.819	0.831	0.825
XFe bi	0.399	0.394	0.401	0.414	0.395	0.393	0.425	0.403
T (°C)								
H&S	558.5	551.2	560.1	568.3	540.9	550.8	553.1	540
P&L	558.1	553.9	559	562.5	546.8	552.6	555.7	547
I&M (b)	555.3	548.2	555.5	559.5	539.5	549.5	541.7	535.3
F&S	552.3	545	553.8	562.9	535.6	545.5	548.8	535.7
PD et al	557.2	550.9	559.5	564.4	540.7	551.1	564.7	542.6
K&R	558.5	554.2	559.2	563.2	548.3	554.3	555.9	548.5

g-bi	WK182		Geothermometry			
	core data					
XFe g	0.833	0.832	0.832	0.83	0.831	0.83
XFe bi	0.399	0.394	0.4	0.405	0.393	0.401
T (°C)						
H&S	521.5	515.4	523.5	533.3	518.6	528
P&L	536.5	532.9	537.7	542.4	533.7	539.2
I&M (b)	519.1	512.8	519.4	532.4	517.2	526.7
F&S	513.6	507.5	515.6	526.2	511.6	520.9
PD et al	515.6	513.2	521	528.9	516.5	526.4
K&R	534.3	531.7	536.4	542.3	533.8	539.6

g-bi	WK182		THERMOCALC V2.6				
	rim data						
XFe g	0.813	0.8129	0.813	0.8131	0.8192	0.82	0.819
XFe bi	0.399	0.4	0.394	0.401	0.414	0.395	0.393
Pressure (kbar)	T (°C)						
5.6	572	574	569	578	579	548	560
5.9	574	576	570	579	581	549	562
6.2	575	578	572	581	582	551	563
6.5	577	579	573	582	584	552	565
6.8	578	581	575	584	585	554	566
7.1	580	582	576	586	587	555	568

g-bi	WK182		THERMOCALC V2.6			
	core data					
XFe gnt	0.833	0.832	0.832	0.83	0.831	0.83
XFe bi	0.399	0.394	0.4	0.405	0.393	0.401
Pressure (kbar)	T (°C)					
5.6	524	515	522	538	516	527
5.9	525	516	524	539	517	528
6.2	527	517	525	541	519	530
6.5	528	519	527	542	520	531
6.8	530	520	528	544	521	533
7.1	531	522	530	545	523	534

Table A4.5. Results of g-bi thermometry, GASP and g-plag-bi-q barometry on sample PB11.

g-bi	PB11			Geothermometry		
	rim data					
XFe gnt	0.82	0.8202	0.808	0.8076	0.813	0.8134
XFe bi	0.356	0.366	0.377	0.366	0.376	0.367
T (°C)						
H&S	488.4	500.5	537.5	524.5	527	514.4
P&L	519.4	526.7	548.1	540.5	541.8	534.3
I&M (b)	475.8	483.4	516.2	508.5	506.3	498.9
F&S	484.4	496.4	532.9	519.9	522.9	510.3
PD et al	489.8	495.5	530.5	519	520.6	509.4
K&R	517.5	522.3	544.5	537.2	538.4	531.1
ave	495.9	504.1	535.0	524.9	526.2	516.4

g-bi	PB11			Geothermometry		
	interior data					
XFe gnt	0.792	0.791	0.764	0.765	0.777	0.778
XFe bi	0.356	0.3661	0.377	0.366	0.376	0.366
T (°C)						
H&S	536.4	550.1	611.2	595.5	588.6	573.7
P&L	549.2	557.2	594.6	586.1	580.7	572.5
I&M (b)	519.6	528.4	571.1	561.6	554.6	545.7
F&S	528.7	542.4	595.7	580.2	576.9	562.2
PD et al	534.5	541.4	593.1	579.2	574.3	561.2
K&R	544.4	551.1	581.5	573.7	570.7	563.1
ave	535.5	545.1	591.2	579.4	574.3	563.1

g-bi	PB11			Geothermometry				
	core data							
XFe gnt	0.763	0.762	0.76	0.761	0.762	0.7627	0.763	0.764
XFe bi	0.355	0.366	0.356	0.365	0.355	0.365	0.377	0.366
T (°C)								
H&S	584.8	600.4	589	604.7	589.4	605	624.9	609
P&L	579.5	588	581.7	590.3	579.3	587.8	595.4	586.8
I&M (b)	558.5	568.7	563	573.2	571.5	581.8	605.8	595.7
F&S	570.3	585.6	574.2	589.7	578	593.4	616.6	600.9
PD et al	576.5	584.6	580.4	588.7	584.2	592.4	614	599.9
K&R	568.3	576.9	570.5	579.3	572.6	581.5	593.6	586
ave	573.0	584.0	576.5	587.7	579.2	590.3	608.4	596.4

g-bi	PB11			THERMOCALC V2.6		
	rim data					
XFe gnt	0.82	0.8202	0.808	0.8076	0.813	0.8134
XFe bi	0.356	0.366	0.377	0.366	0.376	0.367
Pressure (kbar)	T(°C)					
5.6	478	492	538	517	528	508
5.9	479	493	539	519	530	510
6.2	481	495	541	520	531	511
6.5	482	496	542	522	533	513
6.8	484	497	544	523	534	514
7.1	485	499	545	524	536	515
sdT	86	89	98	94	96	92

g-bi	PB11			THERMOCALC V2.6		
	interior data					
XFe gnt	0.792	0.791	0.764	0.765	0.777	0.778
XFe bi	0.356	0.3661	0.377	0.366	0.376	0.366
Pressure (kbar)	T(°C)					
5.6	530	546	628	602	597	573
5.9	532	548	630	604	598	574
6.2	533	549	631	605	600	576
6.5	535	551	633	607	601	577
6.8	536	552	635	609	603	579
7.1	538	554	636	610	605	580
sdT	96	99	116	111	109	104

g-bi	PB11			THERMOCALC V2.6				
	core data							
XFe gnt	0.763	0.762	0.76	0.761	0.762	0.7627	0.763	0.764
XFe bi	0.355	0.366	0.356	0.365	0.355	0.365	0.377	0.366
Pressure (kbar)	T(°C)							
5.6	592	610	600	618	594	613	646	619
5.9	593	612	601	620	596	614	648	621
6.2	595	613	603	622	597	616	650	623
6.5	597	615	604	623	599	618	651	624
6.8	598	617	606	625	601	619	653	626
7.1	600	618	608	627	602	621	655	628
sdT	108	112	110	114	109	113	121	115

Table A4.5. (continued.)

GASP Calibrations	PB11									
Pressure (bars)	rim data			interior data						
N & H (1981)	5364.1	6511.5	5020.4	3643.9	4372.7					
H & S (1982)	5146.2	6152	4803.1	3438.1	4160.8					
G & S (1984)	4964.1	6041.4	4755.4	3414.7	4091.6					
H & C (1985)	5557.4	6506	5288.2	4044.6	4691.8					
g-pl-bi-q										
Pressure (bars)	rim data			interior data						
Hoisch (a)	4746.8	6215.1	6023.3	4696.3	4745.5	3678.7	3490.7	4320	4131.2	
Hoisch (b)	5459.5	6641.7	6550.3	5339.8	5140.9	3676.6	3586.9	4421.5	4331.4	

GASP Calibrations	PB11							
Pressure (bars)	core data							
N & H (1981)	4013.9	4089.8	5111.2	6091.1				
H & S (1982)	3808.8	3887	4900.9	5873.6				
G & S (1984)	3828.6	3922.3	5047.3	6132.7				
H & C (1985)	4370.1	4427.5	5375.6	6319				
g-pl-bi-q								
Pressure (bars)								
Hoisch (a)	3925.6	4001	5086.2	6311.6	3875.8	3951.2	5073.9	6118.1
Hoisch (b)	4057.1	4108.9	5172.7	6181.3	3939	3990.7	5053.4	6089.1

Table A4.6. Results of g-bi thermometry, GASP and g-plag-bi-q barometry on sample PB12.

g-bi	PB12		Geothermometry				
	rim data						
XFe gnt	0.789	0.813	0.8127	0.813	0.804	0.8037	0.804
XFe bi	0.365	0.404	0.3647	0.371	0.371	0.365	0.357
T (°C)							
H&S	556	561.4	512.3	519.9	537.9	530.1	520.5
P&L	559.1	562.6	534	538.5	548.3	543.7	538
I&M (b)	537.5	551.6	496.8	503.8	523.8	516.5	501.6
F&S	549	556.8	507.7	515.3	532.8	525	515.4
PD et al	568.4	588.9	510.6	518.8	536.4	527.9	513.1
K&R	555.8	561	530.9	535.6	546.1	541.3	533.8
ave	554.3	563.7	515.4	522.0	537.6	530.8	520.4

g-bi	PB12		Geothermometry				
	interior data						
XFe gnt	0.766	0.775	0.7752	0.776	0.777	0.7774	0.778
XFe bi	0.365	0.404	0.364	0.371	0.37	0.365	0.357
T (°C)							
H&S	591.3	635.4	577	586	583.9	575.1	564.3
P&L	583.2	605.3	573.7	578.7	576.3	571.4	565.4
I&M (b)	577.1	623.7	565.9	574.8	574.2	565.4	554.7
F&S	597.6	659	569.1	578.7	578.1	568.6	552.3
PD et al	569.5	590.6	565.6	570.5	570.1	565.3	558
K&R	555.8	561	530.9	535.6	546.1	541.3	533.8
ave	579.1	612.5	563.7	570.7	571.5	564.5	554.8

Table A4.6.(continued.)

g-bi	PB12		Geothermometry			
	core data					
XFe gnt	0.764	0.765	0.7647	0.782	0.781	0.783
XFe bi	0.404	0.365	0.371	0.371	0.365	0.357
T (°C)						
H&S	655.7	594.6	603.9	571.9	563.3	552.7
P&L	617	584.6	589.7	571.5	566.7	560.7
I&M (b)	633.1	566.4	575	545.8	537.8	521.8
F&S	640.9	580.6	589.8	560.7	552.2	541.7
PD et al	677.1	583.8	593.8	564.6	555.3	539.3
K&R	597.6	573.9	578.8	562.5	557.6	550.2
ave	636.9	580.7	588.5	562.8	555.5	544.4

g-bi	PB12		THERMOCALC V2.6			
	rim data					
XFe gnt	0.789	0.813	0.8127	0.804	0.8037	0.804
XFe bi	0.365	0.404	0.371	0.371	0.364	0.357
Pressure (kbar)	T(°C)					
5.6	562	558	518	532	524	516
5.9	563	560	519	534	525	518
6.2	565	561	521	535	527	520
6.5	566	563	522	537	528	521
6.8	568	564	524	538	530	523
7.1	569	566	525	540	531	524
sdT	86	89	98	94	96	92

g-bi	PB12		THERMOCALC V2.6			
	interior data					
XFe gnt	0.766	0.775	0.7749	0.776	0.777	0.778
XFe bi	0.365	0.404	0.3647	0.371	0.371	0.365
Pressure (kbar)	T(°C)					
5.6	598	640	581	591	590	581
5.9	601	641	583	593	592	582
6.2	603	643	585	594	594	584
6.5	604	645	586	596	595	586
6.8	606	647	588	597	597	587
7.1	608	648	589	599	598	589
sdT	86	89	98	94	96	92

g-bi	PB12		THERMOCALC V2.6			
	core data					
XFe gnt	0.764	0.765	0.7647	0.782	0.781	0.783
XFe bi	0.404	0.365	0.371	0.371	0.365	0.357
Pressure (kbar)	T(°C)					
5.6	665	603	613	575	566	557
5.9	667	605	615	577	568	558
6.2	669	607	617	578	569	560
6.5	670	608	618	580	571	561
6.8	672	610	620	582	572	563
7.1	674	612	622	583	574	564
sdT	124	111	112	104	103	102

GASP Calibrations	PB12						
Pressure (bars)	rim data			interior data			
N & H (1981)	5841.5	6725.1	5852.1	4642.5	4485.2	5161.2	
H & S (1982)	5588.1	6264.8	5606.6	4332.8	4280.7	4936	
G & S (1984)	5596.8	6232.8	5553.7	4308.6	4270.8	4953.6	
H & C (1985)	5997.8	6608.3	6009.6	4879.3	4815.9	5406	
g-pl-bi-q							
Pressure (bars)	rim data						
Hoisch (a)	6069.7	6816.2	6376.2	6462.6	5622.8	5536	5420.2
Hoisch (b)	6233.5	6928.9	6892.8	6922.6	5989.5	5959.5	5914.4
g-pl-bi-q							
Pressure (bars)	interior data						
Hoisch (a)	5053.6	4835.4	4399.3	4485	5163	5076.9	4962.1
Hoisch (b)	5039	4599.7	4563.9	4593.5	5269.2	5239.5	5194.7

GASP Calibrations	PB12					
Pressure (bars)	core data					
N & H (1981)	4018.3	4443.4				
H & S (1982)	3818.8	4222.5				
G & S (1984)	3823.8	4110.4				
H & C (1985)	4388.3	4731.5				
g-pl-bi-q						
Pressure (bars)						
Hoisch (a)	4420	4336.5	3985.6	4070.9	4251	4137.1
Hoisch (b)	4099.7	4523.8	4064	4927.8	4494.3	4449.9

Table A4.7. Results of g-bi thermometry, GASP and g-plag-bi-q barometry on sample PBS3.

g-bi	PBS3			Geothermometry				
	rim data					interior data		
XFe gnt	0.795	0.796	0.819	0.804	0.747	0.752	0.78	0.759
XFe bi	0.319	0.346	0.324	0.327	0.324	0.323	0.299	0.325
T (°C)								
H&S	495	527.1	462.3	492.7	565.2	566.1	494.2	553.5
P&L	518.9	537.8	498.2	516.4	569.2	564.3	518.6	557.8
I&M (b)	497.8	532.6	468.7	499.1	541.1	562.8	502.9	545.3
F&S	492.5	525	462	493.7	548.8	556.1	489.9	543.8
PD et al	495	533.4	465	496	550.7	564.2	491.5	547.2
K&R	520.7	542.9	500.3	521.2	556.5	561.7	518.2	553.7
ave	503.3	533.1	476.1	503.2	555.3	562.5	502.6	550.2

g-bi	PBS3			THERMOCALC V2.6				
	rim data							
XFe gnt	0.795	0.796	0.819	0.804	0.747	0.752	0.78	0.759
XFe bi	0.319	0.346	0.324	0.327	0.324	0.323	0.299	0.325
Pressure (kbar)	T(°C)							
5.6	479	521	447	479	565	559	474	547
5.9	480	522	448	480	567	561	475	549
6.2	482	524	450	482	569	562	476	550
6.5	483	525	451	483	570	564	478	552
6.8	484	527	452	484	572	566	479	553
7.1	486	528	454	486	573	567	480	555
sdT	84	92	79	85	100	100	83	97

g-bi	PBS3	Geothermometry		
	core data			
XFe gnt	0.744	0.7436	0.7437	0.7438
XFe bi	0.324	0.325	0.3237	0.3246
T (°C)				
H&S	570.7	571.9	572.1	573.3
P&L	572.3	573	572.1	572.7
I&M (b)	546.3	549.6	556	554
F&S	553.7	554.9	556.4	557.6
PD et al	555.6	558.4	564.7	561.1
K&R	559.5	560.6	561.9	562.2
ave	559.7	561.4	563.9	563.5

g-bi	PBS3	THERMOCALC V2.6		
	core data			
XFe gnt	0.744	0.7436	0.7437	0.7438
XFe bi	0.324	0.325	0.3237	0.3246
Pressure (kbar)	T(°C)			
5.6	479	521	447	479
5.9	480	522	448	480
6.2	482	524	450	482
6.5	483	525	451	483
6.8	484	527	452	484
7.1	486	528	454	486
sdT	84	92	79	85

GASP Calibrations	PBS3							
Pressure (bars)	rim data					interior data		
N & H (1981)	6758	6087	6095	6206	3207	5100	6028	4947
H & S (1982)	6501	5870	5875	5969	3010	4888	5817	4739
G & S (1984)	6700	6106	6111	6271	3145	5215	6170	5008
H & C (1985)	7004	6425	6412	6826	3681	5430	6346	5291
g-pl-bi-q								
Pressure (bars)	rim data							
Hoisch (a)	6559	6078	5515	6270	3099	5111	5622	4865
Hoisch (b)	7209	6512	6443	6961	3352	5324	6307	5158

Table A4.7.(continued.)

GASP Calibrations	PBS3
Pressure (bars)	core data
N & H (1981)	3205.5 3602.2
H & S (1982)	3009.9 3399.8
G & S (1984)	3164.3 3598
H & C (1985)	3674.2 4035.6
g-pl-bi-q	
Pressure (bars)	
Hoisch (a)	3110.2 3562 3130.5 3610.6
Hoisch (b)	3332 3766.4 3346.4 3809.8

Table A4.8. Results of g-bi thermometry, GASP and g-plag-bi-q barometry on sample CM20.

g-bi	CM20			Geothermometry					
	rim data								
XFe gnt	0.769	0.778	0.783	0.786	0.775	0.776	0.786	0.783	0.775
XFe bi	0.397	0.412	0.415	0.426	0.4154	0.4153	0.408	0.407	0.415
T (°C)									
H&S	650	655.9	649.1	661	667.9	665.1	632.1	636.5	667.3
P&L	605.1	608.4	605.1	611.5	614.4	612.9	596.4	598.4	614.9
I&M (b)	647.8	655.7	651.6	659.5	671.8	668.9	643.9	640.2	668.6
F&S	642.9	649.3	642.6	654.4	661	658.2	625.5	630	657.4
PD et al	645.2	649.3	646.5	656	665	662.1	634.9	634.8	661.4
K&R	608.2	614.3	609.9	616.4	620	618.4	602	603	617.9
ave	633.2	638.8	634.1	643.1	650.0	647.6	622.5	623.8	647.9

g-bi	CM20			Geothermometry		
	core data					
XFe gnt	0.77	0.7699	0.778	0.742	0.742	0.741
XFe bi	0.402	0.408	0.423	0.4075	0.412	0.409
T (°C)						
H&S	658	668.6	673	657.4	662.6	659
P&L	609.2	614.7	617.2	610.9	613.6	611.8
I&M (b)	651.6	667.7	679.6	665.2	659.2	651.3
F&S	650.8	661.5	666.3	646.9	652	648.5
PD et al	649.4	662.9	672.5	656.7	656.6	649.9
K&R	612.8	619.4	623	613.4	614.2	612.2
ave	638.6	649.1	655.3	641.8	643.0	638.8

g-bi	CM20		THERMOCALC V2.6		
	core data				
XFe gnt	0.741	0.741	0.742	0.7417	0.74
XFe bi	0.418	0.409	0.408	0.411	0.409
Pressure (kbar)	T(°C)				
5.6	764	786	776	786	784
5.9	766	788	778	788	786
6.2	768	790	780	790	788
6.5	770	792	782	792	790
6.8	773	794	784	794	792
7.1	775	796	786	796	794
sdT	158	164	162	164	164

g-bi	CM20			Thermocalc V2.6						
	rim data									
XFe gnt	0.827	0.769	0.78	0.783	0.77	0.778	0.786	0.785	0.783	0.78
XFe bi	0.422	0.397	0.41	0.407	0.402	0.412	0.408	0.426	0.415	0.407
Pressure (kbar)	T(°C)									
5.6	674	669	666	662	684	686	648	690	675	660
5.9	675	671	667	663	685	687	650	692	677	662
6.2	677	673	669	665	687	689	652	694	679	663
6.5	679	674	671	667	689	691	654	696	680	665
6.8	681	676	673	669	691	693	655	698	682	667
7.1	683	678	675	671	693	695	657	700	684	669
sdT	130	128	129	127	122	135	125	135	131	128

Table A4.8.(continued.)

GASP Calibrations	CM20				with sillimanite					
Pressure (bars)	rim data									
N & H (1981)	5495	5230	5433	5703	5197	5167	5330	5321	5204	5276
H & S (1982)	5100	4838	4516	5196	4642	4733	4867	4859	4739	4860
G & S (1984)	5615	5230	5442	5932	5174	5140	5374	5359	5181	5282
H & C (1985)	5723	5458	5273	5933	5280	5353	5513	5510	5372	5487
GASP Calibrations	with kyanite									
Pressure (bars)	rim data									
N & H (1981)	5544	5327	5493	5714	5300	5276	5409	5402	5306	5365
H & S (1982)	5222	5007	4743	5299	4847	4921	5031	5024	4926	5025
G & S (1984)	5642	5327	5500	5901	5282	5254	5445	5432	5288	5370
H & C (1985)	5900	5681	5532	6075	5535	5594	5727	5724	5610	5705

GASP Calibrations	CM20	with sillimanite		with kyanite		
Pressure (bars)	core data					
N & H (1981)	5495	4385	4903	5544	4633	5056
H & S (1982)	5100	3638	4323	5222	4021	4579
G & S (1984)	5615	4154	4959	5642	4443	5102
H & C (1985)	5723	4338	5115	5900	4753	5398

g-pl-bi-q										
Pressure (bars)	rim data									
Hoisch (a)	5907	5555	6202	6452	5518	5337	5763	5746	5555	5564
Hoisch (b)	5652	5384	5628	5872	5258	5208	5433	5430	5323	5395

g-pl-bi-q				
Pressure (bars)	rim data (cont)			
Hoisch (a)	6158	6408	5646	5575
Hoisch (b)	5628	5873	5218	5283

g-pl-bi-q								
Pressure (bars)	core data							
Hoisch (a)	5942	4729	5673	5677	5945	5663	4848	4859
Hoisch (b)	5646	4488	5092	5049	5603	5310	4568	4593

Table A4.9. Results of g-bi thermometry, GASP and g-plag-bi-q barometry on sample CM19.

g-bi	CM19			Geothermometry					
	rim data								
XFe gnt	0.827	0.804	0.828	0.807	0.801	0.813	0.818	0.817	0.805
XFe bi	0.423	0.425	0.441	0.435	0.423	0.431	0.427	0.431	0.436
T (°C)									
H&S	620.2	622.3	588.6	626.6	627	609.3	591.7	596.7	633.9
P&L	588.6	588.6	570.8	591.6	591	582.1	572.5	575.3	595.2
I&M (b)	618.7	622.8	574.4	613.5	621.8	601.6	584.4	588.7	625.9
F&S	613.8	616.3	582.5	621.1	621.3	603.2	585.3	590.3	628.4
PD et al	612.1	616.7	575.2	615.9	620	600.8	581.7	588	627.7
K&R	593.3	593.4	572.3	594.2	594.7	584.9	575.1	577.6	597.8
ave	607.8	610.0	577.3	610.5	612.6	597.0	581.8	586.1	618.2

Table A4.9.(continued.)

g-bi	CM19		THERMOCALC V2.6					
	rim data							
XFe gnt		0.769	0.78	0.783	0.77	0.778	0.786	0.785
XFe bi	0.422	0.397	0.41	0.407	0.402	0.412	0.408	0.426
Pressure (kbar)	T(°C)							
5.6	598	642	597	645	640	620	601	647
5.9	600	644	599	647	641	622	603	649
6.2	601	645	600	648	643	623	605	650
6.5	603	647	602	650	645	625	606	652
6.8	605	649	604	652	647	627	608	654
7.1	606	651	605	654	648	629	610	656
sdT	117	126	118	128	126	123	118	129

g-bi	CM19 Geothermometry		
	core data		
XFe gnt	0.739	0.7388	0.767
XFe bi	0.426	0.423	0.451
T (°C)			
H&S	781.8	797.2	744.6
P&L	665.6	672.7	654.7
I&M (b)	791	796.6	723.7
F&S	774.6	790.1	734.4
PD et al	772.4	782.4	739.4
K&R	677.5	684	647.2
ave	743.8	753.8	707.3

g-bi	CM19	THERMOCALC	
	rim data		
XFe gnt		0.769	0.78
XFe bi	0.422	0.397	0.41
Pressure (kbar)	T(°C)		
5.6	851	837	780
5.9	54	839	782
6.2	856	842	784
6.5	858	844	786
6.8	860	846	789
7.1	863	848	791
sdT	183	180	163

GASP Calibrations	CM19			with sillimanite					
Pressure (bars)	rim data								
N & H (1981)	5060	5234	5423	5293	5198	5145	5047	5278	5067
H & S (1982)	4615	4568	5053	4637	4563	4586	4470	4737	4512
G & S (1984)	4922	5098	5389	5185	5058	5001	4858	5190	4894
H & C (1985)	5470	5450	5873	5509	5412	5451	5342	5583	5385
GASP Calibrations				with kyanite					
Pressure (bars)	rim data								
N & H (1981)	5185	5238	5484	5377	5299	5255	5174	5365	5191
H & S (1982)	4819	4781	5180	4838	4778	4795	4699	4921	4734
G & S (1984)	5071	5216	5456	5288	5184	5137	5019	5292	5048
H & C (1985)	5693	5678	6024	5727	5646	5678	5588	5786	5623

GASP Calibrations	CM19	with sillimanite		with kyanite		
Pressure (bars)	ore data					
N & H (1981)	6058	6058	4449	6005	6005	4690
H & S (1982)	5338	5338	3669	5414	5414	4054
G & S (1984)	6319	6319	4248	6219	6219	4526
H & C (1985)	6329	6329	4261	6401	6401	4688

g-pl-bi-q									
Pressure (bars)	rim data								
Hoisch (a)	5206	5629	5781	5708	5596	5433	5237	5672	5278
Hoisch (b)	5323	5525	5651	5575	5356	5406	5314	5507	5325

g-pl-bi-q	CM19		
Pressure (bars)	ore data		
Hoisch (a)	7142	7258	5082
Hoisch (b)	6244	6289	4441

Table A4.10. Results of THERMOCALC Average P and PT calculations on sample PB215.

PB215	Average P calculations									
mineral assemblage	rim data g-st-bi-mu-q-fluid					Temperature range 550-630°C				
lst sq P (kbar)	7.68	7.93	8.04	8.09	8.09	6.93	7.98	6.65	7.45	6.42
sd (P)	2.14	2.1	2.1	2.04	2.04	2.16	2.22	2.14	2.2	2.18
σ fit	0.77	0.95	0.78	0.88	0.88	0.91	0.84	1.02	1.04	1.11
σ fit (max)	1.54	1.54	1.54	1.54	1.54	1.54	1.54	1.54	1.54	1.42

PB215	Average P calculations				
mineral assemblage	core data g-bi-mu-q-fluid			Temperature range 450-550°C	
lst sq P (kbar)	5.61	5.56	5.57	5.75	5.99
sd (P)	2.31	2.37	2.16	2.1	2.37
σ fit	0.53	0.48	0.28	0.28	0.23
σ fit (max)	1.73	1.73	1.73	1.73	1.73

PB215	Average PT calculations			
mineral assemblage	core data g-bi-mu-q-fluid			
T (°C)	434	436	472	471
sd (T)	79	80	83	85
P (kbar)	5.5	5.4	5.7	5.9
sd (P)	2.2	2.2	2.1	2.3
σ fit	0.27	0.1	0.26	0.11
σ fit (max)	1.96	1.96	1.96	1.96

PB215	Average PT calculations										
mineral assemblage	rim data g-st-bi-mu-q-fluid										
T (°C)	601	622	630	618	618	604	617	607	620	618	615
sd (T)	54	66	58	60	60	58	56	69	72	60	63
P (kbar)	7.9	7.5	7.6	7.9	7.9	7.1	7.7	6.5	7.1	7.9	7.2
sd (P)	2.2	2.7	2.3	2.3	2.3	2.6	2.4	3	3	2.3	2.6
σ fit	0.98	1.15	0.9	1.07	1.07	1.08	0.98	1.27	1.28	1.07	1.11
σ fit (max)	1.61	1.61	1.61	1.61	1.61	1.61	1.61	1.61	1.61	1.61	1.61

Table A4.11. Results of THERMOCALC Average P and PT calculations on sample PB10.

PB10	Average P calculations								
mineral assemblage	rim data g-st-bi-mu-q-fluid					Temperature range 550-650°C			
lst sq P (kbar)	7.66	7.4	8.05	8.75	8.43	7.9	7.77	7.05	7.69
sd (P)	2.19	2.2	2.37	2.51	2.49	2.47	2.47	2.61	2.42
σ fit	1.04	1.06	1.12	1.2	1.17	1.14	1.15	1.24	1.14
σ fit (max)	1.54	1.54	1.54	1.54	1.54	1.54	1.54	1.54	1.54

PB10	Average P calculations			
mineral assemblage	core data g-st-bi-mu-q-fluid		Temp. range 500-600°C	
lst sq P (kbar)	6.85	6.39	6.34	6.36
sd (P)	2.22	2.23	2.23	2.23
σ fit	0.34	0.38	0.4	0.37
σ fit (max)	1.73	1.73	1.73	1.73

PB10	verage PT calculations				
mineral assemblage	core data g-bi-mu-q-fluid				
T (°C)	543	494	510	534	522
sd (T)	94	84	88	93	91
P (kbar)	6.8	6.3	6.3	6.3	6.3
sd (P)	2.2	2.1	2.1	2.2	2.2
σ fit	0.51	0.33	0.4	0.59	0.48
σ fit (max)	1.96	1.96	1.96	1.96	1.96

Table A4.11. (continued).

PB10	verage PT calculations							
	rim data							
mineral assemblage	g-st-bi-mu-q-fluid							
T (°C)	639	628	646	640	639	647	657	653
sd (T)	70	73	79	80	79	76	85	82
P (kbar)	7.3	7	7.6	7.5	7.3	7.6	8.1	7.9
sd (P)	2.8	3	3.1	3.2	3.1	3	3.3	3.2
σ fit	1.23	1.3	1.33	1.37	1.36	1.29	1.4	1.36
σ fit (max)	1.61	1.61	1.61	1.61	1.61	1.61	1.61	1.61

Table A4.11. Results of THERMOCALC Average P and PT calculations on sample WK71.

WK71	Average P calculations						
	rim data		range 520-650°C		core data		range 450-550°C
mineral assemblage	g-st-bi-mu-q-fluid				g-bi-mu-q-fluid		
lst sq P (kbar)	8.13	7.72	8.52	8.12	5.1	5.9	5.52
sd (P)	2.7	2.5	2.65	2.56	2.98	2.78	2.89
σ fit	1.27	1.17	1.23	1.2	1.44	1.32	1.37
σ fit (max)	1.54	1.54	1.54	1.54	1.54	1.54	1.54

WK71	Average PT calculations			
	rim data			
mineral assemblage	g-st-bi-mu-q-fluid			
	1a rim	1b rim	1d rim	1f rim
T (°C)	628	621	645	632
sd (T)	85	77	82	79
P (kbar)	7.8	7.4	8	7.7
sd (P)	3.5	3.2	3.3	3.3
σ fit	1.49	1.4	1.59	1.39
σ fit (max)	1.61	1.61	1.61	1.61

WK71	Average PT calculations		
	core data		
mineral assemblage	g-bi-mu-q-fluid		
T (°C)	448	474	463
sd (T)	78	83	91
P (kbar)	5	5.5	5.3
sd (P)	2	2.1	2.1
σ fit	0.22	0.31	0.25
σ fit (max)	1.96	1.96	1.96

Table A4.12. Results of THERMOCALC Average P and PT calculations on sample WK182.

WK182	Average P calculations										
	rim data				Temperature range 540-630°C						
mineral assemblage	g-st-bi-mu-q-fluid										
lst sq P (kbar)	7.15	7.12	6.68	6.67	6.95	6.88	7.68	7.06	7.04	7.72	7.62
sd (P)	2.21	2.29	2.55	2.61	2.35	2.18	2.16	2.65	2.29	2.68	2.44
σ fit	1.01	1.05	1.18	1.21	1.14	1.04	1.05	1.23	1.08	1.26	1.15
σ fit (max)	1.54	1.54	1.54	1.54	1.54	1.54	1.54	1.54	1.54	1.54	1.54

WK182	Average P calculations					
	core data			Temperature range 450-550°C		
mineral assemblage	g-bi-mu-q-fluid					
lst sq P (kbar)	5.84	5.98	5.94	5.94	6.1	5.9
sd (P)	2.25	2.26	2.26	2.23	2.24	2.14
σ fit	0.51	0.61	0.59	0.48	0.52	0.47
σ fit (max)	1.73	1.73	1.73	1.73	1.73	1.73

Table A4.12.(continued.)

WK182	Average PT calculations										
mineral assemblage	rim data g-st-bi-mu-q-fluid										
T (°C)	605	609	607	605	627	599	603	601	600	615	605
sd (T)	66	69	87	69	67	76	81	65	83	77	71
P (kbar)	7.1	7.1	7.4	6.8	7.3	7.4	7.3	7.2	7.8	7.5	7.1
sd (P)	2.9	3	3.7	3	2.8	3.2	3.4	2.8	3.6	3.2	3.1
σ fit	1.26	1.3	1.6	1.31	1.25	1.44	1.52	1.25	1.58	1.41	1.34
σ fit (max)	1.61	1.61	1.61	1.61	1.61	1.61	1.61	1.61	1.61	1.61	1.61

WK182	Average PT calculations					
mineral assemblage	core data g-bi-mu-q-fluid					
T (°C)	503	491	498	515	498	502
sd (T)	86	83	85	88	85	85
P (kbar)	5.8	5.9	5.9	5.9	6	5.9
sd (P)	2.1	2.1	2.1	2.2	2.1	2.2
σ fit	0.59	0.68	0.7	0.64	0.54	0.72
σ fit (max)	1.96	1.96	1.96	1.96	1.96	1.96

Table A4.13. Results of THERMOCALC Average PT calculations on sample PB11.

PB11	Average PT calculations THERMOCALC V2.6									
mineral assemblage	rim data g-ky-bi-st-pl-q-fluid						interior data			
T (°C)	631	638	652	646	638	632	645	639	649	642
sd (T)	26	27	30	28	27	26	27	26	27	26
P (kbar)	6.3	6.5	5	4.9	7.3	7.1	4.6	4.5	5.4	5.3
sd (P)	1.1	1.1	1.3	1.2	1.1	1.1	1.2	1.2	1.2	1.1
σ fit	0.96	1	1.11	1.04	0.9	0.83	0.91	0.78	0.89	0.78
σ fit (max)	1.61	1.61	1.61	1.61	1.61	1.61	1.61	1.61	1.61	1.61

PB11	Average PT calculations THERMOCALC V2.6							
mineral assemblage	core data g-ky-bi-pl-q-fluid							
T (°C)	632	640	629	636	625	633	628	621
sd (T)	25	26	25	26	25	26	26	25
P (kbar)	4.8	5.0	4.8	5.0	5.7	5.9	6.6	6.5
sd (P)	1.1	1.1	1.1	1.1	1.0	1.0	1.0	1.0
σ fit	0.59	0.72	0.57	0.7	0.47	0.6	0.7	0.51
σ fit (max)	1.61	1.61	1.61	1.61	1.61	1.61	1.61	1.61

Table A4.14. Results of THERMOCALC Average PT calculations on sample PB12.

PB12	Average PT calculations				THERMOCALC V2.6		
mineral assemblage	rim data g-ky-bi-st-pl-q-fluid						
T (°C)	630	642	641	644	637	634	636
sd (T)	26	35	35	39	34	30	32
P (kbar)	6.7	4.9	4.9	5	6.8	6.7	6.7
sd (P)	1.1	1.6	1.6	1.8	1.5	1.3	1.4
σ fit	0.98	1.34	1.35	1.46	1.27	1.15	1.21
σ fit (max)	1.61	1.61	1.61	1.61	1.61	1.61	1.61

PB12	Average PT calculations				THERMOCALC V2.6	
mineral assemblage	core data g-ky-bi-st-pl-q-fluid					
T (°C)	643	641	644	643	641	643
sd (T)	27	28	32	31	27	29
P (kbar)	5.1	3.8	3.9	5.5	5.4	5.4
sd (P)	1.3	1.3	1.5	1.4	1.3	1.3
σ fit	1.05	1.05	1.19	1.18	1.05	1.09
σ fit (max)	1.61	1.61	1.61	1.61	1.61	1.61

PB12	Average PT calculations				THERMOCALC V2.6		
mineral assemblage	interior data g-ky-bi-st-pl-q-fluid						
T (°C)	642	645	643	646	635	632	632
sd (T)	26	31	29	32	28	26	26
P (kbar)	5.6	4.4	4.3	4.4	5.9	5.9	5.9
sd (P)	1.2	1.4	1.3	1.5	1.3	1.2	1.2
σ fit	0.91	1.14	1.07	1.21	1.1	0.96	0.96
σ fit (max)	1.61	1.61	1.61	1.61	1.61	1.61	1.61

Table A4.15. Results of THERMOCALC Average P and PT calculations on sample PBS3.

PBS3	Average PT calculations				THERMOCALC V2.6			
mineral assemblage	rim data g-ky-bi-pl-q-fluid				interior data			
T (°C)	476	484	471		505	526	483	513
sd (T)	118	121	130		91	100	109	100
P (kbar)	5	4.6	4.5		2.4	4.3	4.4	4
sd (P)	2.1	2	2.2		1.4	1.7	1.8	1.6
σ fit	0.4	0.41	0.04	0.84		0.48	0.24	0.45
σ fit (max)	1.96	1.96	1.96		1.96	1.96	1.96	1.96

PBS3	Average PT calculations			
mineral assemblage	core data g-ky-bi-pl-q-fluid			
T (°C)	515	516	522	522
sd (T)	90	91	92	92
P (kbar)	2.7	2.7	2.9	3
sd (P)	1.4	1.4	1.5	1.5
σ fit	0.85	0.7	0.7	0.69
σ fit (max)	1.96	1.96	1.96	1.96

Table A4.16. Results of THERMOCALC Average PT calculations on sample CM20.

CM20	Average PT calculations				THERMOCALC V2.6						
mineral assemblage	rim data g-ky-bi-sill-q-fluid										
T (°C)	620	609	609	609	613	624	620	637	632	614	608
sd (T)	88	88	82	94	96	105	103	108	106	105	94
P (kbar)	5.9	5.7	5.7	5.7	5.8	6	5.9	6.3	6.2	5.8	5.7
sd (P)	1.9	1.9	1.8	2.1	2.1	2.3	2.3	2.3	2.3	2.3	2.1
σ fit	1.01	1.03	1	0.97	1.01	1.17	1.16	1.16	1.16	1.26	1.14
σ fit (max)	1.73	1.73	1.73	1.73	1.73	1.73	1.73	1.73	1.73	1.73	1.73

Table A4.16. (continued).

CM20	Average PT calculations				
mineral assemblage	core data g-ky-bi-sill-q-fluid				
T (°C)	607	611	595	594	593
sd (T)	112	118	106	115	114
P (kbar)	5.6	5.7	5.4	5.3	5.3
sd (P)	2.4	2.6	2.3	2.5	2.5
σ fit	1.22	1.27	1.18	1.29	1.28
σ fit (max)	1.73	1.73	1.73	1.73	1.73

Table A4.17. Results of THERMOCALC Average PT calculations on sample CM19.

CM19	Average PT calculations					THERMOCALC V2.6				
mineral assemblage	rim data g-ky-bi-sill-q-fluid									
T (°C)	637	636	630	627	646	636	636	633	631	639
sd (T)	23	22	23	22	23	22	23	23	23	23
P (kbar)	6.3	6.3	6.1	6.1	6.5	6.3	6.3	6.2	6.2	6.3
sd (P)	0.5	0.5	0.5	0.5	0.5	0.5	0.5	0.5	0.5	0.5
σ fit	0.95	0.85	0.94	1.07	0.89	0.85	0.8	0.83	0.87	0.77
σ fit (max)	1.49	1.49	1.4	1.49	1.49	1.49	1.49	1.49	1.49	1.49

CM19	Average PT calculations		
mineral assemblage	core data g-ky-bi-sill-q-fluid		
T (°C)	647	651	638
sd (T)	26	32	23
P (kbar)	6.5	6.6	6.3
sd (P)	0.6	0.7	0.5
σ fit	0.98	0.89	0.97
σ fit (max)	1.49	1.49	1.49

Appendix 5

COMPOSITIONAL VARIABLES FOR MINERAL SOLID SOLUTIONS USED IN THERMOCALC

This appendix provides a list of the mineral formulae, compositional variables, mole fraction and activity coefficients used in all phase diagram calculations in this thesis for the NaCaKFMASH, NaKFMASH, CaKFMASH and KFMASH chemical systems. The symbols x_i, y_i, z_i, k_i and c_i represent the variables for a given phase (i) used to derive the ideal mixing activities a_i. For plagioclase the variables are an_c and an_f. Activity coefficient expressions, RT ln γ, ω and Darken's Quadratic Formulism (DQF) Gibbs parameters are given where necessary. The following list constitutes the coded (th d) datafiles required for THERMOCALC to operate, and is taken directly from Worley and Powell, (1998).

staurolite (st) NaCaKFMASH, NaKFMASH, CaKFMASH and KFMASH

variable: $x_{st} = \frac{Fe}{(Fe + Mg)}$

end members : Mg-staurolite (mst) $Mg_4Al_{18}Si_{7.5}O_{48}H_4$

$a_{mst} = (1-x)^4$

: Fe-staurolite (fst) $Fe_4Al_{18}Si_{7.5}O_{48}H_4$

$a_{fst} = x^4$

chlorite (chl) NaCaKFMASH, NaKFMASH, CaKFMASH and KFMASH

variable: $x_{chl} = \frac{Fe}{(Fe + Mg)}$ and $y_{chl} = X_{Al,M2}$

end members : clinoclore (clin) $Mg_4[MgAl]Si_2[AlSi]O_{10}(OH)_8$

$a_{clin} = 16(1-x)^5(1-y)^2y^2$

: daphnite (daph) $Fe_4[FeAl]Si_2[AlSi]O_{10}(OH)_8$

$a_{daph} = 16x^5(1-y)^2y^2$

: amesite (ames) $Mg_4[Al_2]Si_2[Al_2]O_{10}(OH)_8$

$a_{ames} = (1-x)^4y^{42}$

biotite (bi) NaCaKFMASH, NaKFMASH, CaKFMASH and KFMASH

variable: $x_{bi} = \frac{Fe}{(Fe + Mg)}$ and $y_{bi} = X_{Al,M2}$

end members : phlogopite (phl) $KMg[Mg_2]Si_2[AlSi]O_{10}(OH)_2$

$a_{phl} = 0.25(1-x)^3(2-y)^2(1-y)(1+y)$

: annite (ann) $KFe[Fe_2]Si_2[AlSi]O_{10}(OH)_2$

$a_{ann} = 0.25\ x^3(2-y)^2(1-y)(1+y)$

: eastonite (east) $KMg[MgAl]Si_2[Al_2]O_{10}(OH)_2$

$a_{east} = 0.25(1-x)^2y(1-y)(1+y)$

garnet (g) NaCaKFMASH and CaKFMASH

variable: $x_g = \frac{Fe}{(Fe + Mg + Ca)}$ and $z_g = \frac{Ca}{(Fe + Mg + Ca)}$

end members : pyrope (py) $Mg_3Al_2Si_3O_8$

$a_{py}^{ideal} = (1-x-z)^3$

$RT \ln\gamma_{py,g} = \omega_{Mg,Ca}(x+z)$

: almandine (alm) $Fe_3Al_2Si_3O_8$

$a_{alm}^{ideal} = x^3$

$RT \ln\gamma_{alm,g} = \omega_{Mg,Ca}(1-x-z)(-z)$

: grossular (gr) $Ca_3Al_2Si_3O_8$

$a_{gr}^{ideal} = z^3$

$RT \ln\gamma_{gr,g} = \omega_{Mg,Ca}(1-x-z)(1-z)$

NaKFMASH and KFMASH

variable: $x_g = \frac{Fe}{(Fe + Mg)}$

end members : pyrope (py) $Mg_3Al_2Si_3O_8$

$a_{py} = (1-x)^3$

: almandine (alm) $Fe_3Al_2Si_3O_8$

$a_{alm} = x^3$

muscovite (mu) NaCaKFMASH and NaKFMASH

variable: $x_{mu} = \frac{Fe}{(Fe + Mg)}$ $y_{mu} = X_{Al,M2}$ and $k_{mu} = \frac{K}{(K+Na)}$

end members : muscovite (mu) $K\_[Al_2]Si_2[AlSi]O_{10}(OH)_2$

$a_{mu} = y^2(3-2y)^3(2y-1)k$

: celadonite (cel) $K\_[MgAl]Si_2[Si_2]O_{10}(OH)_2$

$a_{cel} = (1-x)(1-y)y(3-2y)^2k$

: Fe-celadonite (fcel) $K\_[FeAl]Si_2[Si_2]O_{10}(OH)_2$

$a_{fcel} = x(1-y)y(3-2y)^2k$

: paragonite (pa) $Na\_[Al_2]Si_2[SiAl]O_{10}(OH)_2$

$a_{pa}^{ideal} = y^2(3-2y)(2y-1)(1-k)$

$RT \ln\gamma_{pa,mu} = I_{pa,mu}$

CaKFMASH and KFMASH

variable: $x_{mu} = \frac{Fe}{(Fe + Mg)}$ and $y_{mu} = X_{Al,M2}$

end members : muscovite (mu) $K\_[Al_2]Si_2[AlSi]O_{10}(OH)_2$

$a_{mu} = y^2(3-2y)^3(2y-1)$

: celadonite (cel) $K\_[MgAl]Si_2[Si_2]O_{10}(OH)_2$

$$a_{cel} = (1-x)(1-y)y(3-2y)^2$$

: Fe-celadonite (fcel) $K\_[FeAl]Si_2[Si_2]O_{10}(OH)_2$

$$a_{fcel} = x(1-y)y(3-2y)^2$$

plagioclase (plag) NaCaKFMASH

C1 region

variable: $an_c = \frac{Ca}{(Na + Ca)}$

end members : albite (ab) $Na[AlSi_3]O_8$

$$a^{ideal}_{ab,C1} = \frac{1}{27}(1-an)(1+an)(3-an)$$

$$RT \ln\gamma_{ab,C1} = \omega_{C1} an^2$$

: anorthite (an) $Ca[Al_2Si_2]O_8$

$$a^{ideal}_{an,C1} = \frac{1}{16} an(1+an)^2(3-an)^2$$

$$RT \ln\gamma_{an,C1} = \omega_{C1}(1+an)^2 + I_{an}$$

I1 region

variable: $an_I = \frac{Ca}{(Na + Ca)}$

end members : albite (ab) $Na[AlSi_3]O_8$

$$a^{ideal}_{ab,I1} = (1-an)$$

$$RT \ln\gamma_{ab,I1} = \omega_{I1} an^2 + I_{ab}$$

: anorthite (an) $Ca[Al_2Si_2]O_8$

$$a^{ideal}_{an,I1} = an$$

$$RT \ln\gamma_{an,I1} = \omega_{I1}(1-an)^2$$

Appendix 6

WHOLE ROCK GEOCHEMISTRY AND CORRELATION DIAGRAMS

This appendix lists the details of whole rock geochemistry, isocon diagrams and bivariate plots discussed in Chapter 7. Data tabulated as 'average granulite' are compilations of geochemical data from the AGSO database which can not be reproduced in entirety due to confidentiality agreements, and therefore has been presented only in its compiled form.

A6.1 Whole rock geochemistry

A6.1.1. Geochemistry of metabasic rocks from the Winnecke area.

Data Source	AGSO	This Study	
Sample No.	ave. mafic	WK55	WK56
Lithology	granulite n=22	amphibolite	amphibolite
SiO_2	50.38	51.01	45.81
TiO_2	1.25	0.84	0.93
Al_2O_3	14.45	21.02	24.51
Fe_2O_3	13.95	11.43	11.40
MnO	0.19	0.15	0.10
MgO	7.41	3.80	3.91
CaO	11.07	0.84	0.05
Na_2O	1.66	1.38	0.74
K_2O	0.24	6.29	7.46
P_2O_5	0.09	0.08	0.06
LOI	0.29	2.06	3.76
Total	100.98	98.90	98.73
Ba	87	2285	3015
Cr	224	160	180
Cu	44	6	4
Ni	66	72	74
Rb	6	171	218
Sr	99	88	90
Zr	83	137	129
Nb		15.1	10.5
Y		18.2	14.6
U		1.3	0.7
Th		26.9	23.2
Ga		31.5	39.4
Sc		22.8	20
Co		35	36
V		134	153
Ce		165	116
Nd		47	105
La		62	171

A6.1.2. Geochemistry of felsic rocks from the Winnecke area.

Data Source	AGSO	This Study	
Sample No.	ave. felsic	WK62	WK61
Lithology	granulite n=40	q-fsp schist	q-fsp schist
SiO_2	75.63	77.56	75.85
TiO_2	0.67	0.32	0.40
Al_2O_3	11.34	7.61	10.96
Fe_2O_3	4.29	6.78	2.56
MnO	0.03	0.05	0.03
MgO	0.91	2.46	2.97
CaO	1.98	1.51	0.48
Na_2O	3.52	1.03	0.23
K_2O	1.41	1.78	3.79
P_2O_5	0.09	0.05	0.34
LOI	0.25	0.42	1.57
Total	100.11	99.57	99.18
Ba	729.4	755.0	1060.0
Cr	4.2	54.0	14.0
Cu	7.7	12.0	3.0
Ni	6.6	20.0	5.0
Rb	35.7	111.7	127.5
Sr	97.5	57.2	19.1
V	25.3	41.0	10.0
Zr	465.8	86.3	272.1
Nb		6.5	14.3
Y		20.3	59.0
U		1.4	2.3
Th		10.2	35.7
Ga		11.0	13.5
Sc		5.1	6.9
Co		34.0	28.0
Ce		62.0	83.0
Nd		25.0	26.0
La		34.0	24.0

A6.1.3. Geochemistry of metapelitic rocks from the Winnecke area.

Data Source	AGSO			This Study				
Sample No.	ave. Mg-rich	ave. g-sill rich	ave. cd-rich	WK57	WK58	WK59	WK59A	WK60
Lithology	m/pelite gran.	m/pelite gran.	m/pelite gran.	m/pelite schist	m/pelite schist	m/pelite schist	m/pelite schist	m/pelite schist
SiO_2	56.26	78.17	77.84	48.92	33.16	56.28	55.36	55.58
TiO_2	0.23	0.36	0.39	0.98	1.70	0.63	0.72	0.65
Al_2O_3	7.49	11.30	11.35	24.68	25.66	17.74	16.15	14.69
Fe_2O_3	12.87	4.14	3.28	14.93	24.82	8.41	9.95	8.64
MnO	0.76	0.03	0.02	0.10	0.38	0.23	0.25	0.20
MgO	17.65	3.20	3.09	3.86	4.44	2.55	2.49	2.87
CaO	4.46	0.33	0.59	0.08	0.10	6.99	6.23	15.70
Na_2O	0.80	1.30	1.73	0.31	0.83	0.18	0.22	0.17
K_2O	0.41	0.76	1.15	3.16	4.80	3.93	5.33	0.05
P_2O_5	0.06	0.02	0.02	0.05	0.09	0.10	0.18	0.14
LOI	0.35	0.55	0.53	2.06	3.07	2.21	2.19	1.48
Total	101.31	100.14	99.98	99.12	99.05	99.25	99.06	100.17
Ba	115	509	533	1266	2027	2480	2819	80
Cr	22	24	5	189	188	114	113	97
Cu	170	5	6	10	7	2	10	3
Ni	9	6	4	93	113	52	50	36
Rb	11	20	31	169	240	231	212	2
Sr	16	25	36	38	51	125	205	838
ZR	85	431	479	148	163	122	146	160
V	14	15	10	141	205	79	78	65
Nb				14.6	27	12.0	14.6	13.6
Y				13.7	16	21.2	34.6	33.2
U				2.5	0.9	1.3	0.4	2.2
Th				25.9	27.4	13.2	6.1	10.4
Ga				38.3	62.0	23.0	21.5	19.1
Sc				21.6	34.4	13.5	12.9	15.7
Co				44.0	50.0	47.0	46.0	53.0
Ce				106.0	182.0	116.0	97.0	85.0
Nd				37.0	49.0	31.0	44.0	36.0
La				47.0	65.0	36.0	58.0	41.0

A6.1.4. Geochemistry of felsic rocks from the Yambah Schist Zone.

Data Source	AGSO	Iyer (1974) Traverse 1		Iyer (1974) Traverse 2		Iyer (1974)			This study	
Sample No.	ave. felsic	A91	A93	A129	A128	A1	A22	A107	YB6	YB8
Lithology	granulite	felsic gran	q-bi schist	felsic gran	q-bi schist	q-fsp schist	q-fsp schist	q-fsp schist	q-fsp schist	q-fsp schist
SiO_2	73.91	73.78	73.96	76.86	76.45	73.84	61.91	73.51	78.80	73.95
TiO_2	0.49	0.10	0.51	0.81	0.81	0.71	0.61	0.25	0.32	0.32
Al_2O_3	11.83	11.03	11.34	11.29	11.29	10.99	17.63	13.85	10.37	7.85
Fe_2O_3	4.81	5.25	4.10	5.65	5.52	4.97	8.67	3.95	2.50	6.12
MnO	0.11	0.03	0.02	0.25	0.00	0.06	0.45	0.05	0.03	0.09
MgO	1.66	1.42	2.02	0.96	1.11	0.75	1.95	0.80	1.50	5.81
CaO	1.33	1.54	1.33	1.88	1.98	1.48	4.10	1.83	1.63	0.10
Na_2O	1.83	2.99	2.16	0.62	0.58	2.69	1.92	1.73	1.72	0.15
K_2O	3.58	2.76	3.61	1.80	1.81	3.12	2.11	2.80	1.71	3.76
P_2O_5	0.12	0.07	0.11	0.30	0.44	0.11	0.06	0.09	0.09	0.05
LOI	0.58	0.75	0.96	730.00	909.00	1.22	0.90	1.62	0.92	0.84
Total	99.86	99.72	100.12	830.42	14.00	99.94	100.31	100.48	99.59	99.03
Ba	765	1304	1707	14	8	718	640	750	297	733
Cr	18					2	86	27	48	73
Cu	10	15	15	8	8	15	15	10	6	3
Ni	11	8	9	10	88	8	31	12	16	30
Pb	16	24	28	41	75	27	30	2	6	2
Rb	124	81	82	89	58	82	100	89	88	177
Sr	63	27	82	63	439	63	239	69	130	4
Zn	65	78	88	40		87	119	66	15	47
Zr	370					537	115	172	176	119
Nb									3.2	13.1
Y									15.1	64.7
U									1.1	1.9
Th									12.4	23.2
Ga									11.6	12.1
Sc									6.2	3.7
Co									52	60
V									29	39
Ce									50	91
Nd									16	54
La									20	71

A6.1.5. Geochemistry of metapelitic rocks from the Yambah Schist Zone.

Data Source	AGSO	Iyer (1974)			This Study		
Sample No.	ave. m/pelitic granulite	A18	A43	A99	YB19	YB30	YB31
Lithology							
SiO2	60.27	59.52	57.58	54.28	53.93	52.75	42.17
TiO2	0.84	0.68	0.76	0.80	0.72	0.53	1.63
Al2O3	17.27	23.59	22.94	22.80	24.20	29.76	27.40
Fe2O3	9.40	8.40	9.21	12.80	9.33	8.02	19.34
MnO	0.07	0.22	0.08	0.10	0.05	0.11	0.20
MgO	5.26	2.94	3.89	2.42	3.00	4.53	3.98
CaO	2.89	0.83	0.44	1.31	0.14	0.09	0.06
Na2O	1.50	0.84	0.56	1.01	0.43	0.17	0.29
K2O	2.02	2.13	3.36	3.54	5.18	2.43	3.22
P2O5	0.07	0.03	0.11	0.07	0.09	0.05	0.03
LOI	0.92	1.61	1.52	1.42	2.29	0.94	1.08
Total	100.50	100.79	100.45	100.55	99.36	99.38	99.40
Ba	383	707	1070	1385	984	403	777
Cr	83	111	138	178	156	169	213
Cu	15	30	4	7	5	1	8
Ni	50	29	47	64	64	46	97
Pb	11	5	7	5	5	4	6
Rb	87	66	133	144	203	118	166
Sr	124	61	57	87	73	3	22
Zn	86	70	114	100	58	108	264
Zr	118	90	101	260	86	121	154
V	167				122	89	141
Nb					11	8.1	18.5
Y					13.3	8.7	12.9
U					0.8	0.1	0.6
Th					21.1	14.9	7.4
Ga					33.8	38.7	70
Sc					18.9	11.1	3.6
Co					38	53	66
Ce					190	55	65
Nd					36	19	9
La					40	24	27

A6.1.6. Geochemistry of metabasic rocks from the Winnecke area.

Data Source	AGSO	Iyer (1974) Traverse		Iyer (1974)				This Study					
Sample no.	ave. mafic	A92	A89	A4	A16	A33	A44	YB2	YB32	YS10	YS148	YS149	YB22
Lithology	granulite	granulite											
SiO_2	49.88	48.14	46.67	52.83	67.76	64.24	63.19	62.82	60.42	26.31	66.14	52.45	60.89
TiO_2	1.28	1.43	0.92	1.83	1.17	0.73	0.68	0.61	0.64	0.60	0.58	0.53	0.64
Al_2O_3	13.96	13.18	14.19	13.63	11.06	15.15	13.73	14.58	16.90	21.10	16.01	13.02	14.30
Fe_2O_3	16.21	15.97	14.73	10.232	6.131	6.45	9.144	8.76	8.69	20.45	9.10	21.31	8.98
MnO	0.26	0.30	0.29	0.12	0.04	0.07	0.11	0.08	0.12	0.06	0.13	0.23	0.06
MgO	6.86	7.18	8.03	8.09	7.51	2.3	2.13	3.07	2.42	19.82	2.03	5.53	2.08
CaO	10.25	9.20	11.62	11.89	2.13	9.85	8.97	8.80	9.42	0.38	5.19	6.81	11.42
Na_2O	1.40	2.02	1.42	0.69	1.03	0.85	0.61	0.54	0.87	0.12	0.40	0.53	0.36
K_2O	0.31	0.47	0.74	0.07	0.09	0.23	0.09	0.19	0.13	0.56	0.06	0.15	0.23
P_2O_5	0.19	0.24	0.11	0.26	0.05	0.2	0.01	0.12	0.12	0.17	0.13	0.11	0.12
LOI	0.57	1.14	1.79	1.54	3.36	0.68	1.38	0.41	0.20	9.28	0.14	-0.18	0.93
Total	101.20	99.27	100.51	100.46	99.97	100.32	99.54	99.98	99.93	98.85	99.92	100.49	100.01
Ba	114.09	216	299	20	125	200	190	184	52	90	74	27	126
Cr	216.45	173		NA	20	113	NA	107	119	96	101	103	104
Cu	54.18	32	13	6	7	2	NA	2	3	4	2	54	14
Ni	77.73	91	104	60	24	63	NA	26	43	104	16	30	23
Pb	10.25	11	17	16	<1	3	2	2.7	6.1	3.2	4.4	0.6	6.7
Rb	4.54	3	12	3	2	ND	ND	3.1	1.2	33.5	1.6	0.4	3.6
Sr	79.38	65	70	177	127	ND	355	469.4	368.3	9.8	291.4	18.6	546.7
Zn	193.08	201	350	101	66	51	28	13	32	42	46	21	6
Zr	90.25	75	43	130	540	185	170	158.6	126.0	167.6	164.1	140.7	157.5
Nb								12.2	11.5	16.1	12.0	10.4	14.2
Y								32.1	30.5	41.2	42.9	42.8	45.0
U								3.4	0.7	0.4	1.9	1.0	6.5
Th								20.5	17.4	22.3	21.3	20.0	19.6
Ga								16.3	21.5	37.0	24.2	17.8	22.8
Sc								13.9	15.4	3.9	11.2	11.3	12.2
Co								29.0	45.0	13.0	53.0	32.0	60.0
V								33.0	51.0	118.0	110.0	42.0	104.0
Ce								92.0	107.0	690.0	110.0	120.0	97.0
Nd								30.0	37.0	340.0	40.0	29.0	33.0
La								37	49	398	54	42	39

A6.1.7. Geochemistry of granulite-facies rocks from the Yambah Schist Zone and Winnecke area.

Data Source	This Study					
Sample No.	YB10	YB11	YB12	YB13	YB14	WK52
Lithology						
SiO_2	75.18	65.11	75.26	73.56	73.25	40.61
TiO_2	0.61	1.17	0.43	0.72	0.65	1.07
Al_2O_3	10.30	13.13	11.83	11.21	11.52	32.11
Fe_2O_3	5.27	9.85	4.49	5.31	4.85	16.2
MnO	0.04	0.11	0.07	0.06	0.06	0.29
MgO	5.86	2.31	4.39	1.28	1.50	6.98
CaO	0.05	5.26	0.19	1.33	1.80	0.33
Na_2O	0.10	2.27	0.21	2.50	2.71	0.3
K_2O	1.30	0.49	1.15	2.66	2.37	0.43
P_2O_5	0.03	0.16	0.03	0.09	0.13	0.05
LOI	0.42	-0.19	0.88	0.63	0.41	1.03
Total	99.15	99.67	98.91	99.37	99.24	99.39
Ba	215	431	352	1336	985	195
Cr	10	59	7	9	24	257
Cu	3	32	1	5	4	6
Ni	7	24	6	4	10	75
Pb	3.0	6.5	5.8	7.4	16.6	7.7
Rb	57.7	5.8	50.9	77.1	64.0	27.2
Sr	-0.4	86.5	3.9	57.0	67.8	21.5
Zn	62	70	81	39	60	240
Zr	599.1	337.3	433.6	440.3	425.9	258.3
Nb	25.4	17	20.1	21.2	21	15.4
Y	72.4	96.6	62.9	106.7	68.3	25.8
U	5	2.1	2.9	2.5	3.7	2.6
Th	30.3	13.7	35	34.9	35.9	65.2
Ga	18.3	18.9	20.3	17.3	17.9	58.3
Sc	8	25.2	3.5	20.8	12.2	11.9
Co	70	54	63	31	35	68
V	23	163	8	52	43	198
Ce	110	97	130	205	129	258
Nd	50	45	65	75	77	105
La	46	39	65	79	74	131

A 6.2 Isocon Diagrams

Isocon diagrams are plots which compare the elemental abundances in an unaltered known precursor rock with those of an altered resultant rock. Major elements are in weight % oxides and trace elements are in ppm, however abundances are scaled by random factors in order to fit them into a convenient range of values which will spread the data across a plot. For example a value of 2 wt% Na would be multiplied by a factor of 10, while 200 ppm Zr would be divided by 10 in order plot them over an equivalent numerical range. Reference lines of constant mass (solid line) and constant volume (broken line) have been added.

A 6.2.1. Isocon diagrams of felsic rocks from the Yambah Schist Zone.

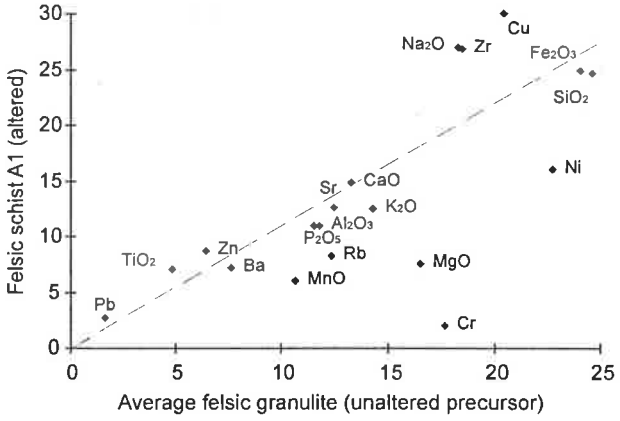

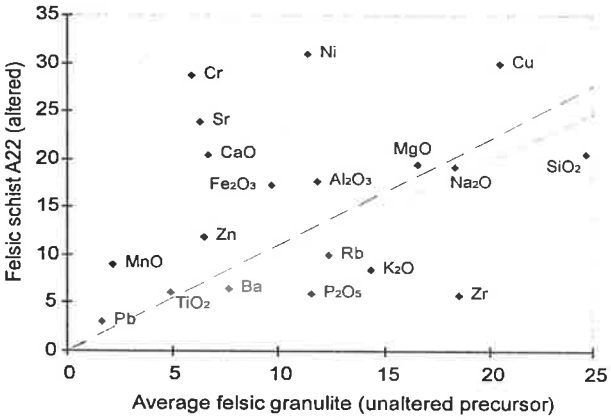

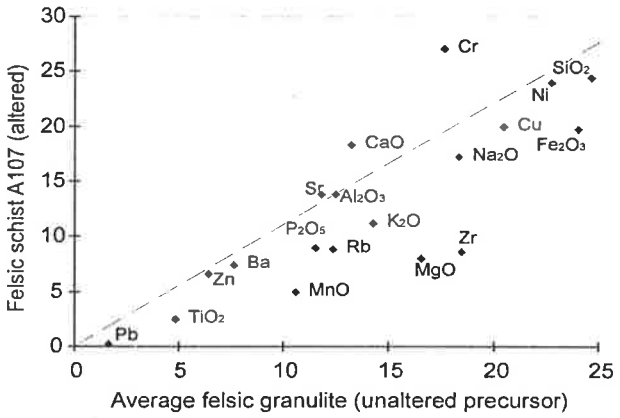

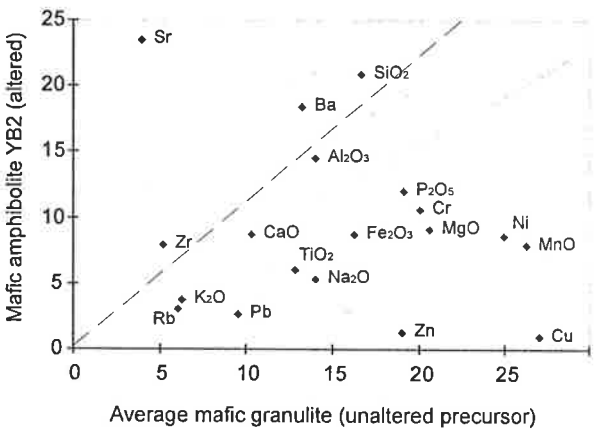

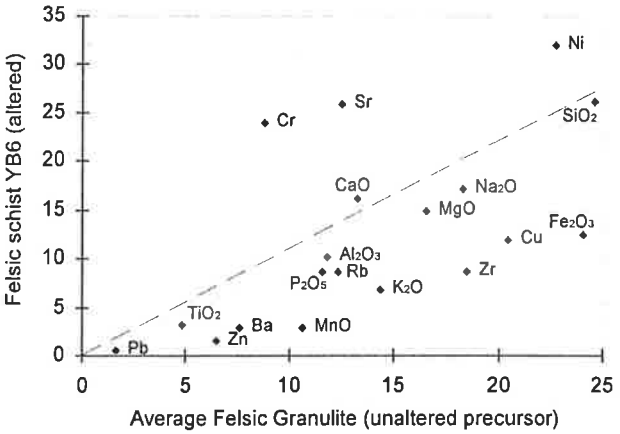

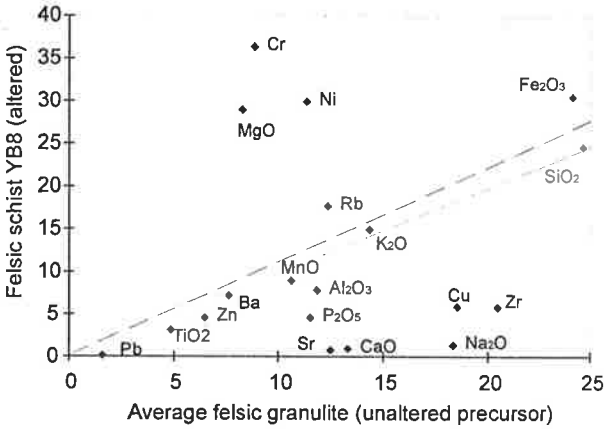

A 6.2.1. (continued).

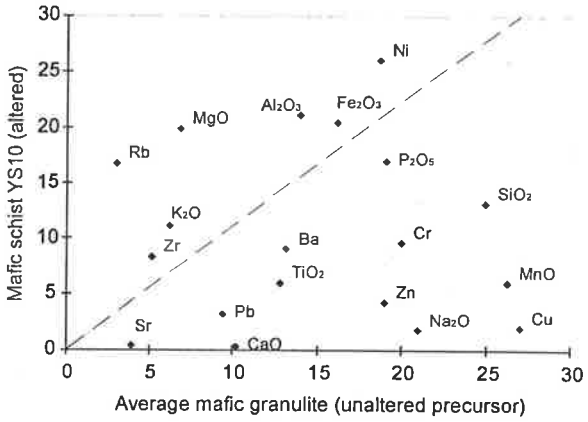

A 6.2.2. Isocon diagrams of 'metapelitic rocks from the Yambah Schist Zone.

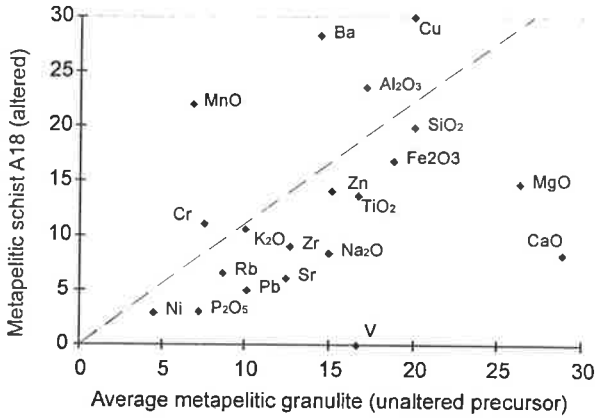

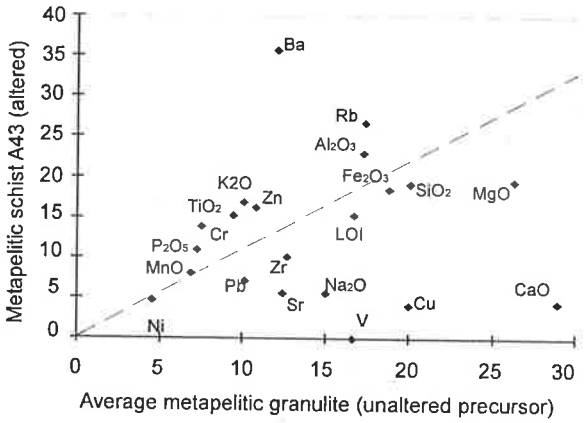

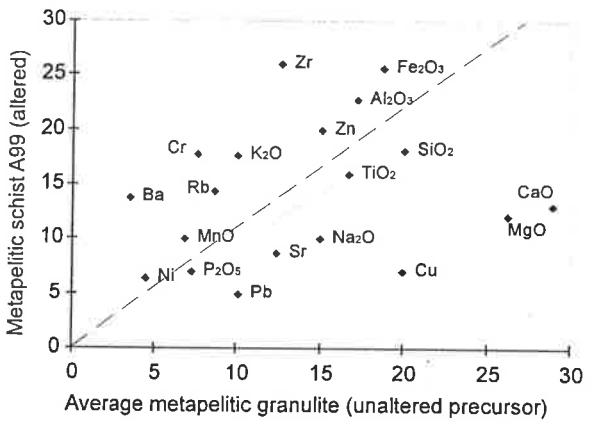

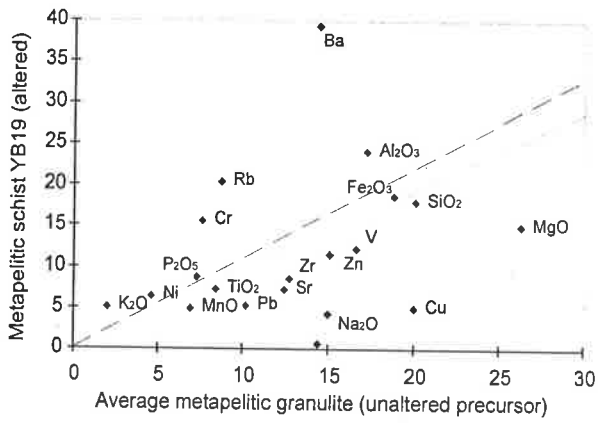

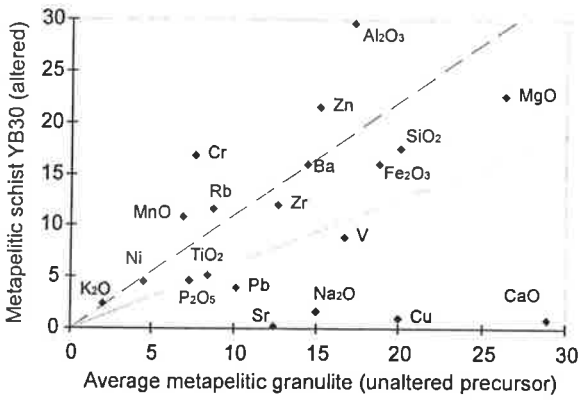

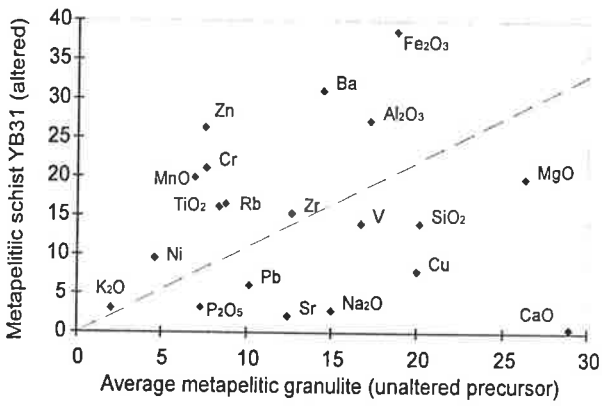

A 6.2.3. Isocon diagrams of 'metabasic rocks from the Yambah Schist Zone.

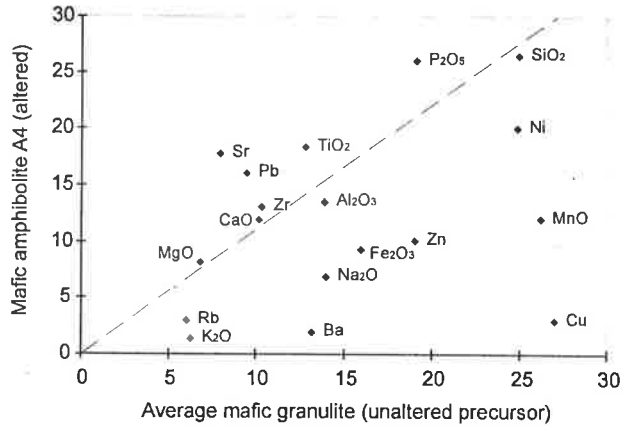

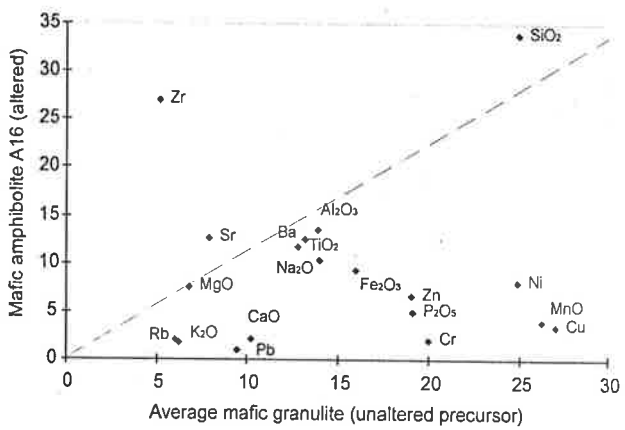

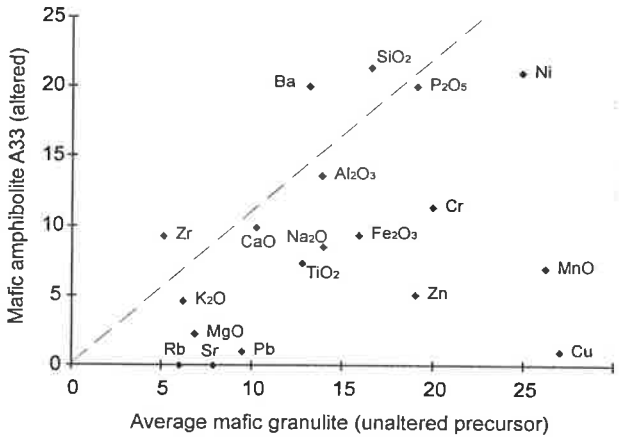

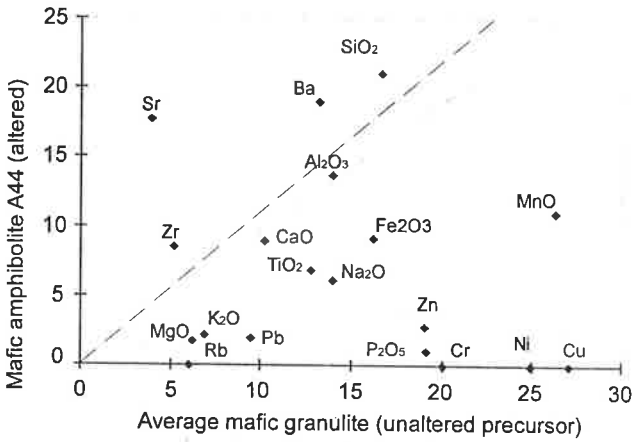

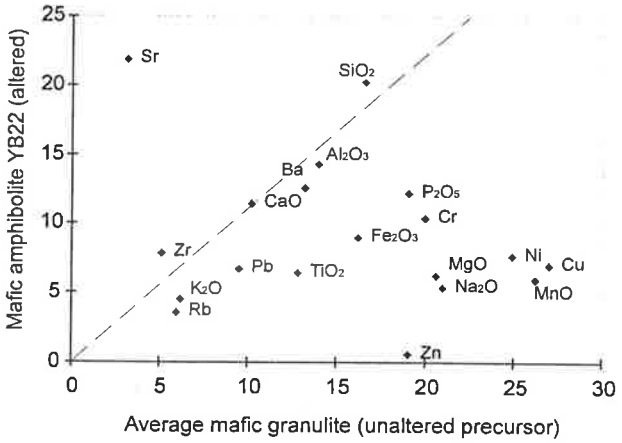

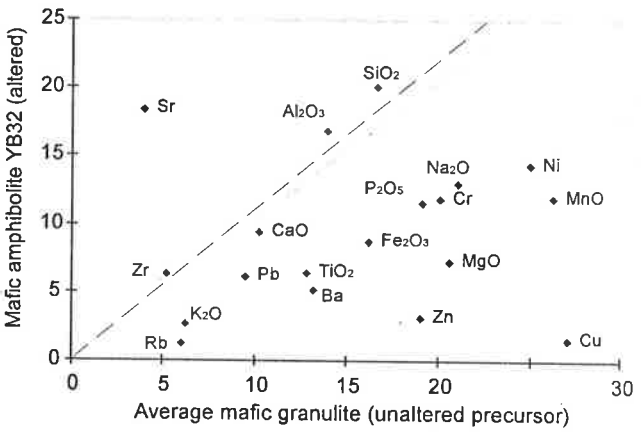

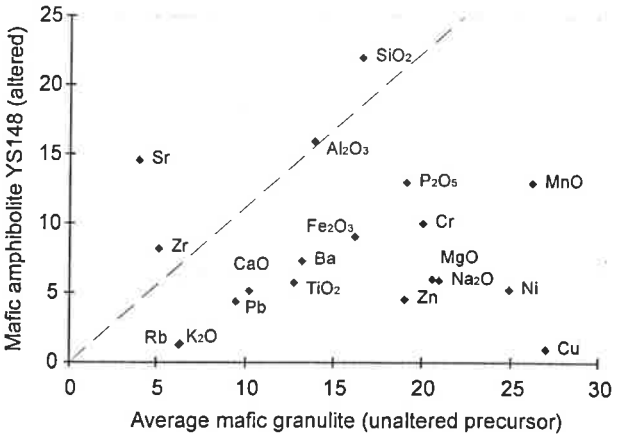

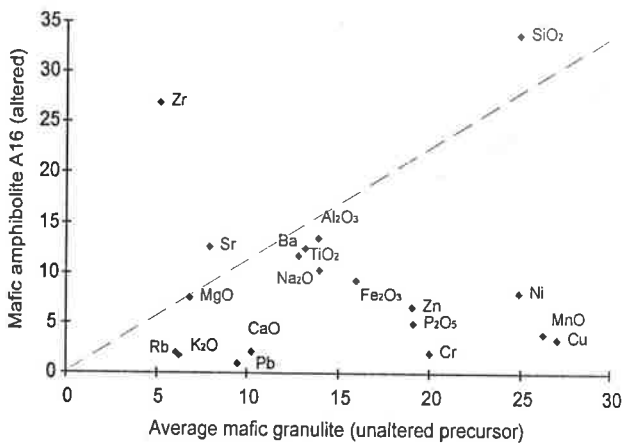

A 6.2.4. Isocon diagrams of felsic rocks from the Winnecke area.

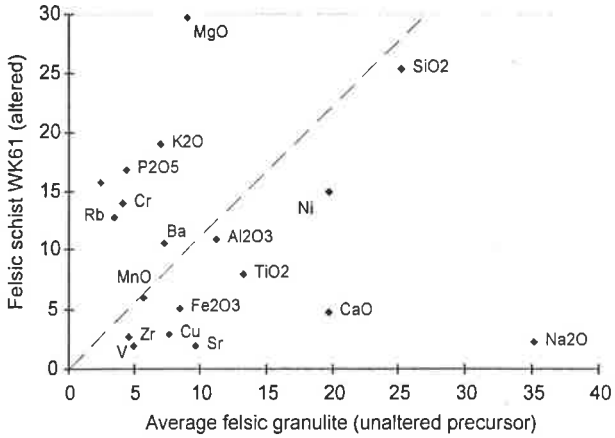

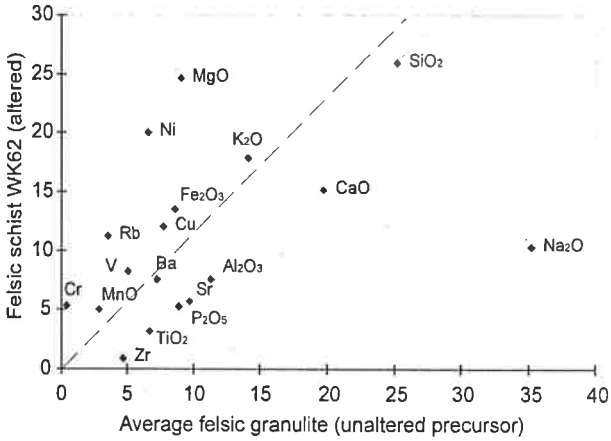

A 6.2.5. Isocon diagrams of metabasic rocks from the Winnecke area.

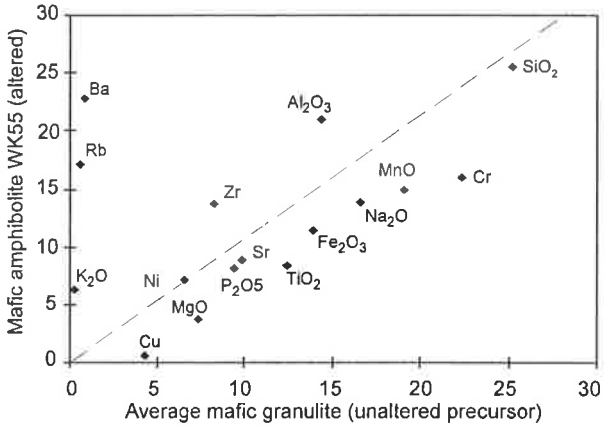

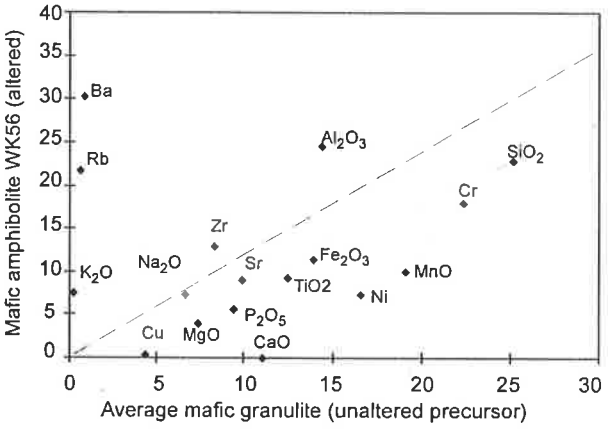

A 6.2.6. Isocon diagrams of metapelitic rocks vs cd-rich granulites from the Winnecke area.

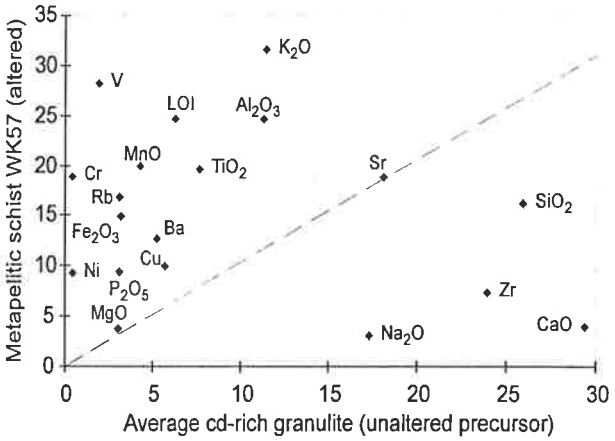

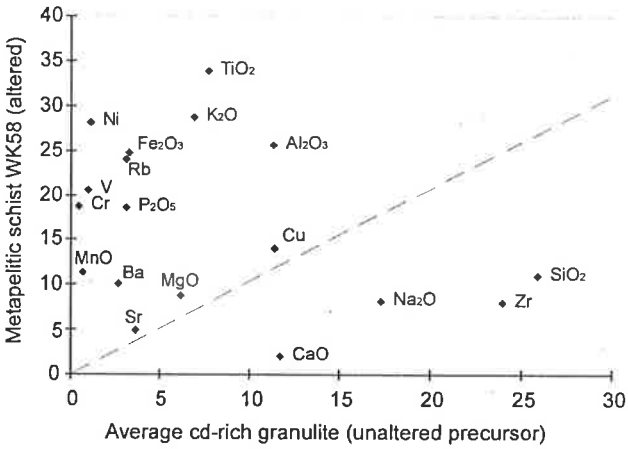

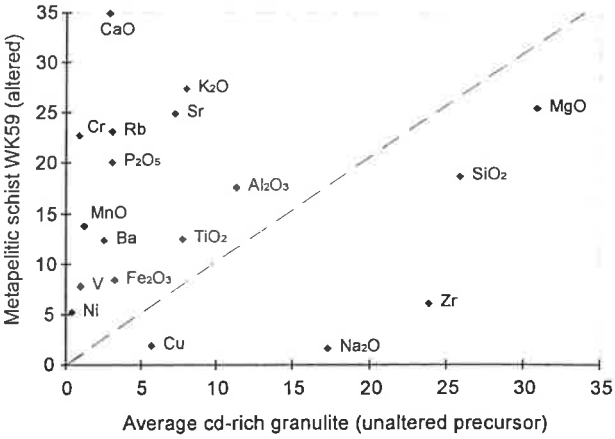

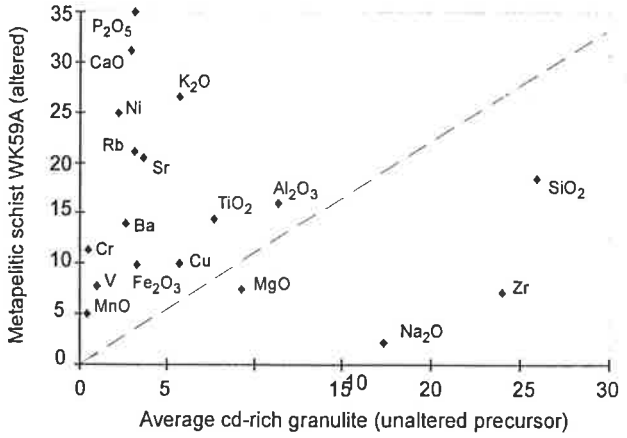

A 6.2.6. (continued).

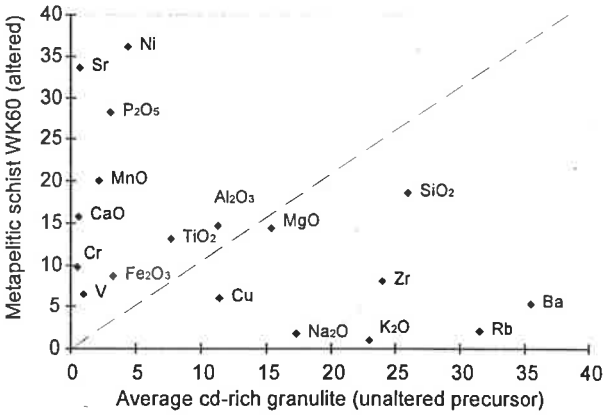

A 6.2.7. Isocon diagrams of metapelitic rocks vs g-sill rich granulites from the Winnecke area.

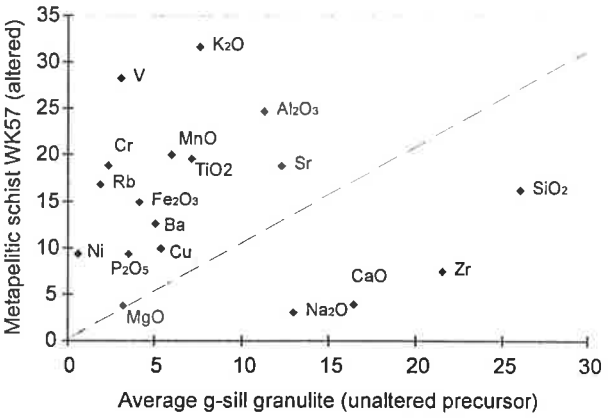

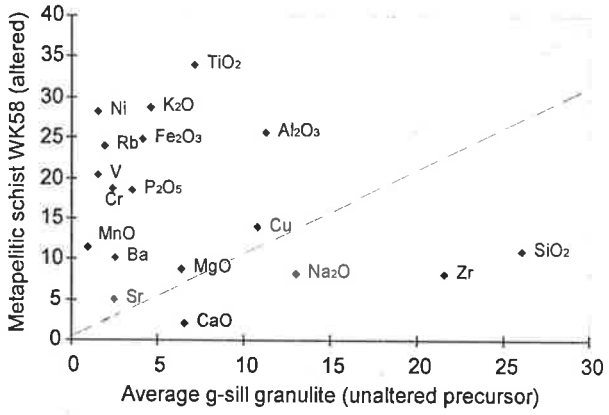

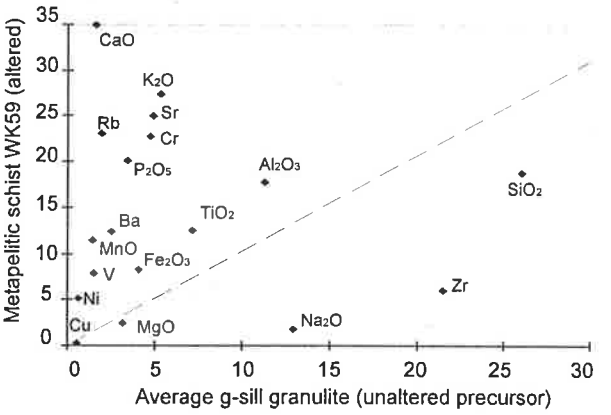

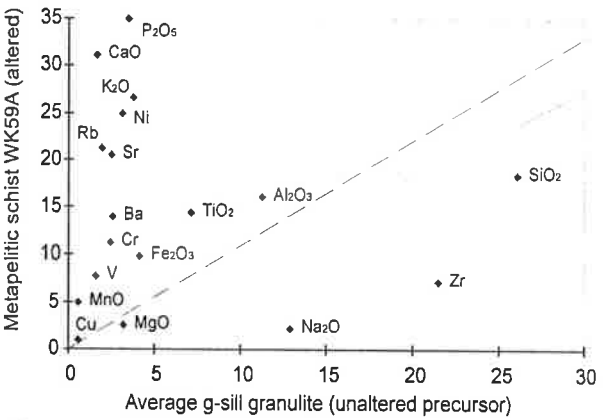

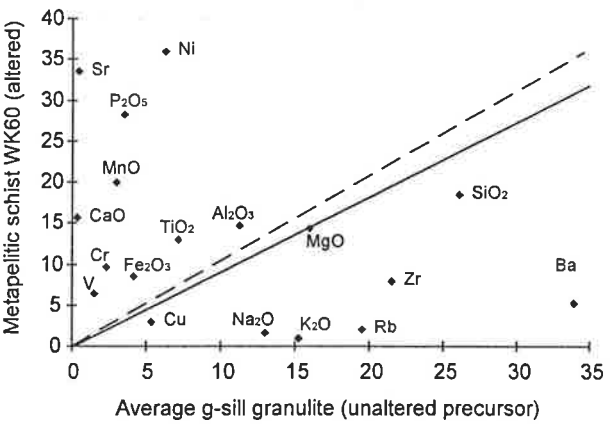

A 6.2.8. Isocon diagrams of metapelitic rocks vs 'magnesian' granulites from the Winnecke area.

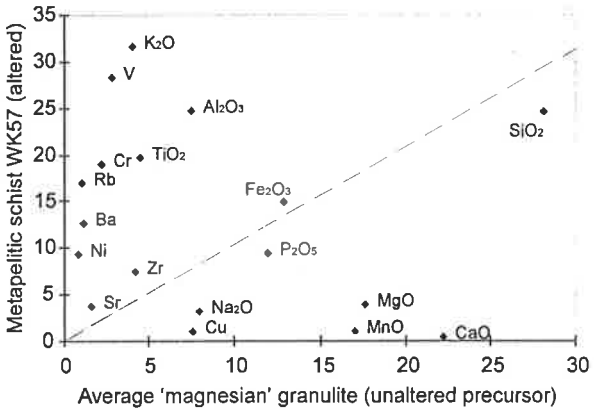

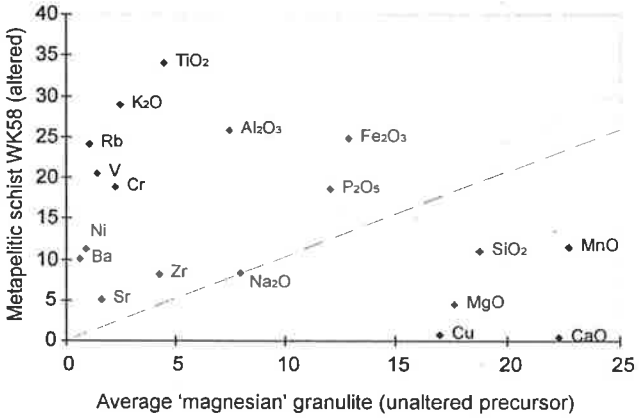

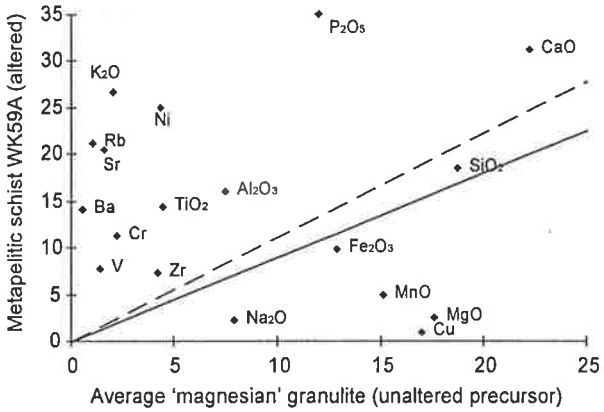

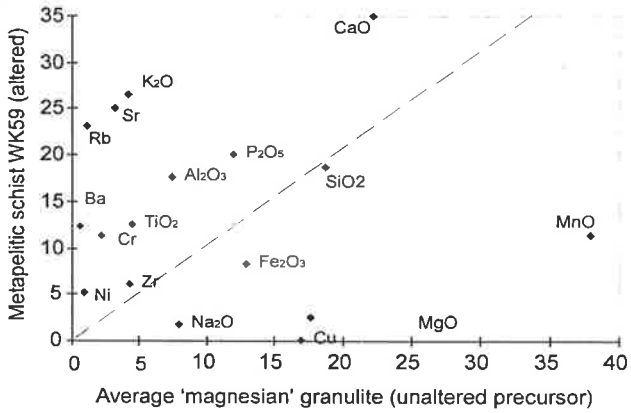

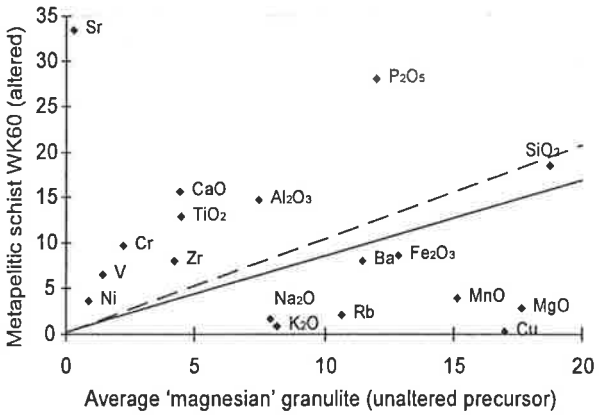

A 6.3. Bivariate plots.

Bivariate plots of potential immobile elements in granulite-facies country rocks and shear zone rocks from the Yambah Schist Zone and Winnecke area are presented in this section. If the ratios of any two elements are consistent then they will define a linear trend through the origin, suggestiing those elements have remaiined immobile. Linear trends which intersect along an axis indicate that one element has been more conserved than the other. Data points from granulites are denoted by a filled diamond, data from shear zone rocks are denoted by an unfilled circle. No well-defined linear trends through the origin are indicated in these plots, thus there is no conclusive evidence to identify elemental immobility.

A 6.3.1. Bivariate plots of felsic rocks from the Yambah Schist Zone.

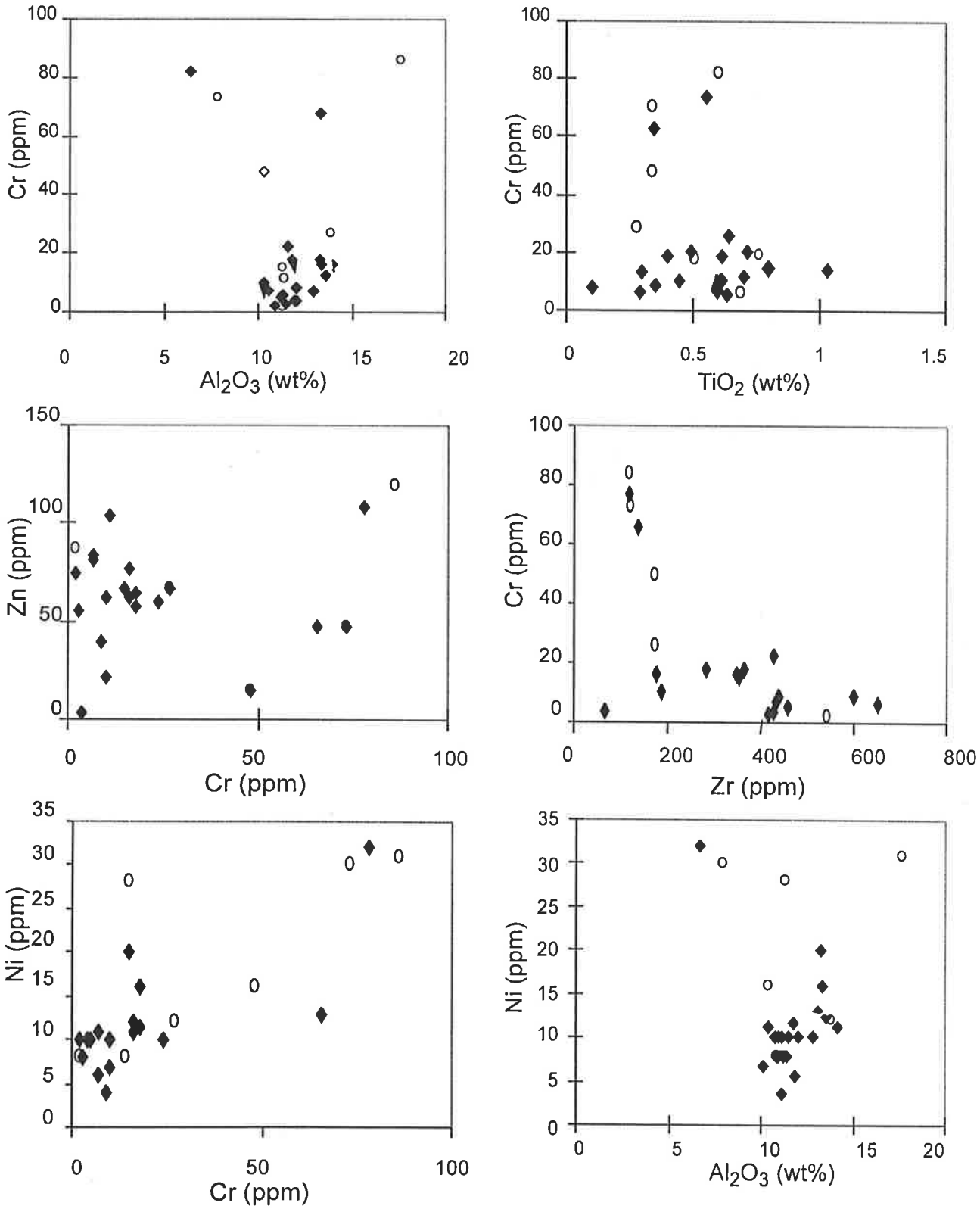

A 6.3.1. (continued).

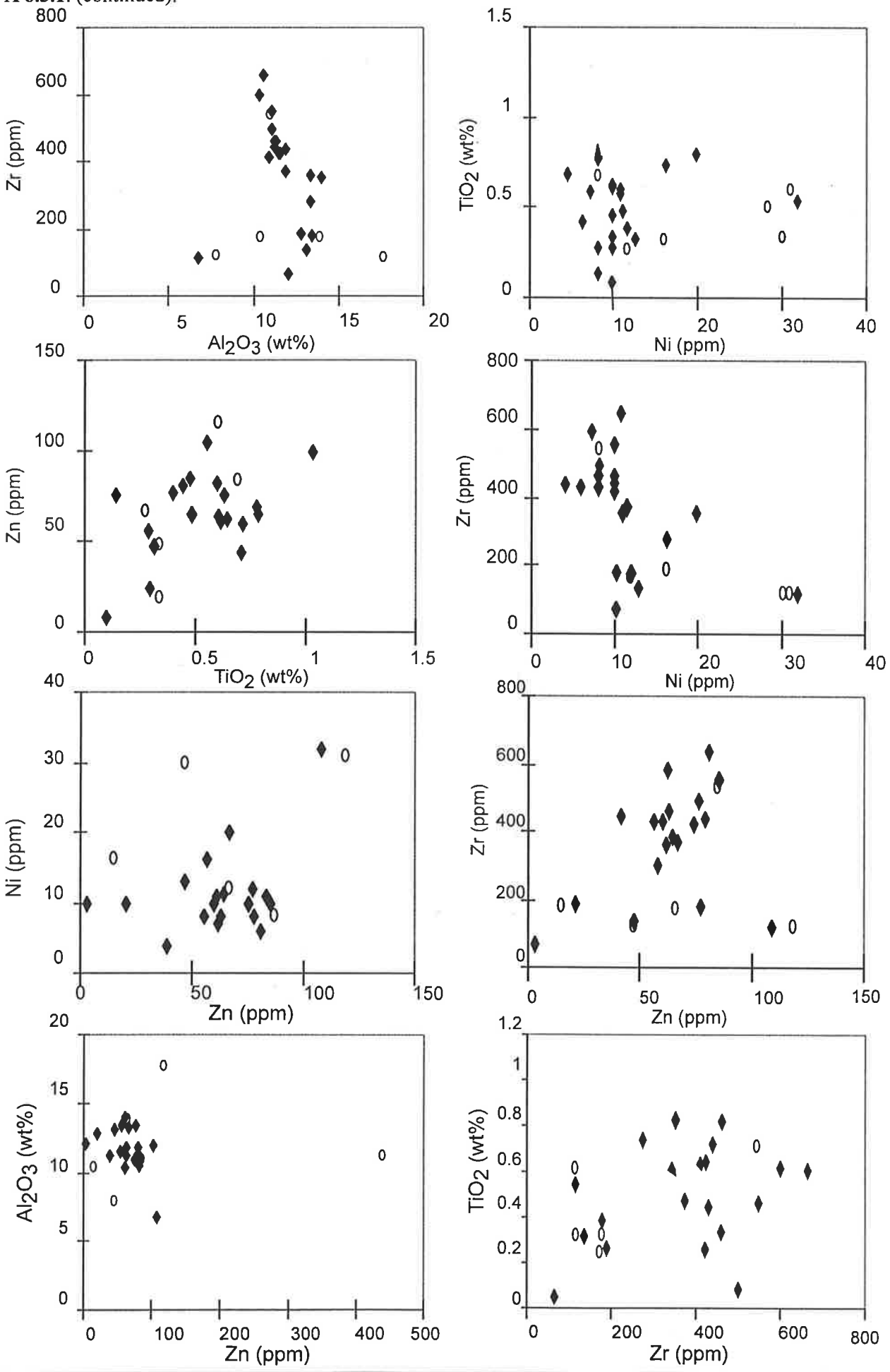

A 6.3.1. (continued).

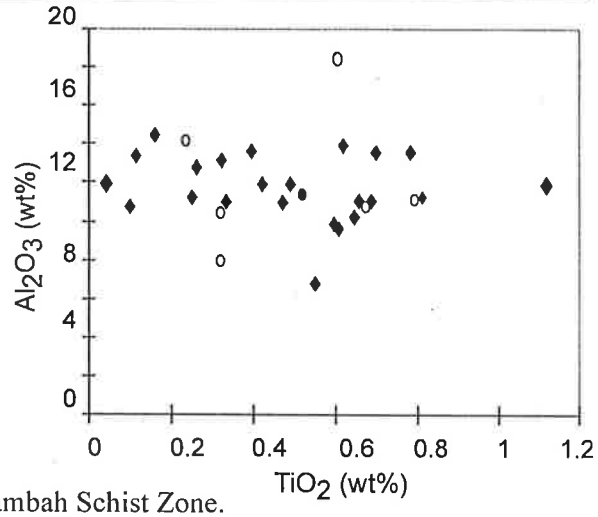

A 6.3.2. Bivariate plots of metabasic rocks from the Yambah Schist Zone.

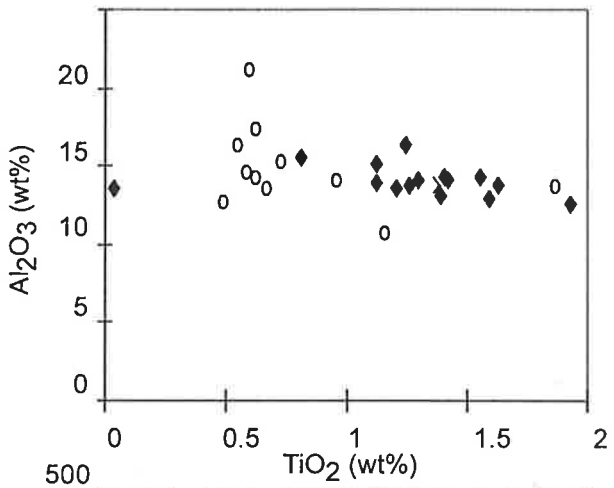

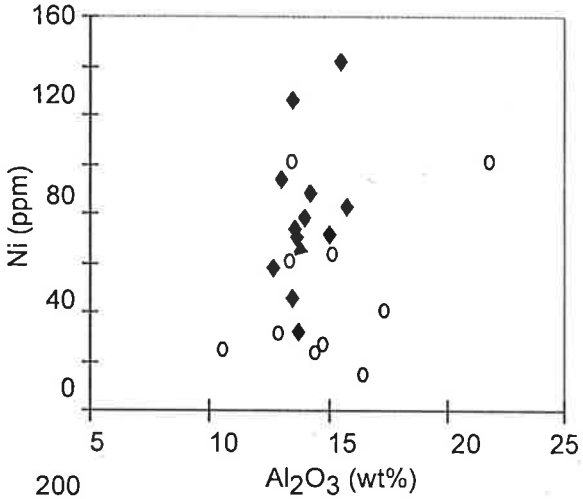

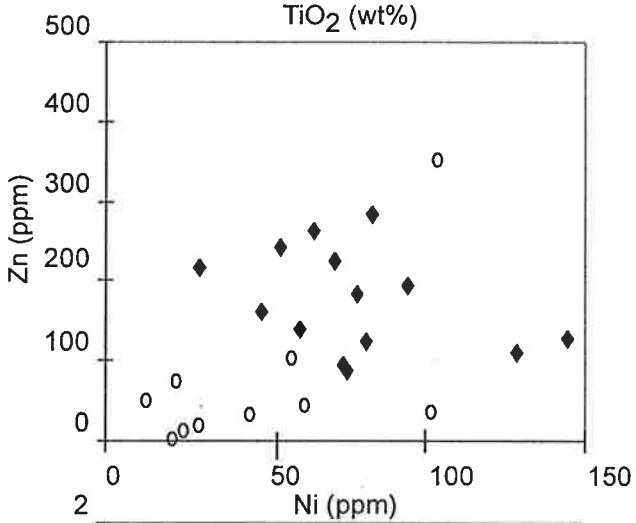

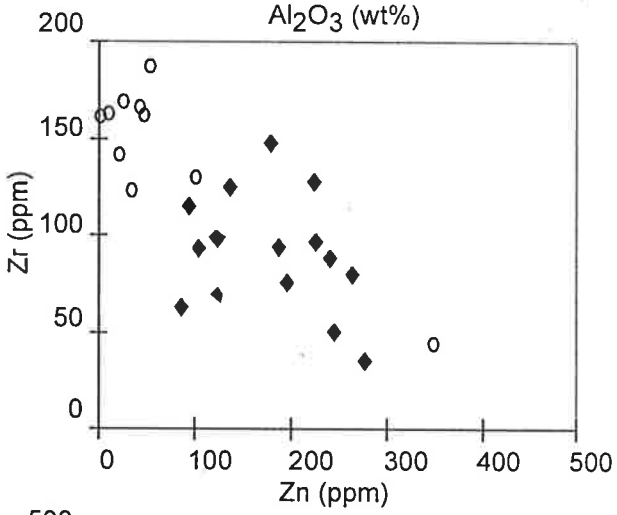

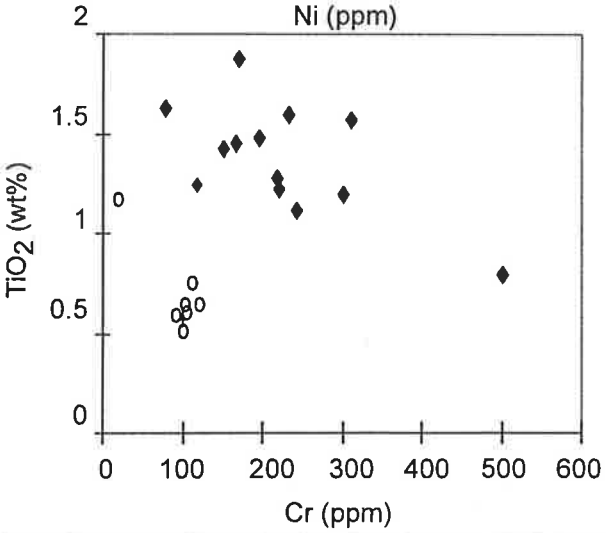

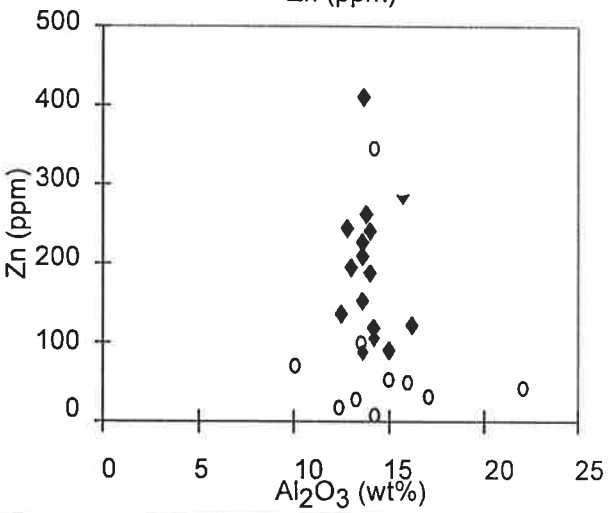

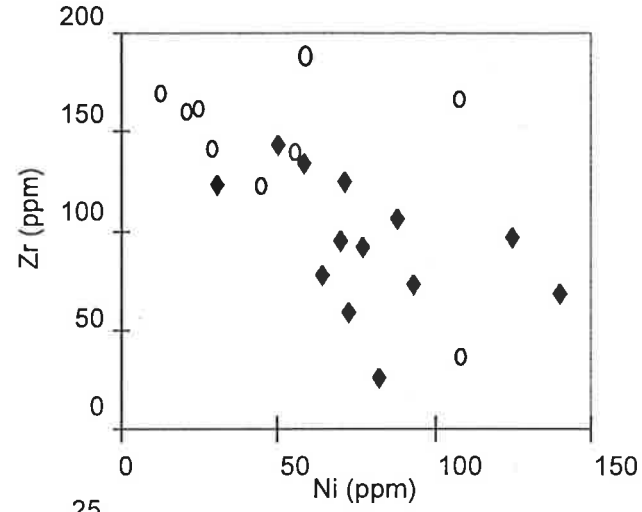
Zr (ppm)
Ni (ppm)
0
50
100
150
200

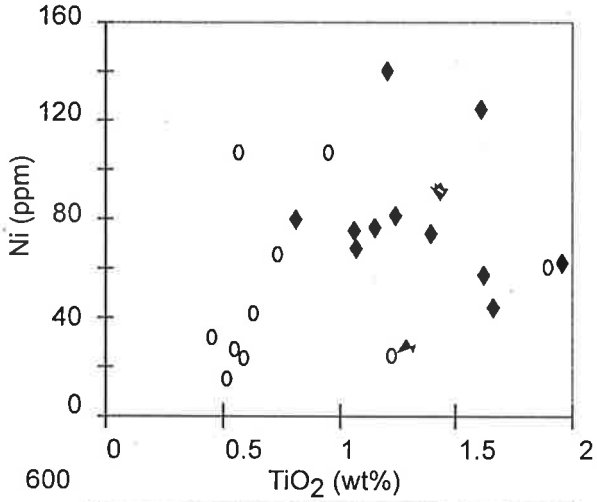
Ni (ppm)
TiO_2 (wt%)
0
40
80
120
160
0.5
1
1.5
2

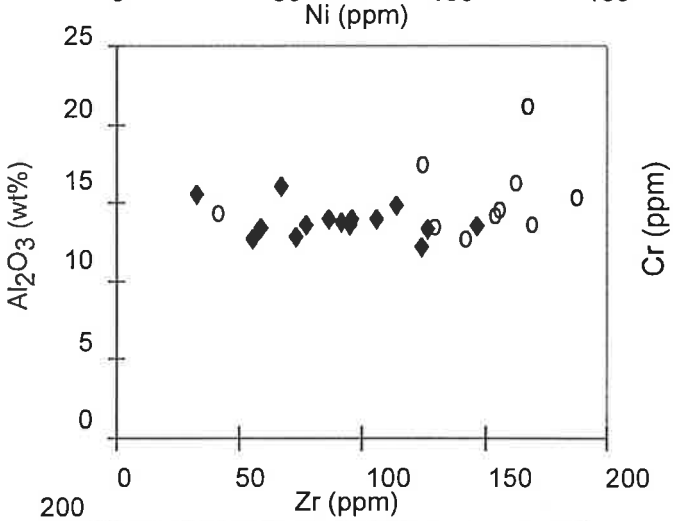
Al_2O_3 (wt%)
Zr (ppm)
0
5
10
15
20
25
50
100
150
200

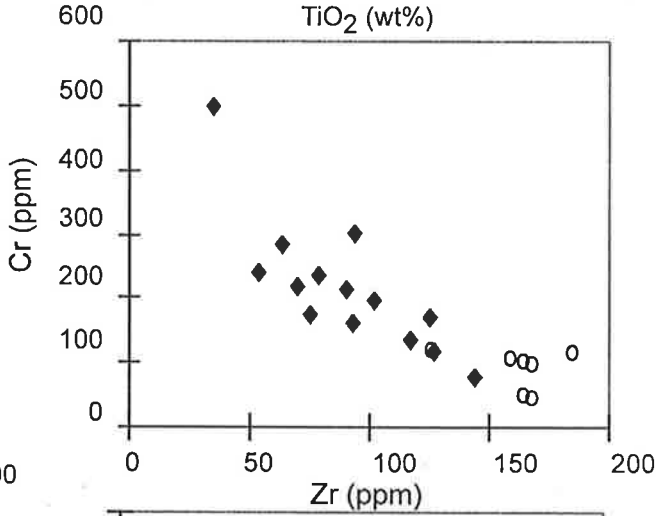
Cr (ppm)
Zr (ppm)
0
100
200
300
400
500
600
50
150

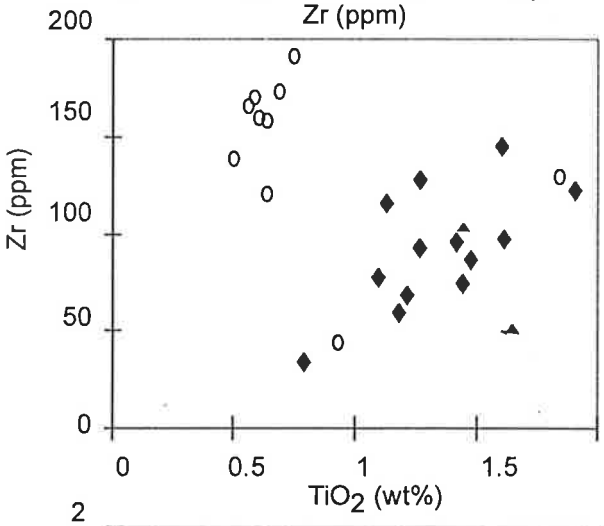
Zr (ppm)
TiO_2 (wt%)
0
50
100
150
200
0.5
1
1.5

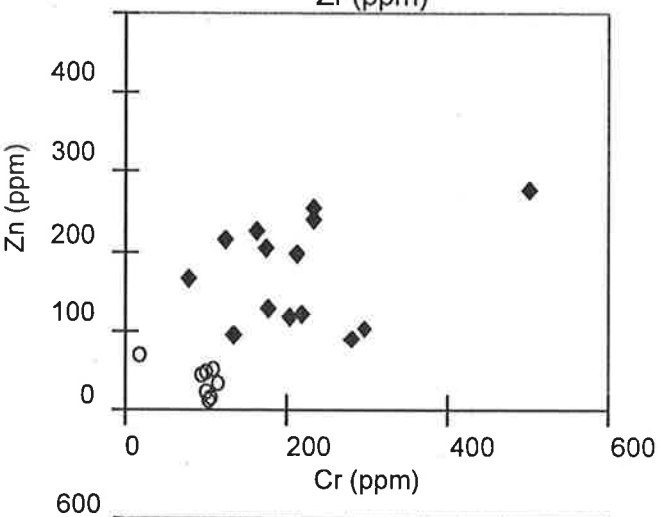
Zn (ppm)
Cr (ppm)
0
100
200
300
400
600

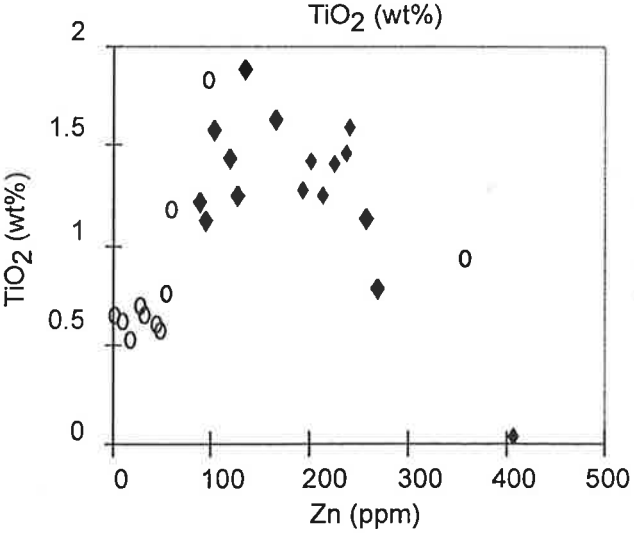
TiO_2 (wt%)
Zn (ppm)
0
0.5
1
1.5
2
100
200
300
400
500

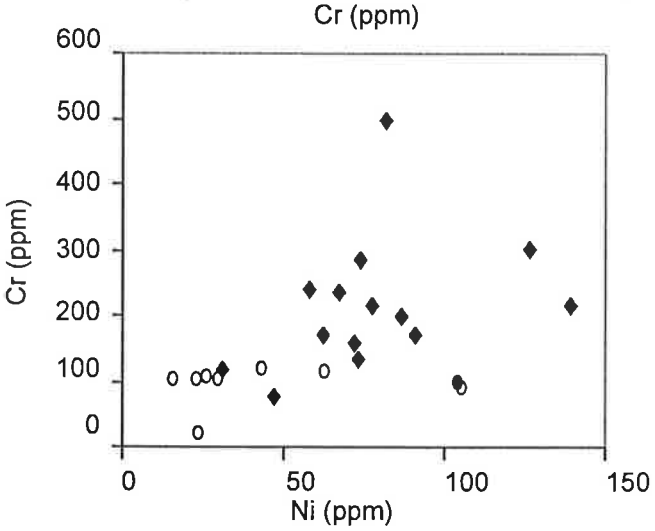
Cr (ppm)
Ni (ppm)
0
100
200
300
400
500
600
50
150

A 6.3.2. (continued).

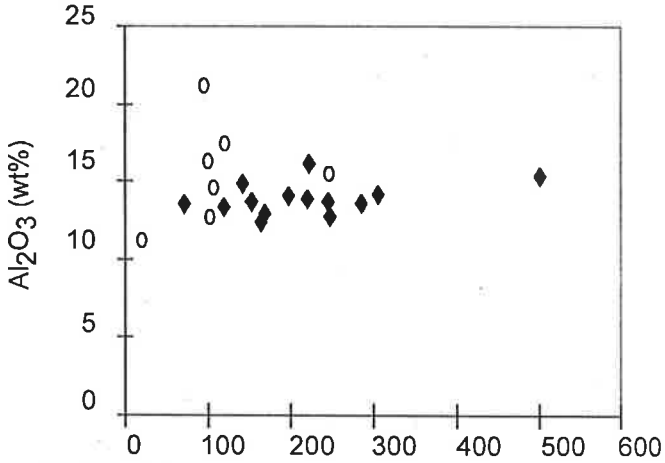

A 6.3.3. Bivariate plots of metapelitic rocks from the Yambah Schist Zone.

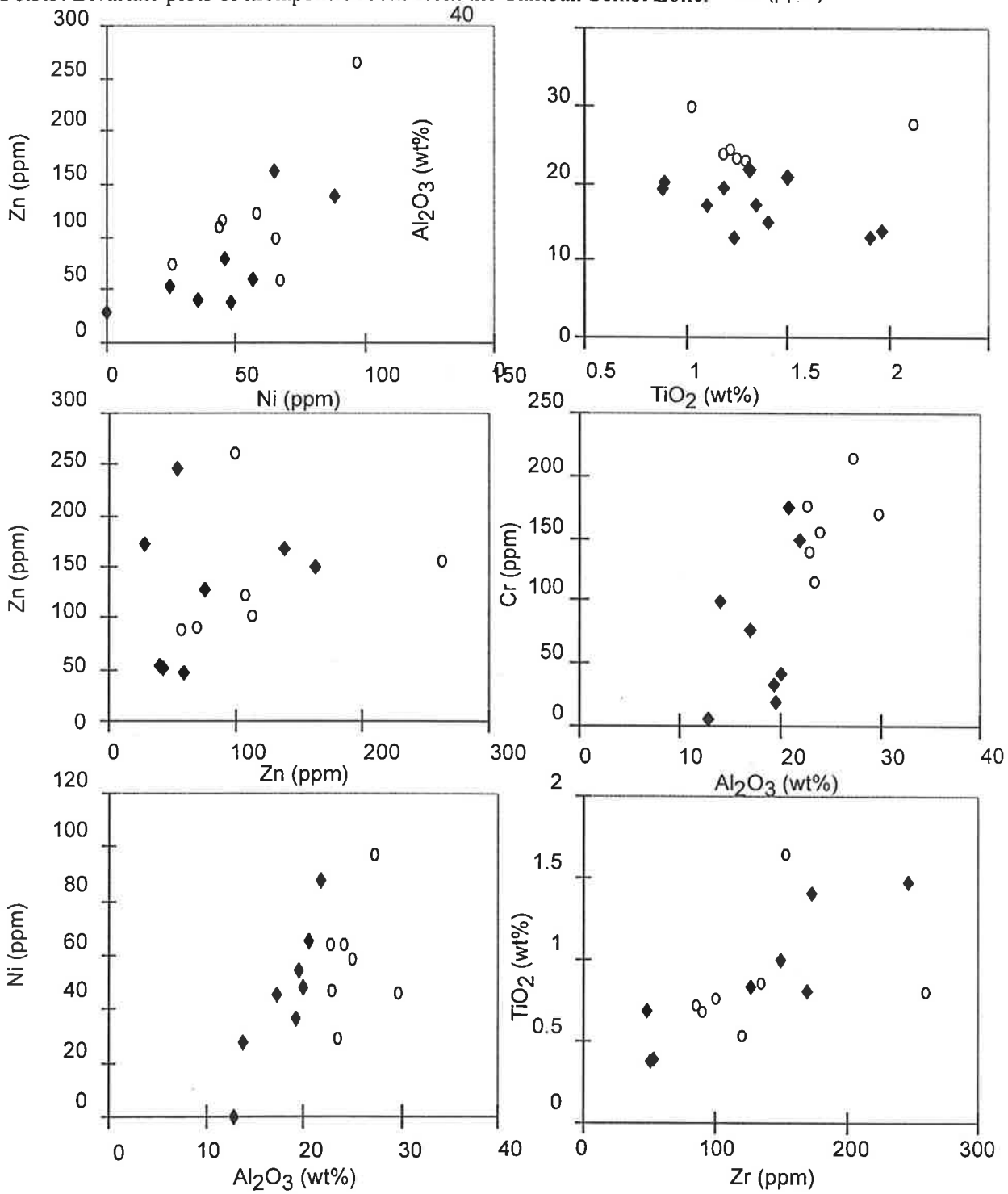

A 6.3.3. (continued).

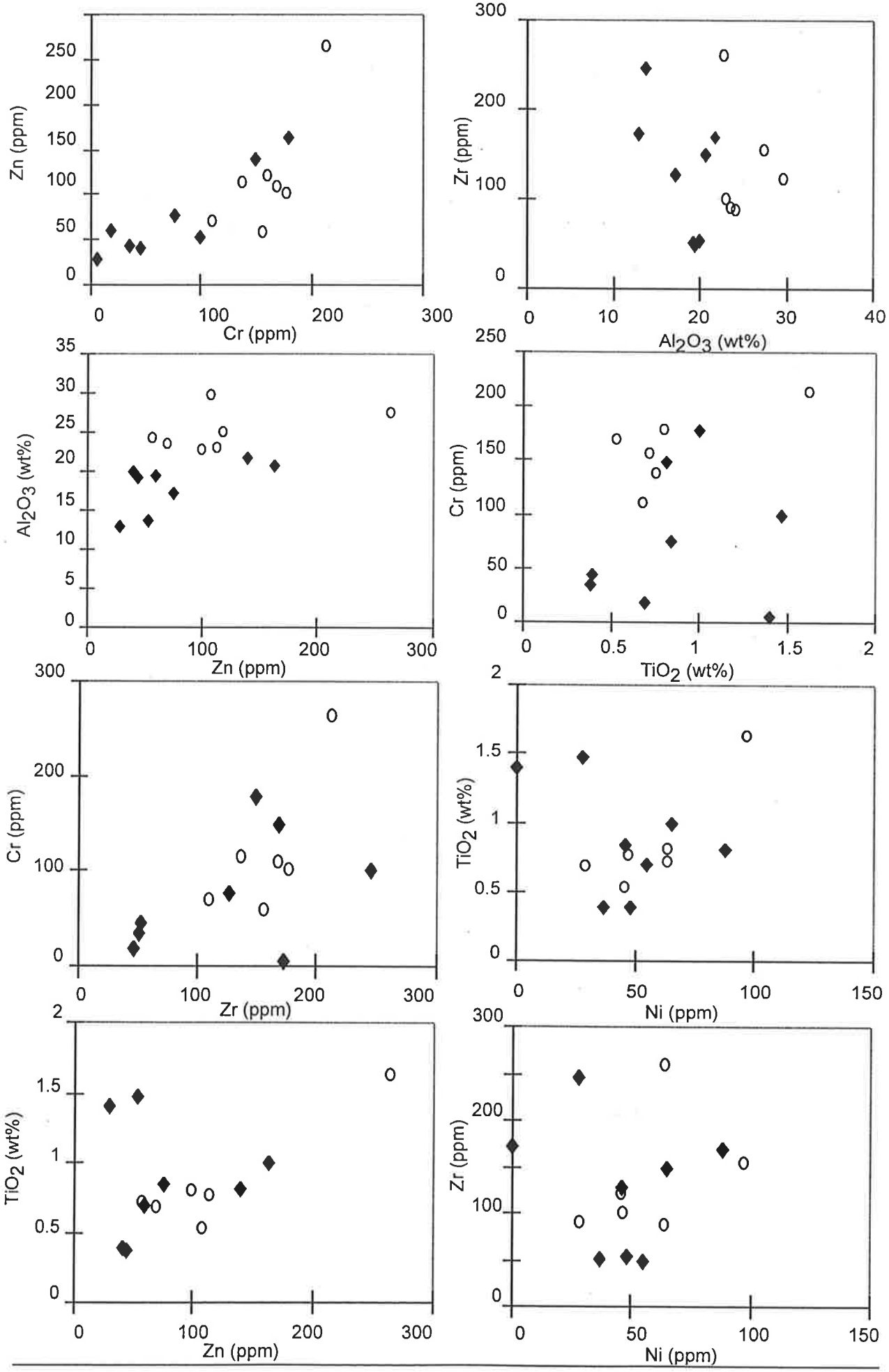

A 6.3.3. (continued).

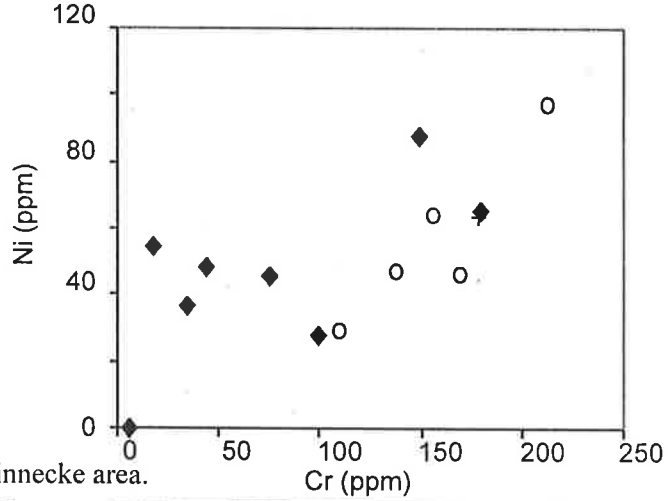

A 6.3.4. Bivariate plots of mafic rocks from the Winnecke area.

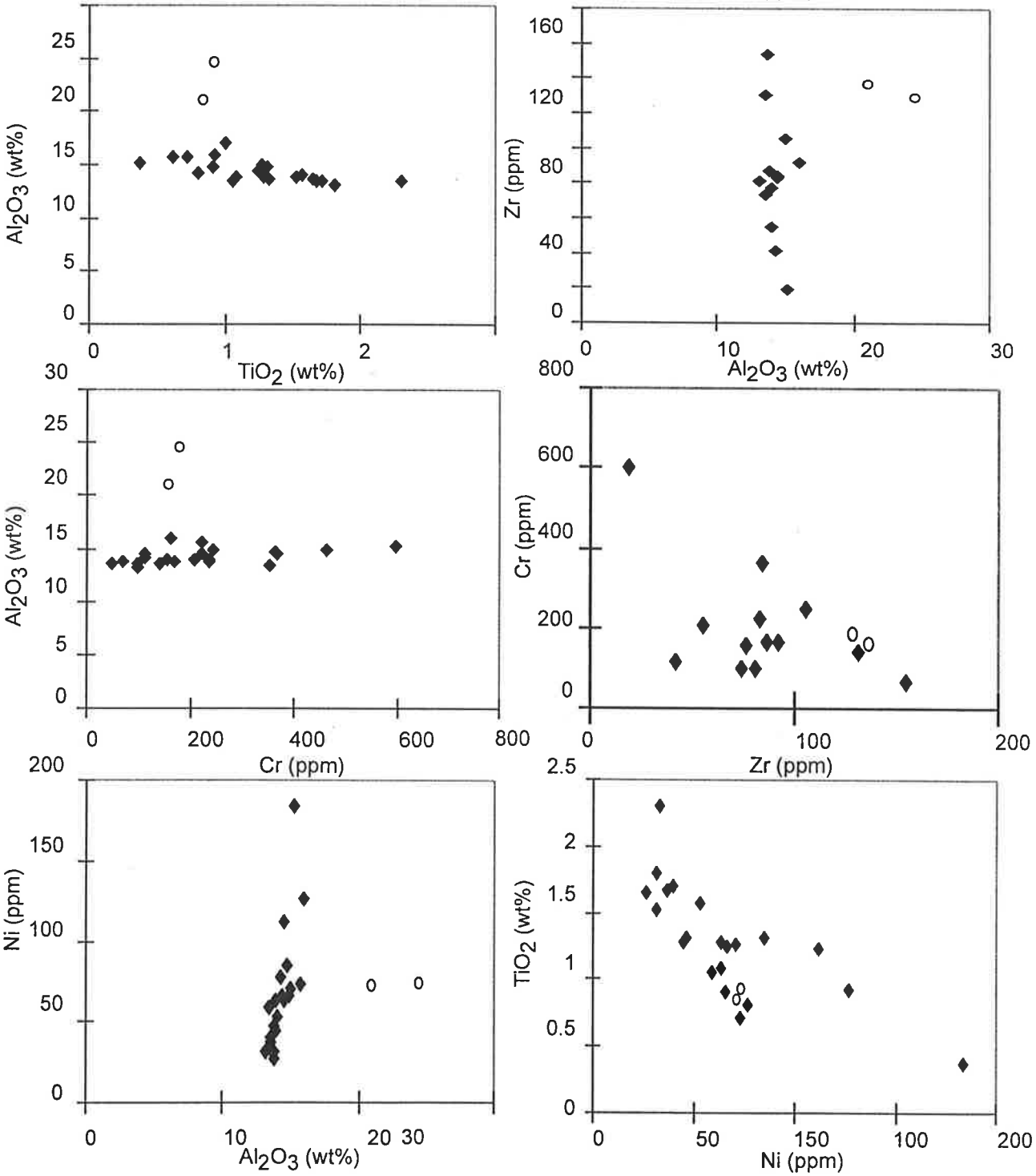

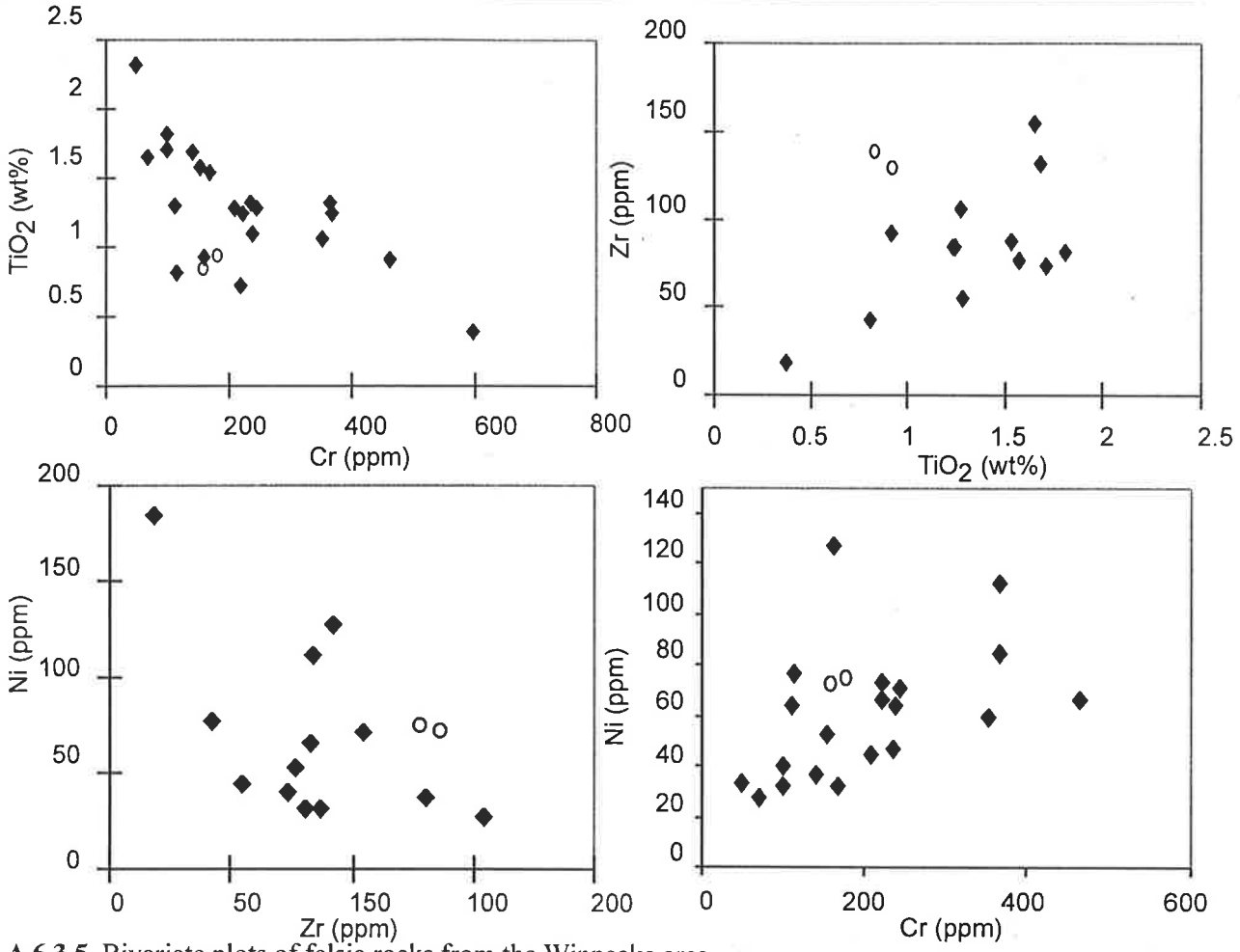

A 6.3.5. Bivariate plots of felsic rocks from the Winnecke area.

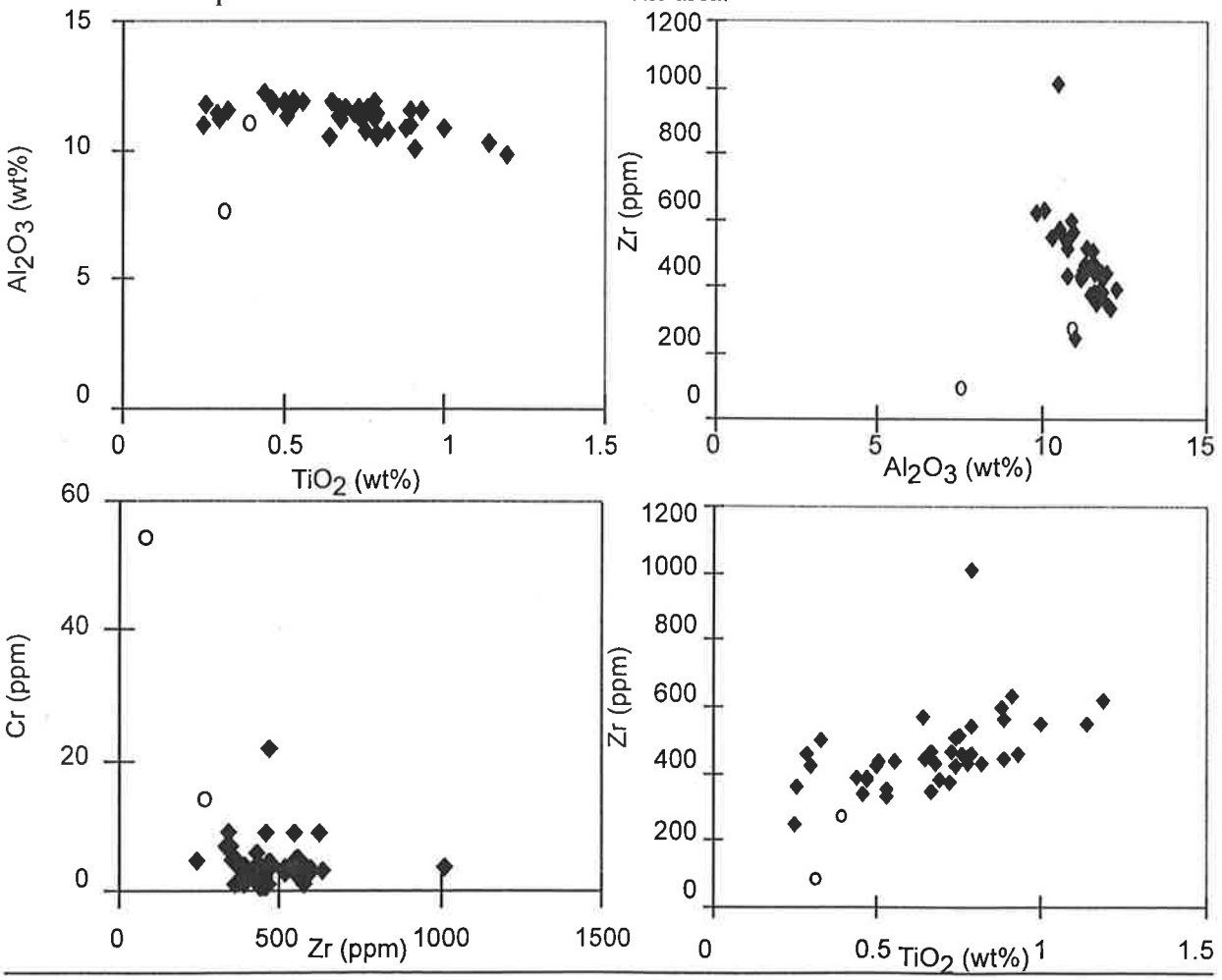

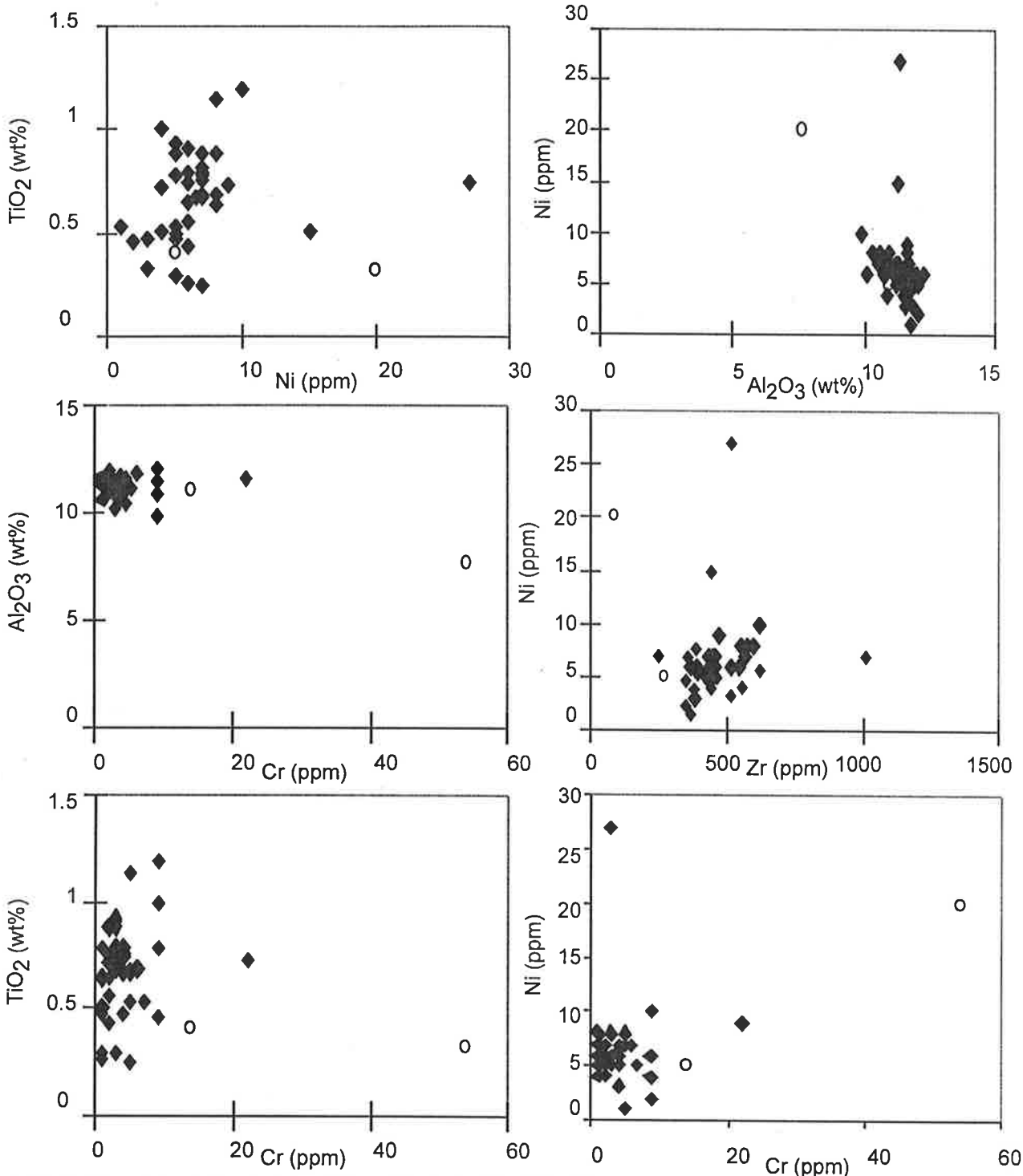

A 6.3.6. Bivariate plots of metapelitic rocks from the Winnecke area.

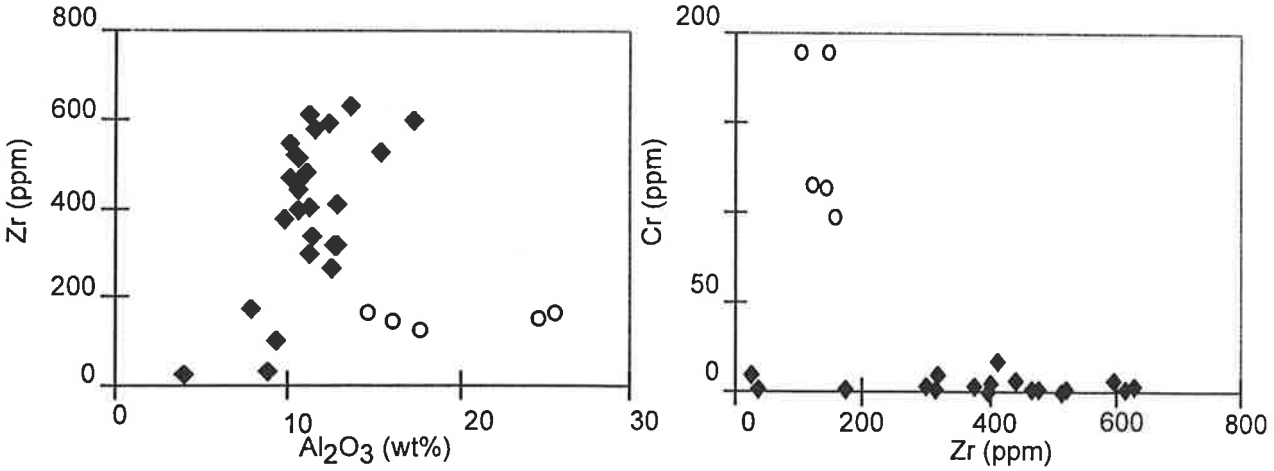

A 6.3.6. (continued).